Magnetic resonance imaging for glioma molecular classification

Dr Stefanie Catherine Thust
FRCR FHEA MD

Student registration number: 100465829

A thesis submitted for the degree of PhD by Publication

School of Medicine,
University of East Anglia,
Norwich, England
November 2024

Declaration

I, Stefanie Thust, confirm that this thesis represents my own work and that I have not previously submitted the contents for a degree at the University of East Anglia or any other university.

Critical analysis word count: 15863

Total word count including publications: ~88382

Abstract

This doctoral thesis discusses a programme of magnetic resonance imaging (MRI) research for predicting molecular characteristics in glioma, a malignant brain tumour, carried out over 8 years.

In 2016, a new classification system mandated the integration of genetics into glioma tissue diagnosis. My research is centred around identifying imaging biomarkers of group specific tumour mutations.

Chapter 1 summarises a pan European survey to investigate conventional and advanced glioma imaging practices in clinical application. Based on responses from 220 hospital institutions, anatomical and diffusion-weighted imaging were judged to be essential, subsequently formulated as consensus guidance. A second survey on advanced MRI practices corroborated the findings.

Chapter 2 reports on research to identify anatomical MRI features associated with glioma molecular characteristics. Candidate morphologies were shaped by testing recently published visual criteria in a pilot study, and by a literature search. Some features, including diffusion, showed limited reproducibility by qualitative inspection.

Chapter 3 discusses apparent diffusion coefficient (ADC) measurements to distinguish early aggressive cancer stages from slower growing gliomas. The accuracy of ADC results differed by tumour contrast enhancement pattern. The performance and interobserver agreement were tested for different ADC parameters.

Chapter 4 describes research into stratifying visual features by reproducibility and combining these with ADC values and age to achieve a prediction of glioma genetic status. An accurate logistic regression model was established and validated in a new glioma MRI data set.

Chapter 5 details the investigation of histogram methods, including a new software (TexRAD), for genotyping of gliomas. No superior diagnostic yield was identified from histogram analysis compared to regional diffusion measurements. Using TexRAD software did not outperform logistic regression in single MRI sequence assessment.

Chapter 6 discusses ongoing research developments and relates the thesis to recently published data on glioma imaging.

Table of contents

List of illustrations

Figure 14. Volume and region of interest examples in non-contrast enhancing glioma.

Figure 15. Boxplots of volumetric and regional ADC measurements in non-contrast enhancing glioma.

Figure 16. Multireader studies of ADC metrics for IDH genotyping – flow diagram of case selection.

Figure 17. Minimum ADC, mean ADC and ADC in normal white matter region of interest placements.

Figure 18. ITK-SNAP volumetric T2-weighted segmentation mask and ADC map overlay.

Figure 19. Boxplots of regional ADC_{mean} values for the WHO 2016 glioma subtypes.

Figure 20. Boxplots of regional ADC_{min} values for the WHO 2016 glioma subtypes.

Figure 21. ROC curves comparison for the prediction of IDH genotype.

Figure 22. Examples of typical WHO grade 2-3 glioma MRI morphologies.

Figure 23. Univariable and multivariable logistic regression analysis to predict IDH status.

Figure 24. Imaging examples of H3 K27M histone-altered diffuse midline glioma.

Figure 25. ADC histograms in H3 K27M histone-altered diffuse midline glioma.

Figure 26. TexRAD freehand segmentation examples in glioma.

Figure 27. Alternative segmentation techniques for T1-weighted contrast enhanced images.

Figure 28. TexRAD filtration steps using scaled texture filters of different sizes.

List of tables

Table 14. WHO grades, IDH and 1p19q status of the glioma population analysed by TexRAD.

Table 15. TexRAD volumetric analysis of T1-weighted contrast enhanced imaging using Segmentation A (WHO grades 2-4) for IDH status prediction.

Table 16. TexRAD volumetric analysis of T1-weighted contrast enhanced imaging using Segmentation A (WHO grade 4).

Table 17. TexRAD volumetric analysis of T1-weighted contrast enhanced imaging using Segmentation B (WHO grades 2-4) for IDH status prediction.

Table 18. TexRAD volumetric analysis of T1-weighted contrast enhanced imaging using Segmentation C (WHO grades 2-4) for IDH status prediction.

Table 19. TexRAD volumetric analysis of T1-weighted contrast enhanced imaging for 1p19q status prediction in IDH^{mut} gliomas.

Table 20. TexRAD volumetric analysis of ADC maps (any enhancement pattern WHO grades 2-4).

Table 21. TexRAD volumetric analysis of ADC maps (solid gliomas, WHO grades 2-4).

Table 22. TexRAD volumetric analysis of ADC maps (non-enhancing gliomas, WHO grades 2-4).

Table 23. Multivariable regression analysis of the best performing TexRad parameters.

Dedication

In loving memory of my mum.

Acknowledgements

Much of the research discussed in this thesis represents my own work. My contributions to individual publications are detailed in Appendix 1.

However, there are others who had important roles in the studies. Amongst my colleagues at the National Hospital for Neurology and Neurosurgery, I particularly thank Professor Sebastian Brandner, Head of the Neuropathology Division, for the support with tissue molecular data.

Dr. Massimo Benenati performed over 250 glioma segmentations during a training fellowship. My students Dr. John Maynard and Dr. Martin Lewis excelled at working with new data in support of molecular predictions. Dr. Sachi Okuchi and Dr. Arian Lasocki were visiting international collaborators on the systematic reviews, and Sachi contributed to interobserver testing. Thank you to everyone involved in the work.

Two physics colleagues deserve special mention: Dr. Laura Mancini supplied the Matlab and Stata analyses to quantify non-enhancing tumour diffusivity in my first study. She also delivered the mathematical justification for using ADC maps from multiple vendors. Dr. Stephen Wastling provided expert technical support, including for transcribing the predictive formula which I developed in Chapter 4.

Dr. Ofran Almossawi, a brilliant colleague with a PhD in statistics, went above and beyond to support my pursuit of a probability calculator. Ofran listened patiently to the idea and taught me how to explore this when success was uncertain.

I am thankful to Professor Rolf Jäger at Queen Square for guidance when I was not his PhD student, and to Professor Marion Smits at Erasmus MC Rotterdam for the resolute direction towards research. Thank you to Dr. Jeremy Rees for insights into the changing clinical management of gliomas. Professor Tarek Yousry and Professor Xavier Golay, academic department heads, have been great teachers. I owe both for funded research time.

Professor Andoni Toms and Dr. Gabriella Baio have been brilliant PhD supervisors and guides to critical discussion. The perspective is quite different to my MD thesis years ago, thanks so much for being by my side for this new task.

I am grateful to my current colleagues, particularly Professor Dorothee Auer, Director of the Nottingham NIHR BRC Magnetic Resonance and Precision Imaging group, for endorsing my UEA enrolment.

A big thanks is due to my family for encouraging my work. To Lily and Ori, you will always be what I am most proud of!

And especially, my thought of thank you goes to the patients involved in research – they are most important in this. I hope that my studies and clinical work can make a positive difference to lives.

Introduction

Definition

Glioma is the most common primary brain malignancy in adults. Gliomas originate from neural stem and glial progenitor cells, which evolve through a hierarchy of molecular aberrations into neoplasia (1). The prognosis differs by glioma type, but the vast majority eventually recur irrespective of therapeutic interventions. Gliomas can spread diffusely and quickly, particularly along white matter tracts with ability to induce synaptic connectivity to healthy neurons (2). This makes it difficult, if not impossible, to achieve a surgical cure. Glioblastoma represents the most frequent and rapidly fatal form of the disease.

Epidemiology

Approximately 12,000 new brain tumours are diagnosed in the UK each year (3). For glioblastoma, this corresponds to an incidence of approximately 6 in 100.000, slightly greater for men (4). Despite global research efforts, the prognosis for glioblastoma shows little improvement over time with a mean survival of 12-18 months. For other diffuse gliomas, survival variably exceeds 5 years with the best prognosis for oligodendrogliomas due to greater chemosensitivity (5). Brain tumours in general, including gliomas, are overall more common towards older age but represent a leading cause of young adult (< 40 years) and childhood cancer deaths.

Histological grading

For several decades, gliomas have been classed according to light microscopy features. By describing cell morphology, tumours were divided into presumed astrocytic or oligodendroglial cell lineage. Additionally, gliomas were assigned a World Health Organisation (WHO) grade from 2-4 based on cell density, microvascular proliferation and evidence of vascular invasion. Glioblastoma lies at the most aggressive end of this spectrum with a WHO grade 4. This system of pathology reporting remained in place for multiple iterations of the WHO classification until 2015 (6). Imperfections of visual grading arise from qualitative elements of inspection, giving rise to interobserver and

intraobserver variability (7). Furthermore, a single time point neuropathologist assessment is not necessarily predictive of future glioma evolution. It has long been recognised that some 'low grade' gliomas grow gradually whereas others progress rapidly, an observation that has been termed 'malignant transformation' (8).

WHO Classification of Central Nervous System Tumors 2016

Consensus recommendations from an International Society of Neuropathology (ISN) meeting held in Haarlem, the Netherlands culminated in a fundamentally different strategy for brain tumour tissue diagnosis (9). For gliomas, this built on the landmark discovery that genetic mutations determine the prognosis, in some cases more than WHO grade (10). This became reflected in the subsequent WHO Classification of Central Nervous System Tumors 2016 (hereforth WHO 2016), which newly mandated an integrated glioma diagnosis based on tumour genetics and microscopy (11). Here, the status of the isocitrate dehydrogenase (IDH) gene appeared particularly relevant to prognosis.

WHO 2016 listed three genetic groups of diffuse glioma: The first group is defined by lack of an IDH mutation (IDH^{wt}), which in many cases corresponds to microscopy findings of WHO grade 4 glioblastoma. Beyond this, glioblastoma is associated with other group-specific genetic mutations such as combined chromosome 7 gain and chromosome 10 loss, epidermal growth factor receptor (EGFR) amplification, and/or telomerase reverse transcriptase (TERT) promoter mutations (12). IDH^{wt} astrocytomas WHO grade 2-3 were adopted into the same genetic group where fulfilling molecular criteria, and these are characterised by a similarly poor prognosis (13,14).

The second group represents astrocytomas with an IDH mutation and intact short arm of chromosome 1 and long arm of chromosome 19 ($IDH^{mut/1p19int}$). The third group are oligodendrogliomas with a combined 1p19q codeletion ($IDH^{mut/1p19del}$). By this, a genetic basis for glioma grouping was established for the first time. In WHO 2016, the spectrum of diffuse gliomas spans the microscopic WHO grades 2-4. Certain WHO grade 1 tumours (e.g. pilocytic astrocytoma) became newly separated by the nomenclature 'circumscript glioma' based on different genetics (15) and are not a subject of this thesis.

Treatment

Prior to WHO 2016, presumed low grade gliomas (LGG, inconsistently represented in the literature as WHO grade 2 and less often as grade 2-3) were often managed with a 'watch and wait' approach (16). Initial observational periods are still to some extent in practice today (17), consisting of tumour size monitoring with resection or debulking in case of progressive growth. Based on survival benefit (18), LGG are increasingly treated surgically whereby the importance of resection appears to vary by genotype (19). Radiotherapy and chemotherapy are typically reserved for gliomas, which have recurred or show aggressive histology features.

Glioblastoma is treated by maximum safe resection, followed by radiotherapy and Temozolomide chemotherapy (Stupp protocol (20)) with new treatment trials evolving alongside this. Based on recent multicentre studies, the importance of (supra)maximal glioblastoma resection has become clearer (21). Furthermore, it increasingly appears that an earlier diagnosis of glioblastoma in the low grade stage could benefit survival through more extensive surgery (22).

MRI before the molecular era

Due to the chronic nature of gliomas, imaging plays a key role in their long-term clinical care. At the time of diagnosis, MRI serves to delineate tumour extent, to estimate malignant potential and to guide considerations of surgical management. Disease extent is typically assessed on T2-weighted (T2w) and T2-fluid attenuated inversion recovery (FLAIR) sequences (**Figure 1**).

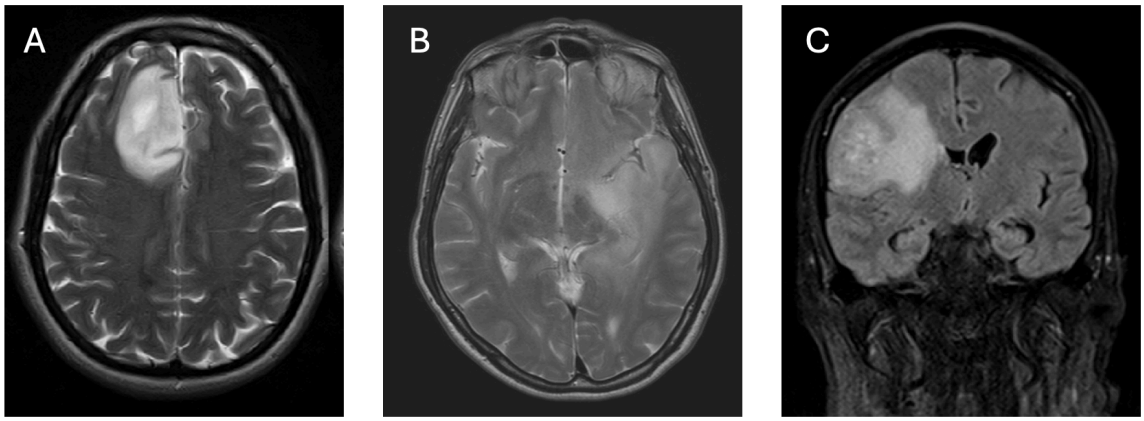

Figure 1. *Axial T2w (A, B) and coronal FLAIR (C) images showing examples of diffuse glioma.*

Many LGG lack gadolinium contrast enhancement on T1-weighted (T1w) MRI. On the contrary, the rapid proliferation of glioblastoma is associated with microscopic hypoxic-ischaemic events and neovascularisation (23), which results in a network of abnormal, friable new vessels and tissue breakdown. The typical imaging finding is of an avidly enhancing, partially necrotic mass. On the contrary, earlier IDH^{wt} glioma stages can appear LGG-like and may lack contrast uptake entirely (**Figure 2**).

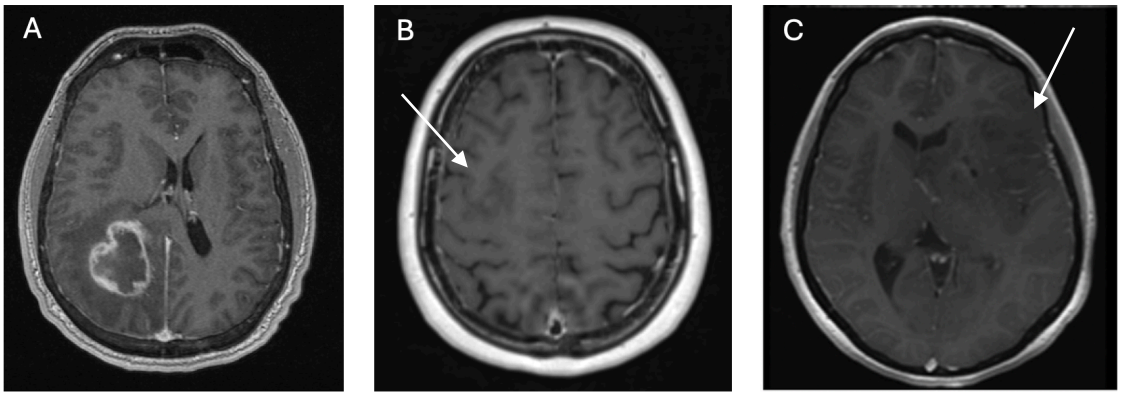

Figure 2. *Post gadolinium contrast T1w (T1CE) images demonstrating IDH^{wt} glioblastoma WHO grade 4 (A), IDH^{wt} astrocytoma WHO grade 3 (B) and IDH$^{mut/1p19del}$ oligodendroglioma WHO grade 2 (C).*

For many years, radiologist practice was limited to characterising gliomas according to contrast uptake. Gadolinium enhancement was considered the best MR imaging predictor of glioma histological grade and malignancy based on older studies (24,25). However, contrast uptake is not specific to glioblastoma and occurs in many tumours, and in other diseases with blood-brain-barrier breakdown.

Non-contrast-enhancing IDH^{wt} gliomas may rapidly progress with development of malignant features of glioblastoma (26,27). It could be argued that for a non-enhancing IDH^{wt} astrocytoma WHO grade 2, a radiologist description as 'low-grade' would be partially correct. However, the benignity inferred by this term is problematic, if no further action follows.

Diffusion-weighted MRI

In diffusion-weighted imaging (DWI), magnetic gradients are applied to measure naturally occurring water movement in tissues. In the brain, this is commonly performed with a baseline gradient of b0, (sometimes b500) and b1000 s/mm^2 (28) to generate a

paired set of images: the DWI (b1000) sequence and the apparent diffusion coefficient (ADC) map. On the ADC map, the magnitude of diffusion is depicted as numerical values in each image voxel.

The application of DWI in cancer is based on the principle that free water movement becomes restricted in tumours compared to normal tissues (**Figure 3**), which are less tightly packed with cells. However, the association between cellularity and diffusion is not linear and varies for different neoplasms (29). Glioma research preceding WHO 2016 suggested that ADC values could be used as a biomarker of cellularity and histological grade (30). ADC mapping has shown reproducibility across different MRI machines, and between vendors (31). It offers quantitative information on tumours, which made it a technique of great interest for glioma research at the time of WHO 2016.

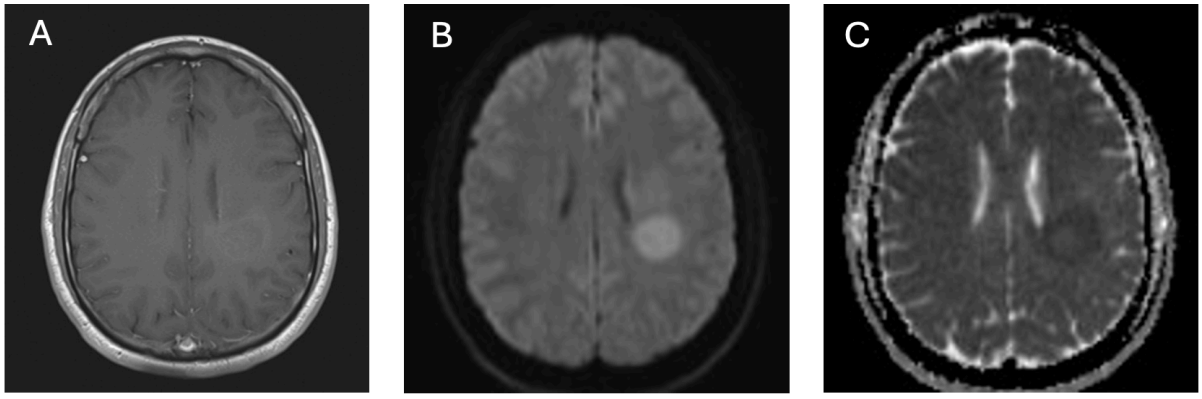

Figure 3*. Axial T1w contrast enhanced (T1CE) image (A), b1000 DWI (B) and ADC map (C) in a patient with suspected low-grade glioma. The tumour is barely contrast enhancing but exhibits high DWI signal with peripheral low ADC signal (partial 'diffusion restriction'). The tissue diagnosis was IDH^{wt} glioblastoma (microscopy WHO grade 4).*

Data availability for studies

The dataset described in this thesis evolved during the timeframe of the research. For all but one of the studies, cases were sourced from the Department of Neuropathology, National Hospital for Neurology and Neurosurgery, Queen Square. All gliomas received the integrated WHO 2016 diagnosis by latest molecular testing standards (32).

In each study, the maximum eligible sample of IDH^{wt} gliomas was studied, however the number of cases included varies by date and methods, such that the largest IDH^{wt} sample is featured in Chapter 4 (n=82). The comparison cohorts of IDH$^{mut/1p19int}$ and IDH$^{mut/1p19del}$ tumours were initially convenience samples (Chapter 2), followed by a partially

randomised sample (Chapter 3). Finally, the entire institutional IDH^{mut} cohort was screened against predefined inclusion and exclusion criteria (Chapter 3 and 4) amounting to the total available data (n=290, of which n=208 IDH^{mut}). The patient cohort in Chapter 5 (33) is derived from consecutive attendances for preoperative MRI with unconfirmed overlap to the remaining studies.

Chapter 1: Glioma imaging practices in Europe

1.0 Background

In response to WHO 2016, the European Society of Neuroradiologists' Diagnostic Committee established a brain tumour working group (ESNR-BTG). The ESNR-BTG convened a workshop on glioma imaging practices at the 38th ESNR Annual Meeting, Naples. This oversubscribed (150+ attendees), inconclusive discussion highlighted a lack of recommendations for glioma MRI in clinical application, particularly regarding physiological methods. To further investigate peer experiences and workflows, a pan-European peer survey was conducted under the auspices of the ESNR (34). This aimed to define current diagnostic neuroradiology practices, infrastructure strengths and hurdles with the application of MRI methods. Research trial guidance published by the United States National Brain Tumor Society (NBTS), Society for Neuro-oncology (SNO) and the European Organisation for Research and Treatment of Cancer (EORTC) (35) was taken into consideration. A second survey on quantitative MRI (qMRI) was conducted in 2019.

1.1 Research questions

- What are the European conventional and advanced imaging practices in glioma?
- Which MRI sequences are widely available to support glioma molecular diagnosis?

1.2 Methods

The ESNR-BTG survey in 2016 asked about MRI practices in glioma using anatomical and advanced (physiological) sequences. The qMRI survey in 2019 examined to what extent advanced MRI sequences are integrated in clinical work generally (not specific to oncology). The results are combined by MRI modality, as this was deemed most illustrative of specific working habits. Both surveys were anonymous without incentives.

1.2.1 ESNR-BTG survey

The ESNR-BTG online questionnaire consisted of a Google form designed with the open access toolbox (Google.com, Mountainview, CA, USA). The final version featured 87 items, divided into multiple choice, single best choice and free text questions on personal

practice, preferred techniques and clinical scenarios ((36), supplement). The survey probed sequence use, acquisition parameters, post-processing, and radiologist reporting. The questionnaire was tested and optimised with peer support, aiming at <10 minutes for completion to increase returns (37). Invitations were emailed to all ESNR members (n=1,662) and non-members linked to ESNR activities (n=6,400). The invitation was distributed via national neuroradiological societies (Netherlands, Belgium and the UK) and social media. To avoid duplicate response bias, participants were asked to list their institution or declare they were the sole respondent from their centre. Results were collated using descriptive statistics in Google Forms and Microsoft Excel.

1.2.2 qMRI survey

The European qMRI survey (38) consisted of 13 topic questions to be answered as free text, or as a combination of multiple, dichotomous, and single-choice answers, published in Google Forms as detailed above. Country of work and employer category (e.g. academic hospital) were mandatory, however institution details were omitted to ensure confidentiality. The results were screened for probable redundancies in the form of duplicate answers. The qMRI questionnaire was disseminated in English, German, Italian, Spanish, French, Turkish, Russian, and Portuguese (emailed to 27 European countries and Russia, Turkey, and Israel) (38). Analyses were performed in Microsoft Excel.

1.3 Results

1.3.1 ESNR-BTG survey

The survey received 227 replies, of which 7 were excluded as duplicates. Professionals from 220 different hospital institutions across 31 European countries completed the glioma imaging survey. A proportion (8.2%) of questionnaires submitted from neuroradiology practice outside Europe were included in the analysis. The demographic and institutional results are displayed in **Table 1**. **Figure 4** provides an overview of the responses by country.

Participant affiliation						
Institution type			Position held			
University hospital	General hospital	Oncology centre	Neuroradiologist	General radiologist	Resident	Other profession
58.7 (129)	37.9 (83)	14.6 (32)	80 (176)	9.5 (21)	5.9 (13)	4.5 (10)
Available services			Physicist support			
Neurosurgery	Radiotherapy	Neuro-oncology	None	General physicist		Neurophysicist
84.5 (186)	81.4 (179)	76.4 (168)	39.5 (87)	35.5 (78)		23.6 (52)

***Table 1**. Responses listing institution details, professions and physics support. Results are shown as % of answers (absolute number of answers).*

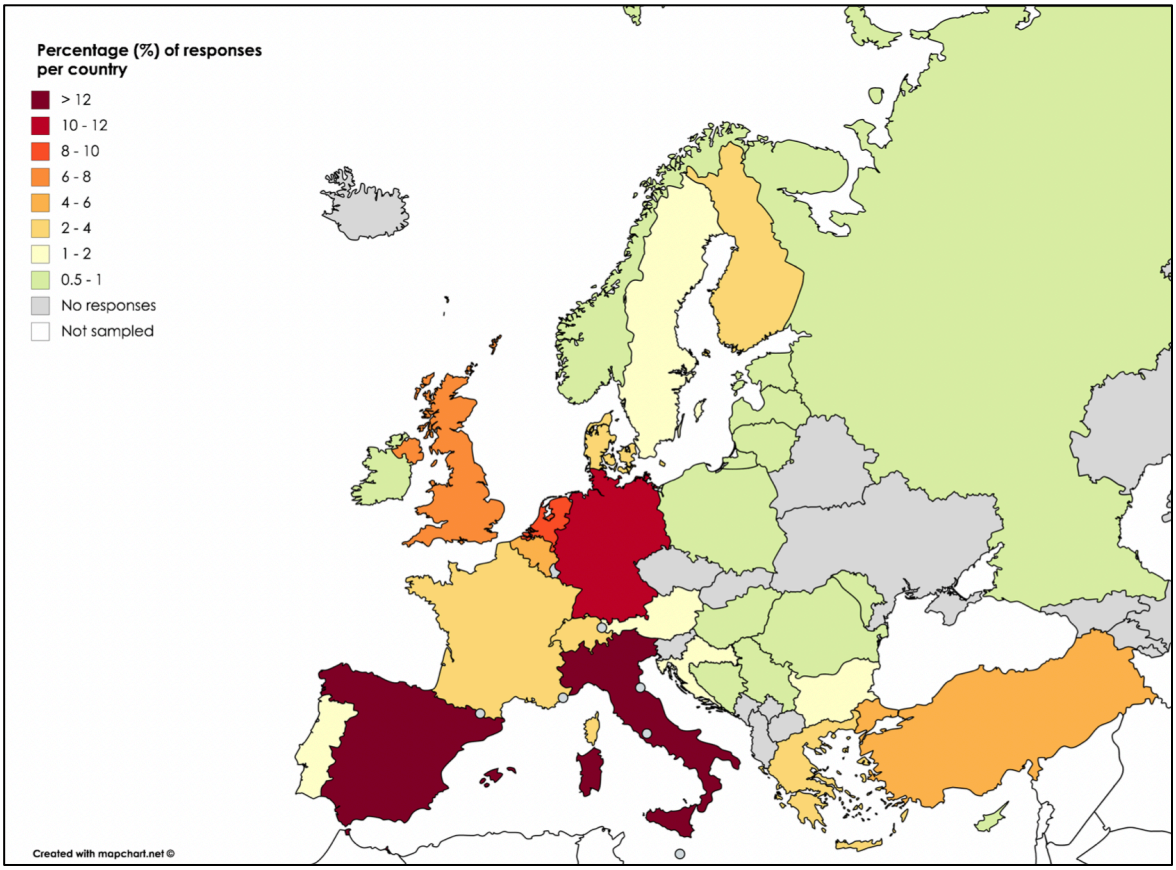

***Figure 4**. Institutional responses by country. Countries with no responses are shaded grey.*

1.3.1.1 Anatomical MRI practices

Most respondents had frequent exposure to glioma MRI reporting (**Table 2**).

Anatomical MRI					
Glioma primary diagnosis			Glioma follow up		
<1 study*	1-5 studies	>5 studies	<5 studies	5-10 studies	>10 studies
16.4 (36)	54.1 (119)	28.6 (63)	26.4 (58)	34.5 (76)	37.3 (82)

Table 2. *Glioma MRI workload in European clinical practice. Results are shown as % of answers (absolute number of answers). *Numbers of glioma MRI reports per week.*

The results for glioma primary diagnosis using MRI demonstrated a congruent application of most anatomical sequences (**Table 3**). A combination of post contrast 2D and 3D T1w imaging (T1CE) was performed, of which fast spoiled gradient echo was the most common (72.3 %) 3D method. Most (77.7 %) institutions used the same protocol for glioma follow-up as for primary diagnosis. A minority of radiologists (17.2.%) performed tumour size measurements as part of glioma follow up, for example post resection.

Anatomical MRI sequences routinely acquired in glioma					
T2w	FLAIR	T1w	T1CE	DWI/ADC	T2* or SWI
95.5 (210)	98.6 (217)	99.1 (218)	99.1 (218)	99.1 (218)	65 (143)

Table 3. *Anatomical MRI practices in Europe. Results are shown as % of answers (absolute number of answers).*

1.3.1.2 Diffusion-weighted MRI (DWI)

Virtually all (99.1%) European centres routinely performed 3-directional diffusion-weighted MRI in glioma. ADC maps were mostly (78.2%) assessed by visual comparison with normal appearing brain, not quantitatively (**Table 4**). In the qMRI survey, 82% of participants used DWI, however measurement practices were not questioned. Advanced diffusion methods (intravoxel incoherent motion imaging (IVIM) and diffusion kurtosis imaging (DKI)) were used by a minority (11.8%, and 3.3%). There were no reports of advanced (beyond 3-directional DWI/ADC with standard b values) diffusion methods for glioma characterisation by histological or molecular grading in either survey.

Diffusion-weighted MRI		
Assessment of ADC map		
Visual only	ROI measurement	Advanced analysis
78.2 (172)	17.7 (39)	3.2 (7)

Table 4*. ENSR-BTG Respondent's practices for apparent diffusion coefficient (ADC) assessment. Results are shown as % of answers (absolute number of answers). ROI=region of interest.*

1.3.1.3 Perfusion

Most institutions (85%) had some experience of perfusion MRI. In the majority this was dynamic susceptibility contrast (DSC) for initial grading and/or glioma follow-up. Free text answers reported usefulness of pMRI in grading (n=36) with no explicit reference made to tumour genetics (**Table 5**). Similarly, in the qMRI survey the predominating method was DSC (72.3% in glioma).

Perfusion MRI (pMRI)						
When do you acquire pMRI?						
Always in glioma		Primary diagnosis only		Follow up only		Upon indication
49.1 (108)		10.9 (24)		3.6 (8)		21.4 (47)
Reasons for using pMRI				pMRI sequence duration		
For clinical diagnosis	Biopsy guidance	To guide therapy	Mainly research	<5 mins	<2 mins	Don't know
79.7 (149)	46 (86)	61.5 (115)	13.4 (25)	83.5 (71)	45 (38)	5 (4)
Reasons for always acquiring pMRI in glioma						
I want it to be available when I need it						43.6 (61)
I (almost) always find it useful						55.7 (78)
It impacts patient care and management						56.4 (79)
Clinicians always want it						7.9 (11)
I acquire it for logistical reasons (e.g. standardised protocols)						30 (42)
For research purposes						24.3 (34)
To maintain radiographers' level of experience						15.7 (22)

Table 5*. Clinical, logistic and personal reasons for using pMRI in glioma. ESNR-BTG results are shown as % of answers (total number of answers).*

Many reporters (43.5%) evaluated perfusion MRI by visual inspection, e.g. of relative cerebral blood volume (rCBV) maps (**Figure 5**). Substantial variability (**Table 6**) in the choice of pMRI sequences, preload application, and analysis methods was evident.

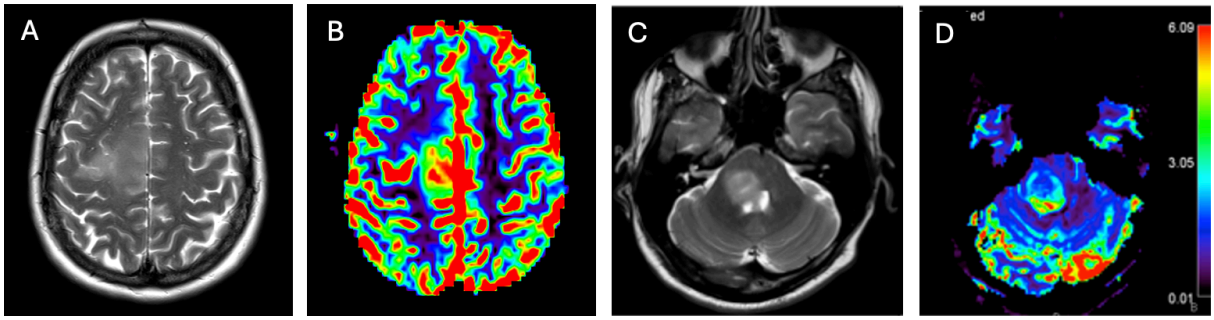

***Figure 5**. Axial T2w and DSC perfusion imaging in two different patients with a cerebral diffuse glioma (A, B) and brainstem glioma (C, D). Adapted from own material, also featured in (39).*

Perfusion MRI continued									
Sequence choice					Preload bolus				
DSC	DCE	ASL	>1 method		Yes	No	Don't know		
82 (153)	29.4 (55)	12.3 (23)	21.4 (40)		46.5 (87)	46 (86)	7.5 (14)		
Preload bolus size*					Total contrast given*				
1/3	½	Full	DK**	Other	Single	1+1/3	1+1/2	Double	DK**
42.5 (37)	16.1 (14)	10.3 (9)	11.5 (10)	19.5 (17)	53.8 (99)	13 (24)	8.2 (15)	14.7 (27)	7.6 (14)
Analysis method					How do you assess glioma perfusion?				
Scanner software	NordicICE	Olea	Other		Qualitatively	ROI comparison NAWM	Other		
78.5 (146)	4.8 (9)	4.8 (9)	7 (13)		43.5 (81)	51.5 (95)	5.4 (10)		

***Table 6**. Perfusion acquisition and post processing methods choices. ESNR-BTG results are shown as % of answers (total number of answers). * Of a typical contrast dose. ** Don't know.*

1.3.1.4 Spectroscopy

Many (ESNR-BTG 80.4%, qMRI 54.8%) institutions reported use of MR spectroscopy (MRS) (**Figure 6**). However, this application was not typically applied for glioma *characterisation*. Instead, the largest group (35.2%) acquired MRS sporadically, predominantly for distinction of tumour from non-neoplastic mimics. MRS was not

routinely (n=21/220) performed for WHO grading. Zero participants reported using oncometabolite spectroscopy (40).

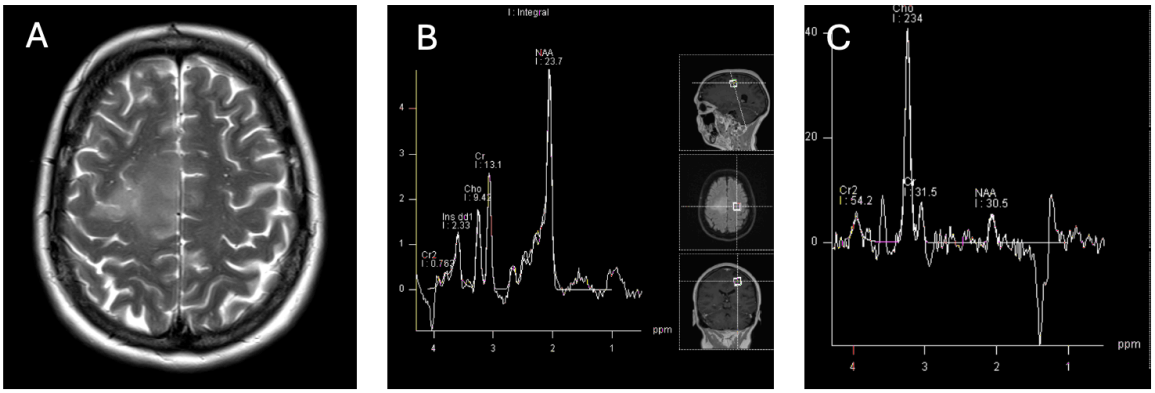

***Figure 6**. An example of MRS in glioma: Axial T2w image (A), normal tissue spectrum in contralateral brain (B) and tumour spectrum (C) characterised by increased Choline and loss of normal neuronal metabolism (N-acetylaspartate, NAA). Adapted from own material, also featured in (39).*

1.4 Discussion

1.4.1 Questionnaire topics

The number of items assessed, particular in the ESNR-BTG glioma survey, was large enough to capture a broad range of practices, technical and educational hurdles. However, we omitted to ask specifically about candidate imaging biomarkers for glioma molecular diagnosis. For example, the technical development of oncometabolite (D2-hydroxyglutarate, 2HG) MRS as a biomarker of IDH-mutant glioma predates WHO 2016 by several years (41). It may have been valuable to enquire about methods in development for genotyping and explicitly ask peer experience, where feasible within the planned questionnaire length. At the same time, the survey almost coincided with WHO 2016, meaning minimal peer experience existed with the new system.

A limitation of the qMRI survey is that this was not targeted at glioma specifically, partially because it followed the ESNR-BTG survey. This means the qMRI survey broadly confirmed the previous results for advanced MRI, but it delivered minimal new data to support glioma diagnosis.

1.4.2 What if more novel modalities had been explored?

A systematic review into an imaging application 'endogenous chemical exchange saturation transfer (CEST) MRI' (42) in glioma performed 3 years after the ESNR-BTG survey indicates that asking about novel methods may not have added clinically meaningful survey data: Of 25 studies on CEST use for untreated glioma characterisation, the majority (n=19) reported no molecular information. Several years after WHO 2016, the data supporting CEST MRI in glioma were limited by what could be termed 'classification lag' with diagnostic test accuracies based on the outdated WHO 2007 reference standard of histological grading only (6). Furthermore, these studies were subject to a high risk of bias with most (80%) lacking data on blinding to tissue results. It thus appears unlikely that probing experience with other novel MRI methods would have substantially altered the survey results on clinical practices.

1.4.3 Survey format

The survey design aimed to capture essential details but remain short enough to avoid omissions or partial entries that could be misinterpreted (43). Nevertheless, the list of 87 ESNR-BTG question items is long. The mix of multiple choice, single best choice and free text questions on personal practice was chosen in consensus. In retrospect, several refinements to the methods could be made: Piloting the entire survey with experts to appraise the content details, not only time taken, could be valuable (44). Randomising the sequence of questions would be ideal. It is unknown if the question wording reflected the topics of interest precisely enough (45), particularly for dynamic techniques, although the breadth of detailed answers suggests that they do. The persons responsible for question design may have favoured MRI modalities over others (e.g. neither lead author relies on spectroscopy), thereby adding unconscious bias to the questionnaire (46).

1.4.4 Number of responses

In both surveys, the number of participating institutions (n>200) was substantial, but the percentage returns were low (<15%). This means a high risk of non-response bias (47), nevertheless pursuing higher response rates may not necessarily improve the validity of results (48). Approaching persons, who are not ESNR members would have increased our

reach to non-specialist hospitals but likely encountered non-returns from those no longer working in neuroradiology. The completed responses are skewed towards specialist practice, and those with interest and experience in glioma imaging would have more enthusiastically responded (48). Disproportionate returns were received for certain countries, with a higher number of Spanish, Italian and German responses received. Given the similarity of anatomical MRI practices between countries, this appears acceptable, but it could have distorted data for rarer methods, or those with technical variability such as dynamic perfusion (49).

1.4.5 Real life transparency

The relatively consistent application of anatomical MRI sequences and DWI/ADC suggests that the survey results captured these sufficiently. However, for the more challenging methods responses could have been influenced by desirability (50), as respondents provided their institution details. Participants may have described what they perceived as best practice rather than daily life. Because the surveys received disproportionately greater responses from academic institutions, typical European clinical practice likely corresponds to the less advanced end of the MRI methods spectrum.

1.4.6 Impact

This research achieved an overview of the applications, strengths and limitations of glioma MRI methods in Europe preceding the new WHO 2016 reference standard. With this, it was possible to formulate international recommendations for clinical imaging. The ESNR consensus protocol (**Figure 7**), technical parameters in (35)) represents a core set of widely available MRI sequences. To mitigate between the aims of best practice and feasibility, 3 protocol alternatives were offered with perfusion made optional. Quantitative MRI assessments were identified as an unmet need, whereby neuroradiologists almost exclusively rely on subjective judgments. The combination of peer survey and imaging recommendations was adopted by other ESNR working groups thereafter (51).

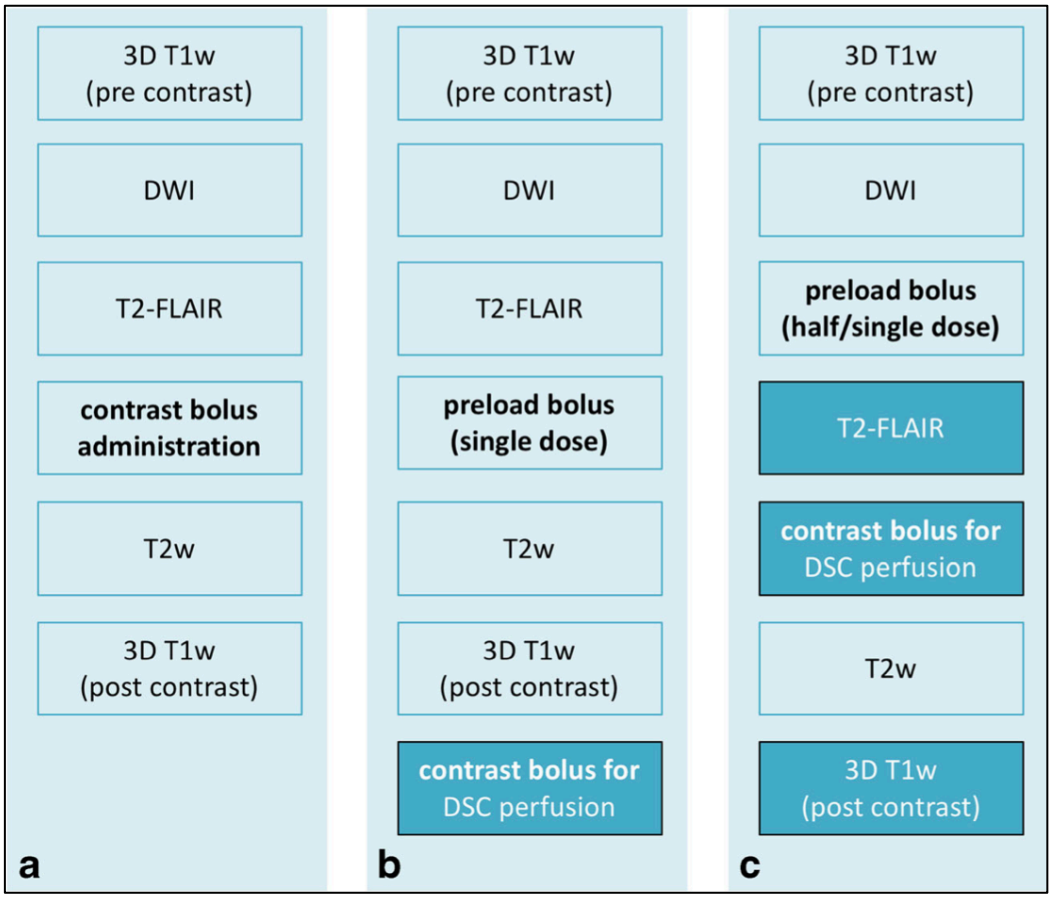

***Figure** 7. ESNR-BTG glioma MRI protocol for clinical practice (a), with the optional additional of perfusion imaging. Acquisition parameters are recommended as specified in EORTC-NBTS (35).*

1.5 Conclusion

Mapping the available infrastructure near the time of the WHO 2016 publication delivered the fundamental data for imaging studies into glioma molecular diagnosis (Chapter 2 onwards). Widely available MRI sequences became the next focus of research to investigate if these could support predictions of the new tissue reference standard inclusive of genetics.

Chapter 2: Morphology for glioma molecular diagnosis

2.1 Study background

Qualitative MRI reporting relies on subjective parameters and is variable. In 2013, a research group at Duke University developed a set of imaging descriptors with the aim to improve report standardisation for glioblastoma, focused on survival prediction (52). This resulted in the publication of the VASARI (Visually AcceSAble Rembrandt Images) feature set, which consists of a lexicon of 24 individual MRI features to describe tumour morphology. The VASARI system was developed via a multireader method, in which at least 3 radiologists each examined a total of n=82 glioblastoma MRIs from The Cancer Genome Atlas (TCGA) (53). The VASARI categories are listed in **Table 7** with image examples from the original user instructions (54) shown in **Figures 8-12**.

VASARI feature set for glioblastoma	
tumour location (f1)	definition of the non-enhancing margin (f13)
side of lesion centre (f2)	proportion of oedema (f14)
eloquent brain (f3)	haemorrhage (f16)
enhancement quality (f4)	diffusion characteristics (f17)
proportion enhancing (f5)	pial invasion (f18)
proportion nCET (f6)	ependymal extension (f19)
proportion necrosis (f7)	cortical involvement (f20)
cysts (f8)	deep white matter invasion (f21)
multifocal or multicentric (f9)	nCET crosses midline (f22)
T1/FLAIR ratio (f10)	CET crosses midline (f23)
thickness of enhancing margin (f11)	satellites (f24)
definition of the enhancing margin (f12)	Calvarial remodelling (f25)

Table 7. *The VASARI feature set as listed in (54). Note that the instructions do not include any category f15.*

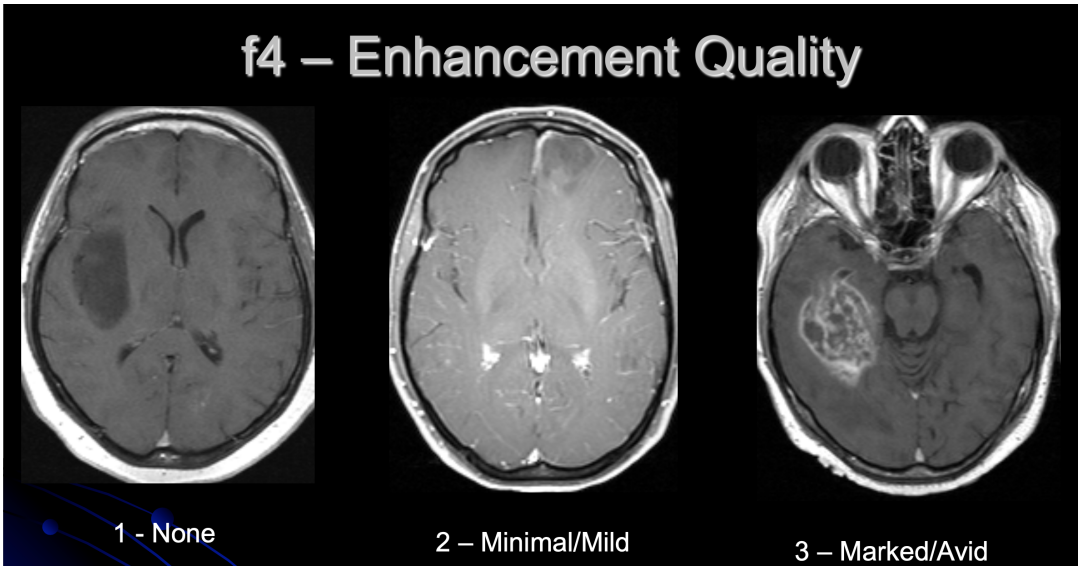

Figure 8**. VASARI user instructions (54) for f4: 'The degree of contrast enhancement should be defined as having all or portions of the tumor that demonstrate significantly higher signal on the postcontrast T1w images compared to pre-contrast T1w images.* ***Mild/ minimal *= when barely a discernible degree of enhancement is present relative to pre-contrast images.* ***Marked/avid*** *= obvious tissue enhancement.'*

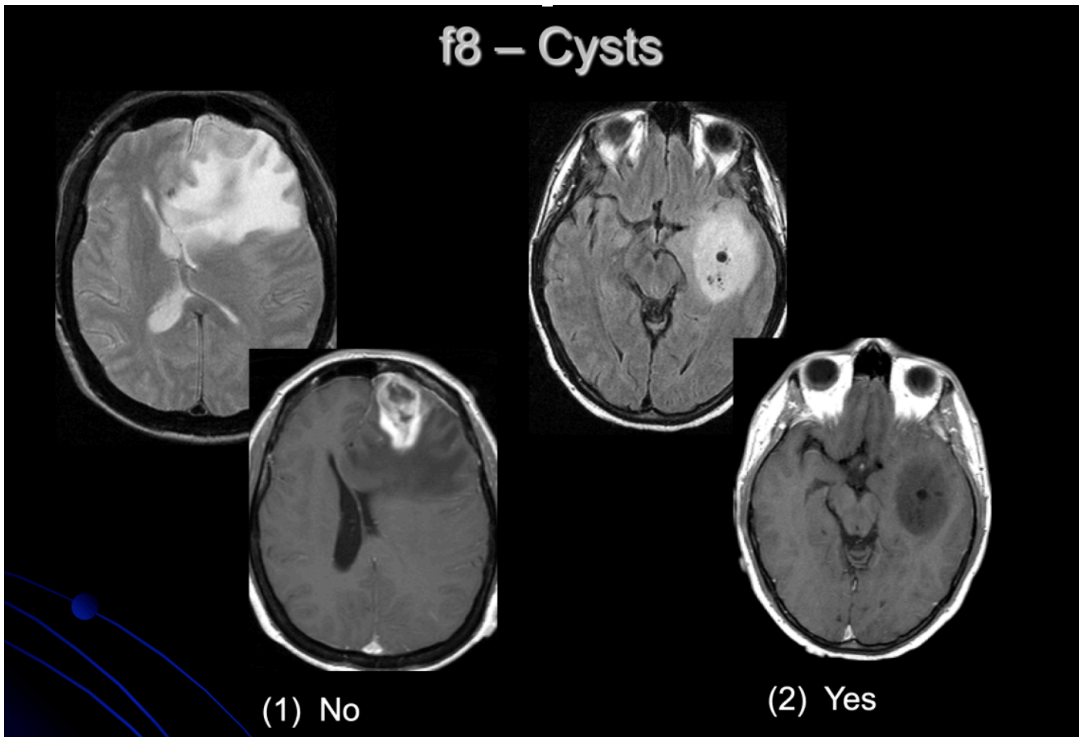

***Figure 9**. VASARI user instructions (54) for f8:' Cysts are well defined, rounded, often eccentric regions of very bright T2W signal and low T1W signal essentially matching CSF signal intensity, with very thin, regular, smooth, non-enhancing or regularly enhancing walls, possibly with thin, regular, internal septations.'*

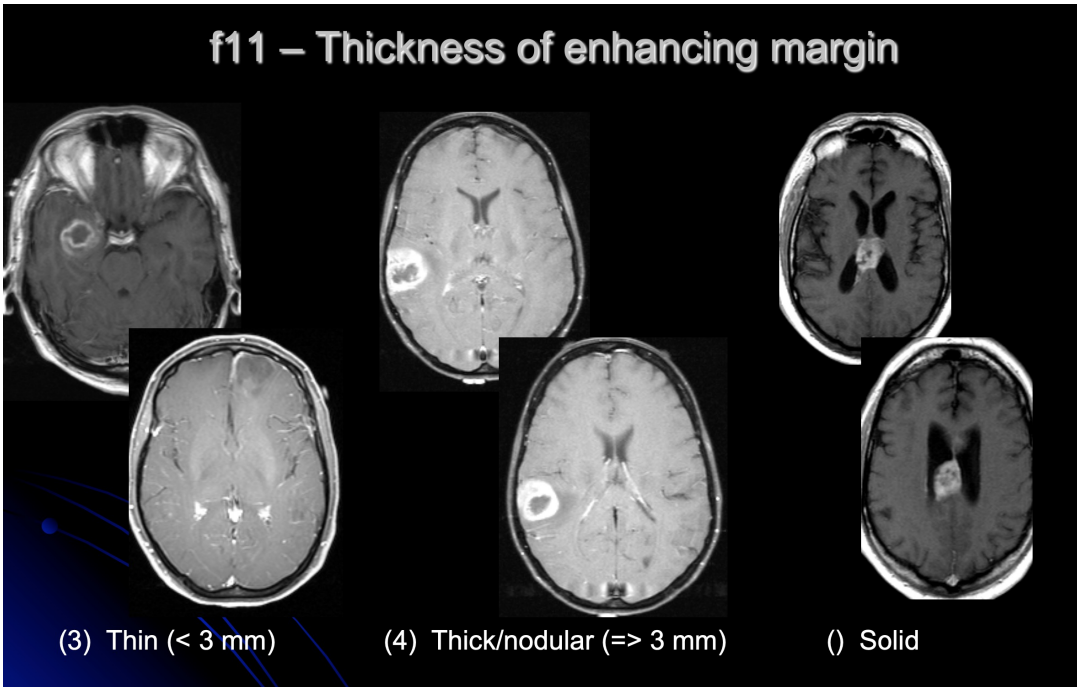

Figure 10. *VASARI user instructions (54) for f11: 'The scoring is not applicable if there is no contrast enhancement. If most of the enhancing rim is thin, regular, and measures < 3 mm in thickness and has homogenous enhancement the grade is* ***thin****. If most of the rim demonstrates nodular and/or thick enhancement, the grade is* ***thick****. If there is only solid enhancement and no rim, the grade is* ***solid****.'*

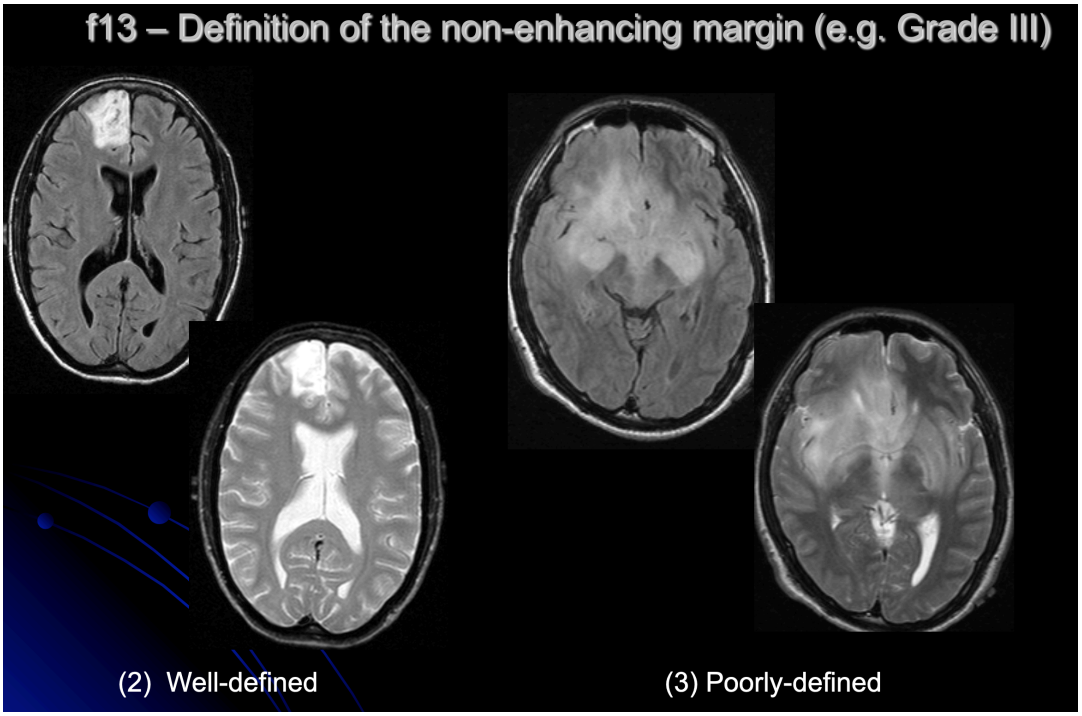

Figure 11. *VASARI user instructions (54) for f13: 'If most of the outside non-enhancing margin of the tumor is well defined and smooth (geographic), versus if the margin is ill-defined and irregular.'*

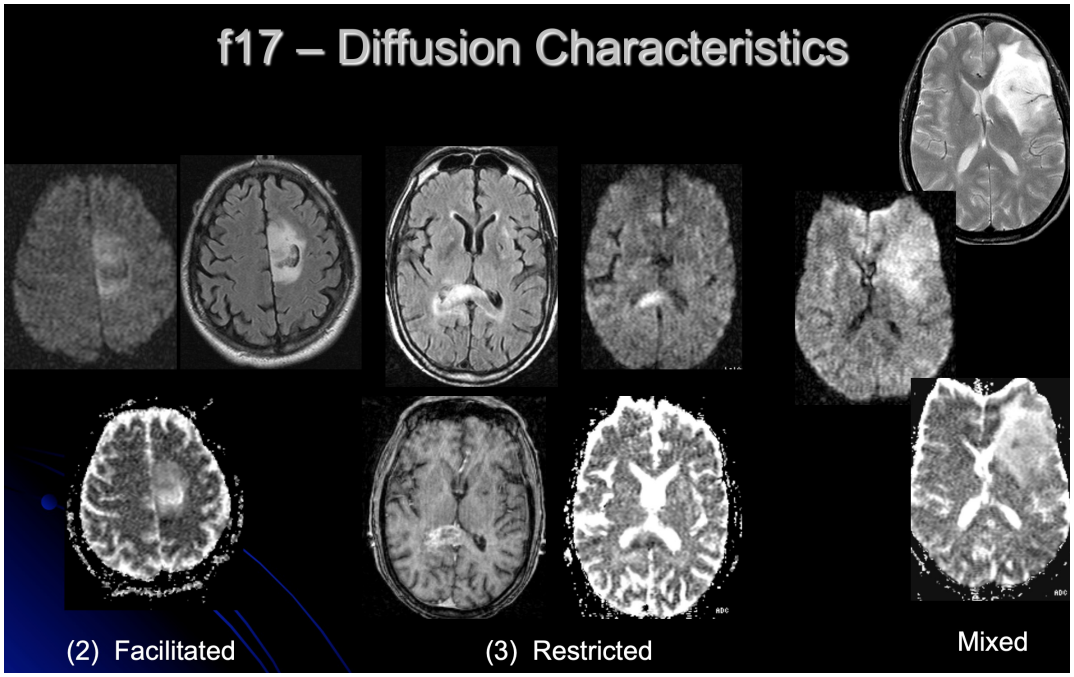

***Figure 12**. VASARI user instructions (54) for f17: 'Predominantly facilitated or restricted diffusion in the enhancing or non-enhancing (nCET) portion of the tumour. (Based on ADC map). [Rate CET alone when present, otherwise use nCET]. Indeterminate = unsure. Mixed = relatively equal proportion of facilitated and restricted. No ADC maps = use no-images. Proportion of tissue not relevant.'*

The VASARI feature set has been used widely in research (55). At the time of publication this represented a new, untested opportunity to obtain glioma data from clinical MRI in a more structured way. A research study was initiated with the hypothesis that VASARI criteria could assist the distinction of IDH^{wt} from IDH^{mut} astrocytomas. This earliest research was focussed on astrocytic tumours, because these were judged to represent the molecular group of interest.

2.2 Research questions

- To investigate if VASARI features differ between IDH^{wt} astrocytomas and other groups.
- To test the performance of VASARI features for predicting IDH status.

2.3 Methods

Consecutive patients (n=146) were retrospectively selected from the neuropathology archives by Hyare et al. (56). These included 52 IDH^{wt} astrocytomas (n=19 WHO grade 2 and n=33 WHO grade 3). Two comparison groups were established consisting of 68 $IDH^{mut/1p19qint}$ astrocytomas (n=53 WHO grade 2 and n=15 WHO grade 3), and 26 IDH^{wt} glioblastomas (WHO grade 4). Initially, two consultant neuroradiologists independently reviewed the MR images of n=33 IDH^{wt} and 30 $IDH^{mut/1p19qint}$ using a picture archiving and communication (PACS) workstation. The VASARI lexicon was applied to preoperative MRI studies with both observers working blinded to the histopathological diagnosis. After the analysis of this subset, modifications were made to VASARI descriptors to capture MRI features, which appeared frequent in lower grade gliomas: A category "not applicable" was added to f5 proportion enhancing, f11 thickness of the enhancing margin and f12 definition of enhancing margin. The category "patchy" was added to f11 thickness of the enhancing margin. This modified VASARI feature set was applied to the remaining data by a clinical fellow. The interrater agreement was assessed in the initial (n=66) training set by kappa statistics. Chi-Square testing was performed to test for differences between the astrocytoma groups. A Bayesian logistic regression model (https://arxiv.org/abs/1611.06649) was populated with 50 variables derived from VASARI scoring in Matlab version 2016b (https://uk.mathworks.com/). The logistic model was then applied to predict IDH status for the entire (n=146) cohort.

2.4 Results

Variable interobserver agreement was demonstrated, which was highest for f1 tumour location (k=0.723) and presence of tumour cysts (k=0.713). The agreement was lowest for the categorical diffusion assessment (restricted, facilitated, mixed) of ADC maps (k=0.357). A consensus review was required for f4 enhancement quality (VASARI categories: none, minimal/mild or marked/avid), f11 thickness of the enhancing margin (<3mm, >3mm or solid) and f12 definition of the enhancing margin (well-defined or poorly-defined).

Statistically significant (Chi-Square $p<0.05$) differences were identified between IDH^{wt} and IDH^{mut} WHO grade 2-3 astrocytomas for patient age (younger in IDH^{mut}), insula

location, eloquent brain location, presence of cysts, multifocality, numerical T1/FLAIR ratio, definition of the non-enhancing margin, deep white matter invasion and presence of satellites (k=0.4-0.75). Qualitative ADC inspection was not associated with IDH status. The final model performed well (AUC=0.92 +/-0.07, sensitivity 83% and specificity 85%) for the prediction of IDH status using the variables of age, tumour location in the thalamus, involvement of speech receptive areas, deep white matter invasion of the brainstem and T1/FLAIR signal ratio.

2.5 Discussion

2.5.1 Astrocytic cohort sample

The 52 IDH^{wt} WHO grade 2-3 astrocytoma group represented the entire sample available at our institution, which was expanded during the study. The IDH^{mut} and glioblastoma groups were convenience samples, which could have introduced selection bias. No $IDH^{mut/1p19qdel}$ oligodendrogliomas were studied. Their inclusion may have altered the selection of variables for the best performing model because of morphological differences compared to IDH^{mut} astrocytomas (57). In the Bayesian model, WHO 2-3 and WHO 4 tumours IDH^{wt} were merged for the IDH status prediction, however their VASARI features tend to markedly differ. Specifically, inclusion of the WHO grade 4 glioblastoma cohort increased the number of rim-enhancing tumours in the IDH^{wt} sample. Glioblastoma is often easily distinguished from IDH^{mut} typical low-grade gliomas by inspection. This may have resulted in overestimating the genotyping model performance.

2.5.2 Criteria suitability for purpose

The application of the VASARI criteria in gliomas has several theoretical advantages. Definition of a fixed vocabulary may reduce variability in wording, possibly even in the visual analysis. Structured image reporting is established in other areas of neuro-oncology, for example as BI-RADS scoring breast cancer (58). In brain tumour clinical assessment, templated reports have been associated with greater reproducibility of documentation and less addenda (59,60). Referrers, more so than radiologists, may welcome standardised reporting (61).

Because the VASARI criteria were developed in glioblastoma, this does not equal their suitability to characterise diffuse gliomas of all grades and genotypes. Subjectively, the feature categories did not apply well to the visual properties of lower grade gliomas, which is reflected in the adaptions. For example, the question about margin enhancement appeared misplaced, as the sample of WHO grade 2-3 gliomas more often exhibited patchy or solid enhancement. Glioblastoma descriptors such as f18 pial invasion and f19 ependymal extension are rarely applicable to IDH^{mut} tumours (55). Adapting feature categories during the study risked inconsistency but did not alter the qualitative assessments (e.g. by addition of a non-enhancement option).

2.5.3 Interobserver study

The interobserver comparison in this study was incomplete. As the initial kappa analysis revealed limited agreement for many VASARI categories, the remainder of the assessment was performed in consensus. Furthermore, a proportion of cases was scored by a non-radiologist supplemented by senior consensus. This effectively amounts to a single senior reader, where visual evaluation is susceptible to observer disagreements generally (62), and specifically in glioblastoma (63). Although the original VASARI study (64) developed feature categories using 3 or more readers, the total number of cases (n=82) contributing to criteria is not large. Binarisation of subjective features (well-defined, poorly defined) is particularly problematic and may not apply to some tumours, even with excellent observer 'skill'. Several of the VASARI categories aim for numerical data (%) but lack a measurement standard, from which substantial disagreements can be expected (65). In this research, the only VASARI categories with good agreement were location and cysts. The concordance for location was lower compared to the original VASARI study (k=0.837, 95% CI 0.807–0.902).

2.5.4 Model clinical translatability

The Bayesian model in this study was developed and implemented by a Matlab expert (PN), using code with partial (BayesReg software package) automation, supplemented by Markov Chain Monte Carlo simulations (66). This provided the opportunity to compute a large hierarchical model (estimated from 50,000 data samples) but involved high dimensional statistics with random number generators (67), which are not easily

accessible to clinical radiologists. Due to the complexity of the method, certain components are analytically intractable meaning that repeated data sampling becomes a statistical substitute to optimise model performance. The obscurity of simulation methods can pose a risk to the quality and reliability of study results, not dissimilar to a single reader assessment (68). The limited transparency of this powerful method could be an important hurdle in the way of clinical implementation. Model validation was performed in a 15% hold out sample, but no independent validation followed.

2.5.5 Impact and learning from this study

The impact of this study on my subsequent research was multiple: unexpectedly, age emerged as a numerical variable with predictive strength for IDH genotyping. In retrospect, the correlation of IDH^{wt} glioblastoma and age appears implicit older prognostic scoring systems (Pignatti score (69)). Integrating age into genotyping predictions may be valuable irrespective of imaging biomarker(s). Interestingly, only in very new imaging literature age is increasingly featured to improve glioma predictive models (70).

Secondly, visual biomarkers for molecular predictive modelling based on clinical MRI may benefit from stratification by reproducibility, if they involve radiologist interaction. Finally, the largest available population should be studied. This should include the $IDH^{mut/1p19q}$ genotype, and validation of any initial research results should be considered.

2.6 Systematic literature review of visual features

Based on the above (56), anatomical MRI features were judged to be potentially valuable for glioma molecular characterisation. However, it remained uncertain which visual characteristic(s) would become preferable for genotyping. To inform the methods design of subsequent research, a systematic literature review was completed.

2.6.1 Literature research questions

- To document candidate morphologies that can be derived from clinical MRI to predict glioma molecular status.
- To summarise existing data on the reliability of these features.

2.6.2 Literature methods

A team of 4 reviewers undertook a systematic literature review (71). This research focused on sequences that could be considered clinical standard in line with ESNR-BTG survey results. The study was carried out according to the Preferred Reporting Items for Systematic Reviews and Meta-Analyses (PRISMA-DTA) criteria (72) and registered in the PROSPERO online database of systematic reviews (CRD42019127655). The reviewers worked in pairs with each publication assessed twice. A step system was used to chronologically randomise abstracts and minimise bias by variable reviewer pairings. Details of the search strategy, inclusion and exclusion criteria are listed in ((73), supplement). All abstracts retrieved in the initial search, and all selected full-text articles were screened independently by two reviewers. The manuscript selection process is detailed in **Figure 13**.

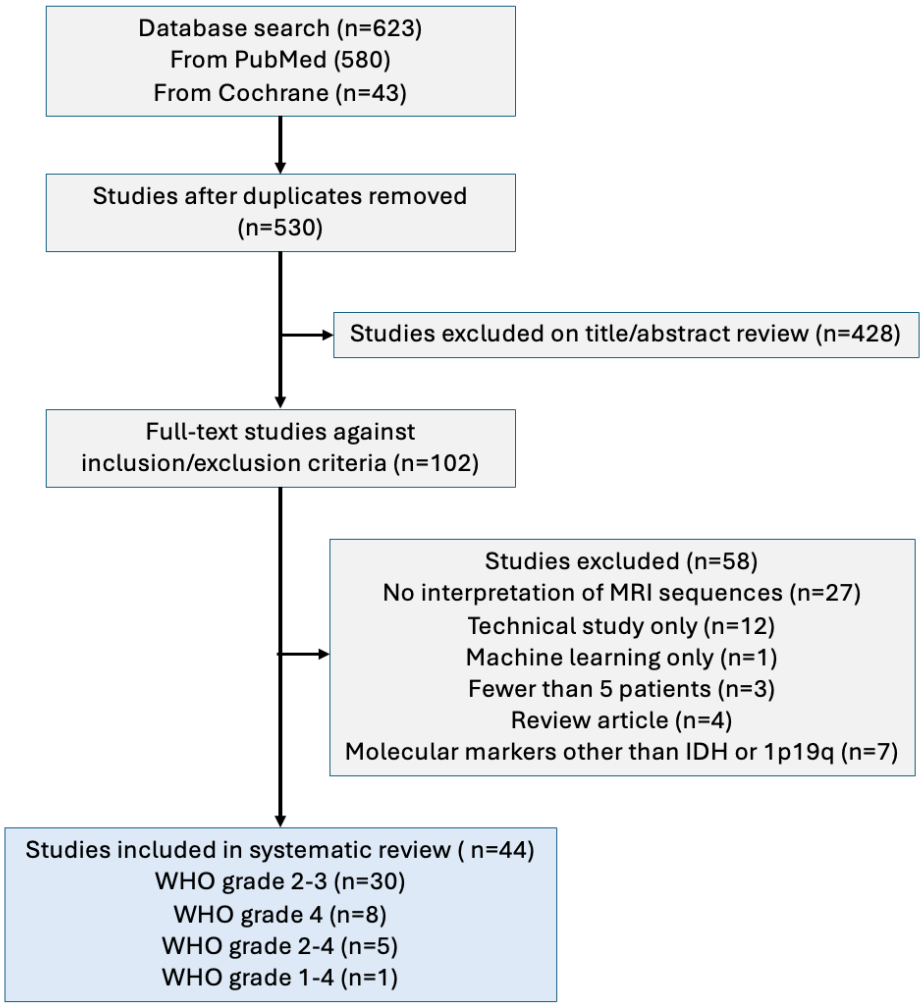

Figure 13. *Flow diagram of manuscript selection for the systematic review (71).*

2.6.3 Literature results

Forty-four studies including a total of 5286 patients fulfilled the inclusion criteria, with a mean of 115.9 (standard deviation 73.1) gliomas analysed in each study. All were retrospective analyses with a mixture of glioma WHO grades reported.

Multiple (n=16) studies assessed the relationship between IDH status and location in WHO grade 2-3 gliomas. Consistently, a predilection of IDH^{mut} tumours for the frontal lobes was reported (74–77), including for the 1p19q codeletion (74,78–80). However, frontal location showed limited (<75%) sensitivity, particularly towards higher WHO grades. A temporal lobe location makes a $IDH^{mut1/p19qdel}$ genotype less likely (77,79,81,82). Associations were reported between IDH^{wt} status and thalamus (56) and brainstem (83) tumours. Multilobar disease was associated with IDH^{wt} status in one (n=175) study (84). WHO grade 2-3 IDH^{mut} lesions were reportedly larger than IDH^{wt} tumours at diagnosis (74,85). Sharp tumour margins were associated with IDH^{mut} status (74,76), while indistinct non-enhancing margins aligned with IDH^{wt} status in multiple publications (56,84,86). However, tumour heterogeneity and poorly-defined margins also correlated with 1p19q codeletion and did not consistently permit IDH genotyping (80,81,87). Cysts appeared more prevalent in IDH^{mut} tumours (83,88).

In WHO grade 2-3 gliomas, contrast enhancement was more common in IDH^{wt} status (88–90). Rim-enhancement and necrosis corresponded to IDH^{wt} status in several studies (77,87,88), also for low grade gliomas (potentially influenced by tissue sampling bias). $IDH^{mut/1p19qdel}$ oligodendrogliomas displayed absent or ill-defined enhancement in several studies [16, 26, 36]. However, anaplastic (WHO grade 3) $IDH^{mut/1p19qdel}$ tumours commonly enhanced with contrast (77).

Three studies concluded that T2w/FLAIR mismatch is 100% specific for an $IDH^{mut/1p19qint}$ astrocytoma, with interobserver agreements between 0.56 and 0.75 (78,91,92). Several studies observed associations with calcifications and haemorrhage, but methods were variable for how these were assessed (CT and/or MRI). Calcification may predict 1p19q codeletion (75,81,93), which aligns to older literature on oligodendroglioma.

Twelve studies reported statistical results for interobserver comparisons of qualitative features, and 13/44 studies performed consensus reads. Twenty-four publications used one reader (7/44) or lacked reader descriptions (12/44). High (>0.9) interobserver agreements were only reported for laterality and location.

2.6.4 Discussion

2.6.4.1 Methods design

This systematic review followed the older edition of the PRISMA checklist (72) with a new version introduced in 2020. It is noted that the 27 item checklist remains unchanged in principle (94). To be exact, PRISMA serves as a reporting tool and is not intended for systematic review design (95).

All eligibility criteria, information sources, search strategy and selection process were defined up front. As the review progressed, the search was appropriately updated prior to final analysis (96). The search term was refined and tested by one researcher. This did not include specific terminology that reflects tumour morphology (e.g. location, size, enhancement) and lacked the term 'VASARI'. Searching the reference lists of all included articles may have yielded additional relevant studies. The data extraction could have benefitted from scrutiny of the reference standard by a neuropathologist to identify studies with incomplete or ambiguous molecular data, both for the IDH^{wt} and IDH^{mut} groups e.g. screening for rarer IDH mutations (97,98).

2.6.4.2 Data extraction and synthesis

All data items for study (research purpose, patient number, WHO grade(s), genetics, MRI field strength and sequences analysed, ROI/VOI methods, number of observers, statistical agreement, feature(s) described and statistical results) were defined up front. On piloting the search, the reviewers judged it to be most appropriate to perform a narrative synthesis because of a perceiving heterogeneity of the methods, cohorts and features reported (99). Care was taken to comprehensively document study results, which in most cases consisted of descriptive statistics. A meta-analysis was avoided because of a perceived difficulty to produce a meaningful result or risk that this could be misleading (96). Excluding studies with substantial bias (up 23% for individual QADAS-2 items) made less data available for meta-analysis. Ideally, a statistics consultation would have been invited to formally confirm the unsuitability for meta-analysis.

2.6.4.3 Application of the QADAS-2 tool

QUADAS-2 (Quality Assessment of Diagnostic Accuracy Studies 2) represents a revised system for critical appraisal in systematic reviews, which is recommended by the U.K. National Institute for Health and Clinical Excellence (NICE) (100). The QADAS framework has been widely used, however the authors had limited experience (n=1) with the tool (42). All QADAS-2 items were defined in advance to optimise the quality analysis. To overcome complexities of nomenclature for reviewers without QADAS-2 experience, example scenarios were discussed prior to study start. Whilst this still leaves a certain room for error (e.g. by confusing index test and reference standard), all discrepant results underwent a consensus involving a third (senior) reviewer.

2.6.4.4 Impact and learning from this study

The combination of the VASARI study for molecular diagnosis and the systematic literature yielded several candidate morphologies for glioma genotyping, which could be further investigated based on clinical MRI sequences.

Key learning points from this research are the importance of studying $IDH^{mut/1p19qdel}$ oligodendrogliomas, because of probable feature overlap (e.g. internal heterogeneity, poorly defined margin) with the IDH^{wt} group, and the need for a clinical predictive model which could be run by radiologists. Furthermore, the paucity of literature data on feature reproducibility would need addressing in future study design.

2.7 Conclusion

Although the observations from studying diffuse glioma morphology were important, one concern was how to obtain quantitative data for molecular characterisation. Anecdotally, my clinical team had observed low ADC values in malignant gliomas (**Figure 3**). I concluded that by applying the VASARI category f17: diffusion characteristics, the gliomas had not been comprehensively studied and hypothesised that measuring ADC values may assist the identification of IDH^{wt} status. The investigation of this topic is detailed in Chapter 3.

Chapter 3: Apparent diffusion coefficient for glioma molecular diagnosis

3.1 Background

Following WHO 2016, emerging data indicated a potential for diffusion-weighted MRI to identify glioma molecular status. One study in 112 cases of WHO 2-4 gliomas applied diffusion tensor-derived ADC values for IDH genotyping (101). In this research, the most accurate results were reported for WHO grade 2 (AUC 0.92), with performance diminished towards WHO grade 4 (AUC 0.66). A further publication reported a stronger association between ADC and IDH status than cell morphology (astrocytoma or oligodendroglioma) in WHO grade 2-3 gliomas (102). The proposed methods differed, whereby one study obtained volumetric measurements and the other regions of interest. As preliminary results, these data supported a new focus on ADC quantification for molecular diagnosis. Two studies followed, of which the first (103) investigated non-contrast enhancing gliomas, and the second (104) analysed the entire WHO grade 2-3 glioma cohort at my institution.

3.2 ADC values in non-contrast-enhancing gliomas

3.2.1 Research Questions

- Do volumetric and/or single slice ADC values correlate with any of the three genetic subtypes of glioma?
- What is the diagnostic accuracy of any resulting correlation?

3.2.2 Methods

A retrospective observational study (n=44) was conducted. All non-enhancing tumours (n=14) from the available WHO grade 2-3 IDH^{wt} cohort were compared to $IDH^{mut/1p19qint}$ molecular astrocytomas (n=16) and $IDH^{mut/1p19qdel}$ oligodendrogliomas (n=14). The IDH^{mut} comparison group was randomly selected for the same period that accrued the IDH^{wt} group.

Tumour volumes (VOI) were segmented using ITK snap Toolbox version 3.6 (105) covering the entire T2 signal abnormality. ADC maps were co-registered to the T2w

segmentation masks using the FLIRT toolbox in FSL (106) and VOI ADC_{mean} values extracted. A second volume of interest was drawn in contralateral centrum semiovale to calculate $rADC_{mean}$ as the ADC_{mean} tumour/ADC_{mean} normal white matter (ADC_{NAWM}) ratio (**Figure 14**).

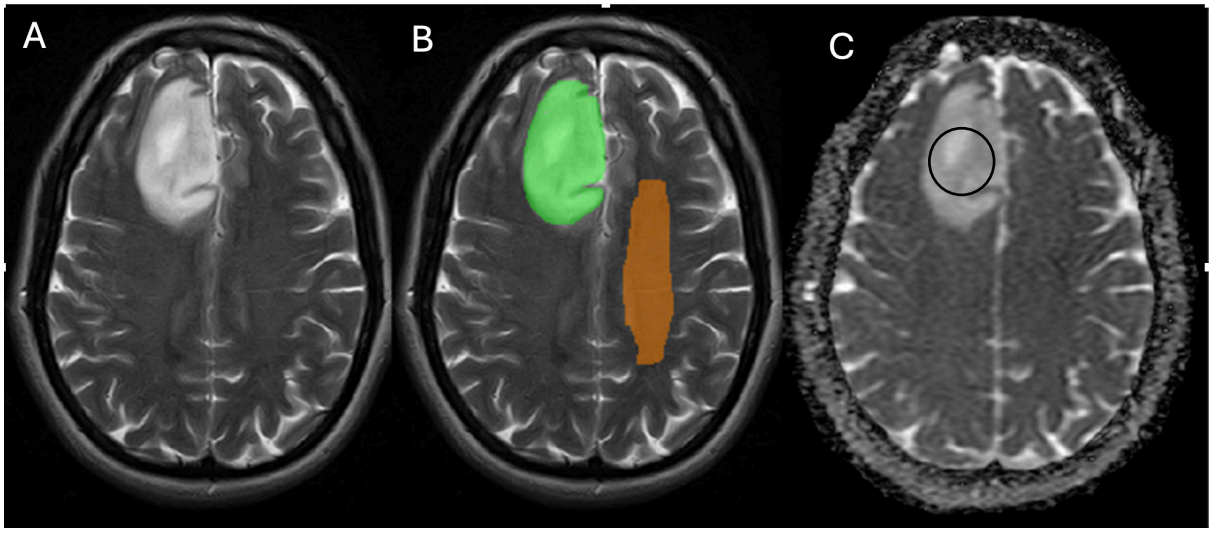

***Figure 14**. T2w images (A, B) and ADC map (C) demonstrating the whole lesion volumetric segmentation (green mask overlaid on right frontal $IDH^{mut/1p19qint}$ glioma), single slice largest tumour cross-section ADC_{mean} (black) and comparative contralateral NAWM ROI placement (brown). Adapted from (103).*

Separately, two observers located each tumour on T2w using the hospital PACS system with the ADC map side by side to draw one region of interest (ROI) ADC_{mean} in the tumour and one ROI ADC_{NAWM} in the centrum semiovale to produce the ROI $rADC_{mean}$.

A linear regression was performed in Stata version 14 to test the association between glioma genotype and ADC values. This was followed by a logistic regression to assess if ADC values could predict non-enhancing glioma IDH status. A receiver operating characteristic (ROC) area under the curve (AUC) analysis was used to assess the diagnostic accuracy of IDH genotyping. Regional and volumetric results were compared, and the ROI results were compared between both observers (intraclass correlation coefficient (ICC)) using a two-way random effects model.

3.2.3 Results

Significant (all $p<0.01$, except $IDH^{mut/1p19qdel}$ $p=0.019$) associations were observed between each ADC metric (VOI ADC_{mean} and VOI $rADC_{mean}$, ROI $rADC_{mean}$) and the three

glioma genotypes. The ADC values were lowest for the IDH^{wt} group, intermediate for the $IDH^{mut/1p19qdel}$ group and highest in the $IDH^{mut/1p19qint}$ group (**Figure 15**).

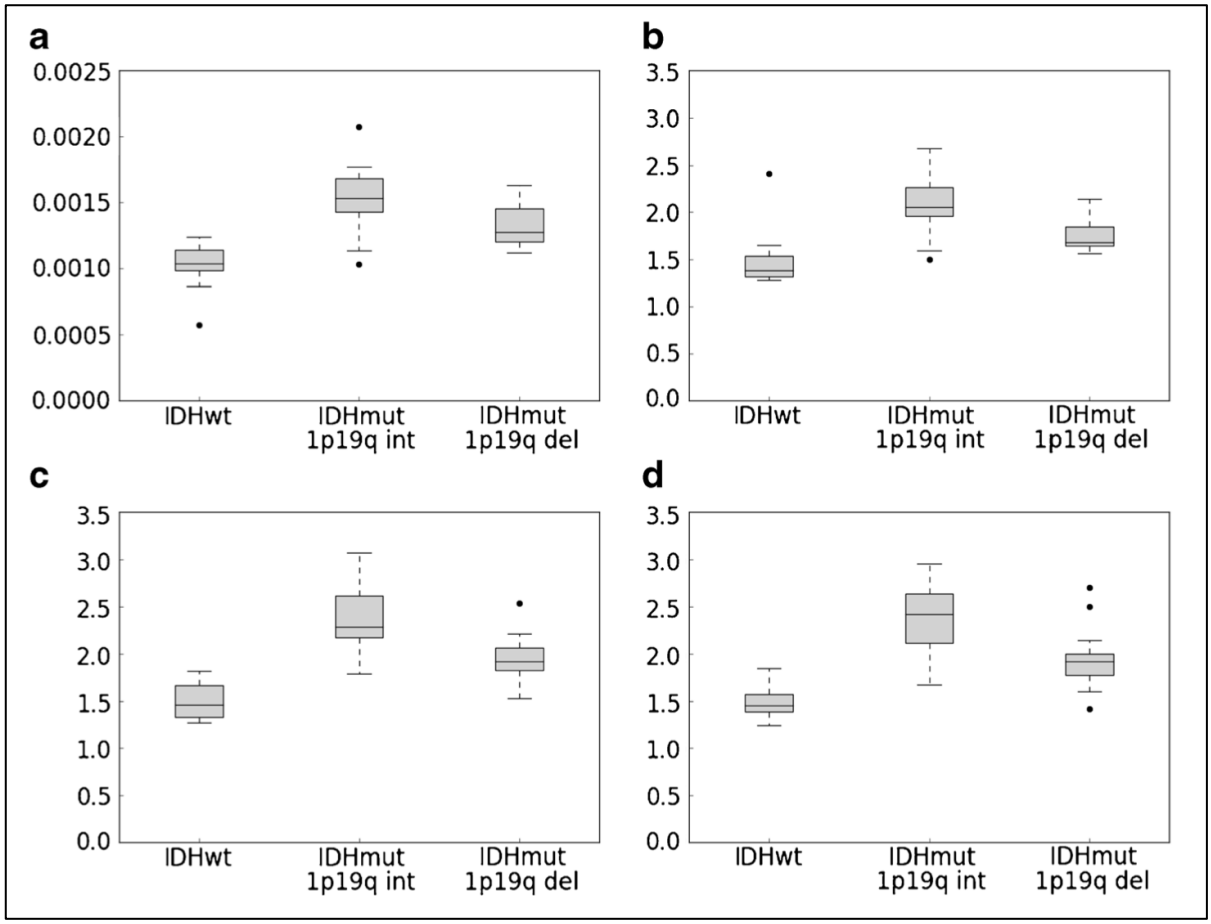

***Figure 15**. Boxplots of the entire tumour VOI ADC_{mean} (a), VOI $rADC_{mean}$ (b), single slice ROI $rADC_{mean}$ for observer 1 (c) and observer 2 (d).*

There was excellent agreement between the ROI measurements of both observers (average ICC 0.92-0.98). For VOI ADC_{mean}, the ROC analysis showed an AUC of 0.94. A VOI ADC_{mean} threshold of 1201×10^{-6} mm^2/s yielded a sensitivity of 83% and a specificity of 86% for the prediction of IDH^{wt} status. For VOI $rADC_{mean}$, the ROC analysis produced an AUC of 0.90 with a sensitivity of 80% and a specificity of 92%. For the single slice measurements, a ROI $rADC_{mean}$ threshold of 1.83 (1.76) achieved a sensitivity of 80% (86%) and specificity of 1 (91%) for observer 1 (observer 2).

3.2.4 Discussion

3.2.4.1 Case selection

Care was taken to assess the entire non-enhancing IDH^{wt} cohort and to randomise the IDH^{mut} cases prior to screening for non-enhancement. Nevertheless, there is a possibility that selection bias could have affected the process of non-enhancing glioma inclusion, because this involved neuroradiologist judgement. In some instances, contrast enhancement can be so minimal that it becomes ambiguous, or T1 shortening may hinder the assessment (pre and post contrast T1w were reviewed in all cases to correct for this) (107). By focussing on gliomas which were clearly non-enhancing, the screening process could have prioritised homogenous tumours. This could be relevant for calcified $IDH^{mut/1p19qdel}$ with potential to impact their ADC_{mean} quantification.

3.2.4.2 STARD fulfilment

This study aligns to the STARD (Standards for Reporting Diagnostic Accuracy Studies) criteria (108) but is not identifiable as a diagnostic accuracy study by title. The eligibility criteria were defined clearly prior to study start but should be described in maximal detail. For example, the two IDH^{mut} comparison groups were chosen randomly to form similar numbers to the IDH^{wt}, from which those without contrast enhancement were selected. The omission of a sample size calculation (maximum IDH^{wt} sample used) and exploratory thresholding should have been discussed in the manuscript. The tissue reference standard description is brief. Information on how ambiguous reference standard results were to be handled could have been included. From memory none accrued, and the IDH^{wt} cohort was assembled in accordance with latest testing standards (32). The reference standard was independent from the index test, however a finding of WHO grade 2-3 IDH^{wt} glioma could have theoretically prompted neuropathologist imaging review. MRI results may become disclosed to pathologists at the MDT with potential to influence the revision of a molecular diagnosis. In summary, this study has partially fulfilled STARD guidance.

3.2.4.3 Types of regression

A linear regression was adopted to associate genotype with ADC values as the continuous numerical outcome. It is unclear if testing was performed by the statistician to confirm data suitability for this operation (109), where the relation between glioma genotypes and ADC is not necessarily linear. A few outliers can be identified in the boxplots, and overlap exists in the ADC_{mean} values of both IDH^{mut} groups with 1p19qdel ADC values consistently lower. The subsequent research resolved testing for group differences and association strength differently (Kruskall-Wallis ANOVA, Eta^2).

To identify whether ADC values can predict IDH status, genotype served as the binary outcome, hence a logistic regression was applied at this point. For the univariable binary logistic regression of ADC parameters, the 1 in 10 rule was narrowly met (n=14 IDH^{wt} outcomes). Whilst this requirement has been challenged (110), it was specifically considered in later categorical grouping (tumour location by epicentre, Chapter 4) to improve the statistical analysis.

3.2.4.4 Area under the curve

ROC AUC plotting represents a widely applied measure of diagnostic test accuracy, in which the true positive rate (y-axis) is plotted against the false positive rate (x-axis). This makes it possible to compare the overall performance of different tests, or of individual metrics such as ADC values, to predict a statistical outcome (in this case genotype). Criticism has been expressed that AUC analysis does not automatically translate into clinically meaningful thresholds (111), and that reciprocal percentage changes in sensitivity and specificity differ for different points along the curve. In this research, achieving a high sensitivity for IDH^{wt} identification was judged to be the priority over specificity. However, it is also important to consider that a marked loss of specificity could be problematic in terms of NHS capacity and molecular testing inequities (112), if an unrealistically large number of suspected high risk tumours require urgent tissue testing.

3.2.4.5 Impact and learning from this study

This research consolidated the emerging role of ADC for glioma molecular diagnosis, particularly to identify the IDH^{wt} high risk status. The results are published in European

Radiology, a journal with reach to the wider (not limited to neuroimaging) radiologist community, who previously relied on contrast patterns to 'grade' gliomas.
Based on the size of this study it was not sufficiently clear, if regional measurements could replace volumetric ADC_{mean}. If both ROI and VOI measurements showed high concordance for different observers, and if both performed equally well for genotyping, the more laborious volume assessments could be omitted. To address this question, a larger study comparing regional and volumetric ADC parameters followed. The purpose of the next study was to comprehensively investigate the performance of several ADC metrics and to assess the entire institutional glioma cohort with available molecular results.

3.3 Multireader studies of ADC metrics for IDH genotyping

3.3.1 Research questions

- Which ADC parameter(s) performs best for WHO grade 2-3 glioma IDH status prediction?
- Are volumetric ADC measurements superior to region of interest placements?
- What is the interobserver agreement for ADC measurements (for any enhancement pattern)?

3.3.2 Methods

Consecutive patients diagnosed from July 2008 to January 2018 were eligible for the research. Inclusion criteria consisted of histologic confirmation of WHO grade 2 or 3 glioma, documented IDH and 1p19q genetic test results, and available pretreatment MR imaging. A flowchart of the case selection process is shown in **Figure 16**.

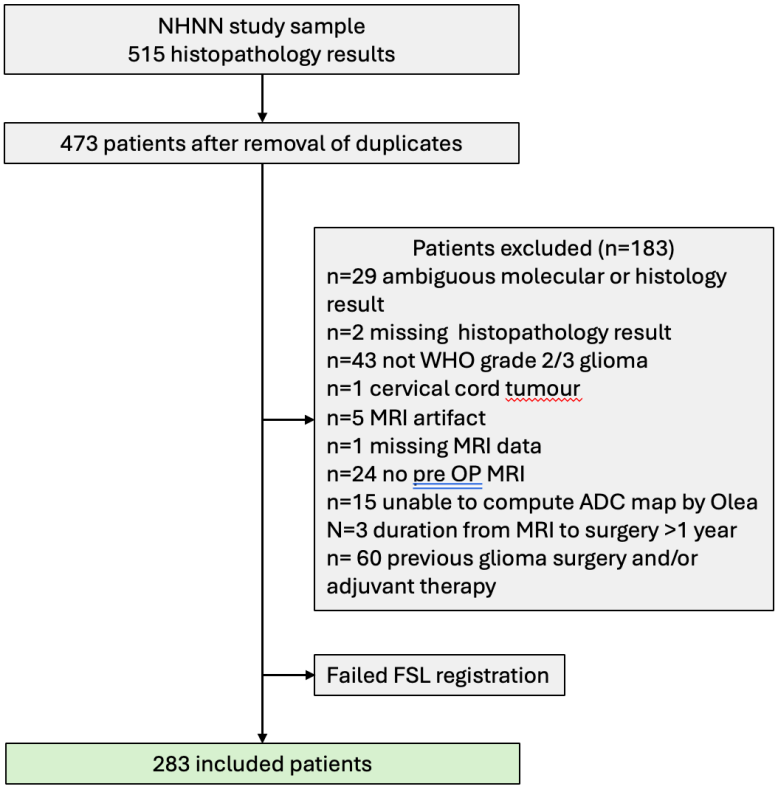

***Figure 16**. Flowchart of WHO grade 2-3 glioma inclusion in the study. NHNN=National Hospital for Neurology and Neurosurgery (113).*

Using an Olea workstation (Olea Sphere, Version 2.3), a circular region of interest ROI was drawn into the largest solid tumour cross-section on the ADC map with T2w and b0 viewed side-by-side to obtain ROI ADC_{mean}. One ADC_{NAWM} was placed to calculate ROI $rADC_{mean}$ as in (103).

Three small (30-40 mm^2) ROIs were drawn in the perceived lowest ADC regions of solid tumour and averaged to obtain ROI ADC_{min} (114). From this, ROI $rADC_{min}$ was calculated using the same ADC_{NAWM}. Each ADC value was measured by 2 observers (observer 1 n=290, observer 2 n=75, observer 3 n=215), blinded to each other's results and tissue data, amounting to n=2900 ADC measurements (**Figure 17**).

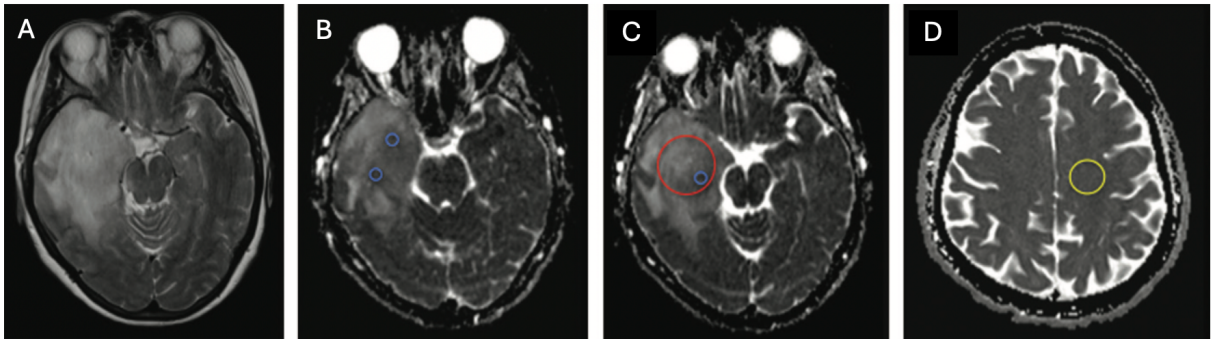

***Figure 17**. An example of the ROI ADC measurements in a right temporal IDH^{wt} glioma. T2w image (A) and ADC maps (B-D) with regions of interest (ROI) placed in the 3 perceived lowest ADC components (ADC_{min}, blue), largest tumour cross-section (ADC_{mean}, red) and normal appearing white matter ADC_{NAWM}, yellow).*

Separately, entire tumour volumes were outlined on T2w using ITK snap (105) by one observer with directly supervised training. All cases with perceived uncertainty were optimised by the senior reviewer, and further cases were randomly spot-checked for correctness. An additional random sample of segmentations (10%, n=28) was subjected to repeat segmentation by a third observer.

The ADC maps were coregistered to T2w imaging using the FLIRT registration (106) in FSL (**Figure 18**). VOI ADC histogram data were extracted using an in-house script written in Python 2.7. For each tumour, the second and fifth ADC histogram percentiles, ADC_{mean} and total lesion volume were extracted. ADC values <0 were excluded from the analysis.

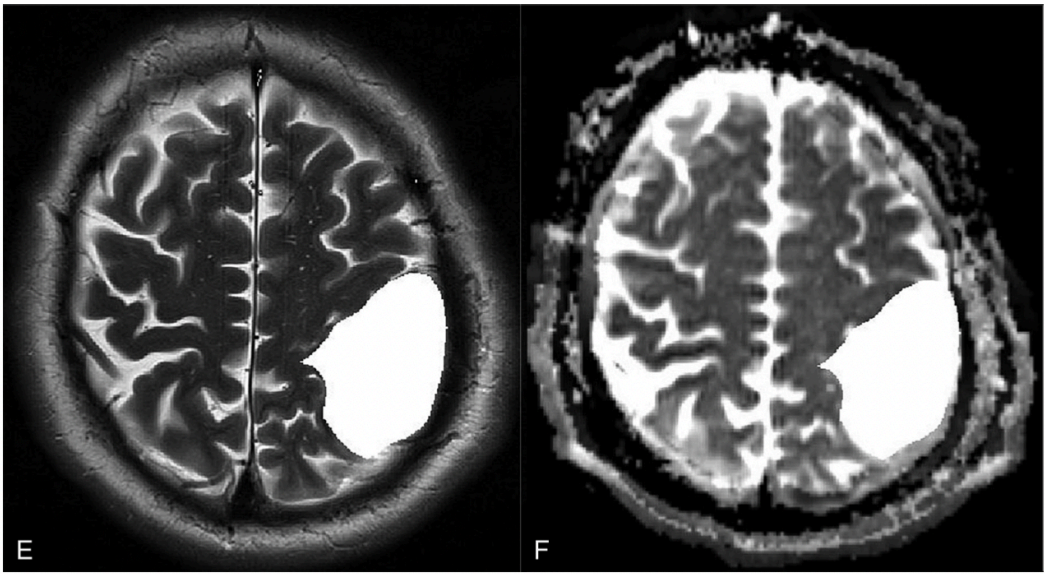

***Figure 18**. An example of the volumetric T2w segmentation mask (white) overlaid onto the ADC map in an IDH$^{mut/1p9qint}$ astrocytoma for subsequent ADC data extraction.*

An analysis for group differences in absolute VOI ADC values and VOI rADC values (derived from the same ROI ADC_{NAWM}) was performed by Kruskal-Wallis ANOVA testing, including Dunn pairwise comparisons with Bonferroni correction. The strength of the association between glioma subtype and ADC metrics was examined using Eta^2. This was followed by univariable binomial logistic regression to assess the performance of each parameter for IDH status prediction.

3.3.3 Results

3.3.3.1 Patient demographics

After exclusion of n=7 failed FSL registrations, n=283 WHO grade 2-3 glioma datasets were available for study. Their genetic data and contrast enhancement patterns are shown in **Table 8**.

	All genotypes	IDH^{wt}	$IDH^{mut/1p19int}$	$IDH^{mut/1p19del}$
Number of patients	283	79	104	100
Median age (IQR) in years	40 (33-53)	59 (43-67)	35 (29-41)	40 (35-48)
Enhancement category				
Non-enhancing	171	33	75	63
Solid-patchy enhancing	87	28	27	32
Rim-enhancing	23	18	0	5

Table 8*. Patient demographics, T1w contrast enhancement patterns, IDH and 1p19q genotypes of the study population (n=283).*

3.3.3.2 Interobserver comparisons

Interobserver agreement (ICC) for the regional ADC metrics ranged from 0.82-0.96 (0.76-0.96 for non-enhancing gliomas) for average measures. The results for average measures and consistency were nearly identical, indicating no systematic difference between observers (**Table 9**).

ROI parameter	ICC measure	All gliomas			Non-enhancing subgroup		
		Average measures ICC (95% CI)	Individual measures ICC (95% CI)	N	Average measures ICC (95% CI)	Individual measures ICC (95% CI)	N
ADC_{min} Observer: 1 vs. 2	Consistency	0.89 (0.82-0.93)	0.80 (0.70-0.87)	75	0.89 (0.8-0.94)	0.80 (0.67-0.88)	51
	Absolute	0.89 (0.82-0.93)	0.80 (0.70-0.87	75	0.89 (0.8-0.94)	0.80 (0.67-0.88)	51
ADC_{min} Observer: 1 vs. 3	Consistency	0.90 (0.86-0.92)	0.81 (0.76 -0.85)	215	0.85 (0.75-0.9)	0.73 (0.60-0.82)	123
	Absolute	0.89 (0.83-0.92)	0.79 (0.71-0.85)	215	0.85 (0.75-0.9)	0.73 (0.6-0.82)	123
ADC_{mean} Observer: 1 vs. 2	Consistency	0.83 (0.73-0.89)	0.71 (0.58-0.81)	75	0.76 (0.57-0.86)	0.61 (0.40-0.76)	51
	Absolute	0.83 (0.73-0.89)	0.71 (0.58-0.81)	75	0.76 (0.57-0.86)	0.61 (0.4-0.76)	51
ADC_{mean} Observer: 1 vs. 3	Consistency	0.96 (0.94-0.97)	0.92 (0.89-0.94)	215	0.95 (0.92-0.96)	0.90 (0.86-0.93)	123
	Absolute	0.96 (0.94-0.97)	0.92 (0.89-0.94)	215	0.95 (0.92-0.96)	0.90 (0.86-0.93)	123
$rADC_{min}$ Observer: 1 vs. 2	Consistency	0.89 (0.83-0.93)	0.81 (0.71-0.87)	75	0.90 (0.82-0.94)	0.81 (0.69-0.89)	51
	Absolute	0.89 (0.83-0.93)	0.81 (0.71-0.87)	75	0.90 (0.82-0.94)	0.81 (0.69-0.89)	51
$rADC_{min}$ Observer: 1 vs. 3	Consistency	0.87 (0.83-0.90)	0.77 (0.71-0.82)	212	0.86 (0.80-0.90)	0.75 (0.66-0.82)	122
	Absolute	0.85 (0.76-0.90)	0.74 (0.61-0.82)	212	0.83 (0.69-0.90)	0.71 (0.53-0.81)	122
$rADC_{mean}$ Observer: 1 vs. 2	Consistency	0.86 (0.77-0.91)	0.75 (0.63-0.83)	75	0.81 (0.66-0.89)	0.68 (0.49-0.80)	51
	Absolute	0.85 (0.75-0.91)	0.74 (0.60-0.83)	75	0.80 (0.65-0.89)	0.67 (0.49-0.80)	51
$rADC_{mean}$ Observer: 1 vs. 3	Consistency	0.93 (0.90-0.94)	0.86 (0.83-0.94)	212	0.92 (0.89-0.94)	0.85 (0.80-0.89)	122
	Absolute	0.92 (0.90-0.94)	0.86 (0.81-0.89)	212	0.92 (0.89-0.94)	0.85 (0.78-0.89)	122
ADC_{NAWM} Observer: 1 vs. 2	Consistency	0.86 (0.77-0.91)	0.75 (0.63-0.83)	75	0.88 (0.79-0.93)	0.78 (0.65-0.87)	51
	Absolute	0.83 (0.65-0.90)	0.70 (0.48-0.82)	75	0.86 (0.70-0.92)	0.75 (0.54-0.86)	51
ADC_{NAWM} Observer: 1 vs. 3	Consistency	0.83 (0.78-0.87)	0.71 (0.64-0.77)	212	0.85 (0.79-0.90)	0.74 (0.65-0.81)	122
	Absolute	0.82 (0.75-0.87)	0.70 (0.60-0.77)	212	0.84 (0.77-0.89)	0.73 (0.63-0.81)	122

***Table 9**. Intraclass correlation coefficients (ICC) for ADC region of interest measurements in the study sample (n=290, prior to exclusion of n=7 cases of failed volumetric registration), all gliomas versus non-contrast-enhancing gliomas.*

3.3.3.3 ADC differences between genotypes

As in the pilot data, the lowest ADC_{mean} values were observed for IDH^{wt} and the highest values for $IDH^{mut/1p19int}$ astrocytomas. Despite their best prognosis of the three groups, $IDH^{mut/1p19qdel}$ oligodendrogliomas exhibited intermediate ADC values, previously attributed to matrix composition (115). **Figures 19 and 20** show boxplots for the regional ADC measurements.

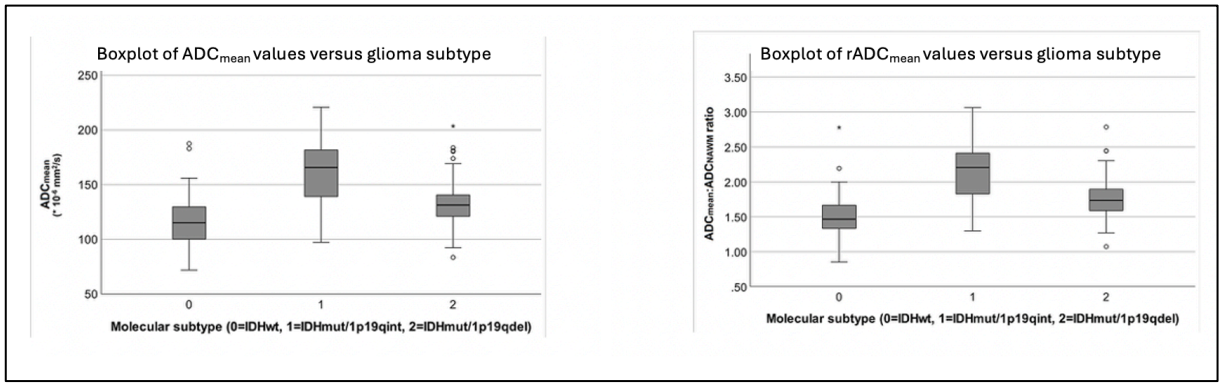

***Figure 19**. Boxplots of regional ADC_{mean} (left) and $rADC_{mean}$ (right) (ADC values averaged between observers) for the WHO 2016 glioma subtypes.*

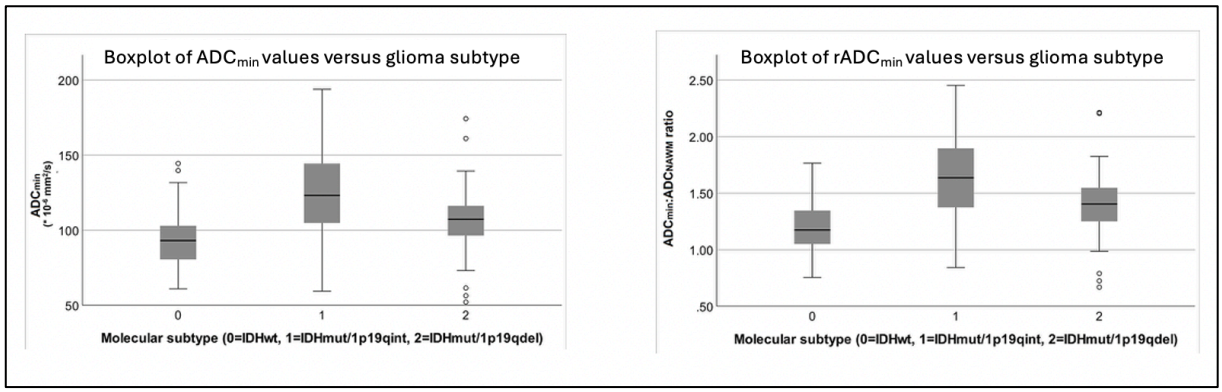

***Figure 20**. Boxplots of regional ADC_{min} (left) and $rADC_{min}$ (right) (ADC values averaged between observers) for the WHO 2016 glioma subtypes.*

3.3.3.4 Associations between ADC and genotype

Significant differences were identified for all ROI parameters, and for most VOI parameters. VOI ADC_{min} and VOI $rADC_{min}$ were not significantly different between IDH^{mut} subgroups (**Table 10**).

Dependent variable	Omnibus test ‡		Pairwise comparisons			N
	VOI*	ROI*	Groups compared	VOI*	ROI*	
ADC_{min}	<0.001†	<0.001	IDH^{wt} vs $IDH^{mut/1p19qdel}$	0.003	<0.001	283
			IDH^{wt} vs $IDH^{mut/1p19qint}$	<0.001	<0.001	
			$IDH^{mut/1p19qint}$ vs $IDH^{mut/1p19qdel}$	0.141	<0.001	
$rADC_{min}$	<0.001†	<0.001	IDH^{wt} vs $IDH^{mut/1p19qdel}$	<0.001	<0.001	280
			IDH^{wt} vs $IDH^{mut/1p19qint}$	<0.001	<0.001	
			$IDH^{mut/1p19qint}$ vs $IDH^{mut/1p19qdel}$	0.483	<0.001	
ADC_{mean}	<0.001	<0.001	IDH^{wt} vs $IDH^{mut/1p19qdel}$	<0.001	<0.001	283
			IDH^{wt} vs $IDH^{mut/1p19qint}$	<0.001	<0.001	
			$IDH^{mut/1p19qint}$ vs $IDH^{mut/1p19qdel}$	<0.001	<0.001	
$rADC^{mean}$	<0.001	<0.001	IDH^{wt} vs $IDH^{mut/1p19qdel}$	<0.001	<0.001	280
			IDH^{wt} vs $IDH^{mut/1p19qint}$	<0.001	<0.001	
			$IDH^{mut/1p19qint}$ vs $IDH^{mut/1p19qdel}$	<0.001	<0.001	

***Table 10**. Kruskal-Wallis ANOVA testing of ADC values for the distinction of glioma subtypes. * denotes volumetric (VOI) and regional (ROI) measurements, † values derived from the 5th histogram percentile (excluding values <0), ‡ p value adjusted (Bonferroni method) for multiple corrections. Vs=versus. Molecular subtype=independent variable for all comparisons. Note n=3 excluded from rADC analysis due to non-measurable NAWM (bilateral glioma).*

Mostly strong Eta^2 associations were identified between glioma IDH genotype and ADC. However, VOI ADC_{min} values showed a weak association, particularly for non-enhancing tumours (**Table 11**). Only VOI ADC parameters, but not ROI derived values, showed a strong association with IDH status in rim-enhancing gliomas.

Volumetric (VOI) ADC				Regional (ROI) ADC			
Measure	Eta^2	Effect size	N		Eta^2	Effect size	N
All gliomas							
ADC_{min}	0.06	Small	283	ADC_{min}	0.28	Large	283
$rADC_{min}$	0.09	Small	280	$rADC_{min}$	0.29	Large	280
ADC_{mean}	0.27	Large	283	ADC_{mean}	0.38	Large	283
$rADC_{mean}$	0.28	Large	280	$rADC_{mean}$	0.38	Large	280
Subgroup analysis, non-enhancing							
ADC_{min}	0.02	Small	171	ADC_{min}	0.24	Large	171
$rADC_{min}$	0.03	Small	170	$rADC_{min}$	0.24	Large	170
ADC_{mean}	0.28	Large	171	ADC_{mean}	0.41	Large	171
$rADC_{mean}$	0.27	Large	170	$rADC_{mean}$	0.39	Large	170
Subgroup analysis, solid-patchy enhancing							
ADC_{min}	0.11	Medium	110	ADC_{min}	0.21	Large	110
$rADC_{min}$	0.19	Large	108	$rADC_{min}$	0.25	Large	108
ADC_{mean}	0.19	Large	110	ADC_{mean}	0.24	Large	110
$rADC_{mean}$	0.23	Large	108	$rADC_{mean}$	0.28	Large	108
Subgroup analysis, rim-enhancing							
ADC_{min}	0.06	Medium	23	ADC_{min}	0.01	Small	23
$rADC_{min}$	0.22	Large	23	$rADC_{min}$	0.08	Medium	23
ADC_{mean}	0.19	Large	23	ADC_{mean}	0.00	None	23
$rADC_{mean}$	0.36	Large	23	$rADC_{mean}$	0.05	Small	23
Tumour volume (mm^3)	0.02	Small	283	N/A			

***Table 11**. Eta^2 associations between ADC values and glioma genotype.*

The AUC values across all gliomas, for non-enhancing and solid-patchy enhancing tumours were similar (AUC 0.81-0.84). **Table 12** demonstrates the sensitivity and specificity values derived by Youden's index for different ADC thresholds. An $rADC_{mean}$ threshold of 1.75 provided 86.8% sensitivity for IDH^{wt} identification.

ADC metric	AUC	N	ADC threshold	Sensitivity	Specificity
All gliomas					
VOI ADC_{mean}	0.78	280	1.19	77.2	64.2
VOI $rADC_{mean}$	0.82	280	1.60	86.8	60.8
ROI ADC_{mean}	0.81	280	1.34	84.8	60.3
ROI $rADC_{mean}$	0.83	280	1.75	86.8	62.3
Subgroup analysis, non-enhancing					
VOI ADC_{mean}	0.81	170	1.19	84.4	68.8
VOI $rADC_{mean}$	0.84	170	1.59	90.6	64.5
ROI ADC_{mean}	0.82	170	1.34	84.4	68.1
ROI $rADC_{mean}$	0.83	170	1.71	84.4	73.9
Subgroup analysis, solid-patchy enhancing					
VOI ADC_{mean}	0.78	85	1.12	76.9	71.2
VOI $rADC_{mean}$	0.80	85	1.51	80.8	67.8
ROI ADC_{mean}	0.79	85	1.16	73.1	79.7
ROI $rADC_{mean}$	0.81	85	1.65	80.8	61.0
Subgroup analysis, rim-enhancing					
VOI ADC_{mean}	0.84	23	1.27	83.3	80.0
VOI $rADC_{mean}$	0.90	23	1.73	88.9	80.0
ROI ADC_{mean}	0.49	23	1.38	83.3	40.0
ROI $rADC_{mean}$	0.61	23	1.5	72.2	60.0

Table 12. *AUC values and ADC thresholds (listed as ^10^{-3} mm^2/s for raw ADC and as ratio for rADC) with corresponding sensitivity and specificity at the threshold.*

Across all gliomas, the most accurate prediction of IDH status was achieved using ROI $rADC_{mean}$ or VOI $rADC_{mean}$ (AUC=0.83 and 0.82, respectively). **Figure 21** shows the ROC curve comparison for the volumetric and regional ADC metrics.

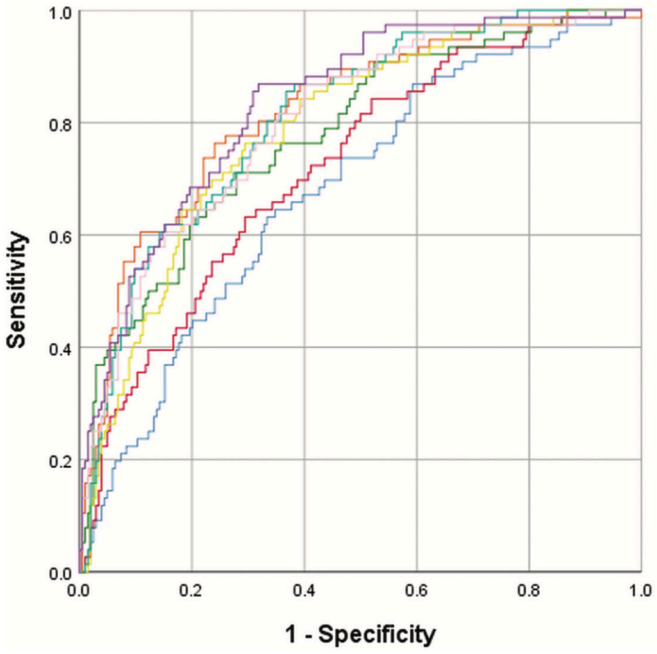

Area Under the ROC Curve (AUC)		
ADC metrics	Area Under the Curve	95% CI
VOI ADC_{min}	0.68	0.61 - 0.75
VOI $rADC_{min}$	0.72	0.66 - 0.79
VOI ADC_{mean}	0.78	0.72 - 0.84
VOI $rADC_{mean}$	0.82	0.76 - 0.88
ROI ADC_{min}	0.79	0.73 - 0.85
ROI $rADC_{min}$	0.81	0.76 - 0.86
ROI ADC_{mean}	0.81	0.75 - 0.86
ROI $rADC_{mean}$	0.83	0.78 - 0.89

***Figure 21**. ROC curves comparison for the prediction of IDH genotype in the study population (n=283).*

3.3.4 Discussion

3.3.4.1 Interobserver agreement

To pursue a system fit for clinical translation, it appeared essential to investigate the reproducibility of ADC measurements. All measurements were obtained by 2 observers in the initial glioma cohort (n=44) and by 3 further observers in the larger (n=283) cohort. Whilst the ICC calculations were performed for pairs of observers, 5 different individuals took part in the readings with similar agreement for all. The reproducibility of ROI ADC_{mean}, $rADC_{mean}$ and ADC_{NAWM} measurements has since been confirmed for an external cohort (n=108, University of Nottingham, average ICC 0.86-0.96) including a larger proportion of WHO grade 4 gliomas (116). Although intraobserver repeatability of measurements was not tested, the many concordant results point towards good reliability.

Where observers participated in diffusion measurements and morphological analyses (Chapter 4), their completion >2 weeks apart served to reduce memory.

3.3.4.2 Simplicity of the ROI ADC_{mean}

According to survey data (34), most radiologists inspect DWI/ADC pairs without quantification. To be feasible, any method for diffusion based molecular grading would need to offer diagnostic value without prolonging clinical workflow. It was hypothesised that a rapid method, if sufficiently accurate, may be favoured in later adoption (117).

As shown in **Figure 17**, the circular ROI ADC_{mean} spares the tumour margin and does not include all of the lesion. This was deliberate, as in a non-spherical tumour, a larger ROI would capture normal brain in some areas. A valid consideration was if to draw a cross-sectional freehand ROI around the entire T2w lesion instead. However, in the Agfa PACS system this function was not available, therefore similar issues were expected at other hospitals.

3.3.4.3 Volumetric ADC diagnostic yield

It was expected that ADC readings from entire gliomas would be superior for genotyping. By definition, analysing all tumour tissue offers more data than a regional measurement. The volumetric segmentations were reproducible between two observers (ICC 0.97-0.98) with the limitation that quantifying the uncertainty corrections (by a third senior observer) should have been considered. It is counterintuitive that volumetric ADC parameters performed less well in some cases. This could be due to erroneous analysis of normal brain margins, either due to oversegmentation or imperfect registration, where the process of FSL registration involves visual judgement. Furthermore, the IDH^{mut} infiltrating $IDH^{mut/1p19qint}$ rim appears more abundant in glial filaments and cellularity than the tumour centre (118). This IDH^{mut} property could be counterproductive to volumetric ADC genotyping.

Conversely, only volumetric ADC values were associated with genotype for rim-enhancing, centrally necrotic gliomas. The failure of ROI in this scenario could be due to microscopic necrosis in IDH^{wt} gliomas perceived as solid (119), which would increase the measured ADC values. Furthermore, ROI placements are more challenging in the presence of macroscopic necrosis. The small number (n=23, of which n=18 IDH^{wt}) of gliomas with necrosis limits the interpretation and generalisability of these results.

3.3.4.4 ADC_{NAWM} for normalisation

A normalisation step has long been applied in DSC perfusion imaging to produce the relative cerebral blood volume (120). In perfusion, this mitigates for dynamic effects of contrast leakage, but this precaution is not applicable to ADC mapping.

The contralateral centrum semiovale (CSO) ADC_{NAWM} was selected as an easily identifiable anatomical marker, which was at the time a subjective decision, but this method is since supported by data (121). The alternative of a mirror-ROI was judged to pose a risk of variability with potential influence from cerebrospinal fluid (CSF), vessels or inadvertent coverage of multiple structures. Use of the posterior limb of internal capsule proposed in another study (101) was avoided, because this is small and less easy to identify by non-expert observers.

Eliminating scanner factors was judged to be a priority in the research design, because the study took place at a specialist referral centre, where the study data originated from 23 different MRI machines. No individual scanner contributed more than 14% of any glioma subtype (104). Therefore normalised metrics were tested, but this may be unnecessary because ADC is mathematically independent from scanner factors (122). In this study, the ADC_{mean} and $rADC_{mean}$ results appeared very similar.

3.3.4.5 Averaging to obtain ROI ADC_{min}

My method to measure ROI ADC_{min} replicated a single centre study, which first attempted IDH genotyping (114). To maximise comparability with this prior research by Xing et al., I adopted the method of averaging multiple measurements. It should be considered that designating a multi-ROI average as ADC_{min} does not represent the lowest ADC in the way that using the lowest value of multiple ADC_{min} regions would. However, the averaging method may potentially safeguard against inadvertent measurement of very low ADC elements such as calcification or blood. Limitations were apparent with the original strategy: Xing et al. obtained 5 non-overlapping ADC_{min} values in each tumour and 5 ADC_{min} values in CSO white matter, totalling a laborious number of 10 small ROIs per patient. This would take time and could be difficult in small lesions. Secondly, no data on interobserver reproducibility was produced. Instead, ADCs were placed by one observer and then checked by a senior neuroradiologist. I reduced the number of measurements to 3 and used a single ADC_{NAWM} for normalisation based on the fact that test

measurements of CSO ADC were extremely similar where the ROI was moved over a short distance. This was quicker and should still capture the lowest region(s) ADC, whilst allowing a degree of comparability to the Xing et al. results. In the volumetric study component, histogram percentiles were extracted, from which the best performing 5th percentile was designated VOI ADC_{min}. Therefore VOI and ROI ADC_{min} are not entirely comparable in my research. ADC values <0 were excluded from the histogram data, as ADC cannot adopt a negative value.

3.3.4.6 Sufficiency of segmentation double reads

The near perfect concordance for the 10% twice segmented cases suggests no systematic error unless made by both observers. However, it is possible that some of the most challenging cases, which were corrected manually, may have become excluded from double reading. The ICC calculation was performed from a volume comparison alone, with no geographic representation as it would be the case by applying a Dice score to quantify visual overlap (123).

3.3.4.7 Impact

To this date, the above research remains one of the largest comparisons of regional and volumetric ADC methods for glioma genotyping (Bhatti et al. in draft). Subsequent studies followed the use of $rADC_{mean}$ for molecular predictions (124,125).

Establishing how to measure, and to ensure sufficient reproducibility was an essential milestone towards predictive modelling. However, the citation number for this methodology research is lower (n=18) than for research focused on clinically relevant predictions (n=88, Chapter 4). Similarly, the multireader comparison of ADC_{NAWM} methods, which established the preference for centrum semiovale normalisation at a leading USA neuro-oncology institute is not yet widely cited (n=5, (126)). These citation figures could be influenced by a perceived lack of novelty in refining clinically available methods.

3.4 Conclusion

Because the accuracy of ADC values for IDH status prediction differed by enhancement pattern, and because certain visual characteristics may support diffuse glioma genotyping, I hypothesised that combining these would improve the molecular characterisation of WHO grade 2-3 diffuse gliomas. This topic is investigated in Chapter 4, including interobserver comparisons for several VASARI type features adapted by the knowledge gain from (56) and (71) .

Chapter 4: ADC, morphology and age for predicting IDH status

4.1 Background

In Chapter 1, the clinical availability of MRI sequences was examined, with a general lack of glioma quantitative assessments uncovered. Chapter 2 reviewed anatomical biomarkers for glioma genotyping and highlighted reproducibility as an unmet model requirement. Chapter 3 investigated the role of ADC values for genotyping, compared different measurement techniques and established interobserver concordance. The upcoming Chapter 4 discusses research into combining ADC, visual parameters and age for glioma characterisation. Because of the marked prognosis difference for the IDH^{wt} molecular group, the choice was made to pursue a new model for their binary distinction from both IDH^{mut} groups.

4.2 Research questions

- Which sufficiently reproducible imaging variable(s), with or without consideration of age, predict(s) IDH^{wt} status most accurately?
- Which multivariable combination predicts IDH^{wt} status most accurately?

4.3 Methods

Patients (n=290) with a tissue diagnosis of diffuse glioma WHO 2-3 were selected as the training cohort. The patient selection process and methods for regional ADC measurements (n=2900) have been described in Chapter 2 (104). $rADC_{mean}$ was adopted for model inputs as the parameter with the highest AUC value (AUC 0.83).

Three observers independently reviewed all MRI data sets blinded to diagnosis, age and to other observers. Feature categories were based on multiple previous publications (56,64,69,71,91). Tumour location, multifocality, enhancement pattern, non-enhancing tumour margin, haemorrhage, calcification, cysts, T2w/FLAIR mismatch, largest diameter and age were recorded. Three contrast patterns were defined: non-enhancing, patchy or solid, or rim enhancing with necrosis. Any avidly enhancing mass with central non-enhancing foci was assigned to the latter group. This was distinguished from cyst(s),

defined as exhibiting fluid signal isointense to cerebrospinal fluid with absent or minimal rim enhancement. T2w/FLAIR mismatch was specified according to Patel et al (20). Examples of different gliomas morphologies are shown in **Figure 22**.

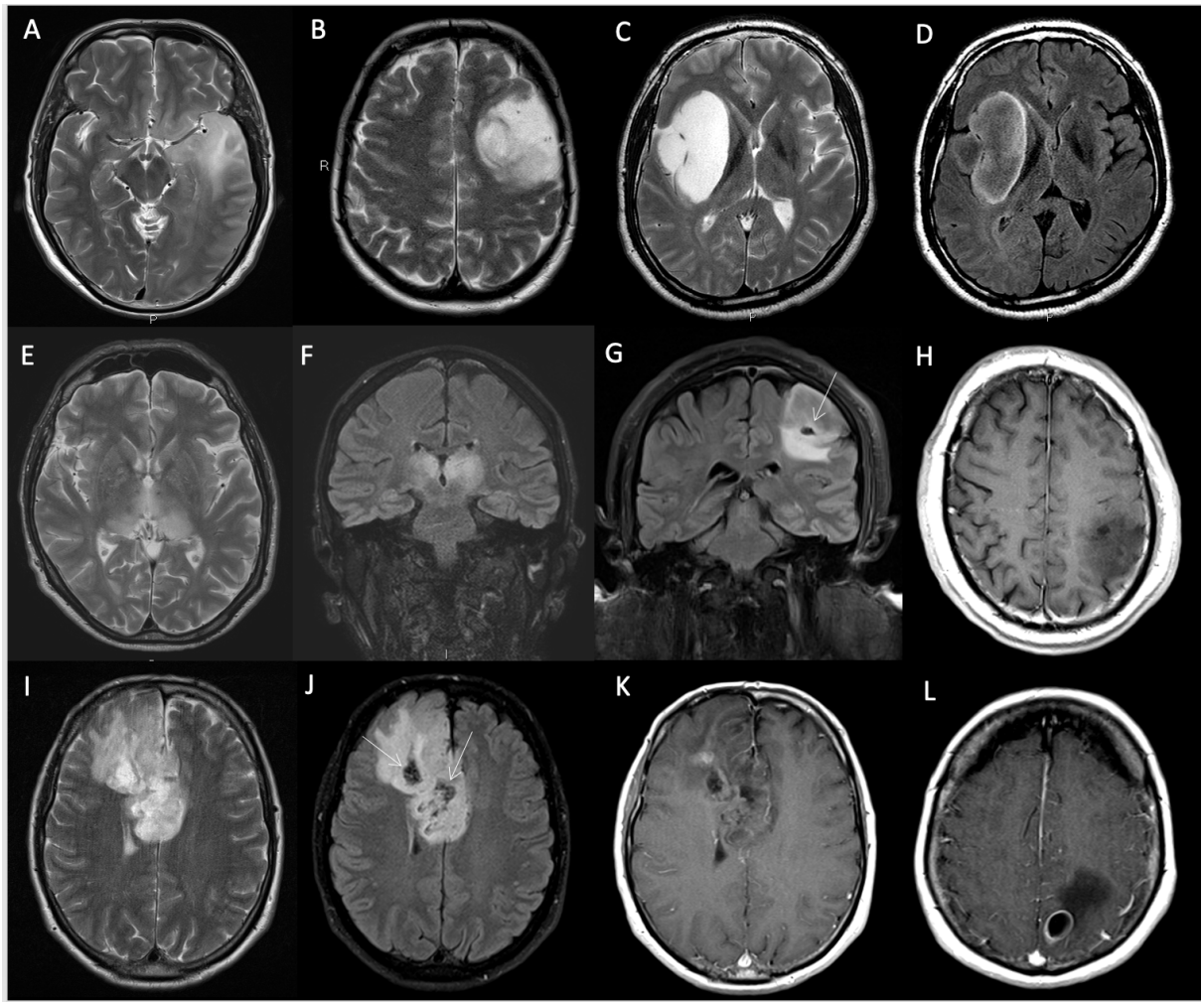

***Figure 22**. An example of typical WHO grade 2-3 glioma morphologies. T2w images showing a temporal IDH^{wt} glioma (a) versus a frontal IDH$^{mut/1p19qdel}$ oligodendroglioma (b). T2w and FLAIR mismatch and distinct margins (c, d) in an IDH$^{mut/1p19qint}$ astrocytoma. Indistinct T2w/FLAIR margins in a bithalamic IDH^{wt} glioma (e, f). FLAIR and T1CE images in a IDH$^{mut/1p19qint}$ astrocytoma with cyst formation (g, h). Larger cyst formation demonstrated on T2w, FLAIR and T1CE in an IDH$^{mut/1p19qdel}$ oligodendroglioma (i-k). T1w rim-enhancement and central necrosis in a parietal IDH^{wt} glioma (l). Featured in (127).*

Cohen's kappa (k) was used to test the observer agreement for morphologic categories, and the majority opinion was designated the final value. Morphologic categories, which achieved k>0.6 were selected for further analysis. Univariable logistic regression was applied to test if age, or morphology could predict IDH^{wt} status. Significant ($p<0.05$) features were tested as predictor variables in a multivariable binomial logistic regression

to predict IDH status. Starting from the highest p value, a backward elimination process (likelihood ratio test) was applied to discard features that did not contribute significantly to the prediction, concluding with the most parsimonious model (Model A). By the same method, an alternative model (Model B) was developed, into which calcification status was not entered.

The multivariable regression results were transcribed into a spreadsheet (Microsoft Excel for Mac version 14.5.2) formula to calculate the IDH^{wt} status probability for individual patients with glioma in an independent test cohort (n=49) of newly recruited gliomas, whereby a probability >0.5 would result in IDH^{wt} classification.

4.4 Results

Tumour location (k=0.81–0.89) and maximum diameter (<6 cm or >6 cm adopted from (69)) demonstrated good agreement (k=0.80–0.82). Calcification reached substantial agreement (k=0.67–0.74) with uncertain results excluded. Cyst identification (k 0.66–0.7) and categorisation of enhancement patterns yielded substantial agreement (weighted k=0.69–0.77). Limited agreement was found for non-enhancing tumour margin (weighted k=0.45–0.61), T2w/FLAIR mismatch (k=0.44–0.62), multifocality (k=0.20–0.46) and haemorrhage (k=0.29–0.51).

Several univariables were significant predictors of IDH genotype, namely age, enhancement category, and tumour location. Locations were grouped according to whether less than one-third, one to two-thirds, or more than two-thirds of tumours represented IDH^{wt} gliomas to reduce the number of variables for statistical analysis. The best performing multivariable model (Model A) consisted of $rADC_{mean}$, age, enhancement pattern, location category (frontal or insula, thalamus or brainstem, or elsewhere), and calcification. Using a likelihood cut-off value of 0.5 (50%), Model A correctly classified 231 of 252 (91.6%; 95% confidence interval [CI]: 88%, 95%) gliomas, with an AUC of 0.96 (95% CI: 0.93, 0.98). In developing this model A, 38 of 290 (13.1%) patients were excluded because of uncertain calcification status. The alternative model (Model B), consisted of $rADC_{mean}$, age, enhancement pattern, location category, and cyst(s). Model B correctly classified IDH status in 259 of 285 (90.9%; 95% CI: 88%, 94%) gliomas (AUC, 0.94; 95% CI: 0.93, 0.98). The results are shown in **Figure 23 and Table 13**.

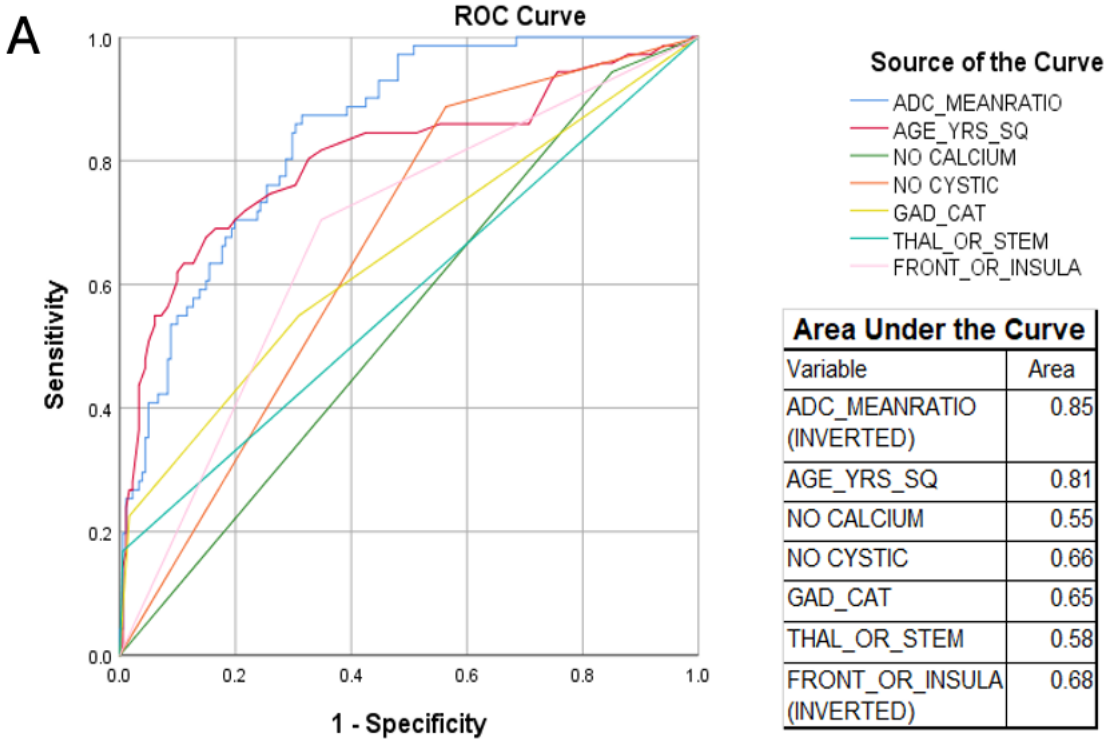

Area Under the Curve

Variable	Area
ADC_MEANRATIO (INVERTED)	0.85
AGE_YRS_SQ	0.81
NO CALCIUM	0.55
NO CYSTIC	0.66
GAD_CAT	0.65
THAL_OR_STEM	0.58
FRONT_OR_INSULA (INVERTED)	0.68

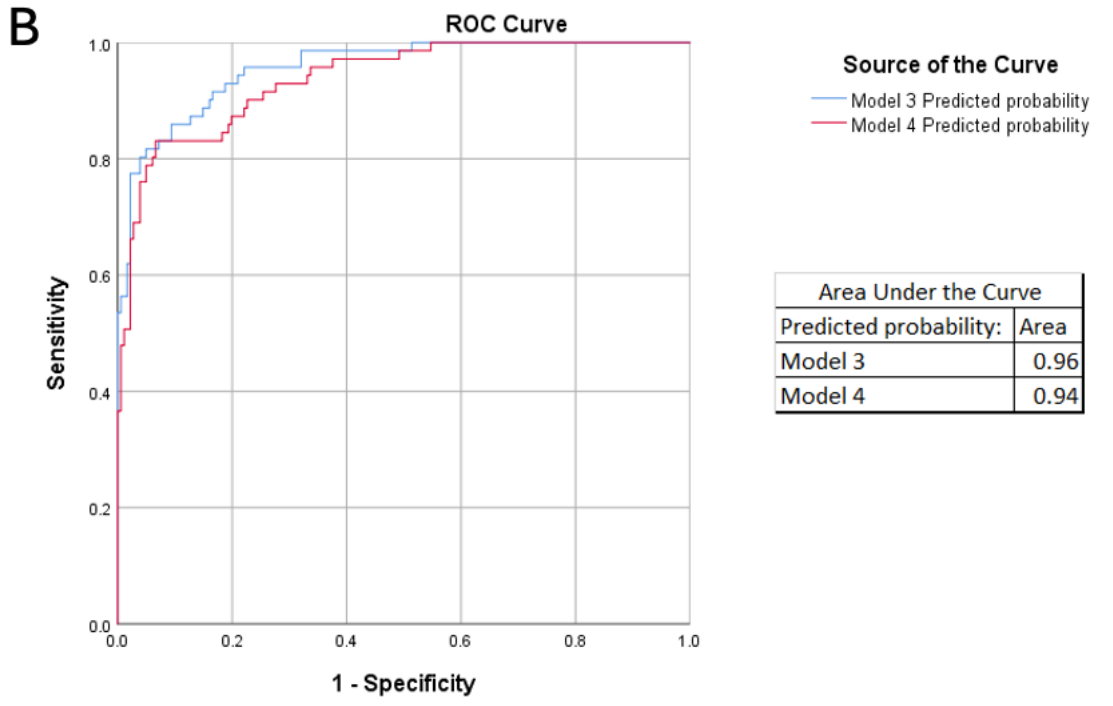

Area Under the Curve	
Predicted probability:	Area
Model 3	0.96
Model 4	0.94

Figure 23. *Univariable (a) and multivariable (b) logistic regression analysis to predict IDH status in the training cohort (n=82 IDH^{wt} and n=208 IDH^{mut}). rADCmean is coded as ADC_MEANRATIO. GAD_CAT refers to the contrast enhancement pattern.*

Using the Microsoft Excel formula (**Appendix 2**), IDH^{wt} status was predicted in a new test cohort (n=49) by a new blinded rater replicating the methods of the main study. In cases of uncertainty regarding calcification (n=5), the negative result (no calcification) was entered to permit results calculation. Model A correctly classified IDH^{wt} mutational status in 40 of 49 gliomas (82%) with 90% sensitivity and 83% specificity. Model B predicted IDH status in 42 of 49 (86%) gliomas, with a lower sensitivity of 75% but greater specificity of 91% (percentage correction aligned to results wording, page 118 (127)).

	Univariable		Model A		Model B	
Parameter	β level	P value	β level	P value	β level	P value
$rADC_{mean}$	-4.4	<0.001	-5.7	<0.001	-3.2	<0.001
age (years)	0.09	<0.001	-0.05	0.71*	-0.1	0.37*
age^2	0.01	<0.001	0.002	0.21*	0.002	0.09*
Enhancement						
None	Ref	Ref	Ref	Ref	Ref	Ref
Solid-patchy	0.64	0.03	-0.31	0.58	0.41	0.4
Rim	2.8	0.001	2.96	0.02	1.7	0.02
Tumour location category						
Front or insula[1]	Ref	Ref	Ref	Ref	Ref	Ref
Other[2]	1.3	<0.001	0.78	0.12	0.9	0.04
Thalamus or brainstem[3]	4.3	<0.001	3.6	0.01	3.6	0.02
Morphology						
Absence of calcification	1.1	0.045	4.3	<0.001	N/A	
Absence of cysts	1.9	<0.001	N/A		1.2	0.02
Constant	N/A		2.2	0.54	3.1	0.31
R^2	N/A		0.75		0.65	

Table 13. *Univariable and multivariable parameters for probability modelling of IDH status. Contents simplified from (127), with numbers previously rounded by one digit for publication. Age and age² are considered joint terms with a combined p<0.001, for which the likelihood ratio test confirmed a significant contribution to the models. [1]Indicates a tumour epicentre in the frontal lobe or insula. [2]Indicates a tumour in a location other than frontal lobe, insula, thalamus or brainstem. [3]Refers to a tumour in the thalamus or brainstem.*

4.5 Discussion

4.5.1 Advantages and drawbacks of kappa thresholding

The process of stratifying the morphological variables by statistical agreement served to increase the future reproducibility of model features. This is essential, as any model that appears excellent in training will not necessarily perform well in validation where human assessments are involved. It is noteworthy that the variable 'non-enhancing margin' yielded a significant result in the astrocytoma VASARI research and in the literature (71), but we omitted this due to limited reproducibility (k 0.45-0.61). It is possible that the inclusion of less reproducible variables could have aided genotype predictions in some cases. Furthermore, the ideal variable selection could differ for computational radiomics approaches, which may overcome subjectivity issues (128).

4.5.1 Category limitations

The VASARI feature set (64) offers a somewhat reproducible strategy to quantify Gadolinium enhancement by percentage and rim thickness but includes minimal pattern descriptions. The contrast categories in my own research are different but also simplistic. This choice was to facilitate interobserver agreement and to limit the number of variables for the model design. Subjectively, the evolution of contrast enhancement in glioblastoma (129) tends to differ from typical findings in IDH^{mut} gliomas (130). It may have been advantageous to perform a systematic search into contrast patterns for lower grade glioma genotyping prior to study start (130). The assessment of calcium and haemorrhage were limited by variable sequence availability. If consistent reviews of CT and SWI had been possible, this may have produced greater certainty and/or agreement for these categories. The exclusion of cases with uncertain calcium results could have risked overestimation of the Model A performance, however this was not confirmed in validation.

4.5.2 Model A or B

In the test cohort, Model A correctly classified IDH mutational status in 40 of 49 (82%) gliomas, and Model B predicted IDH status in 42 of 49 (86%) gliomas. This would make Model B appear slightly preferable. However, the Model B sensitivity was lower (75%)

compared to that of Model A (90%). Model A could thus be the safer option when applied for the purpose of early glioblastoma identification. The development of Model B was in response to statistics advice when discussing practical limitations of calcium identification. No alternative options to arrive at a single best performing model were explored. Both models suffered errors in gliomatosis, where a post hoc analysis revealed 1/9 gliomas misclassified as IDH^{mut} by Model A and 3/9 by Model B. Gliomatosis was previously considered a distinct tumour type but since WHO 2016 is defined as a radiological tumour growth pattern, which can occur in both IDH genotypes (131). In our study, these cases were characterised by relatively high rADC values (1.73–1.87).

4.5.3 Lack of 1p19q status prediction

$IDH^{mut/1p19q}$ oligodendroglioma is the only diffuse glioma to show frequent calcification without prior treatment. Therefore it appears reasonable to assign mineralised gliomas to this class (97% specificity, 100% observer agreement in (93)) without probability modelling. In my research, a narrower model strategy to predict IDH was favoured over attempting to predict three genotypes, because optimisation for two outcomes would reduce the group sizes and could deteriorate model performance for IDH genotyping. Where a three group distinction was recently attempted by a numerical scoring system (132), the 1p19q status prediction in non-enhancing gliomas was solely based on ADC values.

A small number of $IDH^{mut/1p19qdel}$ were falsely classed as IDH^{wt} by Model A and B. For these individuals, an earlier tissue diagnosis would not necessarily be detrimental. The $IDH^{mut/1p19qdel}$ group ultimately undergoes resection or at least a biopsy, and chemotherapy only commences once a definitive tissue diagnosis has been secured.

4.5.4 Considerations for model refinements

It could be valuable to further pursue the development of one final model, possibly by combining cyst and calcification status. The methods in this research were based on the strategy of an intensive care tool (Paediatric Index of Mortality, PIM), which has undergone iterative calibrations (133) by means of multivariable logistic regression using large sets of data. We adopted the PIM convention of entering the 'normal' variable in case of an unknown result, which may not always be justified. The variable coding for 'cyst(s)'

and 'calcification' followed a system of aligning the result with IDH^{wt} status, thus 1=no calcification, 1=no cysts in the model, which is counterintuitive. The variable 'age^2' was developed due to an exponential relationship between age and IDH^{wt} status. In both models, age became adopted as the joint term ($age+age^2$) by backward elimination. The joint term seems to function in the probability formula, however this could appear confusing to new users.

Like many colleagues, I have subsequently focussed on computational research (automated ADC extraction by deep learning methods). Instead it may have been preferable to externally validate the multivariable models. Recently, Model A and B have demonstrated ability to perform IDH genotyping in a second independent cohort (116,134), which is further discussed in Chapter 6.

4.5.5 Impact

I delivered a strategy to predict IDH status immediately in clinic, without the need for software installation or new code. This could be an opportunity to shorten waits to biopsy, particularly for patients with non-enhancing early glioblastoma to avoid initial observation periods.

This study has shaped other research, in which several groups replicated IDH prediction through a combination of visual categories, ADC and age (124,132). The similarities in the choice of morphological descriptors, enhancement patterns and lobar grouping underscore that these are valuable parameters. Nearly identical ADC ROI placements were adopted by Du et al. (Figure 1 in (124)) to good effect. Several citing researchers closely replicated feature stratification by reproducibility (135–137).

IDH genotyping approaches have employed either complex MRI acquisitions, machine learning analyses or both (138,139) without achieving substantial gains in diagnostic accuracy. Interestingly, in one study with imaging parameters similar to ours, a machine learning approach was outperformed by logistic regression (140). Artificial intelligence studies may systematically overestimate T1CE performance for IDH genotyping by including WHO 4 glioblastoma. This is further discussed in Chapter 6.

4.6 Conclusion

By combining individual imaging biomarkers and age, accurate predictions of WHO grade 2-3 glioma were possible. Nevertheless, rADC represents a simplistic measure of tumour diffusivity, which did not predict IDH status in centrally necrotic gliomas. Therefore a further comparison of volumetric and regional ADC for visually heterogenous gliomas was pursued. The question arose if a computational extraction of ADC, T1CE and/or T2w glioma features could assist genotyping. The investigation of these two topics is detailed in Chapter 5.

Chapter 5: Histogram analysis of visually complex gliomas

5.1. Background

In Chapters 3 and 4 the performance of ADC_{mean} and ADC_{min} for glioma genotyping was investigated. In solid tumours, regional measurements appeared equivalent to whole tumour ADC, but in rim-enhancing, necrotic gliomas (n=25) only volumetric measurements were associated with IDH status (104). This raised the question if a detailed volumetric ADC analysis could characterise visually complex gliomas better.
A histogram approach was chosen to visualise the cumulative distribution of ADC signal intensities and to extract statistical data in two studies: Firstly, we examined a rare, newly classified tumour type with heterogenous MRI morphology: Histone-altered diffuse midline glioma (HAG) (141). In brief, HAG are defined by epigenetic alterations, which commonly involve the histone H3 K27M (HAG K27M). HAG K27M are highly aggressive brain tumours with a propensity for adolescent onset, however they can occur at any age. The second study focused on MRI texture analysis in diffuse gliomas (WHO grades 2-4)(33). For this, computer-filtered ADC, T1CE and T2w histograms were analysed using proprietary software (TexRAD).

5.2 Imaging features of H3 K27M histone-altered diffuse midline glioma

5.2.1 Research questions

- What are the ADC histogram observations in HAG K27M, a newly classed type of midline glioma?
- Does the application of a recently published ADC threshold (142) correctly classify the HAG K27M genotype?
- Are ROI derived ADC results in HAG K27M statistically different from volumetric ADC histogram parameters?

5.2.2 Methods

The entire institutional cohort (n=15, age 14–64 years, dates 2016-2019) with a HAG K27M integrated diagnosis was analysed. Tissue was examined microscopically, followed by immunostaining and molecular analysis according to latest protocols (32,143).
Imaging was acquired at multiple institutions as discussed previously (104,127). ADC maps were calculated with Olea Sphere v2.3. Two consultant neuroradiologists placed ADC_{mean}, $rADC_{mean}$, ADC_{min}, $rADC_{min}$ regions of interest (ROIs) according to the prior methods (104,114). An exploratory visual rating was performed to record tumour epicentre, T2w/FLAIR signal characteristics, border definition, enhancement pattern, cysts and necrosis (**Figure 24**).

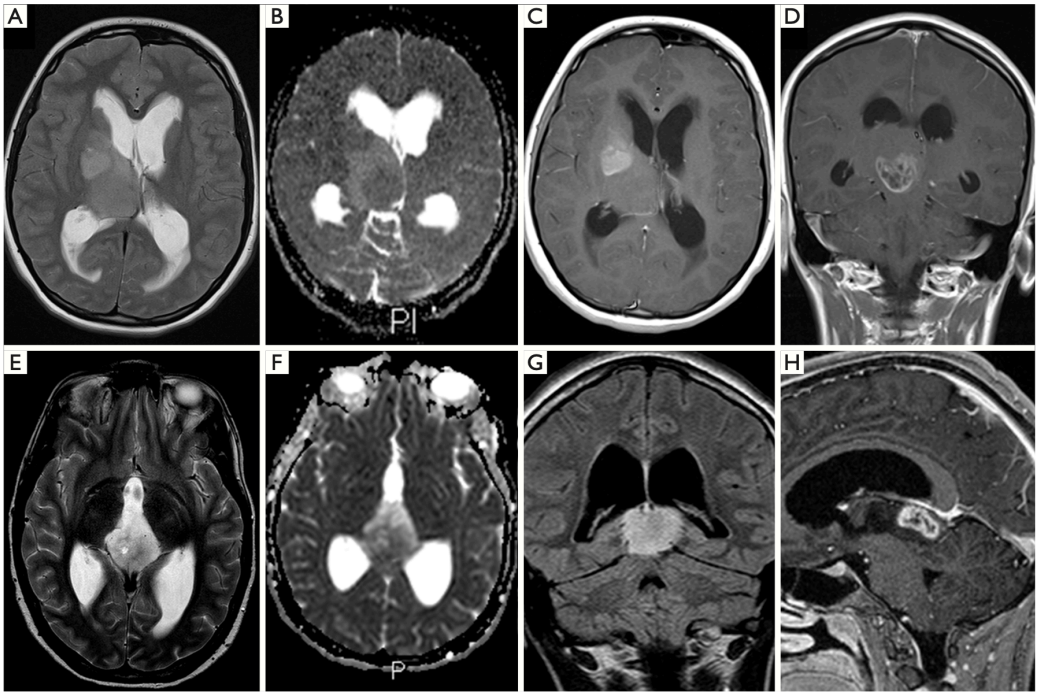

Figure 24*. T2w, ADC and T1CE images in two patients (Case 1 (A-D) and Case 12 (E-H)) with histone-altered (HAG K27M) diffuse midline glioma. Featured in (141).*

Volumetric segmentations (excluding macroscopic necrosis) were completed to produce ADC histogram data. For this, VOIs were drawn onto the b0 images (with T2w and T1CE side by side) in Olea Sphere v2.3 with an automated VOI copy generated on the ADC map. From this ADC volume, a cumulative histogram was extracted for each glioma and transcribed into Microsoft Excel. The T2w (b0) total tumour volumes were recorded. Statistical analysis was performed in SPSS 25 to extract histogram parameters, and to test

for differences between the ROI and VOI histogram values (Wilcoxon signed rank test for related samples).

5.2.3 Results

The HAG K27M group average was calculated for each ADC parameter. For ROI ADC_{min}, this was 0.84 (±0.15 standard deviation, SD) $\times 10^{-3} mm^2/s$. The ROI ADC_{mean} group average was 1.12 (±0.25) $\times 10^{-3} mm^2/s$. The ROI $rADC_{min}$ group average measured 1.097 (±0.149), and the ROI $rADC_{mean}$ group average was 1.466 (±0.299).

Figure 25 shows examples of the ADC histogram curves obtained in the HAG K27M cohort. A biphasic distribution was evident in 2/15 histograms, suspected to represent inclusion of necrotic tissue. A significant difference was observed only between the 2^{nd} centile of the entire tumour ADC histogram and ROI ADC_{min} (p=0.01). Comparisons of ROI ADC_{min} with the 5^{th} and 10^{th} histogram percentiles showed no statistical differences. No differences were identified between ROI $rADC_{min}$ and the VOI $rADC_{5th\ percentile}$. The comparisons between ROI ADC_{mean} and the VOI histogram ADC_{median} and ADC_{mean}, and comparisons between their normalised counterparts were all non-significant (p>0.05). All HAG K27M were in contact with the brain midline. Lesion volumes ranged from 9.2 to 103.1 cm^3. The definition of the non-enhancing tumour margin appeared variable, whereby most lesions demonstrated heterogeneous T2 and FLAIR signal. None of the H3 K27M histone-mutant gliomas exhibited a T2w/FLAIR mismatch. Several tumours contained haemorrhage. No calcification was identified, and two tumours contained cysts. Rim-enhancement surrounding necrosis was present in 10/15 (67%).

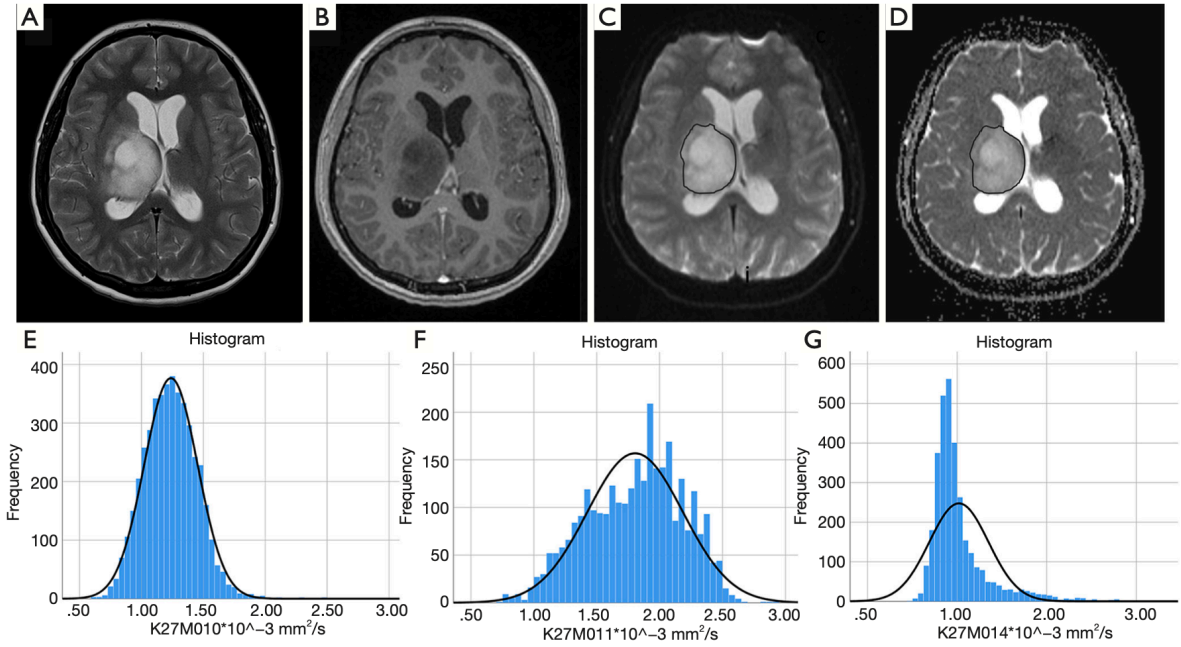

***Figure 25**. ADC histograms in HAG K27M. T2w (A), T1w+contrast (B), b0 (C) and ADC map (D) showing an example segmentation (Case 10). ADC histograms in 3 different patients (Case 10, 11 and 14) (E-G). Featured in (141).*

5.2.4 Discussion

5.2.4.1 Cohort size

Because the maximum institutional sample was small, an observational study was conducted. A diagnostic accuracy study comparing histone-altered and wild-type tumours was omitted, which would have been limited by numbers. Group differences would have been missed in this way. Because of the rarity of HAG K27M care was taken to ensure anonymity in the publication, including consultation of the institutional Caldicott guardian.

An alternative approach would have been to consider waiting, and to collaborate with other centres to enlarge the dataset for the study. Molecular testing for H3 K27M status at NHNN preceded partner institutions, hence an attempt to initiate a retrospective multicentre study could not be taken further at the time. H3 K27M testing methods commenced differently (144), which means possible changes to the reference standard over time, e.g. through novel antibody development (145).

5.2.4.2 Consensus assessment

The structural MRI assessment was conducted in consensus, as the number of cases was small for an observer comparison. The same visual categories were used as in Chapter 4, for which statistical agreement had been tested. The conclusion from this pilot observation is that HAG K27M glioma morphology and ADC values vary substantially. This is not as helpful as a new biomarker, but awareness could potentially avoid dismissing the possibility of this rare tumour type where the imaging does not match textbook examples.

5.2.4.3 Diagnostic yield of the cumulative histograms

The ADC signal intensity plotting as cumulative histograms graphically highlighted heterogenous diffusion within tumours, and differences between individuals with HAG 27M. Diffusivity may vary according to the stage of tumour evolution, whereby growing malignant gliomas can rapidly develop necrosis (146). Histogram differences between individuals were observed despite segmenting solid appearing tissue, which could be attributed to microscopic necrosis, or more broadly to genetic-metabolic differences between cancers of the same WHO class (119,147).

Within the limitations of sample size, no specific ADC percentile cluster was identifiable as a biomarker for HAG K27M. As shown in **Figure 25**, there is case-by-case variability in the histogram shape and its kurtosis, and in the ADC median. Because no statistical differences were observed between most ROI and VOI ADC metrics, it remains unclear if these could be used interchangeably in HAG 27M. The difference between the 2nd histogram percentile and ROI ADC_{min} is explainable by multiple ROI averaging. One comparative study (Aboian et al. n=60) identified no statical difference in ADC histogram parameters for HAG K27M and K27M wild-type midline gliomas (148), whereas another study proposed greater kurtosis and skewness as HAG K27M findings (149).

5.2.4.4 Knowledge gain

This study delivered an important piece of knowledge in the form of a discrepancy: Chen et al. had published data on ADC measurements in HAG K27M (n=19) compared to a K27M wild-type patient group (142). The authors proposed an ADC_{min} threshold of ($0.728\times10^{-3}mm^2/s$) and $rADC_{min}$ threshold of 0.982 for HAG K27M classification.

However, the majority of ADC_{min} (87%) and $rADC_{min}$ (80%) results in the NHNN patient cohort exceeded this threshold. Because Chen's study coincided in time, the NHNN analysis was blinded to their threshold.

The result is important, because the surgical biopsy of midline gliomas carries an increased morbidity risk with some UK centres avoiding tissue diagnosis in the brainstem in favour of empirical therapy. This means that an erroneous diagnosis of a HAG K27M glioma as 'wild-type' with a more favourable risk profile may receive initial undertreatment. This becomes problematic with the HAG K27M prognosis being dismal, often under 12 months (150). Furthermore, patients with a histone H3 K27M alteration could be eligible for a new agent ONC201 (Dordaviprone), after this recently demonstrated survival benefit (151).

5.3 HAG 27M systematic literature review

To move forward from the small observational study, my team performed a systematic literature review to summarise findings in histone altered gliomas, specifically HAG K27M (152). This identified 47 publications, of which 21 were case reports, underscoring the rarity of the disease. The majority (39/47) described HAG K27M altered gliomas (often reported as H3 K27M-mutant, reflecting a recent nomenclature change), and two described both HAG K27M and H3 G34R-mutant gliomas (HAG G34R). HAG G34R are rare cerebral hemispheric gliomas with a more favourable prognosis. These will not be further discussed in the thesis, as no original research was conducted for this genotype. Studies varied substantially in their methods design with all being retrospective and most (n=17) lacking information on whether MRI was analysed blinded to tissue results. HAG K27M occurred most commonly in the paediatric and young adult population (153,154), anywhere along the midline, whereby location propensities were described for the thalamus in adults (155,156) and brainstem in children (148,157). Midline location has recently become a mandatory diagnostic criterion for HAG K27M (158). HAG K27M exhibited variable T2/FLAIR morphology and margins, and contrast patterns in research. No consistent visual distinction of HAG K27M from K27M wild-type midline gliomas was established (142,153). HAG K27M may lack the extensive contrast uptake, which is typical in advanced glioblastoma. The proposal of ADC metrics to predict HAG 27M status remains based on limited data (156,159), and facilitated diffusion does not

exclude this lethal neoplasm. Furthermore, ADC may differ according to specifics of the histone abnormality (160).

In summary, the combination of the pilot study and literature review produced no imaging biomarker for HAG K27M molecular status. The diagnostic contribution from analysing volumetric histogram ADC data was not superior to ROI measurements for this genotype.

5.4 Future research in HAG K27M

To this date, no large imaging studies have investigated HAG K27M. Pooling data for this tumour type may ultimately identify distinctive features, or at least trends. In the NHNN case series, two tumours exhibited high perfusion (rCBV 3.5-5.9). Based on subsequent research, which identified significantly elevated rCBV in the HAG K27M group (n=94)(156)), it could be valuable to further investigate the role of perfusion modalities. This may also support the distinction of therapy effects ('pseudoprogression') as a complication of radiation and chemotherapy, perhaps in a multimodal approach (161). Limits of harmonisation can be expected, especially in paediatric advanced MRI, and technical challenges will arise in smaller brainstem cross-sections. Only one publication exists for HAG K27M genotyping by machine learning (162), where future research may achieve new ways of non-invasive tumour classification.

5.5 Filtration histogram texture analysis in diffuse glioma

5.5.1 Background

Computational imaging analysis has the potential to resolve intricate disease patterns, which are inaccessible to human vision (163). A plethora of methodologies exists by now to characterise cancer by feature extraction, termed radiomics, with or without machine learning. An opportunity arose at UCL to test a new software 'TexRAD' (164) for the purpose of glioma genotyping.

TexRAD employs a process termed filtration-histogram based MR imaging texture analysis (MRTA) to extract 1st order statistical data (165). Using the TexRAD desktop application, MRI sequences are loaded for viewing followed by manual tumour outlining and initiation of the analysis by mouse-click.

TexRAD commences with a filtration step, which aims to remove image noise, extract and enhance tissue features of different sizes before measuring signal intensity histogram parameters. Based on multiple CT studies and initial glioma data (166), my research team hypothesised that TexRAD may improve the MRI based distinction of diffuse glioma genotypes.

5.5.2 Research question

- How accurately can TexRAD derived MRI parameters predict diffuse glioma (WHO grade 2-4) genotypes?
- Which, if any, MRI sequence is preferable for IDH genotyping with TexRAD?

5.5.3 Methods

Cases were identified from attendances for operative planning (n=124) between 2010 and 2016. Fourteen patients were excluded due to a non-glioma histological diagnosis, 11 patients due to prior surgery, and 2 studies had corrupted imaging data. In total, 97 gliomas were eligible for MRTA, amounting to a similar sample size as in prior studies using the same software (166,167). All image interactions were performed blinded to histological and molecular diagnosis using TexRAD version 3.3 (www.texrad.com, part of Feedback Plc, Cambridge, UK).

Segmentations were performed slice by slice with the software's freehand drawing function. On T2w and ADC maps, the entire tumour volumes were segmented. On T1CE, 3 types of segmentation (Seg A, Seg B, Seg C) were completed by a student with training and regular supervision by a consultant. **Figures 26** and **27** show example segmentations.

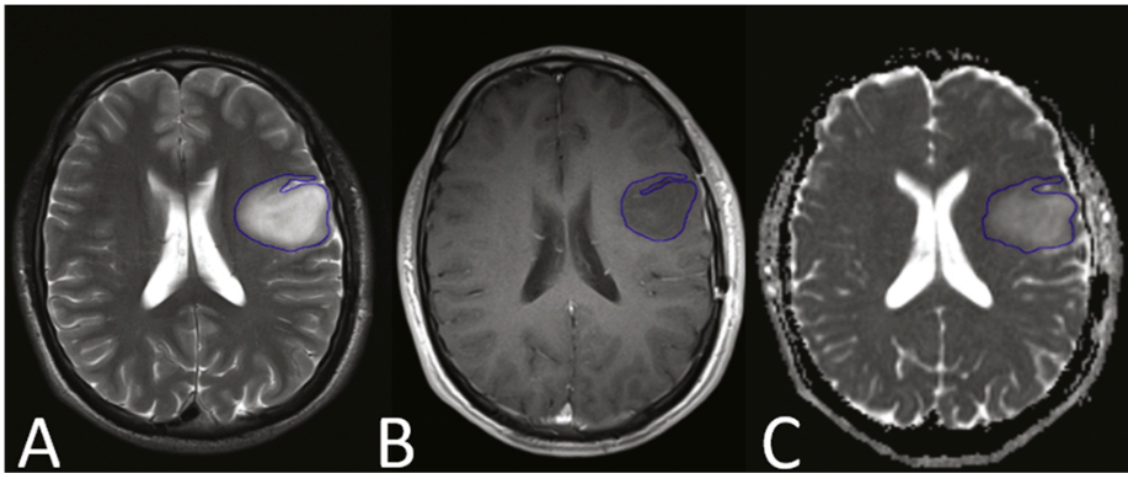

***Figure 26**. TexRAD freehand segmentation of a WHO grade 3 IDH$^{mut/1p19qint}$ glioma by including the entire lesion on T2w (a), T1CE (b) and on the ADC map (c).*

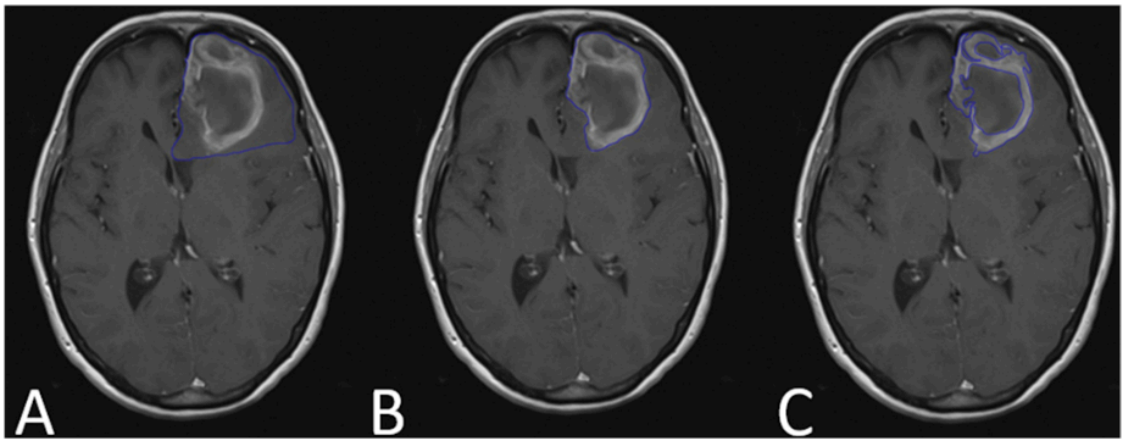

***Figure 27**. An example of the 3 different segmentation techniques for T1CE images: Segmentation of the entire lesion (Seg A), of the enhancing lesion inclusive of necrosis (Seg B) and of the enhancing lesion excluding necrosis (Seg C).*

Slices containing very few (<250) pixels of signal abnormality were excluded to avoid partial volume effects (mean slice size 4803 pixels, range 349–15499). In addition, the image with the largest glioma cross-section based on pixel count was subjected to a single slice evaluation.

5.5.3.1 TexRAD script

TexRAD MRTA follows a published method that was originally developed in CT (168). The filtration employs spatial scale filter (SSF) values of 0, 2mm, 3mm, 4mm, 5mm and 6mm in width (radius). SSF=0 hereby means no filtration, SSF=2 mm equals a fine texture

scale, SSF=3–5 mm a medium texture scale, and SSF=6 mm translates to a coarse texture scale (**Figure 28**).

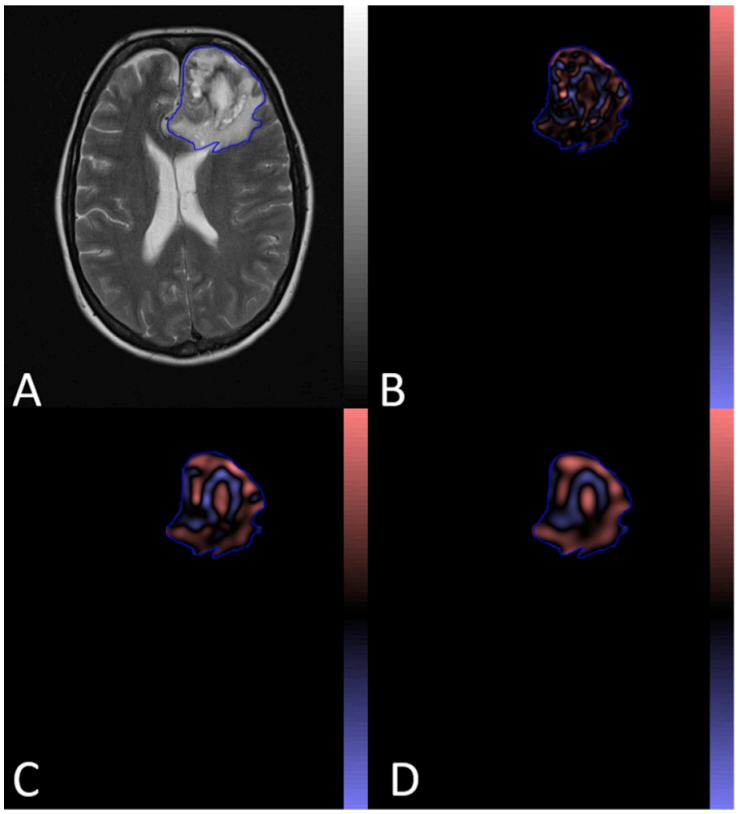

Figure 28*. TexRAD filtration steps consisting of T2w glioma segmentation (a) and volume of interest filtration using scaled texture filters (SSF=2 (b), SSF=4 (c) and SSF=6 (d)). Towards larger filter sizes, larger objects become amplified in the filtered image.*

Following filtration, histogram parameters (mean, standard deviation, entropy, mean of positive pixels, skewness, kurtosis) were extracted from the tumour volumes and slices, respectively. TexRAD automates the statistical process for this.

The ability of texture features to determine genotype was tested by non-parametric (Mann Whitney U for IDH, Kruskal-Wallis ANOVA for three genotypes) testing. This was repeated over different subgroup analyses e.g. according to WHO grade. For statistically significant results, a receiver operating characteristic (ROC) analysis was undertaken, to determine the area under the curve (AUC), and optimum cut-offs for sensitivity and specificity calculations. A multivariable logistic regression model was generated to combine the best results from all sequences for IDH genotyping.

5.5.4 Results

50 females and 47 males with an average age of 43.3 (27–77) years were included in the TexRAD study. The histological, molecular and glioma enhancement characteristics of the patient cohort are shown in **Table 14**.

WHO grade	N	IDH^{wt} (e/e+n)*	$IDH^{mut/1p9qint}$ (e/e+n)*	$IDH^{mut/1p9qdel}$ (e/e+n)*
2	54	4 (0/0)	24 (2/1)	26 (2/0)
3	20	3 (1/0)	7 (1/0)	10 (4/1)
4	23	12 (11/8)	10/5/1)	1
Total	97	19 (12/8)	41 (8/2)	37 (6/1)

***Table 14**. WHO grades, IDH and 1p19q status of the glioma population analysed by TexRAD. *e/e+n denotes solid-patchy enhancing/rim-enhancing + necrosis.*

5.5.4.1 TexRAD T1CE analysis

Filtered T1CE histogram parameters predicted IDH status variably (**Table 15**). Across the combination of WHO grades 2-4 (n=91), the SSF 6-filtered signal intensity mean derived from Seg A (the entire enhancing and non-enhancing tumour) yielded a moderate sensitivity of 72.2%, specificity 74% and AUC = 0.801. Hereby, the T1w signal intensity values were higher in the IDH^{wt} group.

T1CE (VOI)						
Seg A	SSF	Mean	SD	Skewness	Kurtosis	Sens/Spec
WHO 2-4 (IDH^{wt}=18) (IDH^{mut}=73)	0	NS	0.695**	NS	NS	66.7/61.3
	2	0.752	0.743*	0.633**	NS	72.2/71.2
	3	0.764*	0.718**	0.737*	NS	83.3/68.5
	4	0.786*	0.706**	0.759*	NS	83.3/69.9
	5	0.800*	0.697**	0.701*	NS	72.2/69.9
	6	0.801*	0.699**	NS	NS	72.2/74

***Table 15**. TexRAD volumetric analysis of T1CE imaging for Seg A (WHO grades 2-4). SSF = spatial scale factor, *p-value <0.005, **p-value <0.05. NS indicates not significant. Adapted from (33).*

When analysing the glioblastoma (WHO grade 4) group separately, the mean derived from Seg A was the best parameter for IDH genotyping with a sensitivity of 91.7%, specificity 88.9% and AUC 0.935 for SSF 4 (**Table 16**) with n=21 cases contributing to this analysis.

T1CE (VOI)						
Seg A	SSF	Mean	SD	Skewness	Kurtosis	Sens/Spec
WHO 4 (IDH^{wt}=12) (IDH^{mut}=9)	0	NS	0.769*	NS	NS	66.7/100
	2	0.778*	0.870*	0.880**	NS	83.3/89.9
	3	0.861*	0.870*	0.917*	NS	83.3/100
	4	0.935*	0.852*	0.852*	NS	91.7/88.9
	5	0.917*	0.824**	0.769*	NS	83.3/100
	6	0.907*	0.815**	NS	NS	83.3/77.8

***Table 16**. TexRAD volumetric analysis of T1CE imaging for Seg A (WHO grade 4). SSF = spatial scale factor, *p-value <0.005, **p-value <0.05. NS indicates not significant. Adapted from (33).*

If Seg B (enhancing tumour inclusive of necrosis) was analysed, the standard deviation (SD) represented the most distinctive parameter with a sensitivity of 87.5%, specificity 100% and AUC 0.969 (also SSF 4) with n=12 cases contributing to this analysis (**Table 17**).

T1CE (VOI)						
Seg B	SSF	Mean	SD	Skewness	Kurtosis	Sens/Spec
WHO 4 (IDH^{wt}=8) (IDH^{mut}=4)	0	NS	NS	NS	NS	NS
	2	NS	NS	NS	NS	NS
	3	NS	0.938*	NS	NS	75/100
	4	NS	0.969*	NS	NS	87.5/100
	5	NS	0.906*	NS	NS	87.5/100
	6	NS	NS	NS	NS	NS

***Table 17**. TexRAD volumetric analysis of T1CE imaging for Seg B (WHO grade 4). SSF = spatial scale factor, *p-value <0.005. NS indicates not significant. Adapted from (33).*

Using Seg C (solid enhancing tissue only), kurtosis became the best IDH status predictor across all filters with a best sensitivity 91.9%, specificity 100%, AUC = 0.945 (**Table 18**) with n=16 cases in this analysis.

T1CE (VOI)						
Seg C	SSF	Mean	SD	Skewness	Kurtosis	Sens/Spec
WHO 4 (IDH^{wt}=11) (IDH^{mut}=5)	0	NS	NS	NS	0.836*	91.9/100
	2	NS	NS	NS	0.927*	91.9/100
	3	NS	0.855*	0.836*	0.891*	91.9/100
	4	NS	0.891*	0.782*	0.818*	91.9/100
	5	NS	0.873*	NS	0.855*	91.9/100
	6	NS	NS	NS	0.945*	91.9/100

***Table 18**. TexRAD volumetric analysis of T1CE imaging for Seg C (WHO grade 4). SSF = spatial scale factor, *p-value <0.005. NS indicates not significant. Adapted from (33).*

For 1p19q genotyping of lower grade IDH^{mut} gliomas, the TexRAD analysis of Seg A produced a sensitivity of 77.4%, specificity of 77.8% and AUC 0.736 (**Table 19**) with n=64 cases in this analysis.

T1CE (VOI)						
Seg A	SSF	Mean	SD	Skewness	Kurtosis	Sens/Spec
WHO 2-3 IDH^{mut} (1p19int =31) (1p19del =33)	0	NS	NS	0.736*	NS	77.4/77.8
	2	0.725*	NS	NS	NS	75.8/64.5
	3	0.735*	NS	NS	NS	81.8/61.3
	4	0.735*	NS	NS	NS	78.8/61.3
	5	0.738*	NS	NS	NS	75.8/61.3
	6	0.750*	NS	0.659	NS	75.8/61.3

***Table 19**. TexRAD volumetric analysis of T1CE imaging for 1p19q status prediction in IDH^{mut} gliomas (WHO grades 2-3). SSF = spatial scale factor, *p-value <0.005. NS indicates not significant. Adapted from (33).*

5.5.4.2 TexRAD ADC analysis

Table 20 lists the results analysis of ADC values for n=82 cases with available DWI. For the combination of WHO grades 2-4, ADC skewness without filtration performed moderately for IDH genotyping (sensitivity 77.8%, specificity 68.7%, AUC = 0.791). The

unfiltered ADC_{mean} was inferior, for example for a threshold of 1.14 ^$10^{-3}$$mm^2$/s (sensitivity 64.1%, specificity 66.7% and AUC 0.694).

ADC (VOI)						
All gliomas	SSF	Mean	SD	Skewness	Kurtosis	Sens/Spec
WHO 2-4 (IDH^{wt}=18) (IDH^{mut}=64)	0	0.694**	NS	0.791*	0.734*	77.8/68.7
	2	NS	NS	NS	NS	NS
	3	NS	NS	NS	0.694**	66.7/64.9
	4	NS	NS	NS	0.693**	66.7/68.7
	5	0.655**	NS	NS	0.727*	72.2/62.5
	6	0.674**	NS	0.659	0.736*	77.8/67.2

***Table 20**. TexRAD volumetric analysis of ADC maps (all gliomas, WHO grades 2-4). SSF = spatial scale factor, *p-value <0.005, **p-value <0.05. NS indicates not significant. Adapted from (33).*

When excluding cases with macroscopic necrosis (n=11) from the analysis, the ADC_{mean} area under the curve improved with a limited sensitivity 68.3%, specificity 91.9% and AUC 0.82 for SSF 6 (**Table 21**) in n=71 cases available for this analysis.

ADC (VOI)						
Solid gliomas	SSF	Mean	SD	Skewness	Kurtosis	Sens/Spec
WHO 2-4 (IDH^{wt}=11) (IDH^{mut}=60)	0	0.753**	NS	0.811*	0.755**	72.7/88.3
	2	0.785*	NS	NS	0.736**	73.3/81.8
	3	0.809*	NS	NS	0.782*	71.7/81.8
	4	0.791*	NS	NS	0.776*	66.7/81.8
	5	0.800*	NS	NS	0.800*	66.7/81.8
	6	0.818*	NS	NS	0.802*	68.3/91.9

***Table 21**. TexRAD volumetric analysis of ADC maps (solid gliomas, WHO grades 2-4). SSF = spatial scale factor, *p-value <0.005, **p-value <0.05. NS indicates not significant. Adapted from (33).*

For non-enhancing gliomas (n=58), the IDH status prediction using ADC_{mean} was slightly further improved (sensitivity 85.7%, specificity 78.4%, AUC 0.88, also for SSF 6) (**Table 22**). TexRAD single slice ADC_{mean} by drawing around the peripheral tumour margin produced a limited sensitivity of 67.2%, specificity 66.7% and AUC 0.73 for IDH status.

ADC (VOI)						
Non-enhancing	SSF	Mean	SD	Skewness	Kurtosis	Sens/Spec
WHO 2-4 (IDH^{wt}=7 (IDH^{mut}=51)	0	0.733*	NS	0.843*	0.751*	71.4/88.2
	2	0.824*	NS	NS	0.745*	74.5/85.7
	3	0.832*	NS	NS	0.784**	70.6/85.7
	4	0.815*	NS	NS	0.787**	68.6/85.7
	5	0.818*	NS	NS	0.849*	71.4/82.4
	6	0.840*	NS	NS	0.877*	85.7/78.4

***Table 22**. TexRAD volumetric analysis of ADC maps (non-enhancing gliomas, WHO grades 2-4). SSF = spatial scale factor, *p-value <0.005, **p-value <0.05. NS indicates not significant. Adapted from (33).*

For the detection of the 1p19q co-deletion in IDH^{mut} gliomas, unfiltered ADC_{mean} analysis yielded a sensitivity 95.0%, specificity of 85.0% and AUC 0.811, but this excluded IDH^{wt} tumours.

5.5.4.3 TexRAD T2w analysis

All of the T2w results were inferior to T1w+contrast and ADC. These are not listed here in further detail (maximum AUC 0.69) but are visible in (33).

5.5.4.4 TexRAD multivariable model

A logistic regression model was generated combing the best results from T1CE, T2w and ADC volumes for cases with three available MRI sequences, merging WHO grades 2-4 (n=80, 63 IDH^{mut}/17 IDH^{wt}). This produced a highly accurate prediction of IDH status (AUC 0.98, **Table 23**).

Combined sequences (T1CE+ADC+T2w)					
Multivariable	SSF	AUC	Min (95% CI)	Max (95% CI)	Sens/Spec
WHO 2-4 (n=80)	0	0.937*	0.877	0.998	88/88
	2	0.937*	0.887	0.987	86/94
	3	0.942*	0.894	0.990	87/94
	4	0.980*	0.955	1.000	90/94
	5	0.895*	0.857	1.000	90/88
	6	0.937*	0.869	1.000	100/83

***Table 23**. Multivariable regression analysis of the best performing T1CE, ADC and T2w parameters. One individual multivariable model was created for each filter. SSF = spatial scale factor, *p-value <0.005. NS indicates not significant. Adapted from (33).*

5.5.5 Discussion

5.5.5.1 WHO grade 4 sample

IDH^{wt} glioblastoma represents the most common type of adult diffuse glioma. It is correspondingly overrepresented in epidemiology literature (169) and in public imaging databases (170,171). In the TexRAD analysis of n=97 gliomas, the proportion of WHO grade 4 tumours was limited (n=12, 12%). In retrospect, this discrepancy most likely reflects the path of recruitment via clinical science, who provided anonymised preoperative MRI data for the study. Although consecutive gliomas were enrolled, the study population is skewed towards lower WHO grades, most likely because these frequently undergo functional MRI/diffusion tractography planning at NHNN. This explains why WHO grades 2-3 would preferentially appear on the enrolment list for any given time frame, whilst glioblastomas may undergo urgent surgery based on external hospital MRI, with few or no planning sequences repeated. With this, an imbalance of genotypes was present.

Since the TexRAD research, the tumour class 'glioblastoma' has undergone interpretative changes. Since 2021, IDH^{mut} astrocytomas of the WHO grade 4 are no longer termed glioblastoma under consideration of further genetics including CKDN2A/B genetic status (172). The nomenclature WHO grade 4 oligodendroglioma (n=1 in this analysis) is discontinued, reflecting the better prognosis for this genetic group (173). This means limitations to the interpretability of the TexRAD study results and reference standard.

5.5.5.2 TexRAD ADC analysis

ADC mean, skewness and kurtosis were informative histogram parameters to predict glioma IDH status. For ADC kurtosis, the highest AUC values (AUC 0.88, non-enhancing gliomas) were observed. This finding is plausible from a pathophysiological perspective, as rapidly evolving malignancy may translate into tissue heterogeneity. However, the volumetric segmentation derived TexRAD ADC results are barely superior to the single slice ROI $rADC_{mean}$ (AUC 0.84) methods described in Chapter 3.

The TexRAD parameter kurtosis refers to the tailedness of the cumulative histogram curve comprising all ADC voxels in the image segmentation. This differs from diffusion kurtosis imaging (DKI), which represents an advanced diffusion model based on a more complex (including multiple b values >1000 s/mm^2) image acquisition. DKI has been proposed as a biomarker for IDH status, however controversy remains regarding its value above standard DWI/ADC (174).

The TexRAD result for single slice ADC was inferior to a margin-sparing largest tumour cross-section ROI (104). Employing TexRAD software for volumetric ADC read-outs was laborious with each tumour slice requiring manual outlining prior to statistical analysis. Furthermore, it was not possible to copy segmentations onto another sequence (e.g. b0 to ADC). Therefore, the TexRAD tumour volume slightly varied by sequence (as illustrated in Figure 26). The software was freely usable at our institution but would otherwise have required new funding, permissions and installation.

5.5.5.3 Filtration

For all MRI sequences the AUC values varied depending on which TexRAD filter was used. Towards larger filter sizes larger objects become emphasised, yet the biological meaning of this remains unclear from the study. Furthermore, which was the most 'accurate' filter varied by imaging parameter and by tumour grouping. Concerns have been raised about limited repeatability of signal intensity and texture features generally (175), and this may also apply to TexRAD. The MRI studies originated from multiple vendors and machines with unquantified technical variations, and their impact on filtration remains unknown.

5.5.5.4 Alternative T1CE segmentations

When segmenting entire tumours including non-enhancing tissue (Seg A), mean T1w values were most diagnostic of IDH status across WHO grades 2-4. This finding could relate to contrast avidity, where a previous study by Yamauchi et al. observed dense contrast-enhancement preferentially in IDH^{wt} gliomas (75). The result may also be influenced by larger non-enhancing components, which have been observed in IDH^{mut} higher grade tumours (176). Regarding Seg B, greater necrosis is a known feature associated with IDH^{wt} status and poor prognosis (177). The small number of IDH^{wt} tumours in this study precludes any firm conclusions from the data.

The standalone performance of T1CE (AUC 0.8) was inferior to the rapid probability calculation, which was developed in WHO grade 2-3 (Chapter 4, Model A and B). Most avidly enhancing, necrotic tumours are glioblastoma requiring no TexRAD or ADC measurement to achieve the correct working diagnosis.

5.5.5.5 Learning from proprietary MRTA

Although the study confirmed differences between the glioma genotypes, no gain in accuracy or speed was identified above software-free probability modelling. The results were not subjected to further research. A search into other studies using TexRAD reveals numerous statistically significant associations, mostly without independent test sample validation (178).

The diagnostic accuracy of TexRAD appears promising on first glance. Particularly, the multisequence (T2, T1CE, ADC) model was accurate (AUC of 0.98). However, this involved assembly of 6 multivariable models, which could have been subject to overfitting based on the limited dataset and lack of a test sample.

Moreover, for exploring statistical associations the TexRAD technical environment did not support multiple test corrections, where the research would be at risk of type 1 statistical errors (179). The statistical outputs of TexRAD are not transparent, as the best performing parameters vary by sequence, by segmentation and by filter. Thus, potentially spurious findings and statistical associations may result in overestimation of the software performance and are open to misinterpretation.

5.5.5.6 Impact

Several observations from this research are useful. The performance for ADC-based IDH typing of gliomas was slightly better for non-enhancing tumours. This aligns to prior data and means that software could adopt a role in identifying IDH^{wt} gliomas of 'low grade' morphology. Secondly, the T1CE TexRAD performance was improved by excluding necrotic elements. This result could be relevant for future genotyping approaches, in which larger numbers of enhancing gliomas are featured.

The publication of this research has received 38 citations to date (27th September 2024). Although the conclusion 'MRTA is a software platform without machine learning, which can assist the distinction of glioma IDH and 1p19q molecular subtypes' remains broadly warranted, I would hesitate to use this product again.

Computational image analysis is desirable for automation and in this case offered a rapid histogram analysis compared to the Olea-SPSS methods in (141), but the segmentation process was slow. Computing is not universally superior to radiologist analysis in terms of accuracy, reproducibility or, as in this case, time penalty. Furthermore, proprietary software should offer value for money. The TexRAD retail price approximated to £15K, whereby subsequently a science colleague produced a workable histogram extraction script minus filtration in one day (104).

5.6 Conclusion

Major technical advances, particularly in the realm of computing, have occurred since the studies described in Chapters 1-5. The final Chapter 6 is focused on new developments in glioma imaging, and how the outputs of my research relate to these.

Chapter 6: Glioma imaging in 2024 and beyond

From the research discussed in Chapters 1-5, several conclusions follow: Firstly, radiologist assessment using a reproducible feature system may enable glioma molecular diagnosis without new software, training or costs. Secondly, predicting WHO grade 2-3 glioma IDH status is in many cases achievable using clinically available MRI sequences. Finally, no superiority was identified for volumetric ADC histogram analysis in three studies (33,104,141) at a single institution, for an evolving dataset. Yet, the theoretical benefit of more sophisticated analysis methods cannot be negated.

The Models A and B have undergone recent testing at a new centre (University of Nottingham, UoN) in a sample of consecutive gliomas (WHO grade 2-4, January-December 2023). Model A (including calcification) yielded an accuracy of 95.4%, and Model B (including cysts) was 97.2% accurate for IDH status prediction (134) (rater ST, blinded to tissue diagnosis and age). When used by a resident (NM, ST4), Model B (accuracy 91.7%) fractionally outperformed Model A (accuracy 87.0%) with approximately 10% gain over guessing IDH status (116). Unlike the NHNN training cohort, the new grade-unselected sample contained n=81/108 (77%) glioblastomas with WHO grade 4 microscopy results. These data support the role of a probability calculation for a different mix of glioma grades. Model B was preferred by the resident due to uncertainty about calcification status.

The $rADC_{mean}$ measurements (ICC 0.86-0.98) and visual criteria (kappa 0.76-0.9) were reproducible for the UoN cohort. Prospective validation is under consideration, which would ideally extend to further UK centres.

Results from the ADC research have featured in peer education (T. Yousry, ESNR Advanced Course in Neuroradiology (180)) and major textbooks (39,181). Currently, ADC maps still receive mostly qualitative reports, including in neuro-oncology ('restriction' yes/no). In July 2024, my research team completed a statistical meta-analysis (n=32 studies) of ADC performance for glioma genotyping, stratified according to measurement techniques and WHO grade composition (Bhatti et al, submitted to ECR 2025). This demonstrated statistical equivalence of several volumetric and regional ADC parameters for IDH genotyping, together with evidence that white matter normalisation could be omitted. The latter step would not be justified in the Model A/B probability formula (127) without recalibration.

MRI technology is continuously evolving with refinements to hardware, signal generation and postprocessing. This includes new ultra-high field opportunities for preclinical and human scanning (182). Many advanced imaging modalities in development have shown potential for applications in cancer. For example, oncometabolite MRS (40), chemical exchange saturation transfer (CEST) MRI, positron emission tomography (PET) methods (183) and Deuterium metabolic imaging (DMI) (184) may in the future support glioma molecular diagnosis and mapping treatment response.

In 2024, the translation of physiological MRI into clinical neuro-oncology remains partial at best. Advanced MRI biomarkers in glioma are mostly based on level 3 evidence as newly summarised for a European Society of Radiology initiative (ST for DWI, CEST (185,186)). Amongst MRI modalities with clinical availability (34), perfusion and MRS could be considered as today's alternative options for glioma genotyping. In a recent meta-analysis, the performance of DSC perfusion for IDH status identification was moderate (79%, pooled sensitivity and 82% specificity (187). A different meta-analysis advocated 2-hydroxyglutarate magnetic resonance spectroscopy (2HG MRS) for IDH genotyping, based on n=2 studies (188). Cystathionine MRS was recently proposed as a biomarker of 1p19q codeletion (189). Subsequently, the MRS combination of Cystathionine and 2HG achieved excellent specificity but limited sensitivities for genotyping (62% for IDH, 33% for 1p19q)(190). In summary, perfusion and MRS are complimentary but not currently superior for glioma molecular diagnosis.

Artificial intelligence (AI) approaches have flooded the literature in many topic areas, including cancer detection and prediction (191). Computational successes are emerging in glioma using machine learning approaches, including deep learning (DL). DL functions by an artificial neural network, resembling the connectivity of the human brain. It integrates data from multiple assessment 'layers', from which intelligent decision making can solve complex tasks. DL is potentially game-changing through its ability to detect hidden image hallmarks but generates classifications from a myriad of parameters in an obscure ('black-box') way.

Transparent and reliable AI could ultimately outperform simpler strategies and resolve observer dependence for IDH genotyping (192). Automated glioma segmentations have featured in the BraTS challenges with UNet as a particularly successful method (193–195). My UCL research team recently automated the process of T2w volumetric

segmentation and ADC extraction for the NHNN dataset (104), achieving nearly equivalent results (Wu J et al. in draft) based on an nnUNet algorithm.

A different DL algorithm for combined segmentation and classification (196) achieved precise IDH genotyping (AUC 0.99, n=95, Anderson J, MSci Computer Science, UoN 2024) despite limited visual overlap of the DL masks with gliomas. At multiple research sites (Erasmus MC, UoN, UCL), a part-prospective validation study has been delayed by computer scientist staff shortages. Certain workflow issues may improve with greater integration of radiomics scripts into imaging routine (197). Automated approaches are economically attractive, as these could become very time efficient and do not suffer fatigue. However, high level computation does not uniformly translate into diagnostic value, as highlighted by the survival prediction in VASARI-auto (R^2 0.245 (198)). Importantly, task-based AI lacks intuition and may fail at new problem solving.

The high proportion of advanced IDH^{wt} glioblastoma amongst all diffuse gliomas in real life (169) and in public databases (199) probably inflates the performance of AI tools for IDH genotyping (200). Specifically, such cohort compositions may overestimate the contribution of T1CE to molecular diagnosis (201). Indeed, genotypes and WHO grade mixes have the potential to impact research outputs for any imaging biomarker. For example, paucity of $1p19^{codel}$ in a public dataset (202) may ease the distinction of IDH^{wt} from IDH^{mut} ADC values (boxplots, Figure 15). It is also known that rarity of one class limits the learning of AI. Thus, it could be essential to develop tools with a focus on genotyping solid gliomas, if the aim is to identify early IDH^{wt} tumour stages.

As the UK's view has shifted upon improving brain tumour outcomes with the promise of a transformative investment linked to the Tessa Jowell initiative (203), the emphasis on early diagnosis cannot be strong enough (204,205). After all, this has been the stepping stone to revise the prognosis for many systemic cancers.

Appendix 1

Publications in this thesis

This thesis is based on the following peer-review publications, which are presented in the order of appearance in each chapter. Impact factors (IF) and citation figures were obtained on 21st November 2024. My contributions to each manuscript are listed in italics with co-author signatures supplied to the University of East Anglia by separate documentation.

Chapter 1

Thust SC, Heiland S, Falini A, Jäger HR, Waldman AD, Sundgren PC, Godi C, Katsaros VK, Ramos A, Vernooij MW, Yousry T, Bendszus M, Smits M. Glioma imaging in Europe: A survey of 220 centres and recommendations for best clinical practice. Eur Radiol. 2018 Mar 13. doi: 10.1007/s00330-018-5314-5. These are current international imaging recommendations endorsed by the European Society of Neuroradiologists.

Principal author, design of the investigation, conduct of the research, analysis of the outcome, consensus formulation of international guidance, manuscript preparation for publication (IF 5.2, 212 citations).

Manfrini E, Smits M, **Thust S**, Geiger S, Bendella Z, Petr J, Solymosi L, Keil VC. From research to clinical practice: a European neuroradiological survey on quantitative advanced MRI implementation. Eur Radiol. 2021 Aug;31(8):6334-6341.

Collaborator, contributions to design of the investigation, interpretation of the outcome and manuscript preparation for publication. Discussion of this work in the thesis was essential to justify why advanced MRI was omitted from probability modelling. (IF 5.2, 30 citations).

Okuchi S, Hammam A, Golay X, Kim M, **Thust S**. Endogenous chemical exchange saturation transfer imaging for the diagnosis and therapy response assessment of brain tumors: a systematic review. Radiology: Imaging in Cancer 2020. doi.org/10.1148/rycan.2020190036.

Senior author, design of the investigation, conduct of the research (lead for literature searches, lead for consensus), analysis of the outcome, manuscript preparation for publication (IF 5.2, 12 citations).

Chapter 2

Hyare H, Rice L, **Thust S**, Nachev P, Jha A, Milic M, Brandner S, Rees J. Modelling MR and clinical features in grade II/III astrocytomas to predict IDH mutation status. Eur J Radiol. 2019 May;114:120-127.

Collaborator, contributions to conduct of the research and manuscript preparation for publication. Discussion of this work in the thesis was essential to justify the need for feature stratification by reproducibility and for a radiologist-led predictive model. (IF 3.2, 36 citations).

Lasocki A, Anjari M, Örs Kokurcan S, **Thust SC**. Conventional MRI features of adult diffuse glioma molecular subtypes: a systematic review. Neuroradiology. 2021 Mar;63(3):353-362.

Senior author, design of the investigation, conduct of the research (lead for literature searches, 50% data extraction and QADAS-2, lead for consensus), analysis of the outcome, manuscript preparation for publication (IF 3.1, 59 citations).

Chapter 3

Thust SC, Hassanein S, Bisdas S, Rees JH, Hyare H, Maynard JA, Brandner S, Tur C, Jäger HR, Yousry T, Mancini L. Apparent diffusion coefficient for molecular subtyping of non-gadolinium-enhancing WHO grade II/III glioma: volumetric segmentation versus two-dimensional region of interest analysis. Eur Radiol 2018 Sep;28(9):3779-3788.

Principal author, ethics approval, design of the investigation, conduct of the research, interpretation of the outcome, manuscript preparation for publication (IF 5.2, 69 citations).

Thust SC, Maynard JA, Benenati M, Wastling SJ, Mancini L, Jaunmuktane Z, Brandner S, Jäger HR. Regional and Volumetric Parameters for Diffusion-Weighted WHO Grade II and III Glioma Genotyping: A Method Comparison. AJNR Am J Neuroradiol. 2021 Mar; 42(3):441-447.

Principal author, ethics approval, design of the investigation, conduct of the research, analysis of the outcome, manuscript preparation for publication (IF 5, 19 citations).

Chapter 4

Maynard J, Okuchi S, Wastling S, Busaidi AA, Almossawi O, Mbatha W, Brandner S, Jaunmuktane Z, Koc AM, Mancini L, Jäger HR, **Thust S**. World Health Organization Grade II/III Glioma Molecular Status: Prediction by MRI Morphologic Features and Apparent Diffusion Coefficient. Radiology. 2020 Jul;296(1):111-121.

Senior and corresponding author, ethics approval, design of the investigation (including methodology of kappa thresholding, location grouping by incidence), leader of a team of 5 observers, conduct of the research, analysis of the outcome, manuscript preparation for publication (IF 29.1, 91 citations).*

**This project was perceived by UCL examiners as beyond MRes scope. Major contributions to statistical analysis and to all manuscript components, including the 1st draft. Sole manuscript handler through the publication in a leading journal.*

Chapter 5

Thust S, Micallef C, Okuchi S, Brandner S, Kumar A, Mankad K, Wastling S, Mancini L, Jäger HR, Shankar. Imaging characteristics of H3 K27M histone-mutant diffuse midline glioma in teenagers and adults. Quant Imaging Med Surg. 2021 Jan;11(1):43-56.

Principal author, NHS institutional approval, design of the investigation, conduct of the research, analysis of the outcome, manuscript preparation for publication (IF 2.9, 26 citations).

Lasocki A, Abdalla G, Chow G, **Thust SC**. Imaging features associated with H3 K27- altered and H3 G34-mutant gliomas: a narrative systematic review. Cancer Imaging. 2022 Nov 17;22(1):63.

Senior author, design of the investigation, conduct of the research (lead for literature searches and consensus), analysis of the outcome, manuscript preparation for publication (IF 5.6, 18 citations).

Lewis MA, Ganeshan B, Barnes A, Bisdas S, Jaunmuktane Z, Brandner S, Endozo R, Groves A, **Thust SC**. Filtration-histogram based magnetic resonance texture analysis (MRTA) for glioma IDH and 1p19q genotyping. Eur J Radiol. 2019 Apr;113:116-123.

*Senior and corresponding author, ethics approval, design of the investigation, contributions to conduct of the research and analysis of the outcome, manuscript preparation for publication (*IF 3.2, 38 citations).

Appendix 2

Formula

The log odds ratios for Model A and B in (127) were calculated as follows:

Model A: [LA = (25.71 x $rADC_{mean}$) + (20.05 x age) + (0.002 x age^2) + (20.32 x solid contrast enhancement) + (2.96 x rim contrast enhancement) + (0.78 x tumour location = other) + (3.58 x tumour location in thalamus or brainstem) + (4.34 x absent calcification) + 2.24].

Model B: [LB = (-3.23 x $rADC_{mean}$) + (20.1 x age) + (0.002 3 age^2) + (20.41 x solid contrast enhancement) + (1.66 x rim contrast enhancement) + (0.86 x tumour location = other) + (3.64 3 tumour location in thalamus or brainstem) + (1.17 x absent cyst or cysts) + 3.07].

Each tumour is assigned one contrast enhancement category only, meaning a result of 1 is assigned for the tumour's enhancement category and 0 for the contrast categories that are not applicable. Accordingly, the tumour location is designated 1 for the applicable category and 0 if not in this category.

Calcification (Model A) and cysts (Model B) are coded as 1 if present and as 0 if absent. In the case of an uncertain result of calcification, 0=absent is entered.

The probability of IDH^{wt} is calculated for Model A and B by using the following equation: 1/(1 + e2L), where L is the relevant log odds ratio.

Appendix 3

Scientific oral presentations and posters

Bhatti, F, Strobel J, Tench C, Grech-Sollars M, Dineen RA, Sollmann N, **Thust S**. Apparent diffusion coefficient for the characterisation of untreated gliomas: a systematic review and meta-analysis. Submitted to ECR Annual Meeting, Vienna 2025

Bhatti F, Menon N, Maynard J, Wastling S, Morgan P, Smith S, Paine S, **Thust S**. A rapid probability calculator for glioma IDH genotyping: diagnostic gain for rater in-training. Power pitch and scientific poster. BSNR Annual Meeting, Bristol 2024

Bhatti F, Menon N, Maynard J, Wastling S, Morgan P, Smith S, Paine S, **Thust S**. Validation of a rapid probability calculator for glioma IDH genotyping. Scientific poster. ESNR Annual Meeting, Paris 2024

Oliveira-Stahl G, Inglese M, **Thust SC**, Grech-Sollars M. Machine learning based characterisation of glioma shows best performance with post-contrast T1 and diffusion imaging. 3rd prize, scientific poster. BIC-ISMRM Annual Meeting, Aberdeen 2023

Lasocki A, Abdalla G, Chow G, **Thust SC.** Imaging features associated with H3 K27- altered and H3 G34-mutant gliomas: a narrative systematic review. Oral presentation. BSNR Annual Meeting, Liverpool 2022

Thust SC, Micallef C, Okuchi S, Brandner S, Kumar A, Mankad K et al. Diffusion-weighted MR imaging characteristics of H3 K27M histone-mutant diffuse midline glioma in teenagers and adults. Oral presentation. ESNR Annual Meeting, Oslo 2019

Okuchi S, Hammam A, Golay X, Kim M, **Thust S**. Endogenous chemical exchange saturation transfer (CEST) MR imaging for the diagnosis and therapy response assessment of brain tumors: A systematic review. Oral presentation. ESNR Annual Meeting, Oslo 2019

Maynard JA, Okuchi S, Wastling S, Al-Busaidi A, Almossawi O, Mbatha W, ..., **Thust SC**. Clinical MR imaging for WHO grade II/III glioma molecular subtyping: diffusion, age and morphology evaluation system. Oral presentation. ESNR Annual Meeting, Oslo 2019

Mbatha W, Okuchi S, Mancini L, Jaunmuktane Z, Brandner S, Golay X, **Thust SC**. Region of interest derived ADC quantification: interobserver results in WHO grade II/III gliomas. Power pitch and poster. ESNR Annual Meeting, Rotterdam 2018

Okuchi S, Mbatha W, Mancini L, Brandner S, Jaunmuktane Z, Golay X, **Thust SC**. Apparent diffusion coefficient in WHO II/III grade glioma – association with IDH or TERT genotype? Power pitch and poster. ESNR Annual Meeting, Rotterdam 2018

Thust SC, Heiland S, Falini A, Jäger HR, Waldman AD, Sundgren PC et al. Glioma imaging in Europe: A survey of 220 centres and recommendations for best clinical practice. Oral presentation. SNR XXI Symposium Neuroradiologicum, Taipei 2018

Thust SC, Hassanein S, Bisdas S, Rees JH, Hyare H, Maynard JA et al. Apparent diffusion coefficient for molecular subtyping of non-gadolinium-enhancing WHO grade II/III glioma: volumetric segmentation versus two- dimensional region of interest analysis. Oral presentation. SNR XXI Symposium Neuroradiologicum, Taipei 2018

Thust S, Hassanein S, Bisdas S, Rees J, Hyare H, Tur C, Brandner S, Jager R, Mancini L. Diffusion-weighted MR imaging for molecular subtyping of low to intermediate grade glioma lacking Gadolinium contrast enhancement. Oral presentation. BSNR Annual Meeting, Cambridge 2017.

Lewis M, Ganeshan B, Barnes A, Mancini L, Bisdas S, Groves A, Endozo R, **Thust S**. Volumetric texture analysis of clinical MR imaging for the identification of IDH wild type glioma. Oral presentation. BSNR Annual Meeting, Cambridge 2017

Hyare H, Rice L, **Thust SC**, Nachev P, Jha A, Milic M, Islam S, Brander S, Rees J. The effect of IDH mutation status on MR features and clinical outcomes in grade II/III astrocytomas. BSNR Annual Meeting, Cambridge 2017.

Thust S, Bisdas S, Rees JH, Hyare H, Brander S, Hassanein S, Jager R, Siddiqui A, Mancini L. Diffusion MRI may support the identification of non-enhancing IDH wild type astrocytoma. BNOS Annual Meeting, Edinburgh 2017.

Thust S, Yousry T, Bagallo N, Vernooij M, Smits M. Glioma MR imaging practices in Europe: Results from the ESNR Diagnostic Subcommittee Survey on Glioma Imaging. RSNA Annual Meeting, Chicago 2016.

Thust S, Yousry T, Bagallo N, Vernooij M, Smits M. Glioma MR imaging practices in Europe: Results from the ESNR Diagnostic Subcommittee Survey on Glioma Imaging. Oral presentation. ESNR Annual Meeting, Belgrade 2016.

Appendix 4

Further publications

Thorpe J, **Thust SC**, Gillon, G Rowe S, Swain CE, MacArthur DC, Howarth SP, Avula S, Morgan PS, Dineen RA. Comparison of echo planar and turbo spin-echo diffusion-weighted imaging in intraoperative MRI. J Magn Reson Imaging 2024 Oct 10. doi: 10.1002/jmri.29614. Online ahead of print.

Chelliah A, Wood DA, Canas LS, Shuaib H, Currie S, … **Thust SC**… Glioblastoma and Radiotherapy: multi-center AI study for survival predictions from MRI (GRASP study). Neuro Oncol. 2024 Jun 3;26(6):1138-1151.

Gupta M, Anjari M, Brandner S, Fersht N, Wilson W, **Thust S**, Kosmin M. Isocitrate dehydrogenase 1/2 wildtype adult astrocytoma with WHO grade 2/3 histological features: molecular re-classification, progrnostic features, clinical outcomes. Biomedicines 2024 Apr 18;12(4):901.

Karschnia P et al*. A framework for standardized tissue sampling and processing during resection of diffuse intracranial glioma: joint recommendations from four RANO groups. Lancet Oncol, 2023, Nov;24(11):e438-e450.***Thust SC** named expert rater

Cornell I, Al Busaidi A, Wastling S, Anjari M, Cwynarski K… **Thust SC**. Early MRI predictors of relapse in primary central nervous system lymphoma treated with MATRix immunochemotherapy. J Pers Med. 2023 Jul 24;13(7):1182.

Doig D, Thorne L, Rees J, Fersht N, Kosmin M, Brandner S, Jäger HR, **Thust S.** Clinical, Imaging and Neurogenetic Features of Patients with Gliomatosis Cerebri Referred to a Tertiary Neuro-Oncology Centre. J Pers Med. 2023 Jan 27;13(2):222.

McNamara C, Mankad K, **Thust S**, Dixon L, Limback-Stanic C, D'Arco F et al. 2021 WHO classification of tumours of the central nervous system: a review for the neuroradiologist. Neuroradiology. 2022 Oct;66(10):1919-1950.

Shuaib H, Barker GJ, Sasieni P, De Vita E, Chelliah, … **Thust SC** et al. Overcoming Challenges of translating deep learning models for glioblastoma: the ZGBM consortium. Br J Radiol. 2022 May 26;20220206. Doi:10.1259\bjr.20220206.

Le Rhun E, Devos P, Winklhofer S, Lmalen H, Brandsma D, …, **Thust S** et al. Prospective validation of a new imaging scorecard to assess leptomeningeal metastasis: a joint EORTC BTG and RANO effort. Neuro Oncol. 2022 Oct 3;24(10):1726-1735.

Thust S, Veneziano L, Parkinson MH, Bhatia KP, Mantuano E, Gonzalez-Robles C, Davagnanam I, Giunti P. Altered pituitary morphology as a sign of benign hereditary chorea caused by TITF1/NKX2.1 mutations. Neurogenetics. 2022 Apr;23(2):91-102.

Fox CP, Ali AS, McIlroy G, **Thust S**, Martinez-Calle N, Jackson AE et al. A phase 1/2 study of thiotepa-based immunochemotherapy in relapsed/refractory primary CNS lymphoma: the TIER trial. Blood Adv. 2021 Oct 26;5(20):4073-4082.

Okuchi S, Rojas-Garcia A, Ulyte A, Lopez I, Ušinskienė J, Lewis M, Hassanein SM, Sanverdi E, Golay X, **Thust S**, Panovska-Griffiths J, Bisdas S. Diagnostic accuracy of dynamic contrast-enhanced perfusion MRI in stratifying gliomas: A systematic review and meta-analysis. Cancer Med. 2019 Sep;8(12):5564-5573.

Kim M, Torrealdea F, Adeleke S, Rega M, Evans V, Beeston T, Soteriou K, **Thust S**, Kujawa A, Okuchi S, Isaac E, Piga W, Lambert JR, Afaq A, Demetriou E, Choudhary P, Cheung KK, Naik S, Atkinson D, Punwani S, Golay X. Challenges in glucoCEST MR body imaging at 3 Tesla. Quant Imaging Med Surg. 2019 Oct;9(10):1628-1640.

Agn M, Munck Af Rosenschöld P, Puonti O, Lundemann MJ, Mancini L, Papadaki A, **Thust S**, Ashburner J, Law I, Van Leemput K. A modality-adaptive method for segmenting brain tumors and organs-at-risk in radiation therapy planning. Med Image Anal. 2019 May;54:220-237.

Mansoor NM, **Thust S**, Militano V, Fraioli F. PET imaging in glioma: techniques and current evidence. Nucl Med Commun. 2018 Dec;39(12):1064-1080.

Halstead S, Scott G, **Thust S**, Hann G. Review of the new RCR guidelines (2017): The radiological investigation of suspected physical abuse in children. Arch Dis Child Educ Pract Ed. 2019 Dec;104(6):309-312.

Thust SC, van den Bent MJ, Smits M. Pseudoprogression of brain tumours. J Magn Reson Imaging. 2018 May 7;48(3):571-589.

Bisdas S, Shen H, **Thust S**, Katsaros V, Stranjalis G, Boskos C, Brandner S, Zhang J. Texture analysis- and support vector machine-assisted diffusional kurtosis imaging may allow in vivo gliomas grading and IDH-mutation status prediction: a preliminary study. Sci Rep. 2018 Apr 17;8(1):6108.

D'Arco F, O'Hare P, Dashti F, Lassaletta A, Loka T, Tabori U, Talenti G, **Thust S** et al. Volumetric assessment of tumor size changes in pediatric low-grade gliomas: feasibility and comparison with linear measurements. Neuroradiology. 2018 Apr;60(4):427-436.

Szychot E, Seunarine K, Mankad K, **Thust S**, Clark C, Gaze MN, Michalski A. Impact of induction chemotherapy, hyperfractionated accelerated radiotherapy and high-dose thiotepa on brain volume loss and functional status of children with primitive neuroectodermal tumour. Pediatr Blood Cancer. 2017 Nov;64(11). doi: 10.1002/pbc.26619.

Hyare H, **Thust S**, Rees J. Advanced MRI techniques for treatment monitoring of glioma. Curr Opin Neurol. 2017 Mar;19(3):11. doi:10.1007/s11940-017-0445-6.

Zarkali A, Gorgoraptis N, Miller R, John L, Merve A, **Thust S**, Jager R, Kullmann D, Swayne O. CD8+ encephalitis: a severe but treatable HIV-related acute encephalopathy. Pract Neurol. 2017 Jan;17(1):42-46.

Thust SC, Yousry T. Imaging of skull base tumours. Pract Oncol Radiother. 2016 Jul-Aug;21(4):304-18.

Arenas-Pinto A, Stöhr W, Jäger R, Haddow L, Clarke A, Johnson M, Chen F, Winston A, Godi C, **Thust S** et al. PIVOT Neurocognitive function and neuroimaging markers and virologically suppressed HIV-positive patients randomized to ritonavir-boosted protease inhibitor monotherapy or standard combination ART: a cross-sectional substudy from the PIVOT trial. Clin Infect Dis. 2016 Jul 15;63(2):257-64.

Bray TJ, Chandrashekar H, Rees J, Burke A, Merve A, **Thust S.** Venous infarction mimicking a neoplasm in spontaneous intracranial hypotension: an unusual cause of Parinaud's syndrome. J Surg Case Rep. 2016 Mar 17;2016(3):rjw037. doi: 10.1093/jscr/rjw037.

Mahady K, **Thust S**, Berkeley R, Stuart S, Barnacle A, Robertson F, Mankad K. Vascular anomalies of the head and neck in children. Quant Imaging Med Surg. 2015 Dec;5(6):886-97.

Marshall CR, Guerreiro R, **Thust S**, Fletcher P, Rohrer JD, Fox NC. A novel MAPT mutation causing corticobasal syndrome led by progressive apraxia of speech. J Alzheimers Dis. 2015 Oct 27;48(4):923-6.

Erro R, Hersheson J, Ganos C, Menacci N, Stamelou M, Batla A, **Thust S** et al. H-ABC syndrome and DYT4: Variable expressivity or pleiotropy of TUBB4 mutations? Mov Disord. 2015 May;30(6):828-33.

Thust SC, Chong WK, Gunny R, Mazumder A, Poitelea M, Ederies A, Mankad K. Paediatric cerebrovascular CT angiography – towards better image quality. Quant Imaging Med Surg. 2014 Dec;4(6):469-74.

Thust SC, Blanco E, Michalski A, Chong WK, Gaze MN, Phipps K, Mankad K. MRI abnormalities in children following sequential chemotherapy, hyperfractionated accelerated radiotherapy and high-dose thiotepa for high-risk primitive neuroectodermal tumours of the central nervous system. J Med Imaging Radiat Oncol. 2014 Dec;58(6):683-90.

Thust S, Burke C, Siddiqui A. Neuroimaging findings in sickle cell disease. Br J Radiol 2014; 87(1040):20130699.doi: 10.1259/bjr.20130699.

Mayer D, Bartz D, Fischer J, Ley S, del Río A, **Thust S**, Kauczor HU, Heussel CP. Hybrid segmentation and virtual bronchoscopy based on CT images. Acad Radiol. 2004 May;11(5):551-65.

Book chapters

Thust SC, Vollmuth P, Jäger HR. Imaging of CNS Lymphoma. Clinical Neuroradiology - the ESNR Textbook. Springer (2024, 2nd Edition in print).

Thust SC, Kumar A. Extra-axial brain tumours. Clinical Neuroradiology – the ESNR Textbook. Springer (2024, 2nd Edition in print).

Pizzini F, **Thust SC**, Jäger HR. Clinical presentations, differential diagnosis and imaging work-up of cerebral masses. Clinical Neuroradiology – the ESNR Textbook. Springer (2024, 2nd Edition in print).

McNamara M, Brandner S, **Thust S**. Fast Facts: Glioblastoma: New molecular concepts pave the way for advances in diagnosis and treatment. Karger (2020).

Thust SC, Micallef C, Jager HR. Imaging of brain tumours. Grainger and Allison's Diagnostic Radiology 7th edition (2020).

Thust SC, Hyare H, Rees JR. Imaging of Treatment Response and Pseudoresponse in Glioblastoma: State-Of-The-Art Neuroimaging. Nova Science Publishers (2019).

Quirk B, **Thust S**, Yousry T. Imaging of Low Grade Gliomas in Glioblastoma: State-Of-The-Art Neuroimaging. Nova Science Publishers (2019) .

Kim M, Zaiss M, **Thust SC**, Golay X. Quantitative Chemical Exchange Saturation Transfer in Quantitative MRI of the Brain: Principles of Physical Measurement, 2nd Edition, Taylor & Francis 2018.

Thust S, Miszkiel K, Davagnanam. Imaging of the orbit and visual pathways. Grainger & Allison's Diagnostic Radiology (6th edition 2014).

Abbreviations

1p19q	Short arm of chromosome 1 and long arm of chromosome 19
2D	Two dimensional
2HG	D2-hydroxyglutarate
3D	Three dimensional
ADC	Apparent diffusion coefficient (unit mm^2/s)
ADC_{mean}	Apparent diffusion coefficient mean value
ADC_{min}	Apparent diffusion coefficient minimum value
ADC_{NAWM}	Apparent diffusion coefficient in normal appearing white matter
AI	Artificial intelligence
ANOVA	Analysis of variance
ASL	Arterial spin labelling
AUC	Area under the curve
b0	Diffusion gradient of 0 s/mm^2
b500	Diffusion gradient of 500 s/mm^2
b1000	Diffusion gradient of 1000 s/mm^2
BI-RADS	Breast imaging reporting and data system
BTG	Brain tumour working group
CDKN2A/B	Cyclin dependent kinase inhibitor 2A/B

CEST	Chemical exchange saturation transfer
CET	Contrast enhancing tumour
CSF	Cerebrospinal fluid
CSO	Centrum semiovale
CT	Computed tomography
DCE	Dynamic T1-weighted contrast enhanced MRI
DKI	Diffusion kurtosis imaging
DL	Deep learning
DMI	Deuterium metabolic imaging
DSC	Dynamic susceptibility-weighted contrast enhanced imaging
DWI	Diffusion-weighted imaging
EORTC	European Organisation for Research and Treatment of Cancer
ESNR	European Society of Neuroradiologists
FLAIR	T2-weighted fluid attenuated inversion recovery
HAG	Histone altered glioma
HAG K27M	Glioma with a H3 K27M histone alteration
NHS	National Health System
IDH	Isocitrate dehydrogenase
IDH^{wt}	Isocitrate dehydrogenase wild-type

$IDH^{mut/1p19int}$	Isocitrate dehydrogenase mutant with intact 1p19q
$IDH^{mut/1p19del}$	Isocitrate dehydrogenase mutant with 1p19q codeletion
ISN	International Society of Neuropathology
ICC	Intraclass correlation coefficient
IVIM	Intravoxel incoherent motion imaging
k	Kappa
LGG	Low grade glioma
MCMC	Markov Chain Monte Carlo
MRI	Magnetic resonance imaging
MRS	Magnetic resonance spectroscopy
MRTA	MR imaging texture analysis
N	Number
NAA	N-acetylaspartate
NAWM	Normal appearing white matter
NBTS	United States National Brain Tumor Society
nCET	Non contrast enhancing tumour
NICE	National Institute for Health and Clinical Excellence
NHNN	National Hospital for Neurology and Neurosurgery
PACS	Picture archiving and communication

PET	Positron emission tomography
PIM	Paediatric Index of Mortality
pMRI	Perfusion-weighted MRI
PRISMA-DTA	Preferred Reporting Items for Systematic Reviews and Meta-Analyses
QADAS-2	Quality Assessment of Diagnostic Accuracy Studies 2
qMRI	Quantitative magnetic resonance imaging
rCBV	Relative cerebral blood volume
$rADC_{mean}$	Relative apparent diffusion coefficient mean value
$rADC_{min}$	Relative apparent diffusion coefficient minimum value
ROC	Receiver operating characteristic
ROI	Region of interest
SD	Standard deviation
Seg A	Segmentation A
Seg B	Segmentation B
Seg C	Segmentation C
SNO	Society for Neuro-oncology
SSF	Spatial scale filter
STARD	Standards for Reporting Diagnostic Accuracy Studies
SWI	Susceptibility-weighted imaging

T1CE	T1-weighted gadolinium contrast enhanced
T1w	T1-weighted
T2w	T2-weighted
T2*	T2-weighted gradient echo
TCGA	The Cancer Genome Atlas
UCL	University College London
UoN	University of Nottingham
VASARI	Visually AcceSAble Rembrandt Images
VOI	Volume of interest
WHO	World Health Organisation
WHO 2007	WHO Classification of Central Nervous System Tumors 2007
WHO 2016	WHO Classification of Central Nervous System Tumors 2016

Glossary

Absolute agreement

A measure of the numerical agreement between observers in intraclass correlation coefficient testing.

Adjuvant therapy

Additional treatment given after the primary treatment (e.g. surgery) to lower the risk of cancer recurrence. Adjuvant therapy may include radiotherapy and chemotherapy.

Algorithm

A mathematical process or rule applied in calculations or computerised problem-solving operations.

Antibody

An immune system protein, which may be created in a lab, that interacts with specific targets. Antibodies may be applied in diagnostic testing or as a form of cancer therapy.

Arterial spin labelling

A perfusion imaging method which uses magnetically labelled arterial blood water protons as an endogenous tracer.

Astrocyte

A type of glial cell.

Bayesian

Bayesian inference is a statistical method in which Bayes' theorem is used to update the probability for a hypothesis as more information becomes available.

Bias

Any factor that leads to a systematic difference between the true parameters of a population and the statistical estimate of those parameters.

Binomial

A discrete probability distribution that gives only two possible results in an experiment.

Biomarker

A measurable parameter that is a sign of a normal or abnormal physiological condition or disease.

Biopsy

A surgical procedure to remove a piece of tissue or cell sample for testing.

Blood-brain-barrier

A selective endothelial layer, which restricts the passage of potentially harmful substances and infective pathogens to the brain.

Bonferroni correction

A statistical correction method, which may be applied in the circumstance of multiple hypothesis testing to reduce the likelihood of a type 1 error (at the expense of a type 2 error). This can be applied in form of a p value adjustment, whereby each p value is multiplied by the number of tests.

Brainstem

The neural structure that connects the cerebrum of the brain to the spinal cord and cerebellum.

BraTS challenge

The Brain Tumor Image Segmentation (BraTS) benchmark challenge was first organized in conjunction with the MICCAI 2012 conference as a competition for testing of automated glioma segmentation algorithms. In 2024, over 200 publications have arisen from the international BraTS challenges held yearly.

b value

A factor that reflects the strength and timing of the gradients used to generate diffusion-weighted images.

β value

Logistic regression coefficient, see logistic regression.

Caldicott guardian

A senior representative of the NHS responsible for protecting the confidentiality of people's health and care information and making sure it is used appropriately.

Calvarial remodelling

A change in skull shape or contour, typically as a gradual effect due to pressure e.g. from a tumour mass.

Centrum semiovale

The cerebral white matter region situated cranial to the lateral ventricles and corpus callosum.

Cerebrum

The largest part of the human brain, which consists of two hemispheres.

Cerebral blood volume

The volume of blood within a given amount of brain tissue, which can be estimated from dynamic susceptibility contrast enhanced (DSC) perfusion imaging.

Cervical cord

The spinal cord of the neck region.

Chemical exchange saturation transfer

A recently developed MRI method, in which image signal is generated by selective radiofrequency saturation of exchangeable protons followed by measuring saturation transfer, as this becomes amplified in water. The CEST effect is dependent on solute (e.g. protein) concentration and pH, which can be depicted as image contrast.

Chemotherapy

A systemically administered cancer treatment.

Chi square test

A statistical test to assess whether an association exists between two categorical variables.

Cohen's kappa

A measure of agreement between raters of categorical variables.

Combined chromosome 7 gain and chromosome 10 loss

A characteristic molecular alteration in glioblastoma.

Computed tomography

An imaging technique that combines x-rays with computation for generating cross-sectional images of the brain or body.

Consistency of agreement

A measure of the systematic agreement between observers in intraclass correlation coefficient testing.

Contrast bolus

A predefined dose of contrast given over a short duration, typically in seconds.

Contrast enhancement

Increased signal on T1w images post Gadolinium administration, typically as a result of blood brain barrier breakdown.

Coregister

The fusion of two or more image sequences to make them fully overlap.

Cumulative histogram

A statistical plot, which summarises the signal intensity distribution for all voxels of an image.

Cyst

A fluid filled structure surrounded by a thin membrane as a feature of disease or developmental abnormality.

Cystathionine

An intermediate metabolite in the synthesis of cysteine, a semi-essential amino acid which contributes to protein synthesis.

D2-hydroxyglutarate, 2HG

A cancer metabolite which is produced by IDH-mutant gliomas.

Deep learning

A machine learning method which uses artificial neural networks to perform complex tasks such as segmentation or classification.

Deuterium metabolic imaging

An MRI method based on generating signal from heavy water (^2H_2O).

Dice score

A metric used for measuring the visual overlap between two data sets, typically used in the context of image segmentation. The score quantifies how well the predicted region aligns with the ground truth region.

Dunn pairwise comparisons

A type of post hoc correction applied following Kruskall-Wallis ANOVA testing.

Dynamic contrast enhanced (DCE) imaging

A type of perfusion MRI technique in which contrast is rapidly injected for acquiring T1w images.

Dynamic susceptibility contrast enhanced (DSC) imaging

A type of perfusion MRI technique in which contrast is rapidly injected for acquiring T2w gradient echo images.

Epigenetic

The study of changes in gene expression that occur through alterations in the chromosome rather than in the DNA sequence.

Eta^2

A measure of effect size in a statistical association between variables.

Facilitated diffusion

Increased diffusion compared to normal brain parenchyma.

Fluid attenuated inversion recovery

A T2w MRI acquisition in which fluid signal is deliberately suppressed to increase tissue contrast.

Frontal lobe

The anterior part of the cerebrum.

Gadolinium

A commonly used intravenous contrast medium that increases T1 signal by shortening magnetic relaxation time.

Genotype

Belonging to a genetic group.

Glia

A type of cell that provides physical and chemical support to nerve cells and contributes to the physiological blood brain barrier.

Gliomatosis

A glioma growth pattern defined by involvement of three or more brain lobes.

H3 G34R

A glycine 34-to-arginine or valine substitution in the histone gene 3.3.

H3 K27M

A lysine 27-to-methionine substitution in the histone gene 3.3.

Histology

The microscopic study of tissues.

Histone

A protein that provides structural support for a chromosome and plays a role in gene expression.

Insula

A small, deep seated area of cerebral cortex.

Internal septations

Thin strands of tissue, typically within a fluid filled structure such as a cyst.

Intraclass correlation coefficient

A statistical test used to quantify the level of agreement for numerical variables between two observers, or in test-retest application.

Intravoxel incoherent motion imaging

An advanced diffusion-weighted imaging technique, which uses multiple b values and biexponential fitting to model intracellular and extracellular diffusion.

Kappa statistics

A statistical measure used to quantify the level of agreement between two raters of categorical items.

Kruskal-Wallis ANOVA

A non-parametric statistical test to compare two or more groups for a continuous or discrete variable.

Kurtosis

The tailedness of a distribution curve with higher kurtosis corresponding to greater extremity of numerical deviations.

Likelihood ratio test

A statistical test, which compares the goodness of fit of two statistical (e.g. logistic regression) models.

Linear regression

A statistical model that estimates the linear relationship between a dependent response variable and one or more independent explanatory variables.

Logarithm

The inverse of an exponent or power to which a base must be raised to yield a given number.

Log odds ratio

Logarithm of the odds ratio.

Logistic regression

A logistic model estimates the log-odds of an event as a combination of one or more independent explanatory variables. The logistic function converts log odds to a probability between 0 and 1.

Machine learning

A type of artificial intelligence focused on developing computer models that learn from data to make predictions.

Macroscopic

Visible without magnification.

Mann-Whitney U test

A non-parametric statistical test to compare unrelated samples.

Markov Chain Montecarlo method

A high dimensional statistical simulation method to study a probability distribution through repeated data sampling.

Mean

The average value of the sum of all the numbers is divided by the total number of numbers in a sample.

Median

The middle value in a list of given numbers when ordered from smallest to largest.

MR Spectroscopy

An imaging method, which assesses the presence and concentration of metabolites in one or more image voxels.

Multicentric

Multiple spatially distant tumour foci.

Multifocal

Multiple interconnected tumour foci.

Multivariable

Multiple explanatory parameters in a statistical model, e.g. in logistic regression.

Necrosis

Devitalised tissue.

Neovascularisation

Formation of new vessels.

Neural stem cell

A pluripotent cell with ability to differentiate into a range of cell types such as neuron, astrocyte or oligodendrocyte.

Neuron

A nerve cell with ability to generate electric signals for communication within a network of other neurons in the nervous system.

Normal appearing white matter

White matter without macroscopic evidence of tumour infiltration.

Normalisation

The process by which a numerical measurement in tumour is divided by a numerical measurement in normal appearing tissue, for example white matter.

Odds ratio

The odds that an outcome will occur given a particular condition compared to the odds of the outcome occurring in the absence of that condition.

Oligodendrocyte

A type of glial cell.

ONC201

An orally administered agent Dordaviprone, which selectively binds to the G-protein coupled dopamine receptor D2 and the mitochondrial protease ClpP as a treatment for diffuse midline glioma.

Oncogenic

Something that causes cancer.

Oncometabolite

A metabolite which is produced as an effect of cancer.

PACS

Picture archiving and communications system, a digital imaging technology for secure storage and image viewing. Images are stored in DICOM (Digital Imaging and Communications in Medicine) format.

Paediatric index of mortality

A severity scoring system for predicting the outcome of patients admitted to paediatric intensive care units based on data collected within the first hour of admission.

Percentile

A theshold below which a given percentage of a sample falls, e.g. 10^{th} percentile = 10% of the sample falling below the threshold.

Perfusion-weighted MRI

An MRI method, which measures blood flow related parameters based on intravenous injection of gadolinium (DSC, DCE) or endogenous contrast (ASL).

Perfusion post-processing

The computational process, which derives quantitative maps from perfusion raw data.

Pial invasion

Tumour infiltration of the leptomeninx, a thin cover layer surrounding the brain and spinal cord.

Pignatti score

A clinical risk score derived from multiple EORTC glioma trials in 2002. In brief, this identified age >40 years, astrocytoma histology, largest tumour diameter >6 cm, tumour crossing the midline, and neurologic deficit before surgery as unfavorable factors for survival.

Pixel

The smallest unit in a digital image.

Positron emission tomography

An imaging method that uses radioactive tracers to visualise metabolic processes.

Probability

The likelihood of a statistical outcome. This can be calculated as odds/1+odds.

Pseudoprogression

A self-limiting treatment effect, typically following combined radiation and chemotherapy, resulting in temporary enlargement or new appearance of contrast enhancing imaging abnormalities in the absence of true tumour progression.

QUADAS-2

A tool developed at Bristol University to assess the quality of primary diagnostic accuracy studies, separate from and complementary to the data extraction process.

R^2

A goodness of fit measure for a model, representing 'pseudo' R^2 in logistic regression.

Radiomics

The extraction of imaging data to predict a disease state, for example genetics in cancer.

Radiotherapy

Iatrogenic application of radiation, typically to treat cancer.

Receiver operating characteristic curve

A graphical representation of the performance of a classification model at varying threshold values.

Restricted diffusion

Reduced diffusion compared to normal brain parenchyma.

Sample size calculation

A step in research planning with the aim to determine the number of samples or participants required to correctly represent a population.

Satellites

Discrete tumour lesions in addition to a main tumour mass.

Script

A file or code that contains computational commands.

Segmentation

The delineation of a target structure in an image.

Skewness

A measure of the deviation from a symmetric distribution.

Standard deviation

A statistical measure of the variation of the values in a distribution with regards to its mean.

Stupp protocol

The current standard of care protocol for glioblastoma of radiotherapy and concomitant chemotherapy with temozolomide, an alkylating agent. Where possible, this is preceded by maximum safe tumour resection.

Synaptic connectivity

A connection by which nerve cells communicate through electrochemical activity.

Susceptibility

A source of MRI contrast which exploits the magnetic susceptibility differences of various compounds, such as paramagnetic blood, iron, and diamagnetic calcium.

T2/FLAIR mismatch

Bright T2w signal in a glioma with corresponding signal drop out on FLAIR imaging. This represents a specific feature of $IDH^{mut/1p19qint}$ astrocytomas, thought to be caused by microcystic tissue elements.

Telomerase reverse transcriptase promoter

A subunit of the telomerase enzyme complex that adds nucleotides to the ends of telomeres. This process contributes to cell life span and is often upregulated in cancer cells due to a mutation in the promoter region.

Tertiary referral centre

A specialist hospital service that receives referrals from district hospitals and general practice.

Tessa Jowell initiative

Dame Tessa Jowell was a Labour Party politician and MP, who in 2018 made a moving call for action to improve brain tumour outcomes. The Tessa Jowell Brain Cancer Mission has become a national strategy to deliver transformational programmes in the areas of research, trials, training and patient experience.

Test cohort

A sample of cases independent from training cases, typically to test a predictive algorithm.

Texture analysis

A type of image analysis focused on the spatial distribution of signal intensity values in an image.

Thalamus

A paired grey matter structure surrounding the brain midline.

The Cancer Genome Atlas (TCGA)

A landmark cancer genomics program, which molecularly characterized over 20,000 primary cancer samples spanning many cancer types, including glioblastoma, with a linked imaging database.

Training cohort

A sample of cases used for statistical model training.

Type 1 error

A false positive error in statistics resulting in the rejection of the null hypothesis when it is true.

Type 2 error

A false negative error in statistics resulting in failure to reject the null hypothesis when it is false.

Univariable

A single explanatory parameter in a statistical model, e.g. in logistic regression.

Vendors

Commercial manufacturers of MRI machines.

Voxel

The smallest volumetric unit within an image, representing a three-dimensional pixel.

WHO grading

Since 2021, Arabic numerals have been adopted instead of the previous Roman numbering system. This change was implemented to align brain tumour grading with body cancer grading. The numbers can otherwise be used interchangeably.

Wilcoxon signed rank test

A non-parametric statistical test to compare related samples.

Youden's index

A statistical tool for selecting the optimal threshold value or cutoff point along a receiver operating characteristic curve.

References

1. Alcantara Llaguno SR, Parada LF. Cell of origin of glioma: biological and clinical implications. Br J Cancer. 2016 Dec;115(12):1445–50.

2. Krishna S, Choudhury A, Keough MB, Seo K, Ni L, Kakaizada S, et al. Glioblastoma remodelling of human neural circuits decreases survival. Nature. 2023 May;617(7961):599–607.

3. Cancer Research UK [Internet]. 2015 [cited 2024 Jul 29]. Brain, other CNS and intracranial tumours incidence statistics. Available from: https://www.cancerresearchuk.org/health-professional/cancer-statistics/statistics-by-cancer-type/brain-other-cns-and-intracranial-tumours/incidence

4. Wanis HA, Møller H, Ashkan K, Davies EA. The incidence of major subtypes of primary brain tumors in adults in England 1995-2017. Neuro-Oncol. 2021 Apr 9;23(8):1371–82.

5. van den Bent MJ, Brandes AA, Taphoorn MJB, Kros JM, Kouwenhoven MCM, Delattre JY, et al. Adjuvant procarbazine, lomustine, and vincristine chemotherapy in newly diagnosed anaplastic oligodendroglioma: long-term follow-up of EORTC brain tumor group study 26951. J Clin Oncol Off J Am Soc Clin Oncol. 2013 Jan 20;31(3):344–50.

6. Louis DN, Ohgaki H, Wiestler OD, Cavenee WK, Burger PC, Jouvet A, et al. The 2007 WHO classification of tumours of the central nervous system. Acta Neuropathol (Berl). 2007 Aug;114(2):97–109.

7. Aldape K, Simmons ML, Davis RL, Miike R, Wiencke J, Barger G, et al. Discrepancies in diagnoses of neuroepithelial neoplasms. Cancer. 2000;88(10):2342–9.

8. Frazier JL, Johnson MW, Burger PC, Weingart JD, Quinones-Hinojosa A. Rapid malignant transformation of low-grade astrocytomas: report of 2 cases and review of the literature. World Neurosurg. 2010 Jan 1;73(1):53–62.

9. Louis DN, Perry A, Burger P, Ellison DW, Reifenberger G, von Deimling A, et al. International Society of Neuropathology-Haarlem Consensus Guidelines for Nervous System Tumor Classification and Grading. Brain Pathol. 2014;24(5):429–35.

10. Eckel-Passow JE, Lachance DH, Molinaro AM, Walsh KM, Decker PA, Sicotte H, et al. Glioma Groups Based on 1p/19q, IDH, and TERT Promoter Mutations in Tumors. N Engl J Med. 2015 Jun 25;372(26):2499–508.

11. Louis DN, Perry A, Reifenberger G, von Deimling A, Figarella-Branger D, Cavenee WK, et al. The 2016 World Health Organization Classification of Tumors of the Central Nervous System: a summary. Acta Neuropathol (Berl). 2016 Jun;131(6):803–20.

12. Stichel D, Ebrahimi A, Reuss D, Schrimpf D, Ono T, Shirahata M, et al. Distribution of EGFR amplification, combined chromosome 7 gain and chromosome 10 loss, and TERT promoter mutation in brain tumors and their potential for the reclassification of IDHwt astrocytoma to glioblastoma. Acta Neuropathol (Berl). 2018 Nov;136(5):793–803.

13. Tesileanu CMS, Dirven L, Wijnenga MMJ, Koekkoek JAF, Vincent AJPE, Dubbink HJ, et al. Survival of diffuse astrocytic glioma, IDH1/2 wildtype, with molecular features of glioblastoma, WHO grade IV: a confirmation of the cIMPACT-NOW criteria. Neuro-Oncol. 2020 Apr;22(4):515–23.

14. null null. Comprehensive, Integrative Genomic Analysis of Diffuse Lower-Grade Gliomas. N Engl J Med. 2015 Jun 25;372(26):2481–98.

15. Appin CL, Brat DJ. Molecular pathways in gliomagenesis and their relevance to neuropathologic diagnosis. Adv Anat Pathol. 2015 Jan;22(1):50–8.

16. Mandonnet E, Wager M, Almairac F, Baron MH, Blonski M, Freyschlag CF, et al. Survey on current practice within the European Low-Grade Glioma Network: where do we stand and what is the next step? Neuro-Oncol Pract. 2017 Dec;4(4):241–7.

17. Recommendations | Brain tumours (primary) and brain metastases in over 16s | Guidance | NICE [Internet]. NICE; 2018 [cited 2024 Jul 2]. Available from: https://www.nice.org.uk/guidance/ng99/chapter/Recommendations#follow-up-for-brain-metastases

18. Jakola AS, Skjulsvik AJ, Myrmel KS, Sjåvik K, Unsgård G, Torp SH, et al. Surgical resection versus watchful waiting in low-grade gliomas. Ann Oncol [Internet]. 2017 Aug [cited 2024 Jul 29]; Available from: https://www.ncbi.nlm.nih.gov/pmc/articles/PMC5834105/

19. Wijnenga MMJ, French PJ, Dubbink HJ, Dinjens WNM, Atmodimedjo PN, Kros JM, et al. The impact of surgery in molecularly defined low-grade glioma: an integrated clinical, radiological, and molecular analysis. Neuro-Oncol. 2018 Jan 10;20(1):103–12.

20. Stupp R, Hegi ME, Mason WP, van den Bent MJ, Taphoorn MJB, Janzer RC, et al. Effects of radiotherapy with concomitant and adjuvant temozolomide versus radiotherapy alone on survival in glioblastoma in a randomised phase III study: 5-year analysis of the EORTC-NCIC trial. Lancet Oncol. 2009 May;10(5):459–66.

21. Karschnia P, Young JS, Dono A, Häni L, Sciortino T, Bruno F, et al. Prognostic validation of a new classification system for extent of resection in glioblastoma: A report of the RANO resect group. Neuro-Oncol. 2023 May 4;25(5):940–54.

22. Karschnia P, Dietrich J, Bruno F, Dono A, Juenger ST, Teske N, et al. Surgical management and outcome of newly diagnosed glioblastoma without contrast enhancement ('low grade appearance') - a report of the RANO resect group. Neuro-Oncol. 2023 Sep 4;noad160.

23. Markwell SM, Ross JL, Olson CL, Brat DJ. Necrotic reshaping of the glioma microenvironment drives disease progression. Acta Neuropathol (Berl). 2022 Mar 1;143(3):291–311.

24. Pierallini A, Bonamini M, Bozzao A, Pantano P, Stefano DD, Ferone E, et al. Supratentorial diffuse astrocytic tumours: proposal of an MRI classification. Eur Radiol. 1997;7(3):395–9.

25. Watanabe M, Tanaka R, Takeda N. Magnetic resonance imaging and histopathology of cerebral gliomas. Neuroradiology. 1992;34(6):463–9.

26. Ideguchi M, Kajiwara K, Goto H, Sugimoto K, Nomura S, Ikeda E, et al. MRI findings and pathological features in early-stage glioblastoma. J Neurooncol. 2015 Jun;123(2):289–97.

27. Olar A, Raghunathan A, Albarracin CT, Aldape KD, Cahill DP, Powell SZ, et al. Absence of IDH1-R132H mutation predicts rapid progression of nonenhancing diffuse glioma in older adults. Ann Diagn Pathol. 2012 Jun;16(3):161–70.

28. Zhong J. Basics of Diffusion Measurements by MRI. In: Moritani T, Ekholm S, Westesson PL, editors. Diffusion-Weighted MR Imaging of the Brain [Internet]. Berlin, Heidelberg: Springer; 2009 [cited 2024 Jul 15]. p. 1–5. Available from: https://doi.org/10.1007/978-3-540-78785-3_1

29. Surov A, Meyer HJ, Wienke A. Correlation between apparent diffusion coefficient (ADC) and cellularity is different in several tumors: a meta-analysis. Oncotarget. 2017 May 10;8(35):59492–9.

30. Sugahara T, Korogi Y, Kochi M, Ikushima I, Shigematu Y, Hirai T, et al. Usefulness of diffusion-weighted MRI with echo-planar technique in the evaluation of cellularity in gliomas. J Magn Reson Imaging JMRI. 1999 Jan;9(1):53–60.

31. Grech-Sollars M, Hales PW, Miyazaki K, Raschke F, Rodriguez D, Wilson M, et al. Multi-centre reproducibility of diffusion MRI parameters for clinical sequences in the brain. Nmr Biomed. 2015 Apr;28(4):468–85.

32. Reuss DE, Sahm F, Schrimpf D, Wiestler B, Capper D, Koelsche C, et al. ATRX and IDH1-R132H immunohistochemistry with subsequent copy number analysis and IDH sequencing as a basis for an ‘integrated’ diagnostic approach for adult astrocytoma, oligodendroglioma and glioblastoma. Acta Neuropathol (Berl). 2015 Jan;129(1):133–46.

33. Lewis MA, Ganeshan B, Barnes A, Bisdas S, Jaunmuktane Z, Brandner S, et al. Filtration-histogram based magnetic resonance texture analysis (MRTA) for glioma IDH and 1p19q genotyping. Eur J Radiol. 2019 Apr;113:116–23.

34. Thust SC, Heiland S, Falini A, Jäger HR, Waldman AD, Sundgren PC, et al. Glioma imaging in Europe: A survey of 220 centres and recommendations for best clinical practice. Eur Radiol. 2018 Aug;28(8):3306–17.

35. Ellingson BM, Bendszus M, Boxerman J, Barboriak D, Erickson BJ, Smits M, et al. Consensus recommendations for a standardized Brain Tumor Imaging Protocol in clinical trials. Neuro-Oncol. 2015 Sep;17(9):1188–98.

36. Thust SC, Heiland S, Falini A, Jäger HR, Waldman AD, Sundgren PC, et al. Glioma imaging in Europe: A survey of 220 centres and recommendations for best clinical practice. Eur Radiol. 2018 Aug;28(8):3306–17.

37. Fan W, Yan Z. Factors affecting response rates of the web survey: A systematic review. Comput Hum Behav. 2010 Mar 1;26(2):132–9.

38. Manfrini E, Smits M, Thust S, Geiger S, Bendella Z, Petr J, et al. From research to clinical practice: a European neuroradiological survey on quantitative advanced MRI implementation. Eur Radiol. 2021 Aug;31(8):6334–41.

39. Pizzini FB, Thust S, Jäger R. Clinical Presentations, Differential Diagnosis, and Imaging Workup of Cerebral Mass Lesions. In: Barkhof F, Jager R, Thurnher M, Rovira Cañellas A, editors. Clinical Neuroradiology: The ESNR Textbook [Internet]. Cham: Springer International Publishing; 2020 [cited 2024 Jun 29]. p. 1–24. Available from: https://doi.org/10.1007/978-3-319-61423-6_56-2

40. Bhandari A, Sharma C, Ibrahim M, Riggs M, Jones R, Lasocki A. The role of 2-hydroxyglutarate magnetic resonance spectroscopy for the determination of isocitrate dehydrogenase status in lower grade gliomas versus glioblastoma: a systematic review and meta-analysis of diagnostic test accuracy. Neuroradiology. 2021 Nov;63(11):1823–30.

41. Andronesi OC, Kim GS, Gerstner E, Batchelor T, Tzika AA, Fantin VR, et al. Detection of 2-hydroxyglutarate in IDH-mutated glioma patients by in vivo spectral-editing and 2D correlation magnetic resonance spectroscopy. Sci Transl Med. 2012 Jan 11;4(116):116ra4.

42. Okuchi S, Hammam A, Golay X, Kim M, Thust S. Endogenous Chemical Exchange Saturation Transfer MRI for the Diagnosis and Therapy Response Assessment of Brain Tumors: A Systematic Review. Radiol Imaging Cancer. 2020 Jan;2(1):e190036.

43. Safdar N, Abbo LM, Knobloch MJ, Seo SK. Research Methods in Healthcare Epidemiology: Survey and Qualitative Research. Infect Control Hosp Epidemiol. 2016 Nov;37(11):1272–7.

44. KELLEY K, CLARK B, BROWN V, SITZIA J. Good practice in the conduct and reporting of survey research. Int J Qual Health Care. 2003 May 1;15(3):261–6.

45. Ponto J. Understanding and Evaluating Survey Research. J Adv Pract Oncol. 2015;6(2):168–71.

46. Ross PT, Bibler Zaidi NL. Limited by our limitations. Perspect Med Educ. 2019 Aug;8(4):261–4.

47. Fincham JE. Response Rates and Responsiveness for Surveys, Standards, and the Journal. Am J Pharm Educ. 2008 Apr 15;72(2):43.

48. Cheung KL, ten Klooster PM, Smit C, de Vries H, Pieterse ME. The impact of non-response bias due to sampling in public health studies: A comparison of voluntary versus mandatory recruitment in a Dutch national survey on adolescent health. BMC Public Health. 2017 Mar 23;17(1):276.

49. Boxerman JL, Quarles CC, Hu LS, Erickson BJ, Gerstner ER, Smits M, et al. Consensus recommendations for a dynamic susceptibility contrast MRI protocol for use in high-grade gliomas. Neuro-Oncol. 2020 Sep 29;22(9):1262–75.

50. Okamoto K, Ohsuka K, Shiraishi T, Hukazawa E, Wakasugi S, Furuta K. Comparability of epidemiological information between self- and interviewer-administered questionnaires. J Clin Epidemiol. 2002 May 1;55(5):505–11.

51. Hodel J, Vernooij MW, Beyer MK, Severino M, Leclerc X, Créange A, et al. Multiple sclerosis imaging in clinical practice: a European-wide survey of 428 centers and conclusions by the ESNR Working Group. Eur Radiol. 2023 Oct;33(10):7025–33.

52. Mazurowski MA, Desjardins A, Malof JM. Imaging descriptors improve the predictive power of survival models for glioblastoma patients. Neuro-Oncol. 2013 Oct;15(10):1389–94.

53. Comprehensive genomic characterization defines human glioblastoma genes and core pathways. Nature. 2008 Oct 23;455(7216):1061–8.

54. Vasari MR Feature Guide_v1.1.pdf [Internet]. [cited 2024 Jul 17]. Available from: https://portals.broadinstitute.org/pochetlab/demo/Imaging_Features/Vasari%20MR%20Feature%20Guide_v1.1.pdf

55. Azizova A, Prysiazhniuk Y, Wamelink IJHG, Petr J, Barkhof F, Keil VC. Ten Years of VASARI Glioma Features: Systematic Review and Meta-Analysis of Their Impact and Performance. Am J Neuroradiol. 2024 Aug 1;45(8):1053–62.

56. Hyare H, Rice L, Thust S, Nachev P, Jha A, Milic M, et al. Modelling MR and clinical features in grade II/III astrocytomas to predict *IDH* mutation status. Eur J Radiol. 2019 May 1;114:120–7.

57. van Lent DI, van Baarsen KM, Snijders TJ, Robe PAJT. Radiological differences between subtypes of WHO 2016 grade II–III gliomas: a systematic review and meta-analysis. Neuro-Oncol Adv. 2020 Jan 1;2(1):vdaa044.

58. Eghtedari M, Chong A, Rakow-Penner R, Ojeda-Fournier H. Current Status and Future of BI-RADS in Multimodality Imaging, From the AJR Special Series on Radiology Reporting and Data Systems. AJR Am J Roentgenol. 2021 Apr;216(4):860–73.

59. Bink A, Benner J, Reinhardt J, De Vere-Tyndall A, Stieltjes B, Hainc N, et al. Structured Reporting in Neuroradiology: Intracranial Tumors. Front Neurol. 2018;9:32.

60. Zhang JY, Weinberg BD, Hu R, Saindane A, Mullins M, Allen J, et al. Quantitative Improvement in Brain Tumor MRI Through Structured Reporting (BT-RADS). Acad Radiol. 2020 Jun;27(6):780–4.

61. Kelsch R, Saon M, Sutherland E, Tech K, Al-Katib S. Discrepant Reporting Style Preferences Between Clinicians and Radiologists. Curr Probl Diagn Radiol. 2021;50(6):779–83.

62. Schmid AM, Raunig DL, Miller CG, Walovitch RC, Ford RW, O'Connor M, et al. Radiologists and Clinical Trials: Part 1 The Truth About Reader Disagreements. Ther Innov Regul Sci. 2021;55(6):1111–21.

63. Aldape K, Simmons ML, Davis RL, Miike R, Wiencke J, Barger G, et al. Discrepancies in diagnoses of neuroepithelial neoplasms: the San Francisco Bay Area Adult Glioma Study. Cancer. 2000 May 15;88(10):2342–9.

64. VASARI Research Project - The Cancer Imaging Archive (TCIA) Public Access - Cancer Imaging Archive Wiki [Internet]. [cited 2024 Jun 22]. Available from: https://wiki.cancerimagingarchive.net/display/Public/VASARI+Research+Project

65. Provenzale JM, Ison C, DeLong D. Bidimensional Measurements in Brain Tumors: Assessment of Interobserver Variability. Am J Roentgenol. 2009 Dec;193(6):W515–22.

66. Hastings WK. Monte Carlo sampling methods using Markov chains and their applications. Biometrika. 1970 Apr 1;57(1):97–109.

67. Lin Y, Wang F, Liu B. Random number generators for large-scale parallel Monte Carlo simulations on FPGA. J Comput Phys. 2018 May 1;360:93–103.

68. Pawel S, Kook L, Reeve K. Pitfalls and potentials in simulation studies: Questionable research practices in comparative simulation studies allow for spurious claims of superiority of any method. Biom J Biom Z. 2024 Jan;66(1):e2200091.

69. Pignatti F, van den Bent M, Curran D, Debruyne C, Sylvester R, Therasse P, et al. Prognostic factors for survival in adult patients with cerebral low-grade glioma. J Clin Oncol Off J Am Soc Clin Oncol. 2002 Apr 15;20(8):2076–84.

70. Kaiser L, Quach S, Zounek AJ, Wiestler B, Zatcepin A, Holzgreve A, et al. Enhancing predictability of IDH mutation status in glioma patients at initial diagnosis: a comparative analysis of radiomics from MRI, [18F]FET PET, and TSPO PET. Eur J Nucl Med Mol Imaging. 2024 Jul 1;51(8):2371–81.

71. Lasocki A, Anjari M, Örs Kokurcan S, Thust SC. Conventional MRI features of adult diffuse glioma molecular subtypes: a systematic review. Neuroradiology. 2021 Mar;63(3):353–62.

72. McInnes MDF, Moher D, Thombs BD, McGrath TA, Bossuyt PM, and the PRISMA-DTA Group. Preferred Reporting Items for a Systematic Review and Meta-analysis of Diagnostic Test Accuracy Studies: The PRISMA-DTA Statement. JAMA. 2018 Jan 23;319(4):388–96.

73. Okuchi S, Hammam A, Golay X, Kim M, Thust S. Endogenous Chemical Exchange Saturation Transfer MRI for the Diagnosis and Therapy Response Assessment of Brain Tumors: A Systematic Review. Radiol Imaging Cancer. 2020 Jan;2(1):e190036.

74. Darlix A, Deverdun J, Menjot de Champfleur N, Castan F, Zouaoui S, Rigau V, et al. IDH mutation and 1p19q codeletion distinguish two radiological patterns of diffuse low-grade gliomas. J Neurooncol. 2017 May 1;133(1):37–45.

75. Yamauchi T, Ohno M, Matsushita Y, Takahashi M, Miyakita Y, Kitagawa Y, et al. Radiological characteristics based on isocitrate dehydrogenase mutations and 1p/19q codeletion in grade II and III gliomas. Brain Tumor Pathol. 2018 Jul 1;35(3):148–58.

76. Qi S, Yu L, Li H, Ou Y, Qiu X, Ding Y, et al. Isocitrate dehydrogenase mutation is associated with tumor location and magnetic resonance imaging characteristics in astrocytic neoplasms. Oncol Lett. 2014 Jun 1;7(6):1895–902.

77. Sonoda Y, Shibahara I, Kawaguchi T, Saito R, Kanamori M, Watanabe M, et al. Association between molecular alterations and tumor location and MRI characteristics in anaplastic gliomas. Brain Tumor Pathol. 2015 Apr 1;32(2):99–104.

78. Batchala PP, Muttikkal TJE, Donahue JH, Patrie JT, Schiff D, Fadul CE, et al. Neuroimaging-Based Classification Algorithm for Predicting 1p/19q-Codeletion Status in IDH-Mutant Lower Grade Gliomas. Am J Neuroradiol. 2019 Mar 1;40(3):426–32.

79. Johnson DR, Diehn FE, Giannini C, Jenkins RB, Jenkins SM, Parney IF, et al. Genetically Defined Oligodendroglioma Is Characterized by Indistinct Tumor Borders at MRI. Am J Neuroradiol. 2017 Apr 1;38(4):678–84.

80. Kim JW, Park CK, Park SH, Kim YH, Han JH, Kim CY, et al. Relationship between radiological characteristics and combined 1p and 19q deletion in World Health Organization grade III oligodendroglial tumours. J Neurol Neurosurg Psychiatry. 2011 Feb 1;82(2):224–7.

81. Kanazawa T, Fujiwara H, Takahashi H, Nishiyama Y, Hirose Y, Tanaka S, et al. Imaging scoring systems for preoperative molecular diagnoses of lower-grade gliomas. Neurosurg Rev. 2019 Jun 1;42(2):433–41.

82. Sherman JH, Prevedello DM, Shah L, Raghavan P, Pouratian N, Starke RM, et al. MR imaging characteristics of oligodendroglial tumors with assessment of 1p/19q deletion status. Acta Neurochir (Wien). 2010 Nov 1;152(11):1827–34.

83. Villanueva-Meyer JE, Wood MD, Choi BS, Mabray MC, Butowski NA, Tihan T, et al. MRI Features and IDH Mutational Status of Grade II Diffuse Gliomas: Impact on Diagnosis and Prognosis. Am J Roentgenol. 2018 Mar;210(3):621–8.

84. Park YW, Han K, Ahn SS, Bae S, Choi YS, Chang JH, et al. Prediction of IDH1-Mutation and 1p/19q-Codeletion Status Using Preoperative MR Imaging Phenotypes in Lower Grade Gliomas. Am J Neuroradiol. 2018 Jan 1;39(1):37–42.

85. Compes P, Tabouret E, Etcheverry A, Colin C, Appay R, Cordier N, et al. Neuro-radiological characteristics of adult diffuse grade II and III insular gliomas classified according to WHO 2016. J Neurooncol. 2019 May 1;142(3):511–20.

86. Delfanti RL, Piccioni DE, Handwerker J, Bahrami N, Krishnan A, Karunamuni R, et al. Imaging correlates for the 2016 update on WHO classification of grade II/III gliomas: implications for IDH, 1p/19q and ATRX status. J Neurooncol. 2017 Dec 1;135(3):601–9.

87. Reyes-Botero G, Dehais C, Idbaih A, Martin-Duverneuil N, Lahutte M, Carpentier C, et al. Contrast enhancement in 1p/19q-codeleted anaplastic oligodendrogliomas is associated with 9p loss, genomic instability, and angiogenic gene expression. Neuro-Oncol. 2014 May 1;16(5):662–70.

88. Wu CC, Jain R, Radmanesh A, Poisson LM, Guo WY, Zagzag D, et al. Predicting Genotype and Survival in Glioma Using Standard Clinical MR Imaging Apparent Diffusion Coefficient Images: A Pilot Study from The Cancer Genome Atlas. Am J Neuroradiol. 2018 Oct 1;39(10):1814–20.

89. Wang YY, Wang K, Li SW, Wang JF, Ma J, Jiang T, et al. Patterns of Tumor Contrast Enhancement Predict the Prognosis of Anaplastic Gliomas with IDH1 Mutation. Am J Neuroradiol. 2015 Nov 1;36(11):2023–9.

90. Juratli TA, Tummala SS, Riedl A, Daubner D, Hennig S, Penson T, et al. Radiographic assessment of contrast enhancement and T2/FLAIR mismatch sign in lower grade gliomas: correlation with molecular groups. J Neurooncol. 2019 Jan 1;141(2):327–35.

91. Patel SH, Poisson LM, Brat DJ, Zhou Y, Cooper L, Snuderl M, et al. T2-FLAIR Mismatch, an Imaging Biomarker for IDH and 1p/19q Status in Lower-grade Gliomas: A TCGA/TCIA Project. Clin Cancer Res Off J Am Assoc Cancer Res. 2017 Oct 15;23(20):6078–85.

92. Broen MPG, Smits M, Wijnenga MMJ, Dubbink HJ, Anten MHME, Schijns OEMG, et al. The T2-FLAIR mismatch sign as an imaging marker for non-enhancing IDH-mutant, 1p/19q-intact lower-grade glioma: a validation study. Neuro-Oncol. 2018 Sep 3;20(10):1393–9.

93. Lasocki A, Gaillard F, Gorelik A, Gonzales M. MRI Features Can Predict 1p/19q Status in Intracranial Gliomas. Am J Neuroradiol. 2018 Apr 1;39(4):687–92.

94. Salameh JP, Bossuyt PM, McGrath TA, Thombs BD, Hyde CJ, Macaskill P, et al. Preferred reporting items for systematic review and meta-analysis of diagnostic test accuracy studies (PRISMA-DTA): explanation, elaboration, and checklist. BMJ. 2020 Aug 14;370:m2632.

95. Sarkis-Onofre R, Catalá-López F, Aromataris E, Lockwood C. How to properly use the PRISMA Statement. Syst Rev. 2021 Apr 19;10(1):117.

96. Cochrane Handbook for Systematic Reviews of Interventions [Internet]. [cited 2024 Jul 31]. Available from: https://training.cochrane.org/handbook/current

97. Hasselblatt M, Jaber M, Reuss D, Grauer O, Bibo A, Terwey S, et al. Diffuse Astrocytoma, IDH-Wildtype: A Dissolving Diagnosis. J Neuropathol Exp Neurol. 2018 Jun 1;77(6):422–5.

98. Guo J, Zhang R, Yang Z, Duan Z, Yin D, Zhou Y. Biological Roles and Therapeutic Applications of IDH2 Mutations in Human Cancer. Front Oncol [Internet]. 2021 Apr 26 [cited 2024 Aug 1];11. Available from: https://www.frontiersin.org/journals/oncology/articles/10.3389/fonc.2021.644857/full

99. Lensen S. When to pool data in a meta-analysis (and when not to)? Fertil Steril. 2023 Jun 1;119(6):902–3.

100. Whiting PF, Rutjes AWS, Westwood ME, Mallett S, Deeks JJ, Reitsma JB, et al. QUADAS-2: a revised tool for the quality assessment of diagnostic accuracy studies. Ann Intern Med. 2011 Oct 18;155(8):529–36.

101. Tan WL, Huang WY, Yin B, Xiong J, Wu JS, Geng DY. Can Diffusion Tensor Imaging Noninvasively Detect IDH1 Gene Mutations in Astrogliomas? A Retrospective Study of 112 Cases. AJNR Am J Neuroradiol. 2014 May;35(5):920.

102. Leu K, Ott GA, Lai A, Nghiemphu PL, Pope WB, Yong WH, et al. Perfusion and diffusion MRI signatures in histologic and genetic subtypes of WHO grade II-III diffuse gliomas. J Neurooncol. 2017 Aug;134(1):177–88.

103. Thust SC, Hassanein S, Bisdas S, Rees JH, Hyare H, Maynard JA, et al. Apparent diffusion coefficient for molecular subtyping of non-gadolinium-enhancing WHO grade II/III glioma: volumetric segmentation versus two-dimensional region of interest analysis. Eur Radiol. 2018 Sep;28(9):3779–88.

104. Thust SC, Maynard JA, Benenati M, Wastling SJ, Mancini L, Jaunmuktane Z, et al. Regional and Volumetric Parameters for Diffusion-Weighted WHO Grade II and III Glioma Genotyping: A Method Comparison. AJNR Am J Neuroradiol. 2021 Mar;42(3):441–7.

105. Yushkevich PA, Piven J, Hazlett HC, Smith RG, Ho S, Gee JC, et al. User-guided 3D active contour segmentation of anatomical structures: significantly improved efficiency and reliability. NeuroImage. 2006 Jul 1;31(3):1116–28.

106. Jenkinson M, Bannister P, Brady M, Smith S. Improved optimization for the robust and accurate linear registration and motion correction of brain images. NeuroImage. 2002 Oct;17(2):825–41.

107. Ellingson BM, Bendszus M, Sorensen AG, Pope WB. Emerging techniques and technologies in brain tumor imaging. Neuro-Oncol. 2014 Oct;16(Suppl 7):vii12–23.

108. Bossuyt PM, Reitsma JB, Bruns DE, Gatsonis CA, Glasziou PP, Irwig L, et al. STARD 2015: an updated list of essential items for reporting diagnostic accuracy studies. BMJ. 2015 Oct 28;351:h5527.

109. Aggarwal R, Ranganathan P. Common pitfalls in statistical analysis: Linear regression analysis. Perspect Clin Res. 2017;8(2):100–2.

110. van Smeden M, de Groot JAH, Moons KGM, Collins GS, Altman DG, Eijkemans MJC, et al. No rationale for 1 variable per 10 events criterion for binary logistic regression analysis. BMC Med Res Methodol. 2016 Nov 24;16(1):163.

111. Halligan S, Altman DG, Mallett S. Disadvantages of using the area under the receiver operating characteristic curve to assess imaging tests: A discussion and proposal for an alternative approach. Eur Radiol. 2015;25(4):932–9.

112. BNOS Guideline for Tissue Sampling of Brain Tumours [Internet]. BNOS. [cited 2023 Sep 9]. Available from: https://www.bnos.org.uk/bnos-guideline-for-tissue-sampling-of-brain-tumours/

113. University College London Hospitals NHS Foundation Trust [Internet]. [cited 2024 Jul 13]. Brain Tumour Service (Neuro-Oncology). Available from: https://www.uclh.nhs.uk/our-services/find-service/neurology-and-neurosurgery/brain-tumour-service-neuro-oncology

114. Xing Z, Yang X, She D, Lin Y, Zhang Y, Cao D. Noninvasive Assessment of IDH Mutational Status in World Health Organization Grade II and III Astrocytomas Using DWI and DSC-PWI Combined with Conventional MR Imaging. AJNR Am J Neuroradiol. 2017 Jun;38(6):1138–44.

115. Sadeghi N, Camby I, Goldman S, Gabius HJ, Balériaux D, Salmon I, et al. Effect of hydrophilic components of the extracellular matrix on quantifiable diffusion-weighted imaging of human gliomas: preliminary results of correlating apparent diffusion coefficient values and hyaluronan expression level. AJR Am J Roentgenol. 2003 Jul;181(1):235–41.

116. Bhatti F, Menon N, Maynard J, Wastling S, Morgan PS, Smith S, et al. A rapid probability calculator for glioma IDH genotyping: diagnostic gain for rater in-training. In BSNR Annual Meeting. Bristol, UK.; 2024.

117. Van Bostraeten P, Aertgeerts B, Bekkering GE, Delvaux N, Dijckmans C, Ostyn E, et al. Infographic summaries for clinical practice guidelines: results from user testing of the BMJ Rapid Recommendations in primary care. BMJ Open. 2023 Nov 9;13(11):e071847.

118. Fujita Y, Nagashima H, Tanaka K, Hashiguchi M, Hirose T, Itoh T, et al. The Histopathologic and Radiologic Features of T2-FLAIR Mismatch Sign in IDH-Mutant 1p/19q Non-codeleted Astrocytomas. World Neurosurg. 2021 May;149:e253–60.

119. Yee PP, Wang J, Chih SY, Aregawi DG, Glantz MJ, Zacharia BE, et al. Temporal radiographic and histological study of necrosis development in a mouse glioblastoma model. Front Oncol [Internet]. 2022 Oct 14 [cited 2024 Aug 2];12. Available from: https://www.frontiersin.org/journals/oncology/articles/10.3389/fonc.2022.993649/full

120. Law M, Oh S, Johnson G, Babb JS, Zagzag D, Golfinos J, et al. Perfusion magnetic resonance imaging predicts patient outcome as an adjunct to histopathology: a second reference standard in the surgical and nonsurgical treatment of low-grade gliomas. Neurosurgery. 2006 Jun;58(6):1099–107; discussion 1099-1107.

121. Cho NS, Hagiwara A, Sanvito F, Ellingson BM. A multi-reader comparison of normal-appearing white matter normalization techniques for perfusion and diffusion MRI in brain tumors. Neuroradiology. 2023 Mar 1;65(3):559–68.

122. Pipe J. Pulse sequences for diffusion-weighted MRI. In: Diffusion MRI [Internet]. Elsevier Inc.; 2009 [cited 2023 Nov 10]. p. 11–35. Available from: http://www.scopus.com/inward/record.url?scp=84882470958&partnerID=8YFLogxK

123. Ghosal S, Shah P. A deep-learning toolkit for visualization and interpretation of segmented medical images. Cell Rep Methods. 2021 Nov 22;1(7):100107.

124. Du N, Zhou X, Mao R, Shu W, Xiao L, Ye Y, et al. Preoperative and Noninvasive Prediction of Gliomas Histopathological Grades and IDH Molecular Types Using Multiple MRI Characteristics. Front Oncol. 2022;12:873839.

125. Liu S, Zhang Y, Kong Z, Jiang C, Wang Y, Zhao D, et al. Feasibility of evaluating the histologic and genetic subtypes of WHO grade II-IV gliomas by diffusion-weighted imaging. BMC Neurosci. 2022 Dec 5;23(1):72.

126. Cho NS, Hagiwara A, Sanvito F, Ellingson BM. A multi-reader comparison of normal-appearing white matter normalization techniques for perfusion and diffusion MRI in brain tumors. Neuroradiology. 2023 Mar;65(3):559–68.

127. Maynard J, Okuchi S, Wastling S, Busaidi AA, Almossawi O, Mbatha W, et al. World Health Organization Grade II/III Glioma Molecular Status: Prediction by MRI Morphologic Features and Apparent Diffusion Coefficient. Radiology. 2020 Jul;296(1):111–21.

128. Bahrami N, Hartman SJ, Chang YH, Delfanti R, White NS, Karunamuni R, et al. Molecular classification of patients with grade II/III glioma using quantitative MRI characteristics. J Neurooncol. 2018 Sep;139(3):633–42.

129. Campion T, Stoneham S, Al-Busaidi A, Kumar A, Jaunmuktane Z, Brandner S, et al. Diverse imaging features of adolescent glioblastoma. BJR Case Rep. 2022 Mar 10;8(2):20210207.

130. Berberich A, Hielscher T, Kickingereder P, Winkler F, Drüschler K, Riedemann L, et al. Nonmeasurable Speckled Contrast-Enhancing Lesions Appearing During Course of Disease Are Associated With IDH Mutation in High-Grade Astrocytoma Patients. Int J Radiat Oncol Biol Phys. 2018 Dec 1;102(5):1472–80.

131. Georgakis MK, Tsivgoulis G, Spinos D, Dimitriou NG, Kyritsis AP, Herrlinger U, et al. Clinical, neuroimaging and histopathological features of gliomatosis cerebri: a systematic review based on synthesis of published individual patient data. J Neurooncol. 2018 Nov 1;140(2):467–75.

132. Kang KM, Song J, Choi Y, Park C, Park JE, Kim HS, et al. MRI Scoring Systems for Predicting Isocitrate Dehydrogenase Mutation and Chromosome 1p/19q Codeletion in Adult-type Diffuse Glioma Lacking Contrast Enhancement. Radiology [Internet]. 2024 May 7 [cited 2024 Aug 7]; Available from: https://pubs.rsna.org/doi/10.1148/radiol.233120

133. Jung JH, Sol IS, Kim MJ, Kim YH, Kim KW, Sohn MH. Validation of Pediatric Index of Mortality 3 for Predicting Mortality among Patients Admitted to a Pediatric Intensive Care Unit. Acute Crit Care. 2018 Aug;33(3):170–7.

134. Bhatti F, Menon N, Maynard J, Wastling S, Morgan PS, Smith S, et al. Validation of a rapid probability calculator for glioma IDH genotyping. In ESNR Annual Meeting. Paris, France; 2024.

135. Guo Y, Ma Z, Pei D, Duan W, Guo Y, Liu Z, et al. Improving Noninvasive Classification of Molecular Subtypes of Adult Gliomas With Diffusion-Weighted MR Imaging: An Externally Validated Machine Learning Algorithm. J Magn Reson Imaging. 2023;58(4):1234–42.

136. Zhu M, Han F, Gao J, Yang J, Yin L, Du Z, et al. Clinically Available and Reproducible Prediction Models for IDH and CDKN2A/B Gene Status in Adult-type Diffuse Gliomas. Acad Radiol [Internet]. 2024 Jun 29 [cited 2024 Jul 2]; Available from: https://www.sciencedirect.com/science/article/pii/S1076633224003799

137. Nam YK, Park JE, Park SY, Lee M, Kim M, Nam SJ, et al. Reproducible imaging-based prediction of molecular subtype and risk stratification of gliomas across different experience levels using a structured reporting system. Eur Radiol. 2021 Oct 1;31(10):7374–85.

138. Bisdas S, Shen H, Thust S, Katsaros V, Stranjalis G, Boskos C, et al. Texture analysis- and support vector machine-assisted diffusional kurtosis imaging may

allow in vivo gliomas grading and IDH-mutation status prediction: a preliminary study. Sci Rep. 2018 Apr 17;8(1):6108.

139. Yuan Y, Yu Y, Chang J, Chu YH, Yu W, Hsu YC, et al. Convolutional neural network to predict IDH mutation status in glioma from chemical exchange saturation transfer imaging at 7 Tesla. Front Oncol [Internet]. 2023 May 8 [cited 2024 Aug 8];13. Available from: https://www.frontiersin.org/journals/oncology/articles/10.3389/fonc.2023.1134626/full

140. Zhang J, Peng H, Wang YL, Xiao HF, Cui YY, Bian XB, et al. Predictive Role of the Apparent Diffusion Coefficient and MRI Morphologic Features on IDH Status in Patients With Diffuse Glioma: A Retrospective Cross-Sectional Study. Front Oncol. 2021;11:640738.

141. Thust S, Micallef C, Okuchi S, Brandner S, Kumar A, Mankad K, et al. Imaging characteristics of H3 K27M histone-mutant diffuse midline glioma in teenagers and adults. Quant Imaging Med Surg. 2021 Jan;11(1):43–56.

142. Chen H, Hu W, He H, Yang Y, Wen G, Lv X. Noninvasive assessment of H3 K27M mutational status in diffuse midline gliomas by using apparent diffusion coefficient measurements. Eur J Radiol. 2019 May;114:152–9.

143. Jaunmuktane Z, Capper D, Jones DTW, Schrimpf D, Sill M, Dutt M, et al. Methylation array profiling of adult brain tumours: diagnostic outcomes in a large, single centre. Acta Neuropathol Commun. 2019 Feb 20;7(1):24.

144. Zhao H, Fang X, Xue B. Four methods to analyze H3K27M mutation in diffuse midline gliomas. Pathol - Res Pract. 2020 Sep 1;216(9):153065.

145. Tarapore RS, Arain S, Blaine E, Hsiung A, Melemed AS, Allen JE. Immunohistochemistry Detection of Histone H3 K27M Mutation in Human Glioma Tissue. Appl Immunohistochem Mol Morphol AIMM. 2024 Feb 1;32(2):96–101.

146. Toh CH, Castillo M. Early-Stage Glioblastomas: MR Imaging–Based Classification and Imaging Evidence of Progressive Growth. AJNR Am J Neuroradiol. 2017 Feb;38(2):288–93.

147. Castel D, Philippe C, Calmon R, Le Dret L, Truffaux N, Boddaert N, et al. Histone H3F3A and HIST1H3B K27M mutations define two subgroups of diffuse intrinsic pontine gliomas with different prognosis and phenotypes. Acta Neuropathol (Berl). 2015 Dec 1;130(6):815–27.

148. Aboian MS, Tong E, Solomon DA, Kline C, Gautam A, Vardapetyan A, et al. Diffusion Characteristics of Pediatric Diffuse Midline Gliomas with Histone H3-K27M Mutation Using Apparent Diffusion Coefficient Histogram Analysis. AJNR Am J Neuroradiol. 2019 Nov;40(11):1804–10.

149. Raab P, Banan R, Akbarian A, Esmaeilzadeh M, Samii M, Samii A, et al. Differences in the MRI Signature and ADC Values of Diffuse Midline Gliomas with H3 K27M Mutation Compared to Midline Glioblastomas. Cancers. 2022 Mar 9;14(6):1397.

150. Wu G, Broniscer A, McEachron TA, Lu C, Paugh BS, Becksfort J, et al. Somatic histone H3 alterations in pediatric diffuse intrinsic pontine gliomas and non-brainstem glioblastomas. Nat Genet. 2012 Jan 29;44(3):251–3.

151. Arrillaga-Romany I, Gardner SL, Odia Y, Aguilera D, Allen JE, Batchelor T, et al. ONC201 (Dordaviprone) in Recurrent H3 K27M–Mutant Diffuse Midline Glioma. J Clin Oncol. 2024 May;42(13):1542–52.

152. Lasocki A, Abdalla G, Chow G, Thust SC. Imaging features associated with H3 K27-altered and H3 G34-mutant gliomas: a narrative systematic review. Cancer Imaging. 2022 Nov 17;22:63.

153. Daoud EV, Rajaram V, Cai C, Oberle RJ, Martin GR, Raisanen JM, et al. Adult Brainstem Gliomas With H3K27M Mutation: Radiology, Pathology, and Prognosis. J Neuropathol Exp Neurol. 2018 Apr 1;77(4):302–11.

154. Giagnacovo M, Antonelli M, Biassoni V, Schiavello E, Warmuth-Metz M, Buttarelli FR, et al. Retrospective analysis on the consistency of MRI features with histological and molecular markers in diffuse intrinsic pontine glioma (DIPG). Childs Nerv Syst ChNS Off J Int Soc Pediatr Neurosurg. 2020 Apr;36(4):697–704.

155. Qiu T, Chanchotisatien A, Qin Z, Wu J, Du Z, Zhang X, et al. Imaging characteristics of adult H3 K27M-mutant gliomas. J Neurosurg. 2019 Nov 15;133(6):1662–70.

156. Kathrani N, Chauhan RS, Kotwal A, Kulanthaivelu K, Bhat MD, Saini J, et al. Diffusion and perfusion imaging biomarkers of H3 K27M mutation status in diffuse midline gliomas. Neuroradiology. 2022 Aug;64(8):1519–28.

157. Hohm A, Karremann M, Gielen GH, Pietsch T, Warmuth-Metz M, Vandergrift LA, et al. Magnetic Resonance Imaging Characteristics of Molecular Subgroups in Pediatric H3 K27M Mutant Diffuse Midline Glioma. Clin Neuroradiol. 2022 Mar;32(1):249–58.

158. Louis DN, Perry A, Wesseling P, Brat DJ, Cree IA, Figarella-Branger D, et al. The 2021 WHO Classification of Tumors of the Central Nervous System: a summary. Neuro-Oncol. 2021 Aug 2;23(8):1231–51.

159. Seong M, Kim ST, Noh JH, Kim YK, Kim HJ. Radiologic findings and the molecular expression profile of diffuse midline glioma H3 K27M mutant. Acta Radiol Stockh Swed 1987. 2021 Oct;62(10):1404–11.

160. Rameh V, Vajapeyam S, Ziaei A, Kao P, London WB, Baker SJ, et al. Correlation between Multiparametric MR Imaging and Molecular Genetics in Pontine Pediatric High-Grade Glioma. AJNR Am J Neuroradiol. 2023 Jul;44(7):833–40.

161. Calmon R, Puget S, Varlet P, Dangouloff-Ros V, Blauwblomme T, Beccaria K, et al. Cerebral blood flow changes after radiation therapy identifies pseudoprogression in diffuse intrinsic pontine gliomas. Neuro-Oncol. 2018 Jun 18;20(7):994–1002.

162. Li J, Zhang P, Qu L, Sun T, Duan Y, Wu M, et al. Deep Learning for Noninvasive Assessment of H3 K27M Mutation Status in Diffuse Midline Gliomas Using MR Imaging. J Magn Reson Imaging JMRI. 2023 Jan 24;

163. Gillies RJ, Kinahan PE, Hricak H. Radiomics: Images Are More than Pictures, They Are Data. Radiology. 2016 Feb;278(2):563–77.

164. Thomas JV, Abou Elkassem AM, Ganeshan B, Smith AD. MR Imaging Texture Analysis in the Abdomen and Pelvis. Magn Reson Imaging Clin N Am. 2020 Aug;28(3):447–56.

165. Kassner A, Thornhill RE. Texture analysis: a review of neurologic MR imaging applications. AJNR Am J Neuroradiol. 2010 May;31(5):809–16.

166. Skogen K, Schulz A, Dormagen JB, Ganeshan B, Helseth E, Server A. Diagnostic performance of texture analysis on MRI in grading cerebral gliomas. Eur J Radiol. 2016 Apr;85(4):824–9.

167. Skogen K, Schulz A, Helseth E, Ganeshan B, Dormagen JB, Server A. Texture analysis on diffusion tensor imaging: discriminating glioblastoma from single brain metastasis. Acta Radiol Stockh Swed 1987. 2019 Mar;60(3):356–66.

168. Miles KA, Ganeshan B, Hayball MP. CT texture analysis using the filtration-histogram method: what do the measurements mean? Cancer Imaging Off Publ Int Cancer Imaging Soc. 2013 Sep 23;13(3):400–6.

169. Ostrom QT, Price M, Neff C, Cioffi G, Waite KA, Kruchko C, et al. CBTRUS Statistical Report: Primary Brain and Other Central Nervous System Tumors Diagnosed in the United States in 2015–2019. Neuro-Oncol. 2022 Oct 5;24(Supplement_5):v1–95.

170. Calabrese E, Villanueva-Meyer JE, Rudie JD, Rauschecker AM, Baid U, Bakas S, et al. The University of California San Francisco Preoperative Diffuse Glioma MRI Dataset. Radiol Artif Intell. 2022 Oct 5;4(6):e220058.

171. van der Voort SR, Incekara F, Wijnenga MMJ, Kapsas G, Gahrmann R, Schouten JW, et al. The Erasmus Glioma Database (EGD): Structural MRI scans, WHO 2016 subtypes, and segmentations of 774 patients with glioma. Data Brief. 2021 Aug 1;37:107191.

172. Appay R, Dehais C, Maurage CA, Alentorn A, Carpentier C, Colin C, et al. CDKN2A homozygous deletion is a strong adverse prognosis factor in diffuse malignant IDH-mutant gliomas. Neuro-Oncol. 2019 Dec 17;21(12):1519–28.

173. Whitfield BT, Huse JT. Classification of adult-type diffuse gliomas: Impact of the World Health Organization 2021 update. Brain Pathol. 2022 Jul;32(4):e13062.

174. Figini M, Riva M, Graham M, Castelli GM, Fernandes B, Grimaldi M, et al. Prediction of Isocitrate Dehydrogenase Genotype in Brain Gliomas with MRI: Single-Shell versus Multishell Diffusion Models. Radiology. 2018 Dec;289(3):788–96.

175. Hoebel KV, Patel JB, Beers AL, Chang K, Singh P, Brown JM, et al. Radiomics Repeatability Pitfalls in a Scan-Rescan MRI Study of Glioblastoma. Radiol Artif Intell. 2021 Jan;3(1):e190199.

176. Lasocki A, Gaillard F. Non-Contrast-Enhancing Tumor: A New Frontier in Glioblastoma Research. AJNR Am J Neuroradiol. 2019 May;40(5):758–65.

177. Ma H, Zeng S, Xie D, Zeng W, Huang Y, Mazu L, et al. Looking through the imaging perspective: the importance of imaging necrosis in glioma diagnosis and prognostic prediction – single centre experience. Radiol Oncol. 58(1):23–32.

178. Andersen MB, Harders SW, Thygesen J, Ganeshan B, Torp Madsen HH, Rasmussen F. Potential impact of texture analysis in contrast enhanced CT in non-small cell lung cancer as a marker of survival: A retrospective feasibility study. Medicine (Baltimore). 2022 Dec 2;101(48):e31855.

179. Armstrong RA. When to use the Bonferroni correction. Ophthalmic Physiol Opt. 2014 Sep 1;34(5):502–8.

180. ESNR [Internet]. [cited 2024 Sep 27]. Available from: https://www.esnr.org/nav/2nd_level_-_european_course_in_neuroadiology_%28ecnr%29

181. Adam A, Dixon AK, Gillard JH, Schaefer-Prokop C. Grainger & Allison's Diagnostic Radiology, 2 Volume Set E-Book. Elsevier Health Sciences; 2020. 2398 p.

182. author E. Grants on the web [Internet]. Engineering and Physical Sciences Research Council, Polaris House, North Star Avenue, Swindon, SN2 1ET; [cited 2024 Sep 27]. Available from: https://gow.epsrc.ukri.org/NGBOViewGrant.aspx?GrantRef=EP/Y015398/1

183. Galldiks N, Lohmann P, Friedrich M, Werner JM, Stetter I, Wollring MM, et al. PET imaging of gliomas: Status quo and quo vadis? Neuro-Oncol. 2024 Jul 6;noae078.

184. Bitencourt AGV, Bhowmik A, Marcal Filho EFDL, Lo Gullo R, Mazaheri Y, Kapetas P, et al. Deuterium MR spectroscopy: potential applications in oncology research. BJR Open. 2024 Jan;6(1):tzae019.

185. European Society of Radiology [Internet]. [cited 2023 May 27]. Biomarkers Neuro-Tumors. Available from: https://www.myesr.org/biomarkers-inventory/biomarkers-neuro-tumors

186. GliMR2.0 – COST Action CA18206 – Glioma MR Imaging 2.0 [Internet]. 2024 [cited 2024 Jul 13]. Available from: https://glimr.eu/

187. Siakallis L, Topriceanu CC, Panovska-Griffiths J, Bisdas S. The role of DSC MR perfusion in predicting IDH mutation and 1p19q codeletion status in gliomas: meta-analysis and technical considerations. Neuroradiology. 2023 Jul;65(7):1111–26.

188. Suh CH, Kim HS, Jung SC, Choi CG, Kim SJ. Imaging prediction of isocitrate dehydrogenase (IDH) mutation in patients with glioma: a systemic review and meta-analysis. Eur Radiol. 2019 Feb;29(2):745–58.

189. Branzoli F, Liserre R, Deelchand DK, Poliani PL, Bielle F, Nichelli L, et al. Neurochemical Differences between 1p/19q Codeleted and Noncodeleted IDH-mutant Gliomas by in Vivo MR Spectroscopy. Radiology. 2023 Sep;308(3):e223255.

190. Nichelli L, Cadin C, Lazzari P, Mathon B, Touat M, Sanson M, et al. Incorporation of edited MRS into clinical practice may improve care of patients with IDH-mutant glioma. AJNR Am J Neuroradiol. 2024 Jul 12;ajnr.A8413.

191. Abbas T, Fatima A, Shahzad T, Alharbi M, Khan MA, Ahmed A. Multidisciplinary cancer disease classification using adaptive FL in healthcare industry 5.0. Sci Rep. 2024 Aug 12;14(1):18643.

192. Zhang H, Fan X, Zhang J, Wei Z, Feng W, Hu Y, et al. Deep-learning and conventional radiomics to predict IDH genotyping status based on magnetic resonance imaging data in adult diffuse glioma. Front Oncol. 2023;13:1143688.

193. Ronneberger O, Fischer P, Brox T. U-Net: Convolutional Networks for Biomedical Image Segmentation. In: Navab N, Hornegger J, Wells WM, Frangi AF, editors. Medical Image Computing and Computer-Assisted Intervention – MICCAI 2015. Cham: Springer International Publishing; 2015. p. 234–41.

194. Isensee F, Jaeger PF, Kohl SAA, Petersen J, Maier-Hein KH. nnU-Net: a self-configuring method for deep learning-based biomedical image segmentation. Nat Methods. 2021 Feb;18(2):203–11.

195. Li HB, Conte GM, Anwar SM, Kofler F, Ezhov I, van Leemput K, et al. The Brain Tumor Segmentation (BraTS) Challenge 2023: Brain MR Image Synthesis for Tumor Segmentation (BraSyn). ArXiv. 2023 Jun 28;arXiv:2305.09011v5.

196. van der Voort SR, Incekara F, Wijnenga MMJ, Kapsas G, Gahrmann R, Schouten JW, et al. Combined molecular subtyping, grading, and segmentation of glioma using multi-task deep learning. Neuro-Oncol. 2023 Feb 14;25(2):279–89.

197. van Griethuysen JJ, Fedorov A, Parmar C, Hosny A, Aucoin N, Narayan V, et al. Computational Radiomics System to Decode the Radiographic Phenotype. Cancer Res. 2017 Nov 1;77(21):e104–7.

198. Ruffle JK, Mohinta S, Baruteau KP, Rajiah R, Lee F, Brandner S, et al. VASARI-auto: Equitable, efficient, and economical featurisation of glioma MRI. NeuroImage Clin. 2024 Sep 6;44:103668.

199. Yearley AG, Iorgulescu JB, Chiocca EA, Peruzzi PP, Smith TR, Reardon DA, et al. The current state of glioma data registries. Neuro-Oncol Adv. 2022 Jun 24;4(1):vdac099.

200. Usuzaki T, Inamori R, Shizukuishi T, Morishita Y, Takagi H, Ishikuro M, et al. Predicting isocitrate dehydrogenase status among adult patients with diffuse glioma using patient characteristics, radiomic features, and magnetic resonance imaging: Multi-modal analysis by variable vision transformer. Magn Reson Imaging. 2024 May 29;111:266–76.

201. Oliveira-Stahl G, Inglese M, Thust S, Grech-Sollars M. Machine learning based characterisation of glioma shows best performance with post-contrast T1 and diffusion imaging. In BIC ISMRM Annual Meeting. Aberdeen, UK; 2023.

202. Calabrese E, Villanueva-Meyer JE, Rudie JD, Rauschecker AM, Baid U, Bakas S, et al. The University of California San Francisco Preoperative Diffuse Glioma MRI Dataset. Radiol Artif Intell. 2022 Oct 5;4(6):e220058.

203. Watts C, Savage J, Patel A, Mant R, Wykes V, Pohl U, et al. Protocol for the Tessa Jowell BRAIN MATRIX Platform Study. BMJ Open. 2022 Sep 8;12(9):e067123.

204. Oncology TL. More needed to improve early cancer diagnosis. Lancet Oncol. 2024 Jul 1;25(7):823.

205. Barber HR, Perks CM, Kurian KM. Evaluating circulating tumour cell enrichment techniques to establish an appropriate method for clinical application in glioblastomas. Front Neurol. 2024;15:1358531.

Original files

European Radiology (2018) 28:3306–3317
https://doi.org/10.1007/s00330-018-5314-5

NEURO

Glioma imaging in Europe: A survey of 220 centres and recommendations for best clinical practice

S. C. Thust[1,2,3] · S. Heiland[4] · A. Falini[5] · H. R. Jäger[1,2,3] · A. D. Waldman[6] · P. C. Sundgren[7,8] · C. Godi[5] · V. K. Katsaros[9,10,11] · A. Ramos[12] · N. Bargallo[13,14] · M. W. Vernooij[15,16] · T. Yousry[1] · M. Bendszus[4] · M. Smits[15]

Received: 2 August 2017 / Revised: 14 December 2017 / Accepted: 5 January 2018 / Published online: 13 March 2018

Abstract

Objectives At a European Society of Neuroradiology (ESNR) Annual Meeting 2015 workshop, commonalities in practice, current controversies and technical hurdles in glioma MRI were discussed. We aimed to formulate guidance on MRI of glioma and determine its feasibility, by seeking information on glioma imaging practices from the European Neuroradiology community.

Methods Invitations to a structured survey were emailed to ESNR members (n=1,662) and associates (n=6,400), European national radiologists' societies and distributed via social media.

Results Responses were received from 220 institutions (59% academic). Conventional imaging protocols generally include T2w, T2-FLAIR, DWI, and pre- and post-contrast T1w. Perfusion MRI is used widely (85.5%), while spectroscopy seems reserved for specific indications. Reasons for omitting advanced imaging modalities include lack of facility/software, time constraints and no requests. Early postoperative MRI is routinely carried out by 74% within 24–72 h, but only 17% report a percent measure of resection. For follow-up, most sites (60%) issue qualitative reports, while 27% report an assessment according to the RANO criteria. A minority of sites use a reporting template (23%).

Conclusion Clinical best practice recommendations for glioma imaging assessment are proposed and the current role of advanced MRI modalities in routine use is addressed.

Key Points

- *We recommend the EORTC-NBTS protocol as the clinical standard glioma protocol.*
- *Perfusion MRI is recommended for diagnosis and follow-up of glioma.*
- *Use of advanced imaging could be promoted with increased education activities.*
- *Most response assessment is currently performed qualitatively.*
- *Reporting templates are not widely used, and could facilitate standardisation.*

Keywords Brain neoplasms · Magnetic resonance imaging · Surveys and questionnaires · Guideline · Glioma

Abbreviations

ADC	Apparent Diffusion Coefficient
ADNI	Alzheimer's Disease Neuroimaging Initiative
ASFNR	American Society of Functional Neuroradiology
ASL	Arterial Spin Labelling
Cho	Choline
Cr	Creatine
DCE	Dynamic Contrast-enhanced
DSC	Dynamic Susceptibility Contrast
DTI	Diffusion Tensor Imaging
DWI	Diffusion Weighted Imaging
EORTC	European Organisation for Research and Treatment of Cancer
ESNR	European Society of Neuroradiology
FLAIR	Fluid Attenuated Inversion Recovery
fMRI	Functional MRI
FSPGR	Fast Spoiled Gradient Echo
IDH	Isocitrate Dehydrogenase

This paper has been endorsed by the European Society of Neuroradiology (ESNR) and the European Organisation for Research and Treatment of Cancer (EORTC)

Electronic supplementary material The online version of this article (https://doi.org/10.1007/s00330-018-5314-5) contains supplementary material, which is available to authorized users.

✉ M. Smits
marion.smits@erasmusmc.nl

Extended author information available on the last page of the article

ISMRM	International Society for Magnetic Resonance in Medicine
ITSS	Intratumoral Susceptibility Signals
MPRAGE	Magnetization Prepared RApid Gradient Echo
MRI	Magnetic Resonance Imaging
MRS	MR Spectroscopy
NAA	N-acetylaspartate
NBTS	National Brain Tumor Society
NCI	National Cancer Institute
pMRI	Perfusion MRI
rCBV	Relative Cerebral Blood Volume
RANO	Response Assessment in Neuro Oncology
SNO	Society for Neuro-oncology
SPACE	SPAtial and Chemical Shift Encoded Excitation
SWI	Susceptibility Weighted Imaging
WHO	World Health Organisation

Introduction

Gliomas are a diverse group of neoplasms, the principal treatment for which is surgical resection followed by radiation and/or chemotherapy. Despite ongoing efforts to advance treatments, practically all adult gliomas eventually progress and have an overall poor prognosis [1]. Magnetic resonance imaging (MRI) is fundamental to the characterisation of brain tumours, guides the surgical strategy and is required to monitor treatment response. There is a current lack of MRI protocol standardisation [2], which can be problematic for patient management. Differences in scanning protocols (spatial and contrast resolution, image planes, sequences, etc.), whether within the same institution or between institutions, may affect image interpretation, assessment of contrast enhancement and (volume) changes in follow-up examinations [3]. For advanced imaging modalities, the absence of uniform protocols may delay their implementation, hamper the establishment of threshold values, and in the worst case render the technique non-diagnostic.

In 2015, the Diagnostic Committee of the European Society of Neuroradiology (ESNR) held a workshop on glioma imaging practices at its 38th Annual Meeting in Naples, Italy. Among the audience present, the lack of recommendations for MRI in clinical practice was found to be a universal deficit, whilst variations in protocols seemed to exist.

Best practice is defined as the conscientious and judicious use of current best evidence in making decisions about the care of individual patients [4]. The published evidence around brain tumour MRI protocols constitutes a complex and dynamic entity, particularly where advanced techniques are concerned. Key changes have occurred in the understanding of glioma, which are reflected in the recent World Health Organisation (WHO) classification [5]. It is now clear that the biological aggressiveness of glioma subtypes is primarily influenced by their molecular genetic composition, in some cases discrepant from histological results and conventional imaging features [6–8]. MRI protocols must account for the new integrated approach to glioma classification, and should aim to complement and add value in the diagnostic workup. The goal is to develop imaging protocols, which reflect best practice, but also to consider differences between institutions in equipment, levels of expertise, and financial factors in resource-limited healthcare systems. Furthermore, protocol harmonisation could serve as a means of quality assurance and support multicentre research into new treatments.

Consensus recommendations have recently been developed for glioma imaging in clinical trials. The United States National Brain Tumor Society (NBTS), Society for Neuro-oncology (SNO) and the European Organisation for Research and Treatment of Cancer (EORTC) jointly published the EORTC-NBTS protocol [9]. The main aim of this protocol is to enable in a defined group of patients a reproducible assessment of tumour volume change according to the response assessment in neuro-oncology (RANO) criteria [10]. The focus of this protocol is therefore on anatomical T1-weighted (T1w), T2-weighted (T2w) and T2w fluid-attenuated inversion recovery (T2-FLAIR) sequences, and also includes recommendations for diffusion-weighted imaging (DWI).

The question has been raised whether the EORTC-NBTS protocol would be suitable for implementation in a clinical setting. A simple adoption of a trial protocol into the challenging clinical service may, however, be problematic. In the clinical context, a variable number of questions need to be addressed such as diagnosis, differential diagnosis as well as treatment planning, outcome and monitoring. Furthermore, a clinical protocol must be time efficient and applicable in a wide range of medical institutions, and must affect the management of the individual patient. Advanced techniques, which are not relevant in current clinical trials and therefore not included in the EORTC-NBTS protocol, can be important for patient management.

This paper aims to provide best clinical practice recommendations on conventional and advanced MRI of glioma patients and assesses whether the EORTC-NBTS protocol would be suitable for routine clinical practice. To inform the recommendations and to assess their feasibility, information was sought from European institutions about MRI practices, technical parameters and common diagnostic challenges. To this end, a structured survey was carried out to ensure the involvement and representation of the European neuroradiology community in the guidance.

European survey on glioma MRI practices

Method

An online questionnaire was designed using a Google forms open access toolbox (Google.com, Mountainview, CA, USA). The questionnaire featured 87 items, divided into multiple choice, single best choice and free text questions on personal practice, preferred MRI techniques and clinical scenarios (see online Supplement 1). The questionnaire was optimised and tested by peers such that it would take a maximum of 10 min to fill out. This information was given at the start of the questionnaire.

Questions were derived from issues raised at the 38th ESNR annual meeting workshop on brain tumour imaging (attendance ± 150 people), as well as those identified during the development of the EORTC-NBTS protocol. Survey invitations were emailed to all ESNR members (n=1,662), non-members who had expressed their interest in ESNR-activities in the past (n=6,400), European national neuroradiological societies (The Netherlands, Belgium and the UK), and distributed via LinkedIn and Twitter. The survey was open for 1 month, from 1 March to 1 April 2016, with one reminder sent. To avoid duplicate bias, participants were instructed to supply institution details or confirm they were the only person answering from their centre.

Results

Demographic and institution data (online Supplement 2, Table 1)

Two hundred and twenty-seven professionals working in 31 out of 51 European countries completed the survey; seven were duplicates from the same institution, resulting in responses from 220 institutions. A proportion of questionnaires (8.2 %) included in the analysis were submitted by individuals currently working outside Europe. Figure 1 provides an overview of the responses by country.

A number of questions included the option 'other'. If this was answered by < 5 % of individuals, percentages are not quoted in the results. A few undecipherable free text answers were excluded from the analysis.

Primary diagnosis and follow up (online Supplement 2, Table 2)

Typical glioma standard MRI protocols lasted between 20–60 min. The proportion of institutions per country that use protocols shorter than 30 min is displayed in Fig. 2.

In more than 95 %, the protocols included T2w, T2-FLAIR, pre- and post-contrast T1w, and DWI. At many institutions (65 %) T2*w or susceptibility weighted imaging (SWI) were part of the MRI protocol. 3D anatomical sequences were used by most (81.8 %) of the institutions, most commonly post-contrast T1w. In free text answers, reasons given for not using 3D imaging included time pressure (n=10), quality concerns, scanner limitations, financial reasons and lack of technical support (n=2 each). Most (77.7 %) institutions used the same protocol for glioma follow-up as for primary diagnosis. Some chose a different protocol for follow up with omission or selective use of sequences, most frequently MR spectroscopy (MRS) or perfusion MRI (pMRI).

Contrast-enhanced MRI (online Supplement 2, Table 3)

To depict enhancement, the most commonly (72.3 %) performed sequence was FSPGR/MPRAGE. Not all users felt comfortable using this 3D gradient echo sequence as the sole sequence to assess contrast uptake. In free text answers, the most frequently (n=48) reported concern was absent or suboptimal sensitivity to detect enhancement, followed by artefact, reduced sensitivity, and a risk of missing small lesions.

Diffusion-weighted imaging (DWI; online Supplement 2, Table 4)

DWI was almost always (99.1 %) performed in glioma imaging. ADC was much more often (78.2 %) assessed by visual comparison with normal appearing brain than quantitatively. Nearly all users employed b values of 0 and 1,000 s/mm^2, with some acquiring an additional b-value of 500 s/mm^2.

Perfusion MRI (pMRI; online Supplement 2, Table 5)

Most institutions (85 %) applied pMRI (most frequently dynamic susceptibility contrast [DSC; 81.8 %]) for initial grading and/or glioma follow-up. The use of this modality was homogeneously distributed across Europe. Some institutions (21.4 %) reported use of either DSC plus one other perfusion technique, and rarely all three were acquired. Free text answers highlighted usefulness of pMRI in differentiating chemoradiation effects from tumour progression (n=55) and for grading (n=36).

MR Spectroscopy (MRS; online Supplement 2, Table 6)

The majority (80.4 %) of institutions used MRS in clinical brain tumour imaging, but rarely as part of the routine protocol. The largest group (35.2 %) of users acquired MRS occasionally, upon request or for a specific indication. Free text answers regarding MRS indications featured lesion characterisation (n= 56), including distinction of tumour from non-neoplastic conditions, and grading (n=21). Less commonly

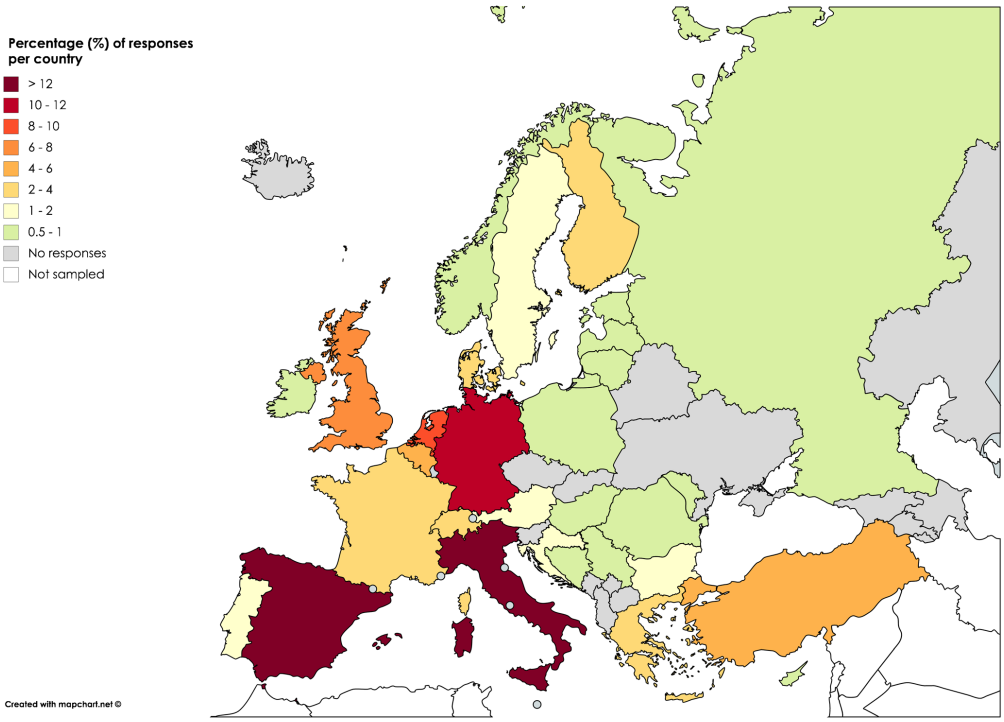

Fig. 1 Institutional responses (%) per country. Countries with no responses are shaded grey

MRS was employed for brain tumours in general or to differentiate therapy effects from tumour recurrence.

Functional MRI (fMRI; online Supplement 2, Table 7)

Approximately half (49.8 %) of participating institutions used fMRI in clinical practice, mostly for surgical planning (95.4 %). Free text answers on the clinical impact reported its value for operative planning, to guide the interventional approach, and to determine tumour resectability. Functions assessed were language lateralisation and localisation, visual cortex localisation and motor cortex localisation (resting state fMRI not assessed). fMRI scan times varied substantially lasting up to 1 h, depending on tasks.

Diffusion-tensor imaging (DTI) tractography (online Supplement 2, Table 8)

Nearly two-thirds (63.7 %) of participating institutions carried out DTI tractography in their practice, generally for presurgical evaluation (88.2 %). Numerous free text answers stated that DTI tractography was useful for operative planning, underscoring the potential of DTI results to change the surgical approach. Some users reported limited impact or experience. The number of acquired directions varied significantly, but over half (58.5 %) of the DTI performing institutions acquired at least 20 directions in their clinical practice.

Clinical scenarios and issues

Early postoperative MRI (online Supplement 2, Table 9) At the majority (74.3 %) of institutions, early postoperative MRI was routinely performed to assess the extent of glioma resection, but few (17.2 %) radiologists provided a percent measure on completeness of resection in their report, with no uniform method identifiable from the free text answers (n=28).

Monitoring of therapy response (online Supplement 2, Table 9) For glioma follow-up, most respondents (60.6 %) undertook a qualitative assessment, and a smaller group (27.1 %) obtained measurements according to the RANO criteria [10]. Less than a quarter (23.3 %) of institutions incorporated a reporting template in their current practice.

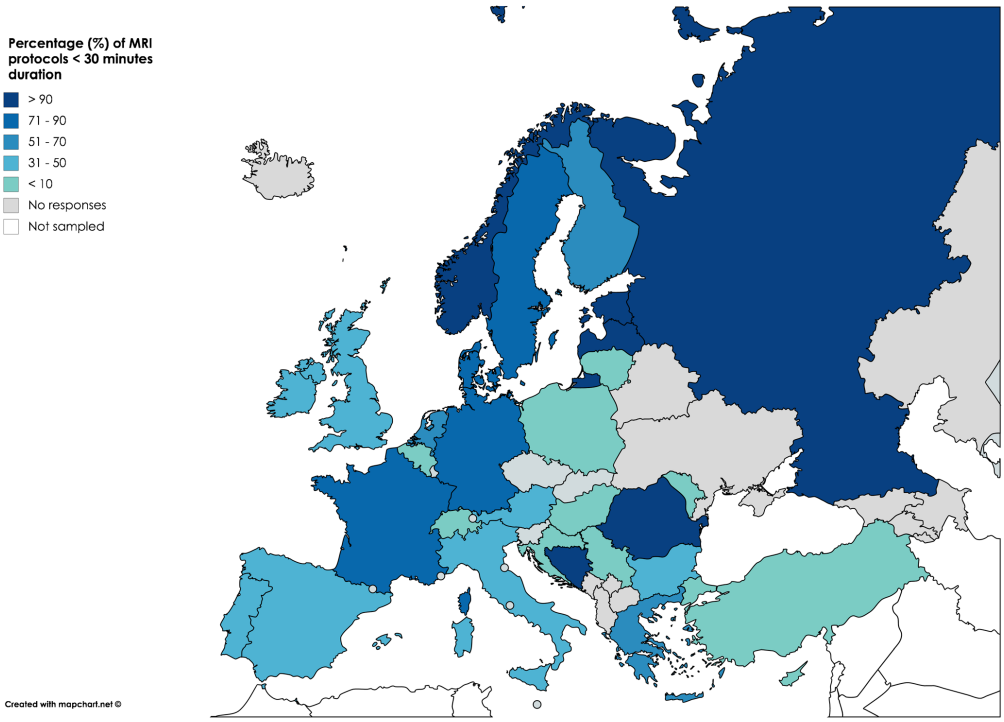

Fig. 2 Percentage of MRI protocols of < 30 min duration for each country. The remaining protocols nearly always lasted between 31 and 60 min. Amongst all 220 responses, only 2.7 % of glioma MRI protocols were longer than 60 min

Post-processing and non-use of advanced imaging (online Supplement 2, Table 10) For all advanced modalities, data post-processing was most commonly carried out by a radiologist. Multiple reasons featured amongst non-use of advanced imaging, with lack of MRI equipment (40.5–49.5 %) slightly dominating for all methods.

Discussion

A conventional MRI protocol consisting of T2w, T2-FLAIR, DWI and pre- and post-contrast T1w appears representative of standard glioma imaging practice in Europe. To the best of our knowledge, level I evidence in the form of randomised controlled trials for the MRI assessment of glioma is currently lacking. Conventional MRI, but also the use of DWI and pMRI for glioma characterisation are supported by some level II evidence, and by numerous level III studies [11]. The current data on the use of MRS, SWI, fMRI and DTI are restricted to level III evidence, mostly in the form of retrospective comparative studies.

3D versus 2D imaging

3D (volumetric) imaging has clear advantages over 2D imaging. First, reconstructions can be made in all planes, allowing not only for a better appreciation of anatomical location, but also for more accurate longitudinal assessment [12]. Second, tumour volumes can be more accurately measured, in particular when this is done automatically [13]. In addition, the higher through-plane resolution of 3D imaging reduces the risk of missing small foci of contrast enhancement due to partial volume effects [14]. FSPGR/MPRAGE appears overall diagnostic for glioma imaging [15] and remains the most widely available T1w 3D technique at present [9]. However, some concerns exist regarding its suitability to depict post contrast enhancement, increased susceptibility to movement or pulsation artifacts, and lack of sensitivity for the detection of leptomeningeal disease. The short repetition times used for FSPGR/MPRAGE sequences are known to result in less marked T1-dependent signal enhancement compared with spin-echo using the same Gadolinium-chelate dose [16]. This effect was not found to be detrimental for small brain

lesions in vivo [17], but potentially superior 3D spin-echo alternatives such as SPACE and CUBE [14, 18] could well supersede FSPGR over time.

Diffusion-weighted imaging

DWI with a maximum b value of 1,000 s/mm^2 matches the EORTC-NBTS protocol and National Cancer Institute (NCI) - International Society for Magnetic Resonance in Medicine (ISMRM) consensus recommendations [19], which specify the preferred use of 3 b-values (0, 500 and 1,000 s/mm^2), but acknowledge the fact that not all scanners have this capability. DWI can non-invasively contribute to estimating tumour cellularity and grade [11, 20–22] and support the assessment of therapy response, although as a single modality its accuracy appears limited for the distinction of tumour and radiation effects [23, 24]. Advanced diffusion techniques could provide greater information on tissue microstructure for the distinction of glioma molecular subgroups [25, 26, 83] and to support early response assessment, e.g. via parametric mapping [27–29], but such methods are not yet a clinical standard.

T2*w and SWI

Susceptibility sensitive sequences may identify haemorrhage or calcification in glioma primary diagnosis, and help depict biopsy tracts. For SWI, an association has been observed between intratumoral susceptibility signals (ITSS), histological WHO grade and relative cerebral blood volume (rCBV) [30]. The latter could provide substitute evidence of neovascularity, where pMRI is unavailable. However, current evidence is confined to a limited number of studies [31]. It remains doubtful what information SWI can offer above other MRI sequences in glioma, with a possible exception of tumour margin delineation on contrast-enhanced SWI [32].

Perfusion MRI (pMRI)

DSC pMRI constitutes the primarily used perfusion method (>80 %) in the European institutions surveyed, which matches published data [33], with nearly half of all users acquiring it for all glioma indications. With DSC, high-grade glioma can be differentiated from low-grade glioma using rCBV values with high (95 %) sensitivity, but specificity is relatively low (70 %) [34, 35]. This finding can be attributed to the misclassification of low-grade gliomas with elevated rCBV, most notably oligodendroglioma [36, 37]. Raised rCBV has recently been highlighted as a characteristic of isocitrate dehydrogenase (IDH) wildtype glioma, even at a histological low grade [38]. Furthermore, rCBV is the most validated perfusion parameter for the distinction of therapy effects from tumour progression [39, 40]. DSC studies consistently demonstrate that rCBV is low in areas of radiation necrosis or pseudoprogression and high in tumour progression, allowing for accurate (generally accuracy >90 %) distinction between these entities [41–44].

Alternative perfusion techniques such as dynamic contrast-enhanced (DCE) perfusion MRI and arterial spin labelling (ASL), though less established, appear beneficial, especially for such gliomas in which susceptibility effects render DSC non-diagnostic. Neither technique has, however, been extensively validated or integrated into clinical glioma imaging practice to date.

Spectroscopy (MRS)

Whilst a high number of institutions have experience with MRS in glioma, the survey results suggest that this method is clinically used for specific indications only. The relative intensity of metabolite spectra is influenced by echo time (TE), with short or intermediate TE (30–144 ms) considered preferable for glioma imaging. The benefit of MRS in the distinction of glioma from non-neoplastic conditions was highlighted in many free text answers, which is well supported by published data [45, 46]. The evidence for the selective use of MRS in the distinction of glioma from other tumours, such as metastases and brain lymphoma, remains indeterminate [47, 48]. A potential advantage of MRS lies in the characterisation of grade II oligodendroglioma, which commonly show elevated rCBV, and may be misclassified as high-grade tumour [49]. Otherwise, MRS finds a less prominent application in grading, tumour classification, biopsy planning and characterisation of radiation effects, with a moderate performance shown for the latter indications in research [50–52]. For glioma grading, Cho/Cr and Cho/NAA ratios have most frequently been reported to increase diagnostic accuracy, but in isolation MRS remains inferior to rCBV measurements [47, 53]. For various thresholds, quantitative MRS suffers from a mismatch between sensitivity and specificity, therefore a clear diagnostic benefit in grading has only been shown through combination with other techniques [34, 50, 53]. For the differentiation of radiation necrosis and recurrent glioma, a systematic meta-analysis revealed a limited performance for MRS, and strongly recommended its use only in combination with other modalities [51].

fMRI and DTI tractography

With a principal clinical application of surgical planning, these modalities are used to determine language lateralisation and localisation of the motor and visual cortex as well as various white matter tracts. Even though there is now substantial literature support for the use of task-based fMRI in glioma in the pre-operative context, reported accuracies for this modality are variable and its impact on clinical practice remains to be

further established [54, 55]. Whilst the notion that DTI may change the surgical approach is supported by data [56, 57] and by the survey results, there are still important limitations to the standardisation and clinical integration of tractography for neurosurgical decision-making [58]. DTI was the only advanced imaging method for which users specifically mentioned limited experience, which is judged to reflect its partial clinical establishment in Europe. Although it has been highlighted that the reliability of DTI may increase according to the number of diffusion directions acquired [57], no consensus was identifiable from the survey results on an optimal number of directions for clinical glioma imaging.

Non-use of advanced imaging

The fact that data processing for all advanced techniques was most commonly carried out by a radiologist suggests that these methods can be user-led. Such an arrangement could however impact neuroradiology workflow. Lack of MRI facility/equipment or software appears to be a greater limiting factor than time pressure. In some countries, advanced techniques are not reimbursed, which can be a significant hurdle. Lack of experience with and not knowing how to implement the techniques appear to be important obstacles, especially for fMRI.

Reporting practices and quantification

With improved outcomes after complete or near-complete glioma removal, postoperative residual measurement can be expected to become a focus of attention [59, 60]. Yet most radiologists do not offer any quantitative information in their report, and the literature provides no established system to assess extent of resection.

In follow up, most respondents relied on a visual estimate of tumour size despite existing RANO guidance. The current RANO criteria incorporate two-dimensional measurements, reflecting evidence indicating that changes in tumour volume correlate with changes in unidimensional or two-dimensional measurements [61–63], especially in high-grade glioma [64, 65]. The debate about whether volumetric glioma measurements would be more accurate than linear measurements and/or would impact clinical management is ongoing, especially for the response assessment of lower grade gliomas, which may be challenged by subtle growth. Conflicting results exist regarding the reliability of low-grade glioma segmentations [66, 67]. An additional hurdle is that currently available semi-automated volumetric segmentation algorithms tend to require manual editing [67–70].

An important issue revealed by the survey is the limited use of quantification methods for physiological parameters such as ADC and rCBV. Lack of available software tools and/or familiarity with how to use them, as well as time pressure may be contributing factors to the limited quantification of findings [22, 71].

Survey limitations

From all persons contacted, only a small proportion (14 % of ESNR members) responded, meaning the survey results may not represent the entire neuroradiology community, almost certainly introducing a response bias from those with a particular interest or expertise in glioma imaging. Moreover, it is likely that the length of the survey contributed to the low participation rate. Duplicate bias was avoided through only allowing one person answer from each institution. The disadvantage of this approach is that variations in practice within one department may not have been captured. This survey does not cover most of the practices in outpatient general radiology outside neuroradiology. We did not survey imaging practices specific to paediatric glioma. However, a central imaging review has been instituted for more than 20 years for paediatric brain tumour studies and recommendations on imaging and response assessment do exist [72, 73].

Best clinical practice recommendations

The following recommendations for MRI of glioma were formulated taking together the information provided by a peer group (>150 persons) discussion at the 38th ESNR Annual Meeting in 2015, a structured survey of clinical practices at over 200 European hospital institutions from 31 European countries, and the currently available literature on the subject (Fig. 3).

Conventional MRI protocol recommendations

The MRI sequences prescribed by the EORTC-NBTS protocol are widely used and scan durations generally allow for the implementation of the 25–30 min EORTC-NBTS basic protocol in routine clinical practice. It is therefore recommended that this should be used as a minimum clinical standard. As a base structure this will support glioma imaging standardisation across Europe with a view to establishing databases, which could be shared for radiomics and radiogenomic analyses and upon which advanced techniques can further build in the future.

3D imaging is preferable for the aforementioned reasons and to support the transition into volumetric tumour measurements, but it is recognised that further development is required in this area. Where 3D T1w imaging is adopted, this should be performed as isotropic sequences before and after contrast, taking care to ensure consistent and sufficient post contrast timing [9]. FSPGR/MPRAGE remains the most widely available T1w 3D technique as part of the standard MRI vendor Alzheimer's Disease

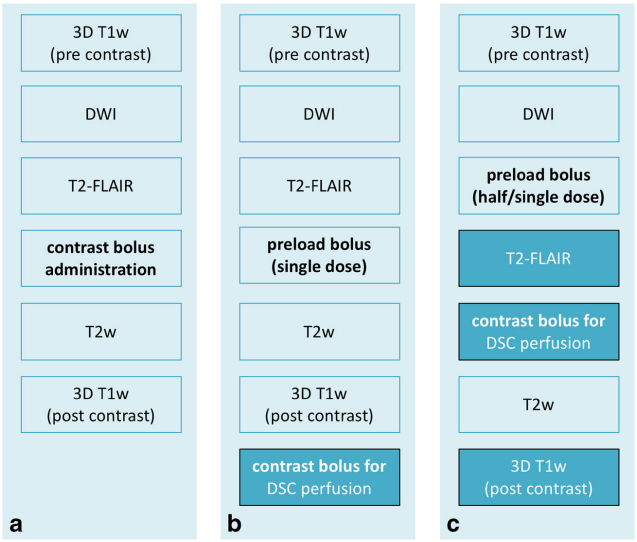

Fig. 3 Three possible options for a glioma imaging protocol in clinical practice based on the EORTC-NBTS protocol (**a**), with the addition of DSC perfusion imaging (**b, c**). Option C has the advantage over option B that it has double the contrast dose for post-contrast T1w imaging. Option B may be preferred if non-contrast enhanced T2-FLAIR is desired. Please see Ellingson et al. [9] for further considerations and vendor-specific sequence details on structural and diffusion-weighted imaging. The moment of contrast administration is indicated in bold

Neuroimaging Initiative (ADNI) protocol [74] and is recommended for clinical brain tumour trials [9]. Its use is again endorsed here as an accessible method for serial glioma imaging in clinical practice, but it could be replaced by 3D spin-echo T1w imaging where this is available, or supplemented with 2D spin-echo sequences where optimisation of the 3D technique fails to be maximally sensitive to contrast enhancement. In individual circumstances where only 2D imaging achieves good quality imaging within a clinically justifiable time, this may be retained as a standard.

For diffusion analysis, quantitative ADC comparison to normal brain is recommended, due to the potential pitfall of visual assessment that a tumour surrounded by oedema will appear dark on the ADC map, even in the absence of diffusion restriction. Because of the limited number of studies on T2*w/SWI, these sequences are considered optional. We would suggest using the same anatomical protocol for both primary diagnosis and follow-up to maximise comparability.

Advanced imaging recommendations

Perfusion MRI should be performed in gliomas of suspected low grade that have not undergone histological evaluation or prior to biopsy [34, 35, 39, 75]. The use of perfusion for serial lesion assessment is recommended to identify malignant transformation and to distinguish therapy effects (pseudoprogression or radiation necrosis) from tumour progression [41–44]. A caveat must be made that threshold values are not simply transferable between institutions, as they very much depend on scan parameters and post-processing methods [76]. Based on currently available data, we recommended DSC as the standard technique. Using pMRI routinely in all glioma patients has several advantages: diagnostic information is available when needed, there is consistency of imaging protocols, and both radiographers and radiologists gain and sustain experience with the technique. The available evidence strongly supports the use of a preload bolus technique, to overcome errors in estimation cerebral blood volume due to contrast leakage effects [40, 77, 78]. Gadolinium contrast dose can – at 3.0T – be kept low by splitting a single dose into preload and bolus injection, as outlined by the American Society of Functional Neuroradiology (ASFNR) in 2015 [40]. The acquisition of an appropriate baseline prior to contrast injection, high temporal resolution (TR<1,500 ms), and fast contrast bolus injection (preferably with a power injector) are important aspects of appropriate DSC acquisition [79]. Consistency of acquisition and post-processing techniques is critical, as differences between software packages, and even algorithm alterations within the same product may produce significantly different quantitative perfusion results [78]. Where sufficient evidence has been gathered within an institution to show the reliability of an alternative technique (DCE, ASL), this could be performed optionally, preferably as an adjunct.

On the basis of the survey results and current data, MRS is recommended in glioma as an optional modality for specific indications as aforementioned. Its clinical indication should be considered on an individual case basis, whereby caution is advised regarding the use of MRS in isolation for some of its less certain indications.

Because of their limited availability and limited use by the survey respondents at the present time, fMRI and DTI will not form part of these recommendations. The authors would like to highlight their potential value, however, and would support their use where adequate facilities, expertise and quality assurance measures exist. Further research into these techniques is desirable and recommended.

Discussion of recommendations

Relatively easy adaptation towards the standard best clinical practice recommendations can be expected, although some variations throughout Europe are likely to remain, depending on reimbursement strategies, practical and logistical setups and availability of scanning facilities.

For advanced techniques, lack of facility, software and experience is likely to hamper their introduction at some institutions, and it is possible that this could be especially the case for centres from which no survey results were available. The neuroradiological community has an important role here to include such technical aspects in their various training programmes.

For anatomical MRI, the use of measurements, bidirectional as a standard (and optionally volumetric, where segmentation software is available) is strongly recommended, as this has been shown to increase diagnostic accuracy in serial follow up [80]. The use of RANO criteria in clinical practice could be facilitated by the introduction of structured reports, which could also have other advantages both in terms of accuracy and effectiveness [81, 82]. These are preferably developed together with treating physicians, to ensure that all relevant information is consistently reported.

Regarding advanced imaging, we would like to emphasise that, where possible, quantification is a powerful tool in clinical practice, since it allows for the formulation of threshold or reference values and avoids certain pitfalls of subjectivity. Validation is, however, required. Multicentre research will be of key importance to establish transferable quantification methods for advanced imaging, which would be applicable across scanners and vendor platforms.

Conclusion

The MRI sequences prescribed by the EORTC-NBTS protocol are well established in glioma imaging practice throughout Europe, and we recommend that this protocol is adopted as the clinical standard for anatomical MRI. Advanced imaging methods may offer crucial diagnostic information, and should be utilised where possible, within the constraints of currently available data and local expertise. The results from the literature review and survey highlight the value of pMRI in glioma, and also potentially important roles for other methods. The relative lack of quantitative assessment and reporting templates reflects a further need for standardisation. The harmonisation of glioma imaging protocols across Europe together with ongoing research should aim to support the development of quantitative biomarkers for brain tumour diagnosis and therapy response assessment.

Funding This publication was supported by the EORTC Cancer Research Fund and by the EORTC Brain Tumour Group and the EORTC Imaging Group.

Compliance with ethical standards

Guarantor The scientific guarantor of this publication is M. Smits, MD PhD.

Conflict of interest The authors of this manuscript declare no relationships with any companies whose products or services may be related to the subject matter of the article.

Statistics and biometry No complex statistical methods were necessary for this paper.

Informed consent Written informed consent was not required for this study because no human subjects/patients were included in this study.

Ethical approval Institutional Review Board approval was not required because no human subjects/patients were included in this study.

Methodology
• Survey and literature review.

References

1. Ostrom QT, Bauchet L, Davis FG et al (2014) The epidemiology of glioma in adults: a "state of the science" review. Neuro Oncol 16: 896–913
2. Wen PY, Cloughesy TF, Ellingson BM et al (2014) Report of the Jumpstarting Brain Tumor Drug Development Coalition and FDA clinical trials neuroimaging endpoint workshop (January 30, 2014, Bethesda MD). Neuro Oncol 16:vii36–vii47
3. Patzig M, Burke M, Brückmann H, Fesl G (2014) Comparison of 3D cube FLAIR with 2D FLAIR for multiple sclerosis imaging at 3 Tesla. Rofo 186:484–488
4. Perleth M, Jakubowski E, Busse R (2001) What is "best practice" in health care? State of the art and perspectives in improving the effectiveness and efficiency of the European health care systems. Health Policy 56:235–250
5. Louis DN, Perry A, Burger P et al (2014) International Society Of Neuropathology–Haarlem consensus guidelines for nervous system tumor classification and grading. Brain Pathol 24:429–435

6. Wiestler B, Capper D, Holland-Letz T et al (2013) ATRX loss refines the classification of anaplastic gliomas and identifies a subgroup of IDH mutant astrocytic tumors with better prognosis. Acta Neuropathol 126:443–451
7. Reuss DE, Sahm F, Schrimpf D et al (2015) ATRX and IDH1-R132H immunohistochemistry with subsequent copy number analysis and IDH sequencing as a basis for an "integrated" diagnostic approach for adult astrocytoma, oligodendroglioma and glioblastoma. Acta Neuropathol 129:133–146
8. Ideguchi M, Kajiwara K, Goto H et al (2015) MRI findings and pathological features in early-stage glioblastoma. J Neurooncol 123:289–297
9. Ellingson BM, Bendszus M, Boxerman J et al (2015) Consensus recommendations for a standardized Brain Tumor Imaging Protocol in clinical trials. Neuro Oncol 17:1188–1198
10. Wen PY, Macdonald DR, Reardon DA et al (2010) Updated response assessment criteria for high-grade gliomas: response assessment in neuro-oncology working group. J Clin Oncol 28:1963–1972
11. Fouke SJ, Benzinger T, Gibson D, Ryken TC, Kalkanis SN, Olson JJ (2015) The role of imaging in the management of adults with diffuse low grade glioma: A systematic review and evidence-based clinical practice guideline. J Neurooncol 125:457–479
12. Reuter M, Gerstner ER, Rapalino O, Batchelor TT, Rosen B, Fischl B (2014) Impact of MRI head placement on glioma response assessment. J Neurooncol 118:123–129
13. Dempsey MF, Condon BR, Hadley DM (2005) Measurement of tumor "size" in recurrent malignant glioma: 1D, 2D, or 3D? AJNR Am J Neuroradiol 26:770–776
14. Kwak HS, Hwang S, Chung GH, Song JS, Choi EJ (2015) Detection of small brain metastases at 3 T: comparing the diagnostic performances of contrast-enhanced T1-weighted SPACE, MPRAGE, and 2D FLASH imaging. Clin Imaging 39:571–575
15. Dodo T, Okada T, Yamamoto A et al (2016) T1-weighted MR imaging of glioma at 3T: a comparative study of 3D MPRAGE vs. conventional 2D spin-echo imaging. Clin Imaging 40:1257–1261
16. Rand S, Maravilla KR, Schmiedl U (1994) Lesion enhancement in radio-frequency spoiled gradient-echo imaging: theory, experimental evaluation, and clinical implications. AJNR Am J Neuroradiol 15:27–35
17. Furutani K, Harada M, Mawlan M, Nishitani H (2008) Difference in enhancement between spin echo and 3-dimensional fast spoiled gradient recalled acquisition in steady state magnetic resonance imaging of brain metastasis at 3-T magnetic resonance imaging. J Comput Assist Tomogr 32:313–319
18. Majigsuren M, Abe T, Kageji T et al (2016) Comparison of Brain Tumor Contrast-enhancement on T1-CUBE and 3D-SPGR Images. Magn Reson Med Sci 15:34–40
19. Padhani AR, Liu G, Koh DM et al (2009) Diffusion-weighted magnetic resonance imaging as a cancer biomarker: consensus and recommendations. Neoplasia N Y N 11:102–125
20. Castillo M, Smith JK, Kwock L, Wilber K (2001) Apparent diffusion coefficients in the evaluation of high-grade cerebral gliomas. AJNR Am J Neuroradiol 22:60–64
21. LaViolette PS, Mickevicius NJ, Cochran EJ et al (2014) Precise ex vivo histological validation of heightened cellularity and diffusion-restricted necrosis in regions of dark apparent diffusion coefficient in 7 cases of high-grade glioma. Neuro Oncol 16:1599–1606
22. Zhang L, Min Z, Tang M, Chen S, Lei X, Zhang X (2017) The utility of diffusion MRI with quantitative ADC measurements for differentiating high-grade from low-grade cerebral gliomas: Evidence from a meta-analysis. J Neurol Sci 373:9–15
23. Chenevert TL, Stegman LD, Taylor JM et al (2000) Diffusion magnetic resonance imaging: an early surrogate marker of therapeutic efficacy in brain tumors. J Natl Cancer Inst 92:2029–2036
24. Zhang H, Ma L, Shu C, Wang YB, Dong LQ (2015) Diagnostic accuracy of diffusion MRI with quantitative ADC measurements in differentiating glioma recurrence from radiation necrosis. J Neurol Sci 351:65–71
25. Xiong J, Tan W, Wen J et al (2016) Combination of diffusion tensor imaging and conventional MRI correlates with isocitrate dehydrogenase 1/2 mutations but not 1p/19q genotyping in oligodendroglial tumours. Eur Radiol 26:1705–1715
26. Hempel J-M, Bisdas S, Schittenhelm J et al (2017) In vivo molecular profiling of human glioma using diffusion kurtosis imaging. J Neurooncol 131:93–101
27. Castellano A, Donativi M, Rudà R et al (2016) Evaluation of low-grade glioma structural changes after chemotherapy using DTI-based histogram analysis and functional diffusion maps. Eur Radiol 26:1263–1273
28. Yoon RG, Kim HS, Kim DY, Hong GS, Kim SJ (2016) Apparent diffusion coefficient parametric response mapping MRI for follow-up of glioblastoma. Eur Radiol 26:1037–1047
29. Hamstra DA, Galbán CJ, Meyer CR et al (2008) Functional diffusion map as an early imaging biomarker for high-grade glioma: correlation with conventional radiologic response and overall survival. J Clin Oncol 26:3387–3394
30. Wang X, Zhang H, Tan Y et al (2014) Combined value of susceptibility-weighted and perfusion-weighted imaging in assessing who grade for brain astrocytomas. J Magn Reson Imaging 39:1569–1574
31. Hsu CC-T, Watkins TW, Kwan GNC, Haacke EM (2016) Susceptibility-Weighted Imaging of Glioma: Update on Current Imaging Status and Future Directions. J Neuroimaging 26:383–390
32. Fahrendorf D, Schwindt W, Wölfer J et al (2013) Benefits of contrast-enhanced SWI in patients with glioblastoma multiforme. Eur Radiol 23:2868–2879
33. Dickerson E, Srinivasan A (2016) Multicenter Survey of Current Practice Patterns in Perfusion MRI in Neuroradiology: Why, When, and How Is It Performed? AJR Am J Roentgenol. https://doi.org/10.2214/AJR.15.15740
34. Law M, Yang S, Wang H et al (2003) Glioma grading: sensitivity, specificity, and predictive values of perfusion MR imaging and proton MR spectroscopic imaging compared with conventional MR imaging. AJNR Am J Neuroradiol 24:1989–1998
35. Law M, Yang S, Babb JS et al (2004) Comparison of cerebral blood volume and vascular permeability from dynamic susceptibility contrast-enhanced perfusion MR imaging with glioma grade. AJNR Am J Neuroradiol 25:746–755
36. Lev MH, Ozsunar Y, Henson JW et al (2004) Glial tumor grading and outcome prediction using dynamic spin-echo MR susceptibility mapping compared with conventional contrast-enhanced MR: confounding effect of elevated rCBV of oligodendrogliomas [corrected]. AJNR Am J Neuroradiol 25:214–221
37. Jenkinson MD, Smith TS, Joyce KA et al (2006) Cerebral blood volume, genotype and chemosensitivity in oligodendroglial tumours. Neuroradiology 48:703–713
38. Tan W, Xiong J, Huang W, Wu J, Zhan S, Geng D (2017) Noninvasively detecting Isocitrate dehydrogenase 1 gene status in astrocytoma by dynamic susceptibility contrast MRI. J Magn Reson Imaging 45:492–499
39. Lacerda S, Law M (2009) Magnetic resonance perfusion and permeability imaging in brain tumors. Neuroimaging Clin N Am 19:527–557
40. Welker K, Boxerman J, Kalnin A et al (2015) ASFNR recommendations for clinical performance of MR dynamic susceptibility contrast perfusion imaging of the brain. AJNR Am J Neuroradiol 36:E41–E51

41. Sugahara T, Korogi Y, Tomiguchi S et al (2000) Posttherapeutic intraaxial brain tumor: the value of perfusion-sensitive contrast-enhanced MR imaging for differentiating tumor recurrence from nonneoplastic contrast-enhancing tissue. AJNR Am J Neuroradiol 21:901–909
42. Hu LS, Kelm Z, Korfiatis P et al (2015) Impact of Software Modeling on the Accuracy of Perfusion MRI in Glioma. AJNR Am J Neuroradiol 36:2242–2249
43. Gasparetto EL, Pawlak MA, Patel SH et al (2009) Posttreatment recurrence of malignant brain neoplasm: accuracy of relative cerebral blood volume fraction in discriminating low from high malignant histologic volume fraction. Radiology 250:887–896
44. Kong D-S, Kim ST, Kim E-H et al (2011) Diagnostic dilemma of pseudoprogression in the treatment of newly diagnosed glioblastomas: the role of assessing relative cerebral blood flow volume and oxygen-6-methylguanine-DNA methyltransferase promoter methylation status. AJNR Am J Neuroradiol 32:382–387
45. Hourani R, Brant LJ, Rizk T, Weingart JD, Barker PB, Horská A (2008) Can proton MR spectroscopic and perfusion imaging differentiate between neoplastic and nonneoplastic brain lesions in adults? AJNR Am J Neuroradiol 29:366–372
46. Majós C, Aguilera C, Alonso J et al (2009) Proton MR spectroscopy improves discrimination between tumor and pseudotumoral lesion in solid brain masses. AJNR Am J Neuroradiol 30:544–551
47. Usinskiene J, Ulyte A, Bjørnerud A et al (2016) Optimal differentiation of high- and low-grade glioma and metastasis: a meta-analysis of perfusion, diffusion, and spectroscopy metrics. Neuroradiology 58:339–350
48. Mora P, Majós C, Castañer S et al (2014) (1)H-MRS is useful to reinforce the suspicion of primary central nervous system lymphoma prior to surgery. Eur Radiol 24:2895–2905
49. Fellah S, Caudal D, De Paula AM et al (2013) Multimodal MR imaging (diffusion, perfusion, and spectroscopy): is it possible to distinguish oligodendroglial tumor grade and 1p/19q codeletion in the pretherapeutic diagnosis? AJNR Am J Neuroradiol 34:1326–1333
50. Wang Q, Zhang H, Zhang J et al (2016) The diagnostic performance of magnetic resonance spectroscopy in differentiating high-from low-grade gliomas: A systematic review and meta-analysis. Eur Radiol 26:2670–2684
51. Zhang H, Ma L, Wang Q, Zheng X, Wu C, Xu BN (2014) Role of magnetic resonance spectroscopy for the differentiation of recurrent glioma from radiation necrosis: a systematic review and meta-analysis. Eur J Radiol 83:2181–2189
52. Weybright P, Sundgren PC, Maly P et al (2005) Differentiation between brain tumor recurrence and radiation injury using MR spectroscopy. AJR Am J Roentgenol 185:1471–1476
53. Fudaba H, Shimomura T, Abe T et al (2014) Comparison of multiple parameters obtained on 3T pulsed arterial spin-labeling, diffusion tensor imaging, and MRS and the Ki-67 labeling index in evaluating glioma grading. AJNR Am J Neuroradiol 35:2091–2098
54. Mohammadzadeh A, Mohammadzadeh V, Kooraki S et al (2016) Pretreatment Evaluation of Glioma. Neuroimaging Clin N Am 26: 567–580
55. Wang LL, Leach JL, Breneman JC, McPherson CM, Gaskill-Shipley MF (2014) Critical role of imaging in the neurosurgical and radiotherapeutic management of brain tumors. Radiographics 34:702–721
56. Mormina E, Longo M, Arrigo A et al (2015) MRI Tractography of Corticospinal Tract and Arcuate Fasciculus in High-Grade Gliomas Performed by Constrained Spherical Deconvolution: Qualitative and Quantitative Analysis. AJNR Am J Neuroradiol 36:1853–1858
57. Wang JY, Abdi H, Bakhadirov K, Diaz-Arrastia R, Devous MD Sr (2012) A comprehensive reliability assessment of quantitative diffusion tensor tractography. Neuroimage 60:1127–1138
58. Pujol S, Wells W, Pierpaoli C et al (2015) The DTI Challenge: Toward Standardized Evaluation of Diffusion Tensor Imaging Tractography for Neurosurgery. J Neuroimaging 25:875–882
59. Li YM, Suki D, Hess K, Sawaya R (2016) The influence of maximum safe resection of glioblastoma on survival in 1229 patients: Can we do better than gross-total resection? J Neurosurg 124:977–988
60. Roelz R, Strohmaier D, Jabbarli R et al (2016) Residual Tumor Volume as Best Outcome Predictor in Low Grade Glioma - A Nine-Years Near-Randomized Survey of Surgery vs. Biopsy. Sci Rep 6:32286
61. Eisele SC, Wen PY, Lee EQ (2016) Assessment of Brain Tumor Response: RANO and Its Offspring. Curr Treat Options Oncol 17: 35
62. Gahrmann R, van den Bent M, van der Holt B et al (2017) Comparison of 2D (RANO) and volumetric methods for assessment of recurrent glioblastoma treated with bevacizumab-a report from the BELOB trial. Neuro Oncol 19:853–861
63. Shah GD, Kesari S, Xu R et al (2006) Comparison of linear and volumetric criteria in assessing tumor response in adult high-grade gliomas. Neuro Oncol 8:38–46
64. Galanis E, Buckner JC, Maurer MJ et al (2006) Validation of neuroradiologic response assessment in gliomas: measurement by RECIST, two-dimensional, computer-assisted tumor area, and computer-assisted tumor volume methods. Neuro-oncol 8:156–165
65. Ellingson BM, Nguyen HN, Lai A et al (2016) Contrast-enhancing tumor growth dynamics of preoperative, treatment-naive human glioblastoma. Cancer 122:1718–1727
66. Ben Abdallah M, Blonski M, Wantz-Mezieres S, Gaudeau Y, Taillandier L, Moureaux JM (2016) Statistical evaluation of manual segmentation of a diffuse low-grade glioma MRI dataset. Conf Proc IEEE Eng Med Biol Soc 2016:4403–4406
67. Bø HK, Solheim O, Jakola AS, Kvistad KA, Reinertsen I, Berntsen EM (2017) Intra-rater variability in low-grade glioma segmentation. J Neurooncol 131:393–402
68. Zhu Y, Young GS, Xue Z et al (2012) Semi-automatic segmentation software for quantitative clinical brain glioblastoma evaluation. Acad Radiol 19:977–985
69. Egger J, Kapur T, Fedorov A et al (2013) GBM volumetry using the 3D Slicer medical image computing platform. Sci Rep 3:1364
70. Artzi M, Aizenstein O, Jonas-Kimchi T, Myers V, Hallevi H, Ben Bashat D (2013) FLAIR lesion segmentation: Application in patients with brain tumors and acute ischemic stroke. Eur J Radiol 82: 1512–1518
71. Lutz K, Wiestler B, Graf M et al (2014) Infiltrative patterns of glioblastoma: Identification of tumor progress using apparent diffusion coefficient histograms. J Magn Reson Imaging 39:1096–1103
72. Gnekow AK (1995) Recommendations of the Brain Tumor Subcommittee for the reporting of trials. SIOP Brain Tumor Subcommittee. International Society of Pediatric Oncology. Med Pediatr Oncol 24:104–108
73. Warren KE, Poussaint TY, Vezina G et al (2013) Challenges with defining response to antitumor agents in pediatric neuro-oncology: a report from the response assessment in pediatric neuro-oncology (RAPNO) working group. Pediatr Blood Cancer 60:1397–1401
74. Wyman BT, Harvey DJ, Crawford K et al (2013) Standardization of analysis sets for reporting results from ADNI MRI data. Alzheimers Dement 9:332–337
75. Weber M-A, Henze M, Tüttenberg J et al (2010) Biopsy targeting gliomas: do functional imaging techniques identify similar target areas? Invest Radiol 45:755–768
76. Patel P, Baradaran H, Delgado D et al (2017) MR perfusion-weighted imaging in the evaluation of high-grade gliomas after treatment: a systematic review and meta-analysis. Neuro Oncol 19:118–127

77. Paulson ES, Schmainda KM (2008) Comparison of dynamic susceptibility-weighted contrast-enhanced MR methods: recommendations for measuring relative cerebral blood volume in brain tumors. Radiology 249:601–613
78. Hu LS, Baxter LC, Pinnaduwage DS et al (2010) Optimized preload leakage-correction methods to improve the diagnostic accuracy of dynamic susceptibility-weighted contrast-enhanced perfusion MR imaging in posttreatment gliomas. AJNR Am J Neuroradiol 31:40–48
79. Boxerman JL, Paulson ES, Prah MA, Schmainda KM (2013) The effect of pulse sequence parameters and contrast agent dose on percentage signal recovery in DSC-MRI: implications for clinical applications. AJNR Am J Neuroradiol 34:1364–1369
80. Vogelbaum MA, Jost S, Aghi MK et al (2012) Application of novel response/progression measures for surgically delivered therapies for gliomas: Response Assessment in Neuro-Oncology (RANO) Working Group. Neurosurgery 70:234–243 discussion 243-244
81. Kahn CE, Genereaux B, Langlotz CP (2015) Conversion of Radiology Reporting Templates to the MRRT Standard. J Digit Imaging 28:528–536
82. Marcovici PA, Taylor GA (2014) Journal Club: Structured radiology reports are more complete and more effective than unstructured reports. AJR Am J Roentgenol 203:1265–1271
83. Leu K, Ott GA, Lai A et al (2017) Perfusion and diffusion MRI signatures in histologic and genetic subtypes of WHO grade II-III diffuse gliomas. J Neurooncol. https://doi.org/10.1007/s11060-017-2506-9

Affiliations

S. C. Thust[1,2,3] · S. Heiland[4] · A. Falini[5] · H. R. Jäger[1,2,3] · A. D. Waldman[6] · P. C. Sundgren[7,8] · C. Godi[5] · V. K. Katsaros[9,10,11] · A. Ramos[12] · N. Bargallo[13,14] · M. W. Vernooij[15,16] · T. Yousry[1] · M. Bendszus[4] · M. Smits[15]

1 Lysholm Neuroradiology Department, National Hospital for Neurology and Neurosurgery, London, UK
2 Department of Brain Rehabilitation and Repair, UCL Institute of Neurology, London, UK
3 Imaging Department, University College London Hospital, London, UK
4 Department of Neuroradiology, University Hospital Heidelberg, Heidelberg, Germany
5 Department of Neuroradiology, San Raffaele Scientific Institute, Milan, Italy
6 Neuroimaging Sciences, University of Edinburgh, Edinburgh, UK
7 Institution for Clinical Sciences/Radiology, Lund University, Lund, Sweden
8 Centre for Imaging and Physiology, Skåne University hospital, Lund, Sweden
9 General Anti-Cancer and Oncological Hospital "Agios Savvas", Athens, Greece
10 Central Clinic of Athens, Athens, Greece
11 University of Athens, Athens, Greece
12 Hospital 12 de Octubre, Madrid, Spain
13 Image Diagnostic Centre, Hospital Clinic de Barcelona, Barcelona, Spain
14 Magnetic Resonance Core Facility, Institut per la Recerca Biomedica August Pi i Sunyer (IDIBAPS), Barcelona, Spain
15 Department of Radiology and Nuclear Medicine, Erasmus MC, Rotterdam, The Netherlands
16 Department of Epidemiology, Erasmus MC, Rotterdam, The Netherlands

European Radiology (2021) 31:6334–6341
https://doi.org/10.1007/s00330-020-07582-2

NEURO

From research to clinical practice: a European neuroradiological survey on quantitative advanced MRI implementation

Elia Manfrini[1,2] · Marion Smits[3,4] · Steffi Thust[4,5] · Sergej Geiger[1] · Zeynep Bendella[1] · Jan Petr[6] · Laszlo Solymosi[1] · Vera C. Keil[1,7]

Received: 20 August 2020 / Revised: 22 October 2020 / Accepted: 1 December 2020 / Published online: 22 January 2021

Abstract

Objective Quantitative MRI (qMRI) methods provide versatile neuroradiological applications and are a hot topic in research. The degree of their clinical implementation is however barely known. This survey was created to illuminate which and how qMRI techniques are currently applied across Europe.

Methods In total, 4753 neuroradiologists from 27 countries received an online questionnaire. Demographic and professional data, experience with qMRI techniques in the brain and head and neck, usage, reasons for/against application, and knowledge of the QIBA and EIBALL initiatives were assessed.

Results Two hundred seventy-two responders in 23 countries used the following techniques clinically (mean values in %): DWI (82.0%, $n = 223$), DSC (67.3%, $n = 183$), MRS (64.3%, $n = 175$), DCE (43.4%, $n = 118$), BOLD-fMRI (42.6%, $n = 116$), ASL (37.5%, $n = 102$), fat quantification (25.0%, $n = 68$), T2 mapping (16.9%, $n = 46$), T1 mapping (15.1%, $n = 41$), PET-MRI (11.8%, $n = 32$), IVIM (5.5%, $n = 15$), APT-CEST (4.8%, $n = 13$), and DKI (3.3%, $n = 9$). The most frequent usage indications for any qMRI technique were tissue differentiation (82.4%, $n = 224$) and oncological monitoring (72.8%, $n = 198$). Usage differed between countries, e.g. ASL: Germany ($n = 13/63$; 20.6%) vs. France ($n = 31/40$; 77.5%). Neuroradiologists endorsed the use of qMRI because of an improved diagnostic accuracy (89.3%, $n = 243$), but 50.0% ($n = 136$) are in need of better technology, 34.9% ($n = 95$) wish for more communication, and 31.3% need help with result interpretation/generation ($n = 85$). QIBA and EIBALL were not well known (12.5%, $n = 34$, and 11.0%, $n = 30$).

Conclusions The clinical implementation of qMRI methods is highly variable. Beyond the aspect of readiness for clinical use, better availability of support and a wider dissemination of guidelines could catalyse a broader implementation.

Key Points

- *Neuroradiologists endorse the use of qMRI techniques as they subjectively improve diagnostic accuracy.*
- *Clinical implementation is highly variable between countries, techniques, and indications.*
- *The use of advanced imaging could be promoted through an increase in technical support and training of both doctors and technicians.*

Keywords Neuroimaging · Perfusion imaging · Magnetic resonance imaging · Surveys and questionnaires

Elia Manfrini and Vera C. Keil contributed equally to this work.

✉ Vera C. Keil
vera.keil@ukbonn.de

[1] Department of Neuroradiology, Bonn University Hospital, Venusberg-Campus 1, 53127 Bonn, Germany

[2] Facoltà di Medicina e Chirurgia, Università Politecnica delle Marche, Via Tronto 10, 60126 Ancona, Italy

[3] Department of Radiology and Nuclear Medicine (Ne-515), Erasmus MC, PO Box 2040, 3000, CA Rotterdam, The Netherlands

[4] National Hospital for Neurology and Neurosurgery, University College London Hospitals, London, UK

[5] Department of Brain Rehabilitation and Repair, UCL Institute of Neurology, Queen Square, London WC1N 3BG, UK

[6] Helmholtz-Zentrum Dresden-Rossendorf, Institute of Radiopharmaceutical Cancer Research, Dresden, Germany

[7] Department of Radiology, Section Neuroradiology, Amsterdam University Medical Center, VUmc, Amsterdam, The Netherlands

Abbreviations

ADC	Apparent diffusion coefficient
APT	Amide-proton transfer
ASL	Arterial spin labelling
BOLD	Blood-oxygen level dependent (imaging)
CEST	Chemical exchange saturation transfer
DCE	Dynamic contrast-enhanced
DKI	Diffusion kurtosis imaging
DSC	Dynamic susceptibility contrast
DTI	Diffusion tensor imaging
DWI	Diffusion-weighted imaging
EIBALL	European Imaging Biomarker Alliance
FatQuant	Fat quantification techniques
fMRI	Functional MRI
GDP	Gross domestic product
GERD	Gross domestic expenditure on research and development as percentage of GDP
IVIM	Intravoxel-incoherent motion
MRI	Magnetic resonance imaging
MRS	Magnetic resonance spectroscopy
QIBA	Quantitative Imaging Biomarkers Alliance
qMRI	Quantitative magnetic resonance imaging

Introduction

Quantitative MRI (qMRI) techniques, both technically and with respect to clinical indication, cover a very broad field of applications [1]. While standard MRI techniques classically provide visual-anatomical information [2], quantitative techniques allow an insight into the physiological activity or biochemical composition of the tissue through quantifiable parameters [3, 4]. qMRI techniques comprise a broad range of sequence applications and, mostly in a research setting, have shown benefits on innumerable levels including vascular and neoplastic diseases, neurodegeneration, or infectious and inflammatory brain lesions [5–12].

Based on the long-standing research efforts and increasing availability of user-friendly post-processing software, one should expect a broad application of advanced MRI techniques in clinical practice. While several of the techniques were first proposed several decades ago: DSC [13], DCE [14], IVIM [15], ASL [16], and relaxometry [17], a routine application is recommended only for a limited range of diseases and techniques, such as DWI and DSC in glioma imaging [18]. For many other techniques, such as IVIM or ASL, a clinical routine introduction is still not within close reach. One of the reasons is that methodological standardisation remains low and standards for acquisition and processing are limited [19–21].

In the long term, the routine clinical implementation of innovative qMRI techniques is pivotal to justify future research in the field and its funding. It is, however, very difficult to estimate how far the process of clinical implementation has advanced without conducting a wider investigation.

The aim of this European survey was to find out which, how, and to what extent qMRI techniques are applied to solve neuroradiological questions in a primarily clinical setting. The in-depth analysis also focuses on the reasons for the lack of clinical application and general knowledge of qMRI.

Materials and methods

Questionnaire

The online questionnaire had a total of 13 main questions to be answered as free text, or multiple, dichotomous, and single-choice answers (online supplement 1). Google Forms was used to implement the questionnaire (Google Inc.). To enhance clarity, techniques that provide quantitative morphometric measurements but are based on conventional MRI sequences were not included in this survey. Brain and head/neck were surveyed as separate organ systems.

The survey was anonymous, voluntary without incentives and all responses were treated confidentially. Information on the country of work and categorisation of the employing institution were mandatory. By design, it was therefore impossible to reliably identify multiple answers from a single institution and thus determine the exact number of institutions answering. Furthermore, respondents could decide if their institution is classified as a large or small hospital.

Questionnaire distribution

The questionnaire was disseminated in English, German, Italian, Spanish, French, Turkish, Russian, and Portuguese. The questionnaire was emailed to 27 European countries and Russia, Turkey, and Israel as listed in detail in the online supplement 2.

The exact contact procedure is described in the online supplement 3 and technically by Fig. 1 (Fig. 1, online supplement 3). The questionnaire was open from Mid-July 2019 to Mid-October 2019. Invitations were sent out three times. Additional phone interviews were conducted in German-speaking countries dedicated to the locally large number of radiologists working in outpatient practices.

Survey analysis

Numerical analyses were performed in Microsoft Excel. Fisher's exact tests were performed with SPSS® V. 26.0 (IBM Corp.) to identify significant differences between groups where applicable.

Answers from professionals who had multiple workplaces were included, but only their primary working place was

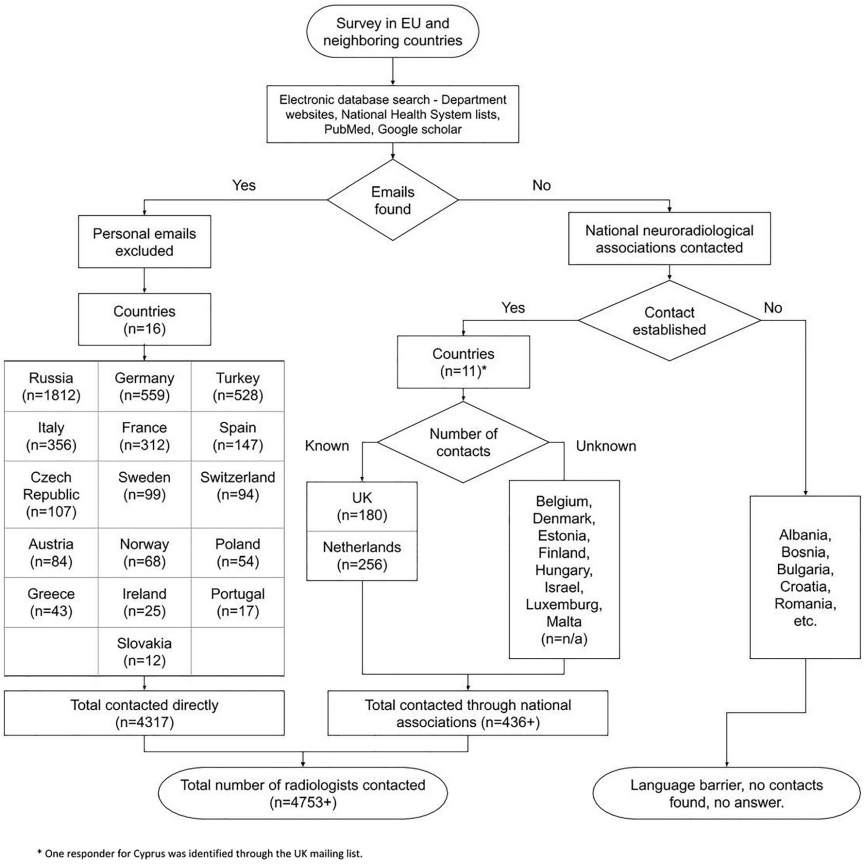

Fig. 1 Flow diagram illustrating the data acquisition process

considered. It was possible that more than one radiologist affiliated with the same institution would fill in and submit the questionnaire, or that the same participant would reply more than once. Therefore, answers were screened for probable redundancies.

If someone denied the use of a certain technique in question 3, but later reported in the detailed answer block (question 6) that she/he used it for several indications, we extrapolated that the responder indeed used the technique, but erroneously forgot to tick the box in the beginning. In the reverse case (with the detailed answers left blank), a non-intentional blank was presumed, e.g. due to oversight.

As advanced MRI needs extra processing and scanning time, we investigated the association between the potential dissemination of knowledge and the presumed economic constraints. qMRI technique dissemination was analysed based on the gross domestic product per person (GDP pP) and the research and development expenditures per country as percentage of GDP (GERD) separating countries of respondents into above or below EU 28 average [22].

Results

Demographic information of respondents

In total, 272 neuroradiologists answered in 23 countries (online supplement 2, Fig. 2). The average return rate per country was 6.7 ± 6.1% (range from 0.0 to 23.5%) of the respondents. The following countries had zero returns: Greece, Slovakia, Hungary, and Poland, or a return rate of < 2%: Russia (1.2%, $n = 22/1812$) and Norway (1.5%, $n = 1/68$).

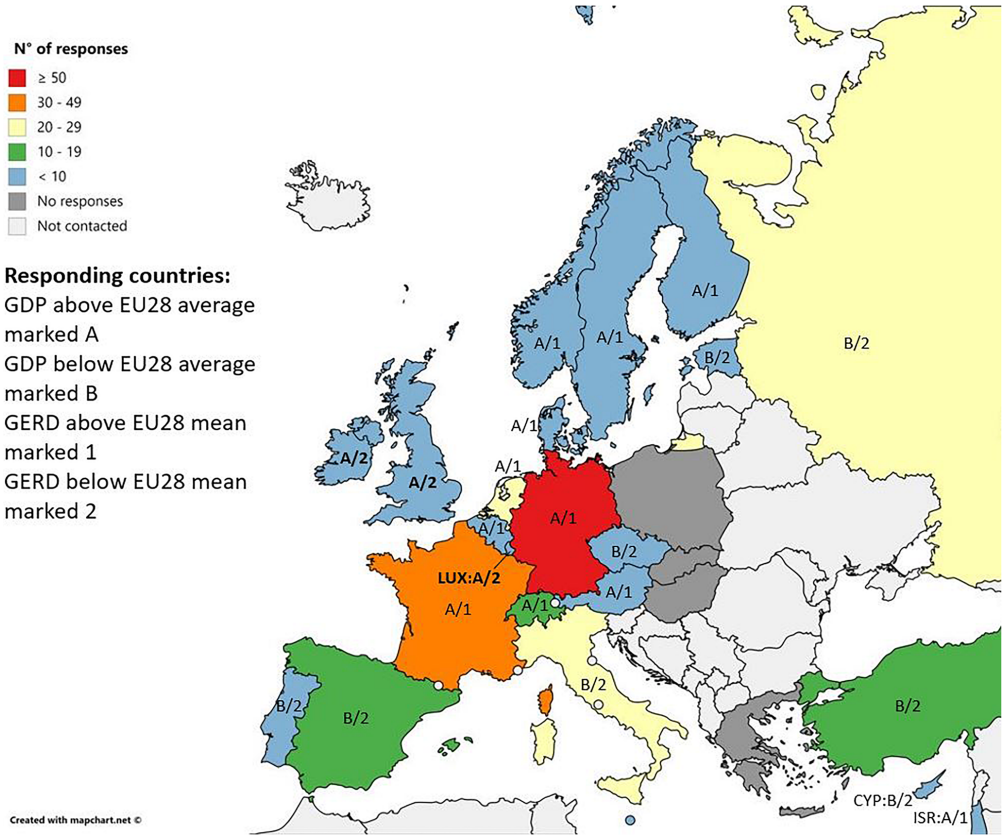

Fig. 2 Map showing the number of radiologists responding by country with GDP and GERD. GDP, gross domestic product per capita in 2018; GERD, gross domestic expenditure on research and development as percentage of GDP (in 2018 except for Switzerland with last numbers from 2017); in bold are countries with discrepancy between economic power and spending on research ("under average spenders")

Most respondents worked in institutions of 6 to 20 doctors (44.9%, n = 122/272). However, 29.0% (n = 79/272) had more than 50 colleagues. Response rates varied by institution type (Table 1).

Table 1 Questionnaire response rates by institution type

Type	Response rate (in % and standard deviation	Range by country (%)
University hospital	19.4 ± 16.3	0.0–60.7
Large hospital	5.9 ± 5.4	0.0–15.4
Small hospital	2.6 ± 3.2	0.0–10.3
Outpatient practice	0.8 ± 1.9	0.0–6.7
Teleradiology centres	0.4 ± 0.7	0.0–1.8
Research institution	0.7 ± 1.3	0.0–3.4

Usage dissemination by sequence and indication

The most commonly applied qMRI sequence based on question 3 was DWI (82.0%), followed by DSC (67.3%) and MRS (64.3%). DCE, BOLD-based techniques, ASL, and fat quantification still had an intermediate dissemination of 43.4%, 42.6%, 37.5%, and 25.0%, respectively. T1 and T2 mapping, PET-MR, IVIM, APT-CEST, and diffusion kurtosis imaging (DKI) were uncommon (15.1%, 16.9%, 11.8%, 5.5%, 4.8%, and 3.3%, respectively) in most institutions.

Sequence usage showed extensive geographical differences (online supplements 4 to 9).

For the detailed clinical indication questions (section II, question 6 of the questionnaire), DWI was not an answer option. A total of 94.9% of respondents used at least one

qMRI technique other than DWI in the brain, while only 31.3% applied qMRI sequences in head and neck MRI.

Tissue differentiation (82.4%) and oncological monitoring (72.8%) were the most common reasons to apply any quantitative technique. qMRI (other than DWI) was less common for stroke imaging (58.8%) and only a minority of respondents used it for neurodegenerative diseases (26.1%) or multiple sclerosis (22.8%).

The most frequently applied techniques for glioma imaging were DSC (73.2%) and MRS (54.8%). DSC (39.3%) and ASL (20.6%) had an intermediate use in stroke diagnostics and oncological monitoring. PET-MRI and APT-CEST were rarely used (10.7% and 0.0%, for general oncological monitoring; 9.6% and 2.2% for glioma diagnostics; 8.1% and 1.1% in lesion differentiation, respectively).

In the head and neck region, lesion differentiation was the single most common reason to apply quantitative techniques, with and DSC (29.0%) or DCE (20.6%) most frequently used (DWI was not an answer option).

Dissemination by institution type and GDP

Clear trends could be observed between the type of institution and the frequency of use of a qMRI technique based on the compulsory country answer and answers to questions 3 of the questionnaire. University hospitals were the most frequent users of a technique, large hospitals second, and small hospitals the least likely users. With DSC as an example, university hospitals used it more often than large hospitals (126/156 vs. 46/70; $p = 0.01$), or small hospitals (13/36; p = 0.01).

The countries with GDP above the EU28 average in 2018 (44,748 USD/capita) used the following techniques significantly more than the countries below this average: DSC ($p = 0.0001$), ASL ($p = 0.02$), DWI ($p = 0.0001$), CEST ($p = 0.04$), T2 mapping ($p = 0.001$), and MRS ($p = 0.003$). DSC ($p = 0.0007$), DWI ($p = 0.0001$), T2 mapping ($p = 0.004$), and MRS ($p = 0.002$) were significantly more often performed in countries with an above-average EU28 GERD (2.03% of GDP; Fig. 2).

Motivation analysis and network knowledge

Figure 3 illustrates the main reasons for and against the use of qMRI based on section III, questions 7 to 9. In summary, the majority of neuroradiologists favoured the usage of qMRI because of an improved diagnostic accuracy (89.3%). Only a small minority (4.0%) did not see any advantages in qMRI.

Scientific reasons (41.5%) were a major impulse to perform additional quantitative sequences.

The greatest impediment for advanced MRI applications seemed a lack of time (39.0%) rather than a lack of financial compensation (12.9%).

Notably, both QIBA and EIBALL as imaging biomarker institutions were not widely known (12.5% and 11.0%, respectively) amongst clinicians.

Discussion

This survey is unique in its purpose and aimed to assess the clinical dissemination of qMRI techniques in neuroradiological practice across Europe. While common usage of DWI, DSC, and MRS was confirmed for certain indications such as glioma imaging, it is apparent that some techniques are rarely used, show variable use by country, or are only performed for a limited number of indications. Our data show that an overwhelming majority of respondents sees a benefit in the use of qMRI for their diagnostic work, but mention a lack of time as the main reason not to implement qMRI techniques. This factor, together with the need for more training, technical adjustments, and an improved exchange of expertise with other institutions, was identified through this survey as the key element hampering the clinical translation of qMRI into clinical neuroradiology.

In most European countries, MRI protocols are being continuously shortened to reduce waiting times for MRI. These waiting times differ largely between countries from an average of 18 days in the Netherlands [23] to 126 days in Ireland [24] and show regional differences within countries (e.g. Italy, North-East 50 days vs. South 111 days [25]). Beyond protocol length, waiting times depend on several factors: number of available MRI scanners, radiologists, and limitations of healthcare budgets [26]. While, e.g., the UK faces a bottleneck for qMRI implementation regarding all of these factors, reasons for limitations of qMRI are different in Germany and have more than four times as many MRI scanners per inhabitant as the UK (37/1M vs. 9/1M inhabitants) [27]. In Germany, insurance compensation frequently has a fixed price per scan without sufficient compensation for additional sequences, which may limit the incentive to add qMRI. This may partially explain the relatively lower usage of many techniques in Germany compared to other above-average GDP and GERD countries, e.g. France—a country with also relatively many respondents, but fewer scanners (14/1M inhabitants; online supplements 5–9). The larger number of scanners in Germany is also not sufficiently reflected in the number of exams performed: 143 MRI exams/1000 inhabitants/year in Germany as opposed to UK and France with 62 and 114, respectively, which makes the possibly lower use of qMRI techniques even more surprising.

Respondents in most countries already use some kind of qMRI technique at least for some indications according to our results. We therefore interpret their claims of impediments and incentives for qMRI as a wish for more extensive use. The questionnaire responses show directions on how to allow

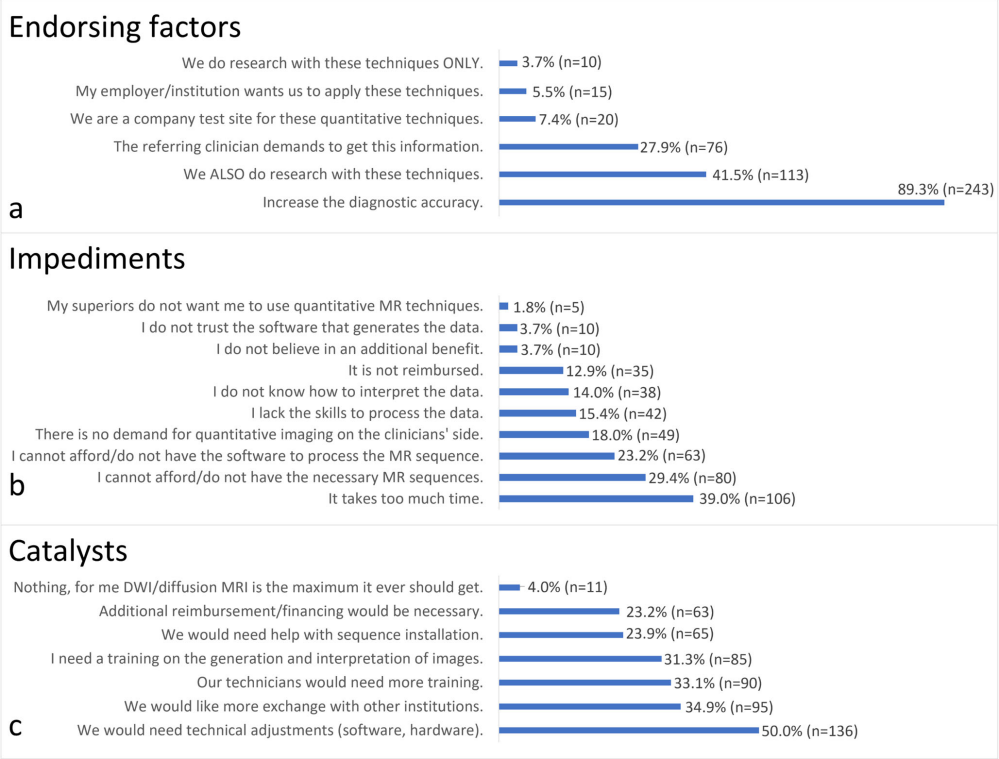

Fig. 3 Factors influencing the use of quantitative advanced MRI sequences in clinical practice. **a** Factors that endorse the use of these quantitative MRI sequences. **b** Factors that impede the use of these quantitative MRI sequences. **c** Factors that could catalyse a greater implementation

qMRI to find a larger entrance into clinical neuroradiology. The level of evidence concerning a diagnostic benefit must be increased, as this is the key to acceptance of a technique into guidelines and eventually financing by the public sector, which is needed to cover costs for technical adjustments, software, and training. DSC in glioma imaging, which is now part of EORTC guidelines, is an example. It had the highest prevalence as an indication in this study and was previously identified as relevant in other surveys on either glioma or perfusion imaging [18, 28, 29]. For some techniques, such as ASL, which is much less used despite reduced risks for the patient and reduced costs compared to DSC, clinical research should possibly be facilitated. Another aspect is the clinical indications for which qMRI techniques. A large discrepancy can be observed between scientific trials and clinical implementation, e.g. concerning neurodegenerative diseases as also testified in this survey. In many countries, patients are still likely to receive a CT scan when dementia is suspected. Although neurodegenerative diseases and also respective imaging receive a lot of funding, there is currently limited evidence to justify qMRI technique implementation. DWI imaging and structural brain volumetric analysis mark the quantitative imaging aspect in this field, as corroborated by very recent clinical data regarding dementia imaging in Europe [30].

In this context, and suggested by our data, one major obstacle to implement qMRI sequences is not a lack of acceptance by clinicians, but indeed a multi-level shortfall of clinical technical skill. Our analyses by institution type uncovered important associations with the likeliness to use qMRI techniques. A clear slope of dissemination was observed from university setting already to large hospitals, and further to small sites. Only DWI would be available at all types of sites in the majority of cases, with all other qMRI techniques mark the exception rather than the norm outside a university setting. This corroborates the slow velocity of trickle-down effects. Therefore, beyond time constraints and financial burdens, clinicians in smaller institutions are also in the need of better knowledge transfer as a motivation

for implementation. Here, not only scientists but also vendors are required to act through hands-on trainings at a low financial and knowledge threshold. The involvement of non-university sites in scientific projects can be another meaningful way to accelerate clinical dissemination of qMRI techniques. An example can be Denmark, which integrates smaller hospitals into large national trials and facilitates also the implementation of private-public partnership projects [31]. Such advances must however be supported by an interaction of the national- and European-level political forces of both the healthcare and science sectors. Here, institutions such as the ESR and in particular EIBALL could act as important lobbyists, but must still be better known according to our data and assuming an over-average interested group of Neuroradiologists as respondents. The radiological training curriculum has the potential to be extended concerning advanced imaging data processing and interpretation. One should remember that many countries do not provide a strictly hierarchical structure of primary to tertiary healthcare providers. Small institutions can, therefore, also be confronted with complex cases that may benefit from qMRI.

A worrying revelation of this study is the possible association between qMRI usage and GDP as well as GERD. Living in a lower GDP European country negatively affects the patients' chances to receive a neuroradiological examination that includes DSC and DWI—two qMRI methods, which are considered an important part of glioma MRI protocols [32, 33]. While political solutions to achieve the desired equal standards of European healthcare are one aspect, neuroradiological societies and scientific European initiatives can contribute their share, too, e.g. through knowledge exchange and provision of free software solutions.

This study has a few limitations starting with a selection bias due to the variable modes of contact to the radiologists. Only a proportion of radiologists were contactable in every country with university centres being, partially deliberately, overrepresented. The resulting data distortions reduce the representativeness of the survey data. Another aspect is the uneven response rate. One reason could be the mode of communication that may have excluded, some respondents, e.g. due to language barriers. Furthermore, it must be assumed that despite the anonymous nature of the survey, respondents may not have felt comfortable providing realistic answers. They may have also mixed up a clinical implementation with research implementation performed in a clinical setting, e.g. an experimental CEST sequence as part of a clinical programme. Neuroradiologists frequently working with quantitative techniques were probably also more willing to answer the survey, biasing results towards a wider use. There remains minimal survey data on the topic, and this survey is unique in its focus. It served as a first attempt to clarify the extent of the current clinical use of qMRI in neuroradiology in Europe and can, also due to the size, not be considered fully representative. The additive value of qMRI techniques must be explored in prospective blinded comparative studies elsewhere and was not attempted to be answered within this survey.

Conclusion

Usage of qMRI techniques in neuroradiology is not standardised throughout Europe. Its clinical translation varies substantially between techniques as well as geographically. Local healthcare policies and variable sharing of expertise can be presumed as underlying reasons, while neuroradiologists in principle feel positive about qMRI opportunities. This survey highlights an unmet need to promote qMRI through larger clinical studies showing a convincing benefit, improved networking between clinicians and scientists as well as training.

Supplementary Information The online version contains supplementary material available at https://doi.org/10.1007/s00330-020-07582-2.

Funding Open Access funding enabled and organized by Projekt DEAL.

Compliance with ethical standards

Guarantor The scientific guarantor of this publication is Vera C. Keil, MD, PhD.

Conflict of interest Prof. Smits and Dr. Keil regularly are invited to present scientific talks about qMRI also in settings organized by MRI vendors. These are partially paid (Smits, GE Healthcare; Keil, Philips Healthcare).

Statistics and biometry No complex statistical methods were necessary for this paper.

Informed consent Written informed consent was not required for this study because no human subjects/patients were included in this study.

Ethical approval Institutional Review Board approval was not required because no human subjects/patients were included in this study.

Methodology
- Survey research
- literature review

References

1. Carnevale L, Lembo G (2019) Innovative MRI techniques in neuroimaging approaches for cerebrovascular diseases and vascular cognitive impairment. Int J Mol Sci 20(11). https://doi.org/10.3390/ijms20112656
2. Lerch JP, van der Kouwe AJ, Raznahan A et al (2017) Studying neuroanatomy using MRI. Nat Neurosci 20(3):314–326. https://doi.org/10.1038/nn.4501
3. Pope WB, Djoukhadar I, Jackson A (2016) Neuroimaging. Handb Clin Neurol 134:27–50. https://doi.org/10.1016/B978-0-12-802997-8.00003-7
4. Chen JJ (2019) Functional MRI of brain physiology in aging and neurodegenerative diseases. Neuroimage 187:209–225. https://doi.org/10.1016/j.neuroimage.2018.05.050
5. Bandettini PA (2012) Twenty years of functional MRI: the science and the stories. Neuroimage 62(2):575–588. https://doi.org/10.1016/j.neuroimage.2012.04.026
6. Meijer FJ, Goraj B (2014) Brain MRI in Parkinson's disease. Front Biosci (Elite Ed) 6:360–369
7. Giorgio A, De Stefano N (2016) Advanced structural and functional brain MRI in multiple sclerosis. Semin Neurol 36(2):163–176. https://doi.org/10.1055/s-0036-1579737
8. Widmann G, Henninger B, Kremser C, Jaschke W (2017) MRI sequences in head & neck radiology - state of the art. Rofo 189(5):413–422. https://doi.org/10.1055/s-0043-103280
9. Shukla G, Alexander GS, Bakas S et al (2017) Advanced magnetic resonance imaging in glioblastoma: a review. Chin Clin Oncol 6(4):40. https://doi.org/10.21037/cco.2017.06.28
10. Yousaf T, Dervenoulas G, Politis M (2018) Advances in MRI methodology. Int Rev Neurobiol 141:31–76. https://doi.org/10.1016/bs.irn.2018.08.008
11. Bonm AV, Ritterbusch R, Throckmorton P, Graber JJ (2020) Clinical imaging for diagnostic challenges in the management of gliomas: a review. J Neuroimaging 30(2):139–145. https://doi.org/10.1111/jon.12687
12. Fujima N, Kameda H, Shimizu Y et al (2020) Utility of a diffusion-weighted arterial spin labeling (DW-ASL) technique for evaluating the progression of brain white matter lesions. Magn Reson Imaging 69:81–87. https://doi.org/10.1016/j.mri.2020.03.005
13. Edelman RR, Mattle HP, Atkinson DJ et al (1990) Cerebral blood flow: assessment with dynamic contrast-enhanced T2*-weighted MR imaging at 1.5 T. Radiology 176(1):211–220. https://doi.org/10.1148/radiology.176.1.2353094
14. Tofts PS, Kermode AG (1989) Blood brain barrier permeability in multiple sclerosis using labelled DTPA with PET, CT and MRI. J Neurol Neurosurg Psychiatry 52(8):1019–1020
15. Le Bihan D (1988) Intravoxel incoherent motion imaging using steady-state free precession. Magn Reson Med 7(3):346–351
16. Williams DS, Detre JA, Leigh JS, Koretsky AP (1992) Magnetic resonance imaging of perfusion using spin inversion of arterial water. Proc Natl Acad Sci U S A 89(1):212–216. https://doi.org/10.1073/pnas.89.1.212
17. Damadian R (1971) Tumor detection by nuclear magnetic resonance. Science 171(3976):1151–1153. https://doi.org/10.1126/science.171.3976.1151
18. Thust SC, Heiland S, Falini A et al (2018) Glioma imaging in Europe: a survey of 220 centres and recommendations for best clinical practice. Eur Radiol 28(8):3306–3317. https://doi.org/10.1007/s00330-018-5314-5
19. Alsop DC, Detre JA, Golay X et al (2015) Recommended implementation of arterial spin-labeled perfusion MRI for clinical applications: a consensus of the ISMRM perfusion study group and the European consortium for ASL in dementia. Magn Reson Med 73(1):102–116. https://doi.org/10.1002/mrm.25197
20. Boxerman JL, Quarles CC, Hu LS et al (2020) Consensus recommendations for a dynamic susceptibility contrast MRI protocol for use in high-grade gliomas. Neuro Oncol. https://doi.org/10.1093/neuonc/noaa141
21. Mutsaerts H, Petr J, Groot P et al (2020) ExploreASL: an image processing pipeline for multi-center ASL perfusion MRI studies. Neuroimage 117031. https://doi.org/10.1016/j.neuroimage.2020.117031
22. OECD (2020) Main science and technology indicators. 2019(2). https://doi.org/10.1787/g2g9ff07-en
23. Statista (2018) Average waiting time for MRI scans in the Netherlands from 2010 to 2016. Statista. https://www.statista.com/statistics/979147/average-waiting-time-for-mri-scans-in-the-netherlands/. Accessed 06 June 2020
24. O'Shea MT (2016) Access to diagnostics used to detect cancer. Irish College of General Practitioners. https://www.lenus.ie/handle/10147/615148. Accessed 06 June 2020
25. Statista (2017) Average waiting time to get an appointment for a magnetic resonance imaging scan in Italy in 2017, by geographic area. Statista. https://www.statista.com/statistics/934110/waiting-time-for-an-mri-by-area-in-italy/. Accessed 06 June 2020
26. Stat ECE Healthcare resource statistics - technical resources and medical technology. https://ec.europa.eu/eurostat/statistics-explained/index.php/Healthcare_resource_statistics_-_technical_resources_and_medical_technology#Use_of_medical_technology. Accessed 06 June 2020
27. OECD (2019) Health at a glance: OECD indicators. OECD Publishing. https://doi.org/10.1787/4dd50c09-en. Accessed 06 June 2020 2020
28. Dickerson E, Srinivasan A (2016) Multicenter survey of current practice patterns in perfusion MRI in neuroradiology: why, when, and how is it performed? AJR Am J Roentgenol 207(2):406–410. https://doi.org/10.2214/AJR.15.15740
29. Freyschlag CF, Krieg SM, Kerschbaumer J et al (2018) Imaging practice in low-grade gliomas among European specialized centers and proposal for a minimum core of imaging. J Neurooncol 139(3):699–711. https://doi.org/10.1007/s11060-018-2916-3
30. Vernooij MW, Pizzini FB, Schmidt R et al (2019) Dementia imaging in clinical practice: a European-wide survey of 193 centres and conclusions by the ESNR working group. Neuroradiology 61(6):633–642. https://doi.org/10.1007/s00234-019-02188-y
31. Schmidt M, Schmidt SAJ, Adelborg K et al (2019) The Danish health care system and epidemiological research: from health care contacts to database records. Clin Epidemiol 11:563–591. https://doi.org/10.2147/CLEP.S179083
32. Ellingson BM, Bendszus M, Boxerman J et al (2015) Consensus recommendations for a standardized Brain Tumor Imaging Protocol in clinical trials. Neuro Oncol 17(9):1188–1198. https://doi.org/10.1093/neuonc/nov095
33. Schmainda KM, Prah MA, Rand SD et al (2018) Multisite concordance of DSC-MRI analysis for brain tumors: results of a National Cancer Institute Quantitative Imaging Network Collaborative Project. AJNR Am J Neuroradiol 39(6):1008–1016. https://doi.org/10.3174/ajnr.A5675

Radiology: Imaging Cancer

ORIGINAL RESEARCH

Endogenous Chemical Exchange Saturation Transfer MRI for the Diagnosis and Therapy Response Assessment of Brain Tumors: A Systematic Review

Sachi Okuchi, MD, PhD • Ahmed Hammam, MD • Xavier Golay, PhD • Mina Kim, PhD • Stefanie Thust, MD, FRCR

From the Department of Brain Repair and Rehabilitation, University College London, Institute of Neurology, London, England (S.O., A.H., X.G., M.K., S.T.); Department of Diagnostic Imaging and Nuclear Medicine, Graduate School of Medicine, Kyoto University, 54 Shogoin-Kawaharacho, Sakyo-ku, Kyoto 606-8507, Japan (S.O.); and Lysholm Department of Neuroradiology, National Hospital for Neurology and Neurosurgery, London, England (S.T.). Received June 4, 2019; revision requested August 9; revision received September 13; accepted October 21. **Address correspondence to** S.O. (e-mail: *sokuchi89@gmail.com*).

This project has received funding from the European Union's Horizon 2020 research and innovation program under grant agreement No. 667510. The work was carried out at University College London/UCL Hospitals, which receives a proportion of funding from the National Institute for Health Research Biomedical Research Centre.

Conflicts of interest are listed at the end of this article.

Radiology: Imaging Cancer 2020; 2(1):e190036 • https://doi.org/10.1148/rycan.2020190036 • Content codes: NR MR OI

Purpose: To generate a narrative synthesis of published data on the use of endogenous chemical exchange saturation transfer (CEST) MRI in brain tumors.

Materials and Methods: A systematic database search (PubMed, Ovid Embase, Cochrane Library) was used to collate eligible studies. Two researchers independently screened publications according to predefined exclusion and inclusion criteria, followed by comprehensive data extraction. All included studies were subjected to a bias risk assessment using the Quality Assessment of Diagnostic Accuracy Studies tool.

Results: The electronic database search identified 430 studies, of which 36 fulfilled the inclusion criteria. The final selection of included studies was categorized into five groups as follows: grading gliomas, 19 studies (area under the receiver operating characteristic curve [AUC], 0.500–1.000); predicting molecular subtypes of gliomas, five studies (AUC, 0.610–0.920); distinction of different brain tumor types, seven studies (AUC, 0.707–0.905); therapy response assessment, three studies (AUC not given); and differentiating recurrence from treatment-related changes, five studies (AUC, 0.880–0.980). A high bias risk was observed in a substantial proportion of studies.

Conclusion: Endogenous CEST MRI offers valuable, potentially unique information in brain tumors, but its diagnostic accuracy remains incompletely known. Further research is required to assess the method's role in support of molecular genetic diagnosis, to investigate its use in the posttreatment phase, and to compare techniques with a view to standardization.

Supplemental material is available for this article.

Gliomas account for most malignant intrinsic brain tumors in adults and, despite being a relatively rare disease, represent a major cause of mortality (1). Diffuse gliomas are categorized into World Health Organization (WHO) grades II to IV, based on histologic evidence of proliferation and vascular invasion. However, histologic (WHO) grade and glioma cell lineage (oligodendroglioma vs astrocytoma) are limited predictors of disease progression, which is predominantly influenced by genetic factors (2). Recent studies have identified molecular markers, such as the isocitrate dehydrogenase (IDH) gene and methylguanyl methyltransferase (MGMT) enzyme, as key determinants of clinical outcomes (1). The optimal treatment and overall prognosis of glioma subtypes depend on the combination of molecular features and histologic grade (1); however, tumor malignant potential remains incompletely captured by clinical imaging techniques (3). In addition, MRI features can overlap between gliomas and different brain tumors (eg, lymphoma, metastases) to such an extent that only tissue diagnosis is conclusive (3). Postoperative radiation and chemotherapy with temozolomide may result in predominantly transient (pseudoprogression) or permanent (radiation necrosis) phenomena, which notoriously resemble contrast-enhancing tumor progression due to breakdown of the blood–brain barrier. Definitive distinction of these entities frequently requires serial imaging with a combination of structural and advanced techniques (4).

Chemical exchange saturation transfer (CEST) is a promising imaging technique that has recently emerged as an alternative contrast mechanism for MRI (5). CEST signal can be generated through application of a radiofrequency "saturation" pulse targeted at the resonance frequency of solute (eg, protein or metabolite bound) protons, from which the saturation is transferred to bulk water via chemical exchange. The much larger water proton pool ensures a continuous flux of unsaturated protons close to the exchangeable sites, thereby leading to a measurable reduction in the water signal amplitude after a few seconds (6). CEST contrasts are classified into diamagnetic CEST, mostly consisting of endogenous agents, and paramagnetic CEST, which usually involves the use of exogenous agent administration (6). Diamagnetic CEST uses chemical compounds

Abbreviations

APT = amide proton transfer, AUC = area under the ROC curve, CEST = chemical exchange saturation transfer, FDG = fluorodeoxyglucose, GBM = glioblastoma, HGG = high-grade glioma, IDH = isocitrate dehydrogenase, LGG = low-grade glioma, MGMT = methylguanyl methyltransferase, MTR = magnetization transfer ratio, MTR_{asym} = magnetization transfer ratio asymmetry, NOE = nuclear Overhauser enhancement, PCNSL = primary central nervous system lymphoma, QUADAS-2 = Quality Assessment of Diagnostic Accuracy Studies 2, ROC = receiver operating characteristic, WHO = World Health Organization

Summary

Chemical exchange saturation transfer can be further developed as a biomarker for metabolically active brain tumors, evidenced by correlations to tissue findings, including proliferative indexes; further study is required to assess its diagnostic power with respect to specific clinical indications.

Key Points

- Endogenous chemical exchange saturation transfer (CEST) methods can support glioma grading, molecular subtyping, and differential diagnosis.
- CEST signal may aid the identification of metabolically active tumor following treatment.
- Study data are heterogeneous with a substantial bias risk, highlighting the importance of future prospective research and technical standardization.

with a range between 0 and 7 ppm from water (eg, -NH,-NH_2,-OH groups), representing the first discovered and most studied CEST contrast (7). CEST techniques can be classified according to the type of molecular construct, such as amide proton transfer (APT), amine CEST, glucoCEST (glucose-based CEST contrast), and gagCEST (CEST contrast originating from glycosaminoglycans) (6). APT imaging targets endogenous mobile proteins and peptides featuring amide protons and is the most widely used CEST imaging method, whereby the APT-weighted signal can be quantified by magnetization transfer ratio (MTR) asymmetry (MTR_{asym}) analysis at +3.5 ppm, using the water peak as reference (5). In addition, nuclear Overhauser enhancement (NOE)–mediated signal arises from mobile protein and lipid spin cross-relaxation effects between 0 and −5 ppm (8). It has been proposed that NOE could also become an imaging biomarker to characterize brain tumors, similar to APT (9).

Numerous single-center studies have highlighted the potential of CEST MRI in stratifying brain tumors; however, the exact diagnostic contribution of the method remains uncertain. To date, a single systematic review and meta-analysis have evaluated the diagnostic performance of only APT in grading gliomas (10). To our knowledge, ours is the first systematic review to explore the diagnostic and prognostic value of endogenous CEST for a variety of brain tumor indications. Our analysis aims to evaluate *(a)* the diagnostic value for grading gliomas, *(b)* the accuracy for predicting glioma molecular subtypes, *(c)* the distinction of glioma from other brain tumor types, *(d)* the assessment of brain tumor therapy response, and *(e)* the power of differentiating tumor recurrence from treatment-related changes.

Materials and Methods

This study was performed according to the Preferred Reporting Items for Systematic Reviews and Meta-Analysis of Diagnostic Test Accuracy Studies criteria (11). The research was registered in the PROSPERO online database of systematic reviews (CRD42019122320).

Search Strategy

In November 2018, a medical researcher performed a systematic search in PubMed, Ovid Embase, and the Cochrane Library. We used the following search key words: ("brain tumor," "glioma," "brain neoplasm," "brain metastasis," "glioblastoma") and ("CEST," "chemical exchange saturation transfer," "amide proton transfer," "magnetization transfer," "chemical exchange," "nuclear Overhauser effect"). Further details of the search strategy are shown in Appendix E1 (supplement).

Selection Criteria

The abstracts of all articles retrieved in the initial search were screened by two board-certified radiologists (S.O. and A.H.) with research experience in neuro-oncology. Selected full-text manuscripts were reviewed in detail to determine their relevance. A stepwise selection was performed by two independent reviewers (S.O. and A.H.) according to the following criteria: The exclusion criteria were as follows: *(a)* no CEST technique (eg, CEST, APT, NOE) performed; *(b)* no patients with brain tumor examined; *(c)* animal and/or laboratory study; *(d)* technical study or diagnostic and/or prognostic value in brain tumors not evaluated; *(e)* comparisons confined to different MRI acquisition technique; *(f)* review article, case report (defined as fewer than five cases), letter, commentary, or conference proceeding; and *(g)* non-English full text. The inclusion criteria were *(a)* CEST technique was performed in patients with brain tumor before, during, or after treatment and *(b)* study assessed diagnostic or prognostic value of CEST parameters in brain tumors or examined pseudoprogression or recurrent tumors. Disagreement was resolved in consensus with a senior reviewer (S.T.).

Data Extraction

The following data were extracted from the included studies: CEST parameter values, diagnostic or prognostic accuracy, and method characteristics. The latter included study design, country of origin, number of patients, participant age, tumor histologic features, and, where available, molecular data, MRI field strength, type of CEST contrast, CEST acquisition parameters, methods of correcting B0 field inhomogeneity, and region-of-interest placements. The same two reviewers independently performed the full-text screening, followed by data extraction, and any discrepancies were resolved in consensus with the third reviewer.

Study Quality Assessment

The study quality was examined by using the Quality Assessment of Diagnostic Accuracy Studies 2 (QUADAS-2) instrument (12). We evaluated concerns regarding applica-

bility in three domains and the risk of bias in four different domains. Each study was independently assessed for quality and potential bias by the same two researchers. Disagreements were resolved as described above.

Statistical Analysis

Descriptive data are presented in the form of a narrative synthesis because of the perceived heterogeneity of research questions, CEST technical parameters, and brain tumor cohorts studied.

Results

Search Results

A total of 430 studies were identified through the electronic database searches. After we removed duplicate studies and screened the studies' titles and abstracts, 68 studies that provisionally satisfied the inclusion criteria remained. Of these, 36 studies were relevant in subsequent full-text screening. We categorized the final selection of 36 studies into five groups as follows: grading gliomas, 19 studies (9,13–30); predicting molecular subtypes of gliomas, five studies (13,14,31–33); distinction of different brain tumor types, seven studies (5,8,34–38); therapy response assessment, three studies (39–41); and differentiating recurrence from treatment-related changes, five studies (25,42–45). Two studies (13,14) contained data on glioma grading and predicting molecular subtypes, and one study (25) was assigned to both glioma grading and differentiating recurrence from treatment-related changes. A flowchart of the study selection process is presented in Figure 1. All studies included in the analysis are summarized in Tables E1–E6 (see supplement).

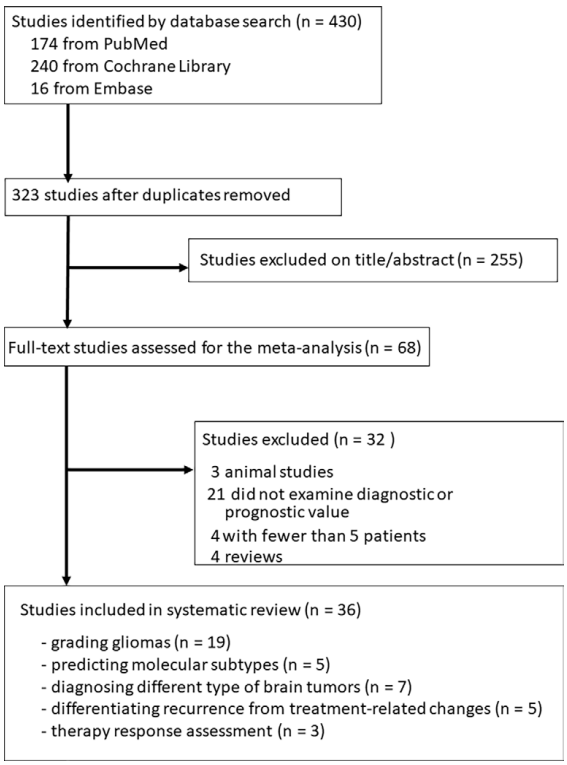

Figure 1: Flowchart describes the study selection process. Two studies contained data on glioma grading and predicting molecular subtypes, and one study was assigned to both glioma grading and differentiating recurrence from treatment-related changes.

CEST Techniques

Thirty-three of the 36 studies used APT-weighted imaging. Six studies presented NOE-weighted images, and four studies assessed amine CEST. Three studies tested conventional magnetization transfer imaging, which depicts semisolid macromolecules in the more solid environment of the cell than APT (37), and one study used fitted magnetization transfer and NOE.

Glioma Grading

A total of 596 patients with glioma (one with WHO grade I, 232 with WHO grade II, 129 with WHO grade III, 193 with WHO grade V, and 41 with WHO grades III or IV) were included from 19 studies. Studies summarized WHO grades I and II into low-grade gliomas (LGGs), whereby WHO grade I corresponds to indolent entities other than diffuse glioma (eg, pilocytic astrocytoma [2]) and WHO grades III and IV into high-grade glioma (HGGs). Seventeen of 19 studies for glioma grading used light microscopic analysis according to the WHO 2007 Classification of CNS Tumors; only two of 19 (more recent) studies adopted the WHO 2016 Classification of CNS Tumors as the diagnostic reference standard. Of these, both studies performed immunohistochemistry testing for *IDH1* status, and one study performed analysis for *MGMT* genetic status. In five of 19 studies, investigators reported the Ki-67 labeling index as a biomarker of tumor cellularity. Seventeen studies used APT-weighted imaging, two studies evaluated amine CEST, two studies presented NOE-weighted images, and one study used fitted magnetization transfer and NOE. Seventeen studies used 3-T MRI and two studies used 7-T MRI. The imaging parameters and grading results are shown in Tables E1 and E2 (see supplement).

Statistically significant differences of APT signals between HGGs and LGGs (with greater and lower signal, respectively) were identified in 16 of 17 studies using APT-weighted images ($P < .0001$–0.0497); the other study by Heo et al (9) found no difference. Furthermore, significant differences were demonstrated between WHO grades II, III, and IV in studies by Bai et al (23) and Togao et al (28). A significant difference between WHO grades II and III but no difference between WHO grades

III and IV was reported in the studies by Zou et al (15) and Jiang et al (21). In contrast, in the studies published by Choi et al (22) and Sakata et al (27), no difference was shown between WHO grade II and III, but WHO III differed significantly from WHO grade IV. Receiver operating characteristic (ROC) curve analyses were carried out in 13 of 17 studies. These demonstrated low to high diagnostic performance with areas under the ROC curve (AUC) of 0.500–1.000.

Paech et al (13) and Heo et al (9) evaluated NOE-weighted MR images by using 7-T imaging. Paech et al (13) showed a lower diagnostic performance for NOE-weighted images than APT-weighted images and downfield-relayed NOE-suppressed APT. Conversely, Heo et al (9) reported that NOE-based signals of HGGs were significantly lower than those of LGGs ($P < .05$), with no statistically significant difference in APT-based signals.

Harris et al (14,26) performed two studies to evaluate diagnostic performance of pH-weighted amine CEST for gliomas. The initial research, in 2016 (26), yielded a statistically significant amine CEST signal difference for glioma of WHO grades II, III, and IV ($P < .05$ for WHO grade III vs grade IV and WHO grade II vs grade IV), but the subsequent study, in 2018 (14), identified a difference only for WHO grade II versus WHO grade IV ($P < .05$). CEST signals increased with increasing tumor grades in both studies.

Some study authors proposed a combination of CEST and multimodal techniques to increase the diagnostic accuracy. Zou et al (15) reported that the combined use of intravoxel incoherent motion resulted in the increase of AUC from 0.957 to 0.986. Sakata et al (17) observed that the combined use of fluorodeoxyglucose (FDG) PET improved the AUC from 0.76 to 0.85, and Choi et al (22) found that the addition of relative cerebral blood volume derived from dynamic susceptibility contrast material–enhanced MRI increased the AUC from 0.877 to 0.923. The correlation of APT signals and MR spectroscopic parameters (choline, choline-to-*N*-acetylaspartate ratio, *N*-acetylaspartate, choline-to-creatine ratio, *N*-acetylaspartate-to-creatine ratio) were investigated in three studies with moderate correlations ($r = 0.4–0.6$).

Predicting Molecular Subtypes of Gliomas

A total of 165 patients with glioma (60 with *IDH* wild type, 44 with *IDH* mutant, 23 with *MGMT* methylated, 17 with *MGMT* unmethylated, 38 with positive MGMT immunostaining, four with negative MGMT immunostaining) were included from five studies. Three of the five studies performed immunohistochemistry testing for *IDH1* status, two of five did so for *MGMT* promotor methylation status, and one of five did so for MGMT protein expression. The *MGMT* methylation status was assessed with a methylation-specific polymerase chain reaction, and MGMT protein expression in tumor cells was reviewed with light microscopy. Four studies used APT-weighted imaging, one study performed amine CEST, one study used NOE-weighted imaging, and one study tested conventional magnetization transfer imaging. Four studies were undertaken by using 3-T and one study using 7-T magnetic field strength. Details of MRI parameters and molecular subtyping results are shown in Tables E1 and E3 (see supplement).

Jiang et al (33) and Paech et al (13) investigated the value of CEST to predict *IDH* mutation status. Jiang et al reported an AUC of 0.89 with use of a maximum region-of-interest value ("hot spot") analysis of APT imaging in WHO grade II gliomas ($n = 27$), with greater APT signal identified in *IDH* wild-type gliomas. Paech et al proposed that downfield-relayed NOE-suppressed APT had a high diagnostic performance (AUC, 0.92–0.98) for *IDH* typing in a mixture of gliomas with various WHO grades (II–IV, $n = 31$) with increased APT signal in *IDH* wild-type gliomas. Harris et al (14) evaluated *IDH* status using pH-sensitive and oxygen-sensitive amine CEST, reporting marginally greater signal in *IDH* mutant ($P = .0434$).

Studies by Su et al (31), Jiang et al (2018) (32), and Paech et al (13) evaluated APT for the prediction of *MGMT* methylation status. Su et al reported a moderate diagnostic accuracy (AUC, 0.849) for a visual scale (qualitative) assessment of APT characteristics. Tumors with greater signal intensity on the solid part or peripheral abnormality tended to be *MGMT*-positive gliomas. Jiang et al observed a moderate performance (AUC, 0.856) using histogram analysis of MTR_{asym} at 3.5 ppm in a comparison of the *MGMT*-unmethylated glioblastomas (GBMs) versus the *MGMT*-methylated GBMs. APT signals were significantly higher in the unmethylated GBMs than in the methylated GBMs (mean APT, $P = .022$; 90th percentile APT, $P = .006$). Paech et al presented APT and NOE results, which achieved low diagnostic accuracy (AUC, 0.61–0.69) although slightly greater compared with perfusion (relative cerebral blood volume AUC 0.59) and diffusion-weighted MRI (apparent diffusion coefficient AUC 0.59). APT and NOE between the unmethylated gliomas and the methylated gliomas had no statistically differences ($P = .13–.39$).

Distinction of Different Brain Tumor Types

A total of 215 patients (124 gliomas [four WHO grade I, 20 WHO grade II, 17 WHO grade III, 77 WHO grade IV, six unclear], 59 metastases, 11 primary central nervous system lymphomas (PCNSLs), eight meningiomas, two pituitary adenomas, three hemangioblastomas, one angiosarcoma, six cavernous malformations, and one angiosarcoma) were included from seven studies. Six brain metastases and nontumor lesions were confirmed by clinical diagnosis, and the remaining tumors were confirmed by histopathologic assessment. The MRI parameters and CEST characteristics are shown in Tables E1 and E4 (see supplement).

Yu et al (34) proposed that APT may help differentiate solitary brain metastases from GBM. In their study of 45 patients with solitary brain metastases versus 43 patients with GBM, APT values in perilesional tissue were significantly lower in the solitary brain metastases group, in which the minimum APT-weighted values produced the highest AUC (0.905) compared with mean APT-weighted values (AUC, 0.868) for lesion discrimination.

Jiang et al (37) reported a high accuracy (AUC, 0.963) for a subtraction parameter (APT $weighted_{max-min}$) to differentiate 11 PCNSLs from 21 HGGs, whereby the PCNSLs had significantly lower APT $weighted_{max-min}$ (mean, 0.76% ± 0.42 [standard deviation]) than the HGGs (2.55% ± 1.20). Jeong et al (36) compared APT signals in hemorrhagic brain lesions

of 16 tumors and seven lesions with nonneoplastic causes, observing that MTR_{asym} in acute to subacute hemorrhage was greater than in surrounding brain, regardless of the underlying pathologic condition.

Park et al (38) analyzed 45 gadolinium-enhanced tumors, consisting of 19 "low-grade" tumors (four pilocytic astrocytomas, two hemangioblastomas, three low-grade astrocytomas, seven low-grade oligodendrogliomas, three pleomorphic xanthoastrocytomas) and 26 "high-grade" tumors (five anaplastic astrocytomas, three anaplastic oligodendrogliomas, two anaplastic oligoastrocytomas, 11 GBMs, five brain metastases), reporting that APT 90th percentile had an AUC of 0.85–0.86 in discriminating low-grade tumors and high-grade tumors. Compared with normalized 90th percentile cerebral blood volume alone, adding APT 90th percentile significantly improved the AUC for the identification of contrast-enhanced low-grade tumor from 0.80–0.82 to 0.97.

Of three studies (5,8,35) featuring gliomas and meningiomas, Jones et al (5) were the first group to demonstrate that the APT effect is quantifiable (eight gliomas and two meningiomas). Shen et al (8) used NOE maps, observing a significantly lower signal within tumor than contralateral normal-appearing white matter for six gliomas ($P < .001$) versus no significant difference for five meningiomas ($P = .116$). Khlebnikov et al (35) used the effect of water T1 relaxation on APT to compare three different metrics of APT contrast: MTR, relaxation-compensated magnetization transfer ratio, and traditional asymmetry (MTR_{asym}) in five gliomas and one meningioma. This study identified a difference that appeared between LGG and HGG in non–gadolinium-enhanced solid tumor regions using MRT and no difference in relaxation-compensated MTR.

Differentiating Tumor Recurrence from Treatment-related Changes

A total of 161 patients with glioma (15 WHO grade II, 15 WHO grade III, 131 WHO grade IV; 108 with tumor progression, 53 with treatment-related effects) and 16 patients with brain metastasis (five with tumor progression, 11 with radiation necrosis) were included from five studies. Final diagnoses were confirmed by second-look surgery or clinical-radiologic follow-up by using the Response Assessment in Neuro-Oncology criteria. All studies used APT-weighted imaging, and one study also assessed magnetization transfer and NOE signals. All studies were completed with 3-T MRI. The patient characteristics and study results are listed in Tables E1 and E5 (see supplement).

One study (43) found a significant difference between tumor progression and radiation necrosis for brain metastases. An ROC analysis was not performed, but NOE MTR and amide MTR differed between tumor progression and radiation necrosis ($P < .0001$). The remaining four studies (25,42,44,45) enrolled patients with glioma (15 with WHO grade II, 15 with WHO grade III, 131 with WHO grade IV). In all four studies, APT signals were significantly higher in tumor progression than in therapy-induced lesion changes; diagnostic accuracies were high (AUC, 0.88–0.98). In a 2018 study, Park et al (42) compared APT and PET imaging and reported greater diagnostic accuracy for APT than carbon 11 (^{11}C) methionine PET. Previously, Park et al (44) had combined gadolinium enhancement features and normalized cerebral blood volume with APT, resulting in increased diagnostic accuracy (AUC, 0.97) over APT alone (AUC, 0.89) for the distinction of glioma recurrence from therapy effects.

Therapy Response Assessment and Prognosis Prediction

Three studies examined therapy response assessment and prognosis prediction by using CEST MRI. Of note, each study differs in its research purposes and investigated different types of brain tumors. The patient characteristics and study results are presented in Tables E1 and E6 (supplement). Regnery et al (39) examined NOE and APT signals at 7-T MRI in 20 patients with GBM to predict early tumor progression after first-line treatment. Pretreatment tumor signal in NOE-Lorentzian difference differed significantly according to responsiveness to first-line treatment (AUC, 0.98).

Desmond et al (40) evaluated the predictive value of various CEST metrics in 25 brain metastases treated with stereotactic radiosurgery at baseline compared with 1 week after treatment and related these to changes in tumor volume at 1 month. A significant association was observed between metastasis volume changes and the relative change in NOE peak amplitude in contralateral normal-appearing white matter.

Harris et al (41) performed pH-weighted imaging in 20 patients with GBM and evaluated differences between acidic tumors and nonacidic tumors in progression-free survival. The median progression-free survival intervals for acidic tumors and nonacidic tumors were 125 days and 450 days, respectively.

Study Quality

The results of the study quality assessment, performed by using the QUADAS-2 tool, are demonstrated in Figure 2. Several studies had a high risk of bias regarding the selection of patients (17 of 36) and/or concerning the conduct or interpretation of the index test (six of 36) due to retrospective design and/or region-of-interest placement by a single researcher. In a high proportion of studies (approximately 80%), it was unclear whether radiologists were blinded to histologic results when placing regions of interest, and in approximately 50% it was unknown whether the interval between imaging and tissue diagnosis was appropriate (ie, when imaging signals were compared to subsequently diagnosed histologic glioma grades).

Discussion

Glioma Grading

Through this systematic review, we identified 36 research studies on the value of endogenous CEST techniques to depict brain tumor metabolism. Approximately half of this research was aimed at predicting glioma histologic (WHO) grades. Broadly, these grading studies indicate a link between greater cellularity in HGGs, higher concentration of proteins and peptides, and APT signal intensity (15,18). Most grading research found higher APT image signals in HGGs than in LGGs, with variable diagnostic accuracy for individual WHO grade distinction. According to the ROC curve analyses, which produced

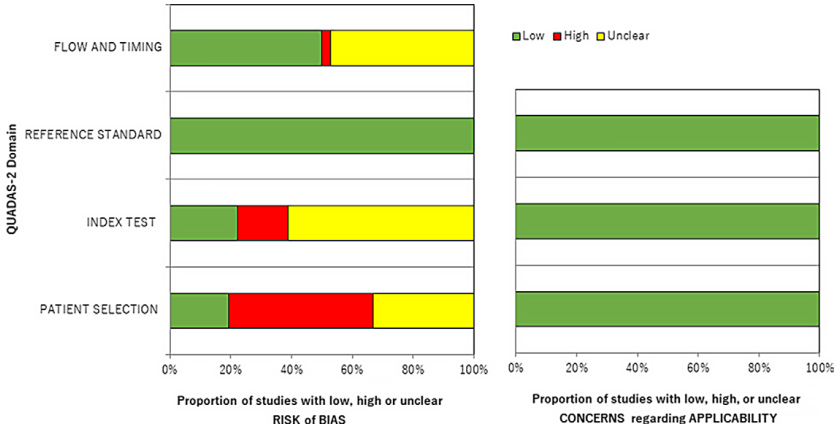

Figure 2: Results of the Quality Assessment of Diagnostic Accuracy Studies 2 (QUADAS-2) quality assessment of the included studies. The risk of bias in four different domains and concerns regarding applicability in three domains are shown.

moderate to high AUC values in many studies (13 of 19), the evidence for the use of CEST in glioma grading is judged to be moderate, whereas the diagnostic accuracy differs among glioma grading studies. For example, Zou et al (15) and Jiang et al (21) reported AUC values of 0.957 and 1.000, respectively, whereas Zhang et al (16) and Sakata et al (27) achieved AUC values of 0.723 and 0.760, respectively, for differentiating between HGGs and LGGs using APT. Aside from technical differences and sampling limitations, the heterogeneity in these data sets is likely to be influenced by the lack of glioma grouping according to molecular genetics. A fundamental change has occurred in the reference standard of the WHO classification of central nervous system tumors from the previous 2007 version (histologic grading only) to the 2016 classification (integrated diagnosis considering histologic grading and molecular markers), whereby most CEST studies carried out for glioma grading (17 of 19) took into account histologic findings only. Specifically, LGGs indistinguishable by histologic criteria may differ in malignant potential (eg, according to *IDH* status), which may affect the CEST signal through difference in the number of solutes (related to the proteasome content) and the pH, depending on the presence or lack of an *IDH* mutation (2,33). Whereas numeric thresholds from individual studies lacking molecular data should be interpreted with caution, in its entirety the research on glioma grading underscores the potential of CEST to quantify malignant metabolism. This is further supported by the statistical associations between APT metrics and Ki-67 in two prospective studies (16,21).

CEST signals contain complex information from various technical factors, whose contributions strongly depend on the experimental setup, such as power, length, and shape of the radiofrequency saturation pulses (24,26), all of which may affect results. A recent meta-analysis by Suh et al (10) focused on the use of APT for glioma grading and attributed variations in radiofrequency saturation power as a probable factor on the heterogeneity of study results.

NOE signals, which are hypothesized to originate from magnetization transfer between water protons and proteins or lipids mediated through intramolecular NOE effects (9), have been identified as valuable to support glioma characterization. However, the extent to which NOE plays a role remains uncertain; Paech et al (13) observed no significant differences for glioma WHO grades, whereas Heo et al (9) reported WHO grade differences for a study of only 10 patients (molecular data unknown). In the study by Paech et al, downfield-relayed NOE-suppressed APT had higher diagnostic performance than conventional APT at 7-T MRI, indicating that NOE contributes to CEST image signal, probably as a confounding effect. Of note, NOE effects are thought to be substantial at 7-T but smaller at 3-T clinical field strength (46).

The comparison of APT CEST with techniques such as diffusion-weighted imaging, FDG PET, and MR spectroscopy for glioma characterization could be of interest for a multimodal diagnostic approach. APT was reported to provide greater diagnostic accuracy for grading than other techniques, and in several studies (13,15,17,22) the combination of CEST with other sequences (intravoxel incoherent motion, FDG PET, and dynamic susceptibility contrast-enhanced MRI) increased diagnostic performance. Therefore, the use of APT together with other modalities has been proposed to aid in grading gliomas. For the combination with APT, it has been reported that intravoxel incoherent motion resulted in an increase in AUC from 0.957 to 0.986 (15), that FDG PET improved the AUC from 0.76 to 0.85 (17), and that dynamic susceptibility contrast-enhanced MRI produced an AUC increase from 0.877 to 0.923 (22). However, the diagnostic accuracy of the combined use of APT and MR spectroscopy has not been comprehensively investigated.

Predicting Molecular Subtypes of Gliomas

Research into the ability of CEST to predict glioma molecular subtypes remains confined to a small number of studies on *IDH* and *MGMT* typing (32,33). *IDH*-mutant gliomas predominantly consist of WHO II–III gliomas and rarely (<10%)

of secondary GBM, with an overall better clinical prognosis (1). Distinct from this are *IDH* wild-type gliomas, many of which correspond to the genetic equivalent of primary GBM with a similarly dismal prognosis, regardless of WHO grade (1). Key disturbances of cellular metabolism, including alterations of amino acid concentrations and reduction of protein expression, are caused by mutations in *IDH* gene-encoded enzymes (33). In addition, *IDH* mutations result in accumulation of the oncometabolite 2-hydroxygluterate, which inhibits oxidative phosphorylation and promotes aerobic glycolysis (14). However, lactic acidosis due to anaerobic glycolysis in the context of nutrient depletion and growing tumor hypoxia is a key property of *IDH* wild-type gliomas, which could confound a pH-based distinction (47). The reported diagnostic accuracy for *IDH* typing by Jiang et al (21) at 3 T (AUC, 0.89) and Paech et al (13) at 7 T (AUC, 0.98, including downfield-relayed NOE suppression) is very high. These results are promising, with the caveat that no information on blinding to immunohistochemistry is stated for either. Larger studies, including multicenter research on CEST imaging for glioma characterization, would be desirable, for example to investigate LGGs, which carry other mutational risk factors for malignant progression (48).

MGMT is a DNA repair enzyme, the activity of which determines glioma susceptibility to alkylating chemotherapy (temozolomide), whereby the methylated *MGMT* promoter status increases chemosensitivity. Both immunohistochemical MGMT protein expression and *MGMT* promoter methylation status are prognostic markers of survival in patients with gliomas (31,32). With regard to AUC, the results of Su et al (31) correlating APT signals with MGMT protein expression are similar to those of Jiang et al (32) assessing *MGMT* promoter methylation status, but differences in the glioma cohorts and analysis methods limit direct comparability. It has been proposed that *MGMT* promoter methylation in gliomas produces a decrease of protein expression, which may affect other protein activity downstream of MGMT (31). Therefore, CEST could be considered as a biomarker for predicting *MGMT* methylation status, but whether it has accuracy sufficient to affect clinical decisions is yet unclear (13).

Paech et al (13) compared CEST with diffusion-weighted imaging and dynamic susceptibility contrast-enhanced MRI for predicting *IDH* and *MGMT* status and found the diagnostic performance of CEST was marginally better than that of the other modalities.

The number of studies aimed at predicting glioma molecular subtypes is still limited, and the evidence for CEST in this context, although promising, is uncertain. Further research is desirable to confirm the method's role in predicting specific genetic signatures and/or tumor biologic behavior.

Diagnosing Different Types of Brain Tumors

The study reporting the highest diagnostic accuracy (37) for differentiating PCNSL from GBM (AUC, 0.963) used a parameter not studied in other research, derived from a calculation ($APT_{max\text{-}min}$) as opposed to one measurement. However, the result is noteworthy, possibly reflecting greater APT signal heterogeneity in GBM, which is known to contain areas of rapid proliferation mixed with (metabolically inactive) necrosis. Also of interest is the finding of greater APT signal in GBM perilesional tissue compared with metastases (34) because it raises the possibility that CEST could improve the delineation of MRI-occult GBM infiltration.

Park et al (38) reported that adding APT to dynamic susceptibility contrast-enhanced MRI increased the diagnostic accuracy in characterizing brain tumors. This finding suggests that a multiparametric approach could be valuable for differentiating malignant gliomas, PCNSL, and brain metastatic disease.

The CEST data on the distinction of different types of brain tumors are limited by small patient numbers (5,8,35), different purposes (34,36–38), and quantitative metrics presented, so that the evidence supporting CEST for this clinical indication remains uncertain.

Differentiating Recurrence from Treatment-related Changes

Conventional MRI sequences are unreliable for differentiating treatment-related changes from tumor recurrence (44) and, even with use of advanced techniques, the distinction can be challenging. Thus, there remains an unmet clinical need for a serial imaging method to provide information on tumor viability. The high reported accuracy in several studies (AUC, 0.88–0.98) suggests that APT may dramatically improve the diagnostic value of MRI for this clinical question. In fact, the performance of APT for differentiating recurrence from treatment-related changes appears to be higher than for differentiating LGGs and HGGs. Recurrent tumors include more protein species, whereas there are fewer proteins in regions of treatment-related changes due to reduced cell density and cytoplasm disruption (49). These metabolic conditions could explain differences in APT signals between recurrence and treatment-related changes. Both APT and methionine PET aim to depict endogenous protein metabolism. Park et al (42) observed a higher diagnostic accuracy for APT than for ^{11}C methionine PET, which could be influenced by differences in protein metabolism. APT signal depends on mobile protein concentration, whereas methionine PET signal originates from actively synthesized proteins. In addition, methionine accumulation may contribute to disruption of the blood–brain barrier in HGGs (42). As in many studies on the distinction of brain tumor recurrence from therapy effects, the reference standard in this study included both cases where the final diagnosis was secured via second-look operation and imaging-only follow-up (using the Response Assessment in Neuro-Oncology criteria).

The evidence for the use of CEST in differentiating recurrence from treatment-related changes is judged to be weak, with study numbers as the main limitation. Those studies consistently report positive results, and more evidence is required for evaluating the efficacy of CEST in differentiating recurrence from treatment-related changes.

Therapy Response Assessment and Prognosis Prediction

In the posttherapy phase, APT may be able to depict baseline and dynamic changes in lesion acidity as a biomarker signature of viable GBM, as suggested by Harris et al (41). This evidence originates from a single-center study and requires validation,

particularly as certain metabolic features of therapy changes and disease recurrence are known to overlap (50).

In a study following stereotactic radiosurgery, Desmond et al (40) identified dynamic changes in normal-appearing white matter, which correlated with volume changes in recently treated brain metastases. As such, CEST signal measurement in normal-appearing tissue may be of interest in monitoring disease progression and disease response. Given these few studies evaluating the relationships between CEST and therapy response or prognosis, the evidence in support of this indication is uncertain.

In summary, CEST techniques can provide information on brain tumor pathologic metabolism and tissue viability in humans at clinical magnetic field strength. But many complexities are unresolved. In particular, the current evidence is shaped by a majority of studies, which solely examined image signals in relation to glioma histologic grade. This limits the clinical impact of these data in the context of WHO 2016 integrated brain tumor diagnosis. The heterogeneity of brain tumor cohorts, acquisition, and interpretative approaches is problematic, including a high risk of bias for a substantial proportion of the published data. From the QUADAS-2 analysis, there was no relationship identifiable between the severity of bias risk and diagnostic accuracy.

Conclusion

Endogenous CEST imaging offers valuable, potentially unique information on brain tumors, but its diagnostic accuracy is incompletely known. Further research is required to assess the method's role in support of molecular genetic diagnosis, to investigate its use in the posttreatment phase, and to compare methods with a view to technical standardization.

Author contributions: Guarantors of integrity of entire study, S.O., M.K., S.T.; study concepts/study design or data acquisition or data analysis/interpretation, all authors; manuscript drafting or manuscript revision for important intellectual content, all authors; approval of final version of submitted manuscript, all authors; agrees to ensure any questions related to the work are appropriately resolved, all authors; literature research, S.O., A.H., M.K., S.T.; clinical studies, S.O., S.T.; and manuscript editing, all authors

Disclosures of Conflicts of Interest: S.O. disclosed no relevant relationships. **A.H.** disclosed no relevant relationships. **X.G.** Activities related to the present article: Received grant funding through the European Commission. Activities not related to the present article: CEO of Gold Standard Phantoms Limited. **M.K.** disclosed no relevant relationships. **S.T.** disclosed no relevant relationships.

References

1. Lapointe S, Perry A, Butowski NA. Primary brain tumours in adults. Lancet 2018;392(10145):432–446.
2. Louis DN, Perry A, Reifenberger G, et al. The 2016 World Health Organization Classification of Tumors of the Central Nervous System: a summary. Acta Neuropathol (Berl) 2016;131(6):803–820.
3. Al-Okaili RN, Krejza J, Woo JH, et al. Intraaxial brain masses: MR imaging-based diagnostic strategy--initial experience. Radiology 2007;243(2):539–550.
4. Thust SC, van den Bent MJ, Smits M. Pseudoprogression of brain tumors. J Magn Reson Imaging 2018 May 7 [Epub ahead of print].
5. Jones CK, Schlosser MJ, van Zijl PC, Pomper MG, Golay X, Zhou J. Amide proton transfer imaging of human brain tumors at 3T. Magn Reson Med 2006;56(3):585–592.
6. Kim M, Zaiss M, Thust S, Golay X. CEST: Chemical exchange saturation transfer. In: Cercignani M, Dowell N, Tofts P, eds. Quantitative MRI of the Brain Principles of Physical Measurement. 2nd ed. Boca Raton, Fla: CRC, 2018.
7. Guivel-Scharen V, Sinnwell T, Wolff SD, Balaban RS. Detection of proton chemical exchange between metabolites and water in biological tissues. J Magn Reson 1998;133(1):36–45.
8. Shen Y, Xiao G, Shen Z, et al. Imaging of nuclear Overhauser enhancement at 7 and 3 T. NMR Biomed 2017;30(9):e3735.
9. Heo HY, Jones CK, Hua J, et al. Whole-brain amide proton transfer (APT) and nuclear overhauser enhancement (NOE) imaging in glioma patients using low-power steady-state pulsed chemical exchange saturation transfer (CEST) imaging at 7T. J Magn Reson Imaging 2016;44(1):41–50.
10. Suh CH, Park JE, Jung SC, Choi CG, Kim SJ, Kim HS. Amide proton transfer-weighted MRI in distinguishing high- and low-grade gliomas: a systematic review and meta-analysis. Neuroradiology 2019;61(5):525–534.
11. McInnes MDF, Moher D, Thombs BD, et al. Preferred Reporting Items for a Systematic Review and Meta-analysis of Diagnostic Test Accuracy Studies: the PRISMA-DTA statement. JAMA 2018;319(4):388–396.
12. Whiting PF, Rutjes AW, Westwood ME, et al. QUADAS-2: a revised tool for the quality assessment of diagnostic accuracy studies. Ann Intern Med 2011;155(8):529–536.
13. Paech D, Windschuh J, Oberhollenzer J, et al. Assessing the predictability of IDH mutation and MGMT methylation status in glioma patients using relaxation-compensated multipool CEST MRI at 7.0 T. Neuro Oncol 2018;20(12):1661–1671.
14. Harris RJ, Yao J, Chakhoyan A, et al. Simultaneous pH-sensitive and oxygen-sensitive MRI of human gliomas at 3 T using multi-echo amine proton chemical exchange saturation transfer spin-and-gradient echo echo-planar imaging (CEST-SAGE-EPI). Magn Reson Med 2018;80(5):1962–1978.
15. Zou T, Yu H, Jiang C, et al. Differentiating the histologic grades of gliomas preoperatively using amide proton transfer-weighted (APTW) and intravoxel incoherent motion MRI. NMR Biomed 2018;31(1):e3850.
16. Zhang J, Zhu W, Tain R, Zhou XJ, Cai K. Improved differentiation of low-grade and high-grade gliomas and detection of tumor proliferation using APT contrast fitted from Z-spectrum. Mol Imaging Biol 2018;20(4):623–631.
17. Sakata A, Okada T, Yamamoto Y, et al. Addition of amide proton transfer imaging to FDG-PET/CT improves diagnostic accuracy in glioma grading: a preliminary study using the continuous net reclassification analysis. AJNR Am J Neuroradiol 2018;39(2):265–272.
18. Togao O, Hiwatashi A, Yamashita K, et al. Grading diffuse gliomas without intense contrast enhancement by amide proton transfer MR imaging: comparisons with diffusion- and perfusion-weighted imaging. Eur Radiol 2017;27(2):578–588.
19. Su C, Liu C, Zhao L, et al. Amide proton transfer imaging allows detection of glioma grades and tumor proliferation: comparison with Ki-67 expression and proton MR spectroscopy imaging. AJNR Am J Neuroradiol 2017;38(9):1702–1709.
20. Sakata A, Fushimi Y, Okada T, et al. Diagnostic performance between contrast enhancement, proton MR spectroscopy, and amide proton transfer imaging in patients with brain tumors. J Magn Reson Imaging 2017;46(3):732–739.
21. Jiang S, Eberhart CG, Zhang Y, et al. Amide proton transfer-weighted magnetic resonance image-guided stereotactic biopsy in patients with newly diagnosed gliomas. Eur J Cancer 2017;83:9–18.
22. Choi YS, Ahn SS, Lee SK, et al. Amide proton transfer imaging to discriminate between low- and high-grade gliomas: added value to apparent diffusion coefficient and relative cerebral blood volume. Eur Radiol 2017;27(8):3181–3189.
23. Bai Y, Lin Y, Zhang W, et al. Noninvasive amide proton transfer magnetic resonance imaging in evaluating the grading and cellularity of gliomas. Oncotarget 2017;8(4):5834–5842.
24. Togao O, Hiwatashi A, Keupp J, et al. Amide proton transfer imaging of diffuse gliomas: effect of saturation pulse length in parallel transmission-based technique. PLoS One 2016;11(5):e0155925.
25. Park JE, Kim HS, Park KJ, Kim SJ, Kim JH, Smith SA. Pre- and posttreatment glioma: comparison of amide proton transfer imaging with MR spectroscopy for biomarkers of tumor proliferation. Radiology 2016;278(2):514–523.
26. Harris RJ, Cloughesy TF, Liau LM, et al. Simulation, phantom validation, and clinical evaluation of fast pH-weighted molecular imaging using amine chemical exchange saturation transfer echo planar imaging (CEST-EPI) in glioma at 3 T. NMR Biomed 2016;29(11):1563–1576.
27. Sakata A, Okada T, Yamamoto A, et al. Grading glial tumors with amide proton transfer MR imaging: different analytical approaches. J Neurooncol 2015;122(2):339–348.
28. Togao O, Yoshiura T, Keupp J, et al. Amide proton transfer imaging of adult diffuse gliomas: correlation with histopathological grades. Neuro Oncol 2014;16(3):441–448.
29. Zhou J, Zhu H, Lim M, et al. Three-dimensional amide proton transfer MR imaging of gliomas: Initial experience and comparison with gadolinium enhancement. J Magn Reson Imaging 2013;38(5):1119–1128.

30. Zhou J, Blakeley JO, Hua J, et al. Practical data acquisition method for human brain tumor amide proton transfer (APT) imaging. Magn Reson Med 2008;60(4):842–849.
31. Su L, Gao P, Lin S, et al. Predicting O6-methylguanine-DNA methyltransferase protein expression in primary low- and high-grade gliomas using certain qualitative characteristics of amide proton transfer-weighted magnetic resonance imaging. World Neurosurg 2018;116:e814–e823.
32. Jiang S, Rui Q, Wang Y, et al. Discriminating MGMT promoter methylation status in patients with glioblastoma employing amide proton transfer-weighted MRI metrics. Eur Radiol 2018;28(5):2115–2123.
33. Jiang S, Zou T, Eberhart CG, et al. Predicting IDH mutation status in grade II gliomas using amide proton transfer-weighted (APTw) MRI. Magn Reson Med 2017;78(3):1100–1109.
34. Yu H, Lou H, Zou T, et al. Applying protein-based amide proton transfer MR imaging to distinguish solitary brain metastases from glioblastoma. Eur Radiol 2017;27(11):4516–4524.
35. Khlebnikov V, Polders D, Hendrikse J, et al. Amide proton transfer (APT) imaging of brain tumors at 7 T: The role of tissue water T1 -Relaxation properties. Magn Reson Med 2017;77(4):1525–1532.
36. Jeong HK, Han K, Zhou J, et al. Characterizing amide proton transfer imaging in haemorrhage brain lesions using 3T MRI. Eur Radiol 2017;27(4):1577–1584.
37. Jiang S, Yu H, Wang X, et al. Molecular MRI differentiation between primary central nervous system lymphomas and high-grade gliomas using endogenous protein-based amide proton transfer MR imaging at 3 Tesla. Eur Radiol 2016;26(1):64–71.
38. Park JE, Kim HS, Park KJ, Choi CG, Kim SJ. Histogram analysis of amide proton transfer imaging to identify contrast-enhancing low-grade brain tumor that mimics high-grade tumor: increased accuracy of MR perfusion. Radiology 2015;277(1):151–161.
39. Regnery S, Adeberg S, Dreher C, et al. Chemical exchange saturation transfer MRI serves as predictor of early progression in glioblastoma patients. Oncotarget 2018;9(47):28772–28783.
40. Desmond KL, Mehrabian H, Chavez S, et al. Chemical exchange saturation transfer for predicting response to stereotactic radiosurgery in human brain metastasis. Magn Reson Med 2017;78(3):1110–1120.
41. Harris RJ, Cloughesy TF, Liau LM, et al. pH-weighted molecular imaging of gliomas using amine chemical exchange saturation transfer MRI. Neuro Oncol 2015;17(11):1514–1524.
42. Park JE, Lee JY, Kim HS, et al. Amide proton transfer imaging seems to provide higher diagnostic performance in post-treatment high-grade gliomas than methionine positron emission tomography. Eur Radiol 2018;28(8):3285–3295.
43. Mehrabian H, Desmond KL, Soliman H, Sahgal A, Stanisz GJ. Differentiation between radiation necrosis and tumor progression using chemical exchange saturation transfer. Clin Cancer Res 2017;23(14):3667–3675.
44. Park KJ, Kim HS, Park JE, Shim WH, Kim SJ, Smith SA. Added value of amide proton transfer imaging to conventional and perfusion MR imaging for evaluating the treatment response of newly diagnosed glioblastoma. Eur Radiol 2016;26(12):4390–4403.
45. Ma B, Blakeley JO, Hong X, et al. Applying amide proton transfer-weighted MRI to distinguish pseudoprogression from true progression in malignant gliomas. J Magn Reson Imaging 2016;44(2):456–462.
46. Zhou J, Hong X, Zhao X, Gao JH, Yuan J. APT-weighted and NOE-weighted image contrasts in glioma with different RF saturation powers based on magnetization transfer ratio asymmetry analyses. Magn Reson Med 2013;70(2):320–327.
47. Khurshed M, Molenaar RJ, Lenting K, Leenders WP, van Noorden CJF. In silico gene expression analysis reveals glycolysis and acetate anaplerosis in IDH1 wild-type glioma and lactate and glutamate anaplerosis in IDH1-mutated glioma. Oncotarget 2017;8(30):49165–49177.
48. Korshunov A, Casalini B, Chavez L, et al. Integrated molecular characterization of IDH-mutant glioblastomas. Neuropathol Appl Neurobiol 2019;45(2):108–118.
49. Zhang P, Guo Z, Zhang Y, et al. A preliminary quantitative proteomic analysis of glioblastoma pseudoprogression. Proteome Sci 2015;13(1):12.
50. Zhang H, Ma L, Wang Q, Zheng X, Wu C, Xu BN. Role of magnetic resonance spectroscopy for the differentiation of recurrent glioma from radiation necrosis: a systematic review and meta-analysis. Eur J Radiol 2014;83(12):2181–2189.

European Journal of Radiology 114 (2019) 120–127

Contents lists available at ScienceDirect

European Journal of Radiology

journal homepage: www.elsevier.com/locate/ejrad

Research article

Modelling MR and clinical features in grade II/III astrocytomas to predict *IDH* mutation status

Harpreet Hyare[a,b,*], Louise Rice[c], Stefanie Thust[a,c], Parashkev Nachev[a], Ashwani Jha[a], Marina Milic[c], Sebastian Brandner[d,e], Jeremy Rees[a,c]

[a] Department of Brain Repair and Rehabilitation, UCL Institute of Neurology, London, UK
[b] Imaging Department, UCLH NHS Trust, London, UK
[c] National Hospital for Neurology and Neurosurgery, Queen Square, London, UK
[d] Division of Neuropathology, National Hospital for Neurology and Neurosurgery, Queen Square, London, UK
[e] Department of Neurodegenerative Diseases, UCL Institute of Neurology, London, UK

ARTICLE INFO

Keywords:
MRI
VASARI
IDH
Astrocytoma

ABSTRACT

Background and purpose: There is increasing evidence that many *IDH* wildtype (*IDH*wt) astrocytomas have a poor prognosis and although MR features have been identified, there remains diagnostic uncertainty in the clinic. We have therefore conducted a comprehensive analysis of conventional MR features of *IDH*wt astrocytomas and performed a Bayesian logistic regression model to identify critical radiological and basic clinical features that can predict *IDH* mutation status.

Materials and methods: 146 patients comprising 52 *IDH*wt astrocytomas (19 WHO Grade II diffuse astrocytomas (A II) and 33 WHO Grade III anaplastic astrocytomas (A III)), 68 *IDH*mut astrocytomas (53 A II and 15 A III) and 26 GBM were studied. Age, sex, presenting symptoms and Overall Survival were recorded. Two neuroradiologists assessed 23 VASARI imaging descriptors of MRI features and the relation between *IDH* mutation status and MR and basic clinical features was modelled by Bayesian logistic regression, and survival by Kaplan-Meier plots.

Results: The features of greatest predictive power for IDH mutation status were, age at presentation (OR = 0.94 +/−0.03), tumour location within the thalamus (OR = 0.15 +/−0.25), involvement of speech receptive areas (OR = 0.21 +/−0.26), deep white matter invasion of the brainstem (OR = 0.10 +/−0.32), and T1/FLAIR signal ratio (OR = 1.63 +/−0.64). A logistic regression model based on these five features demonstrated excellent out-of-sample predictive performance (AUC = 0.92 +/−0.07; balanced accuracy 0.81 +/−0.09). Stepwise addition of further VASARI variables did not improve performance.

Conclusion: Five demographic and VASARI features enable excellent individual prediction of*IDH* mutation status, opening the way to identifying patients with *IDH*wt astrocytomas for earlier tissue diagnosis and more aggressive management.

Summary of importance

This study adds to existing evidence by highlighting the significantly worse prognosis of low to intermediate grade *IDH* wildtype (*IDH*wt) astrocytomas compared to their IDH mutant (*IDH*mut) counterparts, with a striking similarity in Overall Survival (OS) between WHO III *IDH*wt and GBM, demonstrating the significant effect of WHO tumour grade. *IDH*wt astrocytomas are suspected to represent 'early GBM' making it vital to identify these patients for early and aggressive treatment. From a comprehensive analysis of structural MR imaging in *IDH*wt grade II and grade III astrocytomas, we identify five critical imaging and demographic features with substantial power to predict *IDH* mutation status. The current strategy of 'imaging only' observational management for gliomas of presumed low grade, without diagnostic biopsy, may thus be modified by probabilistically stratified risk of adverse tumour genetics.

1. Introduction

The recently published World Health Organization Classification of tumours [1] has now incorporated molecular parameters to complement histological features in the definition of tumour entities. In the updated WHO guidelines, WHO grade II diffuse astrocytomas (A II) and WHO grade III anaplastic astrocytomas (A III) are now divided into *IDH*

* Corresponding author at: Department of Brain Repair and Rehabilitation, UCL Institute of Neurology, Queen Square, London, WC1N 3BG, UK.
E-mail address: harpreet.hyare@nhs.net (H. Hyare).

https://doi.org/10.1016/j.ejrad.2019.03.003
Received 16 July 2018; Received in revised form 12 February 2019; Accepted 9 March 2019

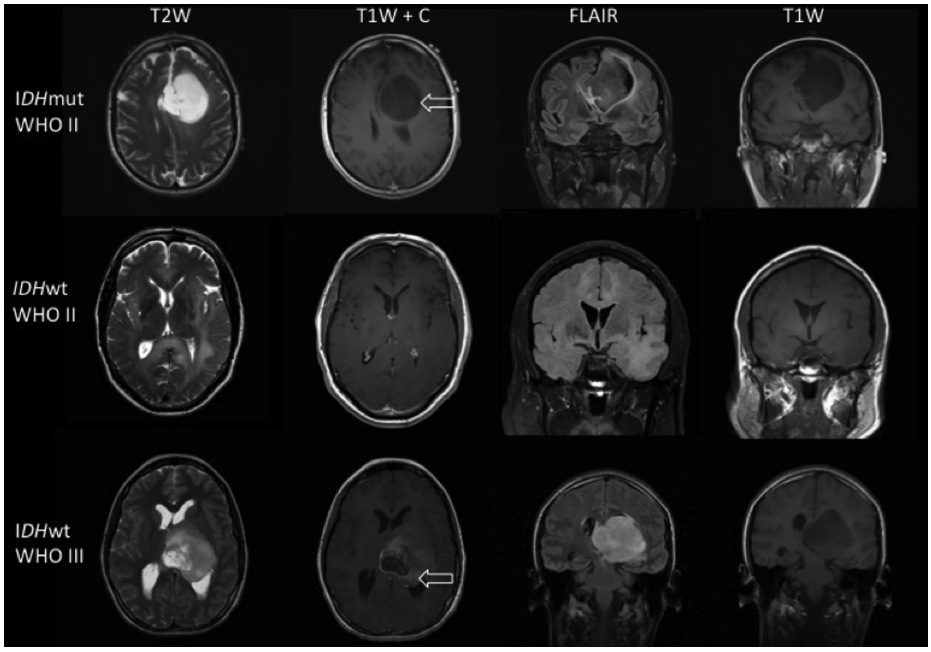

Fig. 1. Illustration of effect of IDH mutation status on VASARI MRI features. legend: *IDH*mut WHO grade II tumour in left frontal lobe demonstrating a well-defined nonenhancing margin on T2W, patchy enhancement on T1W + C and T1¯FLAIR ratio. *IDH*wt WHO grade II tumour centred on the left temporal lobe, demonstrating a poorly-defined non enhancing margin with gliomatosis on T2W, no contrast enhancement on T1W + C and T1 < < FLAIR ratio. *IDH*wt WHO grade III thalamic tumour demonstrating a well-defined tumour margin on T2W, thick/nodular enhancement > 3mm on T1W + C and T1¯FLAIR ratio.

mutant (*IDH*mut), *IDH* wildtype (*IDH*wt) and not otherwise specified (NOS) categories. A recent study of more than 160 adult *IDH*wt astrocytomas demonstrated that 78% were the molecular equivalent of conventional glioblastoma (GBM) based on molecular profiles and hallmark DNA alterations with similar poor survival profiles [2].

There are now numerous reports predicting *IDH* mutation status using both conventional and quantitative MRI. *IDH*wt tumours have been shown to have an indistinct tumour margin [3], tend to involve the temporal lobes, demonstrate lower ADC and have a higher rCBV [4] compared to *IDH*mut tumours. Whilst these findings are important, in isolation these MR features are non-specific, leading to diagnostic uncertainty.

At our institution, we have also observed that a number of patients with histology suggestive of astrocytoma WHO grade II or III, but molecular features of primary glioblastoma, including *IDH*wt, 7p gain or EGFR amplification, 10q loss and TERT promoter mutation, have behaved clinically similar to GBM. The purpose of this study was to identify a robust set of clinical and radiological features that could accurately identify this group of 'early stage GBM'.

We performed a comprehensive qualitative imaging analysis of *IDH*wt astrocytomas using the VASARI (Visually Accessible Rembrandt Images) MR feature set [5] and compared with two reference sets of *IDH*mut astrocytomas and GBM. A Bayesian logistic regression model was then used to identify the critical MR and demographic features with substantial power to predict IDH mutation status.

2. Materials and methods

2.1. Patient population

146 consecutive patients undergoing surgery were selected from the archives of the Neuropathology Department at our Institution betwwen 2012 and 2017, following appropriate institutional review board approval. They comprised 52 *IDH*wt astrocytomas (19 A II and 33 A III), 68 *IDH*mut astrocytomas (53 A II and 15 A III) and 26 *IDH*wt GBM.

Clinical information (age, sex) and overall survival was available in all cases and presenting symptom was available in all WHO grade II/III astrocytoma cases. Overall survival was defined as the number of months between the date of the initial pathological diagnosis and time to death (or point of censure if patient was still alive). In addition, the proportion of patients still alive at two years was determined in each group. Pre-surgical MRI data were available in all cases, of which contrast images were not available in 4 cases (3 *IDH*mut, 1 *IDH*wt) fluid attenuated inversion recovery (FLAIR) images were not available in 6 patients (2 *IDH*wt, 4 *IDH*mut), ADC maps were not available in 18 patients (7 *IDH*wt and 11 *IDH*mut) and the presence of haemorrhage could not be determined in 35 patients (12 *IDH*wt and 23 *IDH*mut).

2.2. Radiological features

The VASARI lexicon for MRI annotation contains 25 imaging descriptors based on different MRI modalities, including T1 and T2/FLAIR sequences, and was developed for use in analyzing GBMs. The exact description of all the features can be found at the National Cancer Institute's Cancer Imaging Archive (https://wiki.cancerimagingarchive.net/display/Public/VASARI+Research+Project).

For the purposes of this study, the most commonly used MRI features were assessed: f1 tumor location, f2 side of lesion center, f3. eloquent brain, f4 enhancement quality, f5 proportion enhancing, f6 proportion non-contrast enhancing tumor (nCET), f7 proportion necrosis, f8 cysts, f9 multifocal or multicentric, f10 T1/FLAIR ratio, f11 thickness of enhancing margin, f12 definition of the enhancing margin, f13 definition of the nonenhancing margin, f14 proportion of edema, f16 hemorrhage, f17 diffusion characteristics, f18 pial invasion, f19 ependymal invasion, f20 cortical involvement, f21 deep white matter invasion, f24 satellites, and f25 calvarial remodeling.

In a subset of 33 patients with *IDH*wt astrocytomas and 30 patients with *IDH*mut astrocytomas, two board-certified neuroradiologists (HH and ST) independently reviewed the MR images on a PACS workstation, blinded to histopathological diagnosis, and recorded a set of mark-ups for imaging features describing the location and morphology of the tumour. After initial review of this subset, modifications were made to some of the VASARI feature set to capture MRI features, which appeared unique to diffuse astrocytomas and anaplastic astrocytomas compared to GBMs. As a number of tumours demonstrated no contrast enhancement, an additional category "Not applicable" was added to f5 proportion enhancing, f11 thickness of enhancing margin and f12 definition of enhancing margin. In addition, an extra category "patchy" was added to f11 thickness of the enhancing margin to better describe the ill-defined enhancement perceived in many of the diffuse and anaplastic astrocytomas (Fig. 1).

The modified VASARI features were recorded on the remaining dataset by a clinical research fellow and checked by neuroradiologist HH.

2.3. Interrater agreement

We assessed the interrater agreement in the training set of each of the VASARI criteria by using the Kappa statistic. Values close to 1 indicate high interrater agreement for that particular feature, whereas values close to 0 signify that interrater agreement is due to chance. Interrater agreement for the lesion size measurements was assessed by means of the intraclass correlation coefficient. Finally, for each patient image set, a consensus review was performed for f4 enhancement quality, f11 thickness of enhancing margin, f12 definition of enhancing margin and f17 diffusion characteristics. For the remaining MR features, the consensus value was equal to the median of the neuroradiologists' measurements.

2.4. Histopathology and molecular analysis

Paraffin blocks containing tissue of adult patients (above 18 years) with *IDH*wt A II or A III were collected from the archives of the Neuropathology department at our Institution and analysed according to previously published data [6].

2.5. Association between MRI features and genomics

For descriptive purposes, a univariate analysis of the association of each of the 25 VASARI features with the clinical label was performed with a Chi-Squared test, uncorrected for multiple comparisons.

Independently, we sought to derive a multivariable statistical model that could be used to predict the genetic mutation status (IDHwt versus IDHmut) of grade II and grade III astrocytomas, based on a combination of basic clinical and radiological criteria. To achieve this, the genetic mutation status of 120 subjects with grade II/III astrocytomas (52 IDHwt, 68 IDHmut) was subjected to a Bayesian penalized logistic multiple regression model using the fully automated BayesReg software package (https://arxiv.org/abs/1611.06649), running in Matlab version 2016b (https://uk.mathworks.com/). Independent variables included age at presentation, gender, and the VASARI imaging descriptors. Each ordinal VASARI criterion (such as F10 T1/FLAIR ratio) was modelled as a single covariate using dummy coding of the categorial levels. Nominal variables were parameterized with categorial expansion: for example F1 Tumour location is thereby decomposed into 8 categorial variables corresponding to each anatomical location. The following variables with fewer than 2 occurrences were removed from the dataset: F1 Tumour Location (Brainstem); F1 Tumour Location (Occipital Lobe); F3 Eloquent Brain (Vision); F11 Thickness of enhancing margin (Thin); F17 Diffusion (Restricted)).

This reparameterisation resulted in a logistic multiple regression model with 50 independent variables. Where the number of independent variables is large relative to the number of cases in the data, estimating a model with conventional statistical methods can lead to extreme and unstable model parameters with high variance, resulting in poor out-of-sample predictive power. We therefore used penalised regression, applying a penalty to extreme model parameter estimates. In the Bayesian setting, this is robustly achieved by applying a shrinkage prior: a hyperparameter of the regression coefficients, whose distribution has a substantial mass around zero. Here we used the default ridge prior in the BayesReg package which is a half-Cauchy function with mean of zero and scale parameter of 1.

High-dimensional models are analytically intractable and so marginal likelihoods and posterior parameter estimates were estimated using Markov Chain Monte Carlo (MCMC) sampling using Gibbs procedure. The model was estimated from 50,000 samples (2000 samples burn-in and every 5th sample was included (thinning)). Odds ratios are presented as maximum a posteriori (MAP) estimates +/- standard deviation (sd).

Following estimation of the full model with the entire dataset, we investigated the predictive power of model with a reduced number of independent variables. For this stage, each regression coefficient was ranked according to a Bayesian feature ranking algorithm (Malik and Schmidt, 2011), where higher ranks indicate a stronger relationship between the dependent variable and the independent variable in question. We created 50 variants of the regression model, incrementally adding independent variables on order of their rank (from 1 variable up to 50 variables). The same MCMC settings were used as for the full model. In order to avoid overfitting, each model was estimated 100 times holding out 15% of the data and model performance was measured with out-of-sample predictive performance as quantified by the mean +/- sd of the area under the curve (AUC) of the Receiver operating characteristic (ROC) curve and mean +/- sd of the balanced accuracy.

Note an advantage of adopting a Bayesian framework is intelligibility of null results, allowing us to infer not only that a feature is associated but also that it is not.

3. Results

3.1. Interrater agreement

Interrater agreements were moderate to high. The highest agreement was seen for f1 tumour location (0.723) and f8 presence of tumour cyst(s) (0.713). The lowest agreement was for f17 diffusion characteristics (0.357) prior to consensus review.

3.2. Patient features and mutation status

Patients with *IDH*wt astrocytomas were significantly older than patients with *IDH*mut astrocytomas (mean 54 (21–76) years compared to 37 (20–63) years) and with GBM (mean age 42 (29–68) years (Table 1). No significant differences were observed for gender or presenting symptoms (Table 1). Seizure was the most common presenting symptom, seen in 39 of 68 *IDH*mut patients, 20 of 52 *IDH*wt patients and 12 of 26 GBM patients followed by motor paresis and dysphasia.

Table 1
Differences in VASARI MR features between the study set.

Variable	GBM (n = 26)	*IDH*wt (n = 52)	*IDH*mut (n = 68)	*IDH*wt vs *IDH*mut	*IDH*wt vs GBM
Age (year)	42 (29–68)	54 (21–76)	37 (20–63)	< **0.001**	0.274
Sex (male:female)	13:13	34:18	38:30	0.292	0.793
Presenting complaint				0.377	0.230
Cognitive disorder	2	5	3		
Dizziness	0	2	2		
Dysphasia	0	7	4		
Gait disturbance	2	1	1		
Headache	3	3	3		
Incidental	0	3	5		
Isolated CN	0	2	3		
Motor paresis	7	8	3		
Seizure	12	20	39		
Sensory disturbance	0	1	2		
Visual field disturbance	0	0	1		
F1 Tumour Location					
Cerebellum	0	1	0		
Corpus Callosum	0	2	1		
Frontal Lobe	11	13	37		
Insula	1	4	4	**0.001**	0.682
Occipital Lobe	1	1	0		
Parietal Lobe	4	5	8		
Temporal Lobe	6	15	18		
Thalamus	3	11	0		
F2 Side of lesion				0.235	0.681
Center/Bilateral	1	5	2		
Left	12	26	32		
Right	13	21	34		
F3 Eloquent Brain				**0.007**	0.726
Motor	4	8	8		
No Eloquent Brain	18	30	44		
Speech motor	0	3	13		
Speech receptive	3	11	2		
Vision	1	0	1		
F4 Enhancement Quality				0.663	**0.003**
	18	9	8		
Marked/avid	8	18	21		
Minimal/Mild	0	24	36		
No Contrast Enhancement	0	1	3		
No Contrast given					
F5 Proportion Enhancing				0.773	< **0.001**
68-95%	6	1	1		
34-67%	6	7	5		
6-33%	13	16	21		
< 5%	1	3	2		
None	0	24	36		
N/A	0	1	3		
F6 Proportion Non-Contrast				0.538	< **0.001**
68-95%	12	42	59		
34-67%	7	7	5		
6-33%	7	1	1		
< 5%	0	2	3		
F7 Proportion Necrosis				0.872	< **0.001**
68-95%	1	0	0		
34-67%	8	4	3		
6-33%	10	3	5		
< 5%	2	1	1		
None	5	44	59		
F8 Cysts				0.022	0.176
Present	**20**	2	12		
Absent	**6**	50	56		
F9 Multifocal or Multicentric				**0.005**	0.190
Focal	23	32	58		
Gliomatosis	0	11	8		
Multifocal	3	9	2		
F10 T1/FLAIR ratio				< **0.001**	**0.002**
No FLAIR images	4	2	4		
T1 < < FLAIR	4	27	9		
T1 < FLAIR	4	13	22		
T1¯FLAIR	14	10	33		
F11 Thickness of enhancing margin				0.388	**0.003**
Patchy	4	13	20		
Solid	3	5	2		
Thick/nodular	15	7	4		
Thin	4	1	0		
Minimal	0	1	3		
N/A	0	25	39		
F12 Definition of the enhancing margin				0.138	**0.011**
Poorly defined	13	17	23		
Well defined	13	10	6		
N/A	0	25	39		
F13 Definition of the non-enhancing margin				< **0.001**	0.162
Poorly defined	15	40	28		
Well defined	11	12	40		
F14 Proportion of Edema				0.160	**0.003**
34-67%	3	1	1		
6-33%	10	5	3		
< 5%	10	18	14		
None	3	28	50		
F16 Haemorrhage				0.434	0.375
Cannot determine	6	12	23		
No	15	37	42		
Yes	5	3	3		
F17 Diffusion Characteristics				0.713	**0.001**
No ADC Images	4	7	11		
Facilitated	4	27	37		
Mixed	14	18	19		
Restricted	4	0	1		
F18 Pial Invasion				0.232	**0.023**
Absent	20	51	63		
Present	6	1	5		
F19 Ependymal Extension	24	50	63		
Absent	2	2	5	0.697	0.494
Present					
F20 Cortical Involvement				**0.034**	0.109
Absent	10	15	8		
Present	16	37	60		
F21 Deep White Matter Invasion				< **0.001**	0.916
Brainstem	1	6	0		
Corpus Callosum	3	9	10		
Internal Capsule	7	15	6		
None	15	22	52		
F24 Satellites				**0.042**	1.000
Absent	24	46	67		
Present	2	6	1		
F25 Calvarial Remodeling		49	67	0.315	1.000
Absent	24	3	1		
Present	2				

Note. GBM: glioblastoma, *IDH*wt: isocitrate dehydrogenase wild type, *IDH*mut: isocitrate dehydrogenase mutated, VASARI: Visually Accessible Rembrandt Images.

3.3. Patient survival

Overall Survival was available in 120 patients (13 GBM, 59 *IDH*mut and 48 *IDH*wt) and is shown by Kaplan-Meier plots for each tumour category in Fig. 2. As can be seen, the *IDH*wt A III and *IDH*wt A II

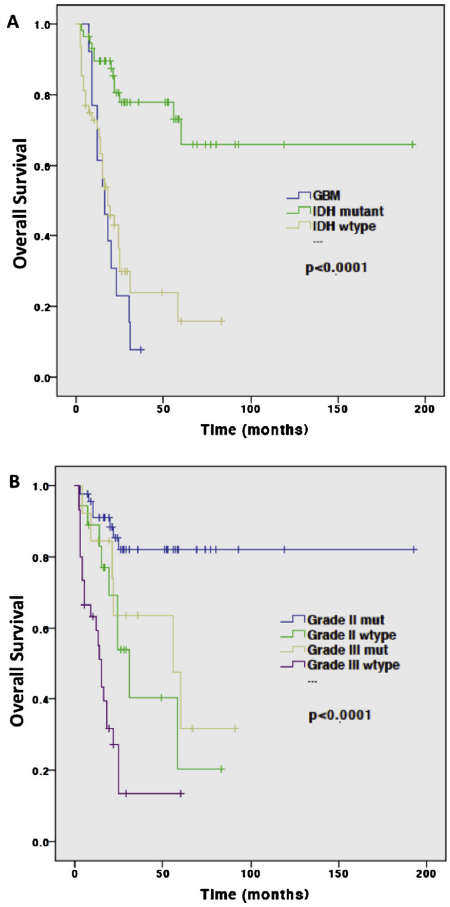

Fig. 2. Kaplan Meier survival curves illustrating effect of tumour grade and *IDH* mutation on Overall Survival. legend: Kaplan Meier survival curves demonstrating: (A) significantly poorer survival in *IDH*wt compared to *IDH*mut astrocytomas ($p < 0.0001$) but similar survival to GBM, (B) poorer survival in Grade III *IDH*mut astrocytomas compared to Grade II *IDH*mut ($p = 0.031$) and Grade III *IDH*wt compared to Grade II *IDH*wt astrocytomas ($p = 0.013$).

demonstrated poorer survival compared to the *IDH*mut reference set ($p < 0.001$) and, as expected, the GBM patients demonstrated the poorest overall survival. The median survival for *IDH*wt was 18.3 months compared to 37.8 months for the *IDH*mut patients, similar to GBM (18.4 months).

3.4. MRI features and mutation status

The univariate descriptive analysis of the difference between *IDH*wt and *IDH*mut, highlighted 8 of the VASARI features: f1 location, f3 eloquent brain, f9 multifocal, f10 T1/FLAIR ratio, f13 definition of nonenhancing margin, f20 cortical, f21 deep white matter invasion and f24 satellites (Table 1). *IDH*wt tumours were more likely to demonstrate a lower T1/FLAIR ratio (27/52) compared to 9 of 68 *IDH*mut astrocytomas, suggestive of an infiltrative rather than expansive pattern. The definition of the non-enhancing margin was poorly defined in 40 of 52 *IDH*wt astrocytomas compared to 28 of 68 *IDH*mut tumours. A higher proportion of *IDH*wt tumours demonstrated deep white matter invasion (30 of 52 (6 brainstem, 9 corpus callosum, 15 internal capsule) compared to 16 of 68 *IDH*mut astrocytomas.

*IDH*wt astrocytomas were more likely to be multifocal (9 of 52) or demonstrate a gliomatosis pattern (11 of 52) compared with 2 of 68 multifocal and 8 of 68 gliomatosis in the *IDH*mut reference set. There was a difference in tumour location between *IDH*wt and *IDH*mut tumours. The most common anatomical location for *IDH*wt tumours was the temporal lobe (15 of 52) whereas the frontal lobe was the most frequently involved site in *IDH*mut tumours. A higher proportion of *IDH*wt tumours were located in the thalamus (11 of 52) whereas the thalamus was not involved in any of the *IDH*mut cases. A higher proportion of *IDH*wt tumours involved eloquent brain, specifically speech receptive: (11 of 52 *IDH*wt compared to 2 of 68 *IDH*mut).

There were no significant differences in any of the MRI features describing contrast enhancement between *IDH*wt and *IDH*mut astrocytomas. 24 of the 52 IDHwt tumours and 36/68 IDHmut astrocytomas demonstrated no enhancement, whereas all the GBM cases demonstrated enhancement. Where enhancement was present, it was more likely to be patchy in the *IDH*wt astrocytomas (13 of 27) similar to the *IDH*mut reference set (20 of 30) whereas the GBM cases were more likely to be thick/nodular (7 of 13).

There were also no significant difference observed in diffusion characteristics between the *IDH*wt and *IDH*mut astrocytomas with the majority of lesions demonstrating facilitated diffusion (27/52 *IDH*wt and 37/68 *IDH*mut) rather than restricted diffusion. The GBM cases were more likely to demonstrate mixed diffusion with 3 cases demonstrating restricted diffusion.

3.5. Predicting mutation status from imaging features

Our Bayesian logistic regression model was used to estimate the odds ratios for each demographic and imaging feature within a probabilistic multivariable inferential framework. These ratios, ranked by strength of association, are shown in Fig. 3. In agreement with the univariate analysis, only a subset of the features were strongly associated with IDH mutation status. To quantify the optimal number of features to incorporate in a model with potential clinical predictive utility, we evaluated a set of 50 models with increasing numbers of independent variables, entered in order of their rank. The cross-validated performance of these models is shown in Fig. 4. Note that excellent performance (AUC = 0.92 +/-0.07; balanced accuracy 0.81 +/- 0.09) was achieved with only the top five variables: age at presentation (OR = 0.94 +/-0.03), tumour location within the thalamus (OR = 0.15 +/-0.25), involvement of speech receptive areas (OR = 0.21 +/-0.26), deep white matter invasion of the brainstem (OR = 0.10 +/-0.32), and T1/FLAIR signal ratio (OR = 1.63 +/-0.64).

An ROC curve for this five variable model is shown in Fig. 4. At the optimal decision threshold, this corresponds to a sensitivity of 0.83 and specificity of 0.85.

4. Discussion

In this comprehensive analysis of *IDH*wt and *IDH*mut WHO Grade II/III astrocytomas, we have shown that *IDH*wt have a survival equivalent to that of GBM, and much less than *IDH*mut astrocytomas, irrespective of histological grade. We have identified five most strongly predictive variables of *IDH* mutation status, and demonstrated—within a Bayesian framework that allows us to make this inference positively—that other imaging features are not contributory. A model based on these five features: older age at presentation, tumour location within the thalamus, involvement of speech receptive areas, deep white matter involvement of the brainstem and lower T1/FLAIR ratio shows excellent predictive performance for *IDH*wt astrocytomas, potentially alerting the clinician to *IDH*wt status and consequently earlier more

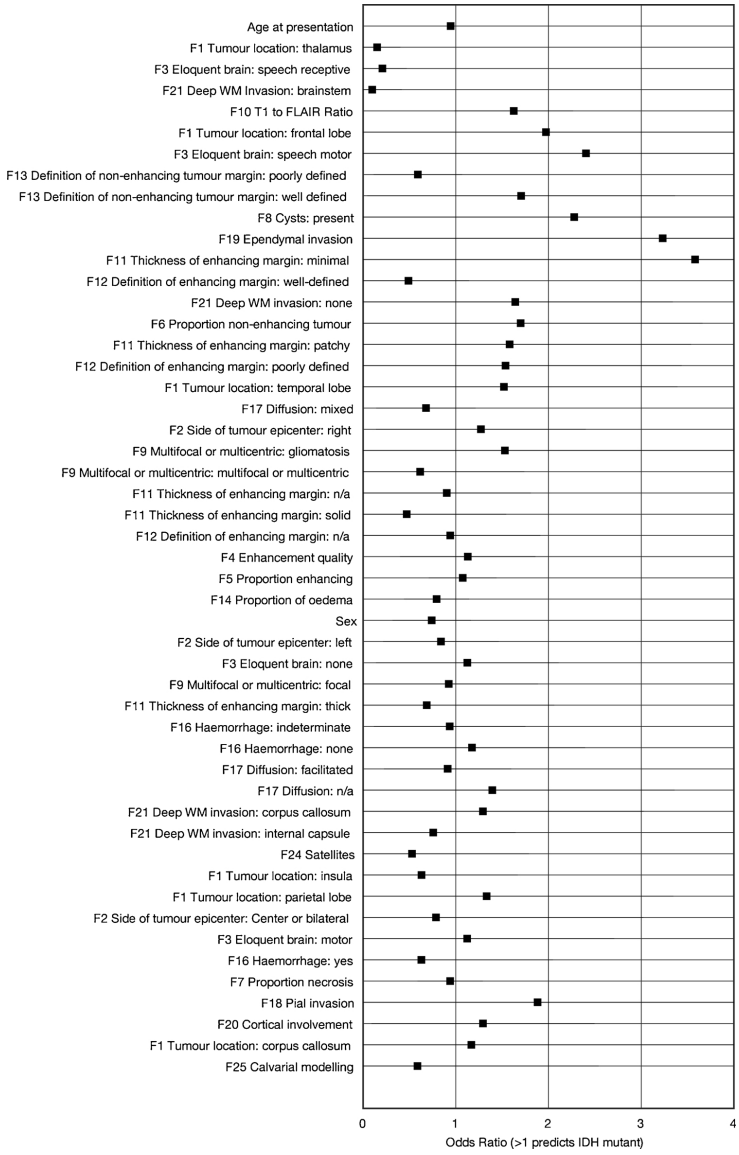

Fig. 3. Odds ratios of IDH status predictive demographic and VASARI features. legend: Forest plot of the odds ratio of demographic and VASARI features predictive of IDH mutation status, reparameterised to enable multivariable modelling within a Bayesian penalized logistic regression model. The features are ranked in order of decreasing strength of association. The black squares indicated the estimated mean, with their associated lines indicating +/- 1 standard deviation of the parameter.

aggressive management.

The revised WHO classification of gliomas [1] has provided an opportunity to re-examine the imaging features of these tumours with potential for additional validation and potential for an imaging-based classification that could complement the genomic classification. This would be particularly useful in unresectable tumours where a policy of surveillance may be preferred without recourse to a histological and molecular diagnosis. Our study findings of a more invasive imaging phenotype in *IDH*wt astrocytomas is supported by a recent radiogenomic study of 110 WHO grade II and III astrocytomas from The Cancer Genome Atlas [7], reporting that the 25 *IDH*wt tumours were more likely to be associated with an irregular tumour boundary and a poorer outcome. The authors used a computer algorithm approach to analyze tumour shape in two or three dimensions and hypothesized that

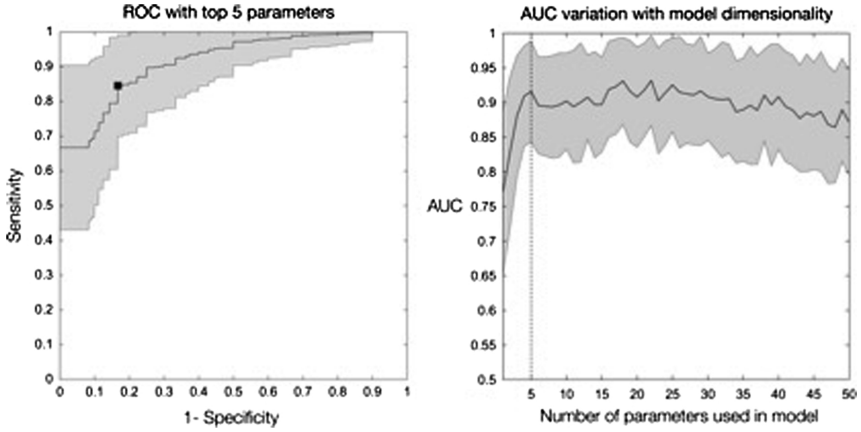

Fig. 4. Predicting IDH mutation status from demographic and VASARI features. legend: The plot on the right shows the estimated AUC (black line) tested on a held out random sample of 15% of the dataset with logistic regression models incorporating incrementally larger number of features, from 1 to 50, added in order of the rank displayed in Fig. 3. The grey lines indicate +/- 1 standard deviation of the parameter, estimated by running each model with randomly resampled training and testing data 50 times. Note that there is no substantial increase in performance beyond the top five features. The plot on the left shows the receiver operating characteristic (ROC) curve for the 5 parameter model, with +/- 1 standard deviation given in grey. The black square shows the optimal decision point. Note excellent predictive performance.

the irregular tumour boundary corresponded to an "invasive" phenotype. In another study of 198 diffuse low grade gliomas, the 34 *IDH*wt astrocytomas were more likely to have an indistinct tumour margin [8]. The authors also reported an association with anatomical location, similar to our findings, where *IDH*wt astrocytomas were more likely to be temporo-insular lesions compared to the more frequently observed frontal location in *IDH*mut astrocytomas. The temporo-insular predominance of *IDH*wt astrocytomas corresponds to the increased involvement of eloquent brain observed in our study with the speech receptive area being most affected.

We also observed an increased incidence of thalamic involvement in the *IDH*wt tumours, seen in 11 of the 52 (21.1%) *IDH*wt astrocytomas compared to no thalamic involvement in any of the 68 *IDH*mut astrocytomas and 3 of the 26 (11.5%) GBM tumours. A recent study of 331 gliomas reported an incidence of 6.4% in the deep structures of the cerebrum but did not investigate anatomical location according to *IDH* mutation status [9]. Our findings, not previously reported in the literature, may be due to institutional bias of increased referrals for complex inoperable tumours. Nevertheless, our findings suggest that thalamic involvement is more likely to be seen in *IDH*wt astrocytomas and should be referred for early biopsy.

The importance of the T1/FLAIR ratio is an interesting finding in our study. It is well-established in high grade gliomas that the surrounding nonenhancing region represented by T2W and FLAIR signal abnormality is a mixture of infiltrative tumour and oedema [10]. In GBM, multiple studies investigating the qualitative extent of peritumoural oedema/nonenhancing disease have shown that the presence and extent of FLAIR signal abnormality is a negative prognostic factor [11–13] with increased resection of FLAIR abnormalities correlating positively with progression-free survival [14]. The inclusion of FLAIR assessment in the recently updated RANO criteria also highlights the importance of FLAIR signal in monitoring treatment response [15]. Whilst recent reports have described an ill-defined border on FLAIR sequences predictive of *IDH*wt tumours [3,16,17] to our knowledge, there are no reports of T1/FLAIR ratio assessment in low-grade gliomas. This MR descriptor offers potential as an important prognosticator in these predominantly non-enhancing tumours.

Our patient survival data supports the growing literature that *IDH*wt grade II/III astrocytomas have a poorer survival than their *IDH*mut equivalents [18,19]. The TCGA study of 31 *IDH*wt grade II/III astrocytomas found an intermediate overall survival between *IDH*mut grade II/III and GBM as we have shown here [20]. As seen in our study, WHO grade had a significant influence on survival. Whilst survival was more similar to GBM than *IDH*mut, our *IDH*wt reference set was radiologically more similar to the *IDH*mut astrocytomas than GBM: less likely to show enhancement, macroscopic necrosis and haemorrhage. In particular, the majority of *IDH*wt and *IDH*mut tumours were non-enhancing and where enhancement was present, tended to be patchy rather than thick/nodular or solid, as seen in GBMs.

It is well established that diffusion can support glioma grading and survival prediction in GBM and diffuse gliomas [21–23]. A recent study of 65 WHO grade II and III astrocytomas demonstrated a lower ADC in *IDH*wt astrocytomas compared to *IDH*mut [24]. However, we were unable to detect a significant difference in diffusion characteristics between *IDH*wt and *IDH*mut astrocytomas. The absence of an available ADC map in 22 patients may have limited our power to detect significant differences. Low inter-rater agreements may have been due to T2 effects and attempting to describe heterogeneous diffusion appearances within the predefined VASARI diffusion categories.

Radiologist-made measurements are potentially open to user bias. In this study the neuroradiologists were blinded to *IDH* mutation status and histopathological grade and where agreement was poor, a consensus review was performed. Studies building radiogenomic maps using quantitative features have shown that these may be a useful complementary strategy to non invasive GBM management [25]. Such studies are currently underway at our institution and we expect the preliminary findings in this study to be validated in a larger dataset.

5. Conclusion

Our results provide further evidence that *IDH*wt astrocytomas demonstrate poorer survival, more equivalent to that for GBM, than *IDH*mut astrocytomas. These tumours are more likely to be located in eloquent areas, show deep white matter invasion and demonstrate more infiltrative radiological features with lower T1/FLAIR ratio when compared to their *IDH*mut counterparts.

We believe that these findings may help clinicians to predict *IDH* mutation status on imaging, identifying those patients that are more likely to have an *IDH*wt tumour for early biopsy/resection and more GBM-like treatment. This could have important implications for diagnostic decision-making, by alerting clinicians to the presence of early stage glioblastoma.

Disclosures

No author disclosures.

Conflict of interest

None.

Acknowledgments

This study was undertaken at University College London Hospitals/University College London which received a proportion of funding from the National Institute of Health Research Biomedical Research Centre. PN is funded by the Wellcome Trust, the Department of Health, and the NIHR UCLH BRC.

References

[1] D.N. Louis, A. Perry, G. Reifenberger, et al., The 2016 World Health Organization classification of tumors of the central nervous system: a summary, Acta Neuropathol. (131) (2016) 803–820.
[2] D.E. Reuss, A. Kratz, F. Sahm, et al., Adult IDH wild type astrocytomas biologically and clinically resolve into other tumor entities, Acta Neuropathol. 130 (2015) 407–417.
[3] R.L. Delfanti, D.E. Piccioni, J. Handwerker, et al., Imaging correlates for the 2016 update on WHO classification of grade II/III gliomas: implications for IDH, 1p/19q and ATRX status, J. Neurooncol. (135) (2017) 601–609.
[4] W. Tan, J. Xiong, W. Huang, et al., Noninvasively detecting Isocitrate dehydrogenase 1 gene status in astrocytoma by dynamic susceptibility contrast MRI, J. Magn. Reson. Imaging 45 (2017) 492–499.
[5] M.A. Mazurowski, A. Desjardins, J.M. Malof, Imaging descriptors improve the predictive power of survival models for glioblastoma patients, Neuro Oncol. 15 (2013) 1389–1394.
[6] D.E. Reuss, A. Kratz, F. Sahm, et al., Adult IDH wild type astrocytomas biologically and clinically resolve into other tumor entities, Acta Neuropathol. 130 (2015) 407–417.
[7] M.A. Mazurowski, K. Clark, N.M. Czarnek, et al., Radiogenomics of lower-grade glioma: algorithmically-assessed tumor shape is associated with tumor genomic subtypes and patient outcomes in a multi-institutional study with the cancer genome Atlas data, J. Neurooncol. 133 (2017) 27–35.
[8] A. Darlix, J. Deverdun, C.N. Menjot de, et al., IDH mutation and 1p19q codeletion distinguish two radiological patterns of diffuse low-grade gliomas, J. Neurooncol. 133 (2017) 37–45.
[9] S. Larjavaara, R. Mantyla, T. Salminen, et al., Incidence of gliomas by anatomic location, Neuro Oncol. 9 (2007) 319–325.
[10] A.T. Parsa, S. Wachhorst, K.R. Lamborn, et al., Prognostic significance of intracranial dissemination of glioblastoma multiforme in adults, J. Neurosurg. 102 (2005) 622–628.
[11] M.A. Hammoud, R. Sawaya, W. Shi, et al., Prognostic significance of preoperative MRI scans in glioblastoma multiforme, J. Neurooncol. 27 (1996) 65–73.
[12] W.B. Pope, J. Sayre, A. Perlina, et al., MR imaging correlates of survival in patients with high-grade gliomas, AJNR Am. J. Neuroradiol. 26 (2005) 2466–2474.
[13] K. Schoenegger, S. Oberndorfer, B. Wuschitz, et al., Peritumoral edema on MRI at initial diagnosis: an independent prognostic factor for glioblastoma? Eur. J. Neurol. 16 (2009) 874–878.
[14] J.L. Yan, A. van der Hoorn, T.J. Larkin, et al., Extent of resection of peritumoral diffusion tensor imaging-detected abnormality as a predictor of survival in adult glioblastoma patients, J. Neurosurg. 126 (2017) 234–241.
[15] P.Y. Wen, D.R. Macdonald, D.A. Reardon, et al., Updated response assessment criteria for high-grade gliomas: response assessment in neuro-oncology working group, J. Clin. Oncol. 28 (2010) 1963–1972.
[16] B. Zhang, K. Chang, S. Ramkissoon, et al., Multimodal MRI features predict isocitrate dehydrogenase genotype in high-grade gliomas, Neuro Oncol. 19 (2017) 109–117.
[17] H. Zhou, M. Vallieres, H.X. Bai, et al., MRI features predict survival and molecular markers in diffuse lower-grade gliomas, Neuro Oncol. 19 (2017) 862–870.
[18] Y. Suzuki, K. Shirai, K. Oka, et al., Higher pAkt expression predicts a significant worse prognosis in glioblastomas, J. Radiat. Res. 51 (2010) 343–348.
[19] C. Hartmann, B. Hentschel, W. Wick, et al., Patients with IDH1 wild type anaplastic astrocytomas exhibit worse prognosis than IDH1-mutated glioblastomas, and IDH1 mutation status accounts for the unfavorable prognostic effect of higher age: implications for classification of gliomas, Acta Neuropathol. 120 (2010) 707–718.
[20] The Cancer Genome Atlas Research Network, Comprehensive, integrative genomic analysis of diffuse lower-grade gliomas, N. Engl. J. Med. 372 (2015) 2481–2498.
[21] W.B. Pope, X.J. Qiao, H.J. Kim, et al., Apparent diffusion coefficient histogram analysis stratifies progression-free and overall survival in patients with recurrent GBM treated with bevacizumab: a multi-center study, J. Neurooncol. 108 (2012) 491–498.
[22] W.B. Pope, H.J. Kim, J. Huo, et al., Recurrent glioblastoma multiforme: ADC histogram analysis predicts response to bevacizumab treatment, Radiology 252 (2009) 182–189.
[23] A. Hilario, J.M. Sepulveda, A. Perez-Nunez, et al., A prognostic model based on preoperative MRI predicts overall survival in patients with diffuse gliomas, AJNR Am. J. Neuroradiol. 35 (2014) 1096–1102.
[24] K. Leu, G.A. Ott, A. Lai, et al., Perfusion and diffusion MRI signatures in histologic and genetic subtypes of WHO grade II-III diffuse gliomas, J. Neurooncol. (2017).
[25] O. Gevaert, L.A. Mitchell, A.S. Achrol, et al., Glioblastoma multiforme: exploratory radiogenomic analysis by using quantitative image features, Radiology 273 (2014) 168–174.

Neuroradiology (2021) 63:353–362
https://doi.org/10.1007/s00234-020-02532-7

DIAGNOSTIC NEURORADIOLOGY

Conventional MRI features of adult diffuse glioma molecular subtypes: a systematic review

Arian Lasocki[1,2] · Mustafa Anjari[3] · Suna Örs Kokurcan[3,4] · Stefanie C. Thust[3,5]

Received: 1 June 2020 / Accepted: 17 August 2020 / Published online: 25 August 2020

Abstract

Purpose Molecular parameters have become integral to glioma diagnosis. Much of radiogenomics research has focused on the use of advanced MRI techniques, but conventional MRI sequences remain the mainstay of clinical assessments. The aim of this research was to synthesize the current published data on the accuracy of standard clinical MRI for diffuse glioma genotyping, specifically targeting IDH and 1p19q status.

Methods A systematic search was performed in September 2019 using PubMed and the Cochrane Library, identifying studies on the diagnostic value of T1 pre-/post-contrast, T2, FLAIR, T2*/SWI and/or 3-directional diffusion-weighted imaging sequences for the prediction of IDH and/or 1p19q status in WHO grade II-IV diffuse astrocytic and oligodendroglial tumours as defined in the WHO 2016 Classification of CNS Tumours.

Results Forty-four studies including a total of 5286 patients fulfilled the inclusion criteria. Correlations between key glioma molecular markers, namely IDH and 1p19q, and distinctive MRI findings have been established, including tumour location, signal composition (including the T2-FLAIR mismatch sign) and apparent diffusion coefficient values.

Conclusion Consistent trends have emerged indicating that conventional MRI is valuable for glioma genotyping, particularly in presumed lower grade glioma. However, due to limited interobserver testing, the reproducibility of qualitatively assessed visual features remains an area of uncertainty.

Keywords Glioma · Glioblastoma · Magnetic resonance imaging · Radiogenomics · Imaging genomics

Introduction

Diffuse astrocytic and oligodendroglial brain tumours occur along a continuum from World Health Organization (WHO) grade II (diffuse astrocytoma and oligodendroglioma) and grade III (anaplastic astrocytoma and anaplastic oligodendroglioma) to grade IV (glioblastoma, GBM) [1]. The latest 2016 WHO update to the Classification of Tumours of the Central Nervous System has acknowledged the prognostic importance of molecular parameters, which now constitute a key component of glioma diagnosis, providing an integrated phenotypic and genotypic diagnosis [1]. This has generated a new clinical need for correlating imaging features with glioma genotypes, known as radiogenomics or imaging genomics.

In the current (2016) WHO classification, grade II and III gliomas are considered together (lower grade gliomas, LGG), but distinct from GBM [1]. Irrespective of grade, the first step in glioma molecular characterisation is isocitrate dehydrogenase (IDH) testing [1]. Most LGG (> 70%) harbour an IDH

Electronic supplementary material The online version of this article (https://doi.org/10.1007/s00234-020-02532-7) contains supplementary material, which is available to authorized users.

✉ Arian Lasocki
arian.lasocki@petermac.org

[1] Department of Cancer Imaging, Peter MacCallum Cancer Centre, Grattan St, Melbourne, Victoria 3000, Australia

[2] Sir Peter MacCallum Department of Oncology, The University of Melbourne, Parkville, Australia

[3] Lysholm Department of Neuroradiology, National Hospital for Neurology and Neurosurgery, London, UK

[4] Department of Diagnostic Neuroradiology, Health Science University, Bakirkoy Dr Sadi Konuk Training and Research Hospital, Istanbul, Turkey

[5] Department of Brain Repair and Rehabilitation, Neuroradiological Academic Unit, UCL Institute of Neurology, London, UK

mutation (IDH-mutant, IDH^{mut}), which is associated with significantly longer survival [2]. For IDH^{mut} LGG, 1p19q genotyping follows to distinguish between tumours with 1p19q codeletion (molecular oligodendrogliomas, demonstrating combined loss of both the short arm of chromosome 1 and long arm of chromosome 19, $IDH^{mut}/1p19q^{codel}$) and those without (molecular astrocytoma, $IDH^{mut}/1p19q^{intact}$) [1]. In contrast, LGG without an IDH mutation are known as IDH-wildtype (IDH^{wt}), and can be considered "molecular GBM" if also associated with other characteristic mutations [3, 4]. For tumours with histological evidence of GBM, IDH testing suffices [1]. IDH^{mut} GBMs are rare (< 10% of all GBMs) [2] and hypothesised to arise from LGG, with correspondingly better outcomes than IDH^{wt} [2].

This molecular characterisation gives rise to 3 prognostically relevant groups for imaging research in glioma: IDH status of LGG; 1p19q status of LGG; and IDH status of GBMs. Radiogenomics studies have primarily focused on the use of advanced MRI techniques for genotyping, including perfusion, spectroscopy and computational algorithms. However, specialist neuro-oncology centres receive referrals, and thus imaging, from a variety of outside institutions, which often utilize less comprehensive protocols. Repeating imaging and/or performing additional advanced sequences pending tissue diagnosis is often impractical, and while such a practice is valuable from a research perspective, it may not necessarily change management. As a result, anatomical MRI sequences remain the basis of the pre-operative MRI characterisation. In addition, the methodology around advanced techniques – both in acquisition and post-processing – is variable, limiting reproducibility and clinical translation. Computational imaging approaches such as machine learning offer new opportunities for the recognition of microstructural tissue patterns, but most have not undergone in-depth clinical testing. Specifically, there is a risk of "over-fitting" when training with a fixed set of imaging parameters in research, with accuracy decreasing when encountering the more variable clinical environment. In this context, human observers may more flexibly recognize morphological differences without a substantial detriment to accuracy.

It remains uncertain to what extent assessments in routine clinical practice can predict glioma genotypes. What can be considered "conventional" in MRI has evolved over time, but is largely based around anatomical sequences. Ellingson et al. have outlined a consensus brain tumour protocol for clinical trials, which consists of axial T2-weighted imaging (T2WI), axial (or volumetric) FLAIR (fluid attenuated inversion recovery), axial DWI (diffusion-weighted imaging) and pre- and post-contrast volumetric T1-weighted imaging (T1WI) [5]. DWI and susceptibility-sensitive sequences such as T2* and susceptibility-weighted imaging (SWI) are routinely performed in many institutions [6], and may nowadays also be considered part of basic MRI protocols.

To date, a limited number of reviews have summarized conventional imaging features of glioma molecular subtypes [7], whereas the bulk of literature on this topic was published in recent years and is constantly evolving. The aim of this research was to systematically review and synthesize currently available data on the accuracy of standard clinical MRI for diffuse glioma genotyping. For the purpose of this study, we have considered sequences as "conventional" in line with recently published guidance on glioma imaging [5, 6], on the proviso that the results description was not solely based on advanced analytic techniques (e.g. computational learning).

Methods

This research was carried out according to the Preferred Reporting Items for Systematic Reviews and Meta-Analyses (PRISMA-DTA) criteria [8]. The study has been registered in the PROSPERO online database of systematic reviews (CRD42019127655).

Data sources

A systematic search was performed in September 2019 using PubMed and the Cochrane Library (until September 2019). The following search key words were used: ("brain tumo(u)r", "glioma", "glioblastoma", "astrocytoma", "oligodendroglioma") AND ("isocitrate dehydrogenase", "IDH", "1p19q", "1p/19q", "molecular", "WHO 2016") AND ("magnetic resonance imaging"). Further details of the search strategy are shown in Supplementary Material 1.

Study selection

The abstracts of all articles retrieved in the initial search were screened independently by two reviewers (board-certified radiologists with research experience in neuro-oncology). All selected full-text manuscripts were reviewed independently by two reviewers (from a team of four board-certified reviewers), with abstracts chronologically randomized and reviewer pairings varied to avoid bias. A stepwise selection was performed independently by each reviewer according to the same method. The exclusion criteria were: no interpretation of conventional MRI sequences (defined as T1 pre-/post-contrast, T2, FLAIR, T2*/SWI and/or 3-directional DWI [6]); animal/laboratory measurements only; technical comparison between different MRI acquisition technique(s); studies confined to physiological MRI (e.g. perfusion, spectroscopy, diffusion tensor or kurtosis imaging, functional imaging methods) or machine learning; studies restricted to predicting WHO histological grade; studies lacking glioma molecular subtype information; studies reporting on prognosis only; review articles; case reports of < 5 cases; studies only examining

molecular markers other than IDH and 1p19q; conference abstracts; or no English full text. The inclusion criteria were: studies examining the diagnostic value of MRI regarding IDH and/or 1p19q in the context of WHO grade II-IV gliomas; assessment of conventional MRI sequences (as defined above) performed on glioma patients pre-treatment; and description of qualitative and/or quantitative glioma feature(s). In cases of disagreement, each full-text article was reviewed and the discrepancy resolved in consensus with a third (senior) reviewer. A summary of inclusions and exclusions is provided in Fig. 1.

Data analysis

The results of the included studies were documented with the use of a data extraction form to derive the glioma molecular information tested, diagnostic MRI sequence(s) used, descriptive and statistical results, and method characteristics. The latter included study design and institute of origin, number of patients, participant age, tumour histology and molecular data, MRI field strength, contrast agent, feature description, quantification (e.g. region of interest (ROI) placements) and interobserver testing. Each of the reviewers independently performed the full-text screening followed by the data extraction with two reviewers analysing each publication. Discrepancies were resolved in consensus with a third reviewer. A summary of the data extraction table is presented in Supplementary Material 2.

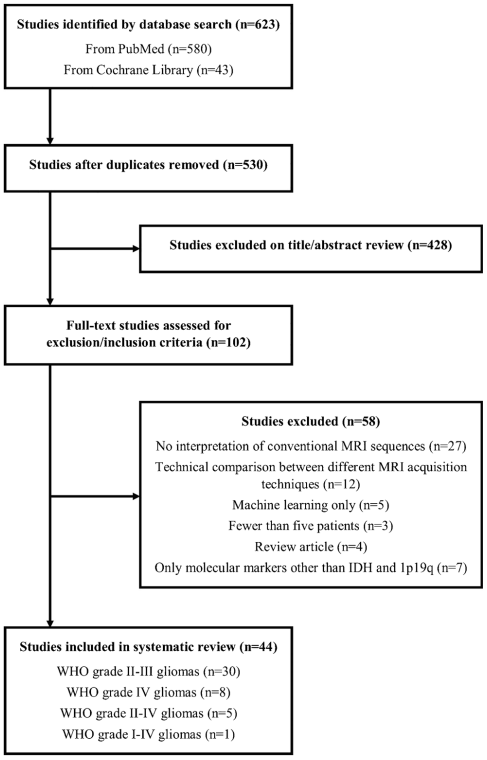

Fig. 1 CONSORT diagram of the study selection process

Study quality assessment

The study quality was examined using the Quality Assessment of Diagnostic Accuracy Studies (QUADAS-2) instrument [9]. We evaluated concerns regarding applicability in three domains (low, high, unclear) and the risk of bias in four different domains (patient selection, index test, reference test, timing). Each study was independently assessed for quality and potential bias by two reviewers. Disagreements were resolved by consensus with a senior reviewer.

Statistical analysis

Descriptive data are presented in the form of a narrative synthesis, because of the perceived heterogeneity of reported imaging features, assessment methods and lack of consistent quantification.

Data synthesis

Results overview

Forty-four studies including a total of 5286 patients fulfilled the inclusion criteria, with a mean of 115.9 (standard deviation 73.1) gliomas analysed in each study. Of these, 30 studies were confined to LGG analysis: 3 studies assessed WHO grade II tumours, 6 evaluated WHO grade III and 21 studies included WHO grades II and III. Grade IV tumours were examined in 8 studies. Five studies assessed WHO grade II-IV gliomas, while one further study included WHO grades I-IV. 18 studies examined IDH alone, 6 1p19q alone, and 20 studies assessed both. 7 studies identified only investigated molecular markers other than IDH and 1p19q, and were thus excluded from further analysis.

All included studies were retrospective analyses. Twelve studies reported statistical results (kappa, κ) for interobserver comparisons of qualitative features, 2 studies reported intraclass correlation coefficient (ICC) values for quantitative glioma properties, 13/44 studies performed consensus reads using ≥ 2 observers, and 24 publications used either a single reader (7/44) or lacked comprehensive information on reader methods (12/44).

WHO grade II/III glioma (LGG) genotyping

IDH

Tumour location Sixteen studies assessed the relationship between tumour location and IDH status in LGG. A predilection of IDH^{mut} tumours to occur in the frontal lobes was identified by multiple research groups [10–17]. Most of these studies showed statistical significance, but only one study provided sensitivity (72.2%) and specificity (63.3%) [12]. A smaller number of studies reported correlations between IDH^{wt} status and other locations, specifically thalamus (11/52 IDH^{wt} compared with 0/68 IDH^{mut}; $p = 0.001$) [15] and brainstem (all brainstem tumours in one cohort were reportedly IDH^{wt}, without subgroup numbers provided) [18]. Sonoda et al. observed that anaplastic gliomas sparing the cerebral cortex were more likely IDH^{wt} (13/44 IDH^{wt}, 0/78 IDH^{mut}; $p < 0.0001$) [11]. In a study by Kanazawa et al, non-temporal location was the sole imaging feature that was significantly associated with IDH status, with limited specificity (57.1%) [19]. High interobserver agreements were reported for laterality ($\kappa = 1.00$) and location ($\kappa = 0.723–1.00$) [15, 20].

A study of 193 patients by Qi et al. found that IDH^{mut} tumours more commonly involved a single lobe, whereas IDH^{wt} tumours were predominantly located in combined lobes such as the diencephalon or brainstem ($p < 0.001$) [10]. Park et al. reported that a "nonlobar location" was associated with IDH^{wt} genotype (adjusted odds ratio (OR) 2.38), though a definition of "nonlobar location" was not provided [20]. Multifocality, multicentricity or a gliomatosis cerebri pattern have been identified as predictive of IDH^{wt} status in two further, relatively large study samples (n = 146 and n = 175, respectively) [15, 20]. Contrary to these findings, IDH^{mut} LGG may be larger than IDH^{wt} tumours at diagnosis [13, 21].

Internal signal characteristics and gadolinium enhancement Multiple studies have examined signal characteristics of LGG. IDH^{mut} LGG were more commonly homogeneous in one cohort (79% of 89 IDH^{mut}, compared with 45% of 104 IDH^{wt}) [10], while cystic change appears less frequent in IDH^{wt} tumours [18, 22]. Enhancement is more common in IDH^{wt} tumours: Wu et al. found enhancement in 93% of IDH^{wt} tumours compared with 57% IDH^{mut} [22], and similar results were reported in the cohort of anaplastic gliomas examined by Wang et al. (88% IDH^{wt} and 68% IDH^{mut}) [23]. Providing further support, Juratli et al. found that enhancing gliomas were more common in IDH^{wt} tumours (57%) than both IDH^{mut}/ATRX-inactivated and IDH^{mut}/$1p19q^{codel}$ tumours (28% and 25%, respectively) [24]. IDH^{wt} tumours have also been associated with a greater degree of enhancement [10, 16, 20, 22, 25]. Ring-enhancement of LGG (i.e. MRI evidence of necrosis) correlated with IDH^{wt} status in several studies [11, 22, 26]. In a logistic regression model utilizing Visually AcceSAble Rembrandt Images (VASARI) features [27], the proportion of enhancing lesion necrosis was one of two optimal features (together with tumour size), which moderately predicted IDH status of LGG (area under the curve, AUC 0.73) [28]. Similar to these findings, a different study examining VASARI features identified the proportion of the tumour that was non-enhancing as the single best feature for predicting an IDH mutation, with high accuracy (AUC 0.92) [25].

Tumour margins Sharp tumour margins have been associated with LGG IDH^{mut} status [10, 13], while poor definition of the non-enhancing margin has been correlated with IDH^{wt} status in multiple publications [15, 17, 20]. Of these, only one study, by Park et al, reported interobserver agreement ($\kappa = 0.766$) [20]. One study identified that a lower T1/FLAIR ratio was more frequent in IDH^{wt} gliomas, together with deep white matter invasion, but interobserver agreement was not specifically reported [15]. One study, in which two readers assessed VASARI features in consensus, suggested that oedema was more common in IDH^{wt} LGG [22].

Diffusion-weighted imaging A variety of ADC metrics have been examined, with higher ADC values consistently reported in IDH^{mut} LGG compared with IDH^{wt}. Villaneuva-Meyer et al. observed that ROI-derived minimum, mean and maximum ADC correlated with IDH status; of these, a minimum ADC threshold of 0.9×10^{-3} mm^2/s provided the greatest sensitivity (91%) and specificity (76%), with an AUC of 0.901 [18]. Wasserman et al. performed ROI-based minimum ADC assessments and reported a significant association with IDH genotype, with an optimal cutoff point of 0.95×10^{-3} mm^2/sec (sensitivity 76.9%, specificity 65.2% and AUC 0.711) [12]. Xing et al. investigated minimum ADC and relative minimum ADC (comparing to contralateral normal-appearing white matter) based on multiple ROIs placed in each glioma, with both yielding statistically significant results; the reported optimal minimum ADC threshold was 1.01×10^{-3} mm^2/sec (sensitivity 76.9%, specificity 82.6%; AUC 0.87) [14]. Liu et al. assessed both mean and minimum ADC; results for mean ADC reached statistical significance ($p = 0.028$), while those for minimum ADC did not ($p = 0.069$) [29]. However, there were only 15 WHO grade II/III gliomas in this cohort, and AUC analysis was not presented [29]. Thust et al. assessed single-slice mean ADC normalized to the contralateral centrum semiovale normal-appearing white matter in 44 non-enhancing LGG, achieving AUC of 0.95 for one reader (optimal ADC_{ratio} cutoff 1.83) and AUC of 0.96 (optimal ADC_{ratio} cutoff 1.76) for the other reader [30]. Notably, single-slice ADC measurements correlated strongly with whole lesion assessment in this study [30]. Of these 5 studies, 2 reported ICC results of 0.71–0.91 [18] and 0.98 [30] for ROI-derived ADC values.

1p19q

Tumour location A frontal lobe location has repeatedly been associated with 1p19q codeletion [13, 26, 31–33]. As a potential confounder, some of these studies may have included IDH^{wt} tumours amongst "non-codeleted" gliomas [26, 32, 33]. In the studies specifically comparing $IDH^{mut}/1p19q^{codel}$ and $IDH^{mut}/1p19q^{intact}$ tumours, the results are heterogenous and the lobar association is less compelling. Batchala et al. nevertheless reported a significant association between a frontal lobe location and codeletion in 102 IDH^{mut} LGG (OR 5.68, 95% CI 2.08–15.44; $p = 0.001$) [31]. In contrast, Sonoda found no significant difference in the frequency of a frontal lobe location between the $1p19q^{codel}$ (74%) and $1p19q^{intact}$ tumours (67%; $p = 0.61$) [11]. The lobar distribution was also similar in the cohort of Darlix et al. (frontal location in 45% of $1p19q^{codel}$ and 42% of $1p19q^{intact}$) [13]. Several studies observed that a temporal lobe location reduces the likelihood of $1p19q^{codel}$ genotype ($p = 0.011$–0.034) [11, 19, 32, 34], with one reporting no case of temporal-centred $1p19q^{codel}$ in a cohort of 123 anaplastic gliomas [11]. Sherman et al. found that $1p19q^{codel}$ tumours were more commonly confined to a single lobe than non-codeleted tumours [34]. The data on 1p19q genotype and cortical involvement are ambiguous, with one study demonstrating a statistical association with codeletion ($p = 0.02$) [16], and another showing no significant association [33]. One study reported weak interobserver correlation (42%) for cortical involvement [35].

Internal signal characteristics and gadolinium enhancement As for IDH, internal signal characteristics have been examined by multiple authors. Yamauchi et al. identified that heterogeneous T2 signal was significantly more common in $1p19q^{codel}$ tumours (94%) than both $1p19q^{intact}$ (33%) and IDH^{wt} tumours (50%), using consensus assessments [16]. Three further studies observed that tumour heterogeneity correlated significantly with 1p19q codeletion, but this feature did not permit a reliable IDH genotype distinction [19, 26, 33]. Batchala et al. observed that LGG which were < 75% homogeneous were much more likely to be $1p19q^{codel}$ than $1p19q^{intact}$ ($p < 0.001$), with an OR of 12.33 and $\kappa = 0.69$ [31]. Similarly, Johnson et al. found that, while it was overall uncommon for a tumour to be completely homogeneous, homogeneity was more frequent in $1p19q^{intact}$ LGG (14% and 10% based on T1- and T2-weighted imaging, respectively) than in codeleted gliomas (1%), also by consensus assessment [32].

1p19q codeleted tumours have shown a correlation with either absent or ill-defined enhancement [16, 26, 36], in contrast to more nodular or ring-like enhancement in $1p19q^{intact}$ LGG [36]. One group reported that $1p19q^{codel}$ tumours more commonly demonstrated ≤5% enhancing tumour [37]. In contrast, a different study assessing anaplastic gliomas concluded that $1p19q^{codel}$ tumours more commonly enhance than non-codeleted tumours, but this was assessed in a binary fashion, with no distinction made between different qualities of enhancement [11].

Tumour margins Several studies have assessed tumour margins, most utilizing a binary distinction. Kim et al. found that an indistinct rather than sharp border correlated with 1p19q codeletion on both T1- and T2-weighted imaging ($p = 0.005$ and $p = 0.036$, respectively) [33]. Similarly, Johnson et al. observed that the majority of 1p19q codeleted tumours lacked sharp borders on both T1- and T2-weighted images (97% for each), with $p < 0.0001$ for each marker of border sharpness evaluated, and an odds ratio of 16.35 [32]. Conversely, a sharp border was much more common in non-codeleted tumours, with an incidence of 40% and 38% based on T1- and T2-weighted imaging, respectively [32]. Kanazawa et al. reported a strong correlation ($p = 0.002$), though only assessed tumour borders on T1WI [19]. Some studies have not shown a significant difference [16, 22]. Darlix et al. described tumour borders as sharp, indistinct or intermediate, and found that $1p19q^{codel}$ tumours more commonly had intermediate borders, while indistinct tumour borders were more frequent in IDH^{wt} tumours [13]. No studies reported interobserver statistics for 1p19q tumour border evaluations.

Calcifications, haemorrhage and magnetic susceptibility Several studies have examined associations with calcifications and haemorrhage, but there is substantial variability in the literature in how these are assessed, both regarding whether CT has been performed and with respect to MRI techniques. Calcification has been shown to predict 1p19q codeletion [16, 19, 35]. In one of these studies, paramagnetic susceptibility on T1WI (T1 shortening) was examined and this too was associated with codeletion, but not as strongly [19]. T2* blooming also predicted codeletion in one study [31]. Other studies which used MRI to assess for calcification [33] and paramagnetic susceptibility artefact [32] did not show a difference, but did not pursue a distinction of calcification from blood products based on the phase. Indeed, one study examining MRI suggests that haemorrhage is associated with codeletion, but did not evaluate calcification or discuss how these characteristics were separated [37]. All studies consisted of consensus reads, except one, which reported a moderate interrater agreement for T2* blooming, with $\kappa = 0.74$ [31].

T2-FLAIR mismatch The T2-FLAIR mismatch sign has been examined by several authors since being first described in 2017 [38]. Three studies concluded that the presence of T2-FLAIR mismatch is 100% specific for an $IDH^{mut}/1p19q^{intact}$ tumour, with interobserver agreements between 0.56 and 0.75 [31, 38, 39]. Another study also found that all patients with > 50% T2-FLAIR mismatch were $1p19q^{intact}$, though definitive IDH testing results were not available for patients with

negative IDH1-R132H immunohistochemistry [35]. In contrast, Juratli et al. had a false-positive rate of 28.5% for T2-FLAIR mismatch [24]. This study included enhancing gliomas, and separate results for non-enhancing gliomas in this cohort were not provided [24]. All false-positive cases were 1p19q^{codel}, with no false-positive IDH^{wt} cases reported [24].

Diffusion-weighted imaging With the caveat that a minority of IDH^{wt} tumours (which are associated with lower ADC values as summarized above) may have been included in some of the studies assessing DWI, 1p19q codeletion has consistently been associated with lower mean ADC values compared with IDH^{mut}/1p19q^{intact} LGG ($p = 0.0005$–0.003) [30, 32, 40], with two studies suggesting an ADCmean cutoff in the region of 1.4–1.6 × 10^{-3} mm^2/s for 1p19q genotyping [32, 40].

Glioblastoma

IDH

Tumour location Publications on the geographical distribution of IDH genotypes in GBM broadly correspond to descriptions in LGG, supportive of a continuum of disease. Carrillo et al. found that 11 of 14 (79%) IDH^{mut} GBMs (comprising 7% of all GBMs in their cohort) were located in the frontal lobes, compared with only 69 of 188 (37%) IDH^{wt} [41]. Xing et al. also identified a geographic correlation with IDH status (p = 0.002), with 9 of 10 (90%) IDH^{mut} GBMs being located in the frontal lobes, compared with 23 of 60 (38%) IDH^{wt} [42]. The cohort of Lasocki et al. displayed a similar frequency of frontal lobe location in both IDH^{wt} (38%) and IDH^{mut} (40%) GBMs, but there were only 5 IDH^{mut} GBMs in this study [43]. In contrast, the IDH^{mut} GBMs in the cohort of Hong et al. displayed a higher frequency of an insular location than IDH^{wt} (33% compared with 12%; p = 0.01) [44], and Hata et al. reported that all five IDH^{mut} tumours in their cohort of 92 GBMs involved the insula [45].

Enhancement and noncontrast-enhancing tumour In a study by Yamashita et al, the necrotic area inside the largest cross-sectional enhancing lesion and the largest cross-section necrosis percentage were both associated with IDH status (p < 0.005) [46]. Wang et al. found that IDH^{mut} GBMs were slightly less likely to demonstrate enhancement (73.3%, compared with 94.9% for IDH^{wt}; $p < 0.001$) [47]. When the tumour did enhance, multiple enhancing foci were more common in IDH^{mut} tumours (42.4%, compared with 19.3% for IDH^{wt}; p = 0.003), though the distribution of contrast enhancement patterns did not differ significantly between IDH^{mut} and IDH^{wt} GBMs [47]. The presence of enhancing satellites positively correlated with IDH mutations in another cohort [41].

Similar to these findings, a larger proportion of noncontrast-enhancing tumour (nCET) has been associated with IDH mutations. All 14 IDH^{mut} GBMs in the cohort of Carrillo demonstrated nCET, and a higher percentage of nCET was shown to correlate with IDH^{mut} status; the proportion of IDH^{wt} tumours with nCET was not specified, however [41]. Hong et al. identified a larger T2WI tumour volume in IDH^{mut} GBMs and a higher volume ratio between T2WI and contrast-enhanced T1WI in IDH^{mut} GBMs ($p < 0.05$) [44]. Similarly, in a study by Lasocki et al, 60% of IDH^{mut} GBMs had > 33% nCET, compared with 21% of IDH^{wt}, though this did not reach statistical significance (p = 0.073) [43]. This study highlighted that nCET was also common in IDH^{wt} tumours, with 57% of IDH^{wt} GBMs containing ≥ 5% nCET [43]. To overcome this limited specificity, the same group subsequently proposed that a mass-like morphology of nCET could potentially provide better specificity for the prediction of an IDH mutation than the presence of nCET alone [48]. A larger GBM size at diagnosis and the presence of cysts have also been associated with IDH mutations [41].

Diffusion-weighted imaging In a study of 176 patients by Hong et al, IDH^{mut} GBMs demonstrated higher mean normalized ADC (2 reader ICC 0.97) in both T2-hyperintense non-enhancing (1.64 × 10^{-3} mm^2/s for IDH^{mut}, 1.49 × 10^{-3} mm^2/s IDH^{wt}; p = 0.022; sensitivity 66.7% and specificity 65.2% for ADC > 1.57 × 10^{-3} mm^2/s) and enhancing areas (1.80 IDH^{mut}, 1.54 IDH^{wt}; p = 0.008; sensitivity 77.8% and specificity 53.8% for ADC > 1.53 × 10^{-3} mm^2/s) [44]. Another study (n = 75) by Xing et al. found IDH^{mut} GBMs to have higher relative minimum ADC values in the enhancing region (AUC 0.703) [42].

Study quality

The results of the study quality assessment using the QUADAS-2 tool [9] are summarized in Fig. 2, with additional information available in Supplementary Material 3. Several

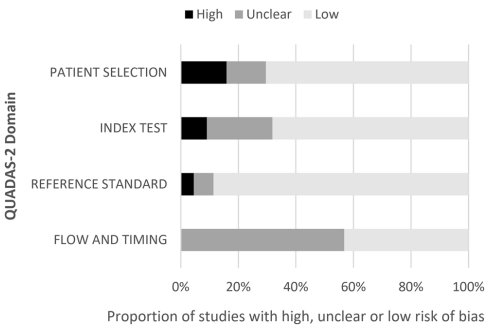

Fig. 2 Results of the QUADAS-2 quality assessment of the included studies. The risk of bias in four different domains is shown

(7/44) studies had a high risk of bias regarding patient selection. In addition, 7/44 studies were unclear about the selection of patients and/or the conduct or interpretation (5/44) of the index test. All research was of retrospective design. 23% (10/44) of studies lacked information on whether index test results were interpreted without knowledge of the reference standard, while 23% of studies gave insufficient information on whether reference standards were defined without knowledge of index test results.

Discussion

This systematic review aimed to summarize and appraise the literature on conventional MRI for glioma radiogenomic predictions. Due to a wide variation in the assessment and reporting methods, we did not proceed to a statistical (meta-analysis) evaluation for any particular sequence or imaging biomarker(s). To group studies with similar topic themes, the LGG and GBM data were presented in separate sections; however, the key results support that molecular-specific imaging features occur on a continuous spectrum across grades. For this reason, the following discussion is structured according to morphology.

Location (by epicentre) appears to be a valuable, static and reproducible tumour property with some of the highest inter-observer ratings (κ) achieved in single centre studies [15, 20] and in multi-rater, multi-timepoint testing (VASARI criteria (laterality $\kappa = 0.943$, 95% CI 0.915–0.982 and tumour location $\kappa = 0.837$, 95% CI 0.807–0.902)) [27]. A frontal lobe location suggests an IDH mutation [10–16], with $1p19q^{codel}$ marginally favoured over $1p19q^{intact}$ [13, 31]. In contrast, an IDH^{mut} tumour located in a temporal lobe is unlikely to be $1p19q^{codel}$ [11, 19, 32]. In glioblastomas, radiogenomic correlations are challenging, due to IDH mutations occurring in a small proportion (< 10%) of GBMs [2, 41, 43, 45, 47]. Corresponding to LGG characteristics, the two more useful GBM features for suggesting an IDH mutation are tumour location (frontal and/or insular) and a greater amount of nCET. However, in the case of a frontal lobe location, the association appears weaker than in LGG. Indeed, frontal location is moderately common in IDH^{wt} tumours, probably greater than for IDH^{mut} GBM in absolute terms [41–43]. Therefore, location can contribute to radiogenomic predictions with limited specificity.

No reliable WHO grade prediction is possible based on glioma enhancement properties for any glioma molecular subtype. IDH^{mut} tumours tend to demonstrate less enhancement than IDH^{wt} [22–24], and $1p19q^{codel}$ tumours may show ill-defined enhancement[17, 19], while ring-enhancement with central necrosis increases the likelihood of an IDH^{wt} glioma [11, 22, 26]. There are challenges with the use of nCET size comparisons; while a larger noncontrast-enhancing tumour proportion may indicate IDH^{mut} status [41], no size threshold is applicable and most IDH^{wt} tumours exhibit nCET to some extent [43]. As such, it may be more appropriate to utilize "lack of nCET" to predict IDH^{wt} status [43].

A homogeneous, well-defined glioma is likely to be $IDH^{mut}/1p19q^{intact}$, while a heterogeneous, ill-defined tumour is likely IDH^{wt} or $1p19q^{codel}$. Provided the glioma does not enhance [24], the presence of T2-FLAIR mismatch allows a confident designation as an $IDH^{mut}/1p19q^{intact}$ astrocytoma [31, 38, 39]. With a published specificity of 100% in three different cohorts [31, 38, 39], this is the single most distinctive conventional MRI feature across both LGG and GBM, with moderate to substantial interobserver agreement. Several studies highlighted the value of indistinct non-enhancing lesion margins to identify IDH^{wt}, but this feature is problematic due to overlap with $1p19q^{codel}$, and for reasons of subjectivity. In particular, the agreement reported for 2 observers by Park et al. ($\kappa = 0.766$) is discrepant from the much lower agreement ($\kappa = 0.374$, 95% CI 0.347–0.514) in multi-reader testing of the original VASARI research, which explicitly casted doubt on the reproducibility of this sign [27]. Calcifications in an untreated glioma suggest $1p19q^{codel}$ [16, 19, 35]; this should ideally be assessed on CT, as intratumoural susceptibility effects due to petechial haemorrhage are common in GBM, and have more recently been associated with IDH^{wt} LGG [49]. Several studies have highlighted an association between cyst formation and IDH^{mut} status [18, 22, 41], which underscores the importance of distinguishing this morphology from rim-enhancing necrosis during imaging assessments.

ADC values are generally highest in $1p19q^{intact}$, lowest in IDH^{wt} and intermediate in $1p19q^{codel}$, which is consistently reported in the literature. Furthermore, ADC is one of few metrics quantifiable on clinical MRI at the time of reporting, with substantial to near perfect interobserver agreement [18, 30]. It remains unclear whether minimum or mean ADC is most accurate, and whether normalizing ADC (e.g. to contralateral normal-appearing white matter) is beneficial. ADC values also appear higher in IDH^{mut} GBM, but there is less evidence for this and the results are not as compelling, with necrosis being a potential confounder of ADC quantification.

The systematic evaluation of genotyping literature was more challenging for LGG than in GBM, because numerous studies investigated either IDH or 1p19q status, or assessed both independently, with a three-group distinction according to the 2016 WHO criteria being less common. Consequently, it is not clear how accurate some particular visual features are for separating the three LGG subtypes in clinical practice, compared with examining a single molecular marker in a binary group distinction, due to a degree of overlap for most visually assessable MRI features across the three subtypes.

A number of strategies, including multivariate regression models, have been proposed to combine imaging features for glioma genotype predictions, but their method variability limits comparison. In general, features that are either specific

(to confidently predict a given molecular subtype) or sensitive (to exclude a subtype) are most suited to such an approach. Lasocki et al. suggested an algorithm combining the T2-FLAIR mismatch sign and the presence of calcifications, being predictive of 1p19q^{intact} and 1p19q^{codel} tumours, respectively, with no overlap between the groups [35]. The main limitation of this algorithm was the sensitivity, as 38 of 59 in this cohort did not exhibit either feature [35]. Kanazawa et al. presented a scoring system for predicting 1p19q codeletion comprised of four features – calcification, indistinct tumour border on T1WI, paramagnetic susceptibility effect on T1WI and a cystic component on FLAIR – and found that the presence of at least three of the four features had a positive predictive value of 96% and specificity of 98% [19]. In the context of glioblastomas, the absence of either a frontal lobe location or at least 33% nCET has been reported as being strongly predictive of IDH^{wt} status [43].

A key finding of this analysis is that most studies performed no interobserver comparisons, so that human factors remain a concern for qualitative visual assessments in clinical practice. Thus, their diagnostic accuracy and variability remain to some extent uncertain, even when summarizing multiple studies.

Conclusions

A substantial body of literature exists on conventional MRI for glioma radiogenomic predictions, detailing findings in several thousand tumours. Despite heterogeneous methods, consistent result themes have emerged in this review with respect to tumour epicentres and signal characteristics, which indicate that conventional MRI is valuable for glioma genotyping, particularly in presumed LGG. However, due to sparse interobserver testing, the reproducibility of qualitative features remains an area of uncertainty.

Authors' contributions All authors contributed significantly to this research and have approved the final manuscript.

Data availability The data extraction table and QUADAS-2 table are provided as Supplementary Material.

Funding information Arian Lasocki was supported by a Peter MacCallum Cancer Foundation Discovery Partner Fellowship. Stefanie Thust receives funding from the University College London/UCL Hospitals National Institute of Health Research Biomedical Research Centre.

Compliance with ethical standards

Conflict of interest None

Ethics approval The study was performed in accordance with the ethical standards as laid down in the 1964 Declaration of Helsinki and its later amendments. Formal ethics committee approval is not required for a study of this nature.

Informed consent Informed consent was obtained from all individual participants included in the study.

Code availability N/A

References

1. Louis DN, Perry A, Reifenberger G, von Deimling A, Figarella-Branger D, Cavenee WK, Ohgaki H, Wiestler OD, Kleihues P, Ellison DW (2016) The 2016 World Health Organization Classification of Tumors of the Central Nervous System: a summary. Acta Neuropathol 131(6):803–820. https://doi.org/10.1007/s00401-016-1545-1
2. Yan H, Parsons DW, Jin G, McLendon R, Rasheed BA, Yuan W, Kos I, Batinic-Haberle I, Jones S, Riggins GJ, Friedman H, Friedman A, Reardon D, Herndon J, Kinzler KW, Velculescu VE, Vogelstein B, Bigner DD (2009) IDH1 and IDH2 mutations in gliomas. N Engl J Med 360(8):765–773. https://doi.org/10.1056/NEJMoa0808710
3. Brat DJ, Aldape K, Colman H, Holland EC, Louis DN, Jenkins RB, Kleinschmidt-DeMasters BK, Perry A, Reifenberger G, Stupp R, von Deimling A, Weller M (2018) cIMPACT-NOW update 3: recommended diagnostic criteria for "Diffuse astrocytic glioma, IDH-wildtype, with molecular features of glioblastoma, WHO grade IV". Acta Neuropathol 136(5):805–810. https://doi.org/10.1007/s00401-018-1913-0
4. Tesileanu CMS, Dirven L, Wijnenga MMJ, Koekkoek JAF, Vincent A, Dubbink HJ, Atmodimedjo PN, Kros JM, van Duinen SG, Smits M, Taphoorn MJB, French PJ, van den Bent MJ (2019) Survival of diffuse astrocytic glioma, IDH1/2-wildtype, with molecular features of glioblastoma, WHO grade IV: a confirmation of the cIMPACT-NOW criteria. Neuro-Oncology 22:515–523. https://doi.org/10.1093/neuonc/noz200
5. Ellingson BM, Bendszus M, Boxerman J, Barboriak D, Erickson BJ, Smits M, Nelson SJ, Gerstner E, Alexander B, Goldmacher G, Wick W, Vogelbaum M, Weller M, Galanis E, Kalpathy-Cramer J, Shankar L, Jacobs P, Pope WB, Yang D, Chung C, Knopp MV, Cha S, van den Bent MJ, Chang S, Yung WK, Cloughesy TF, Wen PY, Gilbert MR (2015) Consensus recommendations for a standardized Brain Tumor Imaging Protocol in clinical trials. Neuro-Oncology 17(9):1188–1198. https://doi.org/10.1093/neuonc/nov095
6. Thust SC, Heiland S, Falini A, Jager HR, Waldman AD, Sundgren PC, Godi C, Katsaros VK, Ramos A, Bargallo N, Vernooij MW, Yousry T, Bendszus M, Smits M (2018) Glioma imaging in Europe: A survey of 220 centres and recommendations for best clinical practice. Eur Radiol 28(8):3306–3317. https://doi.org/10.1007/s00330-018-5314-5
7. Smits M, van den Bent MJ (2017) Imaging Correlates of Adult Glioma Genotypes. Radiology 284(2):316–331. https://doi.org/10.1148/radiol.2017151930
8. McInnes MDF, Moher D, Thombs BD, McGrath TA, Bossuyt PM, Clifford T, Cohen JF, Deeks JJ, Gatsonis C, Hooft L, Hunt HA, Hyde CJ, Korevaar DA, Leeflang MMG, Macaskill P, Reitsma JB, Rodin R, Rutjes AWS, Salameh JP, Stevens A, Takwoingi Y, Tonelli M, Weeks L, Whiting P, Willis BH (2018) Preferred Reporting Items for a Systematic Review and Meta-analysis of Diagnostic Test Accuracy Studies: The PRISMA-DTA Statement. JAMA 319(4):388–396. https://doi.org/10.1001/jama.2017.19163
9. Whiting PF, Rutjes AW, Westwood ME, Mallett S, Deeks JJ, Reitsma JB, Leeflang MM, Sterne JA, Bossuyt PM (2011) QUADAS-2: a revised tool for the quality assessment of diagnostic

accuracy studies. Ann Intern Med 155(8):529–536. https://doi.org/10.7326/0003-4819-155-8-201110180-00009
10. Qi S, Yu L, Li H, Ou Y, Qiu X, Ding Y, Han H, Zhang X (2014) Isocitrate dehydrogenase mutation is associated with tumor location and magnetic resonance imaging characteristics in astrocytic neoplasms. Oncol Lett 7(6):1895–1902. https://doi.org/10.3892/ol.2014.2013
11. Sonoda Y, Shibahara I, Kawaguchi T, Saito R, Kanamori M, Watanabe M, Suzuki H, Kumabe T, Tominaga T (2015) Association between molecular alterations and tumor location and MRI characteristics in anaplastic gliomas. Brain Tumor Pathol 32(2):99–104. https://doi.org/10.1007/s10014-014-0211-3
12. Wasserman JK, Nicholas G, Yaworski R, Wasserman AM, Woulfe JM, Jansen GH, Chakraborty S, Nguyen TB (2015) Radiological and pathological features associated with IDH1-R132H mutation status and early mortality in newly diagnosed anaplastic astrocytic tumours. PLoS One 10(4):e0123890. https://doi.org/10.1371/journal.pone.0123890
13. Darlix A, Deverdun J, Menjot de Champfleur N, Castan F, Zouaoui S, Rigau V, Fabbro M, Yordanova Y, Le Bars E, Bauchet L, Goze C, Duffau H (2017) IDH mutation and 1p19q codeletion distinguish two radiological patterns of diffuse low-grade gliomas. J Neuro-Oncol 133(1):37–45. https://doi.org/10.1007/s11060-017-2421-0
14. Xing Z, Yang X, She D, Lin Y, Zhang Y, Cao D (2017) Noninvasive assessment of IDH mutational status in World Health Organization grade II and III astrocytomas using DWI and DSC-PWI combined with conventional MR imaging. AJNR Am J Neuroradiol 38(6):1138–1144. https://doi.org/10.3174/ajnr.A5171
15. Hyare H, Rice L, Thust S, Nachev P, Jha A, Milic M, Brandner S, Rees J (2019) Modelling MR and clinical features in grade II/III astrocytomas to predict IDH mutation status. Eur J Radiol 114:120–127. https://doi.org/10.1016/j.ejrad.2019.03.003
16. Yamauchi T, Ohno M, Matsushita Y, Takahashi M, Miyakita Y, Kitagawa Y, Kondo E, Tsushita N, Satomi K, Yoshida A, Ichimura K, Narita Y (2018) Radiological characteristics based on isocitrate dehydrogenase mutations and 1p/19q codeletion in grade II and III gliomas. Brain Tumor Pathol 35(3):148–158. https://doi.org/10.1007/s10014-018-0321-4
17. Delfanti RL, Piccioni DE, Handwerker J, Bahrami N, Krishnan A, Karunamuni R, Hattangadi-Gluth JA, Seibert TM, Srikant A, Jones KA, Snyder VS, Dale AM, White NS, McDonald CR, Farid N (2017) Imaging correlates for the 2016 update on WHO classification of grade II/III gliomas: implications for IDH, 1p/19q and ATRX status. J Neuro-Oncol 135(3):601–609. https://doi.org/10.1007/s11060-017-2613-7
18. Villanueva-Meyer JE, Wood MD, Choi BS, Mabray MC, Butowski NA, Tihan T, Cha S (2018) MRI features and IDH mutational status of grade II diffuse gliomas: impact on diagnosis and prognosis. AJR Am J Roentgenol 210(3):621–628. https://doi.org/10.2214/ajr.17.18457
19. Kanazawa T, Fujiwara H, Takahashi H, Nishiyama Y, Hirose Y, Tanaka S, Yoshida K, Sasaki H (2019) Imaging scoring systems for preoperative molecular diagnoses of lower-grade gliomas. Neurosurg Rev 42(2):433–441. https://doi.org/10.1007/s10143-018-0981-x
20. Park YW, Han K, Ahn SS, Bae S, Choi YS, Chang JH, Kim SH, Kang SG, Lee SK (2018) Prediction of IDH1-mutation and 1p/19q-codeletion status using preoperative MR imaging phenotypes in lower grade gliomas. AJNR Am J Neuroradiol 39(1):37–42. https://doi.org/10.3174/ajnr.A5421
21. Compes P, Tabouret E, Etcheverry A, Colin C, Appay R, Cordier N, Mosser J, Chinot O, Delingette H, Girard N, Dufour H, Metellus P, Figarella-Branger D (2019) Neuro-radiological characteristics of adult diffuse grade II and III insular gliomas classified according to WHO 2016. J Neuro-Oncol 142(3):511–520. https://doi.org/10.1007/s11060-019-03122-1
22. Wu CC, Jain R, Radmanesh A, Poisson LM, Guo WY, Zagzag D, Snuderl M, Placantonakis DG, Golfinos J, Chi AS (2018) Predicting genotype and survival in glioma using standard clinical MR imaging apparent diffusion coefficient images: a pilot study from The Cancer Genome Atlas. AJNR Am J Neuroradiol 39(10):1814–1820. https://doi.org/10.3174/ajnr.A5794
23. Wang YY, Wang K, Li SW, Wang JF, Ma J, Jiang T, Dai JP (2015) Patterns of tumor contrast enhancement predict the prognosis of anaplastic gliomas with IDH1 mutation. AJNR Am J Neuroradiol 36(11):2023–2029. https://doi.org/10.3174/ajnr.A4407
24. Juratli TA, Tummala SS, Riedl A, Daubner D, Hennig S, Penson T, Zolal A, Thiede C, Schackert G, Krex D, Miller JJ, Cahill DP (2019) Radiographic assessment of contrast enhancement and T2/FLAIR mismatch sign in lower grade gliomas: correlation with molecular groups. J Neuro-Oncol 141(2):327–335. https://doi.org/10.1007/s11060-018-03034-6
25. Su CQ, Lu SS, Zhou MD, Shen H, Shi HB, Hong XN (2019) Combined texture analysis of diffusion-weighted imaging with conventional MRI for non-invasive assessment of IDH1 mutation in anaplastic gliomas. Clin Radiol 74(2):154–160. https://doi.org/10.1016/j.crad.2018.10.002
26. Reyes-Botero G, Dehais C, Idbaih A, Martin-Duverneuil N, Lahutte M, Carpentier C, Letouze E, Chinot O, Loiseau H, Honnorat J, Ramirez C, Moyal E, Figarella-Branger D, Ducray F (2014) Contrast enhancement in 1p/19q-codeleted anaplastic oligodendrogliomas is associated with 9p loss, genomic instability, and angiogenic gene expression. Neuro-Oncology 16(5):662–670. https://doi.org/10.1093/neuonc/not235
27. Wiki for the VASARI feature set. The National Cancer Institute website. 2015. Available at: https://wiki.cancerimagingarchive.net/display/Public/VASARI+Research+Project. Accessed Dec 2019
28. Zhou H, Vallieres M, Bai HX, Su C, Tang H, Oldridge D, Zhang Z, Xiao B, Liao W, Tao Y, Zhou J, Zhang P, Yang L (2017) MRI features predict survival and molecular markers in diffuse lower-grade gliomas. Neuro-Oncology 19(6):862–870. https://doi.org/10.1093/neuonc/now256
29. Liu T, Cheng G, Kang X, Xi Y, Zhu Y, Wang K, Sun C, Ye J, Li P, Yin H (2018) Noninvasively evaluating the grading and IDH1 mutation status of diffuse gliomas by three-dimensional pseudo-continuous arterial spin labeling and diffusion-weighted imaging. Neuroradiology 60(7):693–702. https://doi.org/10.1007/s00234-018-2021-5
30. Thust SC, Hassanein S, Bisdas S, Rees JH, Hyare H, Maynard JA, Brandner S, Tur C, Jager HR, Yousry TA, Mancini L (2018) Apparent diffusion coefficient for molecular subtyping of non-gadolinium-enhancing WHO grade II/III glioma: volumetric segmentation versus two-dimensional region of interest analysis. Eur Radiol 28(9):3779–3788. https://doi.org/10.1007/s00330-018-5351-0
31. Batchala PP, Muttikkal TJE, Donahue JH, Patrie JT, Schiff D, Fadul CE, Mrachek EK, Lopes MB, Jain R, Patel SH (2019) Neuroimaging-based classification algorithm for predicting 1p/19q-codeletion status in IDH-mutant lower grade gliomas. AJNR Am J Neuroradiol 40(3):426–432. https://doi.org/10.3174/ajnr.A5957
32. Johnson DR, Diehn FE, Giannini C, Jenkins RB, Jenkins SM, Parney IF, Kaufmann TJ (2017) Genetically defined oligodendroglioma is characterized by indistinct tumor borders at MRI. AJNR Am J Neuroradiol 38(4):678–684. https://doi.org/10.3174/ajnr.A5070
33. Kim JW, Park CK, Park SH, Kim YH, Han JH, Kim CY, Sohn CH, Chang KH, Jung HW (2011) Relationship between radiological characteristics and combined 1p and 19q deletion in World Health Organization grade III oligodendroglial tumours. J Neurol

Neurosurg Psychiatry 82(2):224–227. https://doi.org/10.1136/jnnp.2009.178806
34. Sherman JH, Prevedello DM, Shah L, Raghavan P, Pouratian N, Starke RM, Lopes MB, Shaffrey ME, Schiff D (2010) MR imaging characteristics of oligodendroglial tumors with assessment of 1p/19q deletion status. Acta Neurochir 152(11):1827–1834. https://doi.org/10.1007/s00701-010-0743-1
35. Lasocki A, Gaillard F, Gorelik A, Gonzales M (2018) MRI features can predict 1p/19q status in intracranial gliomas. AJNR Am J Neuroradiol 39(4):687–692. https://doi.org/10.3174/ajnr.A5572
36. Xiong J, Tan W, Wen J, Pan J, Wang Y, Zhang J, Geng D (2016) Combination of diffusion tensor imaging and conventional MRI correlates with isocitrate dehydrogenase 1/2 mutations but not 1p/19q genotyping in oligodendroglial tumours. Eur Radiol 26(6):1705–1715. https://doi.org/10.1007/s00330-015-4025-4
37. Peng X, Yishuang C, Kaizhou Z, Xiao L, Ma C (2019) Conventional magnetic resonance features for predicting 1p19q codeletion status of World Health Organization grade II and III diffuse gliomas. J Comput Assist Tomogr 43(2):269–276. https://doi.org/10.1097/rct.0000000000000816
38. Patel SH, Poisson LM, Brat DJ, Zhou Y, Cooper L, Snuderl M, Thomas C, Franceschi AM, Griffith B, Flanders AE, Golfinos JG, Chi AS, Jain R (2017) T2-FLAIR mismatch, an imaging biomarker for IDH and 1p/19q status in lower-grade gliomas: a TCGA/TCIA project. Clin Cancer Res 23(20):6078–6085. https://doi.org/10.1158/1078-0432.Ccr-17-0560
39. Broen MPG, Smits M, Wijnenga MMJ, Dubbink HJ, Anten M, Schijns O, Beckervordersandforth J, Postma AA, van den Bent MJ (2018) The T2-FLAIR mismatch sign as an imaging marker for non-enhancing IDH-mutant, 1p/19q-intact lower-grade glioma: a validation study. Neuro-Oncology 20(10):1393–1399. https://doi.org/10.1093/neuonc/noy048
40. Cui Y, Ma L, Chen X, Zhang Z, Jiang H, Lin S (2014) Lower apparent diffusion coefficients indicate distinct prognosis in low-grade and high-grade glioma. J Neuro-Oncol 119(2):377–385. https://doi.org/10.1007/s11060-014-1490-6
41. Carrillo JA, Lai A, Nghiemphu PL, Kim HJ, Phillips HS, Kharbanda S, Moftakhar P, Lalaezari S, Yong W, Ellingson BM, Cloughesy TF, Pope WB (2012) Relationship between tumor enhancement, edema, IDH1 mutational status, MGMT promoter methylation, and survival in glioblastoma. AJNR Am J Neuroradiol 33(7):1349–1355. https://doi.org/10.3174/ajnr.A2950
42. Xing Z, Zhang H, She D, Lin Y, Zhou X, Zeng Z, Cao D (2019) IDH genotypes differentiation in glioblastomas using DWI and DSC-PWI in the enhancing and peri-enhancing region. Acta Radiol:284185119842288. https://doi.org/10.1177/0284185119842288
43. Lasocki A, Tsui A, Gaillard F, Tacey M, Drummond K, Stuckey S (2017) Reliability of noncontrast-enhancing tumor as a biomarker of IDH1 mutation status in glioblastoma. J Clin Neurosci 39:170–175. https://doi.org/10.1016/j.jocn.2017.01.007
44. Hong EK, Choi SH, Shin DJ, Jo SW, Yoo RE, Kang KM, Yun TJ, Kim JH, Sohn CH, Park SH, Won JK, Kim TM, Park CK, Kim IH, Lee ST (2018) Radiogenomics correlation between MR imaging features and major genetic profiles in glioblastoma. Eur Radiol 28(10):4350–4361. https://doi.org/10.1007/s00330-018-5400-8
45. Hata N, Hatae R, Yoshimoto K, Murata H, Kuga D, Akagi Y, Sangatsuda Y, Suzuki SO, Iwaki T, Mizoguchi M, Iihara K (2017) Insular primary glioblastomas with IDH mutations: Clinical and biological specificities. Neuropathology 37(3):200–206. https://doi.org/10.1111/neup.12362
46. Yamashita K, Hiwatashi A, Togao O, Kikuchi K, Hatae R, Yoshimoto K, Mizoguchi M, Suzuki SO, Yoshiura T, Honda H (2016) MR Imaging-based analysis of glioblastoma multiforme: estimation of IDH1 mutation status. AJNR Am J Neuroradiol 37(1):58–65. https://doi.org/10.3174/ajnr.A4491
47. Wang K, Wang Y, Fan X, Wang J, Li G, Ma J, Ma J, Jiang T, Dai J (2016) Radiological features combined with IDH1 status for predicting the survival outcome of glioblastoma patients. Neuro-oncology 18(4):589–597. https://doi.org/10.1093/neuonc/nov239
48. Lasocki A, Gaillard F, Tacey M, Drummond K, Stuckey S (2018) Morphologic patterns of noncontrast-enhancing tumor in glioblastoma correlate with IDH1 mutation status and patient survival. J Clin Neurosci 47:168–173. https://doi.org/10.1016/j.jocn.2017.09.007
49. Kong LW, Chen J, Zhao H, Yao K, Fang SY, Wang Z, Wang YY, Li SW (2019) Intratumoral susceptibility signals reflect biomarker status in gliomas. Sci Rep 9(1):17080. https://doi.org/10.1038/s41598-019-53629-w

European Radiology (2018) 28:3779–3788
https://doi.org/10.1007/s00330-018-5351-0

NEURO

Apparent diffusion coefficient for molecular subtyping of non-gadolinium-enhancing WHO grade II/III glioma: volumetric segmentation versus two-dimensional region of interest analysis

S. C. Thust[1,2,3] · S. Hassanein[1,3] · S. Bisdas[1,3] · J. H. Rees[4] · H. Hyare[1,2] · J. A. Maynard[2] · S. Brandner[5] · C. Tur[6] · H. R. Jäger[1,2,3] · T. A. Yousry[1,3] · L. Mancini[1,3]

Received: 17 October 2017 / Revised: 26 December 2017 / Accepted: 23 January 2018 / Published online: 23 March 2018

Abstract

Objectives To investigate if quantitative apparent diffusion coefficient (ADC) measurements can predict genetic subtypes of non-gadolinium-enhancing gliomas, comparing whole tumour against single slice analysis.

Methods Volumetric T2-derived masks of 44 gliomas were co-registered to ADC maps with ADC mean (ADC_{mean}) calculated. For the slice analysis, two observers placed regions of interest in the largest tumour cross-section. The ratio (ADC_{ratio}) between ADC_{mean} in the tumour and normal appearing white matter was calculated for both methods.

Results Isocitrate dehydrogenase (IDH) wild-type gliomas showed the lowest ADC values throughout ($p < 0.001$). ADC_{mean} in the IDH-mutant 1p19q intact group was significantly higher than in the IDH-mutant 1p19q co-deleted group ($p < 0.01$). A volumetric ADC_{mean} threshold of 1201×10^{-6} mm^2/s identified IDH wild-type with a sensitivity of 83% and a specificity of 86%; a volumetric ADC_{ratio} cut-off value of 1.65 provided a sensitivity of 80% and a specificity of 92% (area under the curve (AUC) 0.9–0.94). A slice ADC_{ratio} threshold for observer 1 (observer 2) of 1.76 (1.83) provided a sensitivity of 80% (86%), specificity of 91% (100%) and AUC of 0.95 (0.96). The intraclass correlation coefficient was excellent (0.98).

Conclusions ADC measurements can support the distinction of glioma subtypes. Volumetric and two-dimensional measurements yielded similar results in this study.

Key Points

- *Diffusion-weighted MRI aids the identification of non-gadolinium-enhancing malignant gliomas*
- *ADC measurements may permit non-gadolinium-enhancing glioma molecular subtyping*
- *IDH wild-type gliomas have lower ADC values than IDH-mutant tumours*
- *Single cross-section and volumetric ADC measurements yielded comparable results in this study*

Keywords Brain · Diffusion magnetic resonance imaging · Isocitrate dehydrogenase · Glioma · Neuroimaging

Abbreviations

ADC	Apparent diffusion coefficient
AUC	Area under the curve
CS	Centrum semiovale
DKI	Diffusion kurtosis imaging
DTI	Diffusion tensor imaging
DWI	Diffusion-weighted imaging
IDH	Isocitrate dehydrogenase

✉ S. C. Thust
s.thust@ucl.ac.uk

[1] Neuroradiological Academic Unit, Department of Brain Repair and Rehabilitation, UCL Institute of Neurology, London, UK

[2] Imaging Department, University College London Foundation Hospital, London, UK

[3] Lysholm Department of Neuroradiology, National Hospital for Neurology and Neurosurgery, Queen Square, London WC1N 3BG, UK

[4] Department of Clinical Neurology, National Hospital for Neurology and Neurosurgery, London, UK

[5] Department of Neurodegenerative Disease, UCL Institute of Neurology and Division of Neuropathology, London, UK

[6] Queen Square MS Centre. Department of Neuroinflammation, UCL Institute of Neurology, University College London, London, UK

IDH^{wt}	Isocitrate dehydrogenase wild-type
$IDH^{mut}1p19^{int}$	Isocitrate dehydrogenase-mutant 1p19q intact
$IDH^{mut}1p19^{del}$	Isocitrate dehydrogenase-mutant 1p19q co-deleted
ICC	Intraclass correlation coefficient
LGG	Low grade glioma
NAWM	Normal appearing white matter
PACS	Picture archiving and communications system
ROC	Receiver operating characteristic
ROI_{CS}	Centrum semiovale region of interest
ROI_{tum}	Tumour region of interest
TE	Echo time
TR	Repetition time
VOI_{CS}	Centrum semiovale volume of interest
VOI_{tum}	Tumour volume of interest
WHO	World Health Organization
2HG	D2-hydroxyglutarate

Introduction

Gadolinium contrast uptake was previously considered the best MR imaging predictor of glioma histological grade and malignancy[1–3]. On the basis of this, it has been common practice to interpret non-enhancing intrinsic tumours as probable low grade gliomas (LGG) [4]. But conventional MRI has proven to be unreliable in predicting subsequent tumour behaviour, whereby a proportion of presumed LGG may rapidly progress with development of malignant features such as enhancement and necrosis [4–8].

The discovery of several key genetic alterations as principal determinants of glioma prognosis has challenged the reference standard of glioma grouping by histology [9]. Mutations in isocitrate dehydrogenase (IDH) represent a common (> 70%) defining event in the development of LGG, conversely more than 90% of glioblastomas belong to the IDH wild-type group [10, 11]. Despite its oncogenic effect through production of a toxic metabolite D2-hydroxyglutarate (2HG), the presence of an IDH mutation is associated with a favourable prognosis.

The revised 2016 World Health Organization (WHO) classification of brain tumours for the first time incorporates molecular data to augment the diagnosis [12]. For WHO grade II/III gliomas, three molecular subgroups have been defined: IDH wild-type glioma (IDH^{wt}) with survival similar to that of glioblastoma, IDH-mutant glioma with intact 1p19q ($IDH^{mut}1p19^{int}$) and an intermediate prognosis, and IDH-mutant 1p19q co-deleted glioma ($IDH^{mut}1p19q^{del}$) with the best prognosis and greatest chemosensitivity [11]. There is partial overlap with histomorphology, whereby many $IDH^{mut}1p19^{int}$ are astrocytic and the majority of $IDH^{mut}1p19q^{del}$ belong to the oligodendroglioma group [13]. IDH^{wt} gliomas probably constitute a genetically heterogeneous category of lesions, but often exhibit aggressive behaviour and have been suspected to represent early glioblastoma [14–17]. In the emerging literature on MR imaging features of IDH^{wt} glioma, initial lack of enhancement has been reported in some of these tumours [6, 18, 19].

Diffusion-weighted imaging (DWI) is a technique of great interest in cancer, because water diffusivity is impaired in highly cellular tissues, which reflects tumour proliferative rate and aggressiveness [20]. The phenomenon of reduced diffusion preceding fulminant radiological progression of presumed LGG has been observed prior to molecular typing [7], evoking later descriptions of IDH^{wt} glioma serial imaging findings [4]. Quantitative apparent diffusion coefficient (ADC) values have demonstrated high accuracy for glioma grading through meta-analysis [21]. For the non-invasive identification of low to intermediate IDH^{wt} glioma, diffusion tensor imaging (DTI) and diffusion kurtosis imaging (DKI) have shown potential, suggesting that reduced and heterogenous diffusivity are IDH^{wt} features [22–24]. However, advanced diffusion techniques are not universally available outside academic hospital institutions, may require longer scan times and dedicated post-processing.

Mean ADC measurement could be a rapid and practicable approach to assess glioma diffusivity, being computationally non-demanding compared to histograms or texture analysis. Although theoretically superior, there is no conclusive evidence that whole lesion analysis outperforms region-of-interest placement for the identification of malignant gliomas [25].

The study presented sought to (i) investigate whether ADC measurements from routine clinical DWI were associated with glioma molecular subtype and (ii) to compare the performance of volumetric whole tumour ADC with single slice ADC measurements.

Materials and methods

Patients

Following institutional board approval for a retrospective study, we searched the neuropathology records revealing 37 patients with WHO grade II/III IDH^{wt} glioma between 2009 and 2016. For comparison of the molecular groups, control samples of IDH (IDH1-R132H) mutant gliomas (34 $IDH^{mut}1p19q^{int}$ and 32 $IDH^{mut}1p19q^{del}$) were randomly selected. We sought to evaluate ADC for suspected LGG prior to tissue diagnosis. To replicate the clinical situation, only gliomas without gadolinium enhancement were included (2 non-enhancing gliomas were excluded because of missing images and degraded DWI, respectively). The study sample

consisted of 14 IDH^{wt} (7 WHO II and 7 WHO III), 16 $IDH^{mut}1p19q^{int}$ (8 WHO II and 8 WHO III) and 14 $IDH^{mut}1p19q^{del}$ (11 WHO II and 3 WHO III), amounting to 44 non-enhancing gliomas for the three molecular groups (patient selection diagram shown in Fig. 1). No haemorrhagic or necrotic gliomas were featured in the study.

MRI acquisition

Ours is a quaternary neurosurgical centre; therefore the standard (structural and DWI) MRI sequences in this study originated from 10 different referring institutions (institution 1 to institution 10): 29 from our own institutions, 4 from institution 2, 3 from institution 3, 2 from institution 4, and one each from the remaining six institutions. The studies were acquired on 18 different scanners (31 at 1.5 Tesla, and 13 at 3 Tesla) from all major vendors: four General Electric scanners [Discovery MR450 (number of patients n = 5), 2× Signa Excite (n = 1 each), Genesis Signa (n = 2)], seven Siemens scanners [3× Avanto (n = 7, n = 2, n = 1), a Trio (n = 9), Symphony (n = 4), Skyra (n = 3), Espree (n = 1)], six Philips scanners [Ingenia (n = 2), 5× Achieva (n = 1 each)] and one Toshiba scanner (n = 1). All acquisitions included axial T2-weighted images, and axial standard 3-directional whole brain DWI. The median [min, max] values of the parameters of the T2-weighted images were echo time (TE) = 99.5 [80, 141] ms; repetition time (TR) = 4610 [2500, 7480] ms, in-plane resolution = 0.5 × 0.5 [0.3 × 0.3, 0.9 × 0.9] mm^2; slice thickness = 5 [1, 6] mm; gap between slices = 1.5 [0, 2] mm. All DWI acquisitions included diffusion gradient weighting values b = 0 s/mm^2 and b = 1000 s/mm^2; the median [min, max] of other parameters were TE = 90.5 [69.5, 137] ms; TR = 4000 [2837, 10,000] ms, in-plane resolution = 1.25 × 1.25 [0.5 × 0.5, 2.5 × 2.5] mm^2; slice thickness = 5 [4, 6] mm; gap between slices = 1.5 [0, 2] mm. For each patient, the imaging study was performed on average (standard deviation, sd) 2.3 (2.8) months prior to the tissue diagnosis. Image examples for the glioma molecular subgroups are shown in Fig. 2.

Post-processing and ADC analysis

ADC map calculation

In a spin echo diffusion-weighted sequence, the signal S_b [$S_b = S_0\, e^{(-b\ ADC)}$] from each pixel in an image is formed of a first component (S_0) dependent on tissue properties (i.e. 'spin density', T_1 and T_2 relaxation times) and sequence properties (e.g. repetition time, TR); and a second component ($e^{-b\ ADC}$) dependent on the diffusion gradients (b, in units of s/mm^2) and the apparent diffusion coefficient (ADC, in units of mm^2/s).

The ADC is obtained by dividing the image acquired without diffusion gradients ($S_{b=0} = S_0$) by the image acquired with diffusion gradients (S_b):

$$\mathrm{ADC} = (1/b)\ \ln(S_0/S_b) \quad (1)$$

In this division, the dependence of ADC from S_0 (and therefore from T_1, T_2 and TR) is eliminated [26]. The ADC maps were calculated using Eq. 1 and the utility fslmaths from the software library fsl (version 5.0) [27]. Offline whole tumour analysis and single slice analysis were subsequently performed.

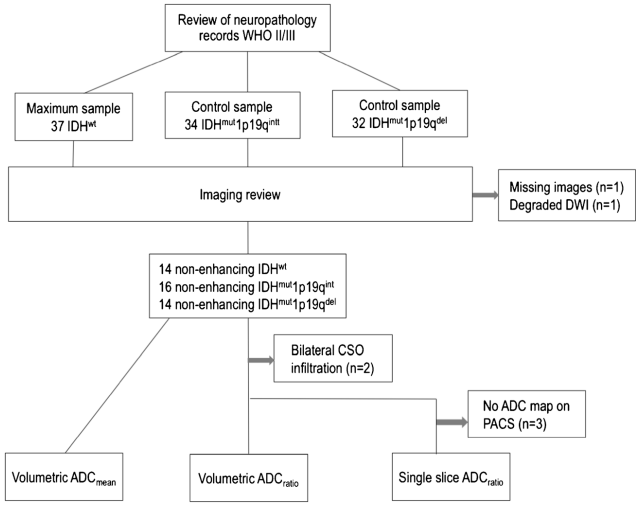

Fig. 1 Flow diagram of patients included and excluded from the analyses

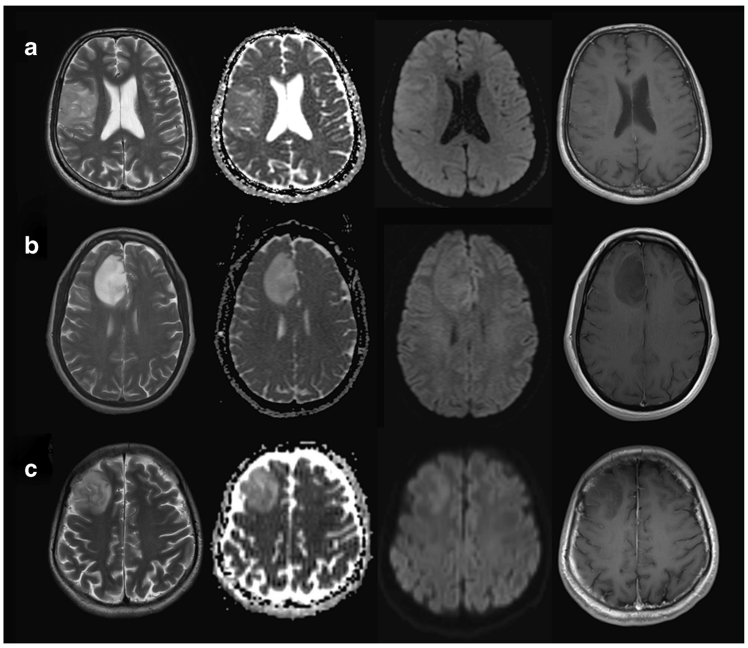

Fig. 2 WHO II/III molecular subgroup examples showing T2-weighted images, *b*1000, ADC maps and T1-weighted post gadolinium images of non-enhancing **a** IDH^{wt}, **b** $IDH^{mut}1p19q^{int}$ and **c** $IDH^{mut}1p19q^{del}$ glioma

Whole tumour (volumetric) ADC analysis

Tumour volumes of interest (VOI_{tum}) were outlined by a neuroradiology resident (S.H.) using ITK snap Toolbox version 3.6 (www.itksnap.org [28]), covering the entire T2 signal abnormality with each segmentation optimised by a board-certified neuroradiologist specialised in brain tumour imaging (S.C.T.). For multicentric gliomas, the total volume of signal abnormality was treated as one lesion. ADC maps were co-registered to T2 imaging using the FLIRT toolbox [29, 30] performing a rigid body transformation with a six-parameter model and 'Normalised Mutual Information' as cost function. Subsequently, ADC_{mean} measurements were obtained for each tumour, using the fslstats utility from fsl [25–27].

To consider possible interindividual variations in brain diffusivity, we assessed the ADC_{mean} in normal appearing white matter (NAWM). For each patient, a standardised second volume of interest (VOI_{CS}) was drawn in the contralateral centrum semiovale (CS). This VOI_{CS} was used to calculate the $ADC_{ratio} = ADC_{mean}(VOI_{tum})/ADC_{mean}(VOI_{CS})$ (Fig. 2). For two IDH^{wt} tumours, the NAWM analysis was omitted because of bilateral tumour infiltration.

Single slice ADC analysis

Standard picture archiving and communication systems (PACS) software (IMPAX 6.5.1.1008, Agfa-Gevaert, Mortsel, Belgium) was used to exploit tools routinely available for reporting of MR images. Two observers blinded to histomolecular results (J.A.M. general radiology trainee = observer 1 and S.C.T. = observer 2) located the tumour on the T2-weighted sequence, selecting two round regions of interest on the ADC map viewed side-by-side: The first region of interest (ROI_{tum}) was drawn in the largest lesion cross-section sparing the tumour margin to avoid partial volume effects. The second round ROI_{CS} aiming for a similar size to ROI_{tum} was placed in contralateral centrum semiovale NAWM, taking care to exclude images with visible ventricular surfaces, cortex and/or sulcal spaces at measurement level. Three patients were excluded from the single slice analysis because of non-availability of an ADC map on PACS. The ratio between the ADC_{mean} in the tumour and CS was calculated [$PACS\_ADC_{ratio} = ADC_{mean}(ROI_{tum})/ADC_{mean}(ROI_{CS})$]. No absolute ADC values were measured by the single slice method, as their workstation display can vary depending on the referring institution. An example of the volumetric segmentation and single slice ADC measurement is demonstrated in Fig. 3.

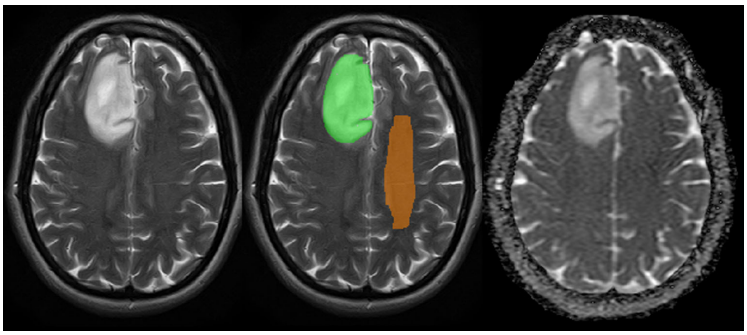

Fig. 3 Image examples demonstrating the whole lesion volumetric segmentation (mask overlaid on right frontal $IDH^{mut}1p19q^{int}$ glioma), single slice largest tumour cross-section ROI_{tum} and comparative contralateral NAWM ROI_{CS} placements

Histopathology and molecular analysis

Paraffin blocks containing tissue were analysed at our institution's neuropathology department according to WHO 2016 guidance and previously published data [16]. IDH R132H immuno-negative tumours underwent multiple gene Sanger sequencing. A quantitative polymerase chain reaction-based copy number assay was used to determine 1p/19q status.

Statistical analysis

For the volumetric and single slice data, the statistical analysis consisted of two steps each: (i) linear regression to assess the association between the tumour type (IDH^{wt}, $IDH^{mut}1p19q^{int}$, $IDH^{mut}1p19q^{del}$) and ADC values, followed by (ii) logistic regression to determine if ADC values can differentiate IDH^{wt} from IDH^{mut} gliomas. A receiver operating characteristic (ROC) analysis was used to quantify the performance of the logistic regression. For the identification of a cut-off point for the logistic regression the 'nearest to (0,1)' method was performed. Statistical significance was set at 5%. The inter-rater agreement was expressed as an intraclass correlation coefficient (ICC) using a two-way random effects model. All statistical analyses were performed using Stata version 14 (College Station, TX: StataCorp LP).

Results

The mean age was greater in the IDH^{wt} group than in the IDH^{mut} groups ($p = 0.0001$ for $IDH^{mut}1p19q^{int}$, $p = 0.005$ for $IDH^{mut}1p19q^{del}$). The larger proportion of WHO II gliomas in the $IDH^{mut}1p19q^{del}$ was not statistically significant (Pearson chi-square test $p = 0.115$ for IDH^{wt} and $p = 0.105$ for $IDH^{mut}1p19q^{int}$). The patient demographic data and tumour volumes are reported in Table 1.

Association between molecular subtype and ADC values

In the volumetric analysis, IDH^{wt} tumours showed significantly lower whole tumour volume $ADC_{mean}(VOI_{tum})$ than $IDH^{mut}1p19q^{int}$ ($p < 0.0005$) and $IDH^{mut}1p19q^{del}$ ($p = 0.001$). The $ADC_{mean}(VOI_{tum})$ in the $IDH^{mut}1p19q^{int}$ group was significantly higher than in the $IDH^{mut}1p19q^{del}$ group ($p = 0.0047$).

IDH^{wt} gliomas had a significantly lower whole tumour ADC_{ratio} than $IDH^{mut}1p19q^{int}$ ($p < 0.0005$) and $IDH^{mut}1p19q^{del}$ ($p = 0.019$). The ADC_{ratio} in the $IDH^{mut}1p19q^{int}$ group was significantly higher than in the $IDH^{mut}1p19q^{del}$ group ($p = 0.0054$).

On single slice assessment, a significantly lower mean $PACS\_ADC_{ratio}$ was observed for IDH^{wt} than for

Table 1 Patient demographic data and tumour volumes

Whole tumour ADC_{mean} (VOI_{tum})					
Patient group	Nr of patients total (male)	Age in years (mean ± sd) (years)	Tumour volume (mean ± sd) (cm^3)	CS NAWM volume (mean ± sd) (cm^3)	Tumour volume for patients with bilateral infiltration (mean ± sd) (cm^3)
IDH^{wt}	14 (9)	53 (± 14)	64 (± 68) ($n = 12$)	11.6 (± 2.5) ($n = 12$)	366 (± 46) ($n = 2$)
$IDH^{mut}1p19^{int}$	16 (6)	33.9 (± 8.6)	60 (± 44)	10.9 (± 2.3)	N/A
$IDH^{mut}1p19^{del}$	14 (7)	38.9 (± 8.3)	48 (± 50)	10.8 (± 2.5)	N/A

$IDH^{mut}1p19q^{int}$ ($p < 0.0005$ observer 1; $p < 0.0005$ observer 2) and for $IDH^{mut}1p19q^{del}$ ($p = 0.001$ observer 1; $p = 0.001$ observer 2). The $PACS\_ADC_{ratio}$ in the $IDH^{mut}1p19q^{int}$ group was higher than in the $IDH^{mut}1p19q^{del}$ group ($p = 0.0008$ for observer 1 and $p = 0.0025$ for observer 2). No statistical associations were demonstrated between the NAWM ADC_{mean} values and molecular subtype.

The intra-rater agreement for the $PACS\_ADC_{ratio}$ measurements was very high: the correlation of measurements made on the same individual was 0.96, while the correlation between mean observer ratings was 0.98. The correlation of measurements equaled the consistency agreement, indicating no systematic difference between the two observers. The single slice ADC_{ratio} values were slightly but systematically higher than the volumetric ADC_{ratio}. The numerical results of the association between tumour type and ADC values for the volumetric and single slice analyses are reported in Table 2. In Table 3, the difference between the ADC values in $IDH^{mut}1p19q^{int}$ and in $IDH^{mut}1p19q^{del}$ is shown. In Table 4 the ICC values are detailed. The boxplots of the ADC_{mean} and ADC_{ratio} values are depicted in Fig. 4.

Table 3 *F* test for the difference between $IDH^{mut}1p19^{int}$ and $IDH^{mut}1p19^{del}$

Analysis type	*p*
ADC_{mean} (VOI_{tum})	0.0047
Whole tumour ADC_{ratio}	0.0054
$PACS\_ADC_{ratio}$ 1st observer	0.0008
$PACS\_ADC_{ratio}$ 2nd observer	0.0025

Diagnostic performance of ADC values

For $ADC_{mean}(VOI_{tum})$, a ROC analysis quantified the accuracy of correctly classifying tumour type to an area under the curve (AUC) of 0.94. The cut-off point for the $ADC_{mean}(VOI_{tum})$ was 1201×10^{-6} mm^2/s, with a sensitivity of 0.83 and a specificity of 0.86. For a decrease in the $ADC_{mean}(VOI_{tum})$ value by 1.0×10^{-5} mm^2/s, the odds of IDH^{wt} increased by 78% ($p = 0.003$).

For the volumetric ADC_{ratio}, the ROC analysis yielded an AUC of 0.90 with a sensitivity of 0.80 and a specificity of 0.92 for a threshold ADC_{ratio} of 1.65. For a decrease in the volumetric ADC_{ratio} value by 0.1, the odds of IDH^{wt} increased by 46% ($p = 0.004$).

Table 2 Results of the linear regression between ADC and tumour type (IDH^{wt} is the reference group)

Whole tumour ADC_{mean} (VOI_{tum})				
Patient group	$ADC_{mean}(VOI_{tum})$ mean (sd) (10^{-6} mm^2/s)	Regression coefficient (10^{-6} mm^2/s)	95% CI of the regr. coeff. (10^{-6} mm^2/s)	*p*
IDH^{wt}	1032 (168)	1032	922–1141	0.0005
$IDH^{mut}1p19^{int}$	1543 (254)	511	361–661	0.0005
$IDH^{mut}1p19^{del}$	1321 (162)	289	134–444	0.001
Whole tumour ADC_{ratio}				
Patient group	ADC_{ratio} mean (sd)	Regression coefficient	95% CI of the regr. coeff.	*p*
IDH^{wt}	1.49 (0.32)	1.49	1.32–1.66	0.0005
$IDH^{mut}1p19^{int}$	2.09 (0.34)	0.59	0.37–0.82	0.0005
$IDH^{mut}1p19^{del}$	1.77 (0.20)	0.28	0.05–0.51	0.019
Single slice $PACS\_ADC_{ratio}$ first observer				
Patient group	$PACS\_ADC_{ratio}$ mean (sd)	Regression coefficient	95% CI of the regr. coeff.	*p*
IDH^{wt}	1.50 (0.21)	1.50	1.33–1.68	0.0005
$IDH^{mut}1p19^{int}$	2.37 (0.35)	0.87	0.63–1.10	0.0005
$IDH^{mut}1p19^{del}$	1.96 (0.27)	0.45	0.20–0.70	0.001
Single slice $PACS\_ADC_{ratio}$ second observer				
Patient group	$PACS\_ADC_{ratio}$ mean (sd)	Regression coefficient	95% CI of the regr. coeff.	*p*
IDH^{wt}	1.48 (0.19)	1.48	1.28–1.68	0.0005
$IDH^{mut}1p19^{int}$	2.37 (0.38)	0.88	0.62–1.14	0.0005
$IDH^{mut}1p19^{del}$	1.96 (0.36)	0.47	0.20–0.75	0.001

Regression coefficient represents the difference in the dependent variable (ADC) between each of the two IDH^{mut} groups and the reference group (IDH^{wt})

Table 4 Inter-rater agreement expressed as intraclass correlation coefficient (ICC)

	Correlation ICC (95% CI)	Consistency ICC (95% CI)
Observer 1 vs observer 2 - PACS_ADC$_{ratio}$		
Individual ICC	0.96 (0.92–0.98)	0.96 (0.92–0.98)
Average ICC	0.98 (0.96–0.99)	0.98 (0.96–0.99)
Observer 1 PACS_ADC$_{ratio}$ vs volumetric ADC$_{ratio}$		
Individual ICC	0.80 (0.35–0.92)	0.87 (0.77–0.93)
Average ICC	0.89 (0.52–0.96)	0.93 (0.87–0.96)
Observer 2 PACS_ADC$_{ratio}$ vs volumetric ADC$_{ratio}$		
Individual ICC	0.79 (0.43–0.91)	0.85 (0.74–0.92)
Average ICC	0.88 (0.60–0.95)	0.92 (0.85–0.96)

A ROC analysis quantified the accuracy of the PACS_ADC$_{ratio}$ logistic regression in correctly classifying tumour type to an AUC of 0.96 for observer 1 and 0.95 for observer 2. The cut-off point for the PACS_ADC$_{ratio}$ for observer 1 (observer 2) was 1.83 (1.76) with a sensitivity of 0.80 (0.86) and a specificity of 1.00 (0.91) at the cut-off point. For a decrease in the single slice ADC$_{ratio}$ value by 0.1, the odds of IDH^{wt} increased by 62% (p = 0.005) for observer 1 and 57% (p = 0.004) for observer 2. The numerical results for glioma subtype prediction are reported in Table 5. The ROC curves are depicted in Fig. 5.

Discussion

In this analysis, we observed that ADC values obtained from standard clinical DWI are a highly significant predictor of non-enhancing glioma IDH status and may permit non-invasive molecular subtyping in accordance with the 2016 WHO classification.

Two recent surveys highlighted clinical practices in caring for patients with presumed LGG, with approximately 50% of neurosurgeons adopting a 'wait and see' approach balanced against surgical risk [31], and only 21% performing an upfront biopsy [32]. Consequently, innocuous appearing IDH^{wt} gliomas may reveal their aggressive nature through progression and receive treatment with a delay.

Low ADC values are associated with increased glioma cellularity and worse prognosis, supported by comparisons of diffusivity, histological specimens and clinical data in multiple studies [5, 33–37]. Low diffusivity predicts poor astrocytoma survival independent from WHO grade [38], although no linear relation exists between ADC and glioma prognosis [39].

Past studies to distinguish astrocytoma and oligodendroglioma using ADC values yielded variable success [40, 41], and in retrospect may have been influenced by the incomplete overlap between histological and molecular groups. Diagnostic focus has shifted to genetic typing, yet immunohistochemistry tests are complex and not infallible, requiring interpretation in in the context of morphological criteria and test type performed to avoid interpretational errors [42].

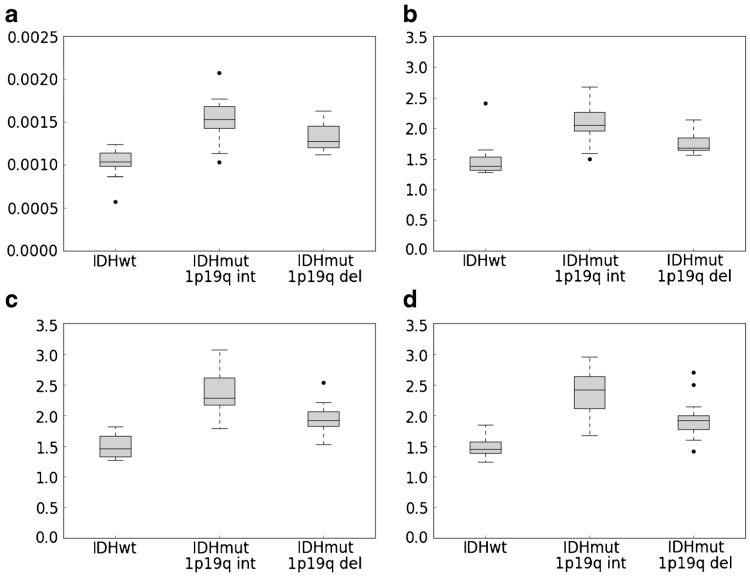

Fig. 4 Boxplot of the values of the **a** whole tumour ADC$_{mean}$(VOI$_{tum}$), **b** whole tumour ADC$_{ratio}$, **c** single slice PACS_ADC$_{ratio}$ first observer and **d** single slice PACS_ADC$_{ratio}$ first observer

Table 5 Cut-off point estimation

Method	Cut-off point	Sensitivity at cut-off point	Specificity at cut-off point	AUC at cut-off point
$ADC_{mean}(VOI_{tum})$	1201 (10^{-6} mm^2/s)	0.83	0.86	0.85
Whole tumour ADC_{ratio}	1.65	0.80	0.92	0.86
PACS_ADC_{ratio} 1st observer	1.83	0.86	1.00	0.93
PACS_ADC_{ratio} 2nd observer	1.76	0.86	0.91	0.88

Recently, Leu et al. were able to assign gliomas to the WHO 2016 molecular groups using ADC; however, their method differed from ours by including enhancing lesions and ADC median values derived from *b*700–1000 gradients with DTI analysed for some patients [43]. To our best knowledge, this is the first IDH typing study to focus on non-enhancing gliomas, using *b*1000 values derived from 3-directional DWI. This is particularly important, as such tumours are usually assumed to be less aggressive in common clinical practice.

We found ADC_{ratio} values to be closely reproducible when comparing whole lesion measurements against single slice region of interest placements, for which there was near complete inter-observer agreement. The similarity of our volumetric and single slice results could be explained by a relative homogeneity of these non-enhancing, non-necrotic gliomas. Both the absolute ADC_{mean} values and ADC_{ratio} appear valuable for this lesion type. The quicker and easier single slice analysis even performed marginally better. This is in line with results of previous imaging research, which suggested that whole lesion diffusivity measurement is not always superior to ROI analysis [25, 44].

The ability of ADC to predict glioma subtypes and optimum thresholds may be subject to ROI placement technique with previous research focusing on minimum ADC value analysis: Xing et al. showed a statistical correlation between ADC and IDH status using a multiple (≥ 5) ROI technique with the mean of the lowest ADC measurement chosen as minimum ADC in consensus [45]. In a similar fashion, a previous DTI study for IDH typing used multiple ROI placements and a two-reader consensus method to obtain minimum ADC values [24].

As a reference ROI, we chose the centrum semiovale for its potentially greater reproducibility compared to a 'mirror' ROI [45], because this could be influenced by tumour location. We

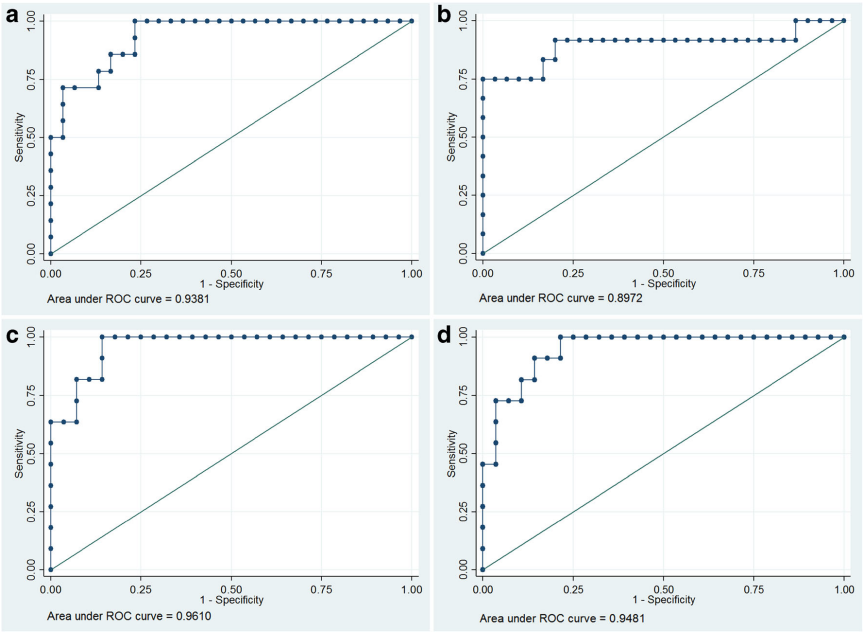

Fig. 5 ROC curves for the **a** whole tumour $ADC_{mean}(VOI_{tum})$, **b** whole tumour ADC_{ratio}, **c** single slice PACS_ADC_{ratio} observer 1 and **d** observer 2

avoided the internal capsule [24], which is a smaller structure and more difficult to locate by an untrained rater.

Lee et al. found ADC mean and ADC histograms useful for IDH typing of WHO grade III and IV gliomas [46]. However, for glioblastoma IDH typing alone, a recent study identified no difference in ADC values [47]. In Tan et al.'s study of grade II–IV gliomas, the accuracy of ADC for IDH typing decreased with higher grade, which may reflect greater lesion heterogeneity [24]. It is probable that in such circumstances advanced diffusion acquisitions (e.g. DKI or multi-*b*-value imaging) could provide greater tissue microstructural information.

The good performance of the single slice ROI technique in IDH typing of non-enhancing lower grade gliomas was unexpected, but is highly relevant. It implies that such easy-to-perform measurements could be incorporated into clinical reports, complementing advanced MR modalities such as perfusion and 2HG spectroscopy [48, 49] pending tissue diagnosis. The origin of data from 18 MRI systems could represent a limitation of this study, but reflects clinical reality. The fact that significant separation of glioma subtypes could be obtained from this dataset further underscores the robustness of ADC.

It remains unknown why intermediate ADC values were observed in the 1p19q co-deleted gliomas, despite their best prognosis. This result is consistent with published data on intermediate diffusivity in oligodendroglioma; interestingly this tumour subtype may also mimic malignant gliomas on MR perfusion studies [39, 50].

In summary, the results from this study suggest that for newly diagnosed non-enhancing gliomas with ADC ratio values of 1.8 or less, further investigation with consideration of early tissue diagnosis is advisable given an increased risk of IDH^{wt} molecular status.

Conclusions

ADC measurement appears to be a simple and powerful method for molecular subtyping of non-enhancing WHO II–III gliomas, specifically to identify IDH^{wt} neoplasms. In our patient cohort, a two-dimensional ROI measurement in the largest lesion cross-section appeared representative of the entire tumour with comparable results.

Funding This study received no specific funding, but was supported by the National Institute for Health Research University College London Biomedical Research Centre.

Compliance with ethical standards

Guarantor The scientific guarantor of this publication is Stefanie Thust.

Conflict of interest The authors of this manuscript declare no relationships with any companies whose products or services may be related to the subject matter of the article.

Statistics and biometry One of the authors (C.T. MD PhD MSc Medical Statistics) has significant statistics expertise.

Informed consent Written informed consent was waived by the institutional review board.

Ethical approval Institutional review board approval was obtained.

Methodology
- retrospective
- diagnostic study/observational
- performed at one institution

References

1. Pierallini A, Bonamini M, Bozzao A et al (1997) Supratentorial diffuse astrocytic tumours: proposal of an MRI classification. Eur Radiol 7:395–399
2. Watanabe M, Tanaka R, Takeda N (1992) Magnetic resonance imaging and histopathology of cerebral gliomas. Neuroradiology 34:463–469
3. Tervonen O, Forbes G, Scheithauer BW, Dietz MJ (1992) Diffuse "fibrillary" astrocytomas: correlation of MRI features with histopathologic parameters and tumor grade. Neuroradiology 34:173–178
4. Ideguchi M, Kajiwara K, Goto H et al (2015) MRI findings and pathological features in early-stage glioblastoma. J Neurooncol 123:289–297
5. Cuccarini V, Erbetta A, Farinotti M et al (2016) Advanced MRI may complement histological diagnosis of lower grade gliomas and help in predicting survival. J Neurooncol 126:279–288
6. Olar A, Raghunathan A, Albarracin CT et al (2012) Absence of IDH1-R132H mutation predicts rapid progression of nonenhancing diffuse glioma in older adults. Ann Diagn Pathol 16:161–170
7. Baehring JM, Bi WL, Bannykh S et al (2007) Diffusion MRI in the early diagnosis of malignant glioma. J Neurooncol 82:221–225
8. Ginsberg LE, Fuller GN, Hashmi M et al (1998) The significance of lack of MR contrast enhancement of supratentorial brain tumors in adults: histopathological evaluation of a series. Surg Neurol 49:436–440
9. Dang L, White DW, Gross S et al (2009) Cancer-associated IDH1 mutations produce 2-hydroxyglutarate. Nature 462:739–744
10. Yan H, Parsons DW, Jin G et al (2009) IDH1 and IDH2 mutations in gliomas. N Engl J Med 360:765–773
11. Cancer Genome Atlas Research Network, Brat DJ, RGW V et al (2015) Comprehensive, integrative genomic analysis of diffuse lower-grade gliomas. N Engl J Med 372:2481–2498
12. Louis DN, Perry A, Burger P et al (2014) International Society of Neuropathology–Haarlem consensus guidelines for nervous system tumor classification and grading. Brain Pathol Zurich Switz 24:429–435
13. Eckel-Passow JE, Lachance DH, Molinaro AM et al (2015) Glioma groups based on 1p/19q, IDH, and TERT promoter mutations in tumors. N Engl J Med 372:2499–2508

14. Abudumijiti A, Chan AK-Y, Shi Z et al (2017) Adult IDH wild-type lower-grade gliomas should be further stratified. Neuro Oncol. https://doi.org/10.1093/neuonc/nox078
15. Suzuki Y, Shirai K, Oka K et al (2010) Higher pAkt expression predicts a significant worse prognosis in glioblastomas. J Radiat Res (Tokyo) 51:343–348
16. Reuss DE, Sahm F, Schrimpf D et al (2015) ATRX and IDH1-R132H immunohistochemistry with subsequent copy number analysis and IDH sequencing as a basis for an "integrated" diagnostic approach for adult astrocytoma, oligodendroglioma and glioblastoma. Acta Neuropathol (Berl) 129:133–146
17. Hartmann C, Hentschel B, Wick W et al (2010) Patients with IDH1 wild type anaplastic astrocytomas exhibit worse prognosis than IDH1-mutated glioblastomas, and IDH1 mutation status accounts for the unfavorable prognostic effect of higher age: implications for classification of gliomas. Acta Neuropathol (Berl) 120:707–718
18. Darlix A, Deverdun J, Menjot de Champfleur N et al (2017) IDH mutation and 1p19q codeletion distinguish two radiological patterns of diffuse low-grade gliomas. J Neurooncol 133:37–45
19. Metellus P, Coulibaly B, Colin C et al (2010) Absence of IDH mutation identifies a novel radiologic and molecular subtype of WHO grade II gliomas with dismal prognosis. Acta Neuropathol (Berl) 120:719–729
20. Patterson DM, Padhani AR, Collins DJ (2008) Technology insight: water diffusion MRI–a potential new biomarker of response to cancer therapy. Nat Clin Pract Oncol 5:220–233
21. Zhang L, Min Z, Tang M et al (2017) The utility of diffusion MRI with quantitative ADC measurements for differentiating high-grade from low-grade cerebral gliomas: Evidence from a meta-analysis. J Neurol Sci 373:9–15
22. Hempel J-M, Bisdas S, Schittenhelm J et al (2017) In vivo molecular profiling of human glioma using diffusion kurtosis imaging. J Neurooncol 131:93–101
23. Xiong J, Tan W, Wen J et al (2016) Combination of diffusion tensor imaging and conventional MRI correlates with isocitrate dehydrogenase 1/2 mutations but not 1p/19q genotyping in oligodendroglial tumours. Eur Radiol 26:1705–1715
24. Tan WL, Huang WY, Yin B et al (2014) Can diffusion tensor imaging noninvasively detect IDH1 gene mutations in astrogliomas? A retrospective study of 112 cases. AJNR Am J Neuroradiol 35:920–927
25. Han X, Suo S, Sun Y et al (2017) Apparent diffusion coefficient measurement in glioma: Influence of region-of-interest determination methods on apparent diffusion coefficient values, interobserver variability, time efficiency, and diagnostic ability. J Magn Reson Imaging JMRI 45:722–730
26. Pipe J (2009) Chapter 2 - pulse sequences for diffusion-weighted MRI. In: Johansen-Berg H, Behrens TEJ (eds) Diffusion MRI. Academic Press, San Diego, pp 11–35
27. Jenkinson M, Beckmann CF, Behrens TEJ et al (2012) FSL. NeuroImage 62:782–790
28. Yushkevich PA, Piven J, Hazlett HC et al (2006) User-guided 3D active contour segmentation of anatomical structures: significantly improved efficiency and reliability. NeuroImage 31:1116–1128
29. Jenkinson M, Bannister P, Brady M, Smith S (2002) Improved optimization for the robust and accurate linear registration and motion correction of brain images. NeuroImage 17:825–841
30. Jenkinson M, Smith S (2001) A global optimisation method for robust affine registration of brain images. Med Image Anal 5:143–156
31. Seiz M, Freyschlag CF, Schenkel S et al (2011) Management of patients with low-grade gliomas - a survey among German neurosurgical departments. Cent Eur Neurosurg 72:186–191
32. Khan OH, Mason W, Kongkham PN et al (2016) Neurosurgical management of adult diffuse low grade gliomas in Canada: a multi-center survey. J Neurooncol 126:137–149
33. Karavaeva E, Harris RJ, Leu K et al (2015) Relationship between [18F]FDOPA PET uptake, apparent diffusion coefficient (ADC), and proliferation rate in recurrent malignant gliomas. Mol Imaging Biol 17:434–442
34. Fudaba H, Shimomura T, Abe T et al (2014) Comparison of multiple parameters obtained on 3T pulsed arterial spin-labeling, diffusion tensor imaging, and MRS and the Ki-67 labeling index in evaluating glioma grading. AJNR Am J Neuroradiol 35:2091–2098
35. Ellingson BM, Malkin MG, Rand SD et al (2010) Validation of functional diffusion maps (fDMs) as a biomarker for human glioma cellularity. J Magn Reson Imaging JMRI 31:538–548
36. Higano S, Yun X, Kumabe T et al (2006) Malignant astrocytic tumors: clinical importance of apparent diffusion coefficient in prediction of grade and prognosis. Radiology 241:839–846
37. Miloushev VZ, Chow DS, Filippi CG (2015) Meta-analysis of diffusion metrics for the prediction of tumor grade in gliomas. AJNR Am J Neuroradiol 36:302–308
38. Zulfiqar M, Yousem DM, Lai H (2013) ADC values and prognosis of malignant astrocytomas: does lower ADC predict a worse prognosis independent of grade of tumor? A meta-analysis. AJR Am J Roentgenol 200:624–629
39. Cui Y, Ma L, Chen X et al (2014) Lower apparent diffusion coefficients indicate distinct prognosis in low-grade and high-grade glioma. J Neurooncol 119:377–385
40. Khayal IS, Vandenberg SR, Smith KJ et al (2011) MRI apparent diffusion coefficient reflects histopathologic subtype, axonal disruption, and tumor fraction in diffuse-type grade II gliomas. Neuro Oncol 13:1192–1201
41. Tozer DJ, Jäger HR, Danchaivijitr N et al (2007) Apparent diffusion coefficient histograms may predict low-grade glioma subtype. NMR Biomed 20:49–57
42. Clark K, Voronovich Z, Horbinski C (2013) How molecular testing can help (and hurt) in the workup of gliomas. Am J Clin Pathol 139:275–288
43. Leu K, Ott GA, Lai A et al (2017) Perfusion and diffusion MRI signatures in histologic and genetic subtypes of WHO grade II-III diffuse gliomas. J Neurooncol. https://doi.org/10.1007/s11060-0172506-9
44. Arponen O, Arponent O, Sudah M et al (2015) Diffusion-weighted imaging in 3.0 Tesla breast MRI: diagnostic performance and tumor characterization using small subregions vs. whole tumor regions of interest. PloS One 10:e0138702
45. Xing Z, Yang X, She D et al (2017) Noninvasive assessment of IDH mutational status in World Health Organization grade II and III astrocytomas using DWI and DSC-PWI combined with conventional MR imaging. AJNR Am J Neuroradiol 38:1138–1144
46. Lee S, Choi SH, Ryoo I et al (2015) Evaluation of the microenvironmental heterogeneity in high-grade gliomas with IDH1/2 gene mutation using histogram analysis of diffusion-weighted imaging and dynamic-susceptibility contrast perfusion imaging. J Neurooncol 121:141–150
47. Yamashita K, Hiwatashi A, Togao O et al (2016) MR imaging-based analysis of glioblastoma multiforme: estimation of IDH1 mutation status. AJNR Am J Neuroradiol 37:58–65
48. Kickingereder P, Sahm F, Radbruch A et al (2015) IDH mutation status is associated with a distinct hypoxia/angiogenesis transcriptome signature which is non-invasively predictable with rCBV imaging in human glioma. Sci Rep 5:16238
49. Andronesi OC, Rapalino O, Gerstner E et al (2013) Detection of oncogenic IDH1 mutations using magnetic resonance spectroscopy of 2-hydroxyglutarate. J Clin Invest 123:3659–3663
50. Lev MH, Ozsunar Y, Henson JW et al (2004) Glial tumor grading and outcome prediction using dynamic spin-echo MR susceptibility mapping compared with conventional contrast-enhanced MR: confounding effect of elevated rCBV of oligodendrogliomas [corrected]. AJNR Am J Neuroradiol 25:214–221

Published January 7, 2021 as 10.3174/ajnr.A6965

ORIGINAL RESEARCH
ADULT BRAIN

Regional and Volumetric Parameters for Diffusion-Weighted WHO Grade II and III Glioma Genotyping: A Method Comparison

S.C. Thust, J.A. Maynard, M. Benenati, S.J. Wastling, L. Mancini, Z. Jaunmuktane, S. Brandner, and H.R. Jäger

ABSTRACT

BACKGROUND AND PURPOSE: Studies consistently report lower ADC values in *isocitrate dehydrogenase* (*IDH*) wild-type gliomas than in *IDH* mutant tumors, but their methods and thresholds vary. This research aimed to compare volumetric and regional ADC measurement techniques for glioma genotyping, with a focus on *IDH* status prediction.

MATERIALS AND METHODS: Treatment-naïve World Health Organization grade II and III gliomas were analyzed by 3 neuroradiologist readers blinded to tissue results. ADC minimum and mean ROIs were defined in tumor and in normal-appearing white matter to calculate normalized values. T2-weighted tumor VOIs were registered to ADC maps with histogram parameters (mean, 2nd and 5th percentiles) extracted. Nonparametric testing (eta^2 and ANOVA) was performed to identify associations between ADC metrics and glioma genotypes. Logistic regression was used to probe the ability of VOI and ROI metrics to predict *IDH* status.

RESULTS: The study included 283 patients with 79 *IDH* wild-type and 204 *IDH* mutant gliomas. Across the study population, *IDH* status was most accurately predicted by ROI mean normalized ADC and VOI mean normalized ADC, with areas under the curve of 0.83 and 0.82, respectively. The results for ROI-based genotyping of nonenhancing and solid-patchy enhancing gliomas were comparable with volumetric parameters (area under the curve = 0.81–0.84). In rim-enhancing, centrally necrotic tumors (n = 23), only volumetric measurements were predictive (0.90).

CONCLUSIONS: Regional normalized mean ADC measurements are noninferior to volumetric segmentation for defining solid glioma *IDH* status. Partially necrotic, rim-enhancing tumors are unsuitable for ROI assessment and may benefit from volumetric ADC quantification.

ABBREVIATIONS: AUC = area under the curve; NAWM = normal-appearing white matter; min = minimum; 1p19q^{codel} = codeletion of the short arm of chromosome 1 and the long arm of chromosome 19; rADC = normalized ADC; WHO = World Health Organization

Diffuse gliomas of World Health Organization (WHO) grades II and III comprise a diverse group of tumors characterized by distinct genetic profiles and varied median survival.[1] Three major types of diffuse gliomas are found in adults: *isocitrate dehydrogenase* (*IDH*) wild-type gliomas with a molecular profile of *IDH* wild-type glioblastoma, *IDH* mutant astrocytoma (with p53 and *ATRX chromatin remodeler* [*ATRX*] mutations), and the *IDH* mutant oligodendroglioma with a codeletion of the short arm of chromosome 1p and the long arm of chromosome 19q (*IDH* mutant/1p19q^{codel}).[2] In addition to these major intrinsic neoplasms, multiple other tumor types exist, for example, with alterations in the map kinase pathway (*B-Raf proto-oncogene, serine/threonine kinase* [*BRAF*] mutations), histone mutations, and the distinct group of ependymal tumors.

IDH wild-type astrocytomas share glioblastoma-specific genetic mutations such as combined chromosome 7 gain and

Received July 11, 2020; accepted after revision October 19.

From the Neuroradiological Academic Unit (S.C.T., J.A.M., S.J.W., L.M., H.R.J.), Department of Brain, Repair and Rehabilitation, UCL Institute of Neurology, London, UK; Lysholm Department of Neuroradiology (S.C.T., J.A.M., M.B., S.J.W., L.M., H.R.J.), National Hospital for Neurology and Neurosurgery, London, UK; Imaging Department (S.C.T., H.R.J.), University College London Foundation Hospital, London, UK; Dipartimento di Diagnostica per Immagini (M.B.), Radioterapia, Oncologia ed Ematologia, Fondazione Policlinico Universitario A. Gemelli Institute for Research, Hospitalization and Health Care, Rome, Italy; and Departments of Clinical and Movement Neurosciences (Z.J.), and Neurodegenerative Disease (S.B.), UCL Queen Square Institute of Neurology, and Division of Neuropathology, National Hospital for Neurology and Neurosurgery, University College London Hospitals NHS Foundation Trust, London, UK.

S.C. Thust, Z. Jaunmuktane, and S. Brandner are supported by the Department of Health's National Institute of Health Research/Biomedical Research Center's funding scheme to the University College London Hospitals. No specific grant is associated with this research.

S.C. Thust, J.A. Maynard, and M. Benenati contributed equally to this work.

Please address correspondence to Stefanie Thust, MD, FRCR, Lysholm Department of Neuroradiology, National Hospital for Neurology and Neurosurgery, Queen Square, London WC1N 3BG, UK; e-mail: s.thust@ucl.ac.uk

Indicates open access to non-subscribers at www.ajnr.org
Indicates article with online supplemental data.
http://dx.doi.org/10.3174/ajnr.A6965

chromosome 10 loss, *epidermal growth factor receptor* (*EGFR*) amplification, and/or *telomerase reverse transcriptase* (*TERT*) promoter mutations[3] and have a short life expectancy.[3,4] Henceforth, with the term "*IDH* wild-type diffuse glioma," we will refer to molecular glioblastoma, *IDH* wild-type.

Rapid glioma genotyping is of prognostic importance and influences therapeutic planning; for example, *IDH* mutant/1p19q^{codel} gliomas are responsive to chemotherapy,[5] whereas in 1p19q intact (*IDH* mutant/1p19q intact) tumors, maximum safe resection appears critical to improve outcomes.[6] It remains uncertain to what extent the strategy of maximal glioblastoma resection[7,8] could prolong survival for diffusely infiltrative *IDH* wild-type gliomas in the WHO grade II and III stages.

A number of imaging techniques have shown the potential for glioma genotype predictions. Of these, conventional MR imaging has the advantage of universal availability, but mostly provides visual-anatomic features, some of which have limited reproducibility.[9,10] Advanced MR imaging techniques such as perfusion and spectroscopy provide physiologic, quantifiable tumor data but can have threshold overlap and lack of technical standardization.[11]

DWI is widely integrated into clinical glioma MR imaging protocols with tissue properties measurable at the time of reporting. DWI exploits the inverse relationship between free water motion in tissues and cellularity.[12] Differences in diffusion-weighted image signals have been shown for glioma WHO grades and, more recently, between genetic subtypes.[13,14] The finding of lower ADC values in *IDH* wild-type diffuse glioma compared with *IDH* mutant tumors is consistently reported; however, the methods and accuracy vary among studies, whereby published techniques include mean and minimum ROI measurements and, in some cases, volumetric ADC quantification.[13-16] Hypothetically, "entire lesion" analysis might provide the most representative information on any individual tumor, whereas ROI placements have the advantage of being minimally time-consuming in clinical workflow.

There are few data comparing regional and volumetric diffusivity measurements for glioma genotyping, currently limited to nonenhancing glioma evaluation. The purpose of this study was to compare the performance of whole-tumor ADC measurements with different ROI parameters for glioma molecular typing, with a focus on *IDH* status prediction.

MATERIALS AND METHODS

Patients

Ethics review board approval (University College London Hospitals and Health Research Authority, United Kingdom) was obtained with informed consent waived for this retrospective imaging data study. Consecutive patients diagnosed at our national brain tumor referral institution from July 2008 to January 2018 were eligible for the research.

Inclusion criteria consisted of histologic confirmation of WHO grade II and III glioma, documented *IDH* and 1p19q genetic test results, and available pretreatment MR imaging. Exclusion criteria were previous glioma treatment; a diagnosis other than WHO grade II and III gliomas; incomplete, inconclusive, or ambiguous molecular results (eg, *IDH* wild-type/1p19q^{codel}); a prolonged ($\geq$ year) interval from MR imaging to surgery; incomplete images; and failed volumetric image registration.

All tissue samples were analyzed at our neuropathology department, using the latest methodology according to the WHO 2016 Classification of CNS Tumors, as described previously.[17,18] Multiple gene Sanger sequencing was completed for *IDH* R132H-negative tumors to identify rarer *IDH* mutations, and the 1p/19q status was established through quantitative polymerase chain reaction–based copy number assay.

MR Imaging Acquisition and Postprocessing

All MR imaging examinations included T2-weighted, T2-FLAIR, and T1-weighted sequences; pre- and postadministration of a gadolinium-based contrast agent; and DWI sequences ($n = 211$ at 1.5T, $n = 79$ at 3T). Because our institution is a quaternary center, the imaging originated from 23 different MR imaging machines with no individual scanner contributing >14% of any glioma subtype. In the generation of an ADC map, the image acquired without diffusion gradients is divided by the image acquired with diffusion gradients, removing dependence on T1, T2, and TR.[19] Sufficient comparability of ADC among scanners has been demonstrated previously.[20] The range of MR imaging parameters used has been described in a prior component of the study.[21] ADC maps were calculated from 3-directional DWI acquired with 2 gradient values ($b = 0$ and $b = 1000$ s/mm^2) using proprietary software (Olea Sphere, Version 2.3; Olea Medical).

ROI Measurements

The ADC regional measurements were performed by 3 independent observers as detailed in Maynard et al,[21] blinded to tissue diagnosis. First, each observer sited small (30–40 mm^2) ROIs 3× into the visually perceived lowest ADC portions of each glioma (within ≥1 axial image slice), while remaining in the solid tumor component and avoiding apparent necrotic, hemorrhagic, or cystic areas or blood vessels, as identified on the relevant accompanying contrast-enhanced and other sequences. From these 3 ROIs, the mean value of the numerically lowest ADC measurement was designated minimum ADC (ADC_{min}) as described in Xing et al.[14]

Thereafter, 1 large ROI (ADC_{mean}) was placed to cover most of the largest axial tumor cross-section, excluding tumor margins, necrosis, macroscopic hemorrhage, and calcifications, as described in Thust et al.[22] Finally, a comparative ROI was positioned in the contralateral normal-appearing centrum semiovale white matter (ADC_{NAWM}), amounting to 5 ROI measurements per patient. Multifocal tumors were measured as 1 glioma.

Observer 1 analyzed all ($n = 290$) gliomas, observer 2 re-analyzed a subset of 75 gliomas, and observer 3 re-analyzed the remaining subset of 215 gliomas, totaling 2900 ADC measurements (ie, 5 ROIs by 2 observers per glioma, ie, 10×290 measurements). From these, the normalized minimum ADC ($rADC_{min}$, defined as ADC_{min}/ADC_{NAWM} ratio) and the mean normalized ADC ($rADC_{mean}$) (defined as ADC_{mean}/ADC_{NAWM} ratio) were calculated, resulting in 4 regional ADC parameters (ROI ADC_{min}, ROI $rADC_{min}$, ROI ADC_{mean}, and ROI

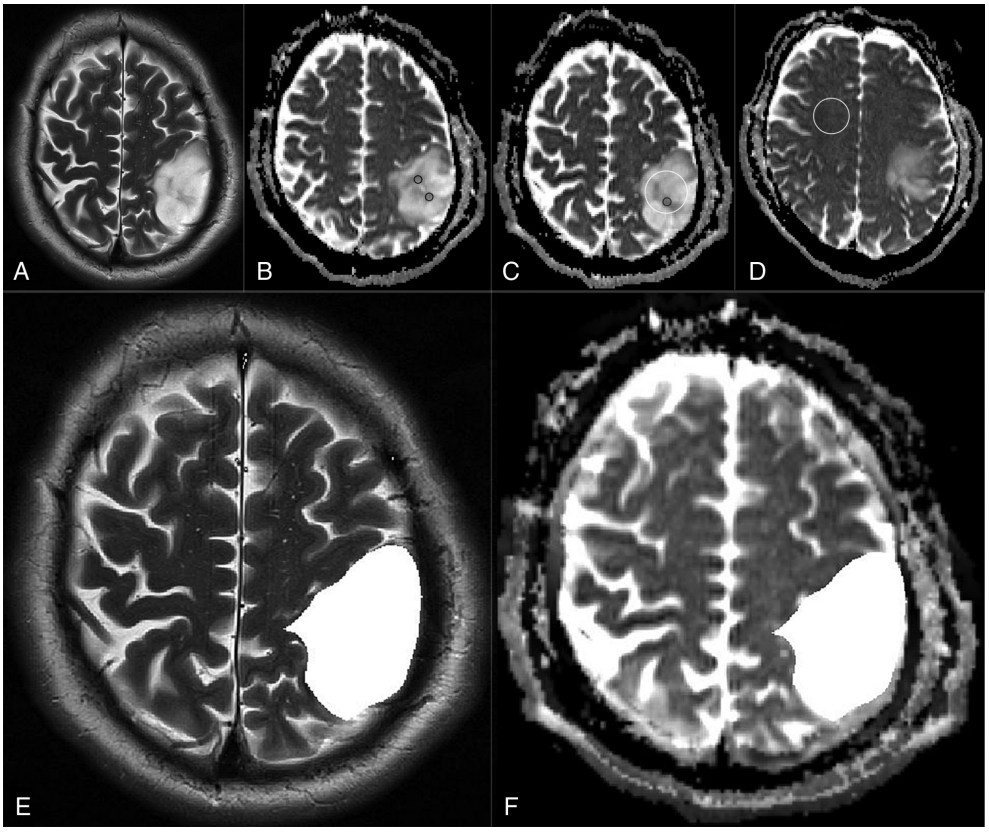

FIG 1. An example of regional and volumetric ADC measurements in a patient with *IDH* mutant 1p19q intact glioma. T2-weighted image (*A*) and ADC maps (*B–D*) show ADC_{min} (3 × 30–40 mm^2 (black, *B* and *C*), ADC_{mean} (white, *C*), and ADC_{NAWM} (white, *D*) ROI measurements. T2-weighted image (*E*) and ADC map (*F*) in the same patient demonstrate the volumetric segmentation and image registration, respectively.

$rADC_{mean}$) per glioma. An example of the ROI placements is shown in Fig 1*A–D*.

Volumetric ADC Histogram Analysis

Whole-tumor VOIs were segmented by a general radiologist (M.B., 5 years' experience) using the ITK-Snap Toolbox, Version 3.6 (www.itksnap.org[23]) following training and under supervision of a neuroradiologist specialized in brain tumor imaging (S.C.T, 9 years' experience). Segmentations incorporated the entire T2-weighted signal abnormality. For multicentric gliomas, the total volume of signal abnormality was treated as 1 lesion. To assess interobserver reproducibility, a proportion (10%) of gliomas was randomly chosen to undergo a repeat unsupervised segmentation by a second neuroradiologist (J.A.M., 4 years' experience, including brain tumor research).

ADC maps were then co-registered to T2-weighted sequences using the FMRIB Linear Image Registration Tool (FLIRT; http://www.fmrib.ox.ac.uk/fsl/fslwiki/FLIRT),[24,25] according to an affine 12-parameter model with the correlation ratio as a cost function, except in 15 cases in which manual review favored optimization of the registration by substitution of Normalized Mutual Information as the cost function. Subsequently, ADC histogram data were obtained for each tumor ROI, using an in-house script written in Python 2.7. For each tumor, the second and fifth ADC histogram percentiles, ADC mean, and the T2-weighted total lesion volume were extracted. Normalized histogram parameters were calculated using the same ROI ADC_{NAWM} value for the regional measurements to maximize direct comparability. An example of the volumetric segmentation is provided in Fig 1*E, -F*.

Enhancement Pattern Subgroup Analysis

Information on tumor enhancement, recorded as part of a preceding study,[21] was used for a subgroup analysis. Thus, the ability of ROI and VOI parameters to predict the *IDH* genotype was assessed separately for 3 morphologic groups: 1) nonenhancing, 2) solid-patchy enhancing, and 3) rim-enhancing, centrally necrotic gliomas. An example of the enhancement pattern distinction is provided in the Online Supplemental Data.

Patient demographics, *IDH*, and 1p19q genotypes of the study population

	All Glioma Subtypes	*IDH* Wild-Type	*IDH* Mutant/ 1p19q Intact	*IDH* Mutant/ 1p19q^{codel}
No. of patients = 283 (male/female = 164:119)	283	79	104	100
Median age (interquartile range) (yr)	40 (33–53)	59 (43–67)	35 (29–41)	40 (35–48)
Enhancement category[a]				
Nonenhancing	171	33	75	63
Solid-patchy enhancing	87	28	27	32
Rim-enhancing	23	18	0	5

Note:—1p19q^{codel} indicates codeletion of the short arm of chromosome 1 and the long arm of chromosome 19.
[a] In 2/283 patients, T1-weighted contrast-enhanced MR images were unavailable.

Statistical Analysis

All statistical testing was performed in SPSS 25 (IBM). The interobserver agreement for the ROI-derived ADC measurements and for the volumetric segmentations was assessed by intraclass correlation coefficient analysis, using a 2-way random effects model. For each ADC ROI, the mean of the observers' measurements was adopted as the final value. For the proportion of tumors that were segmented by 2 observers, the average of the volumetric ADC results was designated as the final value.

To compare the mean ranks of the groups of ADC values and glioma subtypes, we used the nonparametric Kruskal-Wallis ANOVA test, including the Dunn pair-wise comparisons with Bonferroni correction. The strength of the association between glioma subtype and ADC metrics was tested using eta^2 (η^2), which quantifies the percentage of variance in the dependent variable (ADC value) that is explained by >1 independent variable (glioma genotype).

Univariable logistic regression was applied to test which ROI or VOI ADC parameter best predicted glioma *IDH* status (with $P < .05$ considered significant). The Youden index was used to identify diagnostic thresholds for the most predictive parameter, as determined by the area under the curve (AUC). Nonparametric (Wilcoxon signed rank) testing was performed to assess differences between the region-derived and volumetric ADC values.

RESULTS

Patient Demographics

Of 515 patients identified as potentially eligible for the study, 42 were duplicates, and 190 met the exclusion criteria as follows: previous glioma treatment ($n = 60$), tumor other than WHO grade II or III glioma ($n = 43$ and $n = 1$ spinal cord tumor), ambiguous or incomplete molecular results ($n = 29$), no preoperative DWI ($n = 24$ and $n = 15$ ADC maps not computable), unavailable histopathology report ($n = 2$), prolonged (≥ 1 year) interval from MR imaging to surgery ($n = 3$), MRI artefact ($n = 5$), incomplete images ($n = 1$), and failed volumetric image registration ($n = 7$). Finally, 283 patients (median, 40 years of age; interquartile range, 33–53 years; 164 men) were included in the analysis. The demographic details for the study population are listed in the Table.

Observer Comparison

The reproducibility of the ROI ADC parameters and contrast-enhancement patterns among 3 independent raters has been established in preceding research (intraclass correlation coefficient = 0.83–0.96 and Cohen $\kappa = 0.69$–0.72, respectively).[21] In the current study, the concordance between the 2 observers for the twice-segmented tumor volumes ($n = 28$) was near-complete (intraclass correlation coefficient = 0.97–0.98). This information is further detailed in the Online Supplemental Data.

Association between ADC Values and IDH *Genotype*

Box and whisker plots showing a comparison between *IDH* mutant and *IDH* wild-type gliomas for ADC_{mean}, $rADC_{mean}$, ADC_{min}, and $rADC_{min}$ are shown in the Online Supplemental Data (VOI and ROI methods). Detailed results from the statistical analysis with Kruskal-Wallis and η^2 tests are provided in the Online Supplemental Data. For all regional parameters (ROI ADC_{min}, ROI $rADC_{min}$, ROI ADC_{mean}, and ROI $rADC_{mean}$), the ADC values significantly differed among the *IDH* wild-type, *IDH* mutant, 1p19q intact, and *IDH* mutant 1p19q^{codel} glioma groups ($P < .001$). VOI ADC_{mean} and VOI $rADC_{mean}$ also differed among the glioma molecular groups ($P < .001$).

VOI ADC_{min} and VOI $rADC_{min}$ differed between *IDH* wild-type and *IDH* mutant 1p19q^{codel} genotypes ($P = .003$ and $P < .001$, respectively). However, no significant difference in VOI ADC_{min} or VOI $rADC_{min}$ was shown between *IDH* mutant 1p19q intact and *IDH* mutant 1p19q^{codel} gliomas.

Wilcoxon signed rank testing confirmed statistically significant differences between the VOI and ROI results of the absolute and normalized ADC values ($P < .001$). The association between glioma genotype and diffusivity was strongest for ROI ADC_{mean} and ROI $rADC_{mean}$ values ($\eta^2 = 0.38$) across the study population, while also being substantial for ROI ADC_{min} and ROI $rADC_{min}$ ($\eta^2 = 0.28$–0.29).

The subgroup analysis according to the contrast-enhancement pattern revealed associations between ROI ADC_{mean} and ROI $rADC_{mean}$ values and genotype for nonenhancing gliomas ($n = 170$, $\eta^2 = 0.39$–0.41) and solid-patchy enhancing gliomas ($n = 85$, $\eta^2 = 0.24$–0.28). No association was evident between ROI ADC parameters and the rim-enhancing, centrally necrotic glioma *IDH* genotype ($n = 23$, $\eta^2 = 0.0$–0.05). The strongest association for the rim-enhancing gliomas was with VOI $rADC_{mean}$ values ($\eta^2 = 0.36$).

No correlation among *IDH* status, VOI ADC_{min}, and VOI $rADC_{min}$ was identified for nonenhancing gliomas ($\eta^2 = 0.02$–0.03). Across all regional and volumetric parameters, smaller η^2 effect sizes were observed for minimum ADC values compared with mean ADC values. The VOI ADC_{min} was tested as determined by either the 2nd or 5th percentile by histogram analysis, with consistently larger η^2 values observed between ADC_{min} and genotype when the 5th percentile was used. Thereafter, VOI ADC_{min} referred to the 5th percentile only.

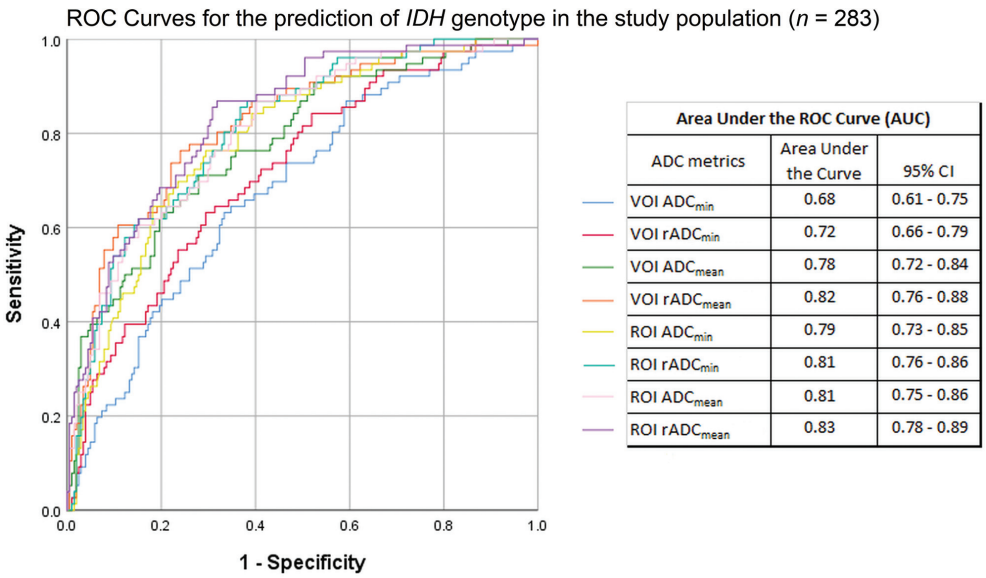

Area Under the ROC Curve (AUC)		
ADC metrics	Area Under the Curve	95% CI
VOI ADC_{min}	0.68	0.61 - 0.75
VOI $rADC_{min}$	0.72	0.66 - 0.79
VOI ADC_{mean}	0.78	0.72 - 0.84
VOI $rADC_{mean}$	0.82	0.76 - 0.88
ROI ADC_{min}	0.79	0.73 - 0.85
ROI $rADC_{min}$	0.81	0.76 - 0.86
ROI ADC_{mean}	0.81	0.75 - 0.86
ROI $rADC_{mean}$	0.83	0.78 - 0.89

FIG 2. ROC curves for the prediction of *IDH* genotype in the study population ($n = 283$).

Univariable Analysis for Prediction of IDH *Status*

The univariable analysis of regional and volumetric ADC metrics, when compared across all ($n = 283$) gliomas, showed that the most accurate prediction of *IDH* status was achieved using ROI $rADC_{mean}$ or VOI $rADC_{mean}$ (AUC = 0.83 and 0.82, respectively). The least accurate predictions were observed for VOI ADC_{min} (AUC = 0.68) and VOI $rADC_{min}$ (AUC = 0.72). The ROC curve analysis is presented in Fig 2, with additional results listed in the Online Supplemental Data.

When assessing nonenhancing gliomas alone, the ROI ADC_{mean} (AUC = 0.82) and ROI $rADC_{mean}$ (AUC = 0.84) results were almost equal to the VOI ADC_{mean} (AUC = 0.81) and VOI $rADC_{mean}$ (AUC = 0.84). For solid-patchy tumors, the ROI ADC_{mean} (AUC = 0.79) and ROI $rADC_{mean}$ (AUC = 0.81) were almost equal to the VOI ADC_{mean} (AUC = 0.78) and VOI $rADC_{mean}$ (AUC = 0.80), respectively.

Conversely, in rim-enhancing centrally necrotic lesions, only volumetric ADC results demonstrated a significant ability to predict *IDH* status (VOI ADC_{mean} [AUC = 0.84], VOI $rADC_{mean}$ [AUC = 0.90]), but not the ROI ADC_{mean} and ROI $rADC_{mean}$ values (AUC = 0.49–0.61). Given the lack of an association between the volumetric ADC_{min} parameters and *IDH* status, these were not further subjected to a subgroup analysis according to enhancement patterns.

DISCUSSION

This study investigated the comparability of region-derived and volumetric ADC values for WHO grade II and III glioma genotyping, specifically their performance for predicting *IDH* status. Our results indicate that the accuracy of regional measurements for solid glioma *IDH* typing is unimproved by performing whole-tumor segmentations (maximum AUC = 0.84 for VOI and ROI $rADC_{mean}$). However, for *IDH* status prediction in the small proportion of rim-enhancing, centrally necrotic tumors ($n = 23$), entire lesion ADC mean parameters were superior to solid-tumor ROI measurements. Throughout the study, mean ADC measurements appeared more accurate than ADC_{min} metrics, particularly if performing a volumetric analysis.

Before the discovery of glioma molecular subgroups, research was focused on testing the ability of ADC to predict glioma histologic grades, showing an inverse correlation between cellularity and diffusion.[26-28] More recently, Leu et al[13] demonstrated a stronger association between glioma ADC values and genotype than WHO grade. Specifically for *IDH* wild-type glioblastoma, no difference in diffusivity may exist between grades II and IV.[29] Villaneuva-Meyer et al[30] previously assessed ROI-derived minimum, mean, and maximum in WHO grade II gliomas: A minimum ADC threshold of 0.9×10^{-3} seconds/mm^2 provided the greatest sensitivity (91%) and specificity (76%) for *IDH* typing, with an AUC of 0.901.[19] ROI-based minimum ADC analysis was also performed by Wasserman et al[15] with a proposed cutoff point of 0.95×10^{-3} seconds/mm^2 (sensitivity of 76.9%, specificity of 65.2%, and AUC = 0.711)[13] and by Xing et al[14] with a suggested minimum ADC threshold of 1.01×10^{-3} seconds/mm^2 (sensitivity of 76.9%, specificity of 82.6%, AUC = 0.87).[15]

By means of ROI measurements, ADC_{min} and $rADC_{min}$ appeared valuable for *IDH* typing in our study, with optimal thresholds in the region of 1.07×10^{-3} seconds/mm^2 (sensitivity of 82.3%, specificity of 61.3%, AUC = 0.79) and 1.40 (sensitivity of 85.5%, specificity of 62.3%, AUC = 0.81), respectively. For an ROI ADC_{mean} threshold of 1.34×10^{-3} seconds/mm^2, a similar

sensitivity of 84.8%, specificity of 60.3%, and AUC of 0.81 were observed. For an $rADC_{mean}$ threshold of 1.75, the results were marginally better (sensitivity of 86.8%, specificity of 62.3, AUC = 0.83).

Across the whole study population, the largest ROI AUC (0.83) was observed for $rADC_{mean}$ values in our research. Liu et al[16] previously assessed glioma mean and minimum ADC, but only the results for mean ADC reached statistical significance ($P = .028$). Recently, in a study of normalized mean measurements for *IDH* typing of non-gadolinium-enhancing WHO grades II and III gliomas, an $rADC_{mean}$ threshold in the region of 1.8 was proposed.[22]

Several studies reported lower ADC values in *IDH* mutant $1p19q^{codel}$ oligodendrogliomas compared with *IDH* mutant 1p19q intact astrocytomas, with 2 studies indicating an ADC_{mean} threshold in the region of $1.4–1.6 \times 10^{-3}$ seconds/mm^2 for 1p19q genotyping.[31,32] However, similar to the reduced specificity of elevated perfusion (blood volume), which may be observed in low-grade oligodendrogliomas, erroneously low ADC values can occur in this tumor type despite its relatively good prognosis. A potential influence from extracellular matrix components is probable.[33] It is also noteworthy that measurements in calcified tumor components may underestimate ADC values and should be avoided.

From our results, it appears that ROI ADC_{mean} and $rADC_{mean}$ are slightly superior to minimum ROI ADC measurements for *IDH* genotyping of WHO grade II and III gliomas. Similarly, Han et al[34] investigated the variability of ADC values according to the ROI technique for glioma grading, with the mean ADC value of single-round ROI showing the highest effect size (0.72) and the greatest AUC (0.872), being superior to minimum measurements for the identification of high-grade gliomas. Within the aforementioned study, minimum ADC values also differed significantly between whole-volume and single-round ROI placements ($P = .003$),[34] indicating that these are not interchangeable.

It has been shown that volumetric tumor diffusivity analysis is not necessarily superior to ROI placements, for example, for WHO grading.[35] In 2 recent studies using ADC for H3 K27M histone-mutant glioma characterization, only the study using ROI measurements was predictive of genotype.[36,37]

It could be hypothesized that the previously reported lower accuracy of ADC for WHO grade IV glioblastoma *IDH* typing[38] could be related to the foci of necrosis. However, in our current study, the best prediction of *IDH* status for such masses was achieved using VOI $rADC_{mean}$ values derived from segmentation inclusive of necrosis, as opposed to ROI measurement in solid lesion components. Indeed, our data suggest that partially necrotic tumors may benefit from a volumetric diffusivity (VOI $rADC_{mean}$) assessment, but the small patient number ($n = 23$) in this subgroup is a limitation of our research. Furthermore, it is possible that in some cases of necrotic tumors, limited tissue sampling resulted in a WHO grade II and III diagnosis instead of glioblastoma.

Imperfections in the volumetric image registration at glioma margins due to ADC map distortion from susceptibility gradients and eddy current effects, which are not visible in the T2-weighted image data, could have contributed to volumetric minimum ADC measurements performing less well in our research.

While the binary discrimination of *IDH* wild-type from *IDH* mutant gliomas is imperfect, noninvasive identification of early glioblastoma stages could help prioritize tissue sampling in such circumstances in which observational management is initially favored or when waiting times to surgery could result in a diagnostic delay.

CONCLUSIONS

Regional diffusivity measurements are noninferior and are possibly preferable to volumetric histogram analysis for *IDH* status prediction of macroscopically solid WHO grade II and III gliomas. ROI $rADC_{mean}$ calculation is rapid and scanner-independent, thus easily introduced into clinical reporting. Partially necrotic, rim-enhancing lesions are unsuitable for ROI assessment and may benefit from volumetric ADC quantification for genotyping.

Disclosures: Stefanie C. Thust—*RELATED*: *Grant*: National Institute of Health Research/Biomedical Research Center funding scheme, *Comments*: University College London/University College London Hospitals receive proportional funding through the UK National Institute of Health Research/Biomedical Research Center funding scheme. No specific grant number is associated with the presented research.* Hans Rolf Jäger—*UNRELATED*: *Royalties*: payment by Springer of £1000, *Comments*: payment for co-editing the textbook *Clincal Neuroradiology*, published by Springer in 2019. *Money paid to the institution.

REFERENCES

1. Brat DJ, Verhaak RG, Aldape KD, et al; Cancer Genome Atlas Research Network. **Comprehensive, integrative genomic analysis of diffuse lower-grade gliomas.** *N Engl J Med* 2015;372:2481–98 CrossRef Medline
2. Louis DN, Perry A, Reifenberger G, et al. **The 2016 World Health Organization Classification of Tumors of the Central Nervous System: a summary.** *Acta Neuropathol* 2016;131:803–20 CrossRef Medline
3. Stichel D, Ebrahimi A, Reuss D, et al. **Distribution of EGFR amplification, combined chromosome 7 gain and chromosome 10 loss, and TERT promoter mutation in brain tumors and their potential for the reclassification of *IDH* wild type astrocytoma to glioblastoma.** *Acta Neuropathol* 2018;136:793–803 CrossRef Medline
4. Tesileanu CM, Dirven L, Wijnenga MM, et al. Survival of diffuse astrocytic glioma, IDH1/2-wild type, with molecular features of glioblastoma, WHO grade IV: a confirmation of the cIMPACT-NOW criteria. *Neuro Oncol* 2020;22:515–23 CrossRef Medline
5. van den Bent MJ, Brandes AA, Taphoorn MJ, et al. **Adjuvant procarbazine, lomustine, and vincristine chemotherapy in newly diagnosed anaplastic oligodendroglioma: long-term follow-up of EORTC brain tumor group study 26951.** *J Clin Oncol* 2013;31:344–50 CrossRef Medline
6. Wijnenga MM, French PJ, Dubbink HJ, et al. **The impact of surgery in molecularly defined low-grade glioma: an integrated clinical, radiological, and molecular analysis.** *Neuro Oncol* 2018;20:103–12 CrossRef Medline
7. Kreth FW, Thon N, Simon M, et al. **Gross total but not incomplete resection of glioblastoma prolongs survival in the era of radiochemotherapy.** *Ann Oncol* 2013;24:3117–23 CrossRef Medline
8. Li YM, Suki D, Hess K, et al. **The influence of maximum safe resection of glioblastoma on survival in 1229 patients: can we do better than gross-total resection?** *J Neurosurg* 2016;124:977–88 CrossRef Medline

9. Mazurowski MA, Desjardins A, Malof JM. **Imaging descriptors improve the predictive power of survival models for glioblastoma patients.** *Neuro Oncol* 2013;15:1389–94 CrossRef Medline
10. Hyare H, Rice L, Thust S, et al. **Modelling MR and clinical features in grade II/III astrocytomas to predict *IDH* mutation status.** *Eur J Radiol* 2019;114:120–27 CrossRef Medline
11. Thust SC, Heiland S, Falini A, et al. **Glioma imaging in Europe: a survey of 220 centres and recommendations for best clinical practice.** *Eur Radiol* 2018;28:3306–17 CrossRef Medline
12. Patterson DM, Padhani AR, Collins DJ. **Technology insight: water diffusion MRI–a potential new biomarker of response to cancer therapy.** *Nat Clin Pract Oncol* 2008;5:220–33 CrossRef Medline
13. Leu K, Ott GA, Lai A, et al. **Perfusion and diffusion MRI signatures in histologic and genetic subtypes of WHO grade II-III diffuse gliomas.** *J Neurooncol* 2017;134:177–88 CrossRef Medline
14. Xing Z, Yang X, She D, et al. **Noninvasive assessment of *IDH* mutational status in World Health Organization grade II and III astrocytomas using DWI and DSC-PWI combined with conventional MR imaging.** *AJNR Am J Neuroradiol* 2017;38:1138–44 CrossRef Medline
15. Wasserman JK, Nicholas G, Yaworski R, et al. **Radiological and pathological features associated with IDH1-R132H mutation status and early mortality in newly diagnosed anaplastic astrocytic tumours.** *PLoS One* 2015;10:e0123890 CrossRef Medline
16. Liu T, Cheng G, Kang X, et al. **Noninvasively evaluating the grading and IDH1 mutation status of diffuse gliomas by three-dimensional pseudo-continuous arterial spin labeling and diffusion-weighted imaging.** *Neuroradiology* 2018;60:693–702 CrossRef Medline
17. Jaunmuktane Z, Capper D, Jones DTW, et al. **Methylation array profiling of adult brain tumours: diagnostic outcomes in a large, single centre.** *Acta Neuropathol Commun* 2019;7:24 CrossRef Medline
18. Reuss DE, Sahm F, Schrimpf D, et al. **ATRX and IDH1-R132H immunohistochemistry with subsequent copy number analysis and *IDH* sequencing as a basis for an "integrated" diagnostic approach for adult astrocytoma, oligodendroglioma and glioblastoma.** *Acta Neuropathol* 2015;129:133–46 CrossRef Medline
19. Pipe J. Pulse sequences for diffusion-weighted MRI. In: Johansen-Berg H, Behrens TE, eds. *Diffusion MRI*. Academic Press; 2009:11–35
20. Grech-Sollars M, Hales PW, Miyazaki K, et al. **Multi-centre reproducibility of diffusion MRI parameters for clinical sequences in the brain.** *NMR Biomed* 2015;28:468–85 CrossRef Medline
21. Maynard J, Okuchi S, Wastling S, et al. **World Health Organization grade II/III glioma molecular status: prediction by MRI morphologic features and apparent diffusion coefficient.** *Radiology* 2020;296:111–21 CrossRef Medline
22. Thust SC, Hassanein S, Bisdas S, et al. **Apparent diffusion coefficient for molecular subtyping of non-gadolinium-enhancing WHO grade II/III glioma: volumetric segmentation versus two-dimensional region of interest analysis.** *Eur Radiol* 2018;28:3779–88 CrossRef Medline
23. Yushkevich PA, Piven J, Hazlett HC, et al. **User-guided 3D active contour segmentation of anatomical structures: significantly improved efficiency and reliability.** *Neuroimage* 2006;31:1116–28 CrossRef Medline
24. Jenkinson M, Bannister P, Brady M, et al. **Improved optimization for the robust and accurate linear registration and motion correction of brain images.** *Neuroimage* 2002;17:825–41 CrossRef Medline
25. Jenkinson M, Smith S. **A global optimisation method for robust affine registration of brain images.** *Med Image Anal* 2001;5:143–56 CrossRef Medline
26. Louis DN, Ohgaki H, Wiestler OD, et al. **The 2007 WHO Classification of Tumours of the Central Nervous System.** *Acta Neuropathol* 2007;114:97–109 CrossRef Medline
27. Hilario A, Ramos A, Perez-Nuñez A, et al. **The added value of apparent diffusion coefficient to cerebral blood volume in the preoperative grading of diffuse gliomas.** *AJNR Am J Neuroradiol* 2012;33:701–07 CrossRef Medline
28. Sugahara T, Korogi Y, Kochi M, et al. **Usefulness of diffusion-weighted MRI with echo-planar technique in the evaluation of cellularity in gliomas.** *J Magn Reson Imaging* 1999;9:53–60 CrossRef Medline
29. Figini M, Riva M, Graham M, et al. **Prediction of isocitrate dehydrogenase genotype in brain gliomas with MRI: single-shell versus multishell diffusion models.** *Radiology* 2018;289:788–96 CrossRef Medline
30. Villanueva-Meyer JE, Wood MD, Choi BS, et al. **MRI Features and *IDH* Mutational Status of Grade II Diffuse Gliomas: Impact on Diagnosis and Prognosis.** *American Journal of Roentgenology* 2018;210:621–28 CrossRef Medline
31. Johnson DR, Diehn FE, Giannini C, et al. **Genetically defined oligodendroglioma is characterized by indistinct tumor borders at MRI.** *AJNR Am J Neuroradiol* 2017;38:678–84 CrossRef Medline
32. Cui Y, Ma L, Chen X, et al. **Lower apparent diffusion coefficients indicate distinct prognosis in low-grade and high-grade glioma.** *J Neurooncol* 2014;119:377–85 CrossRef Medline
33. Sadeghi N, Camby I, Goldman S, et al. **Effect of hydrophilic components of the extracellular matrix on quantifiable diffusion-weighted imaging of human gliomas: preliminary results of correlating apparent diffusion coefficient values and hyaluronan expression level.** *AJR Am J Roentgenol* 2003;181:235–41 CrossRef Medline
34. Han X, Suo S, Sun Y, et al. **Apparent diffusion coefficient measurement in glioma: Influence of region-of-interest determination methods on apparent diffusion coefficient values, interobserver variability, time efficiency, and diagnostic ability.** *J Magn Reson Imaging* 2017;45:722–30 CrossRef Medline
35. Takano K, Kinoshita M, Arita H, et al. **Influence of region-of-interest designs on quantitative measurement of multimodal imaging of MR non-enhancing gliomas.** *Oncol Lett* 2018;15:7934–40 CrossRef Medline
36. Aboian MS, Tong E, Solomon DA, et al. **Diffusion characteristics of pediatric diffuse midline gliomas with histone H3-K27M mutation using apparent diffusion coefficient histogram analysis.** *AJNR Am J Neuroradiol* 2019;40:1804–10 CrossRef Medline
37. Chen H, Hu W, He H, et al. **Noninvasive assessment of H3 K27M mutational status in diffuse midline gliomas using apparent diffusion coefficient measurements.** *Eur J Radiol* 2019;114:152–59 CrossRef Medline
38. Tan WL, Huang WY, Yin B, et al. **Can diffusion tensor imaging noninvasively detect IDH1 gene mutations in astrogliomas? A retrospective study of 112 cases.** *AJNR Am J Neuroradiol* 2014;35:920–97 CrossRef Medline

Radiology

ORIGINAL RESEARCH • NEURORADIOLOGY

World Health Organization Grade II/III Glioma Molecular Status: Prediction by MRI Morphologic Features and Apparent Diffusion Coefficient

John Maynard, FRCR • Sachi Okuchi, PhD* • Stephen Wastling, PhD • Ayisha Al Busaidi, FRCR • Ofran Almossawi, MSc • Wonderboy Mbatha, MD • Sebastian Brandner, FRCPath, PhD • Zane Jaunmuktane, FRCPath, MD • Ali Murat Koc, MD • Laura Mancini, PhD • Rolf Jäger, MD, FRCR • Stefanie Thust, MD, FRCR*

From the Neuroradiological Academic Unit, Department of Brain, Repair and Rehabilitation, UCL Institute of Neurology, London, England (J.M., S.O., S.W., L.M., R.J., S.T.); Lysholm Department of Neuroradiology, National Hospital for Neurology and Neurosurgery, Queen Square, London WC1N 3BG, England (S.W., A.A.B., W.M., A.M.K., L.M., R.J., S.T.); Population, Policy and Practice Research Unit, UCL Great Ormond Street Institute of Child Health, London, England (O.A.); Department of Neurodegenerative Disease, UCL Institute of Neurology and Division of Neuropathology, National Hospital for Neurology and Neurosurgery, London, England (S.B., Z.J.); Department of Radiology, Izmir Bozyaka Education and Research Hospital, Izmir, Turkey (A.M.K.); and Department of Imaging, University College London Foundation Hospital, London, England (R.J., S.T.). Received August 15, 2019; revision requested October 1; revision received January 21, 2020; accepted February 10. **Address correspondence to** S.T. (e-mail: *s.thust@ucl.ac.uk*).

This study originates from University College London Hospitals, which receives a proportion of funding from the National Institute of Health Research Biomedical Research Centre.

* J.M. and S.O. contributed equally to this work.

Conflicts of interest are listed at the end of this article.

Radiology 2020; 296:11111–121 • https://doi.org/10.1148/radiol.2020191832 • Content codes: NR MR

Background: A readily implemented MRI biomarker for glioma genotyping is currently lacking.

Purpose: To evaluate clinically available MRI parameters for predicting isocitrate dehydrogenase (*IDH*) status in patients with glioma.

Materials and Methods: In this retrospective study of patients studied from July 2008 to February 2019, untreated World Health Organization (WHO) grade II/III gliomas were analyzed by three neuroradiologists blinded to tissue results. Apparent diffusion coefficient (ADC) minimum (ADC_{min}) and mean (ADC_{mean}) regions of interest were defined in tumor and normal appearing white matter (ADC_{NAWM}). A visual rating of anatomic features (T1 weighted, T1 weighted with contrast enhancement, T2 weighted, and fluid-attenuated inversion recovery) was performed. Interobserver comparison (intraclass correlation coefficient and Cohen κ) was followed by nonparametric (Kruskal-Wallis analysis of variance) testing of associations between ADC metrics and glioma genotypes, including Bonferroni correction for multiple testing. Descriptors with sufficient concordance (intraclass correlation coefficient, >0.8; $\kappa > 0.6$) underwent univariable analysis. Predictive variables ($P < .05$) were entered into a multivariable logistic regression and tested in an additional test sample of patients with glioma.

Results: The study included 290 patients (median age, 40 years; interquartile range, 33–52 years; 169 male patients) with 82 *IDH* wild-type, 107 *IDH* mutant/1p19q intact, and 101 *IDH* mutant/1p19q codeleted gliomas. Two predictive models incorporating ADC_{mean}-to-ADC_{NAWM} ratio, age, and morphologic characteristics, with model A mandating calcification result and model B recording cyst formation, classified tumor type with areas under the receiver operating characteristic curve of 0.94 (95% confidence interval [CI]: 0.91, 0.97) and 0.96 (95% CI: 0.93, 0.98), respectively. In the test sample of 49 gliomas (nine *IDH* wild type, 21 *IDH* mutant/*1p19q* intact, and 19 *IDH* mutant/*1p19q* codeleted), the classification accuracy was 40 of 49 gliomas (82%; 95% CI: 71%, 92%) for model A and 42 of 49 gliomas (86%; 95% CI: 76%, 96%) for model B.

Conclusion: Two algorithms that incorporated apparent diffusion coefficient values, age, and tumor morphologic characteristics predicted isocitrate dehydrogenase status in World Health Organization grade II/III gliomas on the basis of standard clinical MRI sequences alone.

Online supplemental material is available for this article.

A subgroup of lower-grade gliomas is characterized by genetic overlap with primary glioblastoma and exhibits similarly rapid disease progression (1,2). Such malignant neoplasms are indistinguishable from indolent astrocytomas by assessing proliferative indexes and cell morphologic features (3). Mutations in the isocitrate dehydrogenase (*IDH*) gene, most commonly *IDH1* (*R132H*), define most slow-growing gliomas (>70%) within the World Health Organization (WHO) histologic grades II/III (4). *IDH* mutations (IDH^{mut}) are absent (*IDH* wild-type [IDH^{wt}]) in lower-grade tumors of the primary glioblastoma spectrum, which further differ by genetic hallmarks of combined chromosome-7 gain and chromosome-10 loss, epidermal growth factor receptor amplification, and telomerase reverse transcriptase promoter mutations (2). Among IDH^{mut} gliomas, synchronous deletion of the short arm of chromosome 1 and long arm of chromosome 19 (IDH^{mut}/$1p19q^{del}$) constitutes a specific feature of oligodendrogliomas, whereas IDH^{mut} astrocytomas are mostly *1p19q* intact (IDH^{mut}/$1p19q^{int}$) (5). This genetic grouping serves an important clinical purpose of stratifying tumors with differential susceptibility to adjuvant treatment; for example, IDH^{mut}/$1p19q^{del}$ gliomas have greater sensitivity to alkylating chemotherapy (6).

Abbreviations

ADC = apparent diffusion coefficient, ADC_{mean} = mean ADC, ADC_{min} = minimum ADC, ADC_{NAWM} = ADC in normal-appearing white matter, AUC = area under the receiver operating characteristic curve, CI = confidence interval, FLAIR = fluid-attenuated inversion recovery, *IDH* = isocitrate dehydrogenase, IDH^{mut} = *IDH* mutation, IDH^{wt} = *IDH* wild-type, ROI = region of interest, WHO = World Health Organization

Summary

An algorithm on the basis of standard MRI sequences and age predicted isocitrate dehydrogenase status in lower-grade gliomas without advanced computational methods.

Key Results

- Apparent diffusion coefficient (ADC) measurements supported the distinction of nongadolinium chelate–enhancing and solid enhancing lower-grade glioma genotypes ($P < .001$).
- Glioma location, enhancement characteristics, calcification, and cyst formation were multivariable predictors of isocitrate dehydrogenase (*IDH*) status.
- Two predictive models incorporating ADC, age, and morphologic characteristics defined *IDH* genotype with accuracies of 92% and 91%.

Glioblastoma outcomes are improved with gross total gadolinium-based contrast agent–enhancing lesion resection (7) and potentially beyond this for T2 fluid-attenuated inversion recovery (FLAIR) component removal (8). The similarity between the biology of low-grade IDH^{wt} glioma and glioblastoma makes it crucial to identify glioblastoma early and separate it from the more favorable IDH^{mut} entities.

Diffusion-weighted MRI imaging is routinely used in cancer imaging. It functions on the assumption that free water motion in tissues diminishes with growing tumor cellularity (9). Three-direction diffusion-weighted imaging is widely performed and integrated into clinical glioma imaging protocols, and quantitative results are available immediately at reporting (10). Diffusion-based methods can support grading and have shown capability for *IDH* typing (11–13), including for gliomas in which there is no contrast enhancement (14). Prior studies (15) suggest that lesion properties such as location, internal architecture, and enhancement patterns differ between glioma genetic subtypes. Additionally, consideration of patient age may help diagnosis because it has been shown that IDH^{wt} gliomas are more common in older patients (16). The purpose of our study was to evaluate clinically available MRI parameters for predicting *IDH* status in patients with glioma.

Materials and Methods

Ethics review board approval was obtained and written informed consent was waived for this retrospective study.

Patient Cohort

All patients consecutively diagnosed with WHO grade II/III glioma at our national brain tumor referral institution between July 2008 and January 2018 were eligible for the study. Inclusion criteria were a proven histologic diagnosis of WHO grade II/III glioma, available *IDH* and *1p19q* genetic test results, and MRI examination before treatment.

Exclusion criteria included previous treatment for glioma; a tumor other than WHO grade II/III glioma; missing, inconclusive, or ambiguous molecular results (eg, IDH^{wt}/$1p19q^{del}$); prolonged (≥1 year) interval from MRI to operation; or missing images. In 44 of the 290 patients who were included, mean apparent diffusion coefficient (ADC; ADC_{mean}) values were reported in a previous study (14) that compared volumetric and regional ADC_{mean} measurements. In our study, multiple region-derived ADC metrics and morphologic descriptors were analyzed (by different observers) in these patients. Results derived from the original patient cohort (July 2008 to January 2018) were validated by using a previously unseen test sample of patients included between January 2018 and February 2019 (49 patients).

MRI Parameters

All MRI examinations included T2-weighted, T2-weighted FLAIR, and T1-weighted sequences before and after administration of a gadolinium-based contrast agent and diffusion-weighted imaging (211 examinations at 1.5 T and 79 examinations at 3.0 T). Our institution is a quaternary center and therefore the MRI examinations originated from multiple sites and systems (57 GE systems, 206 Siemens systems, 26 Phillips systems, and one Toshiba system). No machine model contributed more than 14% gliomas of one molecular subtype. The range of MRI parameters is provided in Table E1 (online).

Histopathologic Analysis

All tissue samples were fixed as paraffin blocks and analyzed at our institution's neuropathology department by using the latest method consistent with the WHO 2016 guidance on histopathologic analysis and immunohistochemistry (17). For *IDH R132H*–negative tumors, multiple-gene Sanger sequencing was performed to identify alternative *IDH* mutations. A quantitative polymerase chain reaction–based copy number assay was employed to determine 1p/19q status.

ADC Quantification

The ADC measurements were blinded to tissue diagnosis (reference standard), age, and other observers' results. Three independent observers (M.K., with 6 years of experience, and W.M., with 3 years of experience, both board-certified neuroradiologists; and S.O., a resident in training) placed three different 30–40-mm^2 regions of interest (ROIs) into the visually perceived lowest ADC portions of each glioma. From these, the mean value of the numerically lowest ADC ROI measurement was designated as the ADC minimum (ADC_{min}) as in Xing et al (11). Subsequently, one large ROI (ADC_{mean}) was drawn to cover the largest axial tumor cross-section, excluding tumor margins, necrosis, macroscopic hemorrhage, and calcifications. A comparative ADC ROI was placed in the normal-appearing white matter (ADC_{NAWM}), following a previous study (14), amounting to five ROIs per patient. Multifocal tumors were measured as one glioma. Observer 1 analyzed all 290 gliomas, observer 2 reanalyzed 75 gliomas, and observer 3 reanalyzed the remaining 215 gliomas, amounting to a

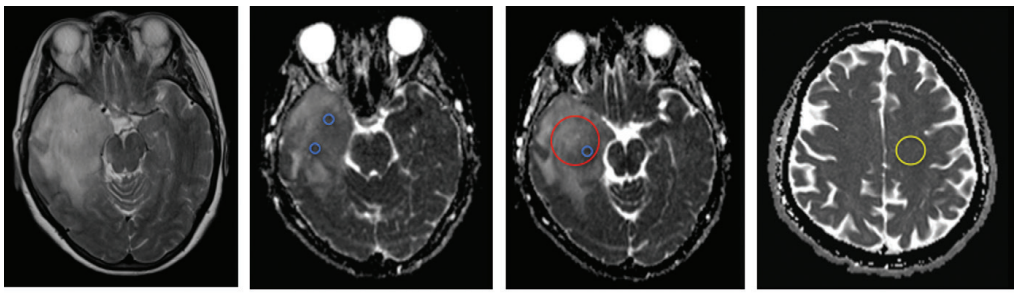

Figure 1: An example of apparent diffusion coefficient (ADC) measurements. **(a)** Axial T2-weighted image of a right temporal isocitrate dehydrogenase (*IDH*) wild-type glioma and **(b–d)** ADC maps showing the regions of interest used to determine minimum ADC (perceived lowest ADC regions [three per patient] blue), mean ADC (largest tumor cross-section measurement, red), and ADC in normal-appearing white matter (contralateral centrum semiovale, yellow). Note that round regions of interest were chosen because this method can be replicated on most picture archiving and communication systems.

total of 2900 ADC measurements. From these, ADC_{min}-to-ADC_{NAWM} and ADC_{mean}-to-ADC_{NAWM} ratios were calculated, resulting in four ADC parameters (ADC_{min}, ADC_{min}-to-ADC_{NAWM} ratio, ADC_{mean}, and ADC_{mean}-to-ADC_{NAWM} ratio) per patient.

For the test sample (n = 49), one researcher newly trained in the ADC method (A.A.B., a board-certified neuroradiologist with 3 years of experience) obtained all ADC values blinded as described. Figure 1 shows examples of the region placements.

Morphologic Assessment

Three observers (S.T., with 8 years of experience, and A.A.B., both board-certified neuroradiologists; and S.O., a resident) independently reviewed 290 MRI data sets and were blinded to diagnosis and the results of other observers. Morphologic readings were performed at a separate time (>2 weeks later than evaluation of ADC measurements). Feature categories were adapted on the basis of previous publications (16,18). Tumor location was specified by epicenter, with locations grouped according to the frequency of IDH^{wt} status to reduce the number of variables for statistical analysis. Multifocality was marked positive if more than one discrete tumor deposit was visible or if three or more lobes were involved. The nonenhancing tumor margin was described by using a visual rating scale as follows: 1, able to clearly draw around the lesion on T2-weighted images; to 4, indistinct margin on T2-weighted and FLAIR images. Hemorrhage and calcification were assessed at T1-weighted imaging together with CT, T2* sequences, and susceptibility-weighted imaging, as available. The option *uncertain* was added for these categories to allow for variability in the diagnostic sequences. The single largest tumor diameter was measured on T2-weighted images according to Pignatti et al (19). Contrast agent uptake was categorized into nonenhancing, patchy or solid, or rim enhancing. Rim enhancement surrounding central necrosis was distinguished from cysts, defined as exhibiting fluid signal isointense to cerebrospinal fluid with absent or minimal rim enhancement. T2-weighted FLAIR mismatch was specified according to Patel et al (20). Examples of different morphologic features of gliomas are shown in Figure 2.

Statistical Analysis

Statistical testing was performed by using software (SPSS 25, IBM, Armonk, NY; and Stata 15, Statacorp, College Station, Tex). The concordance of ADC measurements between observers was examined by intraclass correlation coefficient analysis, with a two-way random-effects model. For each ADC region of interest, the mean of the observers' measurements was adopted as the final value.

Cohen κ testing was used to evaluate the observer agreement for morphologic categories, and the majority opinion of the raters was designated the final value. If three opinions differed, it was resolved in consensus.

The relation between ADC and glioma subtypes was analyzed by using nonparametric testing (Kruskal-Wallis analysis of variance), including Dunn pairwise comparisons with Bonferroni correction. The strength of the association between glioma subtype and ADC metrics was probed by using Eta^2 (η^2). Eta^2 quantifies the percentage of variance in the dependent variable (ADC value) that is explained by one or more independent variables (glioma subtype).

Univariable logistic regression was applied to test if ADC metrics, age, or morphologic criteria could predict IDH^{wt} status. Nagelkerke (Pseudo) R^2 was used as a summary statistic expressing the degree to which the overall model predicts the variation in the outcome (IDH^{wt} status). Youden index was used to identify a diagnostic threshold for the most predictive (by area under the receiver operating characteristic curve [AUC] and R^2) ADC parameter. Morphologic categories with κ values of 0.6 or greater were subjected to univariable analysis. If significant ($P < .05$) at univariable analysis, features with substantial agreement (intraclass correlation coefficient > 0.8; κ > 0.6) were tested as predictor variables in a multivariable binomial logistic regression to predict glioma IDH^{wt} versus IDH^{mut} status. Starting from the highest P value, a backward elimination process by using the likelihood ratio test was applied to discard features that did not contribute significantly to the prediction, concluding with the most parsimonious model to identify *IDH* status. By the same method, an additional backward elimination was performed to develop an alternative model, into which

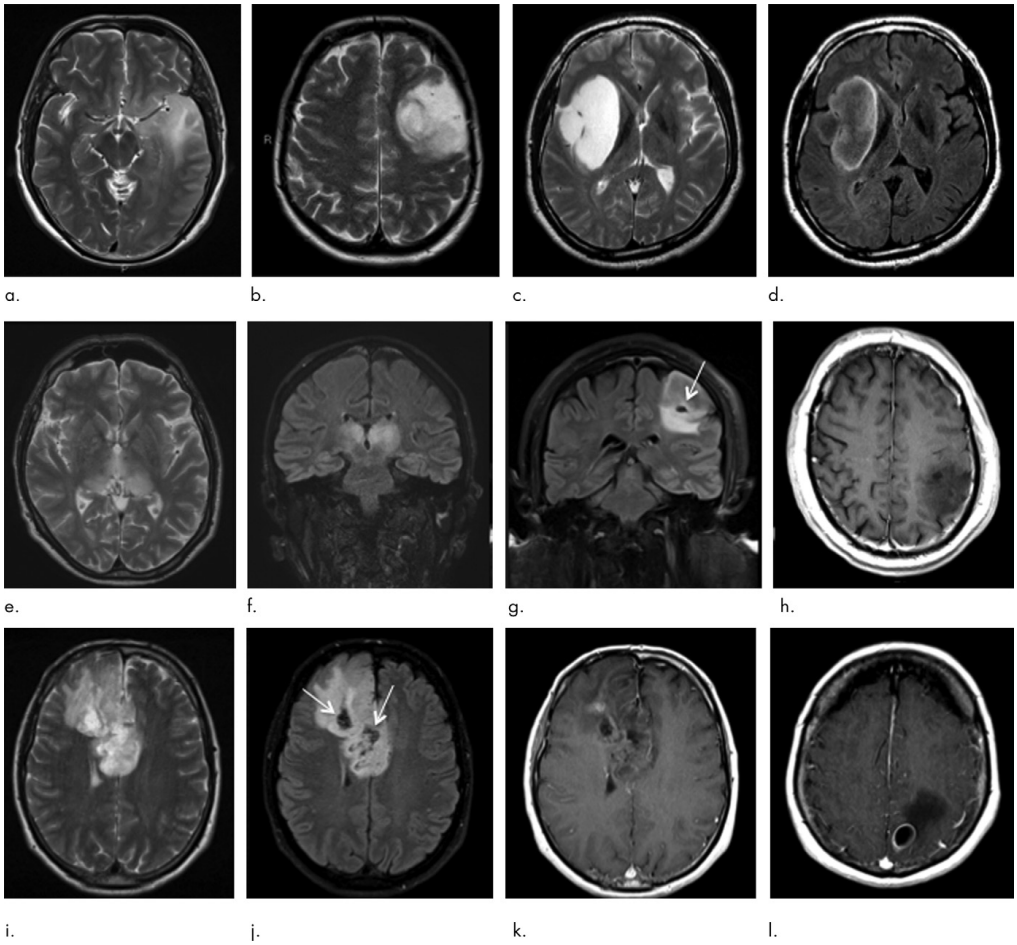

Figure 2: Glioma morphologic characteristics. **(a, b)** T2-weighted images show a temporal isocitrate dehydrogenase (*IDH*) wild-type (IDH^{wt}) glioma (**a**) versus another patient with a frontal *IDH* mutant (IDH^{mut})/*1p19q* codeleted ($1p19q^{del}$) glioma (**b**). Nonenhancing tumor margins: **(c, d)** T2-weighted and fluid-attenuated inversion recovery (FLAIR) images show distinct borders (also a T2-FLAIR mismatch sign) in an IDH^{mut}/*1p19q* intact (IDH^{mut}/$1p19q^{wt}$) glioma versus **(e, f)** the indistinct margin of a bithalamic IDH^{wt} glioma. Cyst formation and enhancement patterns: **(g, h)** IDH^{mut}/$1p19q^{wt}$ astrocytoma show a small cyst (arrow in **g**) nearly isointense to cerebrospinal fluid on FLAIR image without contrast agent uptake; **(i–k)** T2-weighted, FLAIR, and contrast-enhanced T1-weighted images show small cysts (arrows in **j**) and patchy contrast uptake in a IDH^{mut} $1p19q^{del}$ oligodendroglioma; **(l)** contrast-enhanced T1-weighted image shows rim enhancement surrounding central necrosis in an IDH^{wt} glioma.

calcification status was not entered, to allow for the clinical situation in which this may be unavailable from the existing imaging (eg, no CT and no T2*/susceptibility-weighted imaging performed). To assess model discrimination, we used a receiver operating characteristic analysis for both final models.

The numerical results from the multivariable regression developed with the study sample (n = 290) were then transcribed into a spreadsheet (Microsoft Excel for Mac version 14.5.2; Microsoft, Redmond, Wash) formula to calculate the IDH^{wt} status probability for individual patients with glioma in the subsequent test sample (n = 49) of previously unseen gliomas.

Results

Patient Demographics

At the start of the study, 515 patients were eligible for inclusion. After removal of duplicates (n = 42), 183 patients were excluded because of previous treatment for glioma (n = 60), tumor other than WHO grade II/III glioma (n = 43, and one cord tumor), ambiguous molecular result (n = 29), no preoperative diffusion-weighted imaging (n = 24, and 15 ADC map not computable), missing histopathologic report (n = 2), prolonged (≥1 year)

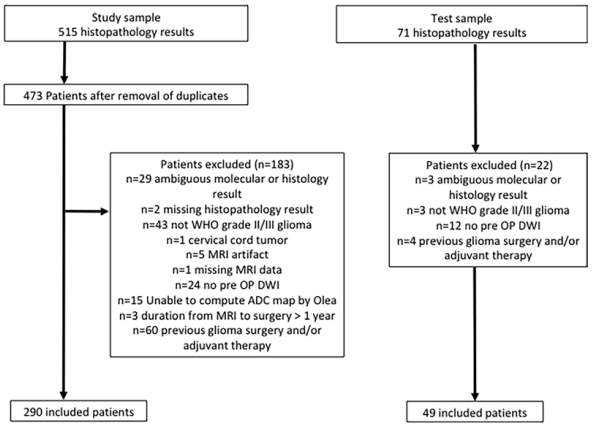

Figure 3: Patient selection flowchart. ADC = apparent diffusion coefficient, DWI = diffusion-weighted imaging, OP = operation, WHO = World Health Organization.

interval from MRI to operation (n = 3), or missing images (n = 1). A total of 290 patients (median age, 40 years; interquartile range, 33–52 years; 169 male patients) were included in the analysis of the study sample (patient inclusion from June 2008 to January 2018). An overview of the case selection process is in Figure 3. An overview of patient demographics and molecular groups is in Table 1. The relation between glioma *IDH* status and age was found to be nonlinear, with an exponential rise in the likelihood of IDH^{wt} status toward older age.

ADC Quantification for Glioma Molecular Subtyping

The interobserver reproducibility was good to excellent for all ADC parameters (intraclass correlation coefficient, 0.83–0.96). Consistency and absolute agreement were identical, indicating no systematic difference between the raters. Detailed intraclass correlation coefficient test results are shown in Table E2 (online). Each of the ADC parameters enabled IDH^{mut}/$1p19q^{del}$ IDH^{mut}/$1p19q^{int}$, and IDH^{wt} glioma discrimination ($P < .01$; Table E3, Fig E1 [online]).

Eta^2 (η^2) testing revealed an association between ADC values and glioma subtype for nongadolinium-enhancing and solidly enhancing tumors (η^2 = 0.28–0.42), but not for rim-enhanced masses (η^2 = 0–0.3) (Table E4 [online]). Across all gliomas, an ADC_{mean}-to-ADC_{NAWM} ratio of 1.8 predicted *IDH* status with a sensitivity of 69 of 79 (87%) and specificity of 124 of 208 (60%). For unenhanced gliomas, an ADC_{mean}-to-ADC_{NAWM} ratio threshold of 1.8 yielded a sensitivity of 28 of 33 (85%) and specificity of 93 of 140 (66%) for IDH^{wt} identification, compared with a sensitivity of 32 of 33 (97%) and specificity of 76 of 140 (54%) for a higher ADC_{mean}-to-ADC_{NAWM} ratio threshold of 1.9 (Fig 4).

Morphologic Assessment

For tumor location, the agreement between the three observers was good (κ = 0.81–0.89; $P < .001$; Table E5 [online]). Measurement of the single longest tumor diameter (<6 cm or ≥6 cm) demonstrated good agreement (κ = 0.80–0.82; $P \leq .001$). Defining calcification as present reached substantial agreement (κ = 0.67–0.74; $P \leq .001$) with uncertain results (eg, missing sequences) excluded. In 63.4% (184 of 290) of patients, one of three raters marked calcification as uncertain. In 11.7% (34 of 290), more than one rater specified calcification status as uncertain. The opinion of the raters regarding tumor cysts showed substantial agreement (κ = 0.66–0.70; $P \leq .001$). The categorization of enhancement patterns yielded substantial agreement (weighted κ = 0.69–0.77; $P \leq .001$).

Moderate interobserver agreement was found for unenhanced tumor margin (weighted κ = 0.45–0.61; $P \leq .001$) and for the T2-weighted FLAIR mismatch sign (κ = 0.44–0.62; $P < .001$). Fair agreement was observed for multifocality (κ = 0.20–0.46; $P < .001$) and hemorrhage (κ = 0.29–0.51; $P < .001$).

Univariable Analysis

The univariable logistic regression results are in Table 2 and Table E6 (online). Several features were statistically significant predictors, including all four ADC metrics (negative association), age (negative association), and several morphologic categories (enhancement pattern, nonenhancing margin, calcification, and cysts). ADC_{mean}-to-ADC_{NAWM} ratio was deemed the best-performing ADC parameter (AUC, 0.83; R^2 = 0.38). For the remaining diffusion parameters, the AUC values were marginally lower (AUCs: ADC_{min}, 0.78; ADC_{min}-to-ADC_{NAWM} ratio, 0.8; and ADC_{mean}, 0.81). Locations were grouped according to whether less than one-third, one- to two-thirds, or more than two-thirds of tumors represented IDH^{wt} gliomas to reduce the number of variables for statistical analysis. The presence of calcification was positively associated (odds ratio, 2.2; $P < .001$) with $1p19q^{del}$ status in IDH^{mut} gliomas (not tabulated). Tumor diameter and T2-FLAIR mismatch sign demonstrated no association with *IDH* status.

Multivariable Logistic Regression Model

The multivariable regression results are listed in Table 2 and Figure 5. The best-performing model (model A) for predicting IDH^{wt} (n = 82) versus IDH^{mut} (n = 208; 107 IDH^{mut}/$1p19q^{int}$ and 101 *IDH* IDH^{mut}/$1p19q^{del}$) genotype consisted of ADC_{mean}-to-ADC_{NAWM} ratio, age in years + age^2 (joint term), enhancement pattern, tumor location category (three groups: frontal or insula region, thalamus or brainstem, or elsewhere), and absence of calcification. On the basis of a likelihood cutoff value of 0.5 (50%), model A correctly classified 231 of 252 (91.6%; 95% confidence interval [CI]: 88%, 95%) gliomas, with an AUC of 0.96 (95% CI: 0.93, 0.98). In developing this model A, 38 of 290 (13.1%) patients were excluded by the statistics software; 33 patients were excluded because of uncertain calcification status as per the majority result of the raters, three patients were excluded because of absent ADC ratio values from tumor infiltration of normal-appearing white matter, one patient was excluded because of absent contrast

Table 1: Patient Demographics

Parameter	All Glioma Subtypes	IDH^{wt}	$IDH^{mut}/1p19q^{int}$	$IDH^{mut}/1p19q^{del}$
No. of patients	290	82	107*	101
Median age (y)	40 (17–77) [33–52]	58.50 (20–77) [24.25]	35 (17–66) [13]	40 (19–76) [13.50]
Enhancement category				
Nonenhancing	174	34	77	63
Patchy enhancing	89	28	28	33
Rim enhancing	25	20	0	5
Tumor location category				
Front or insula†	163	24	69	70
Other‡	113	45	37	31
Thalamus or brainstem§	14	13	1	0
Absence of calcification‖				
Noncalcified	225	70	94	61
Calcified	31	4	4	23
Absence of cyst or cysts				
Noncystic	189	73	58	58
Cystic	101	9	49	43
Hemorrhage#				
None	238	63	96	79
Petechial	7	5	2	0
Macroscopic	11	5	2	4
T2-weighted FLAIR mismatch				
Present	51	0	46	5
Absent	239	82	61	96
Diameter**				
≥6 cm	121	32	47	42
<6 cm	162	43	60	59

Note.—The study sample included 290 patients (169 men and 121 women). Data in parentheses are range and data in brackets are interquartile range. FLAIR = fluid-attenuated inversion recovery, *IDH* = isocitrate dehydrogenase, IDH^{wt} = *IDH* wild type, $IDH^{mut}/1p19q^{int}$ = *IDH* mutant and *1p19q* intact, $IDH^{mut}/1p19q^{del}$ = IDH mutant with synchronous deletion of the short arm of chromosome 1 and long arm of chromosome 19, IQR = interquartile range.

* Two patients within the IDH^{mut}/1p19q^{int} group had no postcontrast imaging available for assessment.

† The lesion was located in the frontal lobe or the insula.

‡ The lesion was in a location other than the frontal lobe, insula, thalamus, or brainstem.

§ The lesion was located in the thalamus or the brainstem.

‖ Calcification status was evaluated as uncertain in a total of 34 patients.

Hemorrhage status was evaluated as uncertain in a total of 34 patients.

** Single largest tumor diameter could not be clearly measured in a total of seven patients.

agent administration, and one patient was excluded because of both absent contrast agent administration and uncertain calcification status.

An alternative model (model B), derived by the same backward elimination method (except for not considering calcification status), performed nearly as well, achieving a correct classification of *IDH* status in 259 of 285 (90.9%; 95% CI: 88%, 94%) gliomas (AUC, 0.94; 95% CI: 0.93, 0.98). In the design of model B, the variable *no_calcification* was intentionally not entered to replicate the clinical situation where this information might be unavailable. Model B consisted of ADC_{mean}-to-ADC_{NAWM} ratio, age in years + age^2 (joint term), enhancement pattern, tumor location category, and absence of tumor cyst or cysts. For additional details on the logistic regression analysis, please see Table E6 (online). The diagnostic contribution from age and tumor morphologic structure is in Figures 6 and 7.

Test Sample

The numerical results from the study sample were transcribed into a software formula (Microsoft Excel for Mac version 14.5.2, Microsoft; see Note in Table 2) to calculate the IDH^{wt} status probability for individual patients with glioma in the subsequent test sample.

In the sample of patients with newly diagnosed glioma (n = 49; nine patients with IDH^{wt}, 21 patients with $IDH^{mut}/1p19q^{int}$, and 19 patients with $IDH^{mut}/1p19q^{del}$), the single blinded rater (A.A.B.) replicated the method of the main study. In cases of uncertainty regarding calcification (n = 5), the term *no calcification* was specified to permit results calculation.

Model A correctly classified *IDH* mutational status in 40 of 49 gliomas (82%; 95% CI: 71%, 93%), with 89% sensitivity and 80% specificity. Model B predicted *IDH* status in 42 of 49 (86%; 95% CI: 76%, 96%) gliomas, with a lower sensitivity of 67% but greater specificity of 90%.

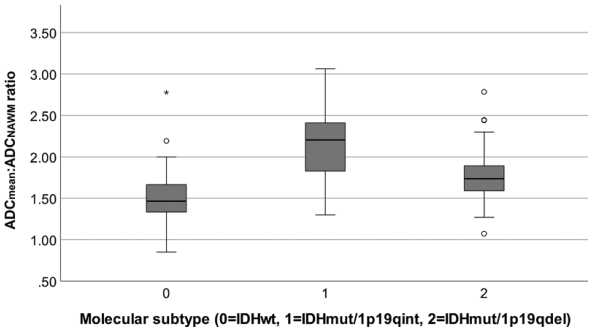

Figure 4: Boxplot shows differences in the apparent diffusion coefficient (ADC) values (mean ADC [ADC_{mean}]-to−normal-appearing white matter ADC [ADC_{NAWM}] ratio) between World Health Organization grade II/III glioma molecular subtypes in the study sample (82 wild-type isocitrate dehydrogenase [*IDH*; *IDH*wt]; 208 *IDH* mutation [*IDH*mut; 107 *IDH*mut/*1p19*qint, and 101 *IDH*mut/*1p19*qdel).

Table 2: Univariable and Multivariable Binomial Logistic Regression Results for Prediction of Glioma *IDH*^{wt} Status in the Study Sample versus *IDH*^{mut}/1p19q^{int} or *IDH*^{mut}/1p19q^{del}

	Univariable Analyses		Multivariable Model A		Multivariable Model B	
Parameter	β Level	*P* Value	β Level	*P* Value	β Level	*P* Value
ADC_{mean}-to-ADC_{NAWM} ratio	−4.4	<.001	−5.7 (−8.1, −3.4)	<.001	−3.2 (−4.9, −1.6)	<.001
Age (y)	.09	<.001	−.05 (−.31, .21)	.71*	−.1 (−.3, .11)	.37*
Age^2 (y)	.01	<.001	.002 (.04 · 10^{-3}, .004)	.21*	.002 (.04 · 10^{-3}, .004)	.09*
Enhancement (categorical)						
Nonenhancing	Ref	Ref	Ref	Ref	Ref	Ref
Patchy enhancing	.64	.03	−.32 (−1.44, .81)	.58	−.41 (−1.4, .6)	.4
Rim enhancing	2.8	<.001	2.96 (.57, 5.34)	.02	1.7 (.3, 3.1)	.02
Tumor location category						
Front or insula†	Ref	Ref	Ref	Ref	Ref	Ref
Other‡	1.3	<.001	.78 (−.21, 1.76)	.12	.9 (.05, 1.7)	.04
Thalamus or brainstem§	4.3	<.001	3.6 (.9, 6.3)	.01	3.6 (1.3, 6.0)	.002
Absence of calcification	1.1	.045	4.3 (2.01, 6.7)	<.001	NA	
Absence of cyst(s)	1.9	<.001	NA		1.2 (.2, 2.2)	.02
Constant	NA		2.2 (−4.9, 9.4)	.54	3.1 (−2.8, 9.0)	.31
R^2	NA		.75		.65	

Note.—Data in parentheses are 95% confidence intervals. Numbers were rounded by one digit for publication. There were 82 patients in the study sample, 107 patients in the *IDH*^{mut}/1p10q^{int} group, and 101 patients in the *IDH*^{mut}/1p19q^{del} group. By using the multivariable regression results, a formula was designed to calculate the likelihood of wild-type isocitrate dehydrogenase (*IDH*) status for individual patients with glioma. The log odds ratios for models A and B are as follows: [L_A = (−5.71 × ADC_{mean}-to-ADC_{NAWM} ratio) + (−0.05 × age) + (0.002 × age^2) + (−0.32 × solid contrast enhancement) + (2.96 × rim contrast enhancement) + (0.78 × tumor location = other) + (3.58 × tumor location in thalamus or brainstem) + (4.34 × absent calcification) + 2.24] and [L_B = (-3.23 × ADC_{mean}-to-ADC_{NAWM} ratio) + (−0.1 × age) + (0.002 × age^2) + (−0.41 × solid contrast enhancement) + (1.66 × rim contrast enhancement) + (0.86 × tumor location = other) + (3.64 × tumor location in thalamus or brainstem) + (1.17 × absent cyst or cysts) + 3.07], respectively, where *solid contrast enhancement* and *rim contrast enhancement* pattern is 1 if present, 0 if absent, with each tumor assigned to one contrast enhancement category only; *tumor location* is 1 if in this category, 0 if not in this category; and *calcification* (model A)/cyst or cysts (model B) is 1 if present, 0 if absent (note the reversal is intentional). The probability of *IDH*^{wt} was calculated for models A and B by using the following equation: $1/(1 + e^{-L})$, where L is the relevant log odds ratio. ADC = apparent diffusion coefficient, ADC_{mean} = mean ADC, ADC_{NAWM} = ADC of normal-appearing white matter, *IDH*^{mut} = *IDH* mutation, *IDH*^{wt} = wild-type *IDH*, NA = not applicable, Ref = reference category.

* Age and age^2 are considered joint terms, hence a joint significance test was applicable. This was significant at $P < .001$, which combined with the likelihood ratio test confirmed a significant contribution of age to the prediction model.

† Indicates that the lesion was in the frontal lobe or the insula.

‡ Indicates that the lesion was in a location other than the frontal, insula, thalamus, or brainstem.

§ Indicates that the lesion was located in the thalamus or the brainstem.

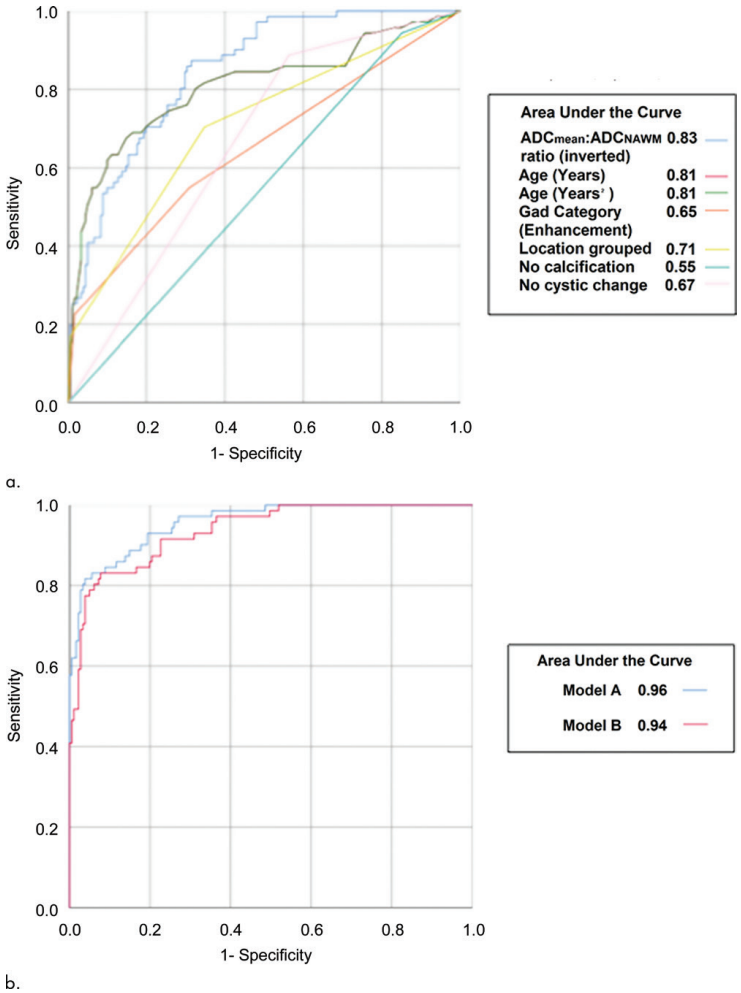

Figure 5: Univariable and multivariable logistic regression analysis to predict isocitrate dehydrogenase (*IDH*) status in the study sample (82 wild-type *IDH* [IDH^{wt}] and 208 *IDH* mutation [IDH^{mut};107 IDH^{mut}/*1p19q*^{int} and 101 IDH^{mut}/*1p19q*^{del}]). **(a)** Receiver operating characteristic curves show age and selected imaging features to predict (IDH^{wt}) glioma and **(b)** receiver operating characteristic curves of the multivariable probabilities for model A and B from Table 2 show similar model performance. Model A consisted of mean ADC (ADC_{mean})-to−ADC in normal-appearing white matter (ADC_{NAWM}) ratio, age in years + age^2 (joint term), enhancement pattern, tumor location category (three groups: frontal or insula region, thalamus or brainstem, or elsewhere), and absence of calcification. Model B consisted of ADC_{mean}-to-ADC_{NAWM} ratio, age in years + age^2 (joint term), enhancement pattern, tumor location category, and absence of tumor cyst or cysts.

Of the IDH^{mut} gliomas that were erroneously diagnosed as IDH^{wt} (eight gliomas by using model A and four gliomas by using model B), 75% (six of eight and three of four, respectively) were IDH^{mut}/*1p19q*^{del} with an average ADC_{mean}-to-ADC_{NAWM} ratio of 1.43 (ranging from 1.21 to 1.76). One IDH^{mut}/*1p19q*^{int} astrocytoma with an ADC_{mean}-to-ADC_{NAWM} ratio of 1.84 was misclassified by both models in an elderly patient (age, 81 years), and one anaplastic IDH^{mut}/*1p19q*^{int} astrocytoma with an ADC_{mean}-to-ADC_{NAWM} ratio of 1.46 was misclassified by model A alone. The IDH^{wt} gliomas erroneously predicted as IDH^{mut} tumors (one of nine, model A; three of nine, model B) had ADC_{mean}-to-ADC_{NAWM} ratio values of 1.73–1.87. At subsequent review, all misclassified IDH^{wt} tumors exhibited a gliomatosis growth pattern with diffusely T2-weighted hyperintense infiltration of three or more lobes. In one IDH^{wt} glioma, the comparison ADC_{NAWM} ROI was sited in artifact (Nyquist ghost of scalp fat).

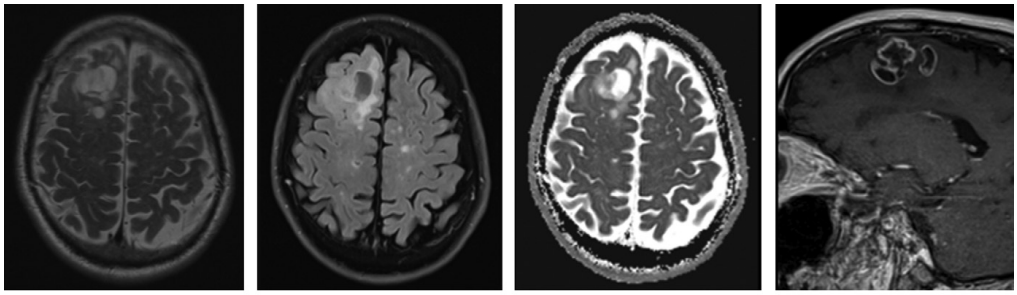

a. b. c. d.

Figure 6: Images in a patient in whom the contribution of age and glioma morphologic structure resulted in correct isocitrate dehydrogenase (*IDH*) status classification over apparent diffusion coefficient alone. **(a)** T2-weighted, **(b)** fluid-attenuated inversion recovery, **(c)** apparent diffusion coefficient (ADC), and **(d)** T1-weighted gadolinium chelate–enhanced images in a male patient age 75 years with an *IDH* wild-type glioma tumor with high solid component diffusivity (mean ADC-to-ADC in normal-appearing white matter ratio, 2.19) and a rim-enhancement pattern.

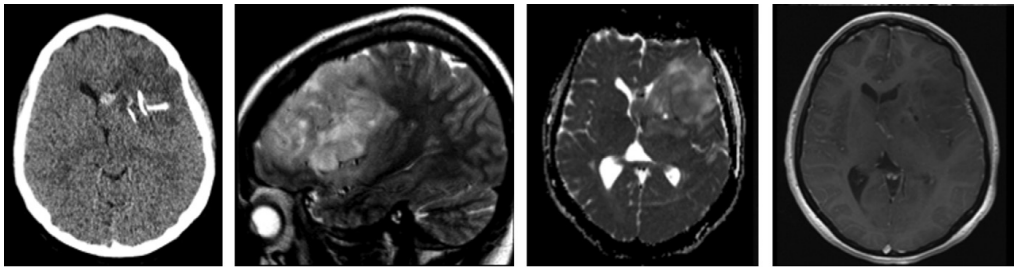

a. b. c. d.

Figure 7: Images in a patient in whom the contribution of age and glioma morphologic structure resulted in correct isocitrate dehydrogenase (*IDH*) status classification over apparent diffusion coefficient (ADC) alone. **(a)** Noncontrast-enhanced CT, **(b)** T2-weighted, **(c)** ADC, and **(d)** T1-weighted gadolinium chelate–enhanced images in a male patient age 45 years with a calcified *IDH* mutant/1p19q codeleted oligodendroglioma (mean ADC-to-ADC in normal-appearing white matter ratio of 1.07).

Discussion

In this study, the combination of apparent diffusion coefficient (ADC) region of interest measurements (mean apparent diffusion coefficient [ADC; ADC_{mean}]-to–normal-appearing gray matter ADC [ADC_{NAWM}] ratio) and morphologic descriptors (enhancement, calcification, and cyst formation) measured at standard MRI (10) permitted isocitrate dehydrogenase (*IDH*) genotyping of lower-grade gliomas (area under the receiver operating characteristic curve [AUC], 0.94–0.96; study sample, 290 patients). Two models, model A (mandating calcification result) and model B (recording cyst formation), were developed, which correctly classified *IDH* status with similar accuracy (82% and 86%, respectively) in a previously unseen test sample (n = 49) of World Health Organization II/III gliomas. By using ADC values alone, significant differences were observed between *IDH* mutation (IDH^{mut})/$1p19q^{del}$, IDH^{mut}/$1p19q^{int}$, and *IDH* wild-type (IDH^{wt}) glioma subtypes ($P < .001$), but the *IDH* status prediction was less precise (AUC, 0.83 for ADC_{mean}-to-ADC_{NAWM} ratio).

Volumetric (12,14) and region-derived minimum (11) and mean (14) ADC measurements were previously used to estimate WHO grade II/III glioma IDH status. Our study confirms excellent (intraclass correlation coefficient, 0.83–0.96) interobserver agreement for ROI measurements, consistent with the reproducibility of ADC values described in other cancer research (21). Whereas ADC values are independent of hardware and field strength at fixed parameters (22), the use of a ratio offers the further advantage of being vendor neutral. Drawing one maximum-size round ADC_{mean} ROI in the largest tumor cross-section is considered feasible on most clinical workstations. Good reproducibility was shown previously for two observers by using ADC_{mean}-to-ADC_{NAWM} ratio regions of interest, representative of entire lesion volumetric measurements (14). In our analysis, three observers used the technique in the study sample, and one observer in the test sample, amounting to a total of six different observers between the studies. It is hypothesized that most lower-grade gliomas are sufficiently homogeneous to make such ROI measurements reliable.

When testing ADC_{mean}-to-ADC_{NAWM} ratio for *IDH* typing, we confirmed a threshold in the region of 1.8 (14), applicable to solid tumors with or without contrast enhancement. ADC values appear unreliable for *IDH* typing in rim-enhanced necrotic gliomas even when measured in macroscopically solid components, which mirrors a previous study (23) of WHO grade IV glioblastoma.

The accuracy of ADC_{mean}-to-ADC_{NAWM} ratio alone for predicting WHO II/III grade glioma *IDH* status in our study (AUC, 0.83 across all tumor morphologic characteristics) exceeded that of published approaches by using multishell diffusion (neurite orientation dispersion and density imaging; AUC maximum, 0.76) (24) and diffusion kurtosis (AUC maximum, 0.72 [25] and 0.79 [26]). The ADC_{mean}-to-ADC_{NAWM} ratio was a highly significant predictor ($P < .001$) in both multivariable models, indicating a strong inverse relationship between ADC and the likelihood of IDH^{wt} status.

Because the qualitative description of glioma features is subjective, we limited the statistical modeling to morphologic categories with substantial agreement such as tumor location. Frontal glioma location has repeatedly been associated with IDH^{mut} status (27,28). Gozé et al (29) found 100% of insula-centered low-grade gliomas to be IDH^{mut}. In our study, both locations were similarly associated with a greater likelihood of IDH^{mut} status, which is also consistent with a report by Xiong et al (30). Conversely, we confirmed that thalamic or brainstem location is predominantly a feature of IDH^{wt}, which may variably be associated with malignant glioma mutations such as *H3 K27M* (31).

In our study, the presence versus absence of solid enhancement was not consistently associated with IDH status (multivariable P = .41–.58). However, glioblastoma morphologic characteristics featuring rim enhancement was a predictor of IDH^{wt} status. We did not test percentage enhancement, which in a study by Delfanti et al (27) failed to predict *IDH* type.

The absence of calcification strongly correlated with IDH^{wt} status and negatively with $1p19q^{del}$ at univariable analysis. In a study by Kanazawa et al (18), both calcification and cysts were significantly related to $IDH^{mut}/1p19q^{del}$. We hypothesize that in many patients undergoing CT at diagnosis, consistent availability of this and/or susceptibility-weighted imaging could further increase observer certainty and concordance. In keeping with our observations (model B), absence of cysts has been proposed previously as an IDH^{wt} glioma feature (32).

In our study sample, there was no association between multifocality and *IDH* status, which was recently proposed as a feature predictive of IDH^{wt} in WHO grade II glioma (33). Our results support that the T2-FLAIR mismatch sign is a specific feature of $IDH^{mut}/1p19q^{int}$ status. However, the interobserver agreement was moderate (κ = 0.44–0.62), closer to the lower 95% CI bound (κ = 0.53) of the original publication by Patel et al (20). The T2-FLAIR mismatch sign did not directly predict *IDH* status because all molecular glioma subtypes can lack this feature. For nonenhancing margin definition, the agreement was moderate, meaning that although IDH^{wt} gliomas are less well demarcated (16,34), subjectivity and overlap with $IDH^{mut}/1p19q^{del}$ indistinct margins (35) limit the reproducibility of this feature.

Our study had some limitations, including its retrospective design and that it lacked a definitive calcification result in a proportion of patients. Both models may have a misclassification risk for low diffusivity $IDH^{mut}/1p19q^{del}$ oligodendrogliomas and for IDH^{wt} tumors exhibiting a T2-weighted and ADC hyperintense gliomatosis growth pattern. We have not tested the models on WHO grade IV gliomas.

In conclusion, the combination of mean apparent diffusion coefficient (ADC)-to–normal-appearing white matter ADC ratio, tumor morphologic characteristics, and age predicted the presence of isocitrate dehydrogenase (*IDH)* wild-type glioma versus *IDH* mutation tumor types with high accuracy.

Author contributions: Guarantors of integrity of entire study, J.M., S.T.; study concepts/study design or data acquisition or data analysis/interpretation, all authors; manuscript drafting or manuscript revision for important intellectual content, J.M., S.W., R.J., S.T.; approval of final version of submitted manuscript, all authors; agrees to ensure any questions related to the work are appropriately resolved, all authors; literature research, J.M., W.M., R.J., S.T.; clinical studies, J.M., S.O., A.A.B., W.M., S.B., A.M.K., R.J., S.T.; statistical analysis, J.M., S.W., O.A., S.T.; and manuscript editing, all authors

Disclosures of Conflicts of Interest: J.M. disclosed no relevant relationships. **S.O.** disclosed no relevant relationships. **S.W.** disclosed no relevant relationships. **A.A.B.** disclosed no relevant relationships. **O.A.** disclosed no relevant relationships. **W.M.** disclosed no relevant relationships. **S.B.** disclosed no relevant relationships. **Z.J.** disclosed no relevant relationships. **A.M.K.** disclosed no relevant relationships. **L.M.** disclosed no relevant relationships. **R.J.** disclosed no relevant relationships. **S.T.** disclosed no relevant relationships.

References

1. Eckel-Passow JE, Lachance DH, Molinaro AM, et al. Glioma Groups Based on 1p/19q, IDH, and TERT Promoter Mutations in Tumors. N Engl J Med 2015;372(26):2499–2508.
2. Stichel D, Ebrahimi A, Reuss D, et al. Distribution of EGFR amplification, combined chromosome 7 gain and chromosome 10 loss, and TERT promoter mutation in brain tumors and their potential for the reclassification of IDHwt astrocytoma to glioblastoma. Acta Neuropathol (Berl) 2018;136(5):793–803.
3. Louis DN, Perry A, Burger P, et al. International Society Of Neuropathology--Haarlem consensus guidelines for nervous system tumor classification and grading. Brain Pathol 2014;24(5):429–435.
4. Yan H, Parsons DW, Jin G, et al. IDH1 and IDH2 mutations in gliomas. N Engl J Med 2009;360(8):765–773.
5. Cancer Genome Atlas Research Network, Brat DJ, Verhaak RG, et al. Comprehensive, Integrative Genomic Analysis of Diffuse Lower-Grade Gliomas. N Engl J Med 2015;372(26):2481–2498.
6. van den Bent MJ, Brandes AA, Taphoorn MJB, et al. Adjuvant procarbazine, lomustine, and vincristine chemotherapy in newly diagnosed anaplastic oligodendroglioma: long-term follow-up of EORTC brain tumor group study 26951. J Clin Oncol 2013;31(3):344–350.
7. Kreth FW, Thon N, Simon M, et al. Gross total but not incomplete resection of glioblastoma prolongs survival in the era of radiochemotherapy. Ann Oncol 2013;24(12):3117–3123.
8. Li YM, Suki D, Hess K, Sawaya R. The influence of maximum safe resection of glioblastoma on survival in 1229 patients: Can we do better than gross-total resection? J Neurosurg 2016;124(4):977–988.
9. Patterson DM, Padhani AR, Collins DJ. Technology insight: water diffusion MRI--a potential new biomarker of response to cancer therapy. Nat Clin Pract Oncol 2008;5(4):220–233.
10. Thust SC, Heiland S, Falini A, et al. Glioma imaging in Europe: A survey of 220 centres and recommendations for best clinical practice. Eur Radiol 2018;28(8):3306–3317.
11. Xing Z, Yang X, She D, Lin Y, Zhang Y, Cao D. Noninvasive Assessment of *IDH* Mutational Status in World Health Organization Grade II and III Astrocytomas Using DWI and DSC-PWI Combined with Conventional MR Imaging. AJNR Am J Neuroradiol 2017;38(6):1138–1144.
12. Leu K, Ott GA, Lai A, et al. Perfusion and diffusion MRI signatures in histologic and genetic subtypes of WHO grade II-III diffuse gliomas. J Neurooncol 2017;134(1):177–188.
13. Hempel JM, Schittenhelm J, Brendle C, et al. Histogram analysis of diffusion kurtosis imaging estimates for in vivo assessment of 2016 WHO glioma grades: A cross-sectional observational study. Eur J Radiol 2017;95:202–211.
14. Thust SC, Hassanein S, Bisdas S, et al. Apparent diffusion coefficient for molecular subtyping of non-gadolinium-enhancing WHO grade II/III glioma: volumetric segmentation versus two-dimensional region of interest analysis. Eur Radiol 2018;28(9):3779–3788.
15. Juratli TA, Tummala SS, Riedl A, et al. Radiographic assessment of contrast enhancement and T2/FLAIR mismatch sign in lower grade gliomas: correlation with molecular groups. J Neurooncol 2019;141(2):327–335.

16. Zhou H, Vallières M, Bai HX, et al. MRI features predict survival and molecular markers in diffuse lower-grade gliomas. Neuro Oncol 2017;19(6):862–870.
17. Reuss DE, Sahm F, Schrimpf D, et al. ATRX and IDH1-R132H immunohistochemistry with subsequent copy number analysis and IDH sequencing as a basis for an "integrated" diagnostic approach for adult astrocytoma, oligodendroglioma and glioblastoma. Acta Neuropathol (Berl) 2015;129(1):133–146.
18. Kanazawa T, Fujiwara H, Takahashi H, et al. Imaging scoring systems for preoperative molecular diagnoses of lower-grade gliomas. Neurosurg Rev 2019;42(2):433–441.
19. Pignatti F, van den Bent M, Curran D, et al. Prognostic factors for survival in adult patients with cerebral low-grade glioma. J Clin Oncol 2002;20(8):2076–2084.
20. Patel SH, Poisson LM, Brat DJ, et al. T2-FLAIR Mismatch, an Imaging Biomarker for IDH and 1p/19q Status in Lower-grade Gliomas: A TCGA/TCIA Project. Clin Cancer Res 2017;23(20):6078–6085.
21. Newitt DC, Zhang Z, Gibbs JE, et al. Test-retest repeatability and reproducibility of ADC measures by breast DWI: Results from the ACRIN 6698 trial. J Magn Reson Imaging 2019;49(6):1617–1628.
22. Ogura A, Tamura T, Ozaki M, et al. Apparent Diffusion Coefficient Value Is Not Dependent on Magnetic Resonance Systems and Field Strength Under Fixed Imaging Parameters in Brain. J Comput Assist Tomogr 2015;39(5):760–765.
23. Tan WL, Huang WY, Yin B, Xiong J, Wu JS, Geng DY. Can diffusion tensor imaging noninvasively detect IDH1 gene mutations in astrogliomas? A retrospective study of 112 cases. AJNR Am J Neuroradiol 2014;35(5):920–927.
24. Figini M, Riva M, Graham M, et al. Prediction of Isocitrate Dehydrogenase Genotype in Brain Gliomas with MRI: Single-Shell versus Multishell Diffusion Models. Radiology 2018;289(3):788–796.
25. Zhao J, Wang YL, Li XB, et al. Comparative analysis of the diffusion kurtosis imaging and diffusion tensor imaging in grading gliomas, predicting tumour cell proliferation and IDH-1 gene mutation status. J Neurooncol 2019;141(1):195–203.
26. Tan Y, Zhang H, Wang X, et al. Comparing the value of DKI and DTI in detecting isocitrate dehydrogenase genotype of astrocytomas. Clin Radiol 2019;74(4):314–320.
27. Delfanti RL, Piccioni DE, Handwerker J, et al. Imaging correlates for the 2016 update on WHO classification of grade II/III gliomas: implications for IDH, 1p/19q and ATRX status. J Neurooncol 2017;135(3):601–609 [Published correction appears in J Neurooncol 2017;135(3):611.].
28. Sonoda Y, Shibahara I, Kawaguchi T, et al. Association between molecular alterations and tumor location and MRI characteristics in anaplastic gliomas. Brain Tumor Pathol 2015;32(2):99–104.
29. Gozé C, Mansour L, Rigau V, Duffau H. Distinct IDH1/IDH2 mutation profiles in purely insular versus paralimbic WHO Grade II gliomas. J Neurosurg 2013;118(4):866–872.
30. Xiong J, Tan W, Wen J, et al. Combination of diffusion tensor imaging and conventional MRI correlates with isocitrate dehydrogenase 1/2 mutations but not 1p/19q genotyping in oligodendroglial tumours. Eur Radiol 2016;26(6):1705–1715.
31. Reyes-Botero G, Giry M, Mokhtari K, et al. Molecular analysis of diffuse intrinsic brainstem gliomas in adults. J Neurooncol 2014;116(2):405–411.
32. Wu CC, Jain R, Radmanesh A, et al. Predicting Genotype and Survival in Glioma Using Standard Clinical MR Imaging Apparent Diffusion Coefficient Images: A Pilot Study from The Cancer Genome Atlas. AJNR Am J Neuroradiol 2018;39(10):1814–1820.
33. Villanueva-Meyer JE, Wood MD, Choi BS, et al. MRI Features and IDH Mutational Status of Grade II Diffuse Gliomas: Impact on Diagnosis and Prognosis. AJR Am J Roentgenol 2018;210(3):621–628.
34. Park YW, Han K, Ahn SS, et al. Prediction of *IDH1*-Mutation and 1p/19q-Codeletion Status Using Preoperative MR Imaging Phenotypes in Lower Grade Gliomas. AJNR Am J Neuroradiol 2018;39(1):37–42.
35. Johnson DR, Diehn FE, Giannini C, et al. Genetically Defined Oligodendroglioma Is Characterized by Indistinct Tumor Borders at MRI. AJNR Am J Neuroradiol 2017;38(4):678–684.

Radiology

Erratum

Originally published in:
Radiology 2020;296(1):111–121
DOI:10.1148/radiol.2020191832

World Health Organization Grade II/III Glioma Molecular Status: Prediction by MRI Morphologic Features and Apparent Diffusion Coefficient

John Maynard, Sachi Okuchi, Stephen Wastling, Ayisha Al Busaidi, Ofran Almossawi, Wonderboy Mbatha, Sebastian Brandner, Zane Jaunmuktane, Ali Murat Koc, Laura Mancini, Rolf Jäger, Stefanie Thust

Erratum in:
DOI:10.1148/radiol.2020209024

The correct second affiliation for Ali Murat Koc should have been listed as follows: **Department of Radiology, Izmir Bozyaka Education and Research Hospital, Izmir, Turkey**.

Original Article

Imaging characteristics of H3 K27M histone-mutant diffuse midline glioma in teenagers and adults

Stefanie Thust[1,2], Caroline Micallef[1,2], Sachi Okuchi[1,2], Sebastian Brandner[3], Atul Kumar[3], Kshitij Mankad[4], Stephen Wastling[1,2], Laura Mancini[1,2], Hans Rolf Jäger[1,2], Ananth Shankar[5]

[1]Neuroradiological Academic Unit, Department of Brain Repair and Rehabilitation, UCL Institute of Neurology, London, UK; [2]Lysholm Department of Neuroradiology, The National Hospital for Neurology and Neurosurgery, University College London Hospitals NHS Foundation Trust, London, UK; [3]Department of Neurodegenerative Disease, UCL Queen Square Institute of Neurology and Division of Neuropathology, The National Hospital for Neurology and Neurosurgery, University College London NHS Foundation Trust, London, UK; [4]Department of Radiology, Great Ormond Street Hospital for Children, London, UK; [5]Teenage and Young Persons' Cancer Unit, Department of Paediatric Oncology, University College London Hospitals NHS Foundation Trust, London, UK

Correspondence to: Stefanie Thust, MD, FRCR. Consultant Neuroradiologist, Honorary Associate Professor, National Hospital for Neurology and Neurosurgery, Queen Square, London WC1N 3BG, UK. Email: s.thust@ucl.ac.uk.

Background: To assess anatomical and quantitative diffusion-weighted MR imaging features in a recently classified lethal neoplasm, H3 K27M histone-mutant diffuse midline glioma [World Health Organization (WHO) IV].

Methods: Fifteen untreated gliomas in teenagers and adults (median age 19, range, 14–64) with confirmed H3 K27M histone-mutant genotype were analysed at a national referral centre. Morphological characteristics including tumour epicentre(s), T2/FLAIR and Gadolinium enhancement patterns, calcification, haemorrhage and cyst formation were recorded. Multiple apparent diffusion coefficient (ADC_{min}, ADC_{mean}) regions of interest were sited in solid tumour and normal appearing white matter (ADC_{NAWM}) using post-processing software (Olea Sphere v2.3, Olea Medical). ADC histogram data (2nd, 5th, 10th percentile, median, mean, kurtosis, skewness) were calculated from volumetric tumour segmentations and tested against the regions of interest (ROI) data (Wilcoxon signed rank test).

Results: The median interval from imaging to tissue diagnosis was 9 (range, 0–74) days. The structural MR imaging findings varied between individuals and within tumours, often featuring signal heterogeneity on all MR sequences. All gliomas demonstrated contact with the brain midline, and 67% exhibited rim-enhancing necrosis. The mean ROI ADC_{min} value was 0.84 (±0.15 standard deviation, SD) $\times 10^{-3}$ mm^2/s. In the largest tumour cross-section (excluding necrosis), an average ADC_{mean} value of 1.12 (±0.25)$\times 10^{-3}$ mm^2/s was observed. The mean $ADC_{min/NAWM}$ ratio was 1.097 (±0.149), and the mean $ADC_{mean/NAWM}$ ratio measured 1.466 (±0.299). With the exception of the 2nd centile, no statistical difference was observed between the regional and histogram derived ADC results.

Conclusions: H3 K27M-mutant gliomas demonstrate variable morphology and diffusivity, commonly featuring moderately low ADC values in solid tumour. Regional ADC measurements appeared representative of volumetric histogram data in this study.

Keywords: Glioma; histones; diffusion magnetic resonance imaging

Submitted Nov 15, 2019. Accepted for publication Jul 07, 2020.
doi: 10.21037/qims-19-954
View this article at: http://dx.doi.org/10.21037/qims-19-954

Introduction

Diffuse midline gliomas are brain tumours with a mean survival of approximately 9 months from diagnosis (1,2). Midline gliomas may arise anywhere near the cerebral or infratentorial brain midline and occasionally develop in the spinal cord (3,4). They demonstrate overlapping anatomical features with the now discontinued World Health Organization (WHO) category of diffuse intrinsic pontine glioma (DIPG) (5).

In 2012, aberrations in a regulatory histone gene (H3) resulting in an amino acid substitution from lysine to methionine (K27M) were discovered in up to 40% of paediatric glioblastomas (6,7). H3 K27M mutations have since been identified as a key genetic trait of midline gliomas, present in up to 80% of childhood DIPG cases and associated with a dismal prognosis (mean survival 0.73 years) compared to midline gliomas lacking a histone mutation (mean survival 4.6 years) (2,8). Although H3 K27M-mutant gliomas tend to manifest at a much younger age (median 10.5, range, 5–23 years) (3) than conventional glioblastoma, they also develop in adults across a wide age spectrum with exceptionally poor survival (9-11).

Histones are nuclear protein complexes, which condense and structure chromosomal DNA into functional units with the potential to modify gene activity (12). Histone octamers, consisting of paired H2A, H2B, H3, and H4 subunits, contain terminal protein terminals as the access point for post-translational modification (6). It has been hypothesised that the genetic code and spatial orientation of these histone terminals direct epigenetic processes, including DNA repair and cell proliferation. Because sixteen nearly identical genes encode histone H3, it is incompletely understood how mutations in a single H3 gene produce tumour growth (13). The transcriptomic profile of H3 K27M resembles mid to late fetal stages of thalamic and corpus striatum development, which could explain the associated tumour locations (3). Consistent with the genetic signature of childhood glioblastoma, adult histone-mutant gliomas are isocitrate dehydrogenase (IDH) wild-type, but may exhibit loss of alpha-thalassaemia-retardation-X (*ATRX*) gene expression and chromosome 10q loss (14). H3 K27M-mutant gliomas in most cases display histological features of glioblastoma, or progress rapidly if discovered in the low grade stage. A distinct entity 'diffuse midline glioma, H3 K27M-mutant, WHO grade IV' has been newly adopted into the latest 2016 WHO Classification of Central Nervous System (CNS) Tumours, thereby replacing the previous (DIPG) nomenclature (15). Imaging is essential in the investigation of H3 K27M-mutant gliomas to estimate the tumour extent, and because the diagnosis may be considered based on lesion site. The deep location within eloquent structures poses a risk to biopsy, in a situation where a rapid diagnosis is required. Midline gliomas may present with obstructive hydrocephalus and critical mass effect (16), particularly if enclosed in the infratentorial compartment. To date, no distinctive structural imaging feature has been identified for histone-mutant gliomas (17). Several MR imaging descriptions exist for DIPG prior to the integrated 2016 WHO diagnosis; it is likely that a substantial proportion of this literature applies to H3 K27M-mutant glioma, but few imaging reviews address the new entity specifically (18). Reduced diffusivity is a well-known feature of cellular gliomas (19) and has been observed as a poor prognostic predictor in DIPG (20). We aimed to analyse morphological and diffusion-weighted imaging data in genotypically confirmed H3 K27M-mutant gliomas, derived from preoperative clinical studies.

Methods

Patient cohort

Institutional ethics approval was obtained, with informed consent waived due to the nature of the disease and retrospective analysis.

Since the classification of H3 K27M histone-mutant glioma (15), 15 individuals aged 14–64 years (median 19 years, 9 female) with a proven diagnosis were treated at our specialist brain tumour unit (between 2016 and 2019). In all cases, MR imaging acquired prior to tissue diagnosis and treatment was analysed.

Histopathology and molecular analysis

All tissues were fixed in formalin for at least 4 hours, followed by processing through graded alcohols and xylene, to paraffin according to standard practice in histology laboratories; 4 µm thick sections of the formalin fixed paraffin embedded samples were mounted on glass slides. All samples were examined initially on haematoxylin and eosin stained sections, followed by immunostaining according to routine diagnostic protocols, including antibodies against IDH1 (R132H), H3 K27M, and ATRX, and Ki67 on a Roche Ventana benchmark platform (21-23).

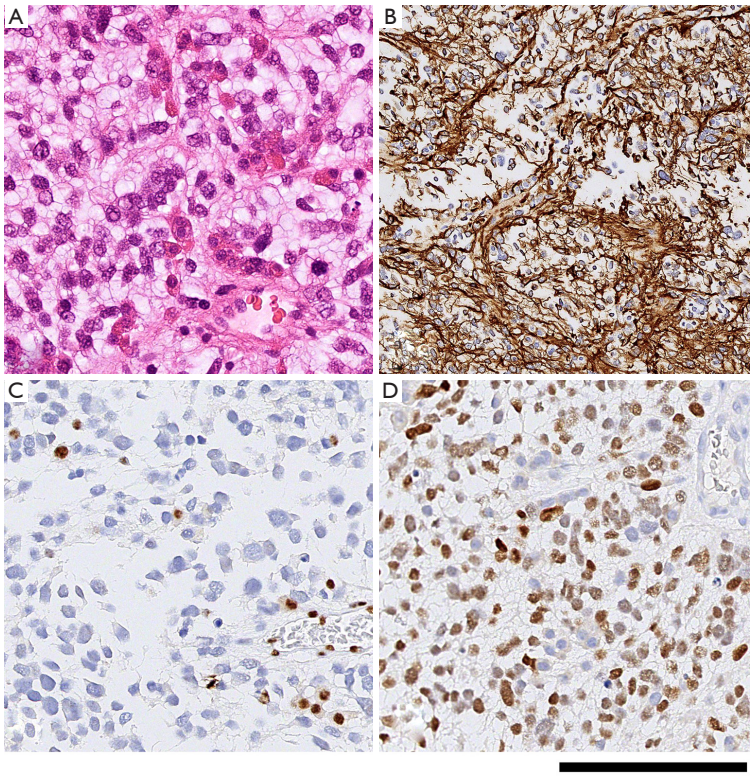

Figure 1 Histological and immunohistochemical features of histone H3 K27M mutant midline glioma (case 15). (A) Tinctorial stain with haematoxylin and eosin shows a moderately cellular glial tumour with relatively monomorphic nuclei. (B) immunohistochemical staining for glial fibrillary acidic protein (GFAP) shows labelling of most tumour cells which are arranged along glial fascicles. (C) Loss of expression of the ATRX protein: brown stained nuclei indicate residual (local) cells with retained ATRX expression whilst tumour cells (blue counterstain) have lost ATRX expression. (D) Immunostaining for mutant histone H3 K27M. The antibody detects the mutant protein only, thus labels all nuclei of tumour cells but not of vascular cells or local glial cells. Scale bar corresponds to 180 µm in (A,C,D) and 360 µm in (B).

Molecular analysis was carried out to confirm the histone mutation according to published protocols (24). All tissue samples fulfilled the histological and molecular criteria for diffuse midline glioma, H3 K27M-mutant (WHO IV). A histopathology imaging example is shown in *Figure 1*.

MR imaging data

Because our institution represents a quaternary referral centre, the MR imaging studies were performed on several 1.5T (n=10) and 3T (n=5) systems, consisting of T2-weighted (T2w), fluid-attenuation inversion recovery (FLAIR), pre- and post-gadolinium T1-weighted (T1w), +/– T2*/susceptibility-weighted (SWI) sequences, and 3-directional diffusion-weighted MRI (DWI) with two b values of 0–1,000 mm^2/s, and in some cases an additional b500 mm^2/s value under the presumption that adding an intermediate image at exactly half the highest b-value will not change the calculated apparent diffusion coefficient (ADC) (25). The conventional imaging parameters were

as follows: T2w (TR/TE, 3,000–6,270/80–380 ms; FOV, 179–231 mm × 220–287 mm; slice thickness, 1–6 mm; matrix, 256–512 × 226–532), FLAIR (TR/TE, 6,000–11,000/81–363 ms; TI, 2,370–2,800 ms; FOV, 193–240 mm × 239–298 mm; slice thickness, 1–6 mm; matrix, 256–328 × 151–241), pre and post contrast-enhanced T1w (TR/TE, 5.25–2,020/1.65–15 ms; FOV, 193–280 × 240–348 mm; slice thickness, 0.9–6 mm; matrix, 256 × 192–256), T2* (TR/TE, 788–857/16–26 ms; FOV, 195–230 mm × 42–286 mm; slice thickness, 5 mm; matrix, 256–320 × 168–256), SWI (TR/TE, 25–49/19–49 ms; FOV, 185–230 mm × 230–286 mm; slice thickness, 1.5–2 mm; matrix, 256–320 × 163–256), and DWI (TR/TE, 3,078–11,500/55–102 ms; FOV, 210–240 mm × 261–298 mm; slice thickness, 2.5–6 mm; matrix, 84–192 × 84–192).

ADC quantification

ADC maps were calculated using clinically integrated post-processing software (Olea Sphere v2.3, Olea Medical). Two board certified neuroradiologists with subspecialisation in neuro-oncology (ST 5-year experience and CM 10-year experience) in consensus placed ADC regions of interest (ROIs) according to published methods (26-28); three small (30–40 mm^2) ROIs were sited in the visually perceived lowest ADC portions of each H3 K27M-mutant glioma on one or more image slices. The mean value of the lowest ADC measurement was designated the minimum ADC value (ADC_{min}) (28). One ROI (ADC_{mean}) was then placed to cover most of the largest axial tumour cross-section as reported in (27), taking care to exclude necrosis, macroscopic haemorrhage and lesion margins. For comparison, an additional ROI was placed into normal appearing centrum semiovale white matter (ADC_{NAWM}). Absolute ADC values, as well as $ADC_{min/NAWM}$ and $ADC_{mean/NAWM}$ ratios were calculated blinded to published thresholds (29) and at an interval to ROI siting to minimise bias. Subsequently, volumetric segmentations (excluding macroscopic necrosis) were completed for each whole tumour in order to produce ADC histogram data. For this, volumes of interest (VOIs) were drawn onto the b0 images in Olea Sphere v2.3 with an automated VOI copy generated on the ADC map. From the ADC volume, a cumulative ADC histogram was generated for each glioma. Statistical testing (Wilcoxon signed rank test for related samples) was performed in SPSS 25 (IBM, New York) to assess for differences between the ROI and VOI histogram derived ADC values.

Visual rating

Tumour location was specified according to the predominant site(s) of expanded tissue abnormality. A T2w-based manual segmentation of each whole lesion was performed to measure tumour volumes. T2w/FLAIR signal characteristics were described, whereby the ability to draw around the lesion on T2w/FLAIR was designated as distinct margin and uncertainty regarding lesion borders as indistinct. Haemorrhage was assessed by inspecting non-contrast T1w and T2w. CT, T2* and/or SWI were taken into consideration, where available. Enhancement patterns were classified as non-enhancing, solid or rim-enhancing. Rim-enhancement surrounding central necrosis was distinguished from cysts, defined as central fluid signal isointense to CSF with absent or minimal contrast uptake. If hydrocephalus was present, it was documented if this was severe enough to require shunting.

Results

Clinical findings

Symptoms of raised intracranial pressure, motor deficits, and seizures, alone or in combination, were the most frequent clinical manifestations identified in the patient group. Other signs included acute onset squint, double vision, swallowing difficulties slurred speech and abnormal gait. Behavioural and mental changes were common in individuals with thalamic tumours. Several patients showed signs of cognitive dysfunction (i.e., language, attention, executive functioning), with deterioration of handwriting and/or speech. Overall, the presenting clinical features appeared predominantly dependent on tumour location, without any H3 K27M-specific symptomatology.

ADC quantification

The median interval between the imaging and tissue diagnosis was 9 days (range, 0–74 days). *Table 1* shows the ADC values obtained in 15 gliomas. The solid tumour ROI ADC_{min} results measured a mean of 0.84 (±0.15 standard deviation, SD) $\times 10^{-3}$ mm^2/s. The solid tumour ROI ADC_{mean} values within the largest cross-section had a mean of 1.12 (±0.25)$\times 10^{-3}$ mm^2/s. A mean of 0.76 (±0.06)$\times 10^{-3}$ mm^2/s was observed for the ADC_{NAWM} values. The ROI $ADC_{min/NAWM}$ ratio values measured a mean of 1.097 (±0.149), and for the ROI $ADC_{mean/NAWM}$ ratio the mean was 1.466 (±0.299). *Table 2* shows the

Table 1 ADC (region of interest derived) measurements in H3 K27M histone-mutant glioma (ADC values displayed as $\times 10^{-3}$ mm^2/s)

Case number	ADC_{min}	ADC_{mean}	ADC_{NAWM}	$ADC_{min}/_{NAWM}$ ratio	$ADC_{mean}/_{NAWM}$ ratio	Physiological MRI
1	0.79	0.94	0.80	0.987	1.183	
2	0.74	0.86	0.76	0.977	1.135	
3	0.79	1.36	0.79	1.009	1.727	18F-Cho avid
4	0.48	0.71	0.59	0.815	1.192	
5	0.71	0.87	0.73	0.973	1.192	
6	1.11	1.38	0.78	1.426	1.771	
7	0.73	0.99	0.72	1.013	1.371	rCBV =5.9
8	0.88	1.34	0.74	1.187	1.818	
9	0.90	0.98	0.81	1.111	1.212	
10	0.95	1.33	0.83	1.145	1.595	
11	1.01	1.42	0.81	1.245	1.751	
12	0.85	1.16	0.76	1.112	1.527	
13	1.04	1.07	0.84	1.236	1.280	
14	0.80	0.92	0.78	1.028	1.179	
15	0.85	1.48	0.73	1.185	2.051	rCBV =3.5
Mean (SD)	0.84 (0.15)	1.12 (0.25)	0.76 (0.06)	1.097 (0.149)	1.466 (0.299)	

ADC, apparent diffusion coefficient; SD, standard deviation.

Table 2 ADC histogram data derived from tumour volumetric segmentation in H3 K27M histone-mutant glioma (ADC values displayed as $\times 10^{-3}$ mm^2/s)

Case number	ADC_{2nd} centile	ADC_{5th} centile	ADC_{10th} centile	$ADC_{5th/NAWM}$ ratio	ADC_{median}	ADC_{mean}	$ADC_{mean/NAWM}$ ratio	Standard deviation (SD)	Kurtosis	Skewness
1	0.69	0.73	0.77	0.92	0.93	0.93	1.16	0.14	14.88	2.00
2	0.72	0.77	0.81	1.01	4.32	3.54	5.72	1.99	−1.38	−0.37
3	0.62	0.73	0.83	0.93	1.21	1.23	1.53	0.35	3.15	0.98
4	0.51	0.55	0.59	0.93	0.69	0.71	1.16	0.12	13.90	2.31
5	0.71	0.75	0.79	1.03	0.99	1.08	1.36	0.31	5.89	1.97
6	0.85	0.93	1.04	1.20	1.36	1.34	1.74	0.23	1.18	0.87
7	0.67	0.71	0.76	0.98	0.91	0.93	1.27	0.22	55.37	5.90
8	N/A	N/A	N/A	N/A	N/A	N/A	N/A	N/A	N/A	N/A
9	0.76	0.82	0.88	1.01	1.09	1.72	1.35	0.94	−1.51	0.56
10	0.84	0.90	0.96	1.09	1.23	1.24	1.48	0.22	1.84	0.54
11	1.03	1.15	1.28	1.41	1.85	1.81	2.27	0.38	−0.60	−0.25
12	0.88	0.94	0.99	1.24	1.30	1.35	1.71	0.31	0.49	0.74
13	0.77	0.84	0.89	1.00	1.08	1.11	1.28	0.21	8.03	1.88
14	0.66	0.71	0.76	0.91	0.92	1.02	1.19	0.33	6.57	2.31
15	0.81	0.86	0.94	1.19	1.40	1.37	1.94	0.33	−0.40	0.12
Mean (SD)	0.75 (0.13)	0.81 (0.14)	0.88 (0.16)	1.06 (0.15)	1.38 (0.89)	1.38 (0.69)	1.80 (1.17)	0.43 (0.49)	7.67 (14.72)	1.40 (1.58)

ADC, apparent diffusion coefficient; SD, standard deviation.

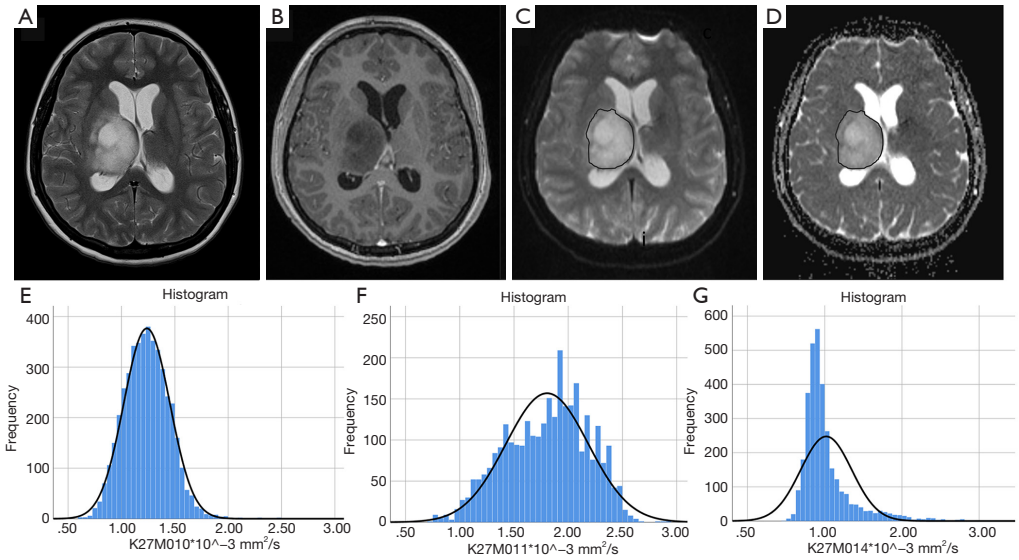

Figure 2 ADC histograms in H3 K27M histone-mutant glioma. T2w image (A), post gadolinium T1w image (B), b0 DWI image (C) and ADC map (D) demonstrating an example of glioma volumetric segmentation (case 10). Segmentations were performed on the b0 images under view of the corresponding anatomical sequences, then copied onto the ADC maps in Olea Sphere v2.3 (Olea Medical). Images (E,F,G) show ADC histograms in 3 different patients (case 10, case 11 and case 14). ADC, apparent diffusion coefficient.

results of the volumetric ADC histogram measurements. *Figure 2* shows an example of different ADC histogram curves observed in the H3 K27M mutant glioma cohort. A biphasic ADC distribution was evident in 2 histograms, with one glioma (case 2) showing a high volumetric ADC_{mean} (3.54 mm^2/s), likely due to inadvertent inclusion of necrotic tissue. In one glioma (case 8), no histogram could be produced due to missing data. A significant difference (P=0.01) was only observed between the 2^{nd} centile of the volumetric ADC histogram and the ROI ADC_{min} values. The comparisons between ROI ADC_{min} and the 5^{th} and 10^{th} histogram percentiles showed no statistical difference (P=0.379 and P=0.177, respectively). No difference was observed between ROI $ADC_{min/NAWM}$ ratio and the $ADC_{5th\ percentile/NAWM}$ ratio measurements (P=0.421). The comparisons between ROI ADC_{mean} and the histogram ADC_{median} and ADC_{mean} were non-significant (P=0.576 and P=0.208). And no statistical difference was apparent between ROI $ADC_{mean/NAWM}$ ratio and the histogram $ADC_{mean/NAWM}$ ratio (P=0.60).

Structural MRI features

An overview of conventional imaging features is shown in *Table 3*. All H3 K27M-mutant gliomas were in contact with the brain midline (*Figure 3*). The lesion volumes ranged from 9.2 to 103.1 cm^3. The definition of the non-contrast enhancing tumour margin appeared variable, whereby most lesions demonstrated heterogeneous T2/FLAIR signal. The observed T2/FLAIR heterogeneity corresponded to visible differences in ADC signal, with facilitated diffusion shown in necrotic glioma components. None of the H3 K27M histone-mutant gliomas exhibited a T2-FLAIR mismatch sign. Several tumours contained haemorrhagic components (*Figure 4*), whereas calcification was not identified, and only two tumours contained cysts. Rim-enhancement surrounding necrosis was present in 10/15 (67%) gliomas; 6/15 (40%) patients required shunting for hydrocephalus. Two gliomas were imaged with dynamic susceptibility contrast enhanced (DSC) perfusion MRI (*Figure 5*), which revealed elevated relative cerebral blood volume (rCBV) indicative of neovascularity.

Table 3 Structural MR imaging findings in diffuse midline glioma, H3 K27M histone-mutant in this case series

Case	Age	Tumour location	T2 volume cm^3	T2/FLAIR margin	T2/FLAIR signal	Haem	Ca^2	Cyst(s)	T1w+Gad pattern	Hydrocephalus
1	17	Thalamus, lentiform	39.2	Distinct	Het	Macro	No	No	Solid, rim enhancing + necrosis	Shunt
2	14	Cerebellum, pons, leptomeninges	33.1	Indistinct	Het	Ukn	Ukn	No	Solid, rim enhancing + necrosis	Shunt
3	17	Pons	38.9	Indistinct	Het	No	No	Yes	Rim enhancing + necrosis	No
4	19	Thalamus, corona radiata midbrain	103.1	Distinct	Het	Macro	No	No	Rim enhancing + necrosis	Shunt
5	30	Thalamus, temporal	85	Indistinct	Het	Macro	No	No	Rim enhancing + necrosis	Mild
6	64	Basal ganglia septum pellucidum, bifrontal	48.4	Indistinct	Het	No	No	No	Non-enhancing	No
7	50	Midbrain, pons	13.9, then 19.4	Distinct	Hom	No	No	No	Non-enhancing*	No
8	15	Thalamus, midbrain	66.85	Distinct	Het	No	No	No	Rim enhancing + necrosis	Mild
9	33	Thalami, tectal plate	11.4	Distinct	Hom	No	No	No	Non-enhancing	Shunt
10	16	Thalami, midbrain	57.1	Indistinct	Het	Petechial	No	No	Solid, rim enhancing + necrosis	Shunt
11	14	Medulla	9.2	Distinct	Het	Ukn	Ukn	No	No Gad given	No
12	17	Tectal plate	13.5	Distinct	Het	No	No	No	Solid, rim enhancing + necrosis	Mild
13	60	Pons	43.4	Indistinct	Het	No	No	No	Solid	No
14	35	Thalamus	54.7	Distinct	Het	No	No	Yes	Rim enhancing + necrosis	Shunt
15	44	Hypothalamus, pituitary, caudate, temporal lobe	24.1	Indistinct	Het	Petechial	No	No	Rim enhancing + necrosis	No

*, in case 7 gadolinium enhancement developed subsequently. Haem, haemorrhage; Macro, macroscopic; Ca^{2+}, calcification; Hom, homogenous; Het, heterogeneous; Ukn, unknown.

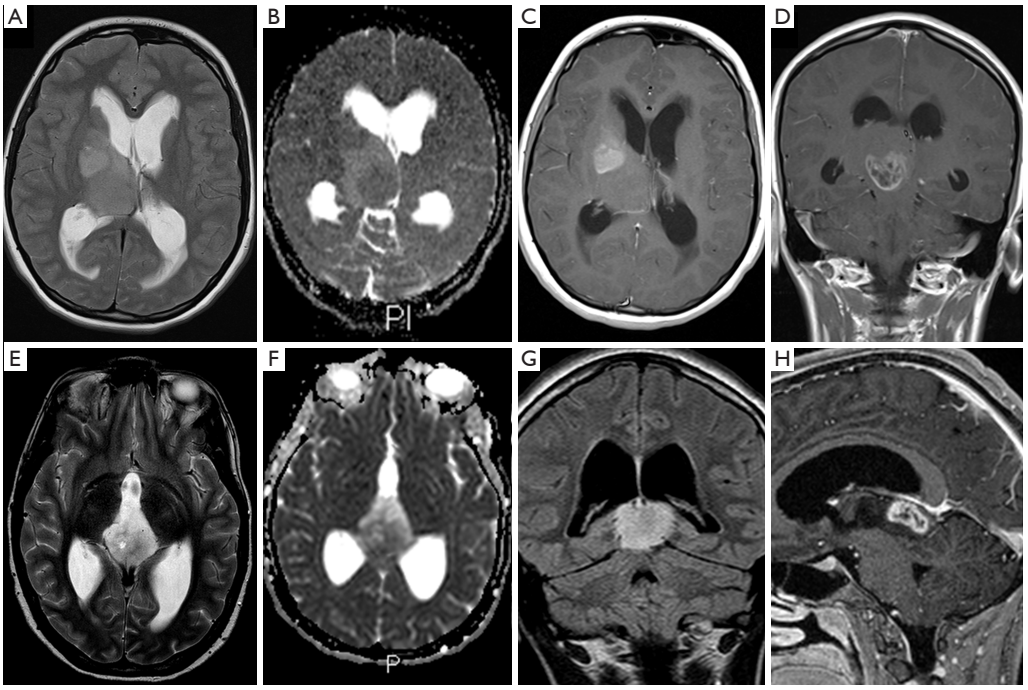

Figure 3 Locations of H3 K27M-mutant diffuse midline glioma. Case 1: T2w (A), ADC map (B), and post gadolinium T1w (C,D) images in a patient with a thalamic glioma. Case 12: T2w (E), ADC map (F), and post gadolinium T1w (G,H) demonstrating a tectal plate tumour epicentre. ADC, apparent diffusion coefficient.

In one case, ^{18}F-choline PET imaging was performed, showing radioactive tracer accumulation within enhancing tumour components (*Figure 6*).

Discussion

Few studies have investigated MR imaging findings in H3 K27M histone-mutant diffuse midline glioma, with most radiological series to date only describing qualitative tumour features (18,30). We quantified ADC values in H3 K27M-mutant solid tumour components, and found diffusivity to be variable, characterised by a relatively narrow spectrum of ADC_{min} values.

Limited extracellular diffusion is recognised as a hallmark feature of cancer, presumed to indirectly reflect tissue cellularity (31). Low diffusivity has been reported in glioblastoma (19,32), in WHO grade II/III malignant gliomas (33) and as an adverse prognostic biomarker in DIPG (20).

The ADC_{min} and ADC_{mean} values in our H3 K27M-mutant glioma cohort are consistent with previous findings in glioblastoma (34). Many of the tumour ADC_{min} values were similar to normal appearing white matter (average $ADC_{min/NAWM}$ ratio 1.097), which is in agreement with published data on ADC quantification in malignant gliomas (28,35). During their research into the conventional imaging morphology of histone-mutant gliomas, Aboian *et al*. observed reduced diffusion (unquantified) on inspection (18), whereas in a recent larger (n=66) series no restricted diffusion was reported (30). H3 K27M-mutant gliomas reportedly have higher cell densities and pronounced nuclear pleomorphism compared to

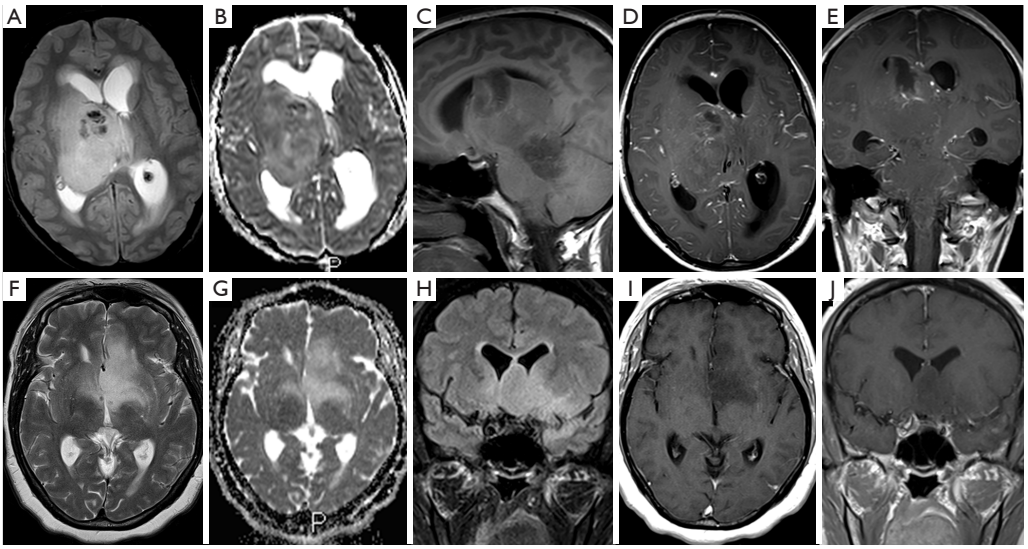

Figure 4 Variable morphology of H3 K27M-mutant diffuse midline glioma. Case 4: T2w (A), ADC map (B), T1w (C) and post Gadolinium T1w (D,E) images demonstrating a large, partially haemorrhagic tumour. Case 6: T2w (F), ADC map (G), FLAIR (H) and post gadolinium T1w (I,J) in a patient with a non-enhancing glioma. ADC, apparent diffusion coefficient.

glioblastoma types (36), which could give rise to the visual observation. On the contrary, indolent low grade gliomas typically show facilitated diffusion, evidenced by higher absolute ADC and ADC ratio values (27).

Chen *et al.* recently compared ADC ROI measurements in H3 K27M-mutant diffuse midline glioma (n=19) to a H3 K27M wild-type patient group (29). This study reported an average ADC_{min} of 0.734 (±0.120 SD) $\times 10^{-3}$ mm^2/s and an average $ADC_{min/NAWM}$ ratio of 0.972 (±0.165)$\times 10^{-3}$ mm^2/s. In our patient group, the results for ADC_{min} [mean 0.84 (±0.15)$\times 10^{-3}$ mm^2/s] and $ADC_{min/NAWM}$ ratio [1.097 (±0.149)$\times 10^{-3}$ mm^2/s] are slightly higher despite using a similar ROI method. Furthermore, the majority of ADC_{min} [13/15 (87%)] and $ADC_{min/NAWM}$ ratio [12/15 (80%)] values in our research exceed the proposed ADC_{min} threshold (0.728×10^{-3} mm^2/s) and $ADC_{min/NAWM}$ ratio threshold (0.982), respectively (29). This deviation may to some extent be explained by technical factors, such as differences in DWI acquisition and modelling. Observer dependence could also play a role, although excellent reproducibility has been demonstrated for region based glioma and NAWM ADC measurements in prior research (27,37).

In our study, less variability (smaller SD) was shown for ADC_{min} compared to ADC_{mean} values, both for the use of the ROI based and the histogram technique. Given the high proportion of necrotic lesions, when using a ROI assessment the ADC_{min} method (using several small ROIs) appears technically more feasible to assess diffusivity in midline gliomas. The placement of a single circular ADC_{mean} ROI in tumours with large portions of necrosis or haemorrhage would invariably exclude parts of the lesion. All (n=3) non-Gadolinium-enhancing, solid H3 K27M-mutant gliomas exhibited ROI $ADC_{mean/NAWM}$ ratio values in the range reported for non-enhancing glioblastoma (27), thus ADC_{mean} measurement could potentially be informative for such cases. The regional NAWM ADC values measured in our study showed the least variation (smallest SD) and were numerically in keeping with previous research in normal white matter (38).

The ROI parameters, specifically ADC_{min} and $ADC_{min/NAWM}$ ratio, appeared representative of the 5th and 10th ADC histogram percentiles. Most tumour histograms showed positive kurtosis and skewness, corresponding to the visually perceived ADC heterogeneity. The clinical impact of

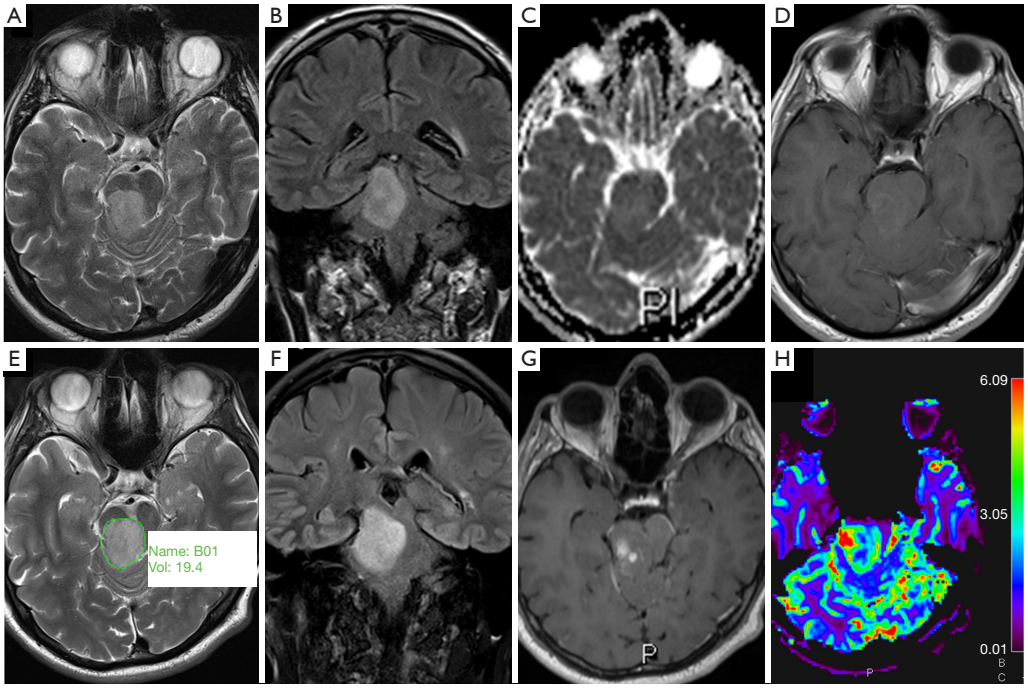

Figure 5 Serial progression and perfusion features of H3 K27M-mutant diffuse midline glioma. Case 7: T2w (A), FLAIR (B), ADC map (C) and post gadolinium T1w images (D) performed on admission showing a non-gadolinium enhancing tumour with ADC signal approximately isointense to surrounding brain. The same patient after 7 months: T2w (E, featuring volumetric segmentation example), FLAIR (F), post gadolinium T1w (G) and DSC perfusion-derived rCBV map (H) revealing interval progression with development of contrast enhancement and pathologically raised blood volume (arrow). ADC, apparent diffusion coefficient; DSC, dynamic susceptibility contrast enhanced perfusion MRI; rCBV, relative cerebral blood volume.

diffusion findings in H3 K27M-mutant glioma remains yet unknown; Aboian *et al.* recently compared ADC histogram statistics between paediatric H3 M27M-mutant and wild-type diffuse midline gliomas observing no difference (39). Conversely, Su *et al.* were recently able to predict H3 K27M glioma genotype using a FLAIR based machine learning algorithm (40) without considering DWI features.

Whilst our study did not include specific testing of ADC repeatability, recent evidence indicates that the majority of diffusion MRI derived parameters, and in particular ADC, are sufficiently robust across 1.5T and 3T scanners and suitable for multi-centre clinical studies (41). Furthermore, in the case of relative ADC measurements normalised to unaffected white matter ($ADC_{min/NAWM}$ ratio and $ADC_{mean/NAWM}$ ratio), any potential effect from scanner variation would be minimised.

Variable T2/FLAIR characteristics, tumour border definition and contrast patterns were encountered, with solid and rim enhancement patterns coexisting. T2 hypointense glioma regions tended to correspond to low ADC signal in keeping with features previously reported for DIPG anaplastic components (42). Haemorrhage was evident in one third of cases, which has been hypothesised to represent a specific feature of H3 K27M-mutant gliomas in the cord (43). The diversity of glioma features and lesion volumes may reflect discovery at different time points during the disease, as suggested by the serial morphology change in case 7. High genomic instability has been

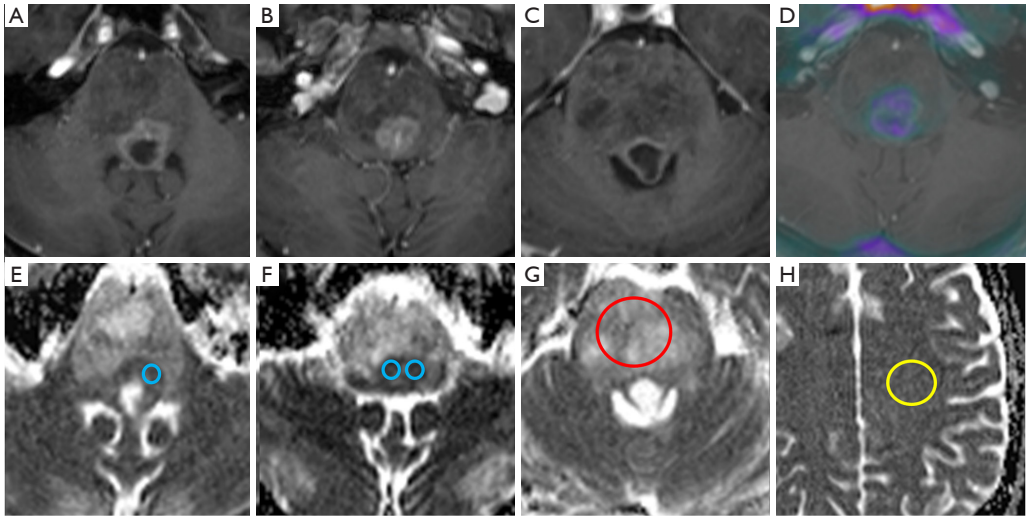

Figure 6 Quantitative ADC measurement in H3 K27M histone-mutant glioma. T2w (A,B), post gadolinium T1w (C) and T1w/18F choline PET fusion image (D) demonstrating a partially necrotic H3 K27M-mutant diffuse midline glioma (case 3) with considerable signal heterogeneity on all image sequences. ADC maps in the same patient featuring superimposed ADC_{min} (E,F), ADC_{mean} (G) and ADC_{NAWM} (H) regions of interest (ADC_{min}=blue, ADC_{mean}=red, ADC_{NAWM}=yellow). ADC, apparent diffusion coefficient.

discovered in histone-mutant gliomas (7), which may be associated with complex lesion architecture and imaging changes over time.

As a limitation, this study did not perform a comparison to other midline glioma genotypes. The cohort is small due to the rarity of the disease and its recent [2016] classification, which limits the generalisability of our results. We minimized potential bias by working according to published, reproducible ROI ADC quantification methods whilst being blinded to published thresholds.

In summary, our analysis underscores the potential role of diffusion-weighted MRI as a biomarker of H3 K27M-mutant glioma. While low diffusivity appears to be a typical feature of this tumour type, we observed a broader spectrum of ADC_{min} and $ADC_{min/NAWM}$ ratio values than previously reported.

Conclusions

Heterogeneous morphology and diffusivity, commonly featuring moderately low ADC values in solid tumour, represents a quantifiable feature of H3 K27M-mutant glioma. Regional ADC measurements appeared representative of volumetric histogram data in this study.

Acknowledgments

Funding: No specific grant funding is associated with the work presented. University College London/UCL Hospitals receive proportional funding from the National Institute for Health Research Biomedical Research Centre.

Footnote

Conflicts of Interest: All authors have completed the ICMJE uniform disclosure form (available at http://dx.doi.org/10.21037/qims-19-954). Dr. KM serves as an unpaid editorial board member of *Quantitative Imaging in Medicine and Surgery*. The other authors have no conflicts of interest to declare.

Ethical Statement: Institutional ethics approval was obtained, with informed consent waived due to the nature of the disease and retrospective analysis.

References

1. Donaldson SS, Laningham F, Fisher PG. Advances toward an understanding of brainstem gliomas. J Clin Oncol 2006;24:1266-72.
2. Wu G, Broniscer A, McEachron TA, Lu C, Paugh BS, Becksfort J, Qu C, Ding L, Huether R, Parker M, Zhang J, Gajjar A, Dyer MA, Mullighan CG, Gilbertson RJ, Mardis ER, Wilson RK, Downing JR, Ellison DW, Zhang, J, Baker SJ. Somatic histone H3 alterations in pediatric diffuse intrinsic pontine gliomas and non-brainstem glioblastomas. Nat Genet 2012;44:251-3.
3. Sturm D, Witt H, Hovestadt V, Khuong-Quang DA, Jones DTW, Konermann C, Pfaff E, Tönjes M, Sill M, Bender S, Kool M, Zapatka M, Becker N, Zucknick M, Hielscher T, Liu XY, Fontebasso AM, Ryzhova M, Albrecht S, Jacob K, Wolter M, Ebinger M, Schuhmann MU, van Meter T, Frühwald MC, Hauch H, Pekrun A, Radlwimmer B, Niehues T, von Komorowiski G, Dürken M, Kulozik AE, Madden J, Donson A, Foreman NK, Drissi R, Fouladi M, Scheurlen W, von Deimling A, Monoranu C, Roggendorf W, Herold-Mende C, Unterberg A, Kramm CM, Felsberg J, Hartmann C, Wiestler B, Wick W, Milde T, Witt O, Lindroth AM, Schwartzentruber J, Faury D, Fleming A, Zakrzewska M, Liberski PP, Zakrzewski K, Hauser P, Garami M, Klekner A, Bognar L, Morrisy S, Cavalli F, Taylor MD, van Sluis P, Koster J, Versteeg R, Volckmann R, Mikkelsen T, Aldape K, Reifenberger G, Collins VP, Majewski J, Korshunov A, Lichter P, Plass C, Jabado N, Pfister S. Hotspot Mutations in H3F3A and IDH1 Define Distinct Epigenetic and Biological Subgroups of Glioblastoma. Cancer Cell 2012;22:425-37.
4. Gilbert AR, Zaky W, Gokden M, Fuller CE, Ocal E, Leeds NE, Fuller GN. Extending the Neuroanatomic Territory of Diffuse Midline Glioma, K27M Mutant: Pineal Region Origin. Pediatr Neurosurg 2018;53:59-63.
5. Louis DN, Ohgaki H, Wiestler OD, Cavenee WK, Burger PC, Jouvet A, Scheithauer BW, Kleihues P. The 2007 WHO Classification of Tumours of the Central Nervous System. Acta Neuropathol (Berl) 2007;114:97-109.
6. Schwartzentruber J, Korshunov A, Liu XY, Jones DTW, Pfaff E, Jacob K, Sturm D, Fontebasso AM, Khuong Quang DA, Tönjes M, Hovestadt V, Albrecht S, Kool M, Nantel A, Konermann C, Lindroth A, Jäger N, Rausch T, Ryzhova M, Korbel JO, Hielscher T, Hauser P, Garami M, Klekner A, Bognar L, Ebinger M, Schuhmann MU, Scheurlen W, Pekrun A, Frühwald MC, Roggendorf W, Kramm C, Dürken M, Atkinson J, Lepage P, Montpetit A, Zakrzewska M, Zakrzewski K, Liberski P, Dong Z, Siegel P, Kulozik AE, Zapatka M, Guha A, Malkin D, Felsberg J, Reifenberger G, von Deimling A, Ichimura K, Collins VP, Witt H, Milde T, Witt O, Zhang C, Castelo-Branco P, Lichter P, Faury D, Tabori U, Plass C, Majewski J, Pfister S, Jabado N. Driver mutations in histone H3.3 and chromatin remodelling genes in paediatric glioblastoma. Nature 2012;482:226-31.
7. Fontebasso AM, Papillon-Cavanagh S, Schwartzentruber J, Nikbakht H, Gerges N, Fiset PO, Bechet D, Faury D, De Jay N, Ramkisson LA, Corcoran A, Jones DTW, Surm D, Johann P, Tomita T, Goldman S, Nagib M, Bendel A, Goumnerova L, Bowers DC, Leonard JR, Rubin JB, Alden T, Browd S, Geyer JR, Leary S, Jallo G, Cohen K, Gupta N, Prados MD, Carret AS, Ellezam B, Crevier L, Klekner A, Bognar L, Hauser P, Garami M, Myseros J, Dong Z, Siegel PM, Malkin H, Ligon AH, Albrecht S, Pfister SM, Ligon KL, Majewski J, Jabado N, Kieran MW. Recurrent somatic mutations in ACVR1 in pediatric midline high-grade astrocytoma. Nat Genet 2014;46:462-6.
8. Khuong-Quang DA, Buczkowicz P, Rakopoulos P, Liu XY, Fontebasso AM, Bouffet E, Bartels U, Albrecht S, Schwartzentruber J, Letourneau L, Bourgey M, Bourque G, Montpetit A, Bourret G, Lepage P, Fleming A, Lichter P, Kool M, von Deimling A, Sturm D, Korshunov A, Faury D, Jones DT, Majewski J, Pfister SM, Jabado N, Hawkins C. K27M mutation in histone H3.3 defines clinically and biologically distinct subgroups of pediatric diffuse intrinsic pontine gliomas. Acta Neuropathol (Berl) 2012;124:439-47.
9. Kleinschmidt-DeMasters BK, Mulcahy Levy JM. H3 K27M-mutant gliomas in adults vs. children share similar histological features and adverse prognosis. Clin Neuropathol 2018;37:53-63.
10. Meyronet D, Esteban-Mader M, Bonnet C, Joly MO, Uro-Coste E, Amiel-Benouaich A, Forest F, Rousselot-Denis C, Burel-Vandenbos F, Bourg V, Guyotat J, Fenouil T, Jouvet A, Honnorat J, Ducray F. Characteristics of

H3 K27M-mutant gliomas in adults. Neuro Oncol 2017;19:1127-34.
11. Schreck KC, Ranjan S, Skorupan N, Bettegowda C, Eberhart CG, Ames HM, Holdhoff M. Incidence and clinicopathologic features of H3 K27M mutations in adults with radiographically-determined midline gliomas. J Neurooncol 2019;143:87-93.
12. Lee J, Solomon DA, Tihan T. The role of histone modifications and telomere alterations in the pathogenesis of diffuse gliomas in adults and children. J Neurooncol 2017;132:1-11.
13. Venneti S, Garimella MT, Sullivan LM, Martinez D, Huse JT, Heguy A, Santi M, Thompson CB, Judkins AR. Evaluation of histone 3 lysine 27 trimethylation (H3K27me3) and enhancer of Zest 2 (EZH2) in pediatric glial and glioneuronal tumors shows decreased H3K27me3 in H3F3A K27M mutant glioblastomas. Brain Pathol 2013;23:558-64.
14. Brandner S, von Deimling A. Diagnostic, prognostic and predictive relevance of molecular markers in gliomas: Molecular markers in gliomas. Neuropathol Appl Neurobiol 2015;41:694-720.
15. Louis DN, Perry A, Reifenberger G, von Deimling A, Figarella-Branger D, Cavenee WK, Ohgaki H, Wiestler OD, Kleihues P, Ellison DW. The 2016 World Health Organization Classification of Tumors of the Central Nervous System: a summary. Acta Neuropathol (Berl) 2016;131:803-20.
16. Fukami S, Nakajima N, Okada H, Akimoto J, Miki T, Fukuhara H, Shishido-Hara Y, Nagao T, Tsuda M, Kohno M. Pathological findings and clinical course of midline paraventricular gliomas diagnosed using a neuroendoscope. World Neurosurg 2018;114:e366-e377.
17. Daoud EV, Rajaram V, Cai C, Oberle RJ, Martin GR, Raisanen JM, White CL 3rd, Foong C, Mickey BE, Pan E, Hatanpaa KJ. Adult Brainstem Gliomas With H3K27M Mutation: Radiology, Pathology, and Prognosis. J Neuropathol Exp Neurol 2018;77:302-11.
18. Aboian MS, Solomon DA, Felton E, Mabray MC, Villanueva-Meyer JE, Mueller S, Cha S. Imaging Characteristics of Pediatric Diffuse Midline Gliomas with Histone H3 K27M Mutation. AJNR Am J Neuroradiol 2017;38:795-800.
19. Gupta A, Young RJ, Karimi S, Sood S, Zhang Z, Mo Q, Gutin PH, Holodny AI, Lassman AB. Isolated diffusion restriction precedes the development of enhancing tumor in a subset of patients with glioblastoma. AJNR Am J Neuroradiol 2011;32:1301-6.
20. Lober RM, Cho YJ, Tang Y, Barnes PD, Edwards MS, Vogel H, Fisher PG, Monje M, Yeom KW. Diffusion-weighted MRI derived apparent diffusion coefficient identifies prognostically distinct subgroups of pediatric diffuse intrinsic pontine glioma. J Neurooncol 2014;117:175-82.
21. Capper D, Preusser M, Habel A, Sahm F, Ackermann U, Schindler G, Pusch S, Mechtersheimer G, Zentgraf H, von Deimling A. Assessment of BRAF V600E mutation status by immunohistochemistry with a mutation-specific monoclonal antibody. Acta Neuropathol (Berl) 2011;122:11-9.
22. Castel D, Philippe C, Calmon R, Le Dret L, Truffaux N, Boddaert N, Pages M, Taylor KR, Saulnier P, Lacroix L, Mackay A, Jones C, Sainte-Rose C, Blauwblomme T, Andreiuolo F, Puget S, Grill J, Varlet P, Debily MA. Histone H3F3A and HIST1H3B K27M mutations define two subgroups of diffuse intrinsic pontine gliomas with different prognosis and phenotypes. Acta Neuropathol (Berl) 2015;130:815-27.
23. Reuss DE, Sahm F, Schrimpf D, Wiestler B, Capper D, Koelsche C, Schweizer L, Korshunov A, Jones DTW, Hovestadt V, Mittelbronn M, Schittenhelm J, Herold-Mende C, Unterberg A, Platten M, Weller M, Wick W, Pfister SM, von Deimling A. ATRX and IDH1-R132H immunohistochemistry with subsequent copy number analysis and IDH sequencing as a basis for an 'integrated' diagnostic approach for adult astrocytoma, oligodendroglioma and glioblastoma. Acta Neuropathol (Berl) 2015;129:133-46.
24. Jaunmuktane Z, Capper D, Jones DTW, Schrimpf D, Sill M, Dutt M, Suraweera N, Pfister SM, von Deimling A, Brandner S. Methylation array profiling of adult brain tumours: diagnostic outcomes in a large, single centre. Acta Neuropathol Commun 2019;7:24.
25. Park MY, Byun JY. Understanding the mathematics involved in calculating apparent diffusion coefficient maps. AJR Am J Roentgenol 2012;199:W784.
26. Ramaglia A, Tortora D, Mankad K, Lequin M, Severino M, D'Arco F, Löbel U, Benenati M, de Leng WJW, de Marco P, Milanaccio C, Rossi A, Morana G. Role of diffusion weighted imaging for differentiating cerebral pilocytic astrocytoma and ganglioglioma BRAF V600E-mutant from wild type. Neuroradiology 2020;62:71-80.
27. Thust SC, Hassanein S, Bisdas S, Rees JH, Hyare H, Maynard JA, Brandner S, Tur C, Jäger HR, Yousry TA, Mancini L. Apparent diffusion coefficient for molecular subtyping of non-gadolinium-enhancing WHO grade

II/III glioma: volumetric segmentation versus two-dimensional region of interest analysis. Eur Radiol 2018;28:3779-88.
28. Xing Z, Yang X, She D, Lin Y, Zhang Y, Cao D. Noninvasive Assessment of IDH Mutational Status in World Health Organization Grade II and III Astrocytomas Using DWI and DSC-PWI Combined with Conventional MR Imaging. AJNR Am J Neuroradiol 2017;38:1138-44.
29. Chen H, Hu W, He H, Yang Y, Wen G, Lv X. Noninvasive assessment of H3 K27M mutational status in diffuse midline gliomas by using apparent diffusion coefficient measurements. Eur J Radiol 2019;114:152-9.
30. Qiu T, Chanchotisatien A, Qin Z, Wu J, Du Z, Zhang X, Gong F, Yao Z, Chu S. Imaging characteristics of adult H3 K27M-mutant gliomas. J Neurosurg 2019;1:1-9.
31. Patterson DM, Padhani AR, Collins DJ. Technology insight: water diffusion MRI--a potential new biomarker of response to cancer therapy. Nat Clin Pract Oncol 2008;5:220-33.
32. Yan R, Haopeng P, Xiaoyuan F, Jinsong W, Jiawen Z, Chengjun Y, Tianming Q, Ji X, Mao S, Yueyue D, Yong Z, Jianfeng L, Zhenwei Y. Non-Gaussian diffusion MR imaging of glioma: comparisons of multiple diffusion parameters and correlation with histologic grade and MIB-1 (Ki-67 labeling) index. Neuroradiology 2016;58:121-32.
33. Leu K, Ott GA, Lai A, Nghiemphu PL, Pope WB, Yong WH, Liau LM, Cloughesy TF, Ellingson BM. Perfusion and Diffusion MRI Signatures in Histologic and Genetic Subtypes of WHO Grade II-III Diffuse Gliomas. J Neurooncol 2017;134:177-88.
34. Yamashita K, Hiwatashi A, Togao O, Kikuchi K, Hatae R, Yoshimoto K, Mizoguchi M, Suzuki SO, Yoshiura T, Honda H. MR Imaging-Based Analysis of Glioblastoma Multiforme: Estimation of IDH1 Mutation Status. AJNR Am J Neuroradiol 2016;37:58-65.
35. Hilario A, Ramos A, Perez-Nuñez A, Salvador E, Millan JM, Lagares A, Sepulveda JM, Gonzalez-Leon P, Hernandez-Lain A, Ricoy JR. The Added Value of Apparent Diffusion Coefficient to Cerebral Blood Volume in the Preoperative Grading of Diffuse Gliomas. Am J Neuroradiol 2012;33:701-7.
36. Neumann JE, Dorostkar MM, Korshunov A, Mawrin C, Koch A, Giese A, Schüller U. Distinct Histomorphology in Molecular Subgroups of Glioblastomas in Young Patients. J Neuropathol Exp Neurol 2016;75:408-14.
37. Maynard J, Okuchi S, Wastling S, Busaidi AA, Almossawi O, Mbatha W, Brandner S, Jaunmuktane Z, Koc AM, Mancini L, Jäger R, Thust S. World Health Organization Grade II/III Glioma Molecular Status: Prediction by MRI Morphologic Features and Apparent Diffusion Coefficient. Radiology 2020;296:111-21.
38. Hakulinen U, Brander A, Ryymin P, Öhman J, Soimakallio S, Helminen M, Dastidar P, Eskola H. Repeatability and variation of region-of-interest methods using quantitative diffusion tensor MR imaging of the brain. BMC Med Imaging 2012;12:30.
39. Aboian MS, Tong E, Solomon DA, Kline C, Gautam A, Vardapetyan A, Tamrazi B, Li Y, Jordan CD, Felton E, Weinberg B, Braunstein S, Mueller S, Cha S. Characteristics of Pediatric Diffuse Midline Gliomas with Histone H3-K27M Mutation Using Apparent Diffusion Coefficient Histogram Analysis. Am J Neuroradiol 2019;40:1804-10.
40. Su X, Chen N, Sun H, Liu Y, Yang X, Wang W, Zhang S, Tan Q, Su J, Gong Q, Yue Q. Automated Machine Learning Based on Radiomics Features Predicts H3 K27M Mutation in Midline Gliomas of the Brain. Neuro Oncol 2020;22:393-401.
41. Grech-Sollars M, Hales PW, Miyazaki K, Raschke F, Rodriguez D, Wilson M, Gill SK, Banks T, Saunders DE, Clayden JD, Gwilliam MN, Barrick TR, Morgan PS, Davies NP, Rositter J, Auer DP, Grundy R, Leach MO, Howe FA, Peet AC, Clark CA. Multi-centre reproducibility of diffusion MRI parameters for clinical sequences in the brain. Nmr Biomed 2015;28:468-85.
42. Löbel U, Sedlacik J, Reddick WE, Kocak M, Ji Q, Broniscer A, Hillenbrand CM, Patay Z. Quantitative Diffusion Weighted Imaging and Dynamic Susceptibility-weighted Contrast-enhanced Perfusion MRI Analysis of T2-hypointense Lesion Components in Pediatric Diffuse Intrinsic Pontine Glioma. AJNR Am J Neuroradiol 2011;32:315-22.
43. Jung JS, Choi YS, Ahn SS, Yi S, Kim SH, Lee SK. Differentiation between spinal cord diffuse midline glioma with histone H3 K27M mutation and wild type: comparative magnetic resonance imaging. Neuroradiology 2019;61:313-22.

Cite this article as: Thust S, Micallef C, Okuchi S, Brandner S, Kumar A, Mankad K, Wastling S, Mancini L, Jäger HR, Shankar A. Imaging characteristics of H3 K27M histone-mutant diffuse midline glioma in teenagers and adults. Quant Imaging Med Surg 2021;11(1):43-56. doi: 10.21037/qims-19-954

Lasocki *et al. Cancer Imaging* (2022) 22:63
https://doi.org/10.1186/s40644-022-00500-3

Cancer Imaging

REVIEW Open Access

Imaging features associated with H3 K27-altered and H3 G34-mutant gliomas: a narrative systematic review

Arian Lasocki[1,2,3*], Gehad Abdalla[4,5], Geoffrey Chow[4,6] and Stefanie C. Thust[4,7]

Abstract

Background: Advances in molecular diagnostics accomplished the discovery of two malignant glioma entities harboring alterations in the H3 histone: diffuse midline glioma, H3 K27-altered and diffuse hemispheric glioma, H3 G34-mutant. Radiogenomics research, which aims to correlate tumor imaging features with genotypes, has not comprehensively examined histone-altered gliomas (HAG). The aim of this research was to synthesize the current published data on imaging features associated with HAG.

Methods: A systematic search was performed in March 2022 using PubMed and the Cochrane Library, identifying studies on the imaging features associated with H3 K27-altered and/or H3 G34-mutant gliomas.

Results: Forty-seven studies fulfilled the inclusion criteria, the majority on H3 K27-altered gliomas. Just under half (21/47) were case reports or short series, the remainder being diagnostic accuracy studies. Despite heterogeneous methodology, some themes emerged. In particular, enhancement of H3 K27M-altered gliomas is variable and can be less than expected given their highly malignant behavior. Low apparent diffusion coefficient values have been suggested as a biomarker of H3 K27-alteration, but high values do not exclude this genotype. Promising correlations between high relative cerebral blood volume values and H3 K27-alteration require further validation. Limited data on H3 G34-mutant gliomas suggest some morphologic overlap with 1p/19q-codeleted oligodendrogliomas.

Conclusions: The existing data are limited, especially for H3 G34-mutant gliomas and artificial intelligence techniques. Current evidence indicates that imaging-based predictions of HAG are insufficient to replace histological assessment. In particular, H3 K27-altered gliomas should be considered when occurring in typical midline locations irrespective of enhancement characteristics.

Keywords: Magnetic resonance imaging, Radiogenomics, H3 K27M-altered glioma, H3 G34-mutant glioma

Introduction

Advances in molecular diagnostic methods have improved the distinction of brain tumors based on characteristic genetic abnormalities, which has been reflected in the 2016 update to the World Health Organization (WHO) Classification of Tumors of the Central Nervous System (forthwith referred to as WHO 2016) and the more recent 2021 WHO Classification (forthwith WHO 2021). WHO 2016 introduced the entity *diffuse midline glioma, H3 K27M-mutant*, which typically occurs in children and young adults, in characteristic midline locations (in particular, thalamus, brainstem and spinal cord) [1]. A midline location is critical for the diagnosis of this neoplasm, and hence the diagnosis cannot be applied to tumors which demonstrate an H3 K27M mutation but occur elsewhere in the brain [2]. Subsequently, gliomas

*Correspondence: arian.lasocki@petermac.org

[1] Department of Cancer Imaging, Peter MacCallum Cancer Centre, Grattan St, Melbourne, Victoria 3000, Australia
Full list of author information is available at the end of the article

with a similar demographic distribution characterized by an H3 G34 mutation have been identified, however these typically arise in the cerebral hemispheres, not in the midline [3, 4]. Growing understanding of these tumors has led to a diagnostic refinement in WHO 2021 [4], in which the two groups are now *diffuse midline glioma, H3 K27-altered* and *diffuse hemispheric glioma, H3 G34-mutant*, respectively. Both are classed WHO grade 4 *pediatric-type diffuse high-grade gliomas* [4].

In parallel with our growing understanding of the molecular mechanisms underlying gliomagenesis, research has correlated imaging features, in particular MRI, with key genetic alterations, known as "radiogenomics" or "imaging genomics". Given their much higher incidence, the majority of this research has examined adult gliomas, predominantly targeting two key genetic markers, IDH mutations and 1p/19q-codeletion (combined loss of the short arm of chromosome 1 and the long arm of chromosome 19) [1, 5], which are absent in histone-altered gliomas (HAG). Earlier radiogenomics research has utilized conventional imaging assessment ("conventional radiogenomics"), while more recent work has investigated augmentation with artificial intelligence (AI) techniques ("AI radiogenomics"), including radiomics [6] and deep learning.

Radiogenomics arguably has greater potential value in HAG than in adult-type gliomas. This is particularly the case for the H3 K27-altered group, given that their midline location increases the morbidity risk associated with obtaining a definitive tissue diagnosis. Because of their rarity and recent discovery, large radiogenomics studies exploring features of HAG are currently limited, and much of the existing literature consists of case reports and short series. The lower incidence of HAG also makes research into AI-augmented diagnostic methods particularly challenging. The purpose of this systematic review was to summarize the existing imaging literature on HAG, with a view to identifying diagnostic trends and targets for future research.

Materials and methods

This research was performed based on the Preferred Reporting Items for Systematic Reviews and Meta-Analyses (PRISMA-DTA) criteria for diagnostic accuracy studies [7]. Acknowledging the limited number of larger series published at this time, case reports and short case series were also examined, but exempt from PRISMA-DTA.

Data sources

A systematic search was performed in March 2022 using PubMed and the Cochrane Library, identifying all relevant papers published at the time of the search. The following search key words were used: (brain tumor OR brain tumour OR glioma OR midline glioma OR diffuse midline glioma OR pontine glioma OR DIPG OR brain neoplasm OR brain cancer OR glioblastoma) AND (magnetic resonance imaging OR imaging) AND (histone OR histone-mutant OR mutant OR mutation OR gene OR H3 OR G34 OR K27M OR H3 OR H3.1 OR H3.3 OR K27M OR H3 G34). The search was deliberately broad, rather than explicitly searching for particular techniques, in order to avoid biasing some techniques over others.

Study selection

The abstracts of all articles retrieved in the initial search were screened independently by two reviewers (board-certified radiologists with research experience in neuro-oncology). All selected full text manuscripts were reviewed independently by the same two reviewers. The exclusion criteria were: no imaging interpretation; animal or laboratory measurements only; study confined to technical comparison between different MRI acquisition technique(s); studies restricted to predicting WHO histological grade or light microscopic features by imaging; or no English full-text. The major inclusion criterion was: contains a description of imaging features associated with diagnosis and/or prognosis of one or more histone-altered glioma subtypes as defined in WHO 2016 or WHO 2021 (based on the search terms described above). References for all studies fulfilling the above criteria were checked, and if additional publications potentially met the criteria, these were also assessed against the exclusion and inclusion criteria as outlined above. Case reports with or without literature review were included, provided that imaging findings were described. In cases of disagreement, each full text article was reviewed by a third (senior) reviewer and the discrepancy was resolved by consensus.

Data analysis

The results of the included studies were documented with the use of a data extraction form to derive the study methods, study population, glioma mutation(s) identified, imaging findings, correlations and statistical results. Greater detail regarding the data extraction table is presented in Table 1. Each of the reviewers independently performed the full-text screening followed by the data extraction with two reviewers analyzing each publication. Discrepancies were resolved in consensus with a third (senior) reviewer.

Study quality assessment

The study quality was examined using the Quality Assessment of Diagnostic Accuracy Studies (QUADAS-2)

Table 1 Data extraction table

Author, year	Study design	Main research purpose	Study population (N, age, gender)	WHO grade(s)	Location	Glioma mutation	MRI sequence(s) analysed	Imaging features described with key statistical results (if any)
Lober RM, 2014 [8]	Retrospective	Using DWI to stratify DIPG subsets with distinct clinical behavior	• $n = 1$ histone mutant / 20 DIPG • 14 yo • M	G3, G4 (NOS for target patient)	Pons/periventricular nodule	H3-K27M	T1wC+, DWI	• Periventricular nodular enhancement • Baseline ADC high = 1393. Follow up ADC mixed = 1172 & 1875. Periventricular lesion: 728
Ishibashi K, 2016 [9]	Case report	To report a pediatric midline glioma with H3F3A K27M mutation before and after malignant transformation	• $n = 1$ • 14 yo • M	G2 on initial biopsy; G3 on resection	Thalamus	H3-K27M	FLAIR, T1wC+	• Non-enhancing • Tumor dissemination at 12 months after diagnosis
Aboian MS, 2017 [10]	Retrospective	Characterize imaging features of DMGs with H3 K27M mutation and determine any specific imaging features correlate with histone mutation	• $n = 24$ histone mutant /$n = 33$ DMGs • Mean age: 108.5 months • 17 M / 7F	Not stated	Pontine/cerebellar peduncle (11), vermis (4), subcallosal (1), thalamic (6), cervical spine (2)	H3-K27M	T2w, FLAIR, T1w, T1wC+, DWI	• 15/24: cystic components or necrosis, 4/24: oedema • 16/24 (67%) enhanced "heterogenous or uniform" • 5/24 multifocal, 18/24 infiltrative, 4/24 mass effect, 18/24 irregular border, 6/24 CSF based metastases, 9/24 direct cortical invasion • No difference between imaging characteristics of histone mutant and wild type gliomas
Yoshimoto K, 2017 [11]	Case series	Examine the prevalence and clinicopathological features of H3F3A and G34R/V mutant high grade gliomas	• $n = 14$ histone mutant ($n = 10$ K27M, $n = 4$ G34R) • Mean age G34R: 10.5 yo; K27M: 15 yo • G34R: 2 M:2F; K27M: 6 M:4F	Not stated	G34R: parietal, multiple lobes, thalamus	H3-K27M, G34R and G34V	T2w, FLAIR, T1w, T1wC+, DWI	• Hyperintense • Absent or faint then marked enhancement (2/4 cases) after tumour progression • G34R: case 1: gliomatosis cerebri growth pattern. Case 2: high density on CT + intratumoral calcification.Central restricted diffusion. Case 3: low density on CT + intratumoral calcification, indefinite tumour margins on MRI
Lopez GY, 2017 [12]	Case series	Describing 2 cases of DMG with mosaic expression of H3.3 K27M mutant protein and its implications with regards to classification and grading.	• $n = 2$ • 30 yo and 69 yo • 1 M and 1F	1) G4 2) G3	Bilateral thalamus	H3 K27M mutant, IDH wild type, ATRX (one lost, another retained)	T1wC+	• Heterogeneously enhancing (both)

Table 1 (continued)

Author, year	Study design	Main research purpose	Study population (N, age, gender)	WHO grade(s)	Location	Glioma mutation	MRI sequence(s) analysed	Imaging features described with key statistical results (if any)
Vettermann FJ, 2017 [13]	Retrospective	Whether malignant tumor progression as observed for IDH-mutated gliomas can also be found in K27M midline gliomas	• $n = 14$ • Median age:21 yo • 8 M, 6F	G2–4	Thalamus (5), brain stem (4), spinal cord (2), mesial temporal (2), cerebellum (1)	H3K27M, ATRX, IDH, FGFR1	T2w, T1w, T1wC+	• 2/14 showed contrast enhancement on follow up, during progression, after 13.1 (case 2) and 3.8 m (case 10). • FET-PET: Maximal tumor-to-background ratio (TBR) - 6/8 with follow up scans 'significant' increase in TBR (> 20%)
Gilbert AR, 2018 [14]	Case report	A case of pineal region DIPG in a child (2nd case of pineal region DIPG overall)	• $n = 1$ • 12 yo • F	G4	Pineal gland	H3-K27M	FLAIR, T1w, T1wC+, MRS	• Hyperintense • Heterogeneous and rim enhancing, with posterior fossa and spinal CSF dissemination on follow up • Hypodense on CT / hydrocephalus. • MRS: suppressed NAA peak and elevated choline, lipid, and lactate peaks
Vettermann FJ, 2018 [15]	Case series	Characterize the imaging features of H3-G34 mutant gliomas using MRI and 18F-FET PET.	• $n = 8$ • Median age: 27 yo • 2 M, 6F	G3 ($n = 2$), G4 ($n = 5$), 1: NOS	Multifocal (2), rest: lobar/ thalamus/ truncus corporis callosi	H3-G34R (all)	T2w and/or FLAIR, 3D T1w, 3D T1wC+	• 4/8 cystic components, 0/8 significant perifocal oedema • 5/8 heterogeneous enhancement • 1/8 hemorrhage and calcification. • 8/8 high uptake intensity on 18F-FET PET with a median TBRmax of 3.4 • Dynamic PET (7/8) short median TTP min = 12.5 minutes
D'Amico RS, 2018 [16]	Case report	Present clinical and pathological features of pineal region GBM	• $n = 1$ histone mutant / 8 GBM • 38 yo • M	G4	Pineal region	H3-K27M, IDH-wild, lost ATRX	FLAIR, DWI, T1w, T1wC+	• Enhancing • Diffuse seeding of the ventricular system with enhancing tumor • Hydrocephalus
Daoud EV, 2018 [17]	Case series	Characterize adult brainstem gliomas, focusing on the H3-K27M radiologic features and clinical outcome	• $n = 7$ histone mutant • Median age: 41 yo • 6 M and 1F	Low grade ($n = 2$), high grade ($n = 5$)	Midbrain tectum (1), midbrain tegmentum (1), pons (2), medulla (1), cerebellar peduncle/pons (2)	H3-K27M, ATRX-retained, p53	FLAIR, T1C+	• 1/7: T2/FLAIR hyperintense • 2/7 exophytic, 3/7 hydrocephalus • 6/7 enhancing: 2/7 heterogeneous, 1/7 minimal amorphous, 1/7 focal, 1/7 poor irregular, 1/7 "enhancing" • No correlation between contrast enhancement and H3-K27M status, p = 0.1

Table 1 (continued)

Author, year	Study design	Main research purpose	Study population (N, age, gender)	WHO grade(s)	Location	Glioma mutation	MRI sequence(s) analysed	Imaging features described with key statistical results (if any)
Dormegny L, 2018 [18]	Case report	Improve accuracy of spinal cord biopsies and analyzing clinical, radiological and surgical features	• $n = 1$ • 21 yo • M	G4	Dorsal thoracic cord T9–11	H3-K27M, IDH (wild-type)	T2w, T1w, T1wC+	• T2 hyperintense; 3 weeks later (no intervention) - heterogeneous • Loss of T2: intralesional hemorrhage • Initial - localized contrast uptake at T10; 3 weeks later (no intervention) - multiple areas of extended contrast uptake form T9 to conus (T12-L1), with nodular uptake in cauda equina
Gao Y, 2018 [19]	Case report	Report a case of DMG with histone H3-K27M mutation which simultaneously showed PNET-like appearance	• $n = 1$ • 51 yo • F	Not stated	Cervical cord C5–7	H3-K27M, IDH wild type, ATRX retained	T2w, T1w, T1wC+	• Hyperintense • Mild enhancement
Puntonet J, 2018 [20]	Retrospective	Correlate the histological and radiological features of G34R mutant high-grade gliomas	• $n = 12$ • Mean age: 16 yo (range = 6–31 yo), • 9 M and 3F	G4 (6), G3 (4), HGG NOS (2)	All supratentorial, predominant temporal lobe (7), basal ganglia (4), all leptomeningeal contact, meningeal invasion (1), ependymal contact (9)	All H3K27M, G34R, GFAP + ve and BRAFv600e wild-type. ATRX lost (9). P53 + ve (9).	T2, FLAIR, T1wC+ (11 patients), DWI (4), PWI (2), T2*w (6)	• T2 hyperintense (7), T2 isointense (5), T2* hypointense (4/6). • Enhancement: 4/11 intense, 5/11 minimal to moderate, 2/11 no enhancement. 3/12 nodular, 3/12 patchy, 3/12 serpiginous, 3/12 ring-like • 3/3 restricted diffusion (ADC ~ 4800.10 − 6 mm2/s) • 8/10 precontrast T1 hyperintensity, 4/12 no necrosis, 4/12 minimal necrosis, 4/12 high necrosis. • 6/11 no oedema, 4/11 minimal oedema, 1/11 moderate oedema. • 2/2 ASL-PWI hyper perfusion (relative CBF: 1.74–2.85). • 2/2 CT hyperdense

Table 1 (continued)

Author, year	Study design	Main research purpose	Study population (N, age, gender)	WHO grade(s)	Location	Glioma mutation	MRI sequence(s) analysed	Imaging features described with key statistical results (if any)
Jung JS, 2019 [21]	Retrospective	Evaluate the imaging characteristics of DMG with H3 K27M mutation in the spinal cord + evaluate predicting the presence of H3 K27M using a machine learning–based classification model.	• $n = 24$ histone mutant / $n = 41$ spinal cord gliomas • Mean age: 35.5 yo • 17 M / 7F	Not stated	Axial location (18/24 central, 6/24 eccentric); Longitudinal location (8/42 cervical, 14/24 thoracic, 2/24 lumbar)	H3-K27M	T2w, T1w, T1wC+, GRE T2*w	• 21/24 hyperintense, 3/24 isointense, 1/24 hypointense; 14/24 edema • 8/24 diffuse enhancement, 9/24 partial, 7/24 none; 5/17 irregular rim enhancement • 6/24 hemorrhage, 4/24 necrosis, 3/24 tumoral cyst, 1/24 syringohydromyelia • 16/24 ill-defined margin • 10/24 CSF-based tumor spread • Significant difference in tumoral hemorrhage between H3-K27M and wildtype, $p = 0.003$ • RF model: sensitivity = 45.8%, specificity = 88.2%, AUC = 0.63, 95% CI (0.45–0.80), accuracy = 63.4%
Qiu T, 2019 [22]	Retrospective	To summarize the imaging characteristics of adult H3 K27M-mutant gliomas	• $n = 66$ histone mutant • Age range: 20–60 yo • 40 M and 26F	Not stated	Thalamus (38), brainstem (6) (2 pons, 4 medulla, all dorsal); cerebellum (2); thalamus (2), whole brain (8), corpus callosum (3), hypothalamus (1), spinal cord (4) (1 in each of cervical, cervicothoracic, thoracic, and lumbar cord), cerebral hemispheres (2)	H3-K27M	T2w, FLAIR, T1w, T1wC+ (in 61/66), DWI	• 10/66 peritumoral oedema • 11/61 none enhancing, 25/61 partial enhancement, 25/61 diffuse (≥ 50% of the whole lesion) • 1/66 hemorrhage; all (4/4) spinal cord lesions spanned 3 or more segments • 8/66 leptomeningeal dissemination • 66/66 unremarkable or moderate restriction.
He P, 2019 [23]	Case report	A rare H3 K27M–mutant glioblastoma in the hypothalamus.	• $n = 1$ • 27 yo • F	Not stated	Hypothalamus, intrasellar, suprasellar	H3-K27M, ATRX &p53& olig2. IDH wild-type	T2w, T1w, T1wC+	• T2 hyperintense • CT: isodense solid mass, local recurrent mass, high rCBV (not mentioned values) • Strongly heterogeneous enhanced solid lesion and nonenhanced cystic lesion • Local recurrent mass: low ADC (1.2806)
Chanchotisatien A, 2019 [24]	Case report	Presenting a slow-growing thalamic glioma with H3-K27M mutation.	• $n = 1$ • 39 yo • M	G2	Thalamus	H3-K27M, ATRX, IDH-wild	T2w, FLAIR, T1wC+	• T2 hyperintense • No enhancement on followup

Table 1 (continued)

Author, year	Study design	Main research purpose	Study population (N, age, gender)	WHO grade(s)	Location	Glioma mutation	MRI sequence(s) analysed	Imaging features described with key statistical results (if any)
Chen H, 2019 [25]	Retrospective	Noninvasively identify MRI markers predictive of H3 K27 M mutational status in diffuse midline tumors.	• $n = 19$ / $n = 38$ DMGs • Mean age: 27 yo • 11 M and 8F	G2 ($n = 4$), G3 ($n = 5$), G4 ($n = 10$)	Thalamus (12), midbrain (1), pons (2), corpus callosum (2), cerebellum (1), hypothalamus (1),	H3-K27M	T2w, FLAIR, T1w, T1wC+, DWI (in 31/38)	• Shape: 12/19 round/oval, 7/19 irregular • 4/19 solid, 15/19 cystic; 3/19 hemorrhage, 7/19 edema, multifocal 9/19 • Tumour margin: 8/19 sharp, 11/19 blurred • 6/19 intra-tumoral rim enhancement, 1/19 marginal, 4/19 heterogeneous, 8/19 none or minimal • DWI in H3-K27M: • Minimal ADC = 0.734 ± 0.120, Ratio of minimal ADC = 0.972 ± 0.165, • Peritumoral ADC = 0.937 ± 0.156, Ratio of peritumoral ADC = 1.240 ± 0.232. • Significant difference in Histone mutant vs wild type in: Younger age ($p = 0.009$), Minimal ADC ($p = 0.020$), Peritumoral ADC ($p = 0.018$), Ratio of minimal ADC ($p = 0.018$), Ratio of peritumoral ADC ($p = 0.013$) • Thresholds: Minimal ADC 0.728, Ratio of minimal ADC 0.982; Peritumoral ADC 1.004, Ratio of peritumoral ADC 1.248 • Combination of DWI parameters: sensitivity = 88.89%, specificity = 76.92%, AUC = 0.872 (0.75–1.00)
Aboian MS, 2019 [26]	Retrospective	Identify differences in imaging diffusion characteristics between H3- K27M mutant and wild-type DMGs	• $n = 23$ • Mean age: 8.9 yo • 14 M and 9F	Not stated	Pons/vermis/4th ventricle (17), thalamus (5), subcallosal (1)	H3-K27M	DWI and ADC map values, FLAIR used for ROI registration	• No significant differences in ADC mean, median, minimum, and percentile values between histone mutant and wild-type gliomas
Miyazaki T, 2019 [27]	Case report	Present first case of DMG with H3-K27M mutation in a pregnant woman followed by fatal hemorrhage during the postpartum period.	• $n = 1$ • 26 yo • F (pregnant)	Not stated	Thalamus/midbrain	H3K27M, IDH-wild	T2w, FLAIR T1w, T2*w, T1wC+, DWI, MRA	• T2 hyperintense, poorly circumscribed • not enhanced • CT: isodense, hydrocephalus

Table 1 (continued)

Author, year	Study design	Main research purpose	Study population (N, age, gender)	WHO grade(s)	Location	Glioma mutation	MRI sequence(s) analysed	Imaging features described with key statistical results (if any)
Karlowee V, 2019 [28]	Retrospective	Analyze the EZH2 expression level and revealed its association with the poor survival of patients with H3K27M mutant-positive tumors.	• $n = 12$ • Age range: 6–56 yo • 8 M and 4F	Not stated	Distant recurrence (9), thalamus (9), pons (1)	H3-K27M, ATRX (4), p53 (8), EZH2 (9)	T2w, FLAIR, T1w, T1wC+, DWI	• 12/12 hyperintense, 2/12 cyst formation • Enhancement: 5/12 partly, 2/12 homogeneously, 3/12 heterogeneously, 2/12 none • 4/12 intratumoral hemorrhage, 9/12 dissemination + distant recurrence • 10/12 high DWI, 1/12 iso, 1/12 low DWI • No relationship between immunohistochemical staining results and clinical or imaging characteristics.
Giagnacovo M, 2020 [29]	Retrospective	Assess consistency between DIPG histo-molecular findings and clinical-radiological features.	• $n = 19$ / $n = 22$ DIPGs • Mean age: 8 yo • 10 M and 9F	G4 ($n = 9$), G3 ($n = 8$), G2 ($n = 2$)	Pons (at least 50% and causing expansion)	H3F3A/HIST1H3B K27M	T2w, FLAIR, T1w, T1wC+ +/− DWI, PWI, DTI, MRS	• Unsharp margins and patchy enhancement in one image for histone mutant
Chiang J, 2020 [30]	Retrospective	Identify variables that correlated with the clinical diagnosis of aDIPG (atypical) and evaluate the consistency of radiographic diagnosis of aDIPG	• $n = 12$ histone mutant / $n = 33$ aDIPGs, • Median age: 9 yo • 6 M and 6F	G1–4	Extra pontine extension (3), eccentric within the pons (7)	H3F3A/HIST1H3B K27M, TP53	T2w, T1w, T1wC+, DWI +/− FLAIR, T2wC+, SWI/T2*w	• 3/12 ring enhancement • K27M: 10/12 ill-defined tumor margin, 7/12 eccentricity within pons, 3/12 extra pontine extension • No significant difference in imaging (or clinical) features of K27M vs wild-type
Garibotto F, 2020 [31]	Retrospective	Compare the clinical behavior of DMGs H3 K27M- mutant and non-histone mutant midline HGGs in NF1 vs. non-syndromic children and to report imaging features of NF1 HGGs.	• $n = 1$ H3-K27M/ $n = 2$ NF1 DMGs; $n = 11$ H3-K27M / $n = 16$ Non-NF1 DMGs • Age: NF1 - 11yo; Non-NF1 - range 3-16yo • NF1: 1 F; Non-NF1: 4 M, 7F	G4 (all)	NF1: pons/midbrain (1); Non-NF1: thalamus (4), pons (4), medulla (1), diencephalon-mesencephalon junction (2)	H3.3 (H3F3A) K27M	T2w, FLAIR, T1w, T1wC+, DWI, FLAIRC+, (MRS in 2 described cases)	• One described case (NF1 H3K27M lesion): • Irregular rim enhancement, adjacent expansile region without enhancement • Irregular central necrotic area in ponto-mesencephalic portion, adjacent expansile portion no necrosis • reduced diffusivity in ponto-mesencephalic portion (minimum absolute ADC value: 0.69×10^{-3} mm^2/s) • Leptomeningeal dissemination • Single voxel MRS: Cho/NAA peak-height ratio: 3.44 and Cho/Cr ratio: 2.91
Tu JH, 2020 [32]	Case report	Report a case of H3 K27M mutant diffuse midline glioma with cartilaginous metaplasia	• $n = 1$ • 56 yo • F	Not stated	Medulla	H3-K27M, GFAP, IDH-wild, lost ATRX, negative BRAFV600E	T2w, T1w, T1wC+	• T2 heterogeneous, cystic degeneration • Ring enhancement • CT: irregular calcification

Table 1 (continued)

Author, year	Study design	Main research purpose	Study population (N, age, gender)	WHO grade(s)	Location	Glioma mutation	MRI sequence(s) analysed	Imaging features described with key statistical results (if any)
Fujioka Y, 2020 [33]	Case report	Report a case of DMG, H3 K27M mutant that mimicked a hemispheric malignant glioma in an elderly patient.	• $n = 1$ • 66 yo • F	Not stated	Bilateral thalamus, left hippocampus, and fronto-parietal lobes	H3-K27M, IDH wild-type, negative BRAFV600E, retained ATRX, GFAP	FLAIR, T1wC+	• Hyperintense • Multiple isolated enhancing lesions. Enhancement disseminated to lateral ventricles
Cheng Y, 2020 [34]	Case series	Examine the prevalence and clinic pathological features of H3F3A and G34R/V mutant HGGs	• $n = 3$ • 15 yo, 15 yo, 28 yo • 2 M and 1F	Not stated	Cases 1 and 2:frontal, case 3: temporal	1) & 3) H3.3 G34V, 2) H3.3 G34R,	T2w	• Variable, homogenous / heterogenous high • Enhancement not stated • Local recurrence in all cases (after 10 or 5 months of 1st operation)
Baroni LV, 2020 [35]	Case series	Report three brainstem tumors with an initial indolent course that later developed classical imaging and clinical features of DIPG.	• $n = 3$ • 3 yo, 11 months, 6 yo • 2 M and 1F	1) Not stated, 2) G4, 3) G4	1) ponto-medullary junction, 2) medulla/pons, 3) brainstem and the pontocerebellar angle	all H3.3 K27M, 2 cases with TP 53	FLAIR, T2w	• All cases: hyperintense • 1) Non-enhancing, 2) non-enhancing, 3) not stated • All cases show increase in size in follow up (range 11 months to 5 years)
Babarczy K, 2020 [36]	Case report	Report one of the oldest patients having so far been reported with an immunohistochemically confirmed DMG, H3 K27M-mutant	• $n = 1$ • 73 yo • F	G4	Cervical cord (C2) extending to medulla, pons, cerebral peduncles, internal capsules bilaterally and right pallidum	H3-K27M, GFAP positive, IDH-wild	T2w, FLAIR, T1w, T1wC+, DWI, MRA, STIR (spine), MRS	• FLAIR hyperintense • No enhancement • No diffusion restriction • MRA: normal • MRS: high metabolism (no values)
Lu VM, 2020 [37]	Case report	Illustrate H3 K27M mutation occurring in cortically-based diffuse gliomas not midline structures and discuss the uncertainties regarding grading and prognostic classification for such tumours.	• $n = 1$ • 9 yo • F	Not stated	Pons	H3-K27M	T1wC+	• Not stated but enhancement highlighted in image • Progression in 2 months time (intracranial/intraspinal metastases)

Table 1 (continued)

Author, year	Study design	Main research purpose	Study population (N, age, gender)	WHO grade(s)	Location	Glioma mutation	MRI sequence(s) analysed	Imaging features described with key statistical results (if any)
Su X, 2020 [38]	Retrospective	Investigate the feasibility of predicting H3 K27M mutation status using an automated machine learning	• $n = 40$ histone mutant / $n = 100$ midline gliomas • Mean age: 23.6 yo • 14 M and 26F	G4	Midline (not otherwise specified)	H3-K27M	T2w, FLAIR, T1w, T1wC+	• 10 important features, including 3 shape, 3 first-order, 2 GLSZM, 1 GLCM, and 1 GLDM, were included. • Tumor shape features important in predicting H3 K27M mutation, maximum 2D diameter of the slice of H3 K27M–mutant tumors was smaller than that of wild-type (41.31 vs 59.35, $P = 0.007$) • Sensitivity range of 10 models: 0.55–0.73 • Specificity range of 10 models: 0.57–0.93 • AUC range for 10 models (0.73–0.90)
Chiba K, 2020 [39]	Retrospective	Investigate the correlation between the original site of thalamic gliomas and patients' clinical outcomes retrospectively and to determine appropriate treatment strategies.	• $n = 4$ Histone mutant / $n = 10$ pediatric thalamic gliomas • Age range: 8–17 yo • 2 M, 2F	G3–4	All thalamopulvinar (TP)	H3-K27M	T2w, T1w, T1wC+, DWI (2/4), methionine-PET (2/4), DTI (1/4)	• T2 hyperintense • 1/4 heterogeneous enhancement, 1/4 mixed faint and homogeneous enhancement, 2/4 faint enhancement • 2/4 high DWI • The presence of H3 K27M mutation and TP location were closely related to each other ($p = 0.0036$)

Table 1 (continued)

Author, year	Study design	Main research purpose	Study population (N, age, gender)	WHO grade(s)	Location	Glioma mutation	MRI sequence(s) analysed	Imaging features described with key statistical results (if any)
Rodriguez Gutierrez D, 2020 [40]	Retrospective	To correlate imaging characteristics and outcome measures of pediatric patients with newly diagnosed non-brainstem HGG with pathologic and molecular data	• $n = 23$ H3K27M, $n = 7$ H3G34R / 113 gliomas • H3K27M: mean 12.1 yo; H3G34R: mean 13.1 yo; H3K27M: 11 M and 12F; H3G34R: 3 M and 4F	G3 ($n = 21$), G4 ($n = 92$)	Cerebral hemispheres and midline	H3F3a K27M, G34R	T2w, FLAIR, T1w, T1wC+	• Perilesional oedema: H3 K27M (10/23 none, 13/23 minor), H3 G34 (1/7 none, 3/7 minor, 2/7 moderate, 1/7 severe) • Necrosis: H3 K27M (16/23 yes, 6/23 no), H3G34 (4/7 yes, 2/7 no) • Enhancement: H3 K27M (14/23 strong, 1/23 moderate, 7/23 minor/none), H3 G34 (1/7 strong, 1/7 moderate, 4/7 minor/none) • Hemorrhage: H3 K27M (7/23 yes, 15/23 no), H3 G34 (4/7 yes, 2/7 no) • Tumor definition: H3 K27M (19/23 well-defined, 5/23 ill-defined/diffuse), H3 G34R (2 well-defined, 5 ill-defined/diffuse) • Versus Midline wildtype, H3 K27M–mutant tumors showed more enhancement ($P < 0.05$) and older age • ADC values were not significantly different between H3 K27M–mutant and Midline WT tumors or between H3G34R and cerebral wildtype. • Versus cerebral wildtype, tumor definition for H3 G34R mutants was significantly different, $p < 0.05$

Table 1 (continued)

Author, year	Study design	Main research purpose	Study population (N, age, gender)	WHO grade(s)	Location	Glioma mutation	MRI sequence(s) analysed	Imaging features described with key statistical results (if any)
Kay MD, 2020 [41]	Case report	Report rare extra cranial metastases from glioblastoma with PNET-like components and demonstrate the utility of FDG PET/CT for revealing distant metastases from glioblastoma	• $n = 1$ • 17 yo • F	G4	Temporal lobe	H3G34, IDH-wild	T2w, T1wC+, PET post resection	• T2 hyperintense • Heterogeneous enhancement • Presented with hematoma • Post resection: invasion into the left greater wing of the sphenoid, leptomeningeal drop and osseous metastases
Onishi S, 2020 [42]	Case series	Describing radiological and immunostaining characteristics of H3.3 G34R-Mutant Glioma	• $n = 3$ • Ages: 13, 19 and 15 yo 1 M and 2F	2/3 glioblastoma, 1/3 HGG	1) frontal, 2) parietal, 3) parieto-occipital	All: H3.3 G34R mutation, IDH-wild BRAF-wildtype, retained 1p/19q	T2w, FLAIR, T1w, T1wC+, DWI, MRS, ASL-PWI	• 3/3 T2/FLAIR moderately hyperintense • 1/3 poor enhancement 2/3 partial enhancement • 3/3 DWI hyperintense (ADC range = 0.625–0.810) • 3/3 mild edema. • 2/3 low tumor blood flow on ASL • 3/3: high choline peak, marked decrease in NAA peak, small lactate peak. • 3/3 iso to hyperdense mass without calcification

Table 1 (continued)

Author, year	Study design	Main research purpose	Study population (N, age, gender)	WHO grade(s)	Location	Glioma mutation	MRI sequence(s) analysed	Imaging features described with key statistical results (if any)
Thust S, 2021 [43]	Retrospective	To assess anatomical and quantitative diffusion-weighted MR imaging features in H3 K27M histone-mutant diffuse midline glioma	• $n = 15$ • Median age: 19 yo • 6 M and 9F	G4	Midline brain	H3-K27M	T2w, FLAIR, T1w, T1wC+, DWI, DSC perfusion MRI (2/15)	• T2/FLAIR signal: 13/15 heterogeneous, 2/15 homogeneous. 2/15 with cysts • Margin: 8/15 distinct, 7/15 indistinct • Enhancement: 4/15 solid enhancement, 6/15 rim enhancing + necrosis, 3/15 none • DWI: • ADCmin in solid tumor = 0.84 (±0.15 SD) ADCmin/NAWM ratio = 1.097 (±0.149) • ADCmean in solid tumor = 1.12 (±0.25) ADCmean/NAWM ratio = 1.466 (±0.299) • Hemorrhage: 3/15 macro, 2/15 petechial • Hydrocephalus: 6/15 requiring shunting • 2/15 elevated rCBV ((5.9, 3.5) • 18F-choline PET (1/15): tracer accumulation • A significant difference (P = 0.01) between the 2nd centile of the volumetric ADC histogram and the ROI ADCmin values. • No statistical significance between ROI ADCmin and the 5th and 10th histogram percentiles, or ROI ADCmin/NAWM ratio and the ADC5th percentile/NAWM ratio or ROI ADCmean and the histogram ADCmedian and ADCmean or ROI ADCmean/NAWM ratio and the histogram ADCmean/NAWM ratio

Table 1 (continued)

Author, year	Study design	Main research purpose	Study population (N, age, gender)	WHO grade(s)	Location	Glioma mutation	MRI sequence(s) analysed	Imaging features described with key statistical results (if any)
Picart T, 2021 [44]	Retrospective	To describe the characteristics of DHG H3G34-mutant in adults and to compare them to those of established types of adult WHO grade IV gliomas	• $n = 17$ H3G34R • Mean age: 25 yo • 11 M and 6F	Not stated	H3.3G34R: frontal (11), parietal (11), temporal (3), occipital (1), corpus callosum (3), midline (4); H3.3K27M: 33/33 midline, 2 with temporal extension	17/17 H3F3a G34R, 14/16 TP53 positive, 13/14 loss of ATRX	T2w, FLAIR, T1w, T1wC+, MRS (9/17), DCE-PWI (8/17)	• H3.3 G34R: 9/16 poorly delineated/infiltrative, 3/16 Initial hemorrhage, 2/16 cyst, 1/16 necrosis; H3.3 K27M: 3/28 cyst, 10/28 necrosis • H3.3 G34R: 4/15 enhancement, 6/15 faint enhancement, 5/15 none; H3.3 K27M: 8/29 enhancement • H3.3 G34R: 12/13 restriction (8/13 focal); H3.3 K27M: 3/23 restriction • 4/8 elevated rCBV (> 1.7). 4/9 elevated Choline/N-Acetyl-Aspartate ratio > 2 and/or of lipid/ lactate peaks • H3 G34-mutant occurred in younger patients ($p = .05$), more frequently involved the parietal lobe ($p < .001$), more frequently presented as a hemorrhagic tumor at diagnosis ($p = .03$), less frequently demonstrated contrast enhancement ($p = .05$) and necrosis ($p = .03$), more frequently displayed ADC restriction ($p < .001$)
Cheng R, 2021 [45]	Case report	Report a pediatric patient with spinal cord H3 K27M-mutant DMG	• $n = 1$ • 7 yo • F	G4	Cervical cord C2–7 intramedullary	H3-K27M	T2w, T1w, T1wC+	• T2 slightly hyperintense • Heterogeneous enhancement
Li Q, 2021 [46]	Retrospective	MRI characteristics of brain DMG-histone mutant using radiomics	• $n = 16$ histone mutant / $n = 30$ DMGs, • Median age: 25.5 yo • 10 M and 6F	Not stated	10/16 thalamus, 6/16 brainstem	H3-K27M	T2w, T1w, T1wC+	• No detailed information. From single selected figure –T2 hyperintense • Faint enhancement • Cyst formation showed sig diff between H3K27M and WT (OR = 7.800, 95% CI 1.476–41.214; $p = 0.024$) • No statistical significance in: necrosis ($p = 0.191$), hemorrhage ($p = 0.657$) and T1/T2 ratio ($p = 0.689$)

Table 1 (continued)

Author, year	Study design	Main research purpose	Study population (N, age, gender)	WHO grade(s)	Location	Glioma mutation	MRI sequence(s) analysed	Imaging features described with key statistical results (if any)
Kandemirli S, 2021 [47]	Retrospective	Machine learning to predict histone mutation	• $n = 50$ histone mutant / $n = 59$ histone wild type • Median age: 10 yo mutant / 30.5 yo histone-wild	Not stated	Thalamus only (17), 12 center in thalamus (12), center in the pons (13), remaining posterior fossa structures (8)	H3K27M	T2w, T1w, T1wC+, FLAIR and ADC	• Median age in the H3K27M mutant group was significantly lower compared with the wild-type cohort • H3K27M-mutant and wild-type tumors show no significant difference in tumor size, enhancement, internal necrotic changes, or infiltrative appearance
Kathrani N, 2022 [48]	Retrospective	Assess DWI and DSC-PWI to predict the H3K27M mutation status in DMGs non-invasively	• $n = 48$ • Mean age: 23 yo • 21 M and 27F	G2–4	Thalamus (28), midbrain (6), pons (10), medulla (2), others (2)	H3-K27M	DWI, DSC (in 34/48)	• Peritumoral ADC = 1.1, nPT ADC = 1.64, min ADC = 0.76, nADC = 1.11 • rCBV = 25.17, nrCBV = 3.44, rCBF = 266.15, uncorrected nrCBV = 3.5 • Significantly lower PT ADC and nPT ADC and higher rCBV, nrCBV, rCBF, uncorrected nrCBV in histone mutant group • Thalamic subgroup analysis: H3K27M showed significantly lower min ADC PT ADC, nADC, nPT ADC and significantly higher nrCBV, rCBF, nrCBF, uncorrected rCBV, uncorrected nrCBV, and corrected rCBV **Predicting histone mutation:** • PT ADC (cut-off = 1.245; AUC 0.6, Sn 47%, Sp 79%), nPT ADC (cut-off = 1.853; AUC = 0.6, Sn 52%, Sp 77%), nrCBV (cut-off = 1.83; AUC = 0.6, Sn 46%, Sp 76%) and uncorrected nrCBV (cut-off = 2.28; AUC = 0.7, Sn 61%, Sp 71%), In thalamic subgroup: nADC (cut-off = 1.129; AUC = 0.7, Sn 61%, Sp 75%), PT ADC (cut-off = 1.185; AUC = 0.65, Sn 68, 68%), nPT ADC (cut-off = 1.853; AUC = 0.65, Sn 64%, Sp 71%), nrCBV (cut-off = 1.83; AUC = 0.703, Sn 47%, Sp 85%), nrCBF (cut- off = 2.73; AUC = 0.74, Sn 71%, Sp 75%), and uncorrected nrCBV (cut-off = 2.27; AUC = 0.759, Sn 60%, Sp 86%)

Table 1 (continued)

Author, year	Study design	Main research purpose	Study population (N, age, gender)	WHO grade(s)	Location	Glioma mutation	MRI sequence(s) analysed	Imaging features described with key statistical results (if any)
Ikeda K, 2022 [49]	Retrospective	Establish high intensity on DWI in non-enhancing tumors (DWI-Gadolinium mismatch sign) as imaging biomarker for H3K27M DMG	• $n=6$ • Median age: 23 yo (range 6–31) • 4 M and 2F	Not stated	6/6 thalamus	H3-K27M, IDH-wild type	T2w, T2*, FLAIR, T1w, T1wC+, DWI	• T2/FLAIR hyperintense • 6/6 enhancement • 6/6 DWI high • 5/6 DWI-Gd mismatch sign positive • DWI-Gd mismatch sign and intratumoral bleeding present in thalamic gliomas than in pons with statistical significance ($p=0.046$ and $p=0.0017$)
Su X, 2022 [50]	Retrospective	Investigate the capacity of quantitative MRI in identifying the H3 K27M mutation status of DMG	• $n=23$ • Age range = 6–47 yo • 13 M and 10F	G4	Juvenile group: hemispheric near midline (1), diencephalon (2), brainstem (8) adult group: diencephalon (3), brainstem (9)	H3K27M	T2, FLAIR, DWI, T1w, T1wC+, PWI, MRS, DTI	• Juvenile group: rADC_M = 1.56, rADC_15th = 1.15, rADC_25th = 1.31, rADC_50th = 1.50, rADC_75th = 1.68, rADC_max = 2.94, Ins/tCr = 1.11, NAA/tCr = 0.62, Cho/NAA = 0.96, Cho/rCr = 0.65, tNAA/tCr = 0.63, Glx/rCr = 0.89. • Adult group: rADC_M = 1.5, rADC_15th = 1.07, rADC_25th = 1.15, rADC_50th = 1.33, rADC_75th = 1.60, rADC_max = 3.05, Ins/tCr = 0.80, NAA/tCr = 0.60, Cho/NAA = 1.11, Cho/rCr = 0.57, tNAA/tCr = 0.86, Glx/rCr = 0.97 • rADC_15th, rADC_25th, rADC_50th, and rADC_75th values were significantly lower in mutation group ($p<0.05$) • Ins/tCr values were lower in the juvenile ($p=0.003$) and the adult ($p=0.025$) mutation subgroups • rMD_mean and rMD_25th/50th/75th values of the mutation group were significantly lower in the adult subgroup ($p<0.001$) • rCBV_mean/25th/50th/75th were slightly higher and the rTTP_mean/50th were slightly lower in the adult mutant subgroup; no significant differences in other PWI metrics • No significant difference in tumor size ($p>0.05$).

Table 1 (continued)

Author, year	Study design	Main research purpose	Study population (N, age, gender)	WHO grade(s)	Location	Glioma mutation	MRI sequence(s) analysed	Imaging features described with key statistical results (if any)
Hohm A, 2021 [51]	Retrospective	Describe and compare MRI of pediatric DMG with known H3 K27 mutation status including H3.1 and H3.3 K27M subgroups	• $n = 52$ • Age: 10.2y (range 1.25–17.75yo) • 26 M and 26F	Not stated	19/52 thalamus/basal ganglia, 0 midbrain tectum, 27/52 pons, 5/52 spinal cord, 1 other (medulla)	H3.1 K27M & H3.3 K27M	T2w, T1w, T1wC+	• T2 hyperintense (44), homogeneous (3), predominantly homogeneous (17), predominantly inhomogeneous (23), inhomogeneous (4). • Margins: well defined (3), moderately defined (23), ill-defined (21). • Necrosis: yes (27); Edema: yes (8); CSF dissemination: (2) • Enhancement: strong (19), intermediate (9), mild (7), no (12), predominantly inhomogeneous (18), inhomogeneous (10); ring enhancement (25) • DWI: DWI hyperintense (22), restriction (5), not restricted (12) • SWI: signal loss (7), hemorrhage: yes (18) • H3.1 younger than H3.3 ($p = 0.004$) • H3K27M more commonly arising in pons and thalamus/BG vs WT widely distributed ($p = 0.001$) • H3 K27M more often T2 hyper intense (44/47, p = 0.02), T1 inhomogeneous (19/46, $p = 0.02$) • Spinal tumors: There were no imaging characteristics that significantly differentiated the two molecular groups
Kim H, 2021 [52]	Retrospective/ one histone mutant case	Report 13 MMRD-associated (9 sporadic and 4 Lynch syndrome) primary brain tumors to determine clinic pathological and molecular characteristics	• $n = 1$ • 11 yo • M	G4	Thalamus (right)	H3-K27M, lost ATRX, IDH-wild type	T2w, T1w, FLAIR, T1wC+ (from images)	• Multiple enhancing solid and cystic masses

Table 1 (continued)

Author, year	Study design	Main research purpose	Study population (N, age, gender)	WHO grade(s)	Location	Glioma mutation	MRI sequence(s) analysed	Imaging features described with key statistical results (if any)
Kurokawa R, 2022 [53]	Case series	Review the demographic, clinical, and neuroradiological features of DHGs-G34m in 3 original cases	• $n = 3$ • Ages: 16, 22 and 19 yo • F/M/F	2/3G4	1/3 frontal, 2/3 parietal	3/3 H3 G34R, 2/3 p53, 3/3 ATRX, 3/3 IDH wild type, BRAF -ve GFAP +ve	CT, T2w, FLAIR T1w, T2*W, T1wC+, DWI, SWI, PWI	• 3/3 T2 hyperintense, 2/3 leptomeningeal contact laterally • 2/3 patchy enhancement, 1/3 heterogeneous enhancement • 3/3 restricted diffusion, ADC values range = 0.53–0.8 • 2/3 hyperdense on unenhanced CT without calcification; 3/3 intratumoral hemorrhage on T2*; 1/3 elevated CBF in enhancing portion
Cheng L, 2021 [54]	Retrospective	Describe the clinical and radiological characteristics of primary spinal H3 K27M-mutant DMG and compare with the H3 K27 wild-type	• $n = 28$ • Age: 28.7 yo • 19 M and 9F	G1 (0), G2 (9), G3 (10), G4 (9)	Cervical (7), cervicothoracic (4), thoracic (11), thoracolumbar (5), holocord (1). Median involved segments = 3	H3K27M p53 (20) ATRX loss (8), Ki-67 >/= 20% (18), IDH-wild type (28)	T2w, T1wC+	• Enhancement: partial (12), diffuse (13); pial enhancement (24) • Ill-defined margin (25) • Edema (16), hemorrhage (4), cysts (4), necrosis (10), syrinx (6) • Fewer H3K27M have syrinx vs WT ($p = 0.017$) • No other imaging features showed statistical significance

Abbreviation key: DWI Diffusion weighted imaging, *DIPG* diffuse intrinsic pontine glioma, *T1wC+* T1 weighted imaging with contrast, *ADC* Apparent diffusion coefficient, *FLAIR* Fluid attenuation inversion recovery, *DMG* Diffuse midline glioma, *G2/3/4* WHO grade 2/3/4, *IDH* Isocitrate dehydrogenase, *T2W* T2 weighted imaging, *FET-PET* Positron emission tomography (PET) using O-(2-[18F] fluoroethyl-)-L-tyrosine, *MRS* Magnetic resonance spectroscopy, *GBM* glioblastoma multiform, *PNET* primitive neuroectodermal tumor, *DL-GNT* Diffuse leptomeningeal glioneuronal tumor, *NOS* not otherwise specified, *PWI* perfusion weighted imaging, *GRE* gradient echo, *rCBV* relative cerebral blood volume, *ROI* region of interest, *MRA* magnetic resonance angiogram, *DTI* diffusion tensor imaging, *SWI* susceptibility weighted imaging, *NF-1* Neurofibromatosis type-1, *STIR* Short Tau Inversion Recovery, *AUC* area under the curve, *HGG* high grade glioma, *FDG* fluorodeoxyglucose, *ASL* arterial spin labelling, *NAWM* normal appearing white matter, *DHG* diffuse hemispheric glioma, *DCE* dynamic contrast-enhanced, *MMRD* Mismatch repair-deficient

instrument [55]. We evaluated concerns regarding applicability in three domains (patient selection, index test and reference standard) and the risk of bias in four different domains (patient selection, index test, reference test and timing). Each study was independently assessed for quality and potential bias by two reviewers. Disagreements were resolved by consensus with a senior reviewer. QUADAS-2 assessment was conducted on all original research, but is not applicable to case reports.

Statistical analysis

Descriptive data are presented in form of a narrative synthesis, because of the heterogeneity of reported imaging features, assessment methods and lack of consistent quantification.

Data synthesis

A total of 47 papers was identified after exclusions [8–54] (Fig. 1). Just under half (21/47) of the included papers were case reports or short series (up to three cases). The majority of the publications (39/47) described only H3 K27-altered gliomas (typically reported as H3 K27M-mutant, reflecting the recency of the change in nomenclature), two described both H3 K27-altered and H3 G34-mutant gliomas, and six reports included only H3 G34-mutant gliomas (in one of these studies, K27-altered were included as a comparator, but were not the focus of the research [44]). The case reports generally described 'novel' features, for example previously undescribed tumor locations, clinical behavior, patient demographics or pathological features. Tumors varied between publications in terms of their histological grade. Despite the mostly high-grade nature of HAG, several tumors with grade 2 histology were described [9, 12, 24], highlighting that the lack of high grade histological features does not negate the need for appropriate molecular testing if the tumor occurs in a typical location [17] or demographic.

Studies assessing larger numbers of patients varied greatly in their method design. Patient demographics were heterogeneous, with studies variably assessing pediatric and/or adult patients. Several cohorts included only HAG, thus were unable to compare imaging appearances with H3-wildtype tumors in a similar location. The majority of studies assessed MRI appearances, with or without CT. Two series (one publication each for H3 K27-altered and H3 G34-mutant gliomas) assessed PET (positron emission tomography) using the amino acid tracer FET (fluorine-18-fluoroethyl-L-tyrosine) [13, 15]. Three recent papers assessed the use of MRI radiomics for predicting H3 K27 status [38, 46, 47].

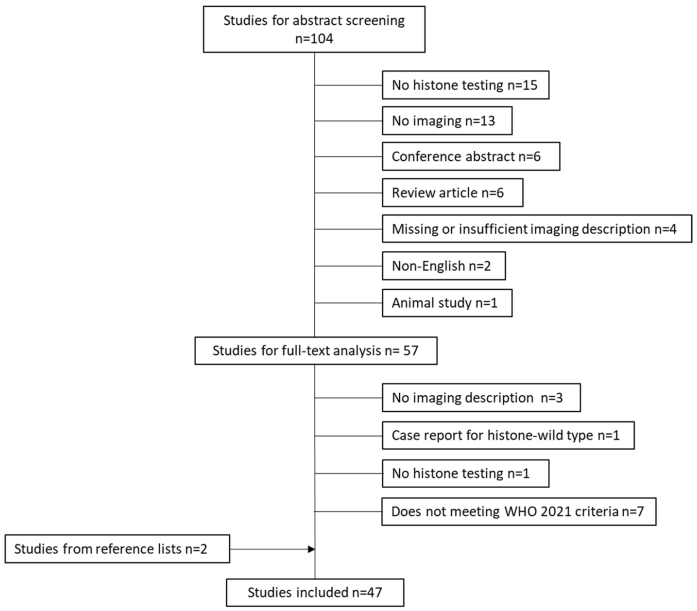

Fig. 1 CONSORT diagram outlining included and excluded studies

H3 K27-altered gliomas

Patient demographics

As would be expected according to incidence, the likelihood of H3 K27 mutations varied depending on the age distributions within the study samples, with H3 K27-alteration being more common in younger age groups. For example, 19 of 22 DIPGs in the pediatric cohort reported by Giagnacovo et al. were H3 K27-altered [29], while only seven (28%) of 25 adult brainstem gliomas reported by Daoud et al. demonstrated H3 K27M mutations [17]. This is also well demonstrated by the cohort of diffuse midline gliomas reported by Chen et al., with H3 K27M-mutant patients being on average 15 years younger than -wildtype patients [25]; a similar finding was reported by Su et al. [50].

Tumor location

Marked heterogeneity in reporting and study design limits assessment of the relative frequency of the different locations. Several studies assessed only tumors in specific locations, for example the pons (diffuse intrinsic pontine glioma, DIPG) or spinal cord, while others included only intracranial tumors. The reporting of tumor location was also variable, for example whether a pontine location was distinguished from other brainstem sites. Nevertheless, the thalami and brainstem (in particular pons) are unambiguously the most common locations. The spinal cord is the third-most-common location, though the data are limited.

There were notable differences in tumor location depending on the age group studied. The thalami were the most common location in cohorts which either largely or exclusively assessed adult patients [22, 25, 28, 46, 48]. In contrast, the brainstem was the most common overall location in studies targeting a pediatric population [10, 13, 31, 51]. Another common theme was that most intracranial H3 K27-altered gliomas were located in either the thalami or brainstem, while H3 K27-wildtype tumors were relatively more evenly distributed across midline locations [48, 51]. There are suggestions that the likelihood of H3 K27-alteration is higher in the brainstem rather than the thalami [48, 51], though this may relate to a brainstem location being more common in younger patients, who inherently have a higher likelihood of H3 K27-alteration. Two studies on spinal cord gliomas suggest that H3 K27M mutations occur in approximately half of cases, with 28/59 in one cohort [54] and 24/41 in another [21].

Beyond demonstration of a midline location, as a key diagnostic criterion [4], few anatomical characteristics have been described to predict H3 K27 status. One study by Chiba et al. subdivided their 10 pediatric thalamic gliomas (four H3 K27M-mutant) into three anatomical groups: anterior, combined thalamic and internal capsular, and thalamopulvinar [39]. All four H3 K27M-mutant gliomas in their cohort were thalamopulvinar, compared to only one H3 K27M-wildtype, and this association was statistically significant ($p = 0.0036$) despite the low number of cases [39]. Chiang et al. found slightly different rates of H3 K27M mutations in pontine tumors stratified as "typical" DIPG (defined radiographically as a poorly-demarcated, T1-hypointense and T2-hyperintense tumor with mass effect occupying ≥75% of the axial diameter of the pons; 50% H3 K27M-mutant), versus "atypical" DIPG (35%) and non-DIPG with an extrapontine epicenter (25%) [30]. Qiu et al. noted that all six of their H3 K27M-mutant gliomas which only involved the brainstem were located dorsally, though such tumors accounted for a minority of their cohort (6/66) [22]. In a cohort of spinal cord gliomas, neither the axial location (central vs eccentric) nor longitudinal location (cervical, thoracic or lumbar) correlated with H3 K27M status [21].

Tumor margins and extent

Individual studies vary in their results, but both well- and ill-defined tumor margins may occur. Fewer studies have specifically assessed tumor size, though most H3 K27-altered appear to be relatively well demarcated. This is supported by the radiomics study of Su et al., which found that the maximal 2D slice diameter was significantly lower for H3 K27M-mutant gliomas compared to -wildtype tumors [38]. Nevertheless, these tumors can occasionally be larger. For example, out of 66 H3 K27M-mutant adult gliomas reported by Qiu et al., eight demonstrated cerebral hemispheric infiltration together with thalamic and/or brainstem involvement [22], and cases of extensive H3 K27M-mutant gliomas in older patients have been reported [33, 36].

Distant tumor spread was identified in several studies. For example, Karlowee et al. observed dissemination and remote recurrence in 75% of 12 H3 K27-altered gliomas [28]. Of the 66 H3 K27M-mutant gliomas described by Qiu et al., leptomeningeal and subependymal dissemination were noted in eight and three patients, respectively [22]. According to publications, such dissemination generally occurred later in the disease course rather than already being manifest at initial diagnosis, although details remained unclear. A midline location itself was associated with leptomeningeal dissemination [40], however, thus it is unclear whether the biology of H3 K27M-altered gliomas predisposes to leptomeningeal dissemination or whether this is simply related to their location. One case report described extracranial HAG metastases [41].

Signal characteristics and contrast-enhancement

The data on signal characteristics, in particular contrast-enhancement, are highly variable, but it is clear that H3 K27M-altered gliomas demonstrate a spectrum of appearances, from a lack of enhancement to ring-enhancement with central necrosis [10]. Thus, a lack of enhancement should not dissuade from considering an H3 K27M-altered glioma. Hohm et al. found that H3 K27M-mutant gliomas in their pediatric cohort were more commonly T2-hyperintense and heterogeneous than H3 K27M-wildtype tumors [51]. A different pediatric study demonstrated significantly more enhancement in H3 K27M-mutant tumors than -wildtype ($p < 0.05$) [40]. However, other studies found no statistically significant differences in the degree of enhancement between H3 K27M-mutant and -wildtype tumors [10, 17, 54]. Information on the specific contrast agent, contrast dose and type of post-contrast T1-weighted imaging sequence(s) used is generally lacking.

Hemorrhage

Results on the incidence of hemorrhage in H3 K27-altered gliomas are variable, but overall this feature seems to have limited predictive value. Hemorrhage was the only imaging feature predictive of H3 K27M mutation in a cohort of spinal cord gliomas, occurring in six of 24 (25%) H3 K27M-mutant gliomas, compared to none of the 17 H3 K27M-wildtype tumors ($p = 0.033$) [21]. However, in another cohort of 59 spinal cord gliomas, the rate of hemorrhage was almost identical (and marginally higher in the wildtype group); the presence of a tumor syrinx (being more common in H3 K27M-wildtype tumors) was the only MRI feature with a statistically significant difference in this study [54]. Similar variability has been reported intracranially, though no other studies have found a statistically significant difference in the rate of hemorrhage between H3 K27-altered and -wildtype tumors. Comparing across studies, there are suggestions that hemorrhage may be more common in pediatric patients than adults [22, 51], but this question has not been specifically investigated.

Apparent diffusion coefficient values

Studies investigating apparent diffusion coefficient (ADC) values have reported variable results, similar to the variability in the conventional imaging appearances, with a recurring trend towards H3 K27-altered gliomas demonstrating lower ADC values. Chen et al. reported that both tumoral and peritumoral apparent diffusion coefficient (ADC) values were significantly lower in H3 K27M-mutant gliomas than -wildtype (ratio of minimal ADC and ratio of peritumoral ADC combined, AUC 0.872) [25]. Another study also found lower ADC values in the peritumoral region of H3 K27M-mutant gliomas [48]; ADC values within the tumoral region were lower in H3 K27M-mutant tumors located in the thalami, but this was not reproduced across their overall cohort [48]. A further study also noted that relative ADC histogram parameters (15th, 25th, 50th and 75th percentiles) were lower in the H3 K27M-mutant group [50]. In contrast, no statistically significant correlations between ADC values and H3 K27 status were identified in two other studies, one having calculated mean, median, minimum and maximum ADC values and percentiles [26], the other having examined average and minimum ADC values [40]. All of the 66 H3 K27M-mutant gliomas reported by Qiu et al. had low or moderate diffusivity, with none demonstrating diffusion restriction on visual inspection [22]. Thust et al. reported moderately low ADC values in some H3 K27M-mutant gliomas, consistent with previous findings in glioblastoma, but highlighted ADC variability [43].

Other advanced MRI techniques

Two out of the 15 H3 K27M-mutant gliomas reported by Thust et al. were imaged with dynamic susceptibility contrast perfusion, both demonstrating elevated relative cerebral blood volume (rCBV; 3.5–5.9) [43]. Kathrani et al. reported higher rCBV in H3 K27M-mutant gliomas compared to -wildtype [48]. Su et al. noted slightly higher rCBV in their discovery cohort, but this was not replicated in the validation cohort [50]. The authors also evaluated several MR Spectroscopy parameters, with lower myo-inositol/total creatine values in the H3 K27M-mutant group being the only parameter with statistical significance [50]. A multivariate model developed from this research achieved AUC = 0.976 in the validation set, but this comprised only 13 patients [50], thus the reproducibility of this model is unknown.

FET-PET

One study assessed the use of FET-PET in H3 K27-altered gliomas [13]. Baseline TBR_{max} (maximal tumor-to-background ratio) did not correlate with histological grade or patient outcome, but was potentially useful to identify a subsequent increase of > 20% in TBR_{max} which predicted tumor progression and poor survival [13]. However, in the case example provided, new contrast-enhancement coincided with the increase in TBR_{max} [13], hence the added diagnostic value of FET-PET is uncertain.

Radiomics

Kandemirli et al. investigated radiomics for the prediction of H3 K27 status in a cohort of 109 tumors, comprising 50 H3 K27M-mutant and 59 -wildtype, with just over half being pediatric cases [47]. Of the two models investigated, better results were obtained using XGBoost

with additional feature selection, which achieved an area under the curve (AUC) of 0.791 in the training set and 0.737 for the test set [47]. Su et al. examined a similar cohort, including 40 H3 K27M-mutant and 60 -wildtype midline gliomas across pediatric and adult age groups, using the Tree-based Pipeline Optimization Tool [38]. This study reported better results, with the best-performing of the 10 models assessed yielding AUC 0.903 in the training cohort and 0.85 in the validation set [38]. Of note, the latter results were obtained utilizing only the FLAIR sequence [38], while Kandemirli et al. incorporated multiple conventional sequences and ADC [47]. Li et al. used principal component analysis in a smaller cohort, comprising 30 tumors, of which 16 were H3 K27M-mutant [46]. They observed overlap between H3 K27M-mutant and -wildtype types, with only cyst formation (favoring a H3 K27M-mutant tumor) showing a statistically significant difference between the two [46]. All three of the above studies extracted features using PyRadiomics [38, 46, 47].

H3 G34-mutant gliomas

Only eight studies reported on H3 G34-mutant gliomas, with small numbers. All cases were high-grade histologically, the majority grade 4 [11, 40, 42, 44, 53]. Yoshimito identified four G34-mutant tumors amongst 411 consecutive gliomas (1.0%) of all ages, compared to 10 H3 K27-altered gliomas [11]. Picart et al. also had fewer H3 G34-mutant gliomas than H3 K27-altered tumors in their cohort (17 compared to 32) [44]. In a pediatric cohort of gliomas divided into midline and cerebral hemispheric locations, H3 G34 mutations were demonstrated in seven of 54 cerebral cases [40].

Tumor margins and location

All four of the H3 G34-mutant tumors reported by Yoshimoto et al. all had ill-defined tumor margins [11]. The gliomas varied in location, and some involved deeper structures such as the basal ganglia [11]. Five of the seven H3 G34-mutant tumors in a pediatric cohort were ill-defined, and tumor definition was significantly different to non-midline H3 G34-wildtype tumors (the majority being well-defined) [40]. Similarly, most of the 17 H3 G34-mutant gliomas reported by Picart et al. were ill-defined [44]. Midline involvement was observed in four of the patients in this cohort, but always as an extension of a primarily hemispheric tumor [44]. In contrast, two of the three H3 G34-mutant gliomas described by Kurokawa et al. were well-defined [53]. Similarly, in a series of 12 H3 G34-mutant gliomas, the tumors were most commonly large and well-delineated, with mild peritumoral edema [20]. Leptomeningeal contact was observed in all 12 [20]. Concordant with these results, the two H3 G34-mutant described by Onishi et al. exhibited little peritumoral edema given their large size [42].

Contrast-enhancement

Eleven of the 17 H3 G34-mutant gliomas reported by Picart et al. demonstrated absent or faint contrast-enhancement initially, but all eight of these which received subsequent MRIs developed nodular or ring-enhancement after a median of 2.6 months [44]. Some other series have demonstrated relatively mild enhancement [11, 42], while a range of enhancement patterns have been reported in other cohorts [15, 20, 53]. As for H3 K27-altered tumors, there is limited information on the specific contrast agent, contrast dose and type of post-contrast T1-weighted imaging sequence(s) used.

Other MRI features

Two of the four H3 G34-mutant tumors reported by Yoshimoto et al. demonstrated calcification [11]. One tumor in a cohort of eight reported by Vetterman et al. demonstrated both calcification and hemorrhage, while four demonstrated cystic components [15]. Microcalcifications have also been noted on histology [20]. All three tumors reported by Kurokawa et al. demonstrated intratumoral hemorrhage, with varying degrees of diffusion restriction [53]. Two tumors in one series had available arterial spin labelling perfusion data and both demonstrated hyperperfusion [20]. One small series described choline elevation and N-acetyl aspartate depletion on Spectroscopy [42].

FET-PET

One study described FET-PET features of eight H3 G34-mutant gliomas, noting high uptake in all (median TBR_{max} 3.4, range 2.5–11.7) [15]. In contrast, the MRI appearances of these tumors were more variable; for example, three tumors did not demonstrate contrast-enhancement, while three demonstrated rim-enhancement with central necrosis [15].

Data quality

Of 47 included publications, 29 were diagnostic accuracy studies proceedable to QUADAS-2 assessment, with the remaining 18 studies being case reports or short series unsuitable for QUADAS-2 assessment. All studies were retrospective, introducing a high risk of bias in the patient selection domain, which parallels other radiogenomics literature. For most ($n = 17$) research, it was unclear whether the imaging was analyzed without knowledge of tissue results, specifically glioma genotypes, thus increasing the risk of bias. For 13 of the 29 publications, images were reviewed by only one observer or no information was provided at all. No formal interobserver comparisons

were reported. The diagnostic reference standard was similar and judged to be appropriate in most ($n=20$) studies. HAG genotype was presumed to represent a static tumor property, therefore the timing between reference standard and target test was considered appropriate for all studies. QUADAS-2 graphs are shown in Fig. 2, while individual study data are presented in Supplementary Material 1.

Discussion

The reported cohort sizes are substantially lower for HAG than in the adult-type diffuse glioma radiogenomics literature, which is expected given their lower incidence, particularly for H3 G34-mutant gliomas. We identified marked heterogeneity of study designs, firstly in the cohorts investigated, but also for visual features assessed and in the definitions of such features, which limits comparability and precluded a meaningful meta-analysis of the data. Results have been conflicting for several features, highlighting that these tumors present a variety of appearances, whereby HAG cannot yet be confirmed or excluded with a high degree of confidence. The heterogeneity of the data indicates a need for more consistent biomarker definitions across studies, and highlights a challenge that could potentially benefit from AI approaches in future research. Despite these diagnostic limitations, some patterns have emerged, in particular for H3 K27-altered gliomas, which are summarized in Table 2. Of particular note, common to both H3 K27-altered and H3 G34-mutant gliomas was the frequent observation of less aggressive MRI appearances, belying their highly malignant histopathological classification.

H3 K27-altered gliomas vary considerably in their degree of enhancement, and often demonstrate less contrast uptake than one would expect for a WHO grade 4 tumor. In contrast, the majority of adult-type grade 4 diffuse gliomas manifest as enhancing, centrally necrotic lesions [56]. Furthermore, a relative paucity of enhancement does not help distinguish between an H3 K27-altered glioma and a low grade adult-type diffuse glioma, which arguably is the more important distinction. Similar variability is evident in terms of tumor margins and ADC values. There have been some promising results with other advanced MRI features, in particular rCBV values, but data are currently limited and further research is warranted. Most H3 K27M-altered

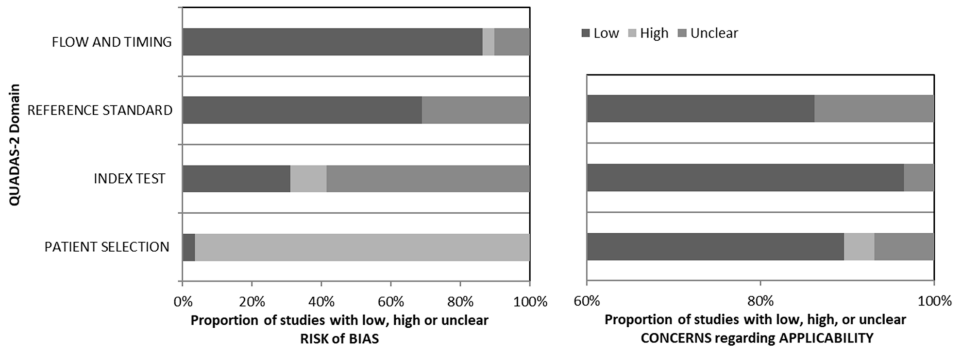

Fig. 2 QUADAS-2 summary results

Table 2 Features of H3 K27M-altered gliomas

Common locations	Less common locations	Tumor margins & extent	Enhancement	ADC values	rCBV
• Thalami (esp. adults) • Brainstem (esp. children) • Spinal cord	• Corpus callosum • Hypothalamus • Pineal gland • Tectum	• Usually well-defined and localized • Occasionally more widely infiltrative • Leptomeningeal dissemination common, esp. later in disease course	• Variable, but often less than expected for a high-grade tumor	• Variable, but generally low	• Variable, but generally increased

gliomas are relatively localized, though more diffusely infiltrative tumors (with a component of midline involvement) can occasionally be seen. Thus, the identification of thalamic and/or brainstem involvement in disseminated tumors could prompt testing for H3 K27-alteration, though the incidence would be expected to be low. There are possible differences in the imaging appearances of H3 K27-altered gliomas depending on their location. Suggestions that a pulvinar location in thalamic gliomas [39] or a dorsal location in pure brainstem gliomas [22] could predict H3 K27M mutation are notable, but require further validation. There is currently minimal information regarding whether a feature combination could provide additional predictive value. While the variability of MRI appearances limits the ability to confidently predict HAG genotypes, it highlights the importance of stereotactic biopsy and molecular testing for candidate lesions (e.g. based on location) even if the MRI appearances suggest a lower-grade tumor, for example based on well-defined margins or a lack of enhancement.

Subtle differences in the results between pediatric and adult studies have been reported. Most convincingly, a thalamic location is most common in adult patients [22, 25, 28, 46, 48], while a brainstem location is relatively more common in children [10, 13, 31, 51]. Beyond location, however, the data are less compelling, and there is clearly substantial overlap in the appearances. A particular challenge relates to methodological differences in the definitions of the assessed features, which make it difficult to compare across studies. In addition, studies combining pediatric and adult patients have generally not compared the two patient populations, and the limited patient numbers within each cohort present a further challenge. More targeted studies, correcting for patient age, would be required to clarify such observations.

The pre-test probability of an H3 K27-altered glioma varies according to each particular location, being highest in the brainstem, thalami and spinal cord. Data on less common midline locations are limited, but these seem to have a lower likelihood of H3 K27M-alteration. In turn, this will alter the role of features predictive of H3 K27M status, analogous to the difference in the ability to confidently predict an IDH mutation in adult-type diffuse gliomas depending on tumor grade (grade 2–3 vs grade 4) [5]. Thus, in a midline location with a higher likelihood of an H3 K27-altered glioma, a particular feature may allow more confident prediction of this genotype. In contrast, it may be difficult to confidently identify an H3 K27-altered glioma in a location with a lower pre-test probability, but instead the absence of features associated with H3 K27M-alteration could make it highly unlikely, such that definitive genetic testing would become redundant. This is particularly valuable given the challenging surgical access to many of these locations.

For G34-mutant gliomas, the existing data are scarce. A particular challenge is that the vast majority of hemispheric gliomas in adults will be H3 G34-wildtype. Nevertheless, some features worthy of further investigation have been reported. Tumors were often noted to be quite large, with relatively mild peritumoral edema. As for H3 K27-altered gliomas, H3 G34-mutant gliomas often demonstrate relatively mild enhancement given their WHO grade 4 status. For some tumors, there was possible morphologic overlap with IDH-mutant, 1p/19q-codeleted oligodendrogliomas: calcifications are characteristic of IDH-mutant, 1p/19q-codeleted oligodendrogliomas [5, 57, 58], but were reported in several H3 G34-mutant gliomas [11, 15]. Therefore, testing for an H3 G34 mutation should be considered for a calcified tumor without 1p/19q-codeletion in a young adult patient.

Very limited AI research exists on HAG. The results presented by Su et al. show promise, though the variability across the described models used raises the possibility over-fitting [38]. The substantial overlap in the features found in H3 K27M-mutant and -wildtype gliomas reported by Li et al. [46] is consistent with the results of conventional MRI radiogenomics studies, though the finding that cyst formation could predict H3 K27-alteration [46] is notable and warrants further investigation. A limitation of all three AI studies identified (and also some of the conventional MRI research) is that both pediatric and adult patients were included, in order to maximize numbers. This raises questions regarding clinical applicability, given that the H3 K27M-wildtype group will have included a mix of neoplasms. We expect that AI research in HAG will increase, but this may need to harness multi-institutional datasets in order to provide more uniform methodology whilst being relevant to clinical practice, for example when distinguishing between pediatric and adult patients and aiming to better characterize the tumors within the H3 K27M-wildtype group.

Conclusion

The existing imaging data on HAG are limited and heterogeneous, but certain patterns have emerged. H3 K27-altered gliomas exhibit variable appearances, thus these tumors should be considered when occurring in typical locations irrespective of their conventional MRI appearances. Low ADC has been proposed as a biomarker of H3 K27-alteration, but results have been variable and facilitated diffusion does not exclude this malignant tumor type. Higher rCBV has also been reported in H3 K27-altered gliomas, but requires further validation. H3 G34-mutant gliomas are commonly large, with relatively mild peritumoral edema and variable, often mild

enhancement. Some of these tumors may exhibit calcification, potentially mimicking IDH-mutant, 1p/19q-codeleted oligodendrogliomas. As a rare disease, HAG research will benefit from collaborative multi-institutional datasets, especially if investigating AI techniques. AI techniques could also be valuable for addressing the issue of heterogeneity of the existing data.

Abbreviations
WHO: World Health Organization; IDH: Isocitrate dehydrogenase; HAG: Histone-altered gliomas; AI: Artificial intelligence; PRISMA-DTA: Preferred Reporting Items for Systematic Reviews and Meta-Analyses; QUADAS-2: Quality Assessment of Diagnostic Accuracy Studies; PET: Positron emission tomography; FET: Fluorine-18-fluoroethyl-L-tyrosine; DIPG: Diffuse intrinsic pontine glioma; ADC: Apparent diffusion coefficient; rCBV: relative cerebral blood volume; TBR_{max} : maximal tumor-to-background ratio.

Supplementary Information

The online version contains supplementary material available at https://doi.org/10.1186/s40644-022-00500-3.

Additional file 1: Supplementary Material 1. QUADAS-2 data for individual studies

Acknowledgements
Nil.

Authors' contributions
AL and ST developed the project. GA and GC performed the systematic analysis, supported by ST. AL drafted the manuscript, supported by GA, GC and ST. All authors read and approved the final manuscript.

Funding
Dr. Arian Lasocki was supported by a Peter MacCallum Cancer Foundation Discovery Partner Fellowship. Dr. Stefanie Thust receives proportional funding from the UCL/UCLH NIHR Biomedical Research Centre.

Availability of data and materials
Not applicable.

Declarations

Ethics approval and consent to participate
Ethics committee approval was not required by our institutions.

Consent for publication
Not applicable.

Competing interests
Nil.

Author details
[1]Department of Cancer Imaging, Peter MacCallum Cancer Centre, Grattan St, Melbourne, Victoria 3000, Australia. [2]Sir Peter MacCallum Department of Oncology, The University of Melbourne, Parkville, Victoria, Australia. [3]Department of Radiology, The University of Melbourne, Parkville, Victoria, Australia. [4]Lysholm Department of Neuroradiology, National Hospital for Neurology and Neurosurgery, London, UK. [5]Department of Radiology, Mansoura University Hospital, Mansoura, Egypt. [6]Department of Radiology, Royal Free Hospital, London, UK. [7]Department of Brain Repair and Rehabilitation, Neuroradiological Academic Unit, UCL Institute of Neurology, London, UK.

Received: 30 August 2022 Accepted: 23 October 2022
Published online: 17 November 2022

References

1. Louis DN, Perry A, Reifenberger G, von Deimling A, Figarella-Branger D, Cavenee WK, et al. The 2016 World Health Organization classification of tumors of the central nervous system: a summary. Acta Neuropathol. 2016;131(6):803–20.
2. Louis DN, Giannini C, Capper D, Paulus W, Figarella-Branger D, Lopes MB, et al. cIMPACT-NOW update 2: diagnostic clarifications for diffuse midline glioma, H3 K27M-mutant and diffuse astrocytoma/anaplastic astrocytoma. IDH-mutant Acta Neuropathol. 2018;135(4):639–42.
3. Brat DJ, Aldape K, Colman H, Holland EC, Louis DN, Jenkins RB, et al. cIMPACT-NOW update 3: recommended diagnostic criteria for "diffuse astrocytic glioma, IDH-wildtype, with molecular features of glioblastoma, WHO grade IV". Acta Neuropathol. 2018;136(5):805–10.
4. Louis DN, Perry A, Wesseling P, Brat DJ, Cree IA, Figarella-Branger D, et al. The 2021 WHO classification of tumors of the central nervous system: a summary. Neuro Oncol. 2021;23(8):1231–51.
5. Lasocki A, Anjari M, Örs Kokurcan S, Thust SC. Conventional MRI features of adult diffuse glioma molecular subtypes: a systematic review. Neuroradiology. 2021;63(3):353–62.
6. Bhandari AP, Liong R, Koppen J, Murthy SV, Lasocki A. Noninvasive determination of IDH and 1p19q status of lower-grade gliomas using MRI Radiomics: a systematic review. AJNR Am J Neuroradiol. 2021;42(1):94–101.
7. McInnes MDF, Moher D, Thombs BD, McGrath TA, Bossuyt PM, Clifford T, et al. Preferred reporting items for a systematic review and Meta-analysis of diagnostic test accuracy studies: the PRISMA-DTA statement. Jama. 2018;319(4):388–96.
8. Lober RM, Cho YJ, Tang Y, Barnes PD, Edwards MS, Vogel H, et al. Diffusion-weighted MRI derived apparent diffusion coefficient identifies prognostically distinct subgroups of pediatric diffuse intrinsic pontine glioma. J Neuro-Oncol. 2014;117(1):175–82.
9. Ishibashi K, Inoue T, Fukushima H, Watanabe Y, Iwai Y, Sakamoto H, et al. Pediatric thalamic glioma with H3F3A K27M mutation, which was detected before and after malignant transformation: a case report. Childs Nerv Syst. 2016;32(12):2433–8.
10. Aboian MS, Solomon DA, Felton E, Mabray MC, Villanueva-Meyer JE, Mueller S, et al. Imaging characteristics of pediatric diffuse midline gliomas with histone H3 K27M mutation. AJNR Am J Neuroradiol. 2017;38(4):795–800.
11. Yoshimoto K, Hatae R, Sangatsuda Y, Suzuki SO, Hata N, Akagi Y, et al. Prevalence and clinicopathological features of H3.3 G34-mutant high-grade gliomas: a retrospective study of 411 consecutive glioma cases in a single institution. Brain Tumor Pathol. 2017;34(3):103–12.
12. Lopez GY, Oberheim Bush NA, Phillips JJ, Bouffard JP, Moshel YA, Jaeckle K, et al. Diffuse midline gliomas with subclonal H3F3A K27M mutation and mosaic H3.3 K27M mutant protein expression. Acta Neuropathol. 2017;134(6):961–3.
13. Vettermann FJ, Neumann JE, Suchorska B, Bartenstein P, Giese A, Dorostkar MM, et al. K27M midline gliomas display malignant progression by imaging and histology. Neuropathol Appl Neurobiol. 2017;43(5):458–62.
14. Gilbert AR, Zaky W, Gokden M, Fuller CE, Ocal E, Leeds NE, et al. Extending the neuroanatomic territory of diffuse midline glioma, K27M mutant: pineal region origin. Pediatr Neurosurg. 2018;53(1):59–63.
15. Vettermann FJ, Felsberg J, Reifenberger G, Hasselblatt M, Forbrig R, Berding G, et al. Characterization of diffuse gliomas with histone H3-G34 mutation by MRI and dynamic 18F-FET PET. Clin Nucl Med. 2018;43(12):895–8.
16. D'Amico RS, Zanazzi G, Wu P, Canoll P, Bruce JN. Pineal region glioblastomas display features of diffuse midline and non-midline gliomas. J Neuro-Oncol. 2018;140(1):63–73.
17. Daoud EV, Rajaram V, Cai C, Oberle RJ, Martin GR, Raisanen JM, et al. Adult brainstem gliomas with H3K27M mutation: radiology, pathology, and prognosis. J Neuropathol Exp Neurol. 2018;77(4):302–11.
18. Dormegny L, Chibbaro S, Ganau M, Santin M, Kremer L, Proust F. Biopsying a spinal cord lesion: a diagnostic dilemma. Case report and review of literature. Neuro-Chirurgie. 2018;64(6):425–30.
19. Gao Y, Feng YY, Yu JH, Li QC, Qiu XS, Wang EH. Diffuse midline gliomas with histone H3-K27M mutation: a rare case with PNET-like appearance and neuropil-like islands. Neuropathology. 2018;38(2):165–70.
20. Puntonet J, Dangouloff-Ros V, Saffroy R, Pagès M, Andreiuolo F, Grill J, et al. Historadiological correlations in high-grade glioma with the histone 3.3 G34R mutation. J Neuroradiol. 2018;45(5):316–22.
21. Jung JS, Choi YS, Ahn SS, Yi S, Kim SH, Lee SK. Differentiation between spinal cord diffuse midline glioma with histone H3 K27M mutation and

wild type: comparative magnetic resonance imaging. Neuroradiology. 2019;61(3):313–22.
22. Qiu T, Chanchotisatien A, Qin Z, Wu J, Du Z, Zhang X, et al. Imaging characteristics of adult H3 K27M-mutant gliomas. J Neurosurg. 2019;15:1-9.
23. He P, Chen W, Qiu XX, Xi YB, Guan H, Xia J. A rare high-grade glioma with a histone H3 K27M mutation in the hypothalamus of an adult patient. World Neurosurg. 2019;128:527–31.
24. Chanchotisatien A, Pan J, Du Z, Qiu T, Yu J, Chu S. Slow-growing thalamic glioma with histone H3 lysine 27-to-methionine mutation: 3-year follow-up before surgical intervention. World Neurosurg. 2019;127:266–8.
25. Chen H, Hu W, He H, Yang Y, Wen G, Lv X. Noninvasive assessment of H3 K27M mutational status in diffuse midline gliomas by using apparent diffusion coefficient measurements. Eur J Radiol. 2019;114:152–9.
26. Aboian MS, Tong E, Solomon DA, Kline C, Gautam A, Vardapetyan A, et al. Diffusion characteristics of pediatric diffuse midline gliomas with histone H3-K27M mutation using apparent diffusion coefficient histogram analysis. AJNR Am J Neuroradiol. 2019;40(11):1804–10.
27. Miyazaki T, Tsuji M, Hagiwara S, Minamoto T, Ishikawa N, Hirato J, et al. Fatal postpartum hemorrhage in diffuse midline glioma with H3-K27M mutation. Case Rep Obstet Gynecol. 2019;2019:8340437.
28. Karlowee V, Amatya VJ, Takayasu T, Takano M, Yonezawa U, Takeshima Y, et al. Immunostaining of increased expression of enhancer of Zeste homolog 2 (EZH2) in diffuse midline glioma H3K27M-mutant patients with poor survival. Pathobiology. 2019;86(2–3):152–61.
29. Giagnacovo M, Antonelli M, Biassoni V, Schiavello E, Warmuth-Metz M, Buttarelli FR, et al. Retrospective analysis on the consistency of MRI features with histological and molecular markers in diffuse intrinsic pontine glioma (DIPG). Childs Nerv Syst. 2020;36(4):697–704.
30. Chiang J, Diaz AK, Makepeace L, Li X, Han Y, Li Y, et al. Clinical, imaging, and molecular analysis of pediatric pontine tumors lacking characteristic imaging features of DIPG. Acta Neuropathol Commun. 2020;8(1):57.
31. Garibotto F, Madia F, Milanaccio C, Verrico A, Piccardo A, Tortora D, et al. Pediatric diffuse midline gliomas H3 K27M-mutant and non-histone mutant midline high-grade gliomas in Neurofibromatosis type 1 in comparison with non-syndromic children: a single-center pilot study. Front Oncol. 2020;10:795.
32. Tu JH, Piao YS, Lu DH, Wang LM, Liu L, Bai DY, et al. An adult case of diffuse midline glioma with H3 K27M mutation. Neuropathology. 2020;40(6):627–31.
33. Fujioka Y, Hata N, Hatae R, Suzuki SO, Sangatsuda Y, Nakahara Y, et al. A case of diffuse midline glioma, H3 K27M mutant mimicking a hemispheric malignant glioma in an elderly patient. Neuropathology. 2020;40(1):99–103.
34. Cheng Y, Bao W, Wu Q. Cerebral hemispheric glioblastoma with PNET-like morphology and histone H3.3 G34 mutation in younger patients: report of three rare cases and diagnostic pitfalls. Indian J Pathol Microbiol. 2020;63(2):262–6.
35. Baroni LV, Solano-Paez P, Nobre L, Michaeli O, Hawkins C, Laughlin S, et al. Indolent course of brainstem tumors with K27M-H3.3 mutation. Pediatr Blood Cancer. 2020;67(3):e28102.
36. Babarczy K, Reisz Z, Szabo E, Rajda C, Vecsei L, Bodi I, et al. A longitudinally extensive H3 K27M-mutant diffuse midline glioma in an elderly patient clinically mimicking central nervous system inflammation: a case report. Folia Neuropathol. 2020;58(4):377–85.
37. Lu VM, Brown DA, Daniels DJ. Rare diffuse intrinsic pontine glioma metastasis throughout the brain and spine. World Neurosurg. 2020;140:301–2.
38. Su X, Chen N, Sun H, Liu Y, Yang X, Wang W, et al. Automated machine learning based on radiomics features predicts H3 K27M mutation in midline gliomas of the brain. Neuro Oncol. 2020;22(3):393–401.
39. Chiba K, Aihara Y, Masui K, Abe K, Komori T, Kawamata T. Pulvinar locus is highly relevant to Patients' outcomes in surgically resected thalamic gliomas in children. World Neurosurg. 2020;134:e530–e9.
40. Rodriguez Gutierrez D, Jones C, Varlet P, Mackay A, Warren D, Warmuth-Metz M, et al. Radiological evaluation of newly diagnosed non-brainstem pediatric high-grade glioma in the HERBY phase II trial. Clin Cancer Res. 2020;26(8):1856–65.
41. Kay MD, Pariury HE, Perry A, Winegar BA, Kuo PH. Extracranial metastases from glioblastoma with primitive neuronal components on FDG PET/CT. Clin Nucl Med. 2020;45(3):e162–e4.
42. Onishi S, Amatya VJ, Karlowee V, Takeshima Y, Sugiyama K, Kurisu K, et al. Radiological and immunostaining characteristics of H3.3 G34R-mutant glioma: a report of 3 cases and review of the literature. Pediatr Neurosurg. 2020;55(5):319–25.
43. Thust S, Micallef C, Okuchi S, Brandner S, Kumar A, Mankad K, et al. Imaging characteristics of H3 K27M histone-mutant diffuse midline glioma in teenagers and adults. Quant Imaging Med Surg. 2021;11(1):43–56.
44. Picart T, Barritault M, Poncet D, Berner LP, Izquierdo C, Tabouret E, et al. Characteristics of diffuse hemispheric gliomas, H3 G34-mutant in adults. Neurooncol Adv. 2021;3(1):vdab061.
45. Cheng R, Li DP, Zhang N, Zhang JY, Zhang D, Liu TT, et al. Spinal cord diffuse midline glioma with histone H3 K27M mutation in a pediatric patient. Front Surg. 2021;8:616334.
46. Li Q, Dong F, Jiang B, Zhang M. Exploring MRI characteristics of brain diffuse midline gliomas with the H3 K27M mutation using Radiomics. Front Oncol. 2021;11:646267.
47. Kandemirli SG, Kocak B, Naganawa S, Ozturk K, Yip SSF, Chopra S, et al. Machine learning-based multiparametric magnetic resonance imaging Radiomics for prediction of H3K27M mutation in midline gliomas. World Neurosurg. 2021;151:e78–85.
48. Kathrani N, Chauhan RS, Kotwal A, Kulanthaivelu K, Bhat MD, Saini J, et al. Diffusion and perfusion imaging biomarkers of H3 K27M mutation status in diffuse midline gliomas. Neuroradiology. 2022;64(8):1519-28.
49. Ikeda K, Kolakshyapati M, Takayasu T, Amatya VJ, Takano M, Yonezawa U, et al. Diffusion-weighted imaging-gadolinium enhancement mismatch sign in diffuse midline glioma. Eur J Radiol. 2022;147:110103.
50. Su X, Liu Y, Wang H, Chen N, Sun H, Yang X, et al. Multimodal MR imaging signatures to identify brain diffuse midline gliomas with H3 K27M mutation. Cancer Med. 2022;11(4):1048–58.
51. Hohm A, Karremann M, Gielen GH, Pietsch T, Warmuth-Metz M, Vandergrift LA, et al. Magnetic resonance imaging characteristics of molecular subgroups in pediatric H3 K27M mutant diffuse midline glioma. Clin Neuroradiol. 2022;32(1):249–58.
52. Kim H, Lim KY, Park JW, Kang J, Won JK, Lee K, et al. Sporadic and lynch syndrome-associated mismatch repair-deficient brain tumors. Lab Invest. 2022;102(2):160–71.
53. Kurokawa R, Baba A, Kurokawa M, Pinarbasi ES, Makise N, Ota Y, et al. Neuroimaging features of diffuse hemispheric glioma, H3 G34-mutant: a case series and systematic review. J Neuroimaging. 2022;32(1):17–27.
54. Cheng L, Wang L, Yao Q, Ma L, Duan W, Guan J, et al. Clinicoradiological characteristics of primary spinal cord H3 K27M-mutant diffuse midline glioma. J Neurosurg Spine. 2021;24:1–12.
55. Whiting PF, Rutjes AW, Westwood ME, Mallett S, Deeks JJ, Reitsma JB, et al. QUADAS-2: a revised tool for the quality assessment of diagnostic accuracy studies. Ann Intern Med. 2011;155(8):529–36.
56. Lasocki A, Tsui A, Tacey MA, Drummond KJ, Field KM, Gaillard F. MRI grading versus histology: predicting survival of World Health Organization grade II-IV astrocytomas. AJNR Am J Neuroradiol. 2015;36(1):77–83.
57. Lasocki A, Gaillard F, Gorelik A, Gonzales M. MRI features can predict 1p/19q status in intracranial gliomas. AJNR Am J Neuroradiol. 2018;39(4):687–92.
58. Saito T, Muragaki Y, Maruyama T, Komori T, Tamura M, Nitta M, et al. Calcification on CT is a simple and valuable preoperative indicator of 1p/19q loss of heterozygosity in supratentorial brain tumors that are suspected grade II and III gliomas. Brain Tumor Pathol. 2016;33(3):175–82.

Publisher's Note

European Journal of Radiology 113 (2019) 116–123

Contents lists available at ScienceDirect

European Journal of Radiology

journal homepage: www.elsevier.com/locate/ejrad

Research article

Filtration-histogram based magnetic resonance texture analysis (MRTA) for glioma IDH and 1p19q genotyping☆

Martin A. Lewis[a], Balaji Ganeshan[b], Anna Barnes[b], Sotirios Bisdas[c,d], Zane Jaunmuktane[e], Sebastian Brandner[e], Raymond Endozo[b], Ashley Groves[b], Stefanie C. Thust[c,d,*]

[a] Institute of Neurology, University College London, London, UK
[b] Institute of Nuclear Medicine, University College London Hospitals NHS Foundation Trust, London, UK
[c] Lysholm Department of Neuroradiology, National Hospital for Neurology and Neurosurgery, University College London Hospitals NHS Foundation Trust, London, UK
[d] Department of Brain Rehabilitation and Repair, UCL Institute of Neurology, Queen Square, London, UK
[e] Division of Neuropathology, National Hospital for Neurology and Neurosurgery, University College London NHS Foundation Trust, London, UK

ARTICLE INFO

Keywords:
Glioma
Brain tumour
Texture analysis
Isocitrate dehydrogenase
1p19q codeletion

ABSTRACT

Background: To determine if filtration-histogram based texture analysis (MRTA) of clinical MR imaging can non-invasively identify molecular subtypes of untreated gliomas.

Methods: Post Gadolinium T1-weighted (T1 + Gad) images, T2-weighted (T2) images and apparent diffusion coefficient (ADC) maps of 97 gliomas (54 = WHO II, 20 = WHO III, 23 = WHO IV) between 2010 and 2016 were studied. Whole-tumor segmentations were performed on a proprietary texture analysis research platform (TexRAD, Cambridge, UK) using the software's freehand drawing tool. MRTA commences with a filtration step, followed by quantification of texture using histogram texture parameters. Results were correlated using non-parametric statistics with a logistic regression model generated.

Results: T1 + Gad performed best for IDH typing of glioblastoma (sensitivity 91.9%, specificity 100%, AUC 0.945) and ADC for non-Gadolinium-enhancing gliomas (sensitivity 85.7%, specificity 78.4%, AUC 0.877). T2 was moderately precise (sensitivity 83.1%, specificity 78.9%, AUC 0.821). Excellent results for IDH typing were achieved from a combination of the three sequences (sensitivity 90.5%, specificity 94.5%, AUC = 0.98). For discriminating 1p19q genotypes, ADC produced the best results using unfiltered textures (sensitivity 80.6%, specificity 89.3%, AUC 0.811).

Conclusion: Preoperative glioma genotyping with MRTA appears valuable with potential for clinical translation. The optimal choice of texture parameters is influenced by sequence choice, tumour morphology and segmentation method.

1. Introduction

Gliomas exhibit considerable genetic and clinical diversity, even amongst tumors of the same World Health Organization (WHO) histological grade [1]. Over 100 DNA mutations have been implicated in glioma genesis [2], from which tumors may be stratified into distinct molecular subgroups of prognostic and predictive value [2–4]. As a biomarker, the Isocitrate Dehydrogenase (IDH) gene is pivotal, because a de novo IDH mutation (IDH^{mut}) probably represents the initiating event that distinguishes lower grade (WHO II-III) gliomas from primary glioblastoma (WHO IV) [5]. The most common mutation is IDH1R132H, present in > 90% of lower grade gliomas and in secondary glioblastoma [6]. Absence of an IDH mutation (IDH wild-type, IDH^{wt}) is a key feature of primary glioblastoma and defines malignant lower grade gliomas within the same genetic disease spectrum [3]. IDH^{mut} gliomas with combined deletion of the short arm of chromosome 1 and the long arm of

Abbreviations: IDH, Isocitrate Dehydrogenase; IDH^{mut}, Isocitrate Dehydrogenase mutation; IDH^{wt}, Isocitrate Dehydrogenase wild type; $IDH^{mut}1p19q^{del}$, Isocitrate Dehydrogenase mutant gliomas with combined deletion of the short arm of chromosome 1 and the long arm of chromosome 19; $IDH^{mut}1p19q^{int}$, Isocitrate Dehydrogenase mutant gliomas with intact short arm of chromosome 1 and long arm of chromosome 19; MRTA, magnetic resonance imaging texture analysis; SSF, spatial scale filter; WHO, World Health Organization; s.d., standard deviation; m.p.p., mean of positive pixels

☆ **Work originated**: UCL Institute of Neurology, Queen Square, London WC1N 3BG and Institute of Nuclear Medicine, University College Hospitals NHS Foundation Trust, 5th Floor Tower, 235 Euston Road, London NW1 2BU, UK.

* Corresponding author at: Lysholm Department of Neuroradiology, National Hospital for Neurology and Neurosurgery, Neuroradiological Academic Unit, Department of Brain Rehabilitation and Repair, Queen Square, London, WC1N 3BG, UK.
E-mail addresses: s.thust@ucl.ac.uk, steffi.thust@nhs.net (S.C. Thust).

https://doi.org/10.1016/j.ejrad.2019.02.014
Received 21 November 2018; Accepted 12 February 2019

chromosome 19 ($IDH^{mut}1p19q^{del}$) are mostly oligodendrogliomas with a better prognosis, which can be distinguished from 1p19q intact ($IDH^{mut}1p19q^{int}$) gliomas that are predominantly astrocytomas, with an intermediate prognosis. Glioma genotyping by immunohistochemistry depends on tissue sampling and requires facilities for testing, with potential geographical restrictions on turnaround times. Presurgical mutational analysis could influence the timing and extent of tumor resection [7] and predict adjuvant therapy response, for example the sensitivity to temozolomide is greater in IDH^{mut} gliomas [8].

Morphological assessment can contribute to glioma molecular subtyping [9,10], but limitations include observer dependence and lack of quantitative thresholds. Filtration-histogram based MR imaging texture analysis (MRTA) provides quantitative information about tumor microstructure beyond the limits of visual perception, as reflected by the distribution of pixel values within the lesion [11]. MRTA requires no programming skills and is operated by performing a manual tumor segmentation using workstation-integrated software, with calculations initiated via mouse-click. The application commences with a filtration step, which serves to remove image noise, extracts and enhances tissue features of different sizes before measuring signal intensity histogram parameters. The interpretation of results as a reflection of biological processes depends on the tumor type examined, but broadly MRTA provides a measure of tissue heterogeneity. The software has previously undergone a qualification process for glioma histological grading and differential diagnosis [12–14]. In this study, we investigated whether filtration-histogram based MRTA could predict glioma IDH and 1p19q genotypes using MR images acquired in routine clinical practice.

2. Materials and methods

2.1. Patient cohort

Ethics review board approval was obtained with informed consent waived for this retrospective study of anonymized imaging data. Cases were identified randomly from attendances for operative planning (n = 124) between 2010 and 2016. 14 patients were excluded due to a non-glioma histological diagnosis, 11 patients due to prior surgery, and 2 studies had corrupted imaging data. In total, 97 gliomas were eligible for MRTA (Fig. 1, **SHARDS diagram**). The sample size for this analysis was chosen based on previous work with the software algorithm.

2.2. MRI imaging acquisition

96 patients had available T2-weighted (T2) sequences, 91 had T1-weighted post Gadolinium (T1 + Gad) imaging and 82 had ADC maps (ADC). Our institution is a quaternary neurosurgical centre, therefore the conventional MRI sequences in this study originated from multiple referrers. The imaging was acquired on 44 different machines (67 at 1.5 T, 30 at 3 T) from all major vendors: 6 GE, 26 Siemens, 11 Phillips and 1 Hitachi scanner. No single MRI machine supplied more than 20% gliomas of one molecular subtype or WHO grade. The median [min, max] values of the parameters of the T2-weighted images were: TE = 99 [17, 140] ms; TR = 4690 [1205, 6300] ms; in plane resolution 0.65 × 0.5 [0.45 × 0.45, 1.13 × 0.95] mm^2, slice thickness = 5 [4,7] mm. For T1 + Gad, the median [min, max] values of the parameters were: TE = 10 [2.28, 26.38] ms; TR = 470 [160, 740] ms; in plane resolution 0.575 × 0.525 [0.45 × 0.375, 1.5 × 1.9] mm^2, slice thickness = 5 [0.9, 7] mm. All DWI acquisitions included three diffusion gradients with weighting values b = 0 s/mm^2 and b = 1000 s/mm^2; the median [min, max] of the other parameters were: TE = 95 [55, 136] ms; TR = 3972 [2873, 8570] ms; in plane resolution 1.25 × 1.2 [1.15 × 1.15, 1.8 × 1.8] mm^2, slice thickness = 5 [4,6] mm.

2.3. Histopathology

Following fixation as paraffin blocks, all tissue samples underwent analysis at our institution's neuropathology department according to World Health Organization (WHO) 2016 guidance on immunohistochemistry testing and previous published methodology [15]. For IDH R132H immune-negative tumors, multiple gene Sanger sequencing was performed to exclude alternative IDH mutations. A quantitative polymerase chain reaction based copy number assay was used to determine 1p/19q status.

2.4. Image segmentation

All image interactions were performed blinded to histological and molecular diagnosis, using proprietary texture analysis research software (TexRAD version 3.3, TexRAD Ltd, www.texrad.com, part of Feedback Plc, Cambridge, UK). Segmentations were performed slice by slice with the software's freehand drawing function. For T2, the entire volume of signal abnormality was segmented (Fig. 2). For T1 + Gad, 3 different types of segmentation were completed: the entire region of T1 signal

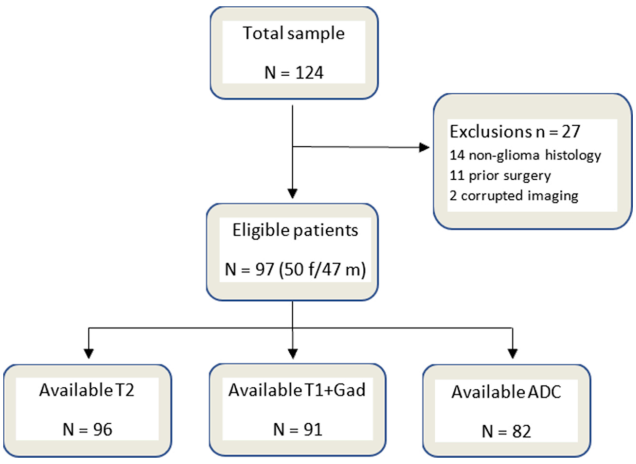

Fig. 1. SHARD flow diagram for patient exclusion and inclusion in the study.

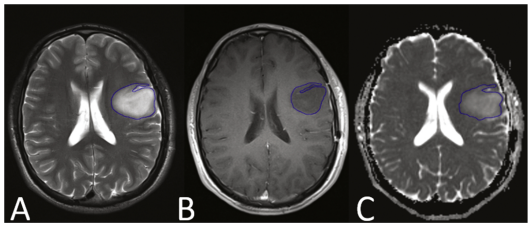

Fig. 2. Freehand segmentation of grade III IDH^{mut} 1p19q^{int} a) entire T2w hyperintense area, b) entire T1 hypointense area, and c) ADC map using T2w as a guide.

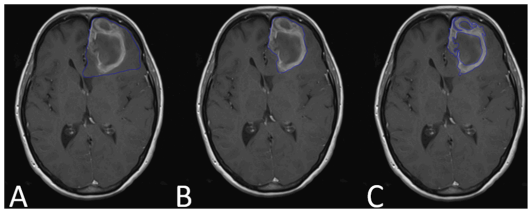

Fig. 3. Example of the 3 different segmentation techniques for T1 + Gad MRTA: a) segmentation of entire mass including enhancing and non-enhancing tissue (**Seg A**), b) segmentation of the enhancing lesion including central necrosis (**Seg B**) and c) segmentation of enhancing tissue only (**Seg C**).

abnormality (enhancing + non-enhancing tissue, **Seg A**), the enhancing lesion inclusive of necrosis (enhancing + necrosis, **Seg B**) and enhancing tissue only (enhancing tissue – necrosis, **Seg C**) (Fig. 3). ADC volumes of interest were defined by manually copying the area of T2 signal abnormality (Fig. 2). Segmentations were undertaken by one researcher (M.L.), trained and supervised by a board-certified radiologist specialized in neuro-oncology (S.T., 7 years experience). Slices containing very few (< 250) pixels of signal abnormality were excluded to avoid partial volume effects (mean slice size 4803 pixels, range 349–15499). In addition, the image with the largest glioma cross-section based on pixel count was subjected to a separate (single slice) evaluation.

2.5. MR texture analysis (MRTA)

MRTA in this study follows a previously published method [13,16]. The filtration used here corresponds to the spatial scale filter (SSF) values of 0, 2 mm, 3 mm, 4 mm, 5 mm and 6 mm in width (radius). SSF = 0 hereby means no filtration, SSF = 2 mm equals a fine texture scale, SSF = 3–5 mm a medium texture scale, and SSF = 6 mm translates to a coarse texture scale (Fig. 4). This was followed by quantification of the image texture via measuring histogram and statistical parameters (mean, standard deviation, entropy, mean of positive pixels, skewness, kurtosis) with slice data mathematically interpolated.

2.6. Statistical analysis

All statistical testing was performed with SPSS 24 (IBM). For each sequence, the ability of the texture features (with and without filtration) to differentiate between the presence and absence of IDH was evaluated using non-parametric Mann Whitney testing. For 1p19q genotyping, Kruskal-Wallis 1 way ANOVA was used. This was repeated over different subgroup analyses e.g. according to WHO grade. For statistically significant results, a receiver operating characteristic (ROC) analysis was undertaken, to determine the area under the curve (AUC), and optimum cut-offs for sensitivity and specificity calculations. A multivariate logistic regression model was generated, to combine the best results from all sequences for IDH genotyping. Pearson coefficient was used to test associations between volumetric and single slice results. Statistics advice was obtained at our institute.

3. Results

3.1. Participants

50 females and 47 males with an average age of 43.3 (27–77) years were included in the study. The histological and molecular characteristics of the patient population are listed in Table 1.

3.2. MRTA using T1 + Gad

3.2.1. T1 + Gad volumes for IDH typing

Table 2 summarizes the most significant T1 + Gad results for molecular subtyping. For IDH typing, filtered texture parameters produced the best results. When examining all Gadolinium enhancing gliomas (WHO II–IV) together, coarse texture mean derived from **Seg A** permitted moderately accurate IDH status prediction (sensitivity 72.2%, specificity 74%, AUC = 0.801), with mean signal intensity values being higher in the IDH^{wt} group.

In glioblastoma, using **Seg A,** mean was the best parameter for IDH genotyping (sensitivity 91.7%, specificity 88.9%, AUC = 0.935). Using **Seg B**, SD represented the most distinctive parameter to predict IDH status (sensitivity 87.5%, specificity 100%, AUC 0.906 – 0.969). With **Seg C**, kurtosis was the best IDH status predictor across all filters (sensitivity 91.9%, specificity 100%, AUC = 0.945) (Fig. 5).

3.2.2. T1 + Gad volumes for 1p19 typing

Combining WHO grades II-III, T1 + Gad using **Seg A** demonstrated moderate results with unfiltered skewness as the best predictor (sensitivity 77.4%, specificity 77.8%, AUC 0.736). For WHO III alone, the algorithm performance for mean was better (AUC 0.871).

3.3. MRTA using ADC maps

3.3.1. ADC volumes for IDH typing

Table 3 summarizes the ROC analysis using ADC volumes for MRTA. Combining WHO II-IV, ADC skewness without filtration performed best for IDH genotyping (sensitivity 77.8%, specificity 68.7%, AUC = 0.791).

Including all gliomas with available ADC maps (n = 82), unfiltered mean ADC performed moderately for a threshold of 1135 mm/s [2]

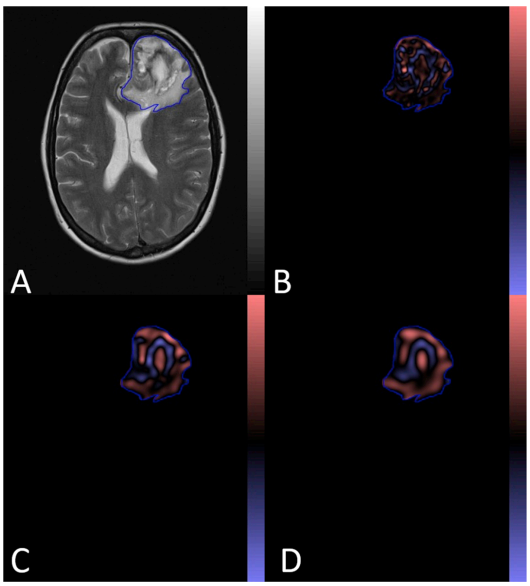

Fig. 4. MRTA filtration step: a) segmentation of entire T2 hyperintense area, b) volume of interest on filter SSF = 2 mm corresponding to fine texture scale, c) volume of interest on filter SSF = 4 mm corresponding to medium texture scale and d) volume of interest on filter SSF = 6 mm corresponding to coarse texture scale. Signal intensities (SI) of bright objects within the filter range are enhanced with concurrent suppression of pixels outside the filter range, highlighting size specific features. With the increase in filter SSF value larger objects are amplified within the segmented volume.

Table 1
WHO grades, IDH and 1p19 genotypes of glioma population.

WHO grade	Number of gliomas	IDH^{wt} (e/e + n)[a]	$IDH^{mut}1p19q^{int}$ (e/e + n)	$IDH^{mut}1p19q^{del}$ (e/e + n)
II	54	4 (0/ 0)	24 (2/1)	26 (2/0)
III	20	3 (1/0)	7 (1/0)	10 (4/1)
IV	23	12 (11/8)	10 (5/1)	1
Total	97	19 (12/8)	41 (8/2)	37 (6/1)

[a] (e/e + n) denotes (enhancing/enhancing + necrotic) gliomas within each molecular subgroup.

(sensitivity 64.1%, specificity 66.7%, AUC 0.694). When excluding cases with macroscopic necrosis (n = 11) from the analysis, the mean ADC area under the curve improved (sensitivity 68.3%, specificity 91.9%, AUC 0.818). By additional exclusion of cases with enhancement lacking necrosis (n = 13), the results improved minimally further. For non-enhancing gliomas, the prediction using ADC mean (sensitivity 70.6%, specificity 100%, AUC 0.840) was near that of kurtosis (sensitivity 85.7%, specificity 78.4%, AUC 0.877). When removing 1p19q codeleted gliomas from the analysis, the accuracy of ADC to distinguish IDH^{wt} and $IDH^{mut}1p19^{int}$ was greater across WHO II-IV with further improved results for ADC mean (AUC 0.888), and kurtosis (AUC 0.949).

The algorithm was less able to distinguish IDH^{wt} and $IDH^{mut}1p19^{del}$ ADC features with only one significant result observed for unfiltered skewness (AUC 0.690). But when applied only to non-enhancing gliomas, mean ADC and kurtosis could separate IDH^{wt} and $IDH^{mut}1p19q^{del}$ better (AUC 0.79, AUC 0.807 respectively).

3.3.2. ADC volumes for 1p19q typing

For the detection of the 1p19q co-deletion in IDH^{mut}, ADC was the most useful sequence. Combining WHO II-III, unfiltered textures predicted 1p19q genotype well (sensitivity 80.6%, specificity of 89.3%, AUC 0.811). The algorithm performance for ADC mean was marginally greater in WHO II alone (sensitivity 90%, specificity 85%, AUC 0.905). In WHO grade III, kurtosis generated the best results (sensitivity 88.9%, specificity 100%, AUC 0.952).

3.4. MRTA using T2

3.4.1. T2 volumes for IDH typing

Table 4 shows the numerical results for the T2 image segmentation. Overall, T2 texture parameters were less distinctive, but the results reached statistical significance. Combining WHO II-IV, the ability to predict IDH status was highest for unfiltered skewness (sensitivity 83.1%, specificity 78.9%, AUC = 0.821). There was no improvement in accuracy when excluding necrotic or non-necrotic enhancing gliomas from the T2 analysis.

3.4.2. T2 volumes for 1p19q typing

T2 appeared more limited for 1p19q typing across WHO grades II-III with medium filtered skewness as the best parameter (sensitivity 75.7%, specificity 62.5%, AUC 0.728). An improved result was observed for WHO III gliomas alone (unfiltered skewness AUC 0.843).

3.5. Sequence combination for IDH typing

A logistic regression model was generated combing the best results from T1 + Gad, T2 and ADC volumes, merging all WHO grades (n = 80, 63 IDH^{mut}/17 IDH^{wt}). Since the filtering precedes MRTA, 6 different logistic regressions were undertaken. Each filter was selected in turn and a regression undertaken using the 18 textures derived from the 3 sequences. This was a fast operation, taking less than 30 seconds after tabulating the texture results. Using a ROC analysis of the predicted probabilities

Table 2
Volumetric analysis using T1 + Gad.

	SSF	Mean	SD	Skewness	Kurtosis	Sens/Spec (%)		SSF	Mean	SD	Skewness	Kurtosis	Sens/Spec (%)
T1 + Gad for IDH genotyping													
WHO II-IV Seg A (IDH^{wt} = 18, IDH^{mut} = 73)	0	NS	**0.695****	NS	NS	66.7/61.3	**WHO IV Seg B** (IDH^{wt} = 8, IDH^{mut} = 4)	0	NS	NS	NS	NS	NS
	2	**0.752***	0.743*	0.633**	NS	72.2/71.2		2	NS	NS	NS	NS	NS
	3	**0.764***	0.718**	0.737*	NS	83.3/68.5		3	NS	**0.938***	NS	NS	75/100
	4	**0.786***	0.706**	0.759*	NS	83.3/69.9		4	NS	**0.969***	NS	NS	87.5/100#
	5	**0.800***	0.697**	0.701*	NS	72.2/69.9		5	NS	**0.906***	NS	NS	87.5/100
	6	**0.801***	0.699**	NS	NS	72.2/74#		6	NS	NS	NS	NS	NS
WHO IV Seg A (IDH^{wt} = 12, IDH^{mut} = 9)	0	NS	**0.769***	NS	NS	66.7/100	**WHO IV Seg C** (IDH^{wt} = 11, IDH^{mut} = 5)	0	NS	NS	NS	**0.836***	91.9/100
	2	0.778*	0.870*	**0.880***	NS	83.3/89.9		2	NS	NS	NS	**0.927***	91.9/100
	3	0.861*	0.870*	**0.917***	NS	83.3/100		3	NS	0.855*	0.836*	**0.891***	91.9/100
	4	**0.935***	0.852*	0.852*	NS	91.7/88.9#		4	NS	0.891*	0.782*	**0.818***	91.9/100
	5	**0.917***	0.824**	0.769**	NS	83.3/100		5	NS	**0.873***	NS	0.855*	91.9/100
	6	**0.907***	0.815**	NS	NS	83.3/77.8		6	NS	NS	NS	**0.945***	91.9/100#
T1 + Gad for 1p19q genotyping of IDH^{mut} glioma													
WHO II-III ($1p19q^{int}$ = 31, $1p19q^{del}$ = 33)	0	NS	NS	**0.736***	NS	77.4/77.8#	**WHO III** ($1p19q^{int}$ = 7, $1p19q^{del}$ = 10)	0	NS	NS	**0.800***	NS	85.7/80
	2	**0.725***	NS	NS	NS	75.8/64.5		2	**0.871***	NS	NS	NS	70/100#
	3	**0.735***	NS	NS	NS	81.8/61.3		3	**0.886***	NS	NS	NS	70/100
	4	**0.735***	NS	NS	NS	78.8/61.3		4	**0.857***	NS	NS	NS	70/100
	5	**0.738***	NS	NS	NS	75.8/61.3		5	**0.871***	NS	NS	NS	70/100
	6	**0.750***	NS	0.659	NS	75.8/61.3		6	**0.871***	NS	0.857*	0.896*	70/100

SSF = spatial scale factor, *p-value < 0.005, **p-value < 0.05, Bold indicates the texture with the highest AUC for which accuracy is displayed, # indicates best accuracy, NS indicates not significant.

(AUC = 0.98 (CI 0.955, 1)), the regression model yielded a high sensitivity of 90.5% and specificity of 94.1% (SSF 4). The model was statistically significant (Hosmer and Lemeshow test = 0.999, omnibus p < 0.001) and demonstrated predictive accuracy (Nagelkerke R Square = 0.826).

3.6. Single slice analysis for IDH typing

For T1 + Gad, mean remained significant in the single slice analysis, with best results achieved for medium to coarse scale filtration, consistent with volumetric results (sensitivity 72.2%, specificity 69.9%, AUC 0.786). ADC results showed a profile comparable to volumetric assessment for unfiltered mean (sensitivity 60.9%, specificity 80.9%, AUC 0.727). The T2 segmentation produced unfiltered skewness as the only significant marker (sensitivity 68.6%, specificity 79.2%, AUC 0.816), also consistent with volumetric analysis. For those textures, which generated significant results in both volumetric and single slice use, the Pearson correlation between the two methods was excellent (r = 0.956) (Fig. 6).

4. Discussion

MRTA has shown ability to identify microstructural disease patterns, including cancer genotypes and chemotherapy response [17,18]. We demonstrated its potential value for the non-invasive assessment of glioma IDH and 1p19q status. To our knowledge, this is the first study to present results for low and high grade glioma molecular subtyping using a filtration histogram approach based on conventional MR sequences. Preoperative genotyping matters for several reasons: in IDH^{mut} astrocytoma even small residual volumes of tumour reduce survival [19], however, molecular results are not usually available during surgery. Glioblastoma therapy is considered appropriate for WHO II-III IDH^{wt} gliomas, consisting of maximum safe resection followed by radiotherapy and chemotherapy. But morphologically 'low grade' IDH^{wt} gliomas are at risk of receiving observation only [20]. All three MRI sequences tested in this study could contribute to non-invasive genotyping, whereby T1 + Gad generated the best results in glioblastoma. Gadolinium enhancement occurs in rapidly proliferating gliomas as a result of pathological neovascularity and blood brain barrier disruption [21]. It has been suggested that the extent and

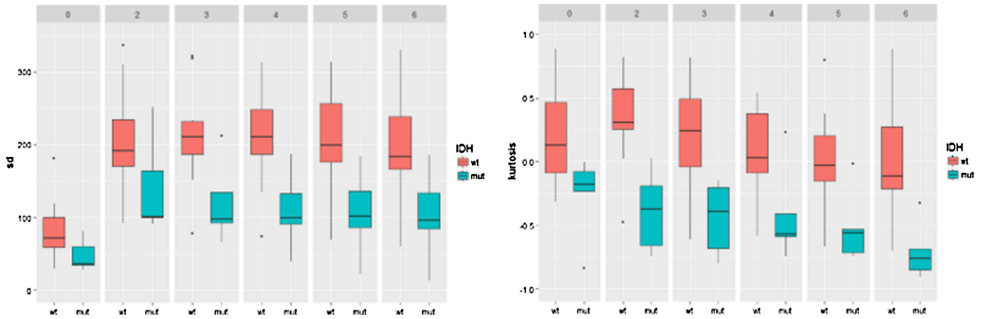

Fig. 5. Boxplots of a) SD and b) Kurtosis showing the separation of T1 + Gad signal intensities between IDH^{wt} and IDH^{mut} gliomas using **Seg C**.

Table 3
Volumetric analysis using ADC values.

ADC for IDH genotyping											
	SSF	Mean	Skewness	Kurtosis	Sens/spec (%)		SSF	Mean	Skewness	Kurtosis	Sens/spec (%)
WHO II-IV (IDH^{wt} = 18, IDH^{mut} = 64)	0	0.694**	**0.791***	0.734**	77.8/68.7#	**WHO II-IV** Non-enhancing (IDH^{wt} = 7, IDH^{mut} = 51)	0	0.733*	**0.843***	0.751*	71.4/88.2
	2	NS	NS	NS	NS		2	**0.824***	NS	0.745*	74.5/85.7
	3	NS	NS	**0.694****	66.7/64.9		3	**0.832***	NS	0.784**	70.6/85.7
	4	NS	NS	**0.693****	66.7/68.7		4	**0.815***	NS	0.787**	68.6/85.7
	5	0.655**	NS	**0.727***	72.2/62.5		5	0.818*	NS	**0.849***	71.4/82.4
	6	0.674**	NS	**0.736***	77.8/67.2		6	0.840*	NS	**0.877***	85.7/78.4#
WHO II-IV Excluding necrotic gliomas (IDH^{wt} = 11, IDH^{mut} = 60)	0	0.753**	**0.811***	0.755**	72.7/88.3#	**WHO II-IV** Non-enhancing (IDH^{wt} = 7, IDH^{mut} $1p19q^{int}$ = 28)	0	0.847*	**0.939***	0.898*	100/85.7
	2	**0.785***	NS	0.736**	73.3/81.8		2	**0.872***	NS	0.796*	85.7/85.7
	3	**0.809***	NS	0.782*	71.7/81.8		3	**0.862***	NS	0.857*	85.7/71.4
	4	**0.791***	NS	0.776*	66.7/81.8		4	**0.852***	NS	0.847*	78.6/71.4
	5	**0.800***	NS	0.800*	66.7/81.8		5	0.857*	NS	**0.949***	100/85.7#
	6	**0.818***	NS	0.802*	68.3/91.9		6	0.888*	NS	**0.934***	100/85.7
ADC for 1p19q genotyping of IDH^{mut} glioma											
	SSF	Mean (WHO II only)		Kurtosis	Sens/spec (%)		SSF	Mean	Skewness	Kurtosis	Sens/spec (%)
WHO II-III ($1p19q^{int}$ = 31, $1p19q^{del}$ = 33)	0	**0.811* (0.905*)**		NS	95/85#	**WHO III** ($1p19q^{int}$ = 7, $1p19q^{del}$ = 9)	0	NS	0.921*	**0.952***	88.9/100#
	2	**0.708* (0.798*)**		NS	75/80		2	NS	**0.873***	NS	100/71.4
	3	**0.722* (0.808*)**		NS	70/75		3	NS	**0.937***	NS	100/71.4
	4	**0.715* (0.793*)**		NS	70/70		4	NS	**0.937***	NS	100/71.4
	5	**0.737* (0.802*)**		NS	75/70		5	NS	**0.905***	NS	100/71.4
	6	**0.736* (0.800*)**		NS	85/65		6	NS	**0.889***	NS	100/71.4

SSF = spatial scale factor, *p-value < 0.005, **p-value < 0.05, Bold indicates the texture with the highest AUC for which accuracy is displayed, # indicates best accuracy, NS indicates not significant.

Table 4
Volumetric analysis using T2 values and single slice results for all sequences.

T2 volumes for IDH genotyping						T2 volumes for 1p19q genotyping of IDH^{mut} glioma					
	SSF	Mean	Skew	Kurtosis	Sens/spec (%)		SSF	Mean	Skew	Kurtosis	Sens/spec (%)
WHO II-IV (IDH^{wt} = 19, IDH^{mut} = 77)	0	NS	**0.821***	0.669**	78.9/83.1#	**WHO II-IV** ($1p19q^{int}$ = 37, $1p19q^{del}$ = 40)	0	NS	**0.722***	NS	73/62.5
	2	**0.696****	NS	NS	NS		2	NS	**0.717***	NS	62.2/70
	3	**0.677****	NS	0.657**	63.6/57.9		3	NS	**0.728***	NS	75.7/62.5#
	4	0.668**	NS	**0.717***	61.0/73.7		4	NS	**0.703****	NS	73/60
	5	0.658**	NS	**0.706***	63.6/73.7		5	NS	**0.678****	NS	64.9/62.5
	6	0.653**	NS	**0.661****	57.1/68.4		6	NS	**0.631****	NS	59.5/55
Single slice T1 + Gad for IDH genotyping						**Single slice ADC for IDH genotyping**					
	SSF	Mean	SD	Entropy	Sens/spec (%)		SSF	Mean	Skew	Kurtosis	Sens/spec (%)
WHO II-IV (IDH^{wt} = 18, IDH^{mut} = 73)	0	0.657**	0.690**	**0.694****	77.8/61.6	**WHO II-IV** (IDH^{wt} = 18, IDH^{mut} = 64)	0	**0.727***	0.722*	0.724*	67.2/66.7
	2	**0.738***	0.711*	0.693**	66.7/76.7		2	NS	**0.753***	NS	77.8/64.1#
	3	**0.747***	0.704**	0.685**	72.2/71.2		3	NS	0.654**	**0.674****	66.7/60.9
	4	**0.778***	0.695**	0.670**	88.9/64.4		4	NS	NS	**0.681****	66.7/57.8
	5	**0.786***	0.684**	NS	72.2/69.9#		5	NS	NS	**0.663****	66.7/64.1
	6	**0.771***	0.667**	NS	77.8/63		6	**0.66****	NS	NS	61.1/56.3
Single slice T2 for IDH genotyping						**Sequence combination for IDH genotyping**					
	SSF	Mean	SD	Skew	Sens/spec (%)		SSF	AUC	Min (95% CI)	Max (95% CI)	Sens/Spec (%)
WHO II-IV (IDH^{wt} = 19, IDH^{mut} = 77)	0	NS	NS	**0.816***	84.2/66.2#	**WHO II-IV** (n = 80)	0	0.937*	0.877	0.998	88/88
	2	NS	NS	NS	NS		2	0.937*	0.887	0.987	86/94
	3	NS	NS	NS	NS		3	0.942*	0.894	0.990	87/94
	4	NS	NS	NS	NS		4	**0.980***	**0.955**	**1.000**	**90/94#**
	5	NS	NS	NS	NS		5	0.895*	0.857	1.000	90/88
	6	NS	NS	NS	NS		6	0.937*	0.869	1.000	100/83

SSF = spatial scale factor, *p-value < 0.005, **p-value < 0.05, Bold indicates the texture with the highest AUC for which accuracy is displayed, # indicates best accuracy, NS indicates not significant.

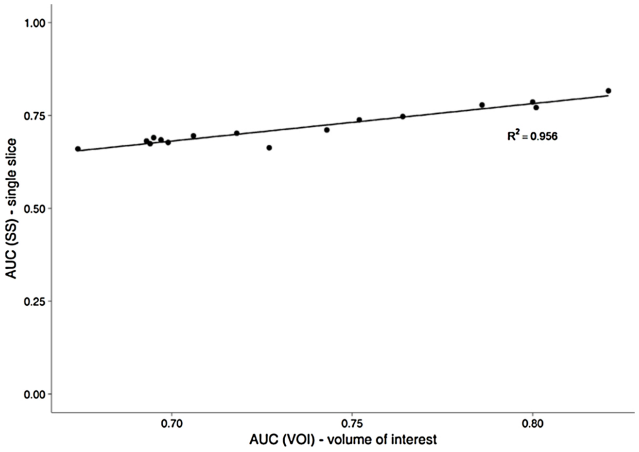

Fig. 6. Scatter plot with Pearson correlation of AUC (VOI – volume of interest) and AUC (SS – single slice) for all T1, T2 and ADC texture parameters, which were significant on both volume and single slice analysis.

morphology of new vessel formation differs by mutational status, with greater vascularity in IDH^{wt} compared to IDH^{mut} [22]. These processes are known to develop gradually and could explain why enhancement patterns become more precisely recognized by MRTA towards WHO IV. The comparison of three different T1 + Gad segmentation methods highlights that the performance of texture parameters is technique-dependent. Using **Seg A**, mean values were most diagnostic of IDH status, which may relate to overall tumor contrast uptake intensity. In support of this, a recent study by Yamauchi et al. observed dense contrast-enhancement preferentially in IDH^{wt} gliomas [23]. With **Seg B**, SD performed best, probably reflecting greater variability of signal intensity values according to the extent of necrosis. Using the same segmentation technique (**Seg B**) and parameter (SD), Skogen et al. were able to non-invasively predict glioma WHO grade with MRTA [13]. When applying **Seg C**, kurtosis was most significant suggesting additional differences in microstructural enhancement heterogeneity, which appeared greater for IDH^{wt} gliomas. Our results are consistent with a recent machine learning study, in which T1 + Gad supported IDH status prediction especially for WHO IV [24]. Diffusion-weighted imaging has been widely recognized as a biomarker of cellularity in neoplasia [25]. Reduced ADC values are a feature of malignant gliomas [26,27], however, the occurrence of increased diffusivity in necrosis may confound quantitative assessment. In a previous diffusion tensor study by Tan et al., the accuracy of ADC for IDH typing diminished towards WHO IV [28]. Our analysis confirms that macroscopic 'high grade' features impact on diffusion quantification: Mean ADC values showed limited sensitivity and specificity when examining WHO II-IV together, with skewness and kurtosis as markers of heterogeneity [29] achieving better results in this context. On the contrary, kurtosis and mean ADC were both valuable for IDH typing of gliomas with 'low grade' appearances. This is consistent with recent studies, which highlighted that low mean ADC values are predictive IDH^{wt} status in lower grade gliomas [10,27,30]. Amongst IDH mutant gliomas, mean ADC values were best at predicting 1p19q genotype in this study, especially for WHO II. $IDH^{mut}1p19^{del}$ glioma ADC values tend to be intermediate, which may impede its distinction from IDH^{wt}, despite marked differences in survival. The T2 texture signatures identified as predictive of IDH status were similar to those identified for ADC. This result is in keeping with previous research showing associations between ADC, T2 signal and tissue cellularity in glioma, medulloblastoma and lymphoma [31]. However, our T2 derived results are less accurate than reported for WHO II gliomas alone [32]. The single slice analysis showed a strong correlation with the volumetric findings, although it was less distinctive. Using this strategy, MRTA appears sufficiently rapid to be integrated into clinical reporting. Further prospective evaluation is required to determine the respective benefits of whole tumor versus largest cross-section texture analysis in terms of precision versus time expense. The combination of T1 + Gad, ADC and T2 sequences appears excellent in the absence of advanced MRI techniques, which might otherwise be employed to assist presurgical glioma subtyping. The diagnostic results presented here are at least equivalent to the best performing D2-Hydroxyglutarate (2HG) MR spectroscopy [33], perfusion [22] and artificial intelligence approaches published to date, with potential advantages for clinical translation. In summary, MRTA is an easily applicable image workstation tool with potential to perform IDH and 1p19q genotyping of untreated gliomas based on conventional MRI sequences.

5. Limitations

Our patient cohort included a limited number of IDH^{wt} tumours, particularly in WHO grade II and III. It is unknown whether with a larger sample the MRTA software could achieve IDH genotyping by solely using T1w post Gadolinium sequences as suggested by one previous study [34]. Further software development is required to optimize transposing regions of interest from one sequence to another, which would increase time efficiency. The origin of MRI sequences from multiple institutions could have influenced measurements, but as no scanner contributed any particular WHO grade or molecular subtype, a systematic error is unlikely. As discussed in prior research, for ADC mapping the dependence from T_1, T_2 and TR settings is mathematically eliminated [30,35].

6. Conclusion

MRTA is a software platform without machine learning, which can assist the distinction of glioma IDH and 1p19q molecular subtypes. Results may be optimized through tailoring the choice of MRI sequence (s) to tumor morphology. It also appears possible to predict genetic status using a sequence combination without considering specific lesion features.

Ethics approval

Ethics review board approval was obtained with informed consent waived for this retrospective study of anonymized imaging data. The study performed in accordance with the Declaration of Helsinki.

Consent for publication

No personal data presented

Availability of data and materials

The datasets used and/or analyzed during the current study are available from the corresponding author on reasonable request

Conflict of interest

ML, AB, SB, ZJ, SB, RE, AG, SC none relevant. BG is a director, part-time employee of TexRAD Ltd (www.texrad.com part of Feedback Plc, Cambridge, England, UK), and shareholder of Feedback Plc (Cambridge, England, UK), company that develops and markets the TexRAD texture analysis algorithm described in this manuscript.

Funding

No specific funding was obtained for this study

Authorship

ML and ST designed and carried out the study, as well as write the manuscript. The statistical analysis was carried out by ML in liaison with the local (University College London) statistics institute. BG supplied the software access and initial training in the use of segmentation tools for this study. RE assisted with anonymization of the images. AB, SB, ZJ, SB, AG reviewed the final manuscript.

Acknowledgements

This study was undertaken at University College London Hospitals/University College London, which receives a proportion of funding from the UK National Institute of Health Research Biomedical Research Centre.

References

[1] D.N. Louis, H. Ohgaki, O.D. Wiestler, W.K. Cavenee, P.C. Burger, A. Jouvet, et al., The 2007 WHO classification of tumours of the central nervous system, Acta Neuropathol. 114 (2) (2007) 97–109.
[2] J.E. Eckel-Passow, D.H. Lachance, A.M. Molinaro, K.M. Walsh, P.A. Decker, H. Sicotte, et al., Glioma groups based on 1p/19q, IDH, and TERT promoter mutations in tumors, N. Engl. J. Med. 372 (26) (2015) 2499–2508.
[3] D.J. Brat, R.G. Verhaak, K.D. Aldape, W.K. Yung, S.R. Salama, L.A. Cooper, et al., Comprehensive, integrative genomic analysis of diffuse lower-grade gliomas, N. Engl. J. Med. 372 (26) (2015) 2481–2498.
[4] H. Suzuki, K. Aoki, K. Chiba, Y. Sato, Y. Shiozawa, Y. Shiraishi, et al., Mutational landscape and clonal architecture in grade II and III gliomas, Nat. Genet. 47 (5) (2015) 458–468.
[5] M. Weller, S.M. Pfister, W. Wick, M.E. Hegi, G. Reifenberger, R. Stupp, Molecular neuro-oncology in clinical practice: a new horizon, Lancet Oncol. 14 (9) (2013) e370–9.
[6] C. Hartmann, J. Meyer, J. Balss, D. Capper, W. Mueller, A. Christians, et al., Type and frequency of IDH1 and IDH2 mutations are related to astrocytic and oligodendroglial differentiation and age: a study of 1,010 diffuse gliomas, Acta Neuropathol. 118 (4) (2009) 469–474.
[7] J. Beiko, D. Suki, K.R. Hess, B.D. Fox, V. Cheung, M. Cabral, et al., IDH1 mutant malignant astrocytomas are more amenable to surgical resection and have a survival benefit associated with maximal surgical resection, Neurooncology 16 (1) (2014) 81–91.
[8] C. Houillier, X. Wang, G. Kaloshi, K. Mokhtari, R. Guillevin, J. Laffaire, et al., IDH1 or IDH2 mutations predict longer survival and response to temozolomide in low-grade gliomas, Neurology 75 (17) (2010) 1560–1566.
[9] J.E. Villanueva-Meyer, M.D. Wood, B.S. Choi, M.C. Mabray, N.A. Butowski, T. Tihan, et al., MRI features and IDH mutational status of grade II diffuse gliomas: impact on diagnosis and prognosis, AJR Am. J. Roentgenol. 210 (3) (2018) 621–628.
[10] S.H. Patel, L.M. Poisson, D.J. Brat, Y. Zhou, L. Cooper, M. Snuderl, et al., T2-FLAIR mismatch, an imaging biomarker for IDH and 1p/19q status in lower-grade gliomas: a TCGA/TCIA project, Clin. Cancer Res. 23 (20) (2017) 6078–6085.
[11] A. Kassner, R.E. Thornhill, Texture analysis: a review of neurologic MR imaging applications, AJNR Am. J. Neuroradiol. 31 (5) (2010) 809–816.
[12] K. Skogen, B. Ganeshan, C. Good, G. Critchley, K. Miles, Measurements of heterogeneity in gliomas on computed tomography relationship to tumour grade, J. Neurooncol. 111 (2) (2013) 213–219.
[13] K. Skogen, A. Schulz, J.B. Dormagen, B. Ganeshan, E. Helseth, A. Server, Diagnostic performance of texture analysis on MRI in grading cerebral gliomas, Eur. J. Radiol. 85 (4) (2016) 824–829.
[14] K. Skogen, A. Schulz, E. Helseth, B. Ganeshan, J.B. Dormagen, A. Server, Texture analysis on diffusion tensor imaging: discriminating glioblastoma from single brain metastasis, Acta Radiol. (2018) Jan 1, 284185118780889.
[15] D.E. Reuss, F. Sahm, D. Schrimpf, B. Wiestler, D. Capper, C. Koelsche, et al., ATRX and IDH1-R132H immunohistochemistry with subsequent copy number analysis and IDH sequencing as a basis for an "integrated" diagnostic approach for adult astrocytoma, oligodendroglioma and glioblastoma, Acta Neuropathol. 129 (1) (2015) 133–146.
[16] K.A. Miles, B. Ganeshan, M.P. Hayball, CT texture analysis using the filtration-histogram method: what do the measurements mean? Cancer Imaging 13 (3) (2013) 400–406.
[17] G.J. Weiss, B. Ganeshan, K.A. Miles, D.H. Campbell, P.Y. Cheung, S. Frank, et al., Noninvasive image texture analysis differentiates K-ras mutation from pan-wildtype NSCLC and is prognostic, PLoS One 9 (7) (2014) e100244.
[18] C.N. De Cecco, B. Ganeshan, M. Ciolina, M. Rengo, F.G. Meinel, D. Musio, et al., Texture analysis as imaging biomarker of tumoral response to neoadjuvant chemoradiotherapy in rectal cancer patients studied with 3-T magnetic resonance, Invest. Radiol. 50 (4) (2015) 239–245.
[19] M.M.J. Wijnenga, P.J. French, H.J. Dubbink, W.N.M. Dinjens, P.N. Atmodimedjo, J.M. Kros, et al., The impact of surgery in molecularly defined low-grade glioma: an integrated clinical, radiological, and molecular analysis, Neurooncology 20 (1) (2018) 103–112.
[20] O.H. Khan, W. Mason, P.N. Kongkham, M. Bernstein, G. Zadeh, Neurosurgical management of adult diffuse low grade gliomas in Canada: a multi-center survey, J. Neurooncol. 126 (1) (2016) 137–149.
[21] K.H. Plate, H.D. Mennel, Vascular morphology and angiogenesis in glial tumors, Exp. Toxicol. Pathol. 47 (2–3) (1995) 89–94.
[22] P. Kickingereder, F. Sahm, A. Radbruch, W. Wick, S. Heiland, A. Deimling, et al., IDH mutation status is associated with a distinct hypoxia/angiogenesis transcriptome signature which is non-invasively predictable with rCBV imaging in human glioma, Sci. Rep. 5 (2015) 16238.
[23] T. Yamauchi, M. Ohno, Y. Matsushita, M. Takahashi, Y. Miyakita, Y. Kitagawa, et al., Radiological characteristics based on isocitrate dehydrogenase mutations and 1p/19q codeletion in grade II and III gliomas, Brain Tumor Pathol. (2018) Jun 19, https://doi.org/10.1007/s10014-018-0321-4.
[24] B. Zhang, K. Chang, S. Ramkissoon, S. Tanguturi, W.L. Bi, D.A. Reardon, et al., Multimodal MRI features predict isocitrate dehydrogenase genotype in high-grade gliomas, Neurooncology 19 (1) (2017) 109–117.
[25] A.R. Padhani, G. Liu, D.M. Koh, T.L. Chenevert, H.C. Thoeny, T. Takahara, et al., Diffusion-weighted magnetic resonance imaging as a cancer biomarker: consensus and recommendations, Neoplasia 11 (2) (2009) 102–125.
[26] K. Kono, Y. Inoue, K. Nakayama, M. Shakudo, M. Morino, K. Ohata, et al., The role of diffusion-weighted imaging in patients with brain tumors, AJNR Am. J. Neuroradiol. 22 (6) (2001) 1081–1088.
[27] K. Leu, G.A. Ott, A. Lai, P.L. Nghiemphu, W.B. Pope, W.H. Yong, et al., Perfusion and diffusion MRI signatures in histologic and genetic subtypes of WHO grade II-III diffuse gliomas, J. Neurooncol. 134 (1) (2017) 177–188.
[28] W.L. Tan, W.Y. Huang, B. Yin, J. Xiong, J.S. Wu, D.Y. Geng, Can diffusion tensor imaging noninvasively detect IDH1 gene mutations in astrogliomas? A retrospective study of 112 cases, AJNR Am. J. Neuroradiol. 35 (5) (2014) 920–927.
[29] J.M. Hempel, J. Schittenhelm, C. Brendle, B. Bender, G. Bier, M. Skardelly, et al., Histogram analysis of diffusion kurtosis imaging estimates for in vivo assessment of 2016 WHO glioma grades: a cross-sectional observational study, Eur. J. Radiol. 95 (2017) 202–211.
[30] S.C. Thust, S. Hassanein, S. Bisdas, J.H. Rees, H. Hyare, J.A. Maynard, et al., Apparent diffusion coefficient for molecular subtyping of non-gadolinium-enhancing WHO grade II/III glioma: volumetric segmentation versus two-dimensional region of interest analysis, Eur. Radiol. 28 (9) (2018) 3779–3788, https://doi.org/10.1007/s00330-018-5351-0 Epub 2018 Mar 23.
[31] A.C. Guo, T.J. Cummings, R.C. Dash, J.M. Provenzale, Lymphomas and high-grade astrocytomas: comparison of water diffusibility and histologic characteristics, Radiology 224 (1) (2002) 177–183.
[32] X. Zhang, Q. Tian, L. Wang, Y. Liu, B. Li, Z. Liang, et al., Radiomics strategy for molecular subtype stratification of lower-grade glioma: detecting IDH and TP53 mutations based on multimodal MRI, J. Magn. Reson. Imaging 48 (4) (2018) 916–926, https://doi.org/10.1002/jmri.25960 Epub 2018 Feb 2.
[33] C. Choi, S.K. Ganji, R.J. DeBerardinis, K.J. Hatanpaa, D. Rakheja, Z. Kovacs, et al., 2-hydroxyglutarate detection by magnetic resonance spectroscopy in IDH-mutated patients with gliomas, Nat. Med. 18 (4) (2012) 624–629.
[34] J. Yu, Z. Shi, Y. Lian, Z. Li, T. Liu, Y. Gao, et al., Noninvasive IDH1 mutation estimation based on a quantitative radiomics approach for grade II glioma, Eur. Radiol. 27 (8) (2017) 3509–3522.
[35] J. Pipe, Chapter 2 - pulse sequences for diffusion-weighted MRI, in: H. Johansen-Berg, Timothy E.J. Behrens (Eds.), Diffusion MRI, Academic Press, San Diego, 2009, pp. 11–35.